# THE INFLUENCE OF METEOROLOGY, URBAN TOPOGRAPHY AND TRAFFIC ON THE VARIABILITY IN CONCENTRATIONS OF A TRAFFIC-RELATED POLLUTANT IN URBAN STREET CANYONS

**John William Douglas Boddy**

Submitted in accordance with the requirements for the degree of PhD

University of Leeds
School of Process, Environmental and Materials Engineering

September 2005

*The candidate confirms that the work submitted is his own and that appropriate credit has been given where reference has been made to the work of others. This copy has been supplied on the understanding that it is copyright material and that no quotation from the thesis may be published without proper acknowledgement.*

He brushed away the thunder, then the clouds,
The colossal illusion of heaven. Yet still
The sky was blue. He wanted imperceptible air.
He wanted to see. He wanted the eye to see
And not be touched by blue ...

Wallace Stevens, *Landscape with Boat*:
in William Boyd's *The Blue Afternoon*, Penguin Books, 1993.

# Acknowledgements

I would like to thank my supervisor, Dr Alison Tomlin, Energy and Resources Research Institute (ERRI) at the University of Leeds, for her support and guidance during the research and for proof-reading the thesis. I also wish to thank Dr Robert Smalley (ERRI) for his advice, enthusiasm and good-humour, particularly during the field experiments, but also throughout the analysis and writing. I am also grateful for the financial support provided for the research by the Natural Environment Research Council (NERC). I also acknowledge the Engineering and Physical Sciences Research Council (EPSRC) for equipment support via the JIF grant. I also wish to thank Dr James Tate, Institute for Transport Studies (ITS), University of Leeds, for providing emissions data, advice and banter. Thanks also to Prof. Margaret Bell and Dr Paul Goodman (ITS) for their help regarding SCOOT and the use of the Instrumented City facility based at ITS. I am indebted to the City of York Council (CYC) who actively supported the research and provided the SCOOT data and additional background meteorological data. Thanks also to Mr Simon Parrett, Urban Traffic Management and Control (UTMC), for providing the closed-circuit television (CCTV) traffic queue length data.

I greatly appreciate the technical advice, time and effort that Mr Martin Hill, School of Earth and Environment at the University of Leeds, gave to the project, particularly during the development of the data acquisition systems. Thanks also to Dr Barbara Brooks, School of Earth and Environment, for writing the code for the sonic anemometers. I would like to thank Prof. Stephen Mobbs, School of Earth and Environment, for the use of the sonic anemometer data loggers. I also wish to thank Dr Nick Dixon (ERRI) for his helpful suggestions, particularly regarding the use of MISKAM, and for his greatly amusing office stoicism. I also am grateful to the support given to me by Mr David Young (ERRI) during the field experiments and throughout the thesis writing. Thanks also to Mr Matthew Buckley, Mr Rod Holt, Mr Ed Woodhouse, Mr Dave McKenzie, and Mr Dave Squires for technical work. Finally, I would like to thank my family, my girlfriend Emma and my friends for their support, encouragement and faith – I would not have got very far without you.

# Abstract

A comprehensive study into the spatial and temporal variations in concentrations of a traffic-related pollutant was undertaken in two urban street canyons located in York, U.K. During the field experiment, investigations were carried out in order to determine the influence of meteorology, urban topography and traffic on the measured concentrations of a traffic-related pollutant. The pollutant measured in this study was carbon monoxide (CO).

Results are presented from simultaneous and continuous measurements of the background (or reference) wind speed and direction, the in-canyon wind and turbulence fields, traffic characteristics and CO concentrations collected over a period of one month. The background wind was found to influence the development of in-canyon wind flow features, which became mechanisms for pollutant dispersion. Under certain background winds, evidence of across-canyon recirculating flows with horizontally- and vertically-aligned axes is presented. During these conditions, turbulence and traffic-related pollutants are likely to have been transported in the across-canyon recirculating flows. During background wind orientated perpendicular to the street axis, the 15-minute mean concentrations of CO were a factor of 2 or 3 higher on the leeward (or upwind) side of the street canyons compared to the windward side. This was caused by the development of an across-canyon recirculating flow with a horizontally-aligned axis. Downdraughts were measured on the windward side of the canyon during these conditions, while updraughts were measured on the leeward side. The wind direction at street level opposed the direction of the above-roof flow, causing the transport of CO towards the leeward side of the street canyon where concentrations increased.

Evidence of counter-rotating corner vortices with vertically-aligned axes are also presented and are thought to have been caused by along-canyon converging flows during certain background winds. However, across-canyon flow during these conditions also accounted for the higher concentrations of CO measured on the leeward side of the canyon, compared to the windward side. Background winds orientated oblique to the street axis were found to produce across-canyon

rearticulating flows. On the other hand, parallel background winds produced channel flows, which had a 'flushing' effect, causing some of the lowest concentrations of CO to be measured during these conditions.

Traffic-produced turbulence was investigated in the street canyon during the field experiment. Comparisons were made between calculated and measured turbulence parameters. The results indicate that the parameterisation performs reasonably well, particularly during weak perpendicular background winds when traffic-produced turbulence effects are likely to have been most dominant.

The traffic was also investigated due to the implications of traffic characteristics on the variability in concentrations of CO. The influence of free-, unstable- and congested-traffic flows on measured CO concentrations was determined. The highest mean concentrations were measured during congested traffic conditions, when the emission levels are likely to have been elevated due to stop-start driving events. The combined influence of the background wind and traffic characteristics was investigated. Results are presented which show that the highest mean CO concentrations were measured during perpendicular background winds and during congested traffic conditions. The implications of using variable emission rates in a computational fluid dynamics (CFD) dispersion model were investigated in a sensitivity study. Results are also presented from the flow model study, which was conducted to help in the interpretation of the field experiment data.

# Table of Contents

ACKNOWLEDGEMENTS ..... III
ABSTRACT ..... IV
TABLE OF CONTENTS ..... VI
TABLE OF FIGURES ..... X
LIST OF TABLES ..... XVI
NOTATION ..... XVII
**CHAPTER 1** MOTIVATION FOR RESEARCH ..... 1
1.1. INTRODUCTION ..... 1
1.2. AIMS AND OBJECTIVES ..... 3
**CHAPTER 2** CONCENTRATIONS OF TRAFFIC-RELATED POLLUTANTS AND THE INFLUENCE OF METEOROLOGY, URBAN TOPOGRAPHY AND TRAFFIC – THE CONTEXT 4
2.1. INTRODUCTION ..... 4
2.1.1. Chapter synopsis ..... 4
2.2. TRAFFIC-RELATED POLLUTANTS ..... 5
2.3. AIR QUALITY MANAGEMENT AREAS ..... 8
2.4. AIR QUALITY MONITORING ..... 10
2.5. AIR QUALITY MODELLING ..... 13
2.5.1. Wind flow modelling ..... 14
2.5.2. Dispersion modelling ..... 15
2.6. STREET CANYON STUDIES ..... 18
2.6.1. Street canyon geometry ..... 18
2.6.2. The influence of meteorology ..... 19
2.6.2.1. Background winds and in-canyon flow features ..... 19
2.6.2.2. Dispersion of traffic-related pollutants ..... 30
2.6.2.3. Population exposure ..... 38
2.6.3. The influence of traffic ..... 39
2.6.3.1. Traffic-produced turbulence ..... 39
2.6.3.2. Traffic flow ..... 43
2.6.3.3. Traffic characteristics and driving mode ..... 45
2.7. SUMMARY AND CONCLUSIONS ..... 47
**CHAPTER 3** INSTRUMENTATION AND TECHNIQUES FOR MEASUREMENT AND ANALYSIS ..... 50
3.1. INTRODUCTION ..... 50
3.1.1. Chapter synopsis ..... 50
3.2. EXPERIMENT OVERVIEW ..... 51
3.3. SITE SELECTION ..... 53
3.4. STREET CANYON GEOMETRIES ..... 57
3.5. INSTRUMENTATION AND MEASUREMENT TECHNIQUES ..... 60
3.5.1. Meteorology ..... 61
3.5.1.1. Wind flow and turbulence ..... 61
3.5.1.1.1. Operating principle of an ultrasonic anemometer ..... 63
3.5.1.1.2. Calculating mean flow and turbulence ..... 65
3.5.1.1.3. Trial runs ..... 72
3.5.1.1.4. Data acquisition systems ..... 74
3.5.1.2. Background wind speed and direction ..... 80
3.5.1.3. Temperature and humidity ..... 82
3.5.2. Concentrations of a traffic-related pollutant ..... 83
3.5.2.1. Operating principle of the streetbox ..... 84
3.5.2.2. Establishing a connection with the streetbox ..... 87
3.5.2.3. Data quality assurance and control procedures for the streetbox ..... 88
3.5.3. Traffic ..... 89
3.5.3.1. Traffic characteristics ..... 89
3.5.3.2. Traffic-produced turbulence ..... 91

3.5.4. Street canyon flow and dispersion modelling ..... 93
3.5.4.1. Description of the MISKAM code ..... 94
3.5.4.2. The model domain ..... 97
3.5.4.3. Running MISKAM ..... 99
3.6. SUMMARY AND CONCLUSIONS ..... 101

CHAPTER 4 MEAN WIND FLOW AND TURBULENCE INSIDE THE GILLYGATE STREET CANYON ..... 102

4.1. INTRODUCTION ..... 102
4.1.1. Perpendicular winds and the classic skimming flow regime ..... 104
4.1.2. Perpendicular winds and the influence of pitched roofs ..... 106
4.1.3. Oblique and parallel background winds ..... 108
4.1.4. Chapter synopsis ..... 108
4.2. EXPERIMENTAL METHOD ..... 109
4.2.1. The site ..... 109
4.2.2. Instrumentation and Experiments ..... 110
4.2.2.1. Background wind speed and direction ..... 110
4.2.2.2. In-canyon wind and turbulence fields ..... 111
4.3. RESULTS ..... 114
4.3.1. Standard deviation of the mean vertical wind velocity ..... 114
4.3.2. Mean in-canyon wind flow for $U_{ref}$ >1.2 m $s^{-1}$ ..... 116
4.3.3. Mean in-canyon turbulence for $U_{ref}$ >1.2 m $s^{-1}$ ..... 123
4.3.3.1. Standard deviation of the mean vertical wind velocity and TKE ..... 123
4.3.3.2. Contribution of each turbulence component to TKE ..... 137
4.4. DISCUSSION ..... 141
4.4.1. Standard deviation of the mean vertical wind velocity ..... 142
4.4.2. Mean in-canyon wind flow for $U_{ref}$ >1.2 m $s^{-1}$ ..... 144
4.4.2.1. Perpendicular SE background winds ..... 145
4.4.2.2. Perpendicular NW background winds ..... 149
4.4.2.3. Oblique background winds ..... 151
4.4.2.4. Parallel background winds ..... 153
4.4.3. In-canyon turbulence for $U_{ref}$ >1.2 m $s^{-1}$ ..... 154
4.4.3.1 Standard deviation of the mean vertical velocity and TKE ..... 156
4.4.3.1.1. Perpendicular SE background winds ..... 156
4.4.3.1.2. Perpendicular NW background winds ..... 162
4.4.3.1.3. Oblique background winds ..... 167
4.4.3.1.4. Parallel background winds ..... 169
4.4.3.2. Contribution of each turbulence component to TKE ..... 170
4.5. SUMMARY AND CONCLUSIONS ..... 173

CHAPTER 5 THE INFLUENCE OF BACKGROUND WINDS ON THE SPATIAL VARIABILITY IN CONCENTRATIONS OF A TRAFFIC-RELATED POLLUTANT ..... 177

5.1. INTRODUCTION ..... 177
5.1.1. Chapter synopsis ..... 180
5.2. EXPERIMENTAL METHOD ..... 181
5.2.1. The site ..... 181
5.2.2. Instrumentation and Experiments ..... 182
5.2.2.1. The background wind speed and direction ..... 182
5.2.2.2. Carbon monoxide concentrations ..... 183
5.2.2.3. The traffic flow characteristics ..... 185
5.3. RESULTS AND DISCUSSION ..... 187
5.3.1. Background winds ..... 187
5.3.2. Spatial variability in CO concentrations in the Gillygate street canyon ..... 188
5.3.2.1. The influence of perpendicular background winds ..... 190
5.3.2.2. The influence of parallel and oblique background winds ..... 191
5.4. SUMMARY AND CONCLUSIONS ..... 201

**CHAPTER 6** THE INFLUENCE OF TRAFFIC-PRODUCED TURBULENCE AS A POTENTIAL POLLUTANT DISPERSION MECHANISM ..... 205

6.1. INTRODUCTION ..... 205
6.1.1. Previous studies ..... 206
6.1.2. Chapter synopsis ..... 208
6.2. THEORETICAL BACKGROUND ..... 209
6.2.1. Low traffic density: no interaction between vehicle wakes ..... 212
6.2.2. Intermediate traffic density: moderate interaction between vehicle wakes ..... 215
6.2.3. High traffic density: strong interaction between vehicle wakes ..... 216
6.2.4. Confusion concerning the calculated spatially averaged turbulence, $\sigma_{ct}^2$ ..... 217
6.3. METHODOLOGY ..... 219
6.3.1. Instrumentation and Experiments ..... 219
6.3.1.1. Background wind speed and direction ..... 219
6.3.1.2. In-canyon wind flow and turbulence ..... 220
6.3.1.3. Traffic flow and speed ..... 220
6.3.1.4. Traffic characteristics ..... 221
6.3.2. TPT parameterisation ..... 226
6.4. RESULTS AND DISCUSSION ..... 229
6.4.1. Comparisons between measured $\sigma_w$ and traffic characteristics ..... 229
6.4.2. Model validation using $\sigma_w$ ..... 234
6.4.2.1. The influence of perpendicular background winds ..... 234
6.4.2.2. The influence of parallel background winds ..... 242
6.4.3. Model validation using TKE ..... 246
6.5. SUMMARY AND CONCLUSIONS ..... 247

**CHAPTER 7** THE INFLUENCE OF TRAFFIC CHARACTERISTICS ON THE SPATIAL VARIABILITY IN CONCENTRATIONS OF A TRAFFIC-RELATED POLLUTANT ..... 249

7.1. INTRODUCTION ..... 249
7.1.1. Chapter synopsis ..... 251
7.2. EXPERIMENTAL METHOD ..... 251
7.2.1. The site ..... 251
7.2.2. Instrumentation and Experiments ..... 252
7.2.2.1. The background wind speed and direction ..... 252
7.2.2.2. Carbon monoxide concentrations ..... 252
7.2.2.3. The traffic flow characteristics ..... 253
7.3. RESULTS AND DISCUSSION ..... 254
7.3.1. Verification of the SCOOT system ..... 254
7.3.2. Traffic flow and detector occupancy ..... 258
7.3.3. Detector occupancy and queue length for Gillygate inbound ..... 261
7.3.4. Spatial and temporal variability in CO concentrations ..... 263
7.3.5. Significance of the study for emissions modelling ..... 266
7.3.6. Combined influence of traffic conditions and background wind flow ..... 274
7.4. SUMMARY AND CONCLUSIONS ..... 277

**CHAPTER 8** SENSITIVITY STUDY INTO THE INFLUENCE OF THE BACKGROUND WIND AND VARIABLE EMISSIONS ALONG GILLYGATE – FINAL DISCUSSIONS ..... 280

8.1. INTRODUCTION ..... 280
8.1.1. Chapter synopsis ..... 281
8.2. METHODOLOGY ..... 281
8.3. RESULTS AND DISCUSSION ..... 286
8.3.1. Longitudinal cross-section ..... 286
8.3.1.1. Parallel background winds ..... 287
8.3.1.2. Oblique background winds ..... 289
8.3.1.3. Perpendicular background winds ..... 292
8.3.2. Transverse cross-section ..... 295
8.4. SUMMARY AND CONCLUSIONS ..... 297

CHAPTER 9 LIMITATIONS OF THE PRESENT STUDY AND RECOMMENDATIONS FOR FURTHER WORK ..... 299

9.1. INTRODUCTION ..... 299
9.1.1. Street canyon field experiments ..... 299
9.1.1.1. Weak background winds ..... 299
9.1.1.2. Moderate and strong background winds ..... 302
9.1.2. Street canyon modelling studies ..... 304
9.1.3. Measurements of other traffic-related pollutant concentrations ..... 305
9.1.4. Population exposure studies ..... 306
9.2. SUMMARY AND CONCLUSION ..... 307

CHAPTER 10 FINAL REMARKS AND CONCLUSIONS ..... 308

10.1. INTRODUCTION ..... 308
10.2. THE BACKGROUND WIND AND STREET CANYON GEOMETRY ..... 308
10.3. IN-CANYON FLOW FEATURES AND RESULTING IN-CANYON CO CONCENTRATIONS ..... 310
10.4. THE BACKGROUND WIND AND TRAFFIC-PRODUCED TURBULENCE ..... 313
10.5. TRAFFIC CHARACTERISTICS AND RESULTING IN-CANYON CO CONCENTRATIONS ..... 314

APPENDIX ..... 316

REFERENCES ..... 319

# Table of Figures

Figure 2.1. The Air Quality Management Area (AQMA) declared for $NO_2$ by the City of York Council (CYC, 2005a)..... 9
Figure 2.2. Schematic of the urban boundary layer including its vertical layers and scales. The Urban Boundary Layer (UBL) and Urban Canopy Layer (UCL) are shown (Piringer *et al.*, 2002)..... 20
Figure 2.3. Flow regimes associated with perpendicular background winds in street canyons with different aspect ratios (Oke, 1987). ..... 22
Figure 2.4. Flow inside a street canyon during (a) oblique and (b) perpendicular background winds (adapted from Hoydysh *et al.*, 1974)..... 23
Figure 2.5. Flow features inside a deep street canyon, showing a single across-canyon recirculating vortex and intermittent corner vortices (Hoydysh and Dabberdt, 1988). ..... 24
Figure 2.6. Schematic of the reflection off the windward canyon wall during oblique background winds showing along- and across-canyon flow (adapted from Johnson and Hunter, 1999). ..... 26
Figure 2.7. Flow field at a street intersection with a tall building, illustrating exchanges between the streets and additional mixing processes along the street canyons during oblique background winds (Robins and MacDonald, 2001)..... 27
Figure 2.8. Flow around an isolated building during perpendicular background winds, showing the development of counter-rotating corner vortices, which are likely to produce converging flows in the lee of the building (Hosker, 1985)... 28
Figure 2.9. Schematic of the single across-canyon recirculating flow with a horizontally-aligned axis, showing the transport of pollutants to the leeward side of the canyon (modified from Berkowicz, 2000a)..... 31
Figure 2.10. Schematic showing the position of the shear layer relative to the in-canyon recirculation zone during skimming flow (Louka *et al.*, 2000)..... 35
Figure 3.1. Map showing the city of York and its surroundings. ..... 54
Figure 3.2. Plan of the Bootham and Gillygate street canyons and adjoining streets.56
Figure 3.3. Plan view of the Bootham and Gillygate street canyons and the surrounding building and street layout. Note that the buildings are shown as yellow rectangles. Open spaces and roads are shown in white..... 59
Figure 3.4. Aerial photograph of Bootham (shown by the arrow). Clarence Street, which leads into Gillygate, is also visible. Rows of buildings define Portland Street and Claremont Terrace (photo courtesy of Bootham School, 2003)..... 60
Figure 3.5. Schematic of the Gill R3-50 ultrasonic anemometer showing the positive velocity axes of the $U$, $V$ and $W$ components (a) plan view; (b) side view. Note that the numbers in (a) refer to the transducer pairs (Redrawn from Gill Instruments, 2002). ..... 62
Figure 3.6. Schematic representation of a typical wind speed time-series, showing $u'$ as the gust or deviation of the actual instantaneous wind, $U(t)$, from the local mean, $U$ (redrawn from Stull, 1988)..... 67
Figure 3.7. The aluminium bracket used to attach the Gill R3-50 ultrasonic anemometer to street furniture, such as lampposts. Note that modifications were made to the bracket shown here in order to make the structure lighter. ..... 73

Figure 3.8. Plan view of the study area showing the Bootham and Gillygate street canyons, the lampposts that supported the instruments and the location of the G3-G4 experiment cross-section. The reference anemometer mast and the four SCOOT sensors (arrows indicate the direction of traffic flow measured) are also indicated. ..... 76
Figure 3.9. Comparison between the background wind direction, $\theta_{ref}$, measured at the mast during the October and November 2003 experiment against the wind direction measured in grounds of Bootham Hospital. ..... 81
Figure 3.10. Schematic representation of the Learian streetbox electrochemical cell monitoring unit showing the hardwired and telemetry methods of establishing a connection (Modified from Ropkins *et al.*, 2000). ..... 85
Figure 3.11. Side view of the electrochemical cell of the type fitted in the Learian streetbox (Ropkins *et al.*, 2000). ..... 86
Figure 3.12. Schematic of the flow of information in a SCOOT-based Urban Traffic Control system (SCOOT, 2003). ..... 89
Figure 3.13. Plan view of the buildings in the modelling domain; showing the Gillygate street canyon and adjoining streets. ..... 97
Figure 4.1. Plan view of the Gillygate street canyon, showing the lampposts that support the anemometers and the reference anemometer mast. ..... 110
Figure 4.2. Schematic of the Gillygate canyon cross-section at G3-G4, showing relative locations of the ultrasonic anemometers. ..... 111
Figure 4.3. Standard deviation of the vertical wind velocity, $\sigma_w$, measured at mid-canyon height against the background wind speed, conditioned on background wind directions ⊠ $\theta_{ref}$= 120° ±90° and ⊕ $\theta_{ref}$= 300° ±90° for (a) G3 and (b) G4. — — curve fit for $\theta_{ref}$= 120° ±90° and —— curve fit for $\theta_{ref}$= 300° ±90°. ..... 114
Figure 4.4. Compensated normalised standard deviation of the vertical wind velocity, $\sigma_w/U_{ref}$, measured at mid-canyon height against the background wind speed, $U_{ref}$, for (a) G3 and (b) G4. ..... 115
Figure 4.5. Vertical velocity component, $W$, measured at mid-canyon height on each lamppost as a function of the across-canyon component measured at the mast, $V_{mast}$: ○ G3 and □ G4. —— —— curve fits for SE background winds and — — — predicted curve fits for NW backgrounds based on the analysis of the data corresponding to the SE winds. ..... 116
Figure 4.6. Schematic of the mean horizontal flow vectors computed by MISKAM at a height of 5m for perpendicular background winds from: (a) $\theta_{ref}$ = 300° and (b) $\theta_{ref}$ = 120°. The section of the model domain used was around cross-section G3-G4 and is shown in (c). The buildings are shown as shaded rectangles. The reference wind speed (at 50 m) was configured to 5 m $s^{-1}$. ..... 117
Figure 4.7. The mean flow vectors computed by MISKAM at cross-section G3-G4 for perpendicular background winds from: (a) $\theta_{ref}$ = 300° and (b) $\theta_{ref}$ = 120°. The buildings are shown as shaded rectangles with diagonal hatches. The reference wind speed (at 50 m) was configured to 5 m $s^{-1}$. ..... 118
Figure 4.8. The mean vertical wind velocity measured at mid-canyon height inside Gillygate normalised by the background wind speed, $U_{ref}$, as a function of the background wind direction, $\theta_{ref}$, for (a) ○ G3 and (b) □ G4. ..... 119
Figure 4.9. Vertical wind velocity angle, $\phi$, as a function of background wind direction, $\theta_{ref}$, for: (a) ○ G3 and (b) □ G4. ..... 120
Figure 4.10. In-canyon wind direction, $\eta$, as a function of background wind direction, $\theta_{ref}$, for: (a) ○ G3 and (b) □ G4. ..... 121

Figure 4.11. Sector-averaged horizontal wind speed, $M$, measured at mid-canyon height normalised by the background wind speed, $U_{ref}$, as a function of $\theta_{ref}$: —○— G3 and --□-- G4. ..... 122
Figure 4.12. The standard deviation of the vertical wind velocity measured at mid-canyon height inside Gillygate normalised by the background wind speed, $U_{ref}$, as a function of the background wind direction, $\theta_{ref}$, for (a) ○ G3 and (b) □ G4. ..... 123
Figure 4.13. The standard deviation of the vertical wind velocity measured at mid-canyon height inside Gillygate normalised by the local wind speed, $M$ (i.e. turbulence intensity, $t_w$) on each lamppost as a function of the background wind direction, $\theta_{ref}$, for (a) ○ G3 and (b) □ G4. ..... 124
Figure 4.14. TKE measured at mid-canyon height on each lamppost against the background turbulence kinetic energy, $TKE_{ref}$, for • G3 and □ G4, conditioned on $U_{ref}$>1.2 m s$^{-1}$ and: (a) $\theta_{ref}$ = 120° ±30°; (b) $\theta_{ref}$ = 300° ±30°. —— curve fit for G3 and — — curve fit for G4. ..... 125
Figure 4.15. TKE measured at mid-canyon height on lampposts G3 and G4 against the background turbulence kinetic energy, $TKE_{ref}$, for • G3 and □ G4, conditioned on $U_{ref}$>1.2 m s$^{-1}$ and: (a) $\theta_{ref}$ = 75° ±30°; (b) $\theta_{ref}$ = 165° ±30°. —— curve fit for G3 and — — curve fit for G4. ..... 126
Figure 4.16. TKE measured at mid-canyon height on each lamppost against the background turbulence kinetic energy, $TKE_{ref}$, for • G3 and □ G4, conditioned on $U_{ref}$>1.2 m s$^{-1}$ and: (a) $\theta_{ref}$ = 30° ±30°; (b) $\theta_{ref}$ = 210° ±30°. —— curve fit G3 and — — curve fit for G4. ..... 127
Figure 4.17. TKE measured on lampposts G3 and G4 normalised by the local horizontal wind speed against the background wind direction, $\theta_{ref}$, for (a) • G3 at $z/H$ = 0.46 and (b) □ G4 at $z/H$ = 0.48. ..... 128
Figure 4.18. TKE measured on lampposts G3 and G4 normalised by the local horizontal wind speed, $M$, against the background wind direction, $\theta_{ref}$, for (a) ○ G3 at $z/H$ = 0.60 and (b) △ G4 at $z/H$ = 0.84. ..... 129
Figure 4.19. TKE measured on lamppost G3 normalised by the local horizontal wind speed, $M$, against the background wind direction, $\theta_{ref}$, for (a) ▲ $z/H$ = 0.60; (b) ○ $z/H$ = 0.46; and (c) ▽ $z/H$ = 0.30. ..... 130
Figure 4.20. TKE measured on each lamppost normalised by $U_{ref}^2$ as a function of the TKE measured close to the shear layer at $z/H$ = 0.84 on lamppost G4 conditioned on $\theta_{ref}$ = 120° ±30° for (a) G4 at $z/H$ = 0.48, (b) G3 at $z/H$ = 0.46 and (c) G3 at $z/H$ = 0.60. ..... 131
Figure 4.21. Contour plots of TKE (m$^2$ s$^{-2}$) computed by MISKAM for perpendicular background winds at the G3-G4 experiment cross-section for (a) $\theta_{ref}$ = 120° and (b) $\theta_{ref}$ = 300°. The buildings are shown as shaded rectangles with diagonal hatches. The reference wind speed (at 50 m) was configured to 5 m s$^{-1}$. ..... 132
Figure 4.22. TKE measured on lamppost G3 normalised by $U_{ref}^2$ as a function of the normalised TKE measured close to the shear layer at $z/H$ = 0.84 on lamppost G4 conditioned on $\theta_{ref}$ = 120° ±30° for (a) $z/H$ = 0.30, (b) $z/H$ = 0.46 and (c) at $z/H$ = 0.60. ..... 133
Figure 4.23. TKE measured on each lamppost normalised by $U_{ref}^2$ as a function of the normalised TKE measured close to the shear layer at $z/H$ = 0.84 on lamppost G4 conditioned on $\theta_{ref}$ = 300° ±30° for (a) G4 at $z/H$ = 0.48, (b) G3 at $z/H$ = 0.46 and (c) G3 at $z/H$ = 0.60. ..... 134

Figure 4.24. TKE measured on lamppost G3 normalised by $U_{ref}^2$ as a function of the normalised TKE measured close to the shear layer at $z/H = 0.84$ on lamppost G4 conditioned on $\theta_{ref} = 300° \pm 30°$ for (a) $z/H = 0.30$, (b) $z/H = 0.46$ and (c) at $z/H = 0.60$. ..... 135
Figure 4.25. Schematic representation of the building cavity vortex that may have formed adjacent to lamppost G4 on Gillygate during near-parallel background winds of $\theta_{ref} = 45°$. ..... 136
Figure 4.26. Normalised variance of each wind velocity component, $\sigma_i^2/2{\cdot}TKE_{G3}$, measured on lamppost G3 at (a) $z/H = 0.60$, (b) $z/H = 0.46$ and (c) $z/H = 0.30$ against $\theta_{ref}$, for: ◇ $\sigma_u^2$; □ $\sigma_v^2$; and △ $\sigma_w^2$. The horizontal line indicates approximate isotropy. ..... 137
Figure 4.27. Normalised variance of each wind velocity component, $\sigma_i^2/2{\cdot}TKE_{G4}$, measured on lamppost G4 at (a) $z/H = 0.84$ and (b) $z/H = 0.48$ against $\theta_{ref}$, for: ◇ $\sigma_u^2$; □ $\sigma_v^2$; and △ $\sigma_w^2$. The horizontal line indicates approximate isotropy. ... 138
Figure 5.1. Plan view of the study area showing the street canyons, the lampposts that support the instruments, the reference anemometer mast, the locations of the significant trees and the four SCOOT sensors (arrows indicate the direction of traffic flow measured). ..... 181
Figure 5.2. Schematic of the Gillygate canyon cross-section at G3-G4, showing relative instrument locations. ..... 184
Figure 5.3. Total traffic flow during the experiment period for (a) Gillygate and .. 186
Figure 5.4. Frequency distribution of: ▬ mean wind direction; —●— mean wind speed. ..... 187
Figure 5.5. Sector-averaged CO concentrations (ppm) in Gillygate: (a) —■— streetbox $G3_{3.5}$ and —□— streetbox $G3_{7.0}$; (b) —●— streetbox $G4_{3.5}$ and —○— streetbox $G4_{10.0}$. ..... 189
Figure 5.6. Sector-averaged CO concentrations (ppm) in Gillygate: (a) —✳— streetbox $G1_{3.5}$; —○— streetbox $G2_{3.5}$ and —■— streetbox $G3_{3.5}$; (b) Normalised sector-averaged CO concentrations using Equation (5.1) for: —■— $G3_{3.5}$ and —×— $G4_{3.5}$. ..... 194
Figure 5.7. The variability in the mean CO concentrations measured in Portland Street against the background wind direction, $\theta_{ref}$, conditioned on $U_{ref} > 1.2$ ms$^{-1}$ and times between 06:30 and 22:00. The mean concentrations are shown as ▬ and the unit standard deviation is shown as ------. ..... 197
Figure 5.8. Sector-averaged CO concentrations (ppm) in Bootham: (a) —■— streetbox $B1_{3.5}$; and —○— streetbox $B3_{3.5}$ (b) —□— streetbox $B2_{3.5}$ and —●— streetbox $B4_{3.5}$. ..... 200
Figure 6.1. Theoretical representation of the turbulence produced by vehicles travelling at constant speed along a street canyon and with equal distance between consecutive vehicles (modified from Berkowicz, 2000b). ..... 212
Figure 6.2. Pie chart showing the proportion of vehicles manually surveyed in the inbound traffic flow along Gillygate during the TPT field investigations..... 222
Figure 6.3. Theoretical relationship between traffic flow and traffic density for a street with a speed limit of 48 km h$^{-1}$ (or 30 miles h$^{-1}$) and a jam density of 240 veh km$^{-1}$. The free flow, unstable flow and congested traffic flow conditions are indicated (modified from Dirks *et al.*, 2003). ..... 223

Figure 6.4. Inbound traffic flow and detector occupancy measured by SCOOT and averaged over 15-minute periods during the manual traffic counting survey showing the unstable and congested traffic flow conditions based on the criteria used in Chapter 7. Note the absence of free flow conditions. ..... 224
Figure 6.5. Characteristics of the inbound traffic flow using 1-minute averages for: (a) traffic flow and traffic density, and (b) vehicle speed and traffic density... 225
Figure 6.6. Vertical velocity fluctuations $\sigma_w$ against mean vehicle speed conditioned on $U_{ref} > 1.2$ m s$^{-1}$ and $\theta_{ref} = 120° \pm 30°$, measured on lamppost G3 at (a) $z/H$ = 0.09 and (b) $z/H = 0.3$. ..... 230
Figure 6.7. Vertical velocity fluctuations $\sigma_w$ against vehicle speed conditioned on $U_{ref} \leq 1.2$ m s$^{-1}$ and $\theta_{ref} = 120° \pm 30°$, measured at lamppost G3 at (a) $z/H = 0.09$ and (b) $z/H = 0.3$. ..... 232
Figure 6.8. 15-minute mean vertical wind velocity angle, $\phi$, as a function of the background wind direction, $\theta_{ref}$, and $U_{ref} \leq 1.2$ m s$^{-1}$ at (a) $z/H = 0.46$ on G3 and (b) $z/H = 0.48$ on G4. ..... 233
Figure 6.9. Comparison of calculated and measured $\sigma_w$ at $z/H = 0.09$ averaged over 1-minute periods; conditioned on $\theta_{ref} = 120° \pm 30°$ and $U_{ref} \leq 1.2$ m s$^{-1}$ using: (a) Equation (6.13); (b) Equation (6.15); and (c) Equation (6.17). ..... 236
Figure 6.10. Comparison of calculated and measured $\sigma_w$ at $z/H = 0.3$ averaged over 1-minute periods; conditioned on $\theta_{ref} = 120° \pm 30°$ and $U_{ref} \leq 1.2$ m s$^{-1}$ and using: (a) Equation (6.13); (b) Equation (6.15); and (c) Equation (6.17)..... 239
Figure 6.11. Comparison of calculated and measured $\sigma_w$ at $z/H = 0.09$ averaged over 1-minute periods; conditioned on $\theta_{ref} = 120° \pm 45°$ and $U_{ref} \leq 1.2$ m s$^{-1}$ and using: (a) Equation (6.13); (b) Equation (6.15); and (c) Equation (6.17)..... 241
Figure 6.12. Comparison of calculated and measured $\sigma_w$ at $z/H = 0.09$ averaged over 1-minute periods; conditioned on $\theta_{ref} = 300° \pm 30°$ and $U_{ref} \leq 1.2$ m s$^{-1}$ and using: (a) Equation (6.13); (b) Equation (6.15); and (c) Equation (6.17)..... 243
Figure 6.13. Comparison of calculated and measured $\sigma_w$ at $z/H = 0.09$ averaged over 1-minute periods; conditioned on $\theta_{ref} = 30° \pm 30°$ and $U_{ref} \leq 1.2$ m s$^{-1}$ and using: (a) Equation (6.13); (b) Equation (6.15); and (c) Equation (6.17)..... 244
Figure 6.14. Comparison of calculated and measured $\sigma_w$ at $z/H = 0.09$ averaged over 1-minute periods; conditioned on $\theta_{ref} = 210° \pm 30°$ and $U_{ref} \leq 1.2$ m s$^{-1}$ and using: (a) Equation (6.13); (b) Equation (6.15); and (c) Equation (6.17)..... 245
Figure 7.1. Plan view of the study area showing the street canyons, the lampposts that support the instruments, the reference anemometer mast, the traffic signal controlled intersections and the four SCOOT sensors (arrows indicate the direction of traffic flow measured). ..... 252
Figure 7.2. Fifteen-minute mean SCOOT inbound traffic flow against the manual observations of the inbound traffic flow along Gillygate during the period of the field experiment. ..... 256
Figure 7.3. Inbound detector occupancy against time for (a) Gillygate and (b) Bootham. ..... 259
Figure 7.4. Total weekday traffic flow and occupancy along Gillygate for (a) inbound link and (b) outbound link. ..... 260
Figure 7.5. Total weekday traffic flow and occupancy along Bootham for (a) inbound link and (b) outbound link..... 261
Figure 7.6. Vehicle queue length against inbound detector occupancy along Gillygate for (a) 15-minute means and (b) diurnal means..... 262

Figure 7.7. Mean diurnal profiles for Gillygate with — — showing unit standard deviation for (a) — — total traffic flow; (b) —— inbound detector occupancy (c) —o— CO concentration at $G3_{3.5}$; (d) —□— CO concentration at $G4_{3.5}$.... 264
Figure 7.8. Mean diurnal profiles for Bootham with standard deviation lines — — for: ..... 266
Figure 7.9. Mean diurnal CO concentrations along Gillygate conditioned on inbound detector occupancy and total traffic flow: ▽ low occupancy; □ medium occupancy and ▲ high occupancy for (a) $G3_{3.5}$ and (b) $G4_{3.5}$..... 268
Figure 7.10. Mean diurnal CO concentrations along Bootham conditioned on inbound detector occupancy and total traffic flow: ▽ low occupancy; □ medium occupancy and ▲ high occupancy for (a) $B1_{3.5}$ and (b) $B2_{3.5}$. ..... 269
Figure 7.11. Mean diurnal CO concentrations along Gillygate at $G3_{3.5}$ varying with occupancy. Data are segregated according to time-of-day regimes: A, B, C and D. Lines correspond to least-squares regressions over the range of data within each bounded region. Tables 7.3 and 7.4 list the regimes with the corresponding time periods and regression results, respectively..... 271
Figure 7.12. Frequency distribution of CO concentrations on Gillygate and Bootham shown as PDFs (bars) and percentiles (lines) for $G3_{3.5}$ and $B1_{3.5}$..... 275
Figure 7.13. Sector-averaged CO concentrations shown as concentration roses conditioned on inbound detector occupancy: ▽ low occupancy; □ medium occupancy; ▲ high occupancy; ····· all data for (a) $G3_{3.5}$ and (b) $G4_{3.5}$. ..... 276
Figure 8.1. Spatial variations in emission rates of CO interpolated over 2 m sections along Gillygate from the common (Bootham/Gillygate) intersection between 08:30 – 08:45: —— variable emissions; — — constant (mean) emissions (adapted from Tate, 2005)..... 283
Figure 8.2. The modelling domain, showing the building configurations around the Gillygate street canyon. ..... 285
Figure 8.3. Longitudinal cross-section of the mean concentration (mg $m^{-3}$) of the tracer on the SE side of Gillygate during parallel background winds (i.e. $\theta_{ref}$ = 210°) using: (a) the constant and (b) variable emission sources shown in Figure 8.1..... 288
Figure 8.4. Longitudinal cross-section of the mean concentration (mg $m^{-3}$) of the tracer on the leeward (SE) side of Gillygate during oblique background winds (i.e. $\theta_{ref}$ = 165°) using: (a) the constant and (b) variable emission sources shown in Figure 8.1..... 290
Figure 8.5. Longitudinal cross-section of the mean concentration (mg $m^{-3}$) of the tracer on the leeward (SE) side of Gillygate during perpendicular background winds (i.e. $\theta_{ref}$ = 120°) using: (a) the constant and (b) the variable emission sources shown in Figure 8.1..... 293
Figure 8.6. Contour plots of the mean concentration (mg $m^{-3}$) of the tracer derived from MISKAM at the transverse G3-G4 cross-section on Gillygate for perpendicular background winds from (a) $\theta_{ref}$ = 120° and (b) $\theta_{ref}$ = 300°. Buildings are shown as rectangles with diagonal hatching. ..... 296

# List of Tables

Table 2.1. Summary of the UK Air Quality Strategy objectives (modified from the UK National Air Quality Archive, 2005). ..... 6
Table 2.2. The Air Quality Action Plan (AQAP) measures for reducing $NO_2$ concentrations within York's Air Quality Management Area (CYC, 2005b).... 10
Table 3.1. The measurement specifications of the Gill omni-directional (R3-50) research ultrasonic anemometer (Gill Instruments, 2002). ..... 63
Table 3.2. Factors potentially affecting the performance of a radio link..... 78
Table 3.3. Learian streetbox fitted with an electrochemical CO sensor (Learian, 2002). ..... 86
Table 4.1. The mean data collection rate for all ultrasonic anemometers deployed during the experiment. *Note that all instruments were set to sample at 20 Hz except for the reference anemometer located on the mast, which was set at 10 Hz. ..... 112
Table 4.2 Regression analysis of $TKE_{G3}/U_{ref}^2$ and $TKE_{G4}/U_{ref}^2$ measured inside the Gillygate street canyon at various heights on lampposts G3 and G4 as a function of $TKE_{G4}/U_{ref}^2$ measured close to the shear layer at $z/H = 0.84$ on lamppost G4 during perpendicular background winds..... 139
Table 4.3. Regression analysis of $TKE_{G3}/U_{ref}^2$ measured inside the Gillygate street canyon on lamppost G3 as a function of $TKE_{G4}/U_{ref}^2$ measured close to the shear layer at $z/H = 0.84$ on lamppost G4 during perpendicular background winds. 139
Table 4.4. Regression analysis of TKE measured inside the Gillygate street canyon at mid-canyon height on lampposts G3 and G4 as a function of $TKE_{ref}$ measured at the reference mast during oblique background winds. ..... 140
Table 6.1. Estimated traffic parameters showing the drag coefficient $C_D$ and geometric length scale $h$ for each vehicle category. ..... 227
Table 6.2. Regression analysis of the calculated turbulence and measured vertical velocity variance $\sigma_w$ at lamppost G3 conditioned on $U_{ref} \leq 1.2$ m s$^{-1}$ and as a function of background wind direction, $\theta_{ref}$. #Note that NS is an abbreviation for *Not Significant*. ..... 237
Table 6.3. Regression analysis of the calculated turbulence and measured TKE (m$^2$ s$^{-2}$) at lamppost G3 conditioned on $U_{ref} \leq 1.2$ m s$^{-1}$ and as a function of background wind direction, $\theta_{ref}$. #Note that NS is an abbreviation for *Not Significant*. ..... 247
Table 7.1. Manual vehicle observations compared with SCOOT detector performance along Gillygate on 10 November 2003..... 255
Table 7.2. Manual vehicle observations compared with SCOOT detector performance along Bootham on 10 November 2003..... 257
Table 7.3. Possible traffic regimes identified from Figure 7.11 using a time-of-day analysis. The dominant traffic condition contribution to each regime is in bold. ..... 272
Table 7.4. The linear regression results for the traffic regimes identified from Figure 7.11 using a time-of-day analysis. ..... 273
Table 9.1. The mean data collection rate for all ultrasonic anemometers deployed during the trial field experiment from 1 April – 9 April 2003 (inclusive). †Note that ID is an abbreviation for *Insufficient Data*. ..... 303

# Notation

## Roman Symbols, Abbreviations & Contractions

| | |
|---|---|
| **A** | |
| $A$ | Advection of TKE |
| $A_c$ | Vertical cross-sectional (or frontal) area of vehicle |
| $A_p$ | Horizontal cross-sectional (or plan area) of vehicle |
| $Ah$ | Amp hour |
| $a_1$ | Axis-1 velocity |
| $a_2$ | Axis-2 velocity |
| $a_3$ | Axis-3 velocity |
| AD | anno Domini |
| AMS | American Meteorological Society |
| AQAP | Air Quality Action Plan |
| AQMA | Air Quality Management Area |
| ASCII | American Standard Code for Information Interchange |
| arctan or atan | Arc Tangent |
| **B** | |
| B | Bootham |
| $B$ | Bouyant production or consumption of TKE |
| $b$ | Constant related to the vehicle aerodynamic drag coefficient |
| B1 | Lamppost B1 |
| $B1_{3.5}$ | Height of instrument (in meters) on lamppost B1 |
| B2 | Lamppost B2 |
| B3 | Lamppost B3 |
| B4 | Lamppost B4 |
| BBC | British Broadcasting Corporation |
| Br | Bromine |
| **C** | |
| $C_D$ | Drag coefficient |
| $C_\varepsilon$ | Constant |
| $C$ | Concentration |
| $C_{11\text{-}16}$ | Anemometers located in street using radio telemetry system |
| $c$ | Concentration |
| $c_1$ | Constant |
| $c_2$ | Constant |
| $c_3$ | Constant |
| $c_4$ | Constant |
| $c_5$ | Constant |
| CCTV | Closed-Circuit Television |
| CFD | Computational Fluid Dynamics |
| CO | Carbon monoxide |
| $CO_2$ | Carbon dioxide |
| CMEM | Comprehensive Model Emission Model |
| CYC | City of York Council |
| **D** | |
| DAPPLE | Dispersion of Air Pollution and Penetration into the Local Environment |
| DC | Direct Current |
| $df$ | Degrees of Freedom |
| DRACULA | Dynamic Route Assignment Combining User Learning and microsimulAtion |

**E**

| | |
|---|---|
| E | East |
| $e$ | Emission factor |
| ENE | East-North-East |
| EPA | US Environmental Protection Agency |
| EPSRC | Engineering and Physical Sciences Research Council |
| ERRI | Energy and Resources Research Institute |
| ESE | East-South-East |
| EU | European Union |

**F**

| | |
|---|---|
| $F_{Hsfc}$ | Effective surface heat flux |
| FORTRAN | FOR(mula) TRAN(slation) |
| FM | Frequency Modulation |

**G**

| | |
|---|---|
| G | Gillygate |
| g | Gram, a mass unit |
| $g$ | Gravity |
| G3 | Lamppost G3 |
| $G3_{3.5}$ | Height of instrument (in meters) on lamppost G3 |
| G4 | Lamppost G4 |
| G3-G4 | Experiment cross-section (at lampposts G3 and G4) |
| GPS | Global Positioning System |

**H**

| | |
|---|---|
| $H$ | Height of buildings, usually expressed as $H/W$ (aspect ratio) |
| h | Hour |
| $h$ | Geometric vehicle length scale |
| HGV | Heavy Goods Vehicle |
| Hz | Hertz, a unit of frequncy |

**I**

| | |
|---|---|
| $i$ | Index |
| ID | Insufficient Data |
| ITS | Institute for Transport Studies |

**J**

**K**

| | |
|---|---|
| $K$ | Normalised and non-dimensional concentration |
| kg | Kilogram, a mass unit |
| $k$ | TKE, usually expressed with dissipation rate, $\varepsilon$ (e.g. $k$- $\varepsilon$) |
| km | Kilometer, a length unit |

**L**

| | |
|---|---|
| $L$ | Length of street, usually expressed as $L/H$ |
| $L_v$ | Distance between consecutive vehicles, or headway |
| $L_\varepsilon$ | Dissipation length scale |
| LGV | Light Goods Vehicle |
| LES | Large Eddy Simulation |

**M**

| | |
|---|---|
| $M$ | Mean horizontal wind speed measured in the street |
| $M_{11}$ | Anemometer located on mast (reference location) for radio telemetry system |
| M19 | Raw SCOOT data message |
| m | Meter, a length unit |
| MC | Motor-Cycle |
| MHz | Mega Hertz, a unit of frequncy |
| MISKAM | MIcroScale flow and dispersion Model |
| mW | Mega Watt |

**N**

| | |
|---|---|
| N | North |
| $N$ | Number of vehicles |
| n | Number of data values |
| NAEI | National Atmospheric Emission Inventory |
| NAQS | National Air Quality Strategy |
| NDIR | Non-Dispersive InfraRed |
| NE | North-East |
| NERC | Natural Environment Research Council |
| nm | Nanometer, a length unit |
| NNE | North-North-East |
| NS | Not Significant |
| NNW | North-North-West |
| NO | Nitrogen monoxide |
| $NO_2$ | Nitrogen dioxide |
| $NO_X$ | Oxides of nitrogen ($NO + NO_2$) |
| NW | North-West |

**O**

| | |
|---|---|
| O | Atomic Oxygen |
| $O_2$ | Oxygen |
| $O_3$ | Ozone |
| OSPM | Operational Street Pollution Model |
| OX | Total 'oxidant' ($NO_2 + O_3$) |

**P**

| | |
|---|---|
| P | Pressure |
| $P_t$ | Production of TKE by TPT |
| Pb | Lead |
| PCI | Power and Communications Interface |
| ppm | Parts per million |
| $PM_{2.5}$ | Particulate Matter (size range <2.5 microns) |
| $PM_{10}$ | Particulate Matter (size range <10 microns) |

**Q**

| | |
|---|---|
| $Q$ | Emission factor |
| $q$ | Traffic flow |
| QA | Quality Assurance |
| QC | Quality Control |

**R**

| | |
|---|---|
| $r$ | Correlation coefficient |
| $r^2$ | Coefficient of determination |
| RCOM | Gill Instruments Ltd. PC communication software |
| RF | Radio Frequency |
| RMS or rms | Root Mean Square |
| RS232 | Communications standard |
| RS422 | Communications standard |

**S**

| | |
|---|---|
| S | South |
| $S$ | Shear production |
| $S_c$ | Cross-sectional area of street canyon |
| $S_{ct}$ | Constant |
| $S_t$ | Cross-sectional area of street canyon in which TPT is most active |
| s | second |
| SATURN | Simulation and Assignment of Traffic to Urban Road Networks |
| SCOOT | Split Cycle Offset Optimisation Technique |
| SE | South-East |
| $SF_6$ | Sulphur Hexafluoride |
| $SO_2$ | Sulphur Dioxide |
| SSE | South-South-East |
| SSW | South-South-West |
| SW | South-West |

**T**

| | |
|---|---|
| T | Time |
| $\mathcal{T}$ | Total traffic flow |
| $T_r$ | Transport |
| $T_v$ | Absolute virtual air temperature at ground level |
| $t$ | Time |
| $t_w$ | Turbulence intensity |
| TKE | Turbulence Kinetic Energy |
| $TKE_{norm}$ | Normalised Turbulence Kinetic Energy |
| $TKE_{ref}$ | Turbulence Kinetic Energy at mast (reference location) |
| $TKE_t$ | Turbulence Kinetic Energy generated by TPT |
| TPT | Traffic-Produced Turbulence |
| TRAPOS | Optimisation of Modelling Methods for Traffic Pollution in Streets |
| TSP | Total Suspended Particulate matter |

**U**

| | |
|---|---|
| $U$ | Mean along-street wind velocity component ($y$-direction), e.g. $U+$ towards NE |
| $U_{ref}$ | Mean horizontal background (or reference) wind speed |
| $u$ | Along-street wind velocity component ($y$-direction) |
| $u*$ | Friction velocity |
| $\overline{u_i v_j}$ | Reynolds stress |
| $\overline{u_j c}$ | Turbulent flux term |
| UBL | Urban Boundary Layer |
| UCL | Urban Canopy Layer |
| UK | United Kingdom |
| USA | United States of America |
| UTMC | Urban Traffic Management and Control |
| US | United States |
| *UVW* | Operating format of the Gill Instruments Ltd. R3-50 ultrasonic anemometer |

**V**

| | |
|---|---|
| $V$ | Mean across-street wind velocity component ($x$-direction), e.g. $V+$ towards NW |
| $V_{mast}$ | Mean across-street wind velocity at mast (reference location) |
| $V_c$ | Volume of whole street canyon |
| $V_t$ | Volume of layer in which TPT is most active |
| $V_w$ | Volume of vehicle wake |
| v | Kinematic molecular viscosity |
| $v$ | Across-street wind velocity component ($x$-direction) |
| $v_l$ | Wind flow along line of transducer |
| $v_t$ | Eddy viscosity |
| veh | Vehicles |

**W**

| | |
|---|---|
| W | West |
| $W$ | Mean wind velocity component upwards ($z$-direction), e.g. $W+$ towards sky |
| $W$ | Width of street, usually expressed as $H/W$ (aspect ratio) |
| $w$ | Wind velocity component upwards ($z$-direction) |
| WHO | World Health Organisation |
| WNW | West-North-West |
| WSW | West-South-West |

**X**

| | |
|---|---|
| $X$ | Horizontal distance |
| $x$ | $x$-direction (across street), also horizontal distance |

**Y**

| | |
|---|---|
| $y$ | $y$-direction (along street), also horizontal distance |

**Z**

| | |
|---|---|
| $z$ | $z$-direction (upwards), also height above street i.e. vertical distance |
| $z_0$ | Roughness length |

## Greek Symbols

**$B\beta$ Beta**

| | |
|---|---|
| $\beta$ | Sources & sinks of emissions |

**$\Gamma\gamma$ Gamma**

| | |
|---|---|
| $\gamma$ | Speed of sound |

**$\Delta\delta$ Delta**

| | |
|---|---|
| $\Delta$ or $\delta$ | Change of |

**$E\varepsilon$ Epsilon**

| | |
|---|---|
| $\varepsilon$ | Dissipation rate |

**$H\eta$ Eta**

| | |
|---|---|
| $\eta$ | Mean wind direction measured in the street |

**$\Theta\theta$ Theta**

| | |
|---|---|
| $\theta_{ref}$ | Mean background wind direction |

**$K\kappa$ Kappa**

| | |
|---|---|
| $K$ | Eddy diffusivity coefficient |
| $\kappa$ | Traffic density, expressed per unit length of street |
| $\kappa_\varphi$ | Jam density of traffic, expressed per unit length of street |

**$M\mu$ Mu**

| | |
|---|---|
| $\mu$ | micro |

**$N\nu$ Nu**

| | |
|---|---|
| $\nu$ | Average vehicle speed |
| $\nu_0$ | Maximum free-flow vehicle speed |

**$P\rho$ Rho**

| | |
|---|---|
| $P$ | Density of air |

**$\Sigma\sigma$ Sigma**

| | |
|---|---|
| $\Sigma$ | Summation |
| $\sigma$ | Standard deviation, e.g. of vertical wind velocity, $\sigma_\omega$ |
| $\sigma_{mt}$ | Standard deviation of along-street wind velocity generated by TPT |
| $\sigma_{wo}$ | Standard deviation of vertical wind velocity calculated by OSPM |
| $\sigma_\varepsilon$ and $\sigma_k$ | Constants |
| $\sigma^2$ | Variance, e.g. of along-street wind velocity, $\sigma_u^2$ |
| $\sigma_{ct}^2$ | TPT produced over a section of the street canyon |
| $\sigma_{wt}^2$ | TPT produced in a single vehicle wake |

**$T\tau$ Tau**

| | |
|---|---|
| $\tau$ | Lifetime of turbulent wake produced by single vehicle |

**$\Phi\phi$ Phi**

| | |
|---|---|
| $\phi$ | Vertical wind angle |

## Operators

| | |
|---|---|
| $(\bar{\ })$ | Overbar denotes averaging or mean |
| [CO] | Mean concentration, e.g. of CO |
| ° | Degrees |
| ′ | Deviation from mean (or fluctuation) |
| ″ | Inch, a length unit |

# CHAPTER 1

## Motivation for Research

### 1.1. Introduction

All living organisms, in one way or another, pollute. Life is a chemical reaction, where input chemicals such as food and oxygen are converted into growth or motion. The reaction products are waste or, where levels become unacceptable, they are pollutants. Consequently, air pollution is the presence of one or more chemicals in the atmosphere in quantities and duration that cause harm to humans, other forms of life and materials. It is tempting to view air pollution as a recent phenomena associated with modern industry. However, it has a long history dating back to the use of fire by early people when poorly ventilated cooking fires filled dwellings with smoke and other pollutants. Urban air pollution was first documented in AD 61 by Seneca, who wrote about the 'heavy air of Rome' and the 'stink of its chimneys poring forth pestilential vapours and soot.' In recent times, urban air pollution has become a concern in relation to health and urban sustainability issues, with road traffic comprising the major source of air pollution and greenhouse gases. Emissions from motor vehicles in urban areas typically comprise over 70% of the total emissions of air pollutants. The UK National Air Quality Strategy (UKNAQS) has set out proposed objectives for eight pollutants against which the air quality will be assessed (see Chapter 2).

The Environment Act 1995 requires local authorities to be responsible for monitoring and managing local air quality to the legislative targets. Consequently, there is growing pressure on local authorities to look for policies and strategies that help to

reduce pollution and improve air quality. This has also lead to the development of urban traffic management and control strategies. However, the implementation of these strategies and the making of urban planning decisions are dependent upon the prediction of the effects of the proposed changes to the ambient pollution concentrations. The effects are likely to be most significant in existing pollution hot-spots where UKNAQS objectives may be exceeded. This requires the use of accurate dispersion models, which are able to reflect the impact of changes in traffic conditions on pollution levels on relatively short time-scales.

Current urban air pollution modelling often involves the use of simplified Gaussian models for the prediction of averaged pollutant concentrations on relatively unresolved numerical solution grids. This approach gives useful qualitative insight into the pollution climate within a city, and can be used in the initial design of long-term traffic management policies. However, it cannot provide short-term predictions of pollution levels, which could be used for population exposure forecasting. The prediction of purely averaged concentrations ignores the possibility that short time-scale peaks in pollution concentrations may have an influence on the health impact of elevated emissions. Therefore, there is a requirement to develop better predictive tools capable of representing the spatial and temporal variability in concentrations of traffic-related pollutants within urban areas. Given the limitations of some existing models it is crucial that the results are interpreted correctly and those recommendations are made with engineering judgement. This would potentially avoid both the incorrect identification of pollution hot-spots and the implementation of inappropriate traffic management measures.

Emission models have recently been developed to take account of traffic characteristics directly from traffic simulations and are capable of calculating emissions produced by vehicles during driving modes, such as accelerating, decelerating, cruising and idling. The purpose of such models is to provide information on proposed traffic management measures. Therefore, dispersion models must be capable or predicting the influence of the short-term variability in emissions and in the impact of traffic on turbulence production. In order to make such predictions, the influence of meteorology, urban topography and traffic on the variability in concentrations of traffic-related pollutants must be understood.

## 1.2. Aims and Objectives

There are currently several approaches to dispersion modelling that are followed, ranging from simple semi-empirical models to Gaussian models through to more complex turbulence models, such as the MISKAM computational fluid dynamics (CFD) model (e.g. Eichhorn, 1996). The development of accurate dispersion models is essential to describing conditions where high emissions and limited dispersion exist. Therefore, these models are particularly useful in locating pollution hot-spots in urban areas. The development and evaluation of a dispersion model for various building and street configurations requires the collection of experimental data.

The aim and objectives of the research undertaken in this study are:

*Aim*

To determine the influence of urban wind flow features and traffic characteristics on the resulting concentrations of a traffic-related pollutant inside narrow streets of a city through field experiments.

*Objectives*

- To obtain simultaneous and continuous measurements of traffic characteristics and wind, turbulence and pollutant concentration fields inside narrow streets;
- To obtain simultaneous measurements of the mean wind speed and direction above roof-level at a suitable background (or reference) location;
- To obtain simultaneous measurements of traffic-produced turbulence (TPT);
- To provide a comprehensive data set from field experiments for the development and evaluation of flow and dispersion models.

The following Chapter provides the research context. Chapter 3 describes the methodology used, while Chapters 4 – 7 present the study findings. Chapter 8 presents the results of a sensitivity study, which used the MISKAM dispersion model. Chapter 9 describes the limitations of the study and gives recommendations for further work, while Chapter 10 presents the final remarks and conclusions.

# CHAPTER 2

# Concentrations of Traffic-Related Pollutants and the Influence of Meteorology, Urban Topography and Traffic – the Context

## 2.1. Introduction

The transport sector is internationally recognised to be a significant source of air pollution. An emphasis has been placed on road traffic and its influence on urban air quality given the potential exposure to a greater number of people. Recently, there have been significant improvements in fuel and engine technology (e.g. electric, fuel-cell and hybrid powered vehicles) and end-of-pipe technology (e.g. catalytic converters). However, air pollution in modern Western cities is still mostly dominated by traffic emissions (Fenger, 1999; Colvile *et al.*, 2001). Traffic-related pollutants directly emitted into the ambient air or indirectly produced through photochemical reactions represent a serious hazard for human health (Hoek *et al.*, 2000).

### 2.1.1. Chapter synopsis

This Chapter will discuss in detail the main traffic-related pollutants. A discussion is also given into why modern Western cities are often prone to areas of locally high concentrations of traffic-related pollutants. These areas are known as pollutant 'hot-spots' and are often Air Quality Management Areas (AQMAs). It is usually within the streets of an AQMA where the influence of meteorology, urban topography and traffic on the variability in concentrations of traffic-related pollutants is most noticeable. These influences will be discussed in turn.

## 2.2. Traffic-Related Pollutants

Several traffic-related pollutants are listed in Table 2.1, which shows the U.K. air quality objectives. The main traffic-related pollutants are carbon monoxide (CO), oxides of nitrogen ($NO_x$), hydrocarbons and particles (e.g. $PM_{10}$ or particulate matter with aerodynamic diameter <10 μm). A more detailed discussion of each traffic-related pollutant is given below.

CO is produced during the incomplete combustion of carbon containing fuels. CO emissions can be reduced by increasing the air/fuel ratio, however, this increases the risk of forming nitrogen oxides (Fenger, 1999), or by using catalytic converters. Traffic-related pollutants are responsible for both acute and chronic effects on human health (WHO, 2003). CO is an asphyxiating pollutant that reduces the ability of blood to carry oxygen around the body to the different organs (Burnett *et al.*, 1998). Increased incidence of congestive heart disease among the elderly and those with pre-existing conditions has been linked to increases in background concentrations of carbon monoxide (Morris *et al.*, 1995). Therefore, acute health impacts may be caused by short-term exposure to high concentrations of CO. However, toxic pollutants such as benzene have a cumulative effect on human health and, consequently, long-term exposure to high concentrations increases the risk for an individual to suffer from leukaemia and lung cancer (e.g. Cicolella, 1997). Other toxic substances emitted by vehicles include aldehydes and ketones, which may also be carcinogenic and cause short-term irritation to the eyes, respiratory tract and skin (Carpenter, 1998).

Combustion also produces a mixture of nitrogen dioxide ($NO_2$) and nitric oxide (NO). Carslaw and Beevers (2004) revealed useful insights into the potential magnitude of primary $NO_2$ emissions from road vehicles (see Section 2.4). Oxides of nitrogen ($NO_x$), as the name suggests, are formed by the oxidation of atmospheric nitrogen during combustion. The primary non-toxic NO is emitted by vehicles, which is subsequently oxidised in the atmosphere to the secondary pollutant $NO_2$. Exposure to $NO_2$ can cause increased susceptibility to viral infections, such as influenza and may irritate the lungs and cause oedema, bronchitis and pneumonia. $NO_2$ exposure may also result in increased sensitivity to dust and pollen in asthmatics.

Table 2.1. Summary of the UK Air Quality Strategy objectives (modified from the UK National Air Quality Archive, 2005).

| Pollutant | Objective | Measured as | Date to be achieved by |
|---|---|---|---|
| **Benzene**<br>All Authorities | 16.25 $\mu g\ m^{-3}$ | Running Annual Mean | 31/12/2003 |
| **Benzene**<br>Authorities in England and Wales only | 5 $\mu g\ m^{-3}$ | Annual Mean | 31/12/2010 |
| **Benzene**<br>Authorities in Scotland and Northern Ireland only[a] | 3.25 $\mu g\ m^{-3}$ | Running Annual Mean | 31/12/2010 |
| **1,3-Butadiene** | 2.25 $\mu g\ m^{-3}$ | Running Annual Mean | 31/12/2003 |
| **Carbon monoxide**<br>Authorities in England, Wales and Northern Ireland only[a] | 10.0 $mg\ m^{-3}$ | Maximum daily running 8 Hour Mean | 31/12/2003 |
| **Carbon monoxide**<br>Authorities in Scotland only | 10.0 $mg\ m^{-3}$ | Running 8 Hour Mean[b] | 31/12/2003 |
| **Lead** | 0.5 $\mu g\ m^{-3}$ | Annual Mean | 31/12/2004 |
| | 0.25 $\mu g\ m^{-3}$ | Annual Mean | 31/12/2008 |
| **Nitrogen dioxide**[c] | 200 $\mu g\ m^{-3}$<br>Not to be exceeded more than 18 times per year | 1 Hour Mean | 31/12/2005 |
| | 40 $\mu g\ m^{-3}$ | Annual Mean | 31/12/2005 |
| **Nitrogen oxides**** | 30 $\mu g\ m^{-3}$ | Annual Mean | 31/12/2000 |
| **Ozone**[*] | 100 $\mu g\ m^{-3}$ | Running 8 hour Mean<br>Daily maximum of running 8 hr mean not to be exceeded more than 10 times per year | 31/12/2005 |
| **Particles ($PM_{10}$) (gravimetric)**[d]<br>All authorities | 50 $\mu g\ m^{-3}$<br>Not to be exceeded more than 35 times per year | 24 Hour Mean | 31/12/2004 |
| | 40 $\mu g\ m^{-3}$ | Annual Mean | 31/12/2004 |
| **Particles ($PM_{10}$)**<br>Authorities in Scotland only[e] | 50 $\mu g\ m^{-3}$<br>Not to be exceeded more than 7 times per year | 24 Hour Mean | 31/12/2004 |
| | 18 $\mu g\ m^{-3}$ | Annual Mean | 31/12/2004 |

| Pollutant | Objective | Measured as | Date to be achieved by |
|---|---|---|---|
| **Sulphur dioxide** | 266 µg $m^{-3}$ Not to be exceeded more than 35 times per year | 15 Minute Mean | 31/12/2005 |
| | 350 µg $m^{-3}$ Not to be exceeded more than 24 times per year | 1 Hour Mean | 31/12/2004 |
| | 125 µg $m^{-3}$ Not to be exceeded more than 3 times per year | 24 Hour Mean | 31/12/2004 |
| | 20 µg $m^{-3}$ | Annual Mean | 31/12/2000 |
| | 20 µg $m^{-3}$ | Winter Mean (01 October - 31 March) | 31/12/2000 |

**Notes:**

a. In Northern Ireland none of the objectives are currently in regulation. Air Quality (Northern Ireland) Regulations are scheduled for consultation early in 2003.
b. The Quality Objective in Scotland has been defined in Regulations as the running 8-hour mean, in practice this is equivalent to the maximum daily running 8-hour mean
c. The objectives for nitrogen dioxide are provisional.
d. Measured using the European gravimetric transfer sampler or equivalent.
e. These 2010 Air Quality Objectives for $PM_{10}$ apply in Scotland only, as set out in the Air Quality (Scotland) Amendment Regulations 2002.

Motor vehicles also emit a wide range of unburned and chemically transformed hydrocarbons (e.g. benzene, toluene, ethane, ethylene, pentane etc.). Particles of condensed carbonaceous material are emitted predominantly by diesel powered vehicles and vehicles that are poorly maintained, although spark ignition engines also produce ultra-fine particles. Particulate matter (PM) was originally determined as soot or black smoke, although more recently the concept of total suspended particulate matter (TSP) was introduced. However, size fractionating has been attempted by measurements of $PM_{10}$ and $PM_{2.5}$ (e.g. Lingard, *et al.*, 2003; Lingard, 2004). Particulate matter irritates mucous membranes and may initiate a variety of respiratory diseases; while fine particles may cause lung cancer and exacerbate morbidity and mortality from respiratory dysfunctions. Suspended particulates can also adhere to carcinogens emitted by motor vehicles (Pfeffer *et al.*, 1995).

A range of air quality standards have recently been introduced in order to reduce the possible health effects associated with the emission of pollutants. Table 2.1 shows the UK air quality objectives for pollutants with respect to different exposure times. For instance, standards are set for benzene as 1-year averages, whereas the standard for CO is based on 8-hour running averages.

In the built environment, population and traffic flows are relatively high. Consequently, human exposure to traffic-related pollutants is likely to be significantly increased. In streets that form part of a busy arterial network of the city, traffic flow is usually high. Furthermore, these streets often have poor dispersion conditions, caused by the combined influence of meteorology, urban topography and traffic characteristics. As a result, high pollution concentrations have been observed in such streets. Areas of locally high concentrations of traffic-related pollutants are known as pollution 'hot-spots' and are often associated with street canyons. The term street canyon is used to describe streets flanked on both sides by buildings (Section 2.6). Pedestrians, cyclists, drivers and residents travelling within many street canyons are likely to be exposed to concentrations of traffic-related pollutants that exceed current air quality standards. Street canyons are, therefore, often located within AQMAs.

## 2.3. Air Quality Management Areas

The Environment Act 1995 Part IV established a statutory framework for local air quality management in the U.K. The Act places a duty upon all local authorities in Wales and Scotland and on London boroughs, district and unitary councils in England to undertake a local air quality review and assessment. This review was to determine whether air quality objectives (as summarised in Table 2.1) were likely to be achieved by the end of 2005. An AQMA must be designated where an objective is unlikely to be achieved by the end of 2005, according to the local authority. The local authority is then obliged to formulate a local Air Quality Action Plan (AQAP) to improve the air quality. Therefore, many local authorities are currently applying traffic management strategies for pollution hot-spots projected to exceed these targets. These may include: controlling traffic signals; re-locating traffic queues during congested periods; and the introduction of low emission zones and congestion

charging (see Joumard *et al.*, 1996; Fenger, 1999). In many instances local authorities aim to predict the possible influences on roadside pollutant concentrations using air quality dispersion models before applying such measures (see Section 2.5).

The study presented in this thesis is based on results collected from a field experiment conducted inside two street canyons in the city of York, U.K (see Chapter 3). For several years the local authority has had concerns about the reduction in the natural ventilation that may occur within these streets due to the so-called *street canyon effect* (Section 2.6). Consequently, the local authority has designated the two streets as part of York's AQMA. Additionally, several streets within the AQMA have been declared pollution hot-spots, with levels of nitrogen dioxide ($NO_2$) predicted to exceed the annual average objective of 40 $\mu g\ m^{-3}$ by the end of 2005 (City of York Council [CYC], 2005a). The streets included in York's AQMA are shown in red in Figure 2.1. The two street canyons used in the full-scale field campaign presented in the following Chapters are Bootham and Gillygate are also shown. On Gillygate, 66% of $NO_x$ ($NO+NO_2$) is estimated by CYC to derive from traffic-related emissions (see http://www.york.gov.uk/environment/airquality/Gillygate.pdf).

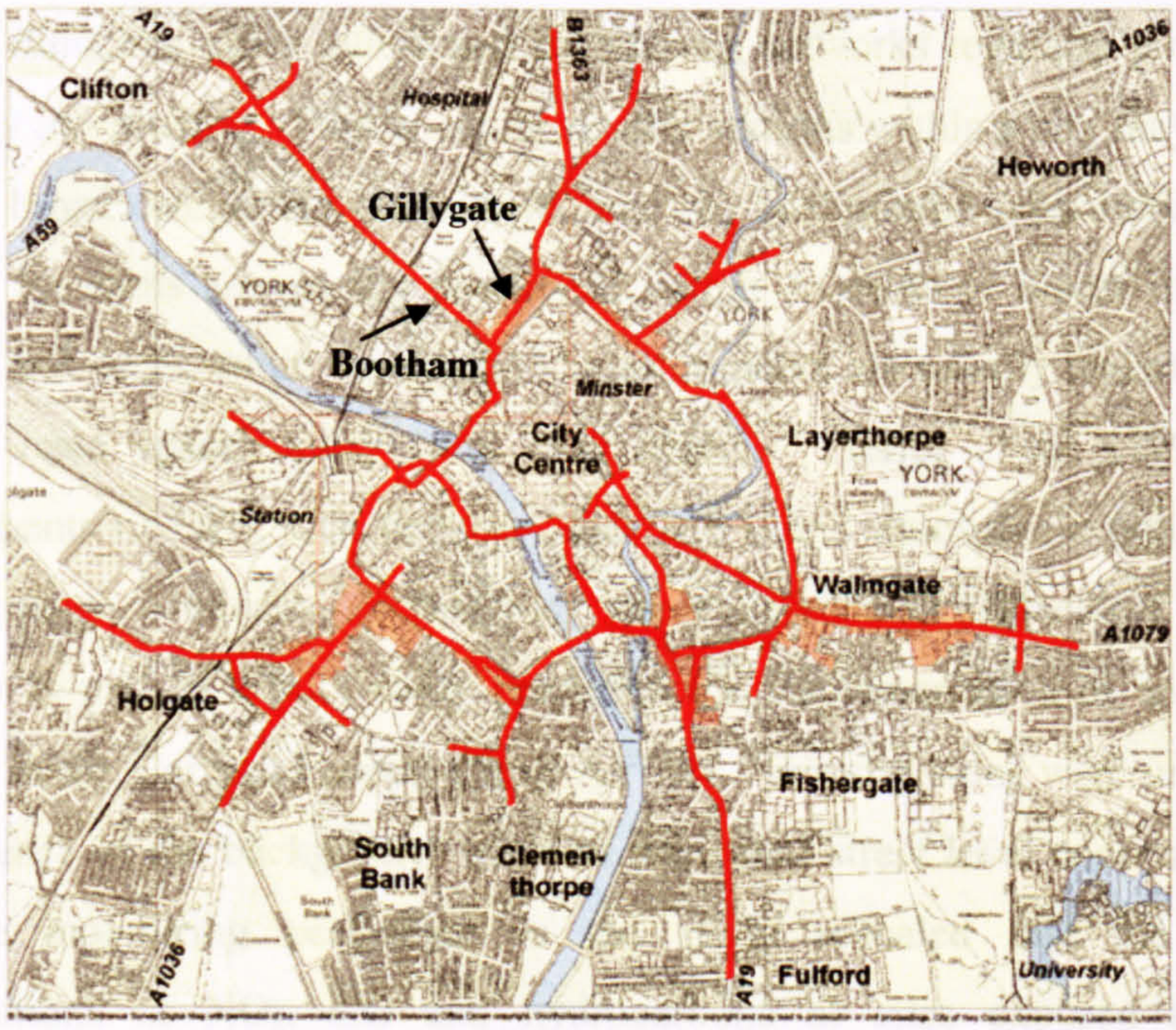


Figure 2.1. The Air Quality Management Area (AQMA) declared for $NO_2$ by the City of York Council (CYC, 2005a).

Details of CYC's Air Quality Action Plan are shown in Table 2.2 as an example of a local authority working towards reducing concentrations of $NO_2$ (CYC, 2005b). Further details of the CYC's Air Quality Action Plan (AQAP) and Local Air Quality Management (LAQM) initiatives can be found on their website (http://www.york.gov.uk).

Table 2.2. The Air Quality Action Plan (AQAP) measures for reducing $NO_2$ concentrations within York's Air Quality Management Area (CYC, 2005b).

1. Reducing the need to travel
2. Encouraging walking and cycling
3. Encouraging use of public transport
4. Reducing the number and distance of trips within the AQMA
5. Encouraging the use of alternative fuels and smaller more fuel efficient vehicles
6. Improving traffic management and reducing congestion
7. Reducing emissions from heavy goods vehicles and buses
8. Reducing emissions from non-transport related sources

## 2.4. Air Quality Monitoring

In many European cities automated monitoring networks regularly provide detailed air quality information. Permanent air quality stations within a city may be classified into two broad categories: (a) kerbside and (b) background measurement locations. Kerbside locations are usually positioned within AQMAs or places of expected air pollution hot-spots, while background measurements are usually undertaken in parks or other open spaces away from road traffic. Pfeffer *et al.* (1995) presented measurements of $NO_2$, CO, benzene, soot and other atmospheric pollutants from a field campaign conducted in two busy street canyons in Düsseldorf and Essen in Germany as part of a pilot study preparing the implementation of new regulations included in the German Federal Clean Air Act. Investigations were undertaken into the influence of the background wind on measured street level concentrations. The extensive monitoring performed in the study revealed that the ambient air concentrations of $NO_x$, CO and hydrocarbons at sites exposed to traffic are considerably higher than at other urban measuring points, which indicates that road traffic is the most important emission source of these compounds. The mean

concentrations of CO and $NO_x$ measured in the Düsseldorf street canyon were found to be more than three and five times higher, respectively, than the mean concentrations at urban background locations. For lead and polycyclic aromatic hydrocarbons the differences are less significant but still discernible. The annual mean concentration of carcinogenic benzene at the Düsseldorf station (reaching 30 μg $m^{-3}$) was six times higher than the overall background level in the Rhine-Ruhr area. According to Pfeffer *et al.* (1995), the carcinogenic risk at sites exposed to traffic, however, is primarily caused by diesel engine emissions of PM.

Gaseous pollutants may be monitored continuously using standard gas analysers or passive electrochemical cells (see Chapter 3). Although not continuous, gaseous pollutants, such as $NO_2$, may also be monitored using diffusive or pumped sampling using tubes filled with an appropriate adsorbent (Laxen and Noordally, 1987). The response times (i.e. the time over which the sample is taken) for standard gas analysers and instruments fitted with electrochemical cells are sufficiently sensitive and fast to give real time measurements of CO, $NO_x$ and ozone ($O_3$). The response times of these instruments are typically 1 – 2 minutes (Vardoulakis *et al.*, 2003).

Diffusive samplers have relatively long response times, usually in the order of weeks, which make them less suitable for observing pollutants responsible for short-term health effects. Furthermore, the long averaging periods prevents comparisons between the diurnal traffic flow average and at even shorter time scales, the influence of meteorological parameters, such as the mean wind flow and turbulence. However, the overall suitability of using passive diffusion tube samplers depends on the objectives of the study. For instance, Laxen and Noordally (1987) demonstrated that as the diffusion tube samplers are portable devices that can easily be attached to street furniture such as lampposts and do not require an electrical power supply they are particularly useful for spatial distribution measurements of $NO_2$. In addition to being suitable for measuring vertical and horizontal concentration distributions, diffusion tubes are also a useful way of measuring long-term pollution trends, which are important for review and assessment procedures undertaken for any AQMA.

Diffusive $NO_2$ sampling has been used in several other field experiments (e.g. Hewitt, 1991; Monn *et al.*, 1997) for establishing the spatial variability of air pollution in urban areas. A criticism of this might be that although $NO_2$ is easily monitored using passive tubes it is not the best indicator for traffic-related pollution. This is because $NO_2$ only represents a small fraction (potentially less than 10%) of the total $NO_x$ directly emitted from traffic. In addition to this, it is highly reactive within very short transport distances and, therefore, is not expected to correlate strongly with other more conservative pollutants like CO and benzene.

Monitoring data from a busy street canyon location in central London and a background site have been used to estimate the potential importance of primary $NO_2$ emissions from road vehicles travelling along the street canyon (Carslaw and Beevers, 2004). By considering the difference in the total 'oxidant', OX (or $NO_2$+$O_3$) between the two sites, insight has been gained into the potential magnitude of primary $NO_2$ emissions from road vehicles. Their findings have shown that the day-of-the-week and hour-of-the-day variation in OX closely matches some attributes of the variation in road traffic flows and vehicle composition. In particular, the variation in OX compares well the variation in estimated $NO_X$ emissions from diesel vehicles by hour-of-the-day and day-of-the-week.

In recent years, however, the development of instruments fitted with passive electrochemical cells has provided a cheaper alternative to the standard gas analysers for continuous measurements of pollutants such as CO, as discussed in Chapter 3. Furthermore, their portability has also allowed for their attachment to street furniture such as lampposts where, in the past, diffusion tube samplers may have been located. Therefore, instruments fitted with passive electrochemical cells have provided a useful method of continuously measuring traffic-related pollutants in street canyons, whilst allowing for the investigation of vertical and horizontal concentration distributions. An additional benefit is associated with the relatively short response times, which allow for the results to be averaged over short time periods in order to compare to the regulatory standards or meteorological and traffic parameters.

It was mentioned earlier that the primary source of CO in street canyons is petrol engine vehicles (Derwent *et al.*, 1995). An additional benefit to measuring CO in

street canyons is related to the fact that it can be regarded as being an inert 'tracer' due to the very short distance between source and receptor and its low reactivity on these short timescales. This is not the case with $NO_2$, which rapidly dissociates in the presence of light, or with NO, which reacts very quickly with ozone (Palmgren *et al.*, 1996). The chemical lifetime of CO is very long (several weeks) compared to other pollutants (Dennis *et al.*, 1996). Therefore, CO can be used as a traffic-related tracer in a study into the influence of dispersion within a street canyon. Furthermore, the mean diurnal concentrations of other traffic-related pollutants such as $NO_x$ (Väkevä *et al.*, 1999) and particle number concentration in the range 0.01 to 10μm (Penttinen *et al.*, 2001, Ketzel *et al.* 2003) have been found to correlate reasonably well with CO close to traffic sources allowing it to be used in the present study as an effective traffic-related tracer. Longley *et al.* (2003) conducted a 2-week measurement campaign to measure size-segregated aerosol in the size range 4.6 nm – 10 μm at a fine timescale (10-minute resolution) in a typical street canyon in Manchester. They discussed their results with particular attention to the influence of background wind direction and traffic flow on number concentrations (see Section 2.6.2.2).

The turbulent mixing of the volume of air inside the street canyon (Section 2.6) implies that any two measurements of a pollutant conducted in close proximity to each other in a street can differ significantly (Croxford *et al.*, 1996). Furthermore, traffic congestion and the characteristic stop-start traffic flows may also provide substantial variability with distance from a traffic-signal controlled intersection (see also Goldstein and Landovitz, 1977a,b; Tate *et al.*, 2005a). It is important to consider these effects in any investigation into the spatial and temporal variability in concentrations of a traffic-related pollutant.

## 2.5. Air Quality Modelling

Dispersion models are now widely used in the assessment of roadside air quality by providing predictions of present and future air pollution concentrations as well as temporal and spatial variations. Some models can also give useful insights into the in-canyon flow and dispersion characteristics. In addition to helping interpret monitoring data, dispersion models are also used in air quality and traffic

management assessments, urban planning, pollution forecasting and population exposure studies. Models have been classified by Vardoulakis *et al.* (2003) into groups according to their physical or mathematical principles e.g. reduced-scale box, Gaussian and computational fluid dynamics (CFD). They may also be classified according to their complexity e.g. screening, semi-empirical and numerical. However, such classifications are not perfect as many categories are often overlapping.

### 2.5.1. Wind flow modelling

The basic equations used to describe the mean flow follow the continuity equation and assume isothermal (i.e. neutral) conditions for an incompressible fluid:

$$\frac{\partial u_i}{\partial x_i} = 0; \tag{2.1}$$

and the steady state momentum conservation equation:

$$u_j \frac{\partial u_i}{\partial x_j} = \frac{\partial}{\partial x_j}\left[ \nu \frac{\partial u_i}{\partial x_j} - \overline{u_i' u_j'} \right] - \frac{1}{\rho}\frac{\partial p}{\partial x_i}; \qquad i = 1,2,3 \tag{2.2}$$

where

- $u_i$ are the three velocity components ($i$=1,2,3 or $x$,$y$,$z$);
- $u_i'$ are the turbulent fluctuation components (deviations from the mean velocity, where over bar refers to time averaging);
- $p$ is pressure;
- $\rho$ is density of air;
- $\nu$ is kinematic molecular viscosity.

In Equations (2.1) and (2.2) the summation convention of repeated indices is implied. The left-hand side of Equation (2.2) describes the advection of mean momentum, while the right-hand side represents the diffusion and pressure forces. Equation (2.2)

cannot be solved directly as it contains new unknowns, which are the Reynolds stresses, $\overline{u_i'u_j'}$. The problem, therefore, is to define an appropriate parameterisation of these stresses, which is often called the *closure concept* as is described in more detail in Chapter 3 (see also Berkowicz *et al.*, 1997a). The wind flow and dispersion modelling (described in the following Section) refer to steady-state rather than transient conditions.

### 2.5.2. Dispersion modelling

The modelling of the dispersion of pollutants in a street canyon is inevitably connected to the modelling of the wind flow and the mathematical principles are basically the same, i.e. the governing equation is the steady-state mass conservation (continuity) equation for a scalar:

$$u_j \frac{\partial c}{\partial x_j} = -\frac{\partial}{\partial x_j} \overline{c'u_j'} + \beta, \tag{2.3}$$

where $c$ denotes the mean concentration and $c'$ is the deviation from the mean, while $\beta$ represents all possible sources and sink terms, such as emissions and chemical reactions. As described for flow modelling, the key problem is once again determining the parameterisation of the turbulent flux term $\overline{c'u_j'}$ and the most common approach is based on the eddy diffusivity concept:

$$\overline{c'u_j'} = -K_t \frac{\partial c}{\partial x_j}, \tag{2.4}$$

where $K$ is the eddy diffusivity coefficient and is usually assumed to be equal to the eddy viscosity, $\nu_t$ (Chapter 3). The mean wind fields and diffusivity coefficients supplied by a particular flow model and Equation (2.3) can be solved numerically subject to appropriate boundary conditions (Berkowicz *et al.*, 1997a). Methods whereby the diffusivity coefficients can be estimated include, among others, the use of the mixing length concept (Lee and Park, 1994) or the $k$-$\varepsilon$ method (Johnson and Hunter, 1995).

However, another approach is based on the stochastic Lagrangian trajectory model and avoids using the diffusivity 'closure' shown in Equation (2.3) for modelling pollutant dispersion. Concentrations of pollutants are calculated by tracing the movement of particles as if they were air parcels. The trajectories are calculated using the mean flow fields upon which a random fluctuation component is superimposed. The statistics of the fluctuating component depend on the turbulence characteristics of the flow and can be derived from the flow model (Berkowicz *et al.*, 1997a). Some examples of stochastic modelling of traffic-related pollutants can be found in Lamb *et al.*, (1979), Schorling (1994), Lanzani and Tamponi (1995), Addison *et al.* (2000), Jicha *et al.* (2000), Xia and Leung (2001a,b) and Smalley *et al.* (2004a).

The MISKAM CFD model consists of a 3-D non-hydrostatic flow model and an Eulerian dispersion model (Eichhorn, 1996) and uses $k$-$\varepsilon$ turbulence closure, where $k$ refers to turbulence kinetic energy (TKE) and $\varepsilon$ is the dissipation rate. MISKAM uses the complete 3-D equations of motion of the flow field and the advection-diffusion equation to determine the concentrations of substances with neutral density (see Sahm *et al.*, 2002). The model, therefore, calculates the stationary flow and pressure field, diffusion coefficients and the concentration field in an area of 500 x 500 m (usually 100 x 100 cells or more in a non-equidistant grid). As with most CFD codes, post-processing of the model outputs produces vector plots of the flow field and contour plots of the concentration field (see Ketzel *et al.*, 2002a). A more detailed description of the MISKAM model is given in Chapter 3. More information can be found on the TRAPOS website (http://www.dmu.dk/Atmospheric-Environment/trapos).

Numerical models that require solving the diffusivity formulation shown in Equation (2.3) or stochastic models with the corresponding flow models are still too complex for practical applications, such as in the review and assessment procedures undertaken for AQMAs. However, they are particularly useful research tools that provide significant insight into in-canyon flow structures and dispersion characteristics that may also be parameterised into semi-empirical models. The Danish model OSPM is a well-known example of a semi-empirical operational street

canyon model (Berkowicz *et al.*, 1997a; Berkowicz, 2000a). OSPM is based on similar principles as the Canyon Plume Box-Model built by Yamartino and Wiegand (1986). Concentrations of traffic-related pollutants are calculated using a combination of a plume model for direct contribution from emissions and a box model for the recirculating flow that develops inside street canyons during skimming flow (Section 2.6). OSPM makes use of a simplified parameterisation of in-canyon flow and dispersion conditions and was deduced from the extensive analysis of experimental data and model tests (Berkowicz *et al.*, 1996). OSPM also includes parameterisation of traffic-produced turbulence (Berkowicz *et al.*, 1997a) and is only one of a few street canyon models to do so (see Chapter 6).

Ketzel *et al.* (2000) undertook mathematical simulations of pollutant dispersion within street canyons using the relatively simple OSPM and the more complex MISKAM code. The results were compared with wind tunnel simulations and field measurements from two permanent monitoring stations in Copenhagen and Hannover. Comparison of the model results, in terms of normalised concentrations, reveals discrepancies between the models, particularly for shorter averaging times and smaller domains. It was found that although the microscale model MISKAM generally performed better than the simple model OSPM there are more parameters that are required to be set by the user in the former model, which may lead to uncertainties in the model results. It was concluded that for microscale models to be a useful practical tool, the procedure of validation needs to be improved and made more transparent by making model input data and processing programs freely available to all users.

Dispersion model predictions are mostly a function of meteorology, street canyon geometry, receptor location, traffic flow and emission factors. The performance of any model clearly depends on the quality of the inputs. Therefore, the acquisition and processing of experimental data is a crucial part of any modelling study. For a more complete review of the dispersion models used in street canyon studies see Berkowicz *et al.* (1997a) and Vardoulakis *et al.* (2003).

## 2.6. Street Canyon Studies

In the past there have been several modelling and experimental field studies that have investigated the pollutant dispersion and transformation patterns (chemical reactions) within street canyons. Although many of the studies had different objectives, different monitoring and modelling techniques have been used. This Section aims to give insight into the influence of meteorology, urban topography and traffic on the variability in concentrations of traffic-related pollutants in the light of the different techniques used. Some studies in the past were purely experimental, i.e. they were exclusively based on full-scale or reduced-scale measurements. Other studies have been entirely theoretical and have focussed on the investigation of different background wind flow regimes and canyon geometries using mathematical models, such as those described in Section 2.5. However, recent studies have commonly combined experimental work and mathematical modelling. For instance, the European research network TRAPOS (Optimisation of Modelling Methods for Traffic Pollution in Streets) has given new insights into a number of issues related to street canyons, many of which will be discussed in turn in the following Section.

However, it should be mentioned that few full-scale experiments have been conducted that have allowed for simultaneous and continuous measurements of the background wind and in-canyon wind, turbulence, pollutant concentrations and traffic characteristics. The simultaneous and continuous monitoring of these parameters inside street canyons of differing geometry would allow for the investigation into the relative importance of the factors influencing high roadside pollutant concentrations. The following Section will describe in detail why this is the case.

### 2.6.1. Street canyon geometry

Street canyons are usually relatively narrow streets with buildings along both sides forming continuous flanks with no significant openings (Nicholson, 1975). However, the term street canyon has also been used more widely to describe much wider streets and even some boulevards with rows of trees on each side of the road (e.g. Sini *et al.*, 1996; Vardoulakis *et al.*, 2002). The term has also been used to describe streets with

openings along the walls of the canyon, particularly where side streets join the study canyon (e.g. Nielsen, 2000).

Therefore, it is useful to express the dimensions of a street canyon by its aspect ratio, or the height (*H*) of the canyon divided by the width (*W*). A regular street canyon has *H/W* of ~1.0 and no significant openings along the walls. A wider boulevard or avenue canyon would have a lower *H/W* of ~0.5. On the other hand, a deep street canyon may have *H/W* of ~2.0. Furthermore, it is often useful to express the distance between two major intersections along a street canyon, or the length, *L*, of the canyon. Short street canyons usually have *L/H* of ~5.0 (e.g. Kastner-Klein *et al.*, 2004). Street canyons are also often classified according to their symmetry, with symmetric canyons having buildings of approximately the same height flanking the street. Asymmetric street canyons, on the other hand, describe significant differences in building height.

### 2.6.2. The influence of meteorology

#### *2.6.2.1. Background winds and in-canyon flow features*

The climate of street canyons is primarily controlled by the micro-meteorological effects of urban geometry rather than the mesoscale forces controlling the climate of the boundary layer (Hunter *et al.*, 1992). Much attention has been directed to the study of the various street canyon airflow regimes (DePaul and Sheih, 1986; Hussain and Lee, 1980; Nakamura and Oke, 1988; Oke, 1987; Johnson and Hunter, 1999), since airflow is responsible for the transport of properties such as turbulence, pollutants, heat and moisture.

Understanding urban climates is critically tied to notions of scale and boundary layer development (Oke, 1987), as illustrated in Figure 2.2. At the smallest scale, which includes individual elements, each building, tree or road creates its own microclimate. Because the city usually possesses repetitive structures, such as rows of buildings, these elements are recombined into larger microscale climate units such as street canyons which generate their own flow features, e.g. across-canyon recirculating flow

(Figure 2.2c). A more detailed discussion of this flow structure and other in-canyon flow features will be given below. It should be mentioned that as these flow features exist beneath roof-level this layer is called the urban canopy layer (UCL) following the analogy with plant stands. A larger neighbourhood comprising several street canyons plus their intervening buildings, gardens and courtyards creates a local scale climate which extends horizontally, but is restricted to the UCL (Figure 2.2b).

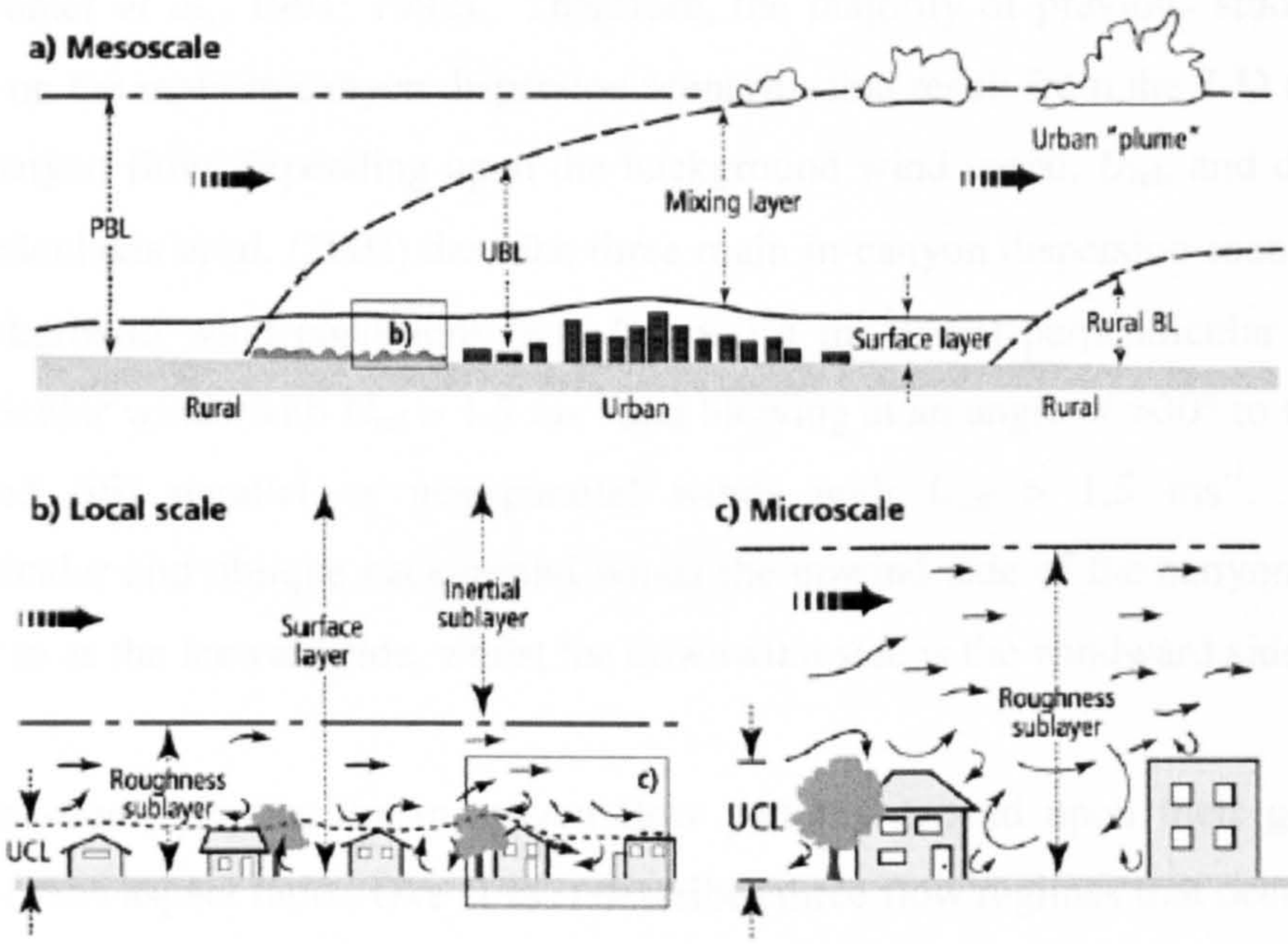


Figure 2.2. Schematic of the urban boundary layer including its vertical layers and scales. The Urban Boundary Layer (UBL) and Urban Canopy Layer (UCL) are shown (Piringer *et al.*, 2002).

The influences of each element also extend above roof-level as a jumbled set of plumes and wakes in the roughness sublayer (see Oke, 1987). Due to the mixing of turbulence these eventually merge to form a more horizontally homogeneous surface layer in which micrometeorological theory for extensive homogeneous surfaces applies (Figure 2.2b,c; Oke, 1987). Distinct urban terrain zones (i.e. areas of different urban topography, such as the type and density of buildings) within a city produce new internal boundary layers, which will form at each zone border. These are mixed together to form the urban boundary layer (UBL) of the whole city (Oke, 1987). This is a mesoscale phenomenon within which the air shows the integrated presence of the city. However, the present study will explore the flow structures that occur at the microscale, i.e. within street canyon environments.

In street canyon studies a distinction should be made between the above-roof or background wind flow and the in-canyon or cavity wind flow (Dabberdt *et al.*, 1973). The emphasis has usually been on the supposed two-dimensional (2-D) nature of the flows and the assumption made that most of the important features can be explained in those terms. For example, in numerical studies the threshold *H/W* ratios for the transition between flow regimes have been evaluated by investigating changes in flow patterns in vertical cross-sections at mid-canyon level aligned with the undisturbed flow (Hunter *et al.*, 1991; 1992). Therefore, the majority of previous studies have focused on the main in-canyon dispersion scenarios that result from the 2-D nature of the in-canyon flow, depending upon the background wind speed, $U_{ref}$, and direction, $\theta_{ref}$. Vardoulakis *et al.* (2003) describe three main in-canyon dispersion scenarios: (i) low background wind conditions (e.g. $U_{ref} \leq 1.5$ ms$^{-1}$); (ii) perpendicular or near-perpendicular winds with $U_{ref} > 1.5$ ms$^{-1}$ and blowing at an angle of >30° to the street axis; and (iii) parallel or near-parallel winds with $U_{ref} > 1.5$ ms$^{-1}$. During perpendicular and oblique background winds the upwind side of the canyon is often referred to as the leeward side, whilst the downwind side is the windward side.

In urban street canyons the in-canyon flow patterns depend upon their geometry, especially the aspect ratio. Oke (1987) describes three flow regimes that occur during perpendicular background winds for street canyons of differing aspect ratios (Figure 2.3). Figure 2.3a shows *isolated roughness* flow for street canyons with widely spaced buildings (i.e. $H/W$ <0.3) and essentially act as isolated roughness elements as there is enough distance for the air to flow downwind of the first building before encountering the next obstacle. Figure 2.3b shows that as buildings become more closely spaced ($H/W \approx 0.5$) the disturbed in-canyon airflow has insufficient distance to readjust before encountering the downwind building, causing *wake interference* flow. Figure 2.3c shows the in-canyon flow features associated with regular street canyons ($H/W \approx 1.0$). During perpendicular winds the majority of the flow skims over the cavity of the canyon, producing the *skimming* flow and characteristic single-across canyon recirculating vortex with a horizontally-aligned axis (see Hunter *et al.*, 1991; 1992).

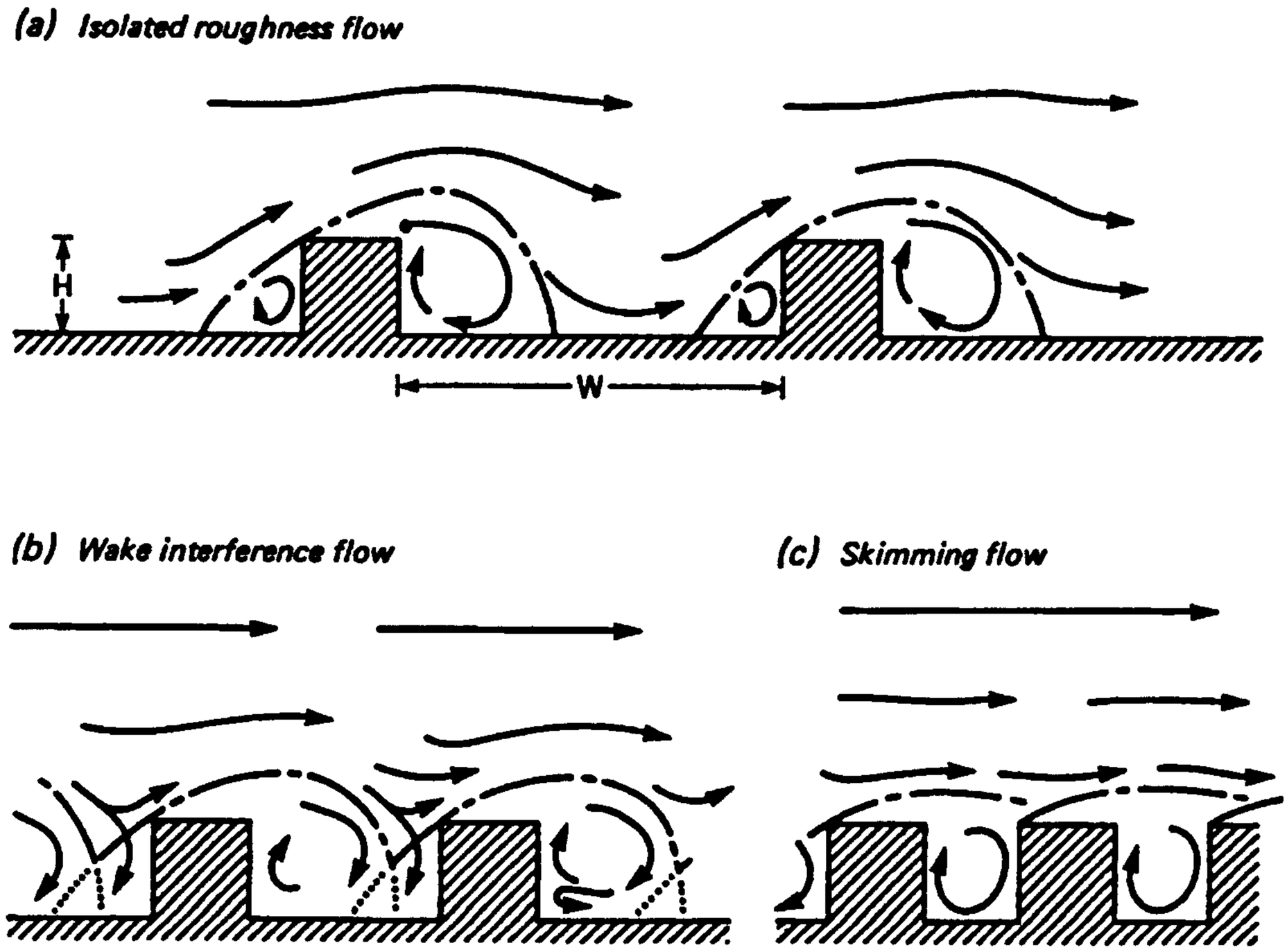


Figure 2.3. Flow regimes associated with perpendicular background winds in street canyons with different aspect ratios (Oke, 1987).

The archetypal street canyon recirculating flow of the type shown in Figure 2.3c consists of a turbulent shear flow above a rectangular cavity during perpendicular background winds. The single across-canyon recirculating flow with a horizontally-aligned axis is also illustrated three-dimensionally in Figure 2.4b. Providing that the background wind speed is strong enough (e.g. $U_{ref} > 1.5 - 2$ m s$^{-1}$) a recirculating flow with a horizontally-aligned axis is established inside a regular street canyon ($H/W \approx 1$) and is driven by momentum transport from the shear layer aloft. Vachon et al. (2000) stated that the across-canyon recirculating vortex associated with skimming flows was not observed for background wind speeds lower than a threshold of between 0.9 and 1.2 m s$^{-1}$ during the field campaign conducted in a street canyon in Nantes, France. However, Vachon *et al.* (2002) present data that suggests that a somewhat weakened recirculating flow may still form during weak perpendicular background winds. This is supported by evidence presented in Chapter 6, which suggests that a recirculating flow still developed inside a street canyon during $U_{ref} \leq 1.2$ m s$^{-1}$.

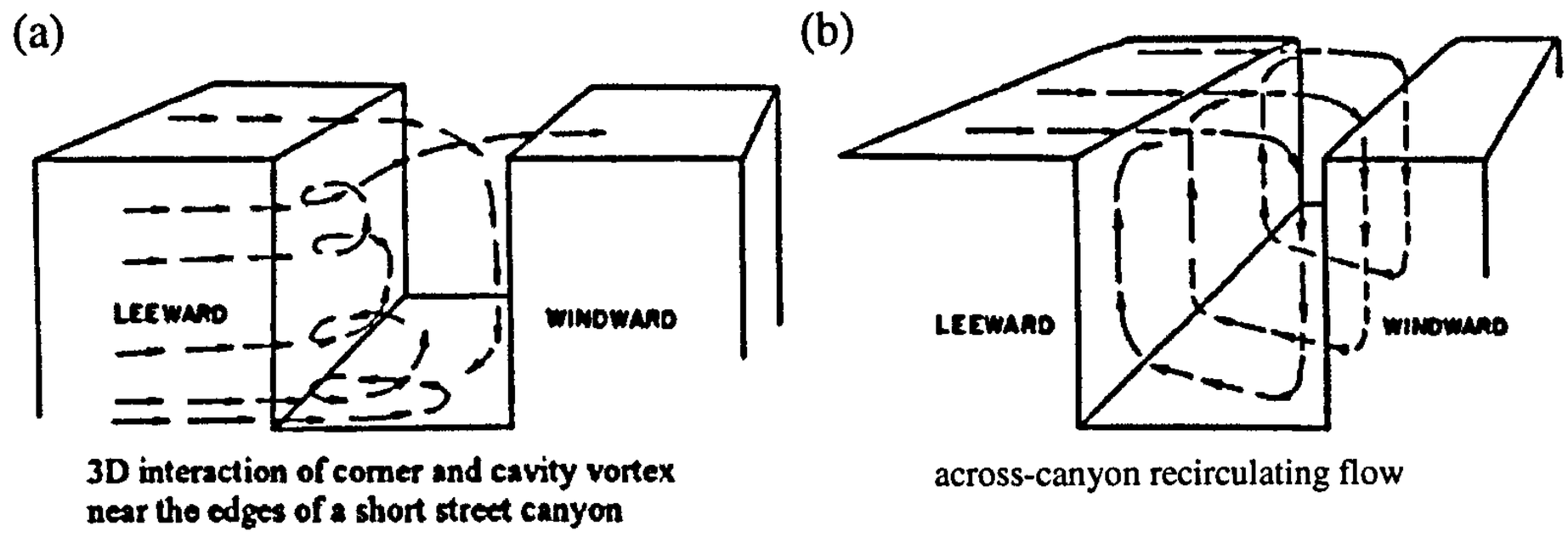


Figure 2.4. Flow inside a street canyon during (a) oblique and (b) perpendicular background winds (adapted from Hoydysh *et al.*, 1974).

Figure 2.4b shows that during skimming flow regimes the street level across-canyon flow is opposite to the direction of the above-roof flow (i.e. towards the leeward side). Typically, the recirculating velocities relative to the above-roof level wind speed are in the order of 0.33 – 0.5 (Nakamura and Oke, 1988) and the turbulence intensities are in the order of 0.1 (see Britter and Hanna, 2003). However, the mean in-canyon wind speed and turbulence will clearly be canyon-specific and will depend upon its aspect ratio, *L/H* ratio, building and roof geometries and the presence of additional roughness elements, such as signs, trees and bus shelters etc. The turbulence intensities measured on the leeward side of the canyon, therefore, may be higher relative to the above-roof turbulence in regular street canyons than in deeper ones.

The recirculating flow, however, is neither steady nor symmetric. The asymmetric recirculating flow is caused by stronger downdraughts on the windward side and weaker, less extensive updraughts on the leeward side. It is also possible that a corner vortex with a vertically-aligned axis may intermittently form within the street canyon during oblique background winds (Figure 2.4a), which is likely to influence the across canyon recirculating flow. This would be particularly the case in short street canyons when the background wind directions switch between perpendicular and oblique to the street axis. Intermittent corner vortices with vertically-aligned axes may also develop inside long and deep street canyons simultaneously with a single across-canyon recirculating flow with a horizontally-aligned axis, as shown schematically in Figure 2.5.

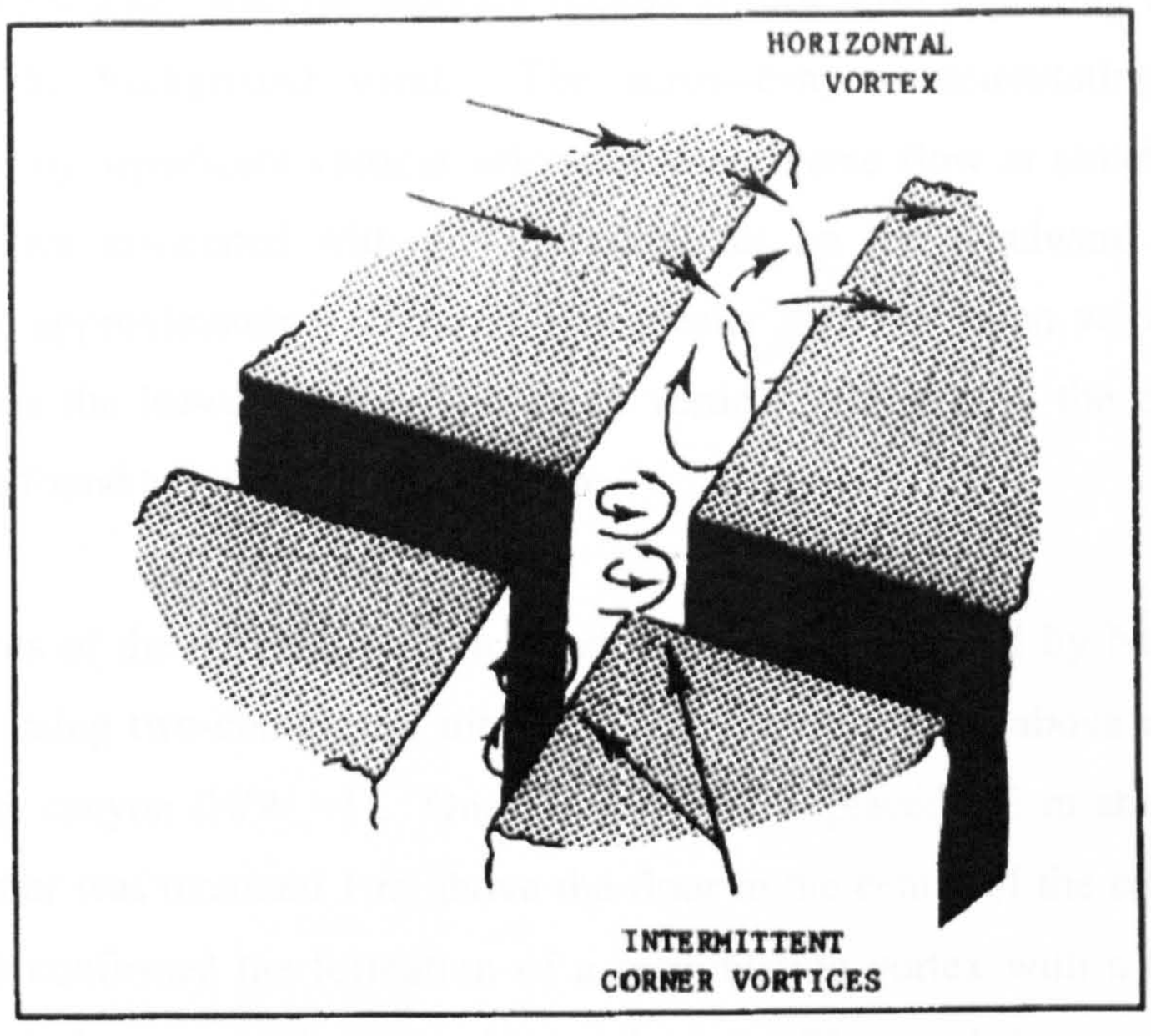


Figure 2.5. Flow features inside a deep street canyon, showing a single across-canyon recirculating vortex and intermittent corner vortices (Hoydysh and Dabberdt, 1988).

Direct measurements of wind flow and turbulence inside street canyons are relatively rare and the results have in the past sometimes been inconclusive. This is due to the fact that only a few point measurements of the wind are usually available and they may be influenced by street furniture (e.g. bus shelters, signs, kiosks) in the street (Berkowicz *et al.*, 1997a). Therefore, it is often not possible to use such measurements to determine the 3-D structure of the in-canyon flow. However, some street canyons without these additional roughness elements are more suited for measurements of the in-canyon wind and turbulence fields, so long as there are several instruments located in an appropriate array.

In the experiment inside a deep street canyon ($H/W \approx 1.3$) conducted by DePaul and Sheih (1986) the mean wind velocities were determined by the analysis of tracer balloons that were released in the canyon and photographed in rapid sequence. The balloon trajectories showed the formation of a recirculating flow with a horizontally-aligned axis within the canyon during perpendicular background winds of $U_{ref} > 1.5 - 2.0$ m s$^{-1}$. An important feature of the in-canyon flow pattern illustrated in Figure 2.3c and Figure 2.4b is that the vertical extent of the cell did not seem to occur

beyond the roof level, with the velocity vectors at roof level appearing to be almost parallel to the background wind. The across-canyon recirculating flow was characterised by significant vertical velocities and reverse flow at street level. The mean velocities associated with the downdraughts on the windward side of the canyon were approximately a factor of two greater than the mean velocities in the updraughts on the leeward side. The mean vertical velocities in the centre of the canyon were found to be approximately zero.

Measurements of the mean in-canyon wind field were conducted by Nakamura and Oke (1988) using two-component ultrasonic anemometers both above and within a regular street canyon (H/W $\approx$1). One instrument was placed 3.6 m above the roof, while the other was mounted 1 m above the floor in the centre of the canyon. Their observations confirmed the formation of a recirculating vortex with a horizontally-aligned axis during perpendicular background winds. The wind flow measured at the floor of the canyon was approximately a 'mirror reflection' of the airflow aloft. During $U_{ref}$ >2 m $s^{-1}$ the street level wind speed was found to be ~2/3 lower. This is in reasonable agreement with the observations of DePaul and Sheih (1986).

The reflection of the wind off the windward canyon wall that was observed during skimming flow conditions (see Nakamura and Oke, 1988; Johnson and Hunter, 1999), revealed that the flow at street level opposed the direction of the above-roof flow (see also Berkowicz *et al.*, 1997a). The reflection is conceptualised in Figure 2.6 where the long dashed arrow indicates true mirror reflection, while the short dashed arrows indicate alternative angles of reflection. According to Johnson and Hunter (1999), a general along-canyon flow is established within the canyon due to the oblique nature of the approach flow, which increases pressure on the windward canyon wall and decreases pressure on the leeward canyon wall. They postulate that this along-canyon component adds momentum to the flow as it enters the canyon at roof level. Once that flow is entrained within the canyon, along-canyon momentum is removed due to friction on the canyon surfaces. This reduction in momentum is less than the increase in momentum at the canyon top. This clearly demonstrates that 3-D flow effects in real street canyons are likely to add a certain amount of complexity to skimming flow regimes of the type described by Oke (1987). During background winds that are

oblique to the street axis, this reflection is likely to induce an along-canyon helical flow.

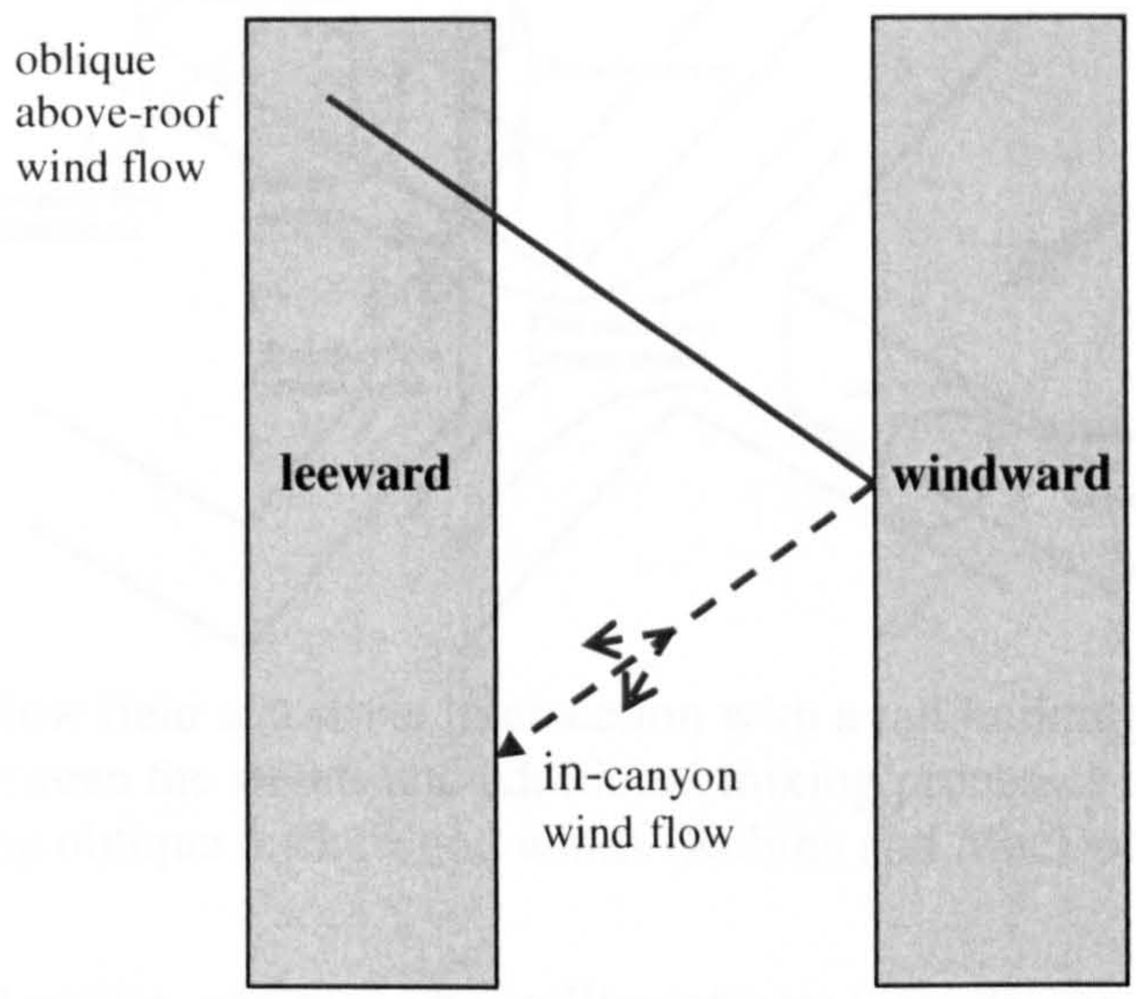


Figure 2.6. Schematic of the reflection off the windward canyon wall during oblique background winds showing along- and across-canyon flow (adapted from Johnson and Hunter, 1999).

In addition to strong along canyon flow components, helical street canyon flows are by nature recirculating phenomena. Therefore, they will also produce street level flow reversal relative to the above-roof wind direction, as shown in Figure 2.7. The oblique wind aloft will therefore drive the recirculation inside the canyon.

Background winds that are parallel to the street axis are likely to produce strong along-canyon channel flows. In the field experiment conducted by Nielsen (2000), parallel background winds were found to enhance the efficiency of the ventilation as a result of turbulent winds causing pulsating circulation patterns. Figure 2.7 also shows that at intersections there are significant lateral exchanges in the airflow with connecting streets. Clearly, these areas of relatively high flow exchange will have significant influences on the resulting concentrations of traffic-related pollutants, particularly as intersections are associated with elevated emission rates due to accelerating driving modes (see Sections 2.6.2.2 and 2.6.3).

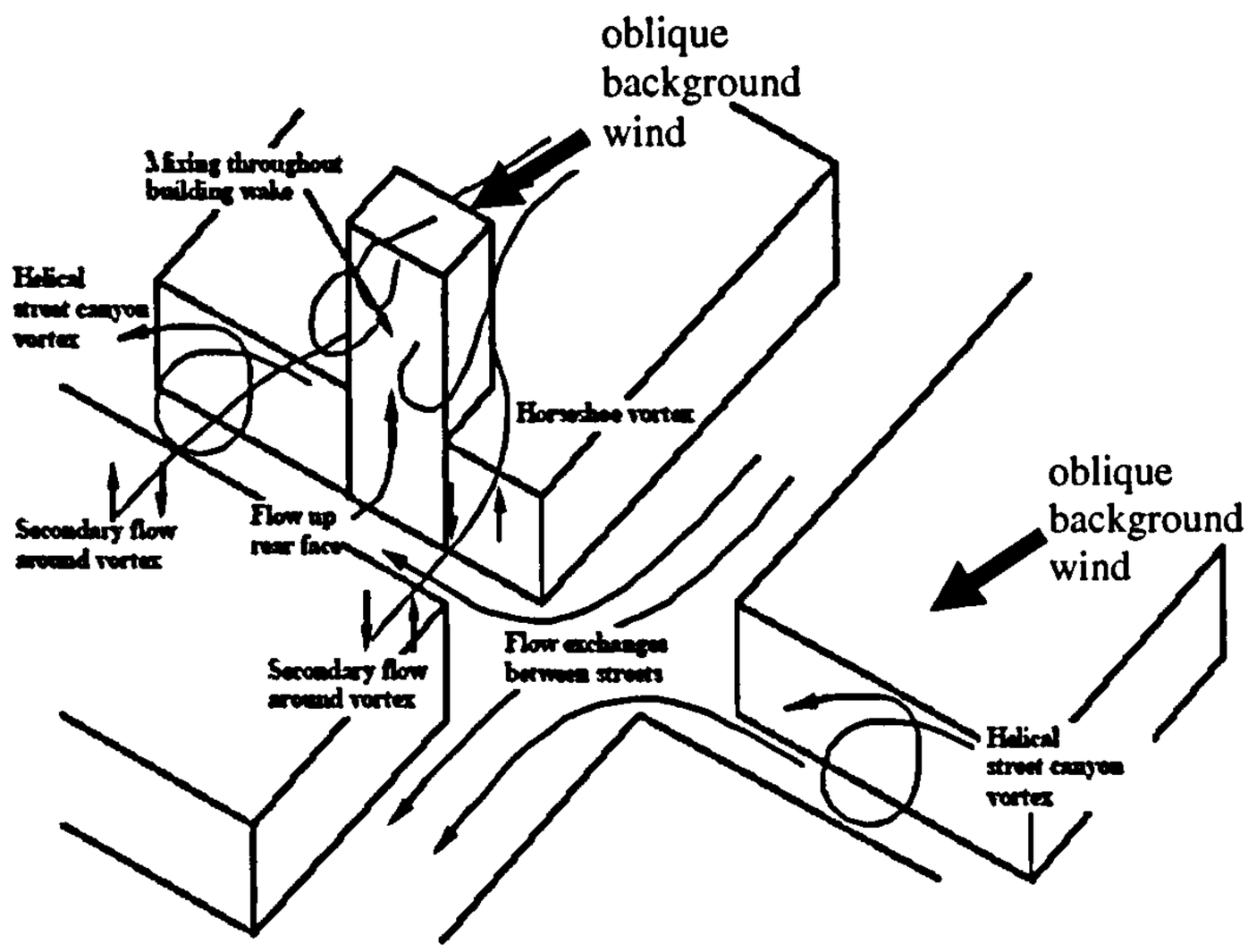


Figure 2.7. Flow field at a street intersection with a tall building, illustrating exchanges between the streets and additional mixing processes along the street canyons during oblique background winds (Robins and MacDonald, 2001).

As mentioned earlier, complex channelling effects may also be produced during other background wind directions. For instance, corner vortices with vertically-aligned axes and strong horizontal components may form at the intersections with the street canyon (Figure 2.4a). In short street canyons ($L/H \approx 5.0$), especially those with side streets that adjoin perpendicular to the street axis, it is likely that counter-rotating corner vortices may develop during perpendicular winds. These corner vortices with vertically-aligned axes may be strong enough to inhibit the development of a single across-canyon recirculating flow with a horizontally-aligned axis of the type shown in Figure 2.3c. This is because the corner vortices induce along-canyon converging flows. Upon convergence, the along-canyon flows produce significant vertical momentum flux (e.g. in the form of updraughts) on both sides of the canyon (see Chapter 4).

The corner vortices, however, are also likely to produce street-level across-canyon flow towards the leeward side of the canyon. Some of these flow features are illustrated in Figure 2.8, although it should be noted that the schematic represents an isolated building rather than a street canyon.

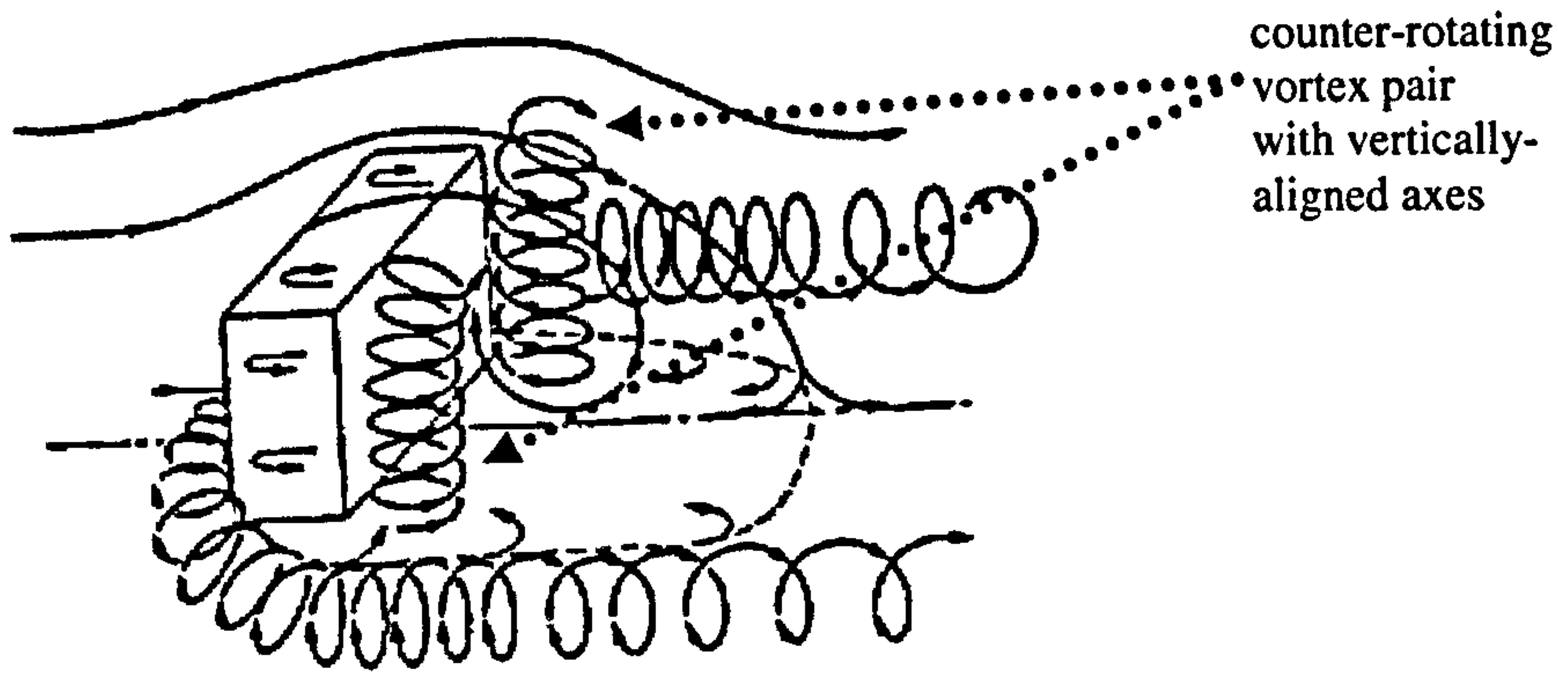


Figure 2.8. Flow around an isolated building during perpendicular background winds, showing the development of counter-rotating corner vortices, which are likely to produce converging flows in the lee of the building (Hosker, 1985).

During perpendicular background winds the counter-rotating vortex pair with vertically-aligned axes located on the leeward side of the upwind building is likely to form within short street canyons with side streets aligned perpendicular to the canyon axis. The influence of corner vortices and the production of extra along-canyon ventilation effects than would occur during classic skimming flow conditions are likely to fade with increasing street canyon length (Theurer, 1999).

The strength of the in-canyon mean wind clearly depends on the strength of the background wind speed. However, moving vehicles may produce additional mechanical turbulence (Di Sabatino *et al.*, 2003; Kastner-Klein *et al.*, 2003) that may affect the in-canyon mean wind and turbulence fields. The influence of traffic-produced turbulence (TPT) will be investigated in Chapter 6. Furthermore, street furniture may act as additional roughness elements, thus, causing additional mechanical turbulence that may also affect the in-canyon mean wind and turbulence. These roughness elements include: trees; balconies; wall cavities; bus shelters; phone kiosks; and pitched roofs (Hoydysh and Dabberdt, 1994; Theurer, 1999).

In addition to the mechanical turbulence that may be produced within some street canyons as a result of flow interaction with street furniture, it also likely that some in-canyon flow features may also be affected by the atmospheric stability (Rotach, 1995). Thermal effects induced by hot exhaust gases emitted from vehicles, particularly during congested traffic flows and the differential heating of the walls and/or the bottom of the canyon may also affect the in-canyon flow features. Uehara

*et al.* (2000) investigated the influence of thermal stratification of the wind flow and turbulence in and above a street canyon in a reduced-scale (i.e. wind tunnel) experiment. The results showed that the single-across canyon recirculating flow with a horizontally-aligned axis becomes weaker when the atmosphere is stable, and stronger when unstable. Stable atmospheric conditions led to a positive feedback effect in which the downward flow into the street canyon weakened due to buoyancy, which facilitated the formation of a more highly stable stratification. Xie *et al.* (2005) investigated the impact of solar heating on street canyon flows using a numerical CFD model. They found that solar heating on the leeward wall of the canyon strengthened the recirculating flow. However, when the windward wall is warmer than the in-canyon air, an upward buoyancy flux opposes the downward advection flux along this wall and divides the recirculating flow structure (with a horizontally-aligned axis) into two counter-rotating cells. The upper vortex cell rotates in a similar direction to the classic recirculating flow, whereas the lower cell rotates in the opposite direction. Thermal effects are unlikely to play a major role in disturbing the mean wind flow, particularly within UK street canyons for climatic reasons, particularly due to the predominance of cloud cover. On the other hand, in street canyons with differential insolation, thermal effects generally only have an influence on the in-canyon flow close to the canyon walls and significant gradients are required to disturb the whole of the canyon flow.

Although wind tunnel studies (see also Kovar-Panskus *et al.*, 2002) and computational studies (see also Sini *et al.*, 1996; Kim and Baik, 2001) suggest that street canyon walls heated by the sun influence the mechanically driven recirculating flow, it seems unlikely to be operationally important in most scenarios (see Britter and Hanna, 2003). Any effect is far less evident in field measurements (Louka *et al.*, 2002) probably because, in the field, the physical width of the free convective boundary layer on the heated wall is small compared to the scale of the mechanically driven motion, which is of course on the street scale (Britter and Hanna, 2003). However, these thermal effects are likely to be of greater consequence during weak background winds, particularly in street canyons with substantial solar radiation.

Variations in the classic single across canyon recirculating flow with a horizontally-aligned axis may occur if the canyon geometry and background wind direction varies.

For example, regular rectangular street canyons with low aspect ratios allow for the possible reattachment of the separating shear layer off the leeward wall to the floor of the canyon (Britter and Hanna, 2003). Furthermore, the classic single across-canyon vortex of the type shown in Figure 2.3c may not be produced in asymmetric street canyons. In step-up canyons the downwind building is higher than the upwind building, whereas in step-down canyons the downwind building is lower than the upwind building. A recirculating vortex may either be entirely absent, particularly in the case of step-down canyons, or the centre of the recirculating vortex may simply be displaced from mid-canyon level (Assimakopoulos *et al.*, 2004). However, it is likely that more than one recirculating vortex will develop inside asymmetric street canyons.

More than one recirculating vortex (with horizontally-aligned axes) may also develop inside deep street canyons ($H/W > 1.3$). In such canyons, the main recirculating flow is usually positioned towards the upper part of the canyon, with almost stagnant air below (DePaul and Sheih, 1986). In even deeper canyons ($H/W \approx 2.0$) a weak counter-rotating secondary vortex may develop at street level (Pavageau *et al.*, 1996). The influence of a single prominent building located along the canyon wall is also likely to affect the in-canyon flow, as shown schematically in Figure 2.7. It is also possible that in even deeper canyons ($H/W \approx 3.0$) a third weak vortex may develop (Jeong and Andrews, 2002). In deep canyons it is likely that small vortices with horizontally-aligned axes develop at street level at the corners of the canyon walls. However, these latter possibilities are more common in idealised laboratory experiments rather than in field experiments (see Britter and Hanna, 2003).

#### *2.6.2.2. Dispersion of traffic-related pollutants*

The dispersion of gaseous traffic-related pollutants in a street canyon generally depends on the rate at which the street exchanges air vertically with the above-roof atmosphere and laterally with connecting streets (Riain *et al.*, 1998; Figure 2.7). It has been demonstrated numerically (e.g. Sini *et al.*, 1996; Leitl and Meroney, 1997) and by using wind tunnel modelling (Hoydysh and Dabberdt, 1988; Kastner-Klein *et al.*, 1997, 2001; Rafailidis, 1997; Park *et al.*, 2004) that wind flow and pollutant dispersion within continuous street canyons essentially depend on the aspect ratio, the

street length and building roof geometry (Theurer, 1999). In regular street canyons, skimming flow of the type shown in Figure 2.3c provides minimal ventilation of the canyon and is relatively ineffective in removing pollutants (Hunter *et al.*, 1992; Berkowicz, 2000a). Figure 2.9 shows a schematic representation of the across-canyon recirculating flow with a horizontally-aligned axis that forms during perpendicular background winds. The direction of the wind at street level is opposite to the background wind direction. The asymmetric recirculating flow is caused by stronger downdraughts on the windward side and weaker updraughts on the leeward side.

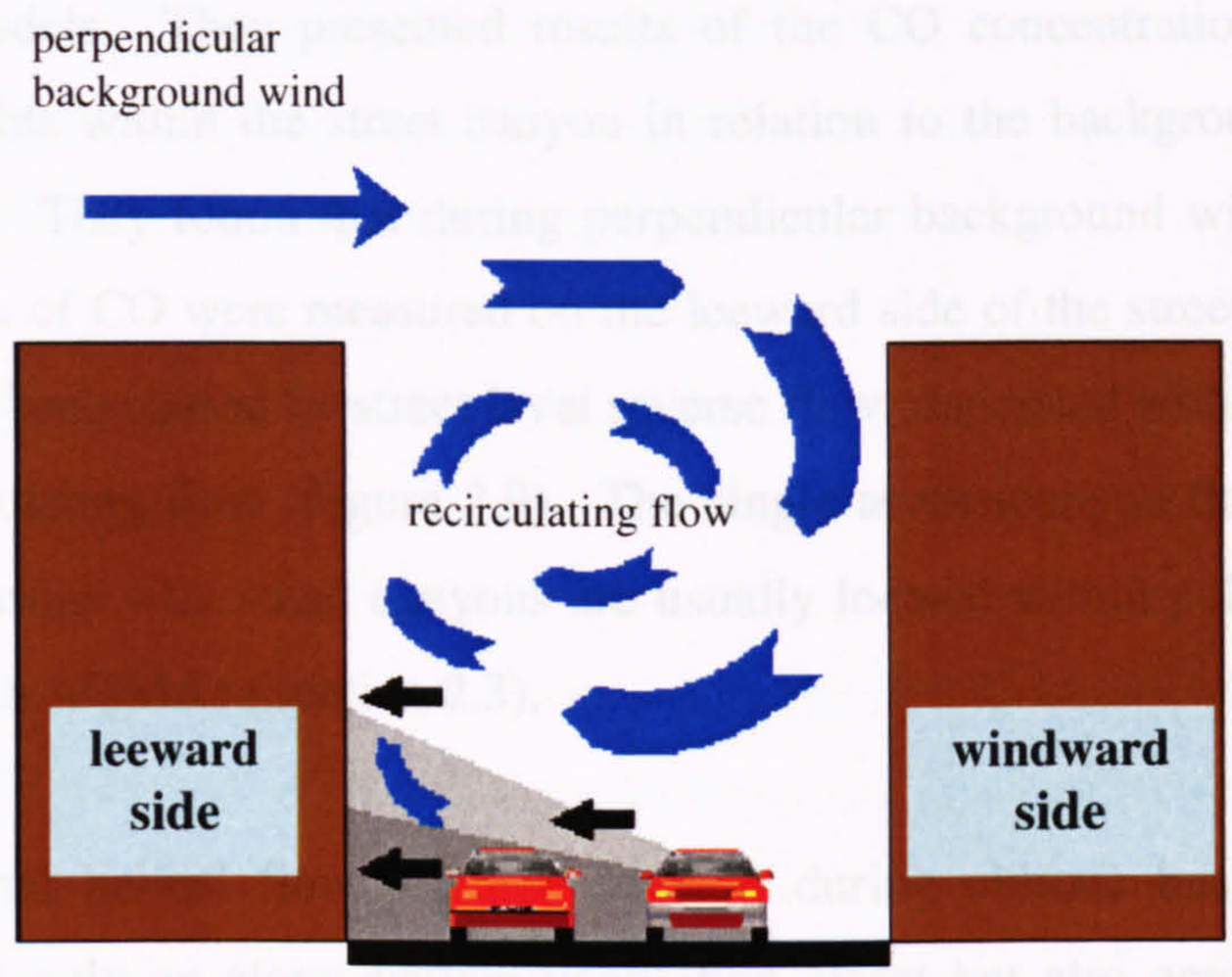


Figure 2.9. Schematic of the single across-canyon recirculating flow with a horizontally-aligned axis, showing the transport of pollutants to the leeward side of the canyon (modified from Berkowicz, 2000a).

The field measurements of DePaul and Sheih (1985), Qin and Kot (1993) and Longley *et al.* (2003) show increased concentrations of traffic-related pollutants on the leeward side of the canyon, with concentrations decreasing with height above the ground on both sides of the street. The background wind direction and, hence the single across-canyon recirculating flow, was found to have a significant influence on the particle number concentrations measured inside the Manchester street canyon (Longley *et al.*, 2003). They found values typically 2-10 times greater in perpendicular flow than the estimated inner-urban background. Longley *et al.* (2004a) confirmed the presence of a recirculating flow during measurements inside

the same street canyon in a second field campaign. Figure 2.9 illustrates how the single-across canyon recirculating vortex advects traffic-related pollutants at street level in the reverse flow portion of the recirculating flow towards the leeward side.

Vachon *et al.* (2000) conducted a full-scale experiment for a period of one month in a section of the Rue de Strasbourg, which is a 3-lane, one-way, highly-trafficked straight street canyon in Nantes, France. Measurements of the mean CO concentration, temperature and wind flow fields were conducted in what was the first campaign of the URBCAP project. The aim of the study was to assess pollutant transformation processes within the urban canopy and to validate small-scale dispersion models. They presented results of the CO concentrations measured at different heights within the street canyon in relation to the background wind speed and direction. They found that during perpendicular background winds the highest concentrations of CO were measured on the leeward side of the street, which is most likely to have been caused by street level reverse flow associated with a single across-canyon recirculating flow (Figure 2.9). The single across-canyon flow, therefore, is one of the reasons why street canyons are usually located within pollution hot-spots associated with AQMAs (Section 2.3).

It is likely that helical flow regimes develop during oblique background winds, producing not only an along-canyon ventilation effect but also across-canyon flow reversal. Consequently, as with classic recirculating flows associated with skimming flow regimes (Figure 2.9), helical recirculating flows are likely to transport pollutants towards the leeward side of the canyon where they may accumulate. Additional recirculation phenomena may occur along a street canyon within small cavities in the building walls.

One of the most systematic investigations into in-canyon dispersion characteristics in a reduced-scale (i.e. wind tunnel) model of urban streets was performed by Hoydysh and Dabberdt (1988) using tracer gas and flow visualisation techniques. Three different canyon configurations were considered in their study: a long regular street canyon; a step-down street canyon; and a step-up street canyon. The street level across-canyon concentration gradients and the vertical concentration gradients were measured for various background wind directions. Their findings confirmed those of

previous studies, whilst also providing several new insights. The vertical concentration profiles were well approximated by an exponential function with the maximum occurring close to the traffic source (i.e. at street level). During perpendicular background winds the concentrations were generally a factor of two or more on the leeward side of the canyon compared to the windward side, except for the step-down canyon where windward concentrations were slightly greater than the leeward concentrations. Concentrations were generally lower in the step-up canyon in relation to the regular and step-down canyon configurations. In the regular street canyon the street level concentrations on the windward side exhibited significant variation with the background wind direction. Perpendicular wind directions produced a local maximum, while oblique winds produced a shallow minimum and a subsequent increase in concentrations approaching parallel to the street axis. Dabberdt and Hoydysh (1994) confirmed these findings.

Schatzmann *et al.* (2000) presented data from a reduced-scale study into pollutant dispersion in urban areas and demonstrated how wind tunnel data can be used to supplement and enhance the value of full-scale measurements for model validation purposes. The street canyon used in the field experiment was located in Hannover, Germany. The German MOBILEV emission model was used to calculate hourly average emissions for the street using information on street geometry, emission factors, driving mode and vehicle fleet composition. Congested traffic and cold-start emissions are also taken into account (see Section 2.6.3). They reported that there was generally reasonable agreement between the results from the full-scale, reduced-scale and modelling studies, with concentrations measured on the leeward side of the canyon being a factor of 2-3 times higher than those measured on the windward side.

Sini *et al.* (1996) built a numerical model to simulate the small-scale atmospheric flows within the urban canopy, based on the standard $k$-$\varepsilon$ two-equation turbulence model, where $k$ refers to the turbulence kinetic energy (TKE) and $\varepsilon$ is the dissipation rate. The model was used to study the flows and vertical exchanges of pollutants within the street and at the interface with the atmospheric layer above the roofs for a street canyon of infinite length. They found that the number and arrangement of vortex structures within the street canyon largely influenced the vertical exchange

rates. Hunter *et al.* (1991; 1992) and Johnson and Hunter (1995) used a $k$-$\varepsilon$ turbulence closure model to investigate the influence of street canyon geometry on in-canyon flow and concentration fields in isolated regular 2-D street canyons. They found an influence of the $L/H$ ratio on the dynamics of the classic single-across canyon recirculating flow.

In similar studies, Chan *et al.* (2001; 2003) investigated the variation in street canyon flow and pollution patterns with changes in the canyon geometry. A regular street canyon was used in the first study, while an asymmetric canyon was used in the numerical $k$-$\varepsilon$ turbulence closure simulations in the latter study. Chan *et al.* (2001; 2003) observed that not only the $H/W$ and $L/H$ ratios have a noticeable influence on street level pollution concentrations, but that the relative height of the buildings flanking the street also influenced the in-canyon flow and concentration fields, with non-uniform roof heights providing better ventilation. Kim and Baik (2003) in another study with a 2-D numerical model found that the in-canyon recirculating flow and street canyon ventilation strengthen with increasing inflow turbulence intensities.

The majority of field experiments conducted within real full-scale street canyons have predominantly investigated the influence of the classic single across-canyon recirculating flow (with a horizontally-aligned axis). The majority of the numerical models currently used to determine the skimming flow regime involve idealised building configurations, i.e. the buildings have rectangular shapes with flat roofs and are arranged in a uniform manner (e.g. Figure 2.3c and Figure 2.9). However, buildings with pitched roofs are more common in the majority of European cities and, therefore, the influence of pitched roof geometries on the in-canyon flow and dispersion must also be determined. The work presented by Louka *et al.* (1998; 2000) has revealed substantially more about the flow and turbulence inside a street canyon with pitched roofs and $H/W \approx 0.7$. The unsteady fluctuations in the position of the shear layer are believed to have forced the unsteady fluctuations in the street. The shapes of the roofs are likely to have affected the depth and strength of the shear layer. Pitched roofs were found to be more associated with energetic eddies (Louka *et al.*, 1998) and stronger turbulence intensities (Rafailidis, 1997; 2000) than flat roofs. Louka *et al.* (2000) presented evidence of an intermittent recirculating flow

(with a horizontally-aligned axis) inside an isolated, traffic-free street canyon with pitched roofs. Figure 2.10 shows the position of the shear layer relative to the in-canyon recirculation zone and the free-stream velocity loft. The shear layer is likely to have been shed off the upstream roof during perpendicular background winds. Louka *et al.* (2000) stated that fluctuations in the position of the shear layer resulted in 'flapping' of the shear layer. Therefore, the strength of the across-canyon recirculating flow is controlled by the flapping of the shear layer, which is situated between the recirculation zone and the above-roof airflow.

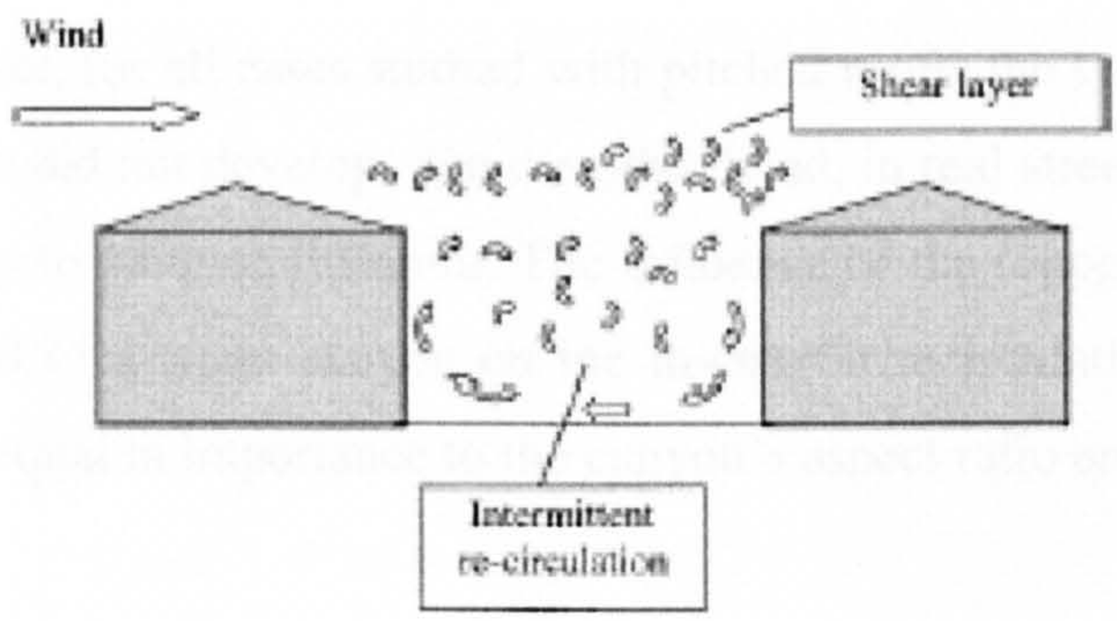


Figure 2.10. Schematic showing the position of the shear layer relative to the in-canyon recirculation zone during skimming flow (Louka *et al.*, 2000).

It was mentioned earlier that the majority of the numerical models currently use idealised building configurations with buildings that have rectangular shapes and flat roofs and are arranged in a uniform manner. However, the wind tunnel studies conducted by Kastner-Klein and Plate (1999) and Rafailidis (1997; 2000) have demonstrated that building and roof geometries (such as pitched roofs) may have significant implications for the dispersion characteristics inside street canyons. Tracer-gas experiments were performed in symmetric and asymmetric street canyons in a neutrally stratified wind tunnel (Kastner-Klein and Plate, 1999). Vehicle emissions were simulated as line sources. Concentration profiles along building walls were measured. Street canyon and roof geometry, upwind building configuration and wind direction were found to be important influences on the in-canyon concentration field. For instance, roof shape can be an important factor determining the vorticity dynamics in the canyon and the intensity of the pollutant transport towards the leeward side of the canyon. In the case of the symmetric, isolated street canyon concentrations were found to be up to ten times higher on the leeward side of the

canyon than on the windward side due to the development of a recirculating flow with a horizontally-aligned axis.

Kastner-Klein *et al.* (2004a) studied the flow patterns in the central vertical plane for three different *L/H* ratios and three different roof configurations for an isolated street canyon with an aspect ratio of unity in a wind tunnel. For all cases with flat roofs, they found that flow separation occurred at the upwind edge of the upwind building and a classic across-canyon recirculating flow with a horizontally-aligned axis formed. Above the roof, a shear zone with increased turbulent velocities developed and the highest turbulence levels were observed above the roof of the upwind building. However, for all cases studied with pitched roofs, the typical street-canyon recirculating flow did not develop. On the other hand, in real street canyons the flow features are likely to be quite different. The influence of the topography of the urban landscape upwind of a street canyon on the in-canyon recirculating flow formation and dynamics is equal in importance to the canyon's aspect ratio and roof geometry.

Meroney *et al.* (1996) investigated the dispersion of a tracer gas in wind tunnel studies of an isolated street canyon in open country and a street canyon in an urban environment. The street canyons had aspect ratios of unity and the roofs were flat. They found that the dynamics and, thus the dispersion characteristics, of the flow were quite different. The isolated canyon was observed to have better ventilation than the urban roughness case. They reported that a recirculating flow formed only intermittently in the isolated street canyon, whereas it was much more stable amidst urban roughness. Recall that in the field study conducted by Louka *et al.* (2000) the intermittent flow recirculation was expected to have been caused by the 'flapping' of the shear layer (Figure 2.10). The results from the full-scale isolated street canyon used by Louka *et al.* (2000) and the reduced-scale isolated street canyons used by Meroney *et al.* (1996) and Kastner-Klein *et al.* (2004a) suggest that greater ventilation may be produced due to shear layer flapping, than in the case of urban roughness where the potential for flapping is reduced. As a result, the mean concentrations of traffic-related pollutants inside non-isolated (i.e. urban roughness) street canyons in real urban topographies would be expected to have worse ventilation conditions during skimming flow regimes as the recirculating flow is likely to be more stable.

Flow visualisation experiments have shown the variability in the strength of the in-canyon flows with horizontally-aligned axes. As a result, pollutants are periodically flushed out of the canyon (Pavageau *et al.*, 1996). It should also be mentioned that in some street canyons the highest in-canyon concentrations may not always be associated with perpendicular skimming flow of the type shown in Figure 2.9. Vardoulakis *et al.* (2002) observed in a relatively long street canyon with $H/W \approx 0.8$ in Paris that the maximum street level concentrations of CO and $NO_x$, normalised by the background wind speed and traffic flow, occurred during parallel background winds. However, this is likely to have been caused by the accumulation of emissions along the line source coupled with the advection of background concentrations into the street canyon from nearby streets. This is supported by the findings of Robins *et al.* (2002), who conducted a wind tunnel study into the dispersion of a tracer gas at a simple urban intersection comprising two perpendicular streets. Concentration and flow field measurements were undertaken in order to determine the importance of the exchange of pollutants between the streets (see also Figure 2.7). The results showed that concentrations on one side of the street were entirely due to emissions from the perpendicular street, whereas concentrations on the opposite side of the street depended upon emissions upwind in the same street as the receptor (see also Hoydysh and Dabberdt, 1994; Robins, 2003).

Weak background winds create a well-known meteorological scenario that favours the accumulation of traffic-related pollutants in urban areas (Qin and Kot, 1993; Vignati *et al.*, 1996; Jones *et al.*, 2000). DePaul and Sheih (1986) observed in a relatively deep street canyon with $H/W \approx 1.3$ that when $U_{ref} < 1.5$ m s$^{-1}$ the across-canyon recirculating flow with a horizontally-aligned axis tended to disappear and the air in the street stagnated. However, in street canyons of $H/W \approx 0.8$ it is more likely that a weaker recirculating flow may still exist during low background winds, as discussed in Chapter 6. During these background wind conditions, the mechanical turbulence produced by vehicles travelling along the street may play a significant role in the dispersion of traffic-related pollutants inside street canyons.

Fine and especially ultrafine particles are expected to disperse in the air like gaseous traffic-related pollutants. The larger sized particles, however, are greatly affected by gravity and consequently have a shorter residence time in the air (Chan and Kwok,

2000). Therefore, the coarse fraction of the total suspended particles (TSP) exhibits larger vertical concentration gradients than those usually observed for gases and fine particles.

Despite the range of idealised numerical studies, few full-scale experiments have been conducted which provide data from simultaneous measurements of in-canyon wind flow and pollutant concentrations, relative to a suitable background wind measurement. Full-scale street canyon experiments, however, are only representative of local conditions and data from more locations are required to identify general properties (Longley *et al.*, 2004a). Inter-comparisons must also be made between street canyons of different geometry, as not all street canyons are symmetrical. Most streets have a non-uniform width or have buildings that differ in height on either side. Dispersion models are widely used in air quality and traffic management, urban planning, pollution forecasting and for predicting personal exposure to pollutants. However, for dispersion models to achieve their full potential, they must be able to accurately represent the influence of traffic emissions on roadside concentrations for a range of street geometries and background wind conditions (see Chapter 8).

*2.6.2.3. Population exposure*

It was mentioned in Section 2.4 that due to the very short distances between sources and receptors, only very fast chemical reactions have a significant influence on the measured concentrations inside street canyons (Berkowicz *et al.*, 1997a). It is expected that the relationship between relatively stable chemical species (e.g. CO) emitted by motor vehicles would not vary significantly in urban streets. This is particularly helpful for epidemiological studies, because a single indicator can be identified for assessing population exposure to traffic-related air pollution (Kingham *et al.*, 2000). Air quality inside street canyons is of major importance from a population exposure point of view, since the highest concentrations and greatest numbers of people often occur in these streets (Hertel *et al.*, 2001). The reduced natural ventilation in street canyons resulting from perpendicular skimming flow (Figure 2.9) results in greater health impacts (e.g. indicated by an increased number of respiratory hospital admissions) and damage costs for the exposed population (Spadaro and Rabl, 2001). Colvile *et al.* (2001) reviewed a number of studies that

provide evidence that fine particles emitted by traffic may be responsible for measurable increases in the manifestations of cardiovascular and respiratory diseases even at the comparatively low levels of air pollution in modern Western cities.

### 2.6.3. The influence of traffic

Traffic is not only a source of pollution, but also provides a mechanism for pollutant dispersion. Therefore, traffic plays a significant role in the variability in concentrations of traffic-related pollutants measured inside street canyons. The following sub-section will continue the theme of in-canyon dispersion mechanisms by exploring the influence of traffic-produced turbulence. The sub-section that follows after that will address the influence of traffic characteristics and driving mode on the variability in emission levels.

#### *2.6.3.1. Traffic-produced turbulence*

High concentrations of traffic-related pollutants in street canyons are often associated with low wind speed conditions. However, operational street canyon dispersion models commonly perform poorly under these conditions. Typically, these models are structured to have an inverse relationship between the concentration field and $U_{ref}$, and this relationship leads to substantial overestimation of the concentrations during low wind speeds (see Britter and Hanna, 2003). Sources of turbulence that may be of greater consequence during weak background wind conditions were mentioned earlier and include thermal production by radiation from the built environment and from vehicle exhausts and engines.

There is also the mechanical production of turbulence from the motion of vehicles, which is known as traffic-produced turbulence (TPT). Therefore, mechanically produced turbulence inside street canyons is assumed to be composed of two parts: one is dependent upon the background wind, which causes shear generated turbulence above roof level (Figure 2.10); and the other is due to TPT. When $U_{ref}$ is low TPT dominates and because the highest concentrations often occur during these conditions, appropriate modelling of these features is crucial (Kastner-Klein *et al.*, 1998; Ketzel *et al.*, 1999).

The generation of turbulence by moving vehicles has been the subject of several theoretical and experimental investigations (Eskridge and Hunt, 1979; Thompson and Eskridge, 1987; Grønskei, 1988; Eskridge *et al.*, 1991; Watkins *et al.*, 1995). However, the TPT effects described in the aforementioned papers are applicable to fast moving cars on open roads. There have been many studies on the dispersion of traffic-related pollutants in street canyons (Bauman *et al.*, 1982; Rotach, 1995; Sini *et al.*, 1996; Louka *et al.*, 1998, 2000; Väkevä *et al.*, 1999; Longley *et al.*, 2004a). However, only a limited number of full-scale field experiments have focused on investigating the influence of TPT on the dispersion of such pollutants. The lack of field measurements of TPT is unsurprising, due to the fact that it is difficult to separate traffic from other sources of turbulence, such as thermally-generated turbulence or shear generated turbulence associated with the background wind. However, DePaul and Sheih (1986) used measurements with hot-wire anemometers inside a deep street canyon with $H/W \approx 1.3$ and found that traffic was significant in increasing turbulence up to heights of approximately 7 m, i.e. $z/H = 0.2$. Qin and Kot (1993) observed that during weak background winds the street-level wind inside a narrow street canyon with $H/W = 1.1$ was dominated by the traffic flow. They found that the influence of TPT extended up to a height of 12 m, i.e. $z/H = 0.8$. The actual height to which TPT effects extend is canyon-specific and is likely to be related to the canyon aspect ratio and/or background wind speed and direction.

Vachon *et al.* (2002) described the influences of traffic motions on the production of turbulence inside a deep three-lane street canyon with one-way traffic and $H/W$ of 1.4. Measurements of velocity components and turbulence were undertaken on a street in Nantes, France. They attributed the increased levels of turbulent kinetic energy (TKE) found in the lower half of the canyon to TPT. They found turbulence enhancement close to the traffic region on both windward and leeward sides of the street. However, the influence was more pronounced on the leeward side and the vertical extent of the TPT region was much larger than on the windward side. Vachon *et al.* (2002) suggest that this is caused by the advection of turbulence produced in the traffic region toward the leeward side due to the wind-induced single across-canyon vortex. A single across-canyon vortex with a somewhat destabilized structure may have developed during weak perpendicular background winds (see also Chapter 6).

These recently obtained wind tunnel and field results have significantly contributed to a better understanding of TPT effects on street canyon airflow and dispersion and their interaction with wind-induced flow phenomena. However, the incorporation of traffic effects in dispersion models is still rudimentary (Di Sabatino *et al.*, 2003). Recently, however, there have been studies into the influence of TPT on street canyon concentration fields using wind tunnel experiments for no traffic, one-way traffic and two-way traffic flows (Kastner-Klein *et al.*, 1998; 1999; 2000; 2001; Di Sabatino *et al.*, 2003). For instance, Kastner-Klein *et al.* (1998; 1999; 2001) released a tracer gas ($SF_6$) at a constant rate from the floor of the canyon and found that during one-way traffic flows, there were pronounced along-canyon airflow and dispersion conditions. The concentration distribution along the canyon displayed strong lateral skewness, with concentrations increasing in the direction of traffic-produced airflow. The results also indicated that street canyon turbulence had a diurnal variation, which followed the traffic flow reasonably well, with concentrations decreasing when traffic flow increased due to TPT. They also showed that for two-way traffic there was little effect of traffic movement on the concentrations field, which was consistent with the small velocity changes that were measured. Therefore, these findings immediately raise the question as to whether TPT is only significant in street canyons with one-way traffic flows and any study into TPT must address this issue.

Pearce and Baker (1997) also used moving model experiments to investigate the effect of vehicle motion. However, the method used was considerably different from the studies of Kastner-Klein *et al.* (1998; 1999; 2000; 2001). Pearce and Baker (1997) fired single and multiple numbers of vehicles along a wind tunnel model of a street canyon with a simulated perpendicular airflow and a tracer gas that was released from the floor of the wind tunnel as a line source along the length of the canyon. Ensemble averaging was used to obtain stable results and it was found that the passage of one vehicle did not seem to affect the concentration field, but a four-vehicle platoon did produce a noticeable effect. For clarity, a vehicle platoon is a line of closely following vehicles. In urban traffic flows there are usually short spaces between consecutive vehicles, i.e. there are short distance headways. Pearce and Baker (1997) also observed a noticeable increase in the concentration of the tracer on the upstream side of the canyon associated with vehicle movement. This was the direction in which the wake would have been translated by the in-canyon airflow.

Di Sabatino *et al.* (2003) estimated the magnitude of TPT, or at least it was an appropriate scaling, from a production-dissipation balance for TKE. They estimated TPT by considering three vehicle-wake conditions: isolated vehicle-wakes, wake-interfering vehicles and totally overlapping wakes. These conditions are analogous to the isolated, wake-interference and skimming flow regimes described by Oke (1988) to explain the effects of buildings on the wind flow (Figure 2.3). TPT effects are likely to reduce with increasing traffic density as the drag coefficient on vehicles following in succession decreases due to slipstream effects.

Kastner-Klein *et al.* (1999) developed and evaluated a scaling concept based on the background wind speed and vehicle speed for pollutant concentration data against field and wind tunnel data. They found that their scaling more realistically described concentration distributions than the standard method, which assumes the concentrations are inversely proportional to $U_{\mathrm{ref}}$. Kastner-Klein *et al.* (2003) compared these results with kerbside measurements of $NO_x$ that were collected over a period of several years in three separate street canyons in Hannover and Berlin in Germany and in Copenhagen, Denmark. They found that the traditional concentration scaling, which uses $U_{\mathrm{ref}}$ as a normalising factor, was inappropriate in urban street canyon situations during low $U_{ref}$. Extreme events are likely to occur during weak background winds and models that ignore TPT will significantly over-predict the magnitude of these events.

The incorporation of TPT into the semi-empirical Operational Street Pollution Model (OSPM) led to a marked improvement in the model performance, especially for the extreme events (Berkowicz, 2000a). According to Di Sabatino *et al.* (2003), the OSPM considers traffic inside a street canyon as the superposition of individual vehicles. They also stated that the TPT parameterisation is based on the assumption that the motion of vehicles produces an overall variance of the velocity fluctuations proportional to the square of the vehicle velocity. The coefficient of proportionality is linked to the drag coefficient of the vehicles and its value is empirically determined by fitting velocity variances and concentration data obtained in field experiments. Kastner-Klein *et al.* (2003) quantified the combined effects of traffic- and wind-generated dispersive motions for different traffic conditions (variable traffic densities, vehicle velocities and vehicle types) and incorporated them into developed

parameterisations. A more detailed discussion of the TPT parameterisation is given in Chapter 6.

Kastner-Klein *et al.* (2003) suggested that the analysed experimental data gave indications of different scaling laws for TPT and resulting concentration fields during different traffic conditions. In particular, they were able to distinguish between light density and intermediate density traffic conditions. However, their analysis had also a number of uncertainties within their field data. For example, traffic velocity was not measured and the estimates used may be erroneous. These uncertainties would also affect the estimation of the emission rates that depend on the traffic characteristics (see Section 2.6.3.2). In order to make more definitive conclusions, therefore, any further field experiments must incorporate a method to include traffic characteristics, particularly traffic speed.

*2.6.3.2. Traffic flow*

It is clear that concentrations of traffic-related pollutants are generally expected to increase as traffic flow increases. Namdeo *et al.* (1999) presented results from a monitoring study of traffic-related particulate pollution in urban areas. Measurements of airborne fine and course particulate matter were taken in an urban street canyon in Nottingham, U.K., and the correlation of the observed concentrations was investigated. Longley *et al.* (2003) conducted a 2-week experimental case study to measure size-segregated aerosol in the size range 4.6 nm–10 μm at a fine time scale (10-minute resolution) in a typical street canyon in Manchester, U.K. The influence of perpendicular background winds and the development of single across-canyon recirculating flows has already been mentioned (see Section 2.6.2.2). However, they also found that number concentrations were inversely related to wind speed and directly related to traffic flow. Coarse mode mass concentrations were generally found to follow urban background $PM_{10}$ concentrations except with a 0–5 μg $m^{-3}$ enhancement related to traffic-induced re-suspension within the canyon (see also Longley 2004a). Longley *et al.* (2004b) reported that number concentrations in the size range 0.1–0.5 μm measured at street level followed a diurnal cycle similar to that observed in Longley *et al.* (2003) in the urban background, with a peak coinciding with the morning peak in traffic flow (see also Longley, 2004).

It was mentioned in Section 2.4 that the mean diurnal concentrations of particle number concentration in the range 0.01 to 10μm (Penttinen *et al.*, 2001, Ketzel *et al.* 2003) have been found to correlate reasonably well with CO close to traffic sources. Vachon *et al.* (2000) presented results from a full-scale experiment conducted in a street canyon in Nantes, France. The findings of the relationship between the mean CO concentrations measured inside the canyon and the background wind speed and direction have already been mentioned (see Section 2.6.2.2). However, they also found that high pollution episodes were associated with increased traffic flow. Venegas and Mazzeo (2000) reported the analysis of 8-hour mean concentrations of CO measured close to the emission source (i.e. traffic) over a period of 3 years in a deep street canyon with H/W ≈1.4 in Buenos Aires, Argentina. They found a high frequency of concentration values that exceeded the World Health Organisation (WHO) health protection guidelines.

The vertical concentration gradients of CO were observed within and above a street canyon in Athens, Greece. The CO concentrations were found to decrease exponentially with height above the street and this observation was used to derive an empirical expression. Bauman *et al.* (1982) measured the vertical gradient of CO and aerosol particles. They reported a dilution for CO concentrations of a factor of 4 between rooftop height (60 m) and street level. They concluded that for CO and particulate lead (Pb) and bromine (Br) there is good mixing and rapid vertical dilution. A large decrease in concentration with height was found to be characteristic of pollutants emitted at street level. They further concluded that the absence of a dilution factor between rooftop height and ground level can be used to determine the presence of transported aerosol, as was the case for particulate sulphur in their study.

Väkevä *et al.* (1999) conducted a similar experiment in a street canyon in Lahti, Finland. In this field study, concentrations of gaseous traffic-related pollutants (CO, $NO_x$ and $O_3$) and aerosol particle concentrations were measured at two different heights ($z$ = 3 m for gases; $z$ = 1.5 m for aerosol particles; and $z$ = 25 m for all pollutant concentrations at roof height). The physical parameters controlling the concentration gradients (e.g. the mean wind flow and turbulence fields) were not directly measured and the conclusions of the study rely mostly on the high-time resolution concentration measurements. It was concluded that dilution and dispersion

reduces the concentrations of pollutants emitted at street level by a factor of roughly 5 between the two sampling heights.

In all of the aforementioned studies, it was found that the concentrations of primary pollutants (e.g. CO) are typically high in urban street canyons with high traffic flows and the concentrations have strong gradients within tens of metres of the road. However, there is very little information available for both street level concentrations and vertical gradients and more data is clearly needed for the characterisation of concentrations and air quality conditions in urban areas (Väkevä *et al.*, 1999). This is particularly important when investigating mixing processes together with the chemical and physical conversion of pollutants at the local scale, during which intensive measurements of both primary and secondary air pollutants (e.g. $NO_x$, $SO_2$ and aerosol particles) are needed.

*2.6.3.3. Traffic characteristics and driving mode*

It was mentioned in Section 2.3 that street canyons are often located within AQMAs. In many instances local authorities aim to predict the possible influences on roadside pollutant concentrations using air quality dispersion models before applying traffic management strategies for pollution hot-spots projected to exceed the national objectives shown in Table 2.1. However, these models are often not able to adequately represent urban driving cycles and ignore elevated emissions that are primarily due to vehicles accelerating. Therefore, in addition to investigating the influence of traffic flow on road-side pollution concentrations, which was largely the focus in the past, it is also important to consider the influence of traffic characteristics and driving mode.

It was mentioned in the previous Section that variability in the traffic flow is likely to lead to variations in emissions and, thus, concentrations of traffic-related pollutants measured inside street canyons. The influence of driving mode on vehicle emissions is of particular importance in street canyon studies as higher emission rates are associated with certain traffic characteristics. The four driving modes that are usually referred to in emission studies are: idling, accelerating, cruising and decelerating. Generally, emission rates are higher for congested traffic conditions with

characteristic stop-start conditions associated with periods of idling followed by acceleration (Waters, 1992; André and Pronello, 1997; De Vlieger, 1997; Holmén *et al.*, 1998; Marsden *et al.*, 2001; Beebe *et al.*, 2003; Midenet *et al.*, 2004). During periods of free flow, where traffic is relatively uninterrupted and cruising mode is usual, emission rates are comparatively low. However, the switching between free flow and congested flow coincides with periods of unstable traffic flow when all four driving modes occur. Rapone *et al.* (2000) studied the emission behaviour of a small capacity catalysed car. The authors found that during highly congested traffic situations the car emits more than twice the amount of CO (g $km^{-1}$) than at higher speeds during free flow. CO emissions are increased further when petrol engines run below optimum temperature, such as cold-start, particularly for vehicles fitted with catalysts, or when the engine runs under low efficiency or choke conditions (Pegg and Ramsden, 1966).

Modern petrol engine vehicles have electronically controlled fuel injection systems that optimise fuel flow rates to ensure stoichiometric combustion conditions (Heywood, 1988). During these conditions there is just enough oxygen available to completely oxidise the fuel. Under such conditions, carbon dioxide ($CO_2$), water and nitrogen are the main products of combustion. The petrol engine management system is also able to command extra fuel (enrichment) to provide peak demand power during periods of high engine load, to prevent engine knock during cold-start and to operate accessories such as air conditioning during idling driving modes (LeBlanc *et al.*, 1994). During enriched operation, CO is emitted as insufficient oxygen is available to fully oxidise the fuel to $CO_2$ (Marsden *et al.*, 2001). Other vehicle characteristics (e.g. engine type and size, vehicle age, and maintenance) have also been found to influence the level of emissions from transport vehicles (Seshadri and Harrison, 1993; Nikolaou, 1999).

## 2.7. Summary and Conclusions

The topography of the urban landscape is extremely variable and is largely dependent upon geographical features and the length of time since major city development. Modern cities are often characterised by clusters of high-rise buildings with wide boulevards, while older cities often have narrower streets with densely-packed buildings of only a few storeys high. These differences in urban topography have a significant impact on the urban climate (see Oke, 1987; 1988). It was not appropriate to give a detailed discussion into all aspects of urban climate on the city-scale in this Chapter. However, a discussion was given into the influence of meteorology on the dispersion of traffic-related pollutants in narrow street canyons that are often found in the older European cities. In-canyon flow features are the cause of spatial and temporal variability in concentrations of traffic-related pollutants that are measured inside a street canyon. The variability in the concentrations of pollutants measured inside street canyons clearly has consequences for population exposure.

In particular, it was demonstrated how unfavourable ventilation conditions often arise in such street canyons during background (above-roof) winds that are perpendicular to the along-street axis. It is during these wind conditions that the most characteristic feature of street canyon wind flow occurs. If the street canyon geometry is such that the height-to-width (aspect) ratio is approximately unity the majority of the roof-top flow skims across the canyon in a skimming flow regime. During skimming flows a classic across-canyon recirculating flow develops and is characterised by street level wind flow opposing the flow aloft. Under such wind conditions pollutants emitted from traffic travelling along the street are transported in the reverse flow portion of the recirculating flow towards the leeward (or upwind) side of the street canyon. Consequently, some street canyons have been declared pollution hot-spots and form part of the Air Quality Management Area (AQMA). In these areas local authorities are obligated to undertake review and assessment procedures in order to determine whether certain traffic-related pollutants meet national air quality objectives. Many of these assessment procedures have required considerable effort in recent years to improve the scientific understanding of dispersion and transformation phenomena in street canyon air quality. Street canyons have attracted the most attention due to the

high numbers of traffic (source) and people (targets of impact). Exposure to traffic-related pollutants inside street canyons, particularly during the skimming flow regime and in-canyon flow recirculation, has resulted in greater health impacts.

Traffic-produced turbulence (TPT) is an additional mechanism for the dispersion of traffic-related pollutants and is likely to be most significant during low background winds. TPT is also likely to be most influential in the transportation of pollutants during certain traffic characteristics. Typically, street canyon dispersion models are structured so as to have an inverse relationship between the concentration field and the background wind speed. Therefore, dispersion models that do not include TPT parameterisations may well over-estimate pollutant concentrations during low wind speed conditions.

Numerical studies using complex flow and dispersion models (e.g. MISKAM) can help in the interpretation of the in-canyon flow and dispersion characteristics, particularly when 3-D effects play a greater role. Using such models can often give greater insight into more complex in-canyon recirculating flows. For instance, certain background wind conditions in short street canyons adjoining side streets may give rise to corner vortices with vertically-aligned axes inside the canyon. These corner vortices are likely to have a significant influence on the horizontal in-canyon flow and are likely to produce across-canyon pollutant transport.

Therefore, 3-D flow effects in real street canyons are likely to add a certain amount of complexity to skimming flow regimes. During background winds that are oblique to the street axis, helical flows are likely to develop inside the street canyon. Whereas, background winds that are parallel to the street axis are likely to produce strong along-canyon channel flows. Parallel background winds often produce the most favourable ventilation conditions as they flush pollutants along and ultimately out the street canyon.

The four driving modes commonly described in street canyon emission studies are: idling; accelerating; cruising and decelerating. However, dispersion models are often not able to adequately represent urban driving cycles and ignore elevated emissions that are primarily due to vehicles accelerating. The variable emission rates along a

street canyon (e.g. with distance from a traffic-controlled intersection) are likely to produce spatial variations in the measured concentrations. Emission rates are higher for congested traffic conditions with characteristic stop-start conditions associated with periods of idling followed by acceleration. On the other hand, periods of free flow traffic conditions have comparatively low emissions.

This Chapter explored the influence of meteorology, urban topography and traffic on the variability in concentrations of traffic-related pollutants in urban street canyons. Reference was made to the work conducted in previous studies. The context for further research was presented. It was stated that previous field experiments have often failed to conduct simultaneous and continuous measurements of: (i) the background wind speed and direction; (ii) the in-canyon wind, turbulence and pollutant concentration fields; and (iii) the traffic characteristics (including TPT). This thesis investigates the influence of meteorology, urban topography and traffic on the dispersion of a traffic-related pollutant. The results presented are predominantly from a comprehensive field experiment conducted in two urban street canyons of differing geometry.

# CHAPTER 3

# Instrumentation and Techniques for Measurement and Analysis

## 3.1. Introduction

In preparing for the investigation into the influence of meteorology, urban topography and traffic on the variability in concentrations of a traffic-related pollutant in street canyons, consideration was given to the consequences of the urban wind field on the dispersion of pollutants. Chapter 2 described the flow regimes that may occur in street canyons, particularly as a result of certain street canyon geometries. Consideration was also given in Chapter 2 to the influence of traffic on the spatial and temporal variability in concentrations of traffic-related pollutants. It was mentioned that not only did traffic characteristics cause variations in driving modes, which produce variable emission rates, particularly during periods of congestion and free-flow, but also how traffic-produced turbulence (TPT) is an additional mechanism for pollutant dispersion.

### 3.1.1. Chapter synopsis

The aim and objectives of the present study were described in Chapter 1. This Chapter will explain in detail the design of the experiment and the methodology used to achieve the aim and objectives. The Chapter first provides an overview of the methodology used during the field experiments. This is followed in turn by detailed descriptions of the site, the instruments used and the experiments conducted during the field campaign. A discussion of mean flow and turbulence analysis is also provided.

### 3.2. Experiment Overview

It was mentioned in Chapter 2 that the two street canyons chosen for the field experiment were Bootham and Gillygate, which are situated along arterial routes to the inner-ring road in the city of York, U.K. A full explanation into the reasons for choosing these street canyons is described in Section 3.3. However, it is useful to note that they are both orientated perpendicular to each other and are characterised by contrasting building and roof geometries. Furthermore, the streets are located within York's AQMA and, therefore, they were known to be sites of severe traffic-related pollution, as mentioned in Chapter 2. While there were geometrical differences between the two streets they were both characterised by similar levels of traffic flow. Thus, the differences in street canyon geometries allowed for the investigation into the influence of in-canyon airflow structures on resulting pollutant concentrations.

The two street canyons chosen for the experiment were not only aligned perpendicular to each other, but they also shared a common signal-controlled intersection. This allowed for the unique opportunity to undertake simultaneous measurements of the background wind, and the in-canyon wind, turbulence and pollution fields and traffic characteristics. The study into the mean in-canyon flow and turbulence fields was conducted in the narrower street canyon as it was more likely that this street would experience skimming flow regimes and, in particular, the classic recirculating flow (and street-level reverse flow) as described in Chapter 2. However, it should be noted that other flow features with significant dispersion mechanisms were also investigated in this study.

Another original feature of the experimental design included the use of a trailer-mounted mast upon which an anemometer was attached in order to achieve simultaneous measurements of the above-roof wind speed and direction. The distance from the ground to the measuring volume of the anemometer was 19.5 m (i.e. 1.8$H$). This allowed for measurements of airflow well above the urban canopy layer, allowing for a more representative measurement of the flow above the street canyons (i.e. the background winds). The advantage of this location is evident following the comparison between this measurement location and the City of York Council automatic weather station location (Section 3.5.1.2). Furthermore, as the

trailer-mounted mast was located between the two street canyons it was suitable to measure the background winds corresponding to both streets.

The design of the October and November 2003 field experiment also included the installation of a lamppost on the NW side of the street approximately opposite an existing lamppost in the narrower street canyon. A more detailed description is given in Section 3.5.1. The height to the top of the lamppost was 10 m, although a lantern and supporting brackets were not installed. Due to Health and Safety issues regarding the amount of space remaining on the pavement for pedestrians, a compromise was met with the lighting contractors employed by the City of York Council when deciding on the exact location of this lighting column. Ultrasonic anemometers were used to measure the wind flow and turbulence inside the narrower street canyon.

Trials with the supporting brackets that were to be used to attach the ultrasonic anemometers to the lampposts in the street were conducted before the field experiment. The brackets used on the pre-existing lamppost (on the SE side of the street) were approximately 0.65 m in length, whereas the brackets used on the installed lamppost (on the NW side) were 1.0 m in length. These brackets were longer in length in order to achieve a greater distance from the adjacent canyon wall. The brackets were all positioned in the same orientation on each lamppost using a plumb line suspended from the upper most brackets. The brackets were orientated off-parallel to the street axis, in order to reduce the likelihood of flow distortion from the lampposts during parallel background winds. These brackets also were aligned at ~10° to the street axis on the SE side of the streets and at ~45° to the street axis on the NW side. This bracket orientation best avoids a cavity formed within the wall of the adjacent building on the NW side of the street. However, some flow distortion during parallel background winds cannot entirely be ruled out.

Anemometers were attached to these brackets at various heights on either side of the street in order to measure the airflow and turbulence at a cross-section of the street canyon. The anemometers were levelled by adjusting the supporting stages. Three anemometers were located on the SE side of the street, with the measuring volumes (i.e. the centres of the transducer arrays) at $z = 3.6$ m, $z = 5.5$ m and $z = 7.2$ m above the pavement. A temporary anemometer, deployed for several hours each day, was

located on a stand beside the same lamppost with the anemometer measuring volume at $z = 1.1$ m. The data from the temporary anemometer was used in the TPT analysis. On the NW side of the street, the anemometer measuring volumes were at $z = 5.7$ m and $z = 10.1$ m, the former allowing comparison with the anemometer at $z = 5.5$ m on the SE side of the street. The anemometer located at the top of the lamppost on the NW side of the street was used to measure the mean wind and turbulence close to the shear layer as the building heights were 12 m at the experiment cross-section.

The turbulent mixing of the in-canyon volume of air, particularly during skimming flow regimes when an across-canyon recirculating flow develops inside narrow street canyons, implies that any two measurements of a pollutant conducted at close proximity to each other in a street can differ significantly. Furthermore, traffic congestion and the characteristic stop-start traffic flows may also provide substantial variability with distance from a traffic-signal controlled intersection. With this in mind, a large spatial coverage of the traffic-related pollutant concentration measurements was achieved by attaching instruments to lampposts at various heights and locations along the two streets (Section 3.5.2).

The traffic characteristics were determined through the use of inductive loop detectors buried in the road surface together with manual observations, which were used to test the reliability of the automatic system in measuring traffic flow in each street. However, manual traffic observations also allowed for the collection of data on traffic speed and vehicle composition, which was used in the TPT analysis (Section 3.5.3.2).

### 3.3. Site Selection

York was a suitable location for the experiment, partly because the surrounding topography is relatively flat, implying that the upwind fetch during the field experiment would be relatively undisturbed by hills and other significant landforms from most directions. Figure 3.1 presents a map of York and its surrounding area.

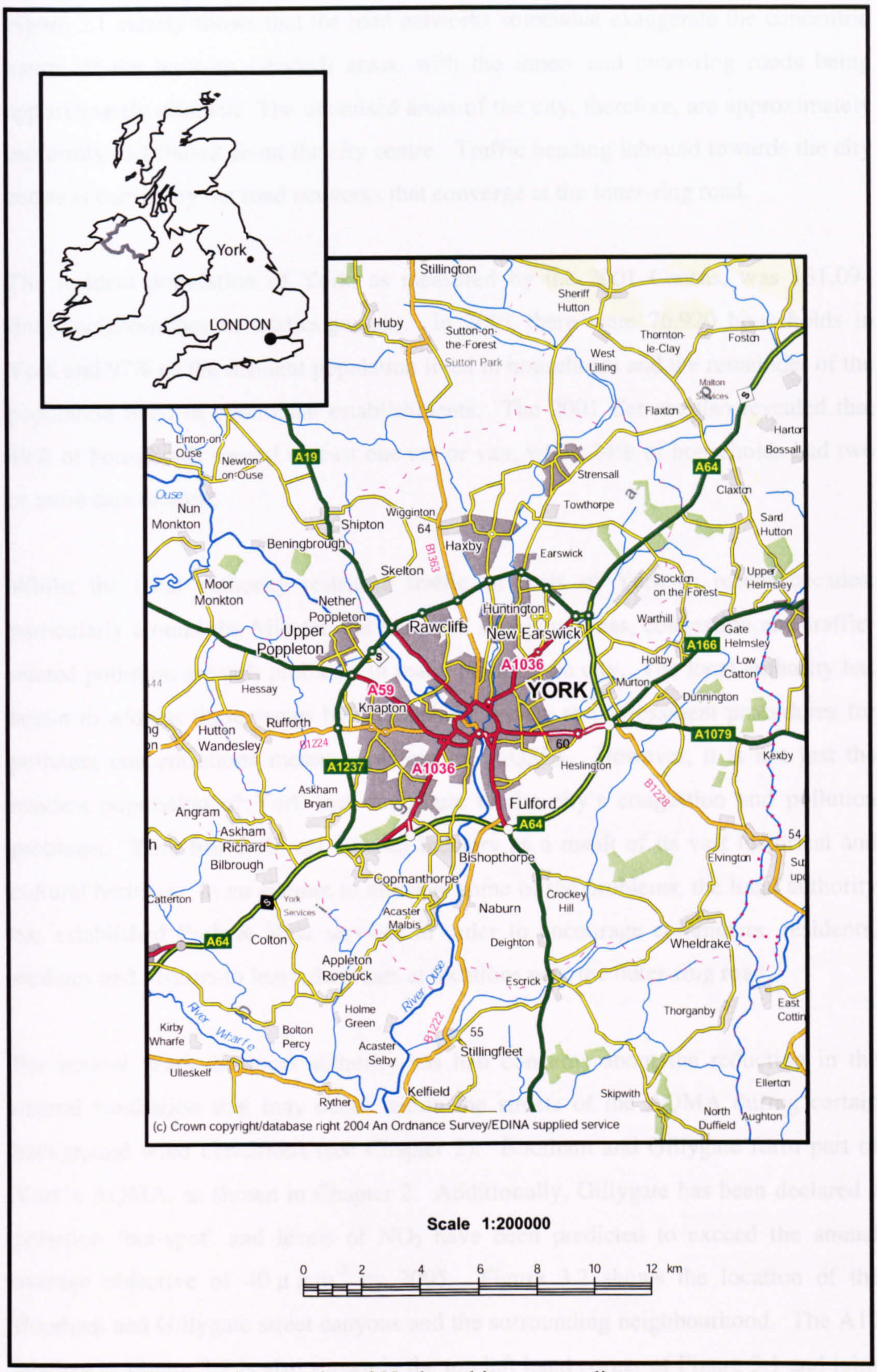


Figure 3.1. Map showing the city of York and its surroundings.

Figure 3.1 clearly shows that the road networks somewhat exaggerate the concentric nature of the built-up (shaded) areas, with the inner- and outer-ring roads being approximately circular. The urbanised areas of the city, therefore, are approximately uniformly distributed about the city centre. Traffic heading inbound towards the city centre is carried by the road networks that converge at the inner-ring road.

The resident population of York, as measured by the 2001 Census, was 181,094 (http://neighbourhood.statistics.gov.uk). In 2001 there were 76,920 households in York and 97% of the resident population lived in households and the remainder of the population lived in communal establishments. The 2001 Census also revealed that 49% of households owned at least one car or van, while 24% of households had two or more cars or vans.

Whilst the local authority restricted traffic in parts of York in recent decades, particularly around the Minster and the main shopping areas, congestion and traffic-related pollution are still problems in many parts of the city. The local authority has begun to address these issues by establishing review and assessment procedures for pollutant concentrations measured within the AQMA. However, it is not just the resident population of York that contribute to the city's congestion and pollution problems. York has a vibrant tourism industry as a result of its vast historical and cultural heritage. In an attempt to alleviate some of the problems, the local authority has established Park & Ride services in order to encourage commuters, residents, students and visitors to leave their cars at locations near the outer-ring road.

For several years the local authority has had concerns about the reduction in the natural ventilation that may occur within the streets of the AQMA during certain background wind conditions (see Chapter 2). Bootham and Gillygate form part of York's AQMA, as shown in Chapter 2. Additionally, Gillygate has been declared a pollution 'hot-spot' and levels of $NO_2$ have been predicted to exceed the annual average objective of $40\,\mu g\,m^{-3}$ by 2005. Figure 3.2 shows the location of the Bootham and Gillygate street canyons and the surrounding neighbourhood. The A19 labelled in Figure 3.2 is also shown in the top left hand corner of Figure 3.1 and joins the outer-ring road in Rawcliffe. The A19 Clifton Road is known as Bootham closer towards the city centre (Figure 3.2).

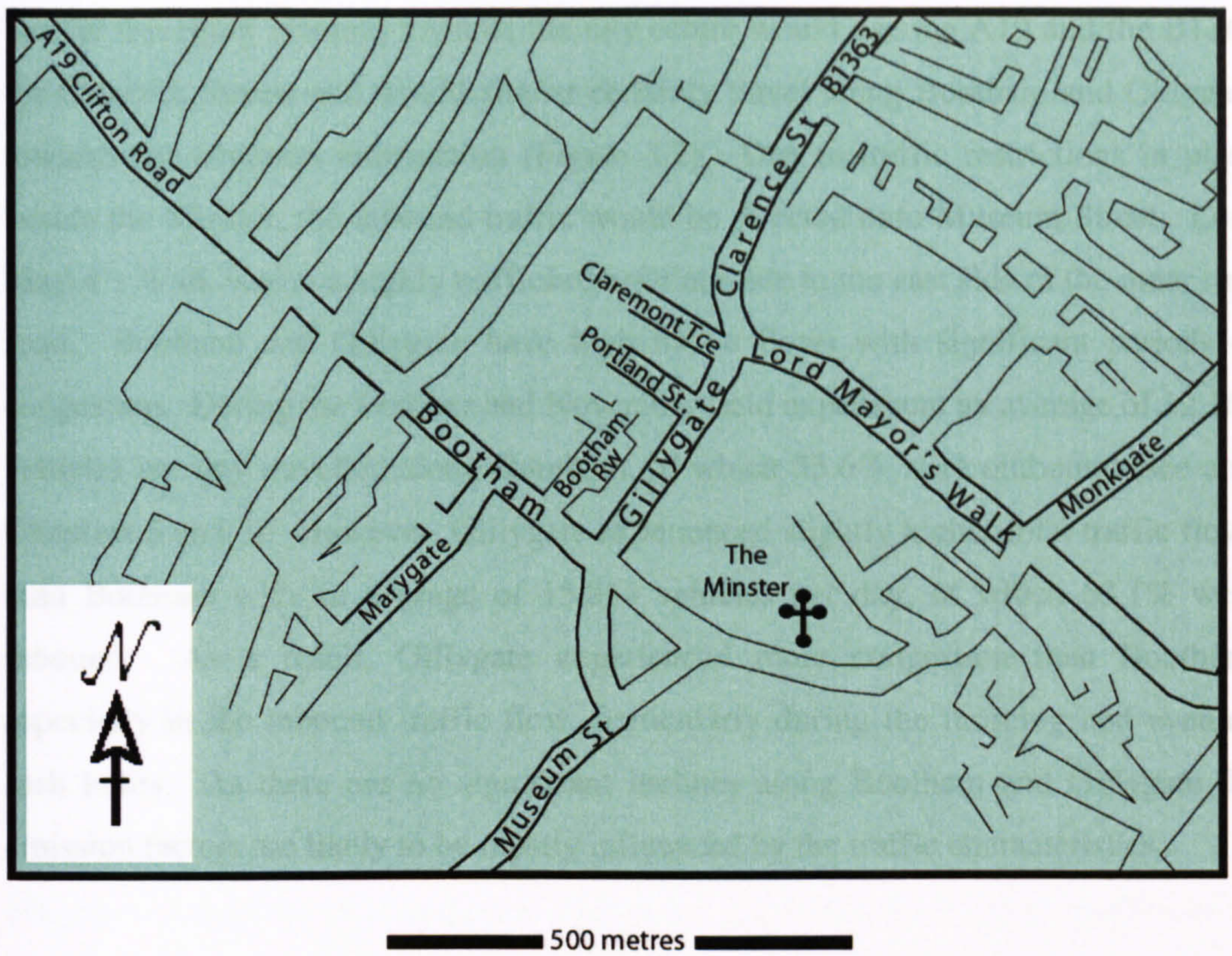


Figure 3.2. Plan of the Bootham and Gillygate street canyons and adjoining streets.

Figure 3.2 shows that Bootham and Gillygate are aligned perpendicular to each other. Bootham is aligned at approximately 312° clockwise from N, while Gillygate is orientated predominantly at 45° from N. However, Gillygate is aligned approximately 30° from N at the opposite end to the common intersection, towards the junction with Lord Mayor's Walk and Clarence Street. Portland Street and Claremont Terrace are two residential streets that adjoin Gillygate perpendicular to the street canyon axis. The orientation of the two street canyons together with their contrasting building and roof geometries (mentioned in detail below) allowed for simultaneous investigations of the influence of different above-roof wind directions. For example, parallel winds along Bootham clearly equated with perpendicular winds over Gillygate. Furthermore, both streets were installed with an automatic traffic counting system, which was a requirement for the investigation.

Traffic travelling inbound towards the city centre would use the A19 and the B1363 (or Clarence Street) and would almost certainly travel along Bootham and Gillygate towards the common intersection (Figure 3.2). Due to traffic restrictions in place beside the Minster, the inbound traffic would be directed onto Museum Street. Lord Mayor's Walk is also a highly trafficked arterial route to the east side of the inner ring road. Bootham and Gillygate have high traffic flows with significant periods of congestion. During the October and November field experiment an average of 12,168 vehicles per day travelled along Bootham, of which 53.6% were outbound (see also Chapters 5 and 7). However, Gillygate experienced slightly higher total traffic flows than Bootham with an average of 15,864 vehicles per day, of which 53.1% were inbound. As a result, Gillygate experienced more congestion than Bootham, especially in the inbound traffic flow, particularly during the morning and evening rush hours. As there are no significant inclines along Bootham and Gillygate the emission factors are likely to be mostly influenced by the traffic characteristics.

### 3.4. Street Canyon Geometries

The height ($H$) of the buildings along Bootham and Gillygate were measured using the angle of inclination method. The angle of inclination of an imaginary line from the observer located on one side of the street to the pitch of the roof on the opposite side was measured using an Abney level. At each survey location the observer's back was positioned against the opposing building wall. The width of each survey cross-section (i.e. the distance across the street from each building) was measured using a measuring wheel. The angles of inclination and the widths of the survey cross-sections were then used to calculate the heights of the buildings, taking into consideration the height of the observer's eye-level.

The roofs of the buildings along Bootham and Gillygate were generally pitched. However, buildings of different heights and with complex roof shapes were more common along Bootham. Overall, Gillygate was a relatively narrow symmetrical street canyon, with a height-to-width ($H/W$), or aspect ratio of ~0.8 and building heights of ~12 m. Figure 3.3 shows the Bootham and Gillygate street canyons and the surrounding building and street layout. The buildings are shown as rectangles

with yellow fill and the open spaces are blank. The figure also shows that there are relatively few openings along the SE wall of the Gillygate street canyon, whereas the NW side is broken by the adjoining side streets of Portland Street and Claremont Terrace. There are also smaller openings along the NW side of the Gillygate street canyon along the section that is closer to the common intersection. The city wall and its embankment, which surrounds the medieval city centre, are shown on the figure and are approximately parallel to Gillygate and Lord Mayor's Walk. The open spaces between the buildings and the city wall are gardens. However, the open spaces surrounding the Minster are part of Dean's park. The open space to the north of Gillygate is a large coach and car park.

Bootham is generally a wider street canyon than Gillygate and the building heights are predominantly greater at ~14 m. However, the street canyon geometry of Bootham is also more varied. Although $H/W$ is nominally 0.65 throughout the canyon, it is asymmetrical in places. Figure 3.3 shows that there are several locations along Bootham where the buildings are set back further from the road, producing much wider canyon spaces, particularly around the junction with Bootham Row. These wider canyon sections are also evident in the aerial photograph of Bootham shown in Figure 3.4.

The traffic-related pollutant concentrations were measured in the section of Bootham that is shown in Figure 3.3 and Figure 3.4 to be the furthest point away from the common intersection. This section of the canyon is close to the arrow that indicates the location of Bootham in Figure 3.4. This section of Bootham has an aspect ratio of $H/W \approx 0.75$ for background winds from the SW, whereas it is approximately 0.6 for background winds from the NE. Figure 3.4 also shows that the roofs of the buildings along Bootham, Portland Street and Claremont Terrace are pitched. Figure 3.4 also shows that trees were located at the kerbside along Bootham towards the NW end of the street (near to the arrow). The open spaces to the NE of Bootham at this end of the canyon comprise of playing fields associated with the nearby Bootham School.

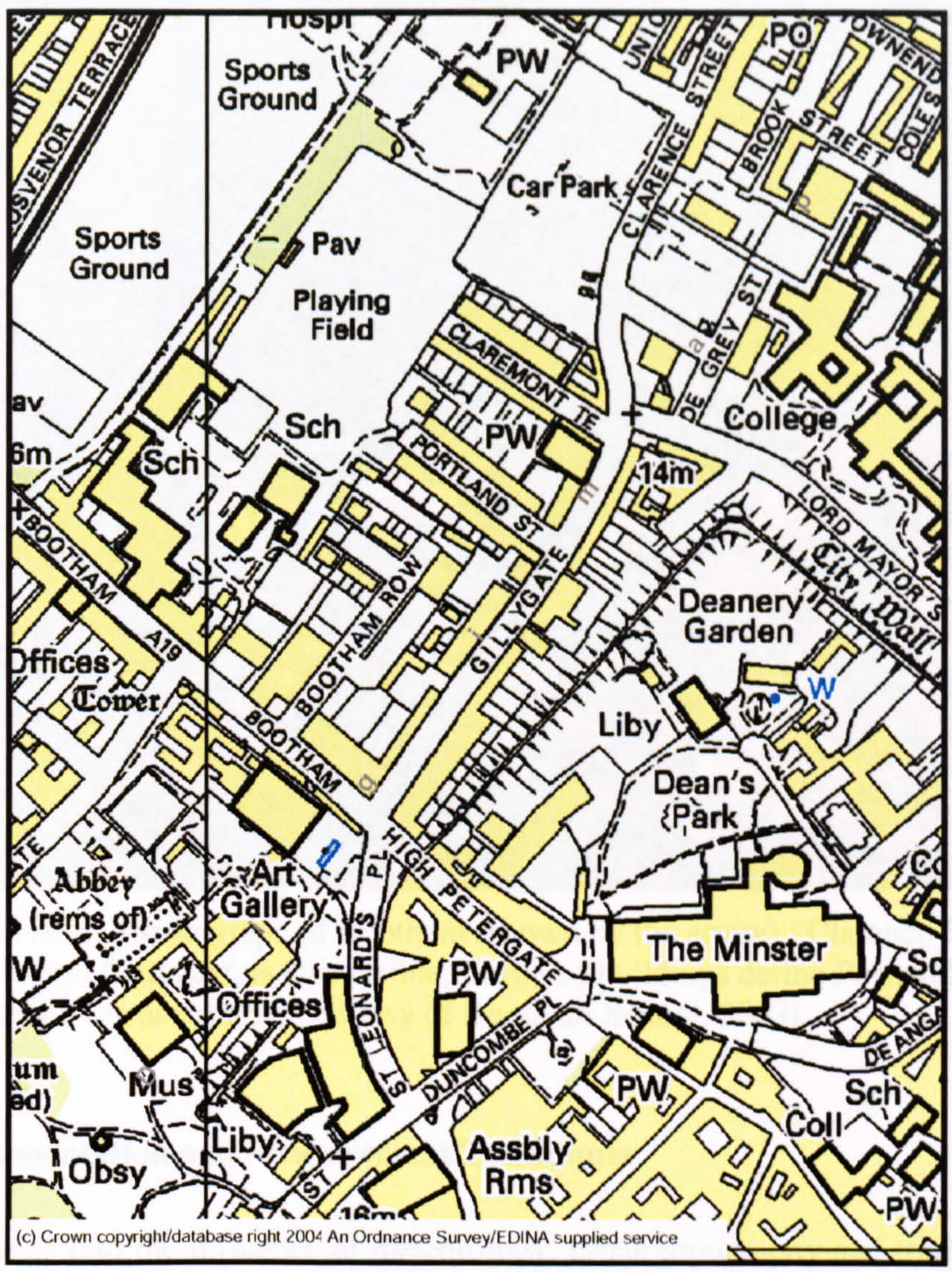


Figure 3.3. Plan view of the Bootham and Gillygate street canyons and the surrounding building and street layout. Note that the buildings are shown as yellow rectangles. Open spaces and roads are shown in white.

Figure 3.4. Aerial photograph of Bootham (shown by the arrow). Clarence Street, which leads into Gillygate, is also visible. Rows of buildings define Portland Street and Claremont Terrace (photo courtesy of Bootham School, 2003).

### 3.5. Instrumentation and Measurement Techniques

Investigations into the influence of meteorology, urban topography and traffic on the dispersion of a traffic-related pollutant where conducted in both street canyons during two separate field experiments. The first experiment was undertaken in March and April 2003, while the second experiment was conducted in October and November 2003. The first experiment was a pilot study during which the instruments were rigorously tested. In the following Chapters, only the analysis of the data collected during the second experiment is presented. A description of the instruments and measurement techniques used in October and November 2003 is shown in this Section. A description of the instruments used in the March and April 2003 experiment is also presented for comparison.

### 3.5.1. Meteorology

The meteorological variables measured during both field experiments were the above-roof (or background) wind speed and direction and the in-canyon wind and turbulence fields. However, during the October and November 2003 the in-canyon temperature and humidity fields were also measured. The following sub-section will describe the instruments used to measure the wind and turbulence in and around the Gillygate street canyon. The sub-section that follows after that will describe the instruments used to measure the temperature and humidity fields.

#### *3.5.1.1. Wind flow and turbulence*

The local right-hand Cartesian coordinates can be used to describe the motion of air. Although it is common to align this system with $x$ pointing east, $y$ pointing north and $z$ pointing upwards, many other alignment systems are used in street canyon studies. For example, the mean wind velocity components $U$, $V$ and $W$ may correspond to mean flow in the $x$, $y$, and $z$ directions, respectively. Figure 3.5 shows the positive velocity axes of the $U$, $V$ and $W$ components. A positive value of $U$, therefore, corresponds to a velocity component from south to north, while negative values relate to flow from north to south. Similarly, $V$ is positive westwards and $W$ is positive upwards. It should be noted that the ultrasonic anemometers used in the field experiments were aligned with the $U$-axis parallel to the street canyon axis. Therefore, the values of $U$ corresponded to parallel reference velocity components, while values of V corresponded to across-canyon velocity components. For clarity, the values of $W$ corresponded to the vertical velocity components.

Measurements of the in-canyon wind and turbulence fields were conducted using Gill Instruments omni-directional (R3-50) ultrasonic anemometers. The dimensions of the R3-50 ultrasonic anemometer were 750 mm from the base to the top of the head framework, whilst the length and diameter of the head framework were 240 mm. Due to its size and relatively light weight (<1 kg) the R3-50 ultrasonic anemometer could easily be fixed to a supporting bracket for use in field experiments. The method of attaching the supporting bracket to street furniture, such as lampposts, is described in Section 3.5.1.1.3. Seven sonic anemometers were located in and around the Gillygate

street canyon during the October and November experiment. The operating principle of an ultrasonic anemometer is described in the following sub-section.

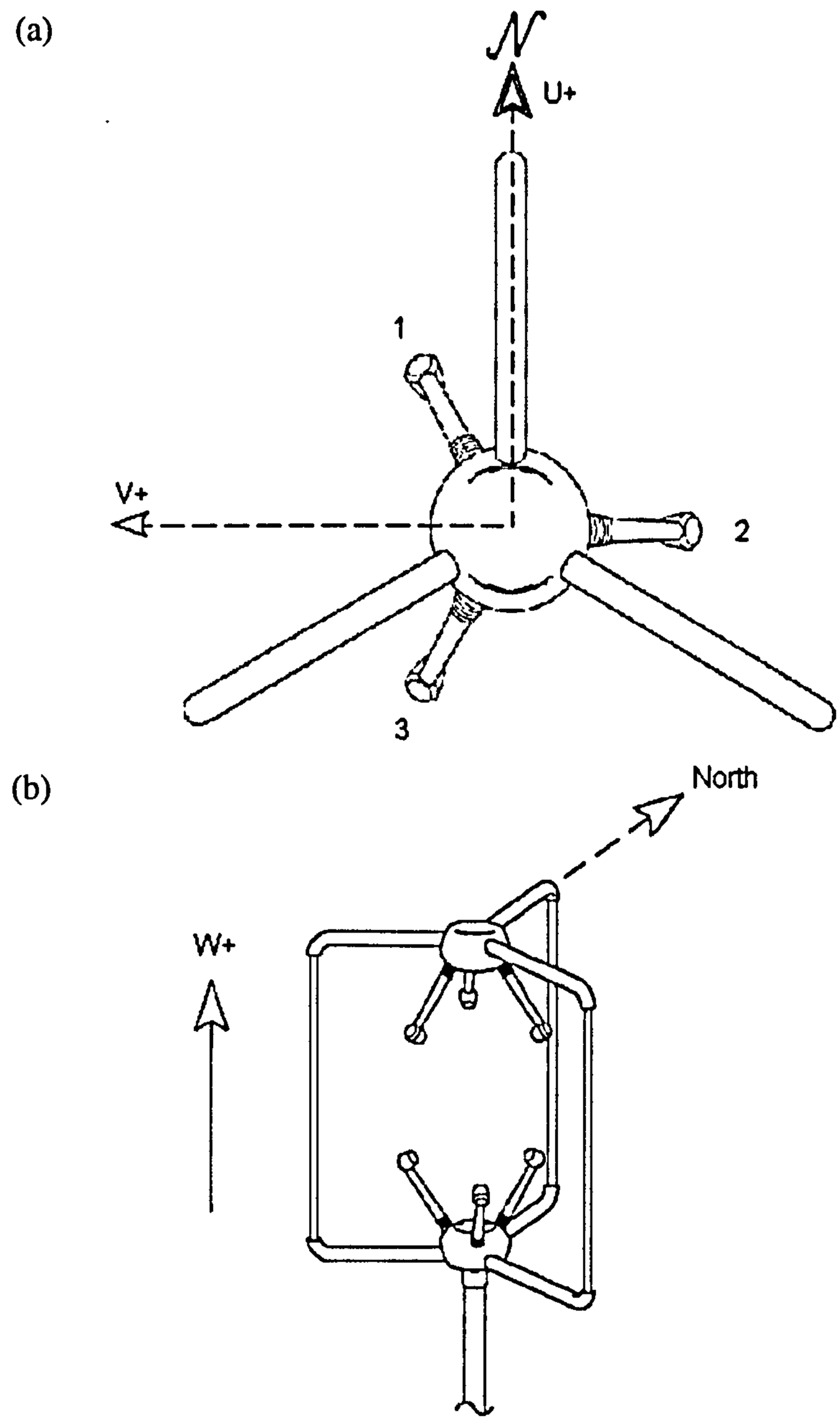


Figure 3.5. Schematic of the Gill R3-50 ultrasonic anemometer showing the positive velocity axes of the *U*, *V* and *W* components (a) plan view; (b) side view. Note that the numbers in (a) refer to the transducer pairs (Redrawn from Gill Instruments, 2002).

*3.5.1.1.1. Operating principle of an ultrasonic anemometer*

The basic time-of-flight operating principle of an ultrasonic anemometer employs fundamental physics and provides vector measurements of air velocity dependent on the dimensions and geometry of the transducer array. As mentioned previously, Figure 3.5 presents a schematic of the R3-50 ultrasonic anemometer showing the positive velocity axes of the *U*, *V* and *W* components.

The head framework that supported the transducer array can also be seen in Figure 3.5b. The three pairs of transducers acted intermittently as transmitters and receivers, sending pulses of high frequency ultrasound between each opposing pair. The operating frequency of the sonic anemometers could be set to 50 Hz. However, the operating frequency was usually set much lower during the experiment in order to improve the quality of the data captured. A further discussion of this is given below in Section 3.5.1.1.3. The wind measurement technical specification of the Gill R3-50 ultrasonic anemometer is detailed below in Table 3.1.

Table 3.1. The measurement specifications of the Gill omni-directional (R3-50) research ultrasonic anemometer (Gill Instruments, 2002).

| | |
|---|---|
| Measurement Rate | 50 $s^{-1}$ (full 3 axis measurement) |
| Data Output Rates | 0.4 – 50 $s^{-1}$ |
| Wind Speed Range | 0 – 45 m $s^{-1}$ |
| Wind Speed Accuracy | <1% rms |
| Wind Speed Resolution | 0.01 m $s^{-1}$ |
| Wind Speed Offset | <±0.01 m $s^{-1}$ |
| Directional Accuracy | <±1° rms |
| Directional Resolution | 1° |

The times of flight in each direction, $t_1$ and $t_2$, are measured (Gill Instruments, 2002). If $\gamma$ is the speed of sound, $l$ is the distance between the transducers and $v_l$ is the air flow along the line of the transducers, the following relationships are derived:

$$t_1 = \frac{l}{\gamma + v_l}, \tag{3.1a}$$

$$t_2 = \frac{l}{\gamma - v_l}. \tag{3.1b}$$

The air flow, $v_l$, is solved explicitly by inverting and subtracting the above equations to give:

$$v_l = 0.5l\left(\frac{1}{t_1} - \frac{1}{t_2}\right). \tag{3.2}$$

The wind vector derivation is not influenced by $\gamma$ or other parameters, such as temperature or contaminant content (Gill Instruments, 2002). Conversely, $\gamma$ is obtained by inverting and adding:

$$\gamma = 0.5l\left(\frac{1}{t_1} + \frac{1}{t_2}\right). \tag{3.3}$$

The air flow, $v_l$, represents the vector component of flow resolved along the line of transducers. The three pairs of transducers were arranged in different orientations (see Figure 3.5) in order to derive unambiguously the direction and magnitude of the incident air flow. Therefore, the transducer pairs do not have to conform to Cartesian axes (Gill Instruments, 2002). The orthogonal arrangement is arranged for optimum undisturbed air flow. The velocities along each transducer axis were calculated using Equations (3.1) – (3.3).

However, the anemometers were configured to operate in *UVW* format (described in Section 3.5.1.1.3) and so vector transformations were calculated in this mode using Equations (3.4a) – (3.4b) shown below. Figure 3.5a shows the plan view of the anemometer head framework and transducer array with the three transducer pairs numbered. The vector transformations were performed in order to derive the transducer axis-1 velocity, where *U*+ was orientated towards north (N). The axis-2 and axis-3 velocities were calculated in a similar way. The *UVW* axis alignment could be set by the user to either '*axis*' (i.e. the *U*-axis is aligned to transducer axis-1 when viewed from above) or '*spar*' (i.e. the *U*-axis is aligned with the north spar, as shown in Figure 3.5a). The equations below show the vector transformations used

when operating in *UVW-axis* format, where $a_1$ is the axis-1 velocity, $a_2$ is the axis-2 velocity and $a_3$ is the axis-3 velocity:

$$U = \frac{(2a_1 - a_2 - a_3)}{2.1213}; \tag{3.4a}$$

$$V = \frac{(a_3 - a_2)}{1.2247}; \tag{3.4b}$$

$$W = \frac{(a_1 + a_2 + a_3)}{2.1213}. \tag{3.4c}$$

The anemometers were also configured to operate in the calibrated mode, implying that a correction operation was applied to exclude flow distortions caused by the transducers and head framework. The *UVW* processed data was then output via the serial port. Section 3.5.1.1.4 describes how the anemometer data was acquired. First, however, it is necessary to describe how mean flow and turbulence can be derived from 3-component measurements.

*3.5.1.1.2. Calculating mean flow and turbulence*

*Mean wind direction and speed*

The raw measurement data collected from each transducer pair were calculated internally within the anemometer in order to derive the three orthogonal wind velocity components of *U*, *V*, and *W* in a right-hand Cartesian coordinate system. Having resolved the direction and magnitude of *U* and *V*, the mean horizontal direction (in degrees from N) for a given averaging period was determined. The arctangent, or atan, of the specified *U* and *V* components of the wind are used to derive the mean horizontal wind direction using the following formula if $V<0$:

$$\theta_{\text{ref}}, \eta = \text{atan}(\frac{-U}{V}) + 360^{\circ}. \tag{3.5}$$

A negative sign was allocated to the $U$ component in order to change from the Cartesian coordinate system to the compass system. However, if $V > 0$ the following formula was used:

$$\theta_{\text{ref}}, \eta = \text{atan}(\frac{-U}{V}). \tag{3.6}$$

This method was used in Chapter 4 to calculate the background wind direction, $\theta_{ref}$, and the in-canyon wind direction, $\eta$. The mean horizontal wind speed, $M$, can be calculated using the mean horizontal velocity components $U$ and $V$, according to the equation:

$$M = \sqrt{(U^2 + V^2)}. \tag{3.7}$$

*Turbulence*

Turbulence refers to irregular fluctuations occurring in fluid motions, such as wind. Concentrations of pollutants emitted by traffic travelling along a street canyon are affected by mean wind and turbulence. The mean wind causes pollutant transport i.e. it blows or advects the pollutants from the source to locations downwind. However, while the plume is advecting turbulent gusts present within the mean flow act to spread, or disperse, the pollutants as they mix with the surrounding air. This is why it is necessary to study both mean and turbulent characteristics of wind in order to determine downwind pollutant concentrations.

As wind consists of mean and turbulent parts, it can be considered to be relatively variable. Stull (2000) describes the total wind speed as the superposition of three types of flow, which can occur individually or in combination:

- mean wind — relatively constant, but varying slowly over the course of hours;
- waves — regular (linear) oscillations of wind, often with periods of ten minutes or longer;
- turbulence — irregular, quasi-random, non-linear variations or gusts, with durations of seconds to minutes.

Using the coordinate system described above, the $x$-direction component of the wind at some instant in time, $t$, can be described as $U(t)$. The values of $U(t)$ are likely to vary over time if the wind is variable. The mean wind in the $U$ component of velocity can be defined by averaging the instantaneous wind measurements over time. The mean wind can be subtracted from the instantaneous wind to give the turbulence or gust, as shown schematically in Figure 3.6. In general, turbulent flows (e.g. $U(t)$) contain a mean flow ($U$) and a random fluctuating component ($u'$). In other words, the turbulence in all three mean wind components can be defined using:

$$u'(t) = U(t) - U\,; \tag{3.8}$$

$$v'(t) = V(t) - V\,; \tag{3.9}$$

$$w'(t) = W(t) - W\,. \tag{3.10}$$

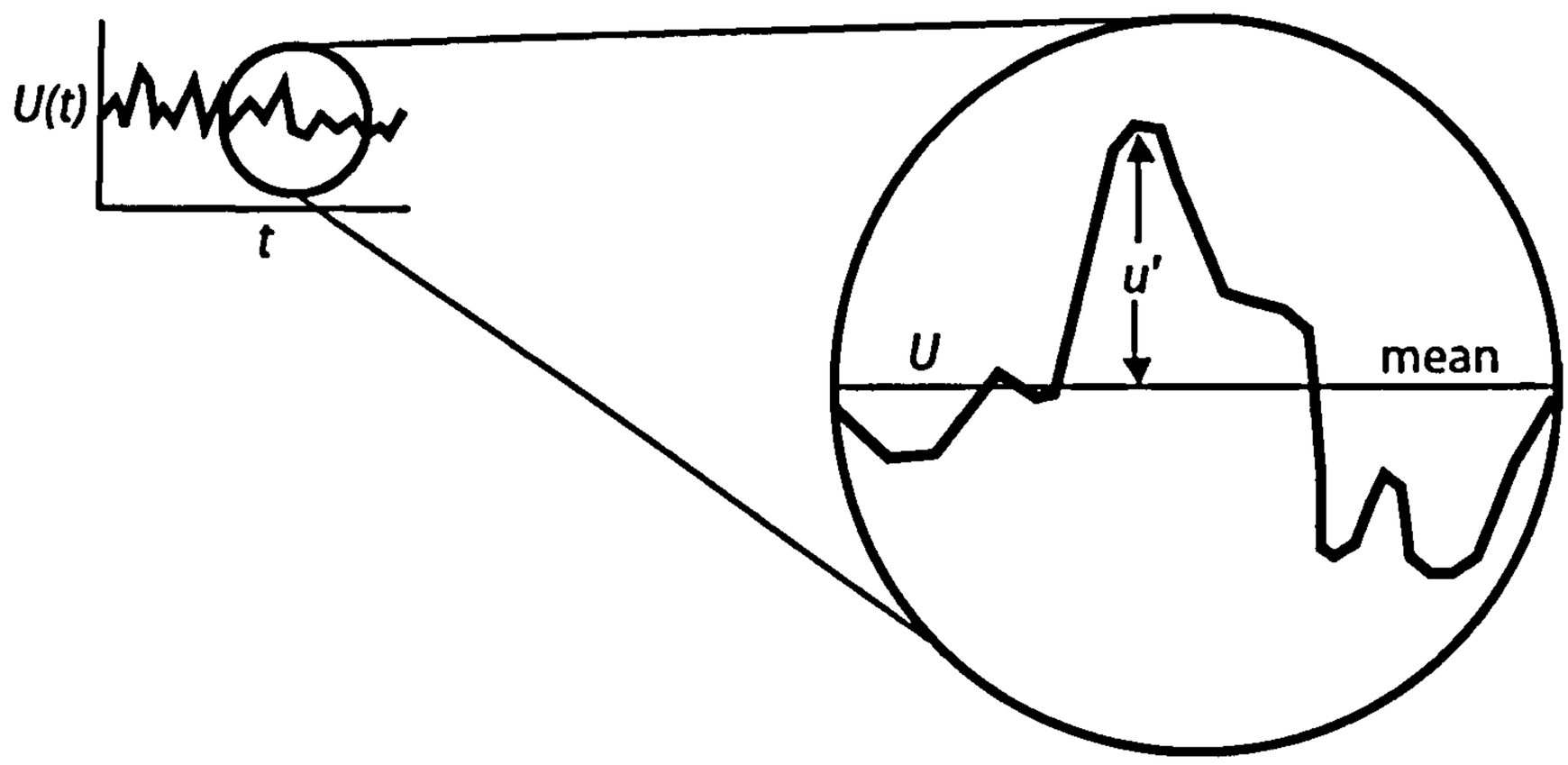


Figure 3.6. Schematic representation of a typical wind speed time-series, showing $u'$ as the gust or deviation of the actual instantaneous wind, $U(t)$, from the local mean, $U$ (redrawn from Stull, 1988).

Thus, the wind can be considered to be the sum of mean and turbulent parts (Stull, 2000). The mean wind velocities described in the above equations are defined over time. For example, the mean vertical velocity, $W$, is calculated as the sum of all individual vertical velocity measurements divided by the total number, $n$, of data points:

$$W = \frac{1}{n}\sum_{i=1}^{n} W_i \,, \tag{3.11}$$

where $W_i$ is the vertical wind speed measured at some time index, $i$.

The short term fluctuations described by the primed quantities in Equations 3.8 – 3.10 are associated with small scale swirls of motion, or eddies. The turbulence in the mean flow consists of the superposition of many such eddies of various scales. For example, $u'$ is highly disordered in space and at any instant in time there is a broad spectrum of eddy sizes within fully developed turbulence. The dissipation of mechanical energy within such flows are concentrated in the smallest eddies.

Friction within eddies is caused by molecular viscosity, which reduces the turbulence intensity. Therefore, turbulence is not a conserved quantity, but is dissipative. In street canyons, turbulence decays and disappears unless there are active processes to generate it. Mechanically produced turbulence in street canyons is caused by wind shear, or the change of wind speed and direction with height, particularly above roof height (see Chapter 2). Traffic passing along the street and convection also generate turbulence and are thought to be particularly significant during weak background winds.

The variance of the vertical velocity, $\sigma_w^2$, is a statistic of gustiness and is defined as:

$$\sigma_w^2 = \frac{1}{n}\sum_{i=1}^{n} (W_i - W)^2 \,; \tag{3.12}$$

$$\sigma_w^2 = \frac{1}{n}\sum_{i=1}^{n} \left(w_i{}'\right)^2 \,; \tag{3.13}$$

$$\sigma_w^2 = \overline{(w')^2} \,. \tag{3.14}$$

The variance of the horizontal components $\sigma_u^2$ and $\sigma_v^2$ can be similarly defined using the above equations. The standard deviation, $\sigma$ , is defined as the square-root of the variance and can be interpreted as an average gust. Therefore, the standard deviation for vertical velocity, $\sigma_w$, can be described by:

$$\sigma_w = \sqrt{\sigma_w^2}\,. \tag{3.15}$$

The variance or standard deviation of the velocity components gives an indication of the turbulence intensity, with larger values corresponding to greater intensities.

*Isotropy*

Turbulence is isotropic if it has the same variance in all three directions. In other words, isotropy occurs if:

$$\sigma_u^2 = \sigma_v^2 = \sigma_w^2. \tag{3.16}$$

In a wind tunnel, turbulence is approximately homogenous and isotropic. However, it cannot be entirely homogeneous or isotropic because it decays along the length of the tunnel and the grid itself may introduce anisotropy. Anisotropy arises from the mechanism which generates or maintains the turbulence. Therefore, turbulence in street canyons is expected to be anisotropic (Chapter 4).

*Turbulence kinetic energy*

An overall measure of the turbulence intensity is the turbulence kinetic energy (TKE) per unit mass:

$$TKE = 0.5 \cdot \left[\overline{(u')^2} + \overline{(v')^2} + \overline{(w')^2}\right]; \tag{3.17}$$

$$TKE = 0.5 \cdot \left[\sigma_u^2 + \sigma_v^2 + \sigma_w^2\right]. \tag{3.18}$$

The nature of the atmospheric turbulence spectrum is directly related to fact that production and dissipation are not happening on the same scales. Production feeds the larger size eddies, while dissipation acts on the smaller ones. The inertial subrange is defined as an intermediate range of turbulent scales or wavelengths that is smaller than the energy-containing eddies but larger than viscous eddies (American Meteorological Society [AMS], 2004). In the inertial subrange, the net energy coming from the energy-containing eddies is in equilibrium with the net energy cascading to smaller eddies where it is dissipated. The transfer can be thought of as happening inertially, i.e. large eddies creating or bumping into smaller ones and transferring some of their inertia in the process. In other words, turbulent energy cascades through the inertial subrange, where the large size eddies drive medium ones, which in turn drive smaller ones. Molecular viscosity is defined as the transport of mass motion momentum solely by the random motions of individual molecules not moving together in coherent groups (AMS, 2004). Molecular viscosity dissipates TKE in the smallest (microscale) eddies into heat. Therefore, TKE is not conserved. The tendency for TKE to increase or decrease was described by Stull (2000) using the TKE budget equation:

$$\frac{\delta TKE}{\delta t} = (A + S + B + Tr) - \varepsilon \tag{3.19}$$

where $A$ is advection of TKE by the mean wind, $S$ is shear generation, $B$ is buoyant production or consumption, $Tr$ is transport by turbulent motions and $\varepsilon$ is viscous dissipation rate.

The mean wind advects TKE from one location to another. The advection term is described by:

$$A = -U \cdot \frac{\delta TKE}{\delta x} - V \cdot \frac{\delta TKE}{\delta y} - W \cdot \frac{\delta TKE}{\delta z}. \tag{3.20}$$

From the above equation it is evident that turbulence at any location can increase or decrease if the wind advects greater or lesser values of TKE from another location.

Wind shear generates turbulence near the ground. By using the mean horizontal wind speed, $M$, wind shear is described as:

$$S = u*^2 \cdot \frac{\Delta M}{\Delta z}, \tag{3.21}$$

where $u*$ is the friction velocity and $\Delta M/\Delta z$ is the wind shear. Compared to weak winds, strong winds near the ground cause greater wind shear and, thus, more turbulence. Shear turbulence is produced in street canyons as the wind flows over the upwind edge of the upwind building, especially during winds orientated perpendicular to the street axis (Chapter 4).

When thermals rise from a heated urban surface they generate TKE, i.e. buoyancy increases turbulence. Conversely, when the ground is cold and the urban boundary layer is statically stable, buoyancy opposes vertical motion and consumes TKE. Stull (2000) describes the rate of buoyant production or consumption of TKE as:

$$B = \frac{g}{T_v} \cdot F_{Hsfc}, \tag{3.22}$$

where $g$ is gravity, $T_v$ is the absolute virtual air temperature near the ground and $F_{Hsfc}$ is the effective surface heat flux and is positive when the ground is warmer than the air above. In street canyons, $F_{Hsfc}$ and $B$ are likely to be positive during the daytime and negative at night.

The transport term used in Equation (3.19) suggests that turbulence can be advected by the mean wind. Therefore, the turbulence produced by shear above roof-level is transported into the street canyon in a single across-canyon recirculating flow (with a horizontally-aligned axis) during perpendicular background winds (Chapter 2). Additional turbulence from sources inside street canyons, such as traffic and thermals, may also be transported in the recirculating flow.

Turbulent motions are dissipated into heat by molecular viscosity. Stull (2000) states that although the amount of heating is small, the amount of TKE consumed is large

and, therefore, dissipation is always a loss. Equations (3.17) – (3.22) demonstrate that TKE is a useful measure of the intensity of turbulence, especially in complex street canyons in which several production and dissipation processes simultaneously interact.

*3.5.1.1.3. Trial runs*

Several trial runs were conducted with the sonic anemometers on Clarendon Road in Leeds prior to the field experiments using a laptop running Gill RCOM software version 4 or RCOM2. During the test runs the anemometer was hardwired to a power and communications interface (PCI) using an RS422 serial link. The full duplex RS422 interface provided the conversion to RS232. The PCI was connected to the laptop using an RS232 serial link. The PCI was powered by DC from a 40 Ah car battery.

The capabilities of the anemometer used in the trial runs were rigorously tested, which involved experimenting with the various settings for the operating and measuring modes. However, the anemometer was usually configured with the absolute temperature reporting and the audible confidence tone disabled. The six analogue inputs were also disabled. The baud rate and operating frequency were usually set to 9600 and 20 Hz, respectively. The alignment of the *U*, *V* and *W* axes were set to "spar", with *U*+ towards north, as shown in Figure 3.5a. The result message string format was set to report continuously in binary. The wind measurement reporting format was set to *UVW* format, i.e. the three components of velocity were reported in 0.01 m $s^{-1}$ units (two's complement signed). The speed of sound reporting format was set to speed of sound rather than sonic temperature and was reported in 0.01 m $s^{-1}$ units (unsigned). For clarity, it should be mentioned that the anemometers were all configured with the same settings prior to the October and November 2003 field experiment. At the end of the trial runs the stored binary files were converted to ASCII by using a modified version of the Gill Convert 3 program. The data files were then able to be read in a text editor or spreadsheet.

These short trial runs also provided the means to perfect the design of the supporting bracket upon which the anemometers were to be fixed in order to allow their

attachment to lampposts in the street. Each anemometer was bolted to an aluminium bracket that weighed approximately 4kg (Figure 3.7). The brackets were ~0.65 m in length. The backplate of the brackets were used for attaching the anemometer to street furniture such as lampposts using Band-It aluminium banding. At the top and bottom of the backplate of each bracket were grooves, which were used to hold the ½" width banding when attaching them to lampposts. The slack in the banding was pulled tight using a banding clamp. Once the bracket was located at the appropriate height the bandings were securely fastened using Band-It buckles. The bracket also had an adjustable stage in order to level the anemometer prior to operation. When the anemometer was mounted on the stage it was insulated by a rubber gasket.

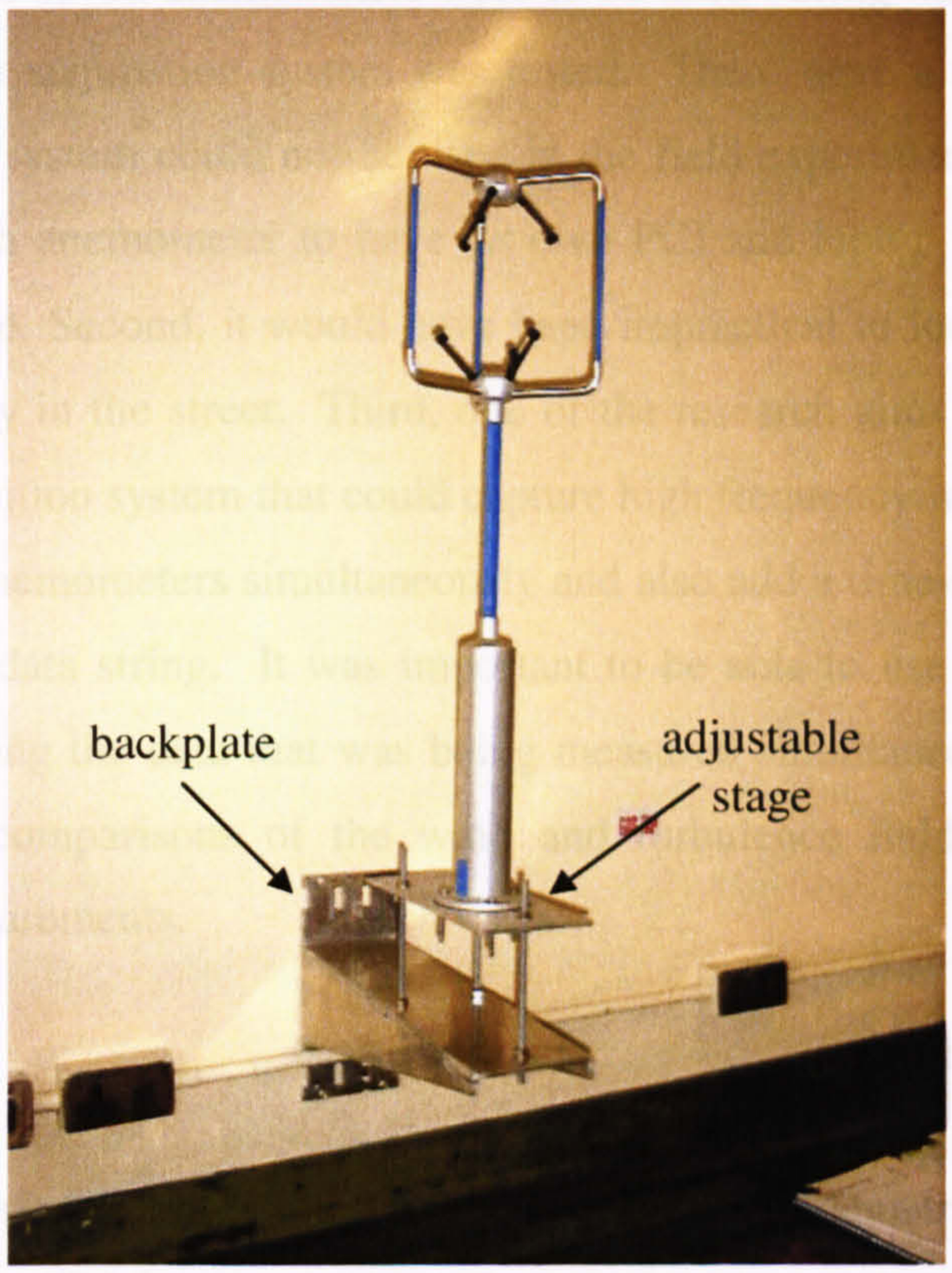


Figure 3.7. The aluminium bracket used to attach the Gill R3-50 ultrasonic anemometer to street furniture, such as lampposts. Note that modifications were made to the bracket shown here in order to make the structure lighter.

The end view of the prototype of the bracket was T-shaped with the centreplate supported on the backplate by a single central fin. However, during the trail runs it was evident that the bracket and anemometer oscillated in strong gusts. The oscillation was reduced by adding two side fins to give further support to the

centreplate and by shortening the bolts of the adjustable stage. Figure 3.7 shows the addition of the two supporting side fins that tapered towards the backplate, causing the end view of the bracket to become m-shaped. However, the design of the bracket was modified further in order to reduce the weight bearing on the lampposts. The modifications consisted of cutting out sections of the aluminium plates, which reduced the overall weight of the bracket by a factor of ~2, whilst retaining its rigidity.

*3.5.1.1.4. Data acquisition systems*

It was mentioned that during the trial runs the data were captured by hardwire serial links. However, as seven anemometers were to be used during the field experiments an alternative data acquisition system was tested. There were a number of reasons why the hardwire system could not be used in the field experiments. First, it would have required each anemometer to have its own PCI and laptop which would have been too expensive. Second, it would have been impractical to locate the equipment securely and safely in the street. Third, one of the research aims was to design and build a data acquisition system that could capture high frequency wind and turbulence data from seven anemometers simultaneously and also add a time-stamp and location identifier to each data string. It was important to be able to use a system that was capable of collecting the data that was being measured simultaneously by the seven anemometers as comparisons of the wind and turbulence fields clearly required synchronous measurements.

*Telemetry*

During the March and April 2003 field experiment a telemetry data acquisition system was tested. Trial runs were conducted along a quiet side street adjoining Clarendon Road with infrequent vehicular activity. Warwick Wireless X7200 synthesised radio modems were used. The Warwick Wireless X7200 radio modems transmitted and received half duplex serial data at baud rates of 1200 to 19200 by means of a FM radio transceiver operating on the UK licence exempt 458.500 MHz to 458.950 MHz band.

The transmitting RS422 radio modem was encased in a custom-built weather-proof box, which was fastened to the anemometer supporting bracket. The anemometer supporting brackets and the transmitting modem boxes were attached to lampposts using Band-It fasteners, as mentioned earlier. Each anemometer was assigned a modem pair. The transmitting modem sent the RS422 data strings from the anemometer to the receiving RS232 modem that was connected by a serial link to a PC located in a nearby office. The transmitting antennae were attached to wooden supports fastened to the lamppost upon which the anemometers were located. During the trial runs various types of antennae were used for the transmitting and receiving modems, including end-fed dipoles and half-wave antennae. However, it was found that the telemetry system operated best by using an end-fed dipole to receive the data from the half-wave antennae. Each modem pair was assigned its own unique radio frequency (RF) channel and station address. In theory, this was to avoid interference with the other modems.

During the trials communication could be made to the anemometers using RCOM2 or HyperTerminal when they were configured to operate at ≤10 Hz. The data was transferred continuously in binary format and was converted to ASCII using the modified Convert 3 program. Experiments were also conducted using a Delphi program written by B. Brooks, School of Earth and the Environment, University of Leeds, to connect to and receive data from each anemometer. The advantage of using the Delphi program over the RCOM2 software was that the former created a time-stamp and anemometer identifier (e.g. serial number) for each data string received. The proportion of clean data from the anemometers and their mean operating frequencies during the trials were high. Further trials of the telemetry system were carried out in the Gillygate street canyon.

The telemetry system was finally deployed in Gillygate for four weeks during the March and April field experiment. Three anemometers were bolted to aluminium brackets that were attached to lamppost G3 on the SE side of the street (see Figure 3.8). Lamppost G3 was also used in the full experiment conducted in October and November. Lamppost G3 was located approximately half way between Portland Street and Claremont Terrace on the opposite side of the street (Figure 3.8). For clarity, lamppost G4 (located opposite G3 on the NW side of the street) was only

installed for the October and November experiment. The heights of the anemometers attached to lamppost G3 were $z$ = 2.5 m, $z$ = 4.5 m and $z$ = 6.5 m. It should be stressed that the anemometer heights referred to in this thesis correspond to the distance from the ground to the centre of the transducer array. The fourth in-canyon anemometer was used occasionally and was attached to a stand at $z$ = 1.1 m.

Figure 3.8. Plan view of the study area showing the Bootham and Gillygate street canyons, the lampposts that supported the instruments and the location of the G3-G4 experiment cross-section. The reference anemometer mast and the four SCOOT sensors (arrows indicate the direction of traffic flow measured) are also indicated.

Each in-canyon anemometer was assigned with a transmitting modem that was housed in a water-tight box fitted with a half-wave antenna. A fifth anemometer was located on a trailer-mounted mast at $z$ = 19.5 m and was used to measure the above-roof wind speed and direction. All five RS422 modems transmitted the data measured at each location to a third floor office in the building opposite lamppost G3. Each receiving RS232 modem was fitted with a half-wave antenna and was connected to the PC comm. ports via serial links. However, experiments were conducted using a single end-fed dipole receiving antenna with an 8-way signal splitter. The receiving antennae were located outside the office window on the sill. Communication was made to each anemometer using RCOM2 or HyperTerminal.

The Delphi program was used to transfer and store the data from each anemometer. The PC time was regularly synchronised to a radio-controlled clock. The Delphi program, therefore, entered an accurate time-stamp for each data string received from each location. The RF channels that allowed for the quickest communication with the anemometer were chosen for each modem pair as it was assumed that they had the least amount of interference from other networks operating nearby. Station addresses were chosen as a means of identifying each modem.

However, the measurements of the above-roof winds and the in-canyon wind and turbulence fields using the telemetry system proved disappointing, given that data from each location was required to be simultaneous and continuous over a suitable period of time. Comparisons of the wind and turbulence fields at each location could only be achieved for ~10 days. In the early part of the experiment, there were too many occasions when one or more of the anemometers were offline to perform statistical analysis of the data in order to achieve the aims and objectives of the research mentioned in Chapter 1. Therefore, it was not possible to accurately determine the influence of in-canyon flow structures on the dispersion of traffic-related pollutants.

Chapter 9 presents the proportion of clean data and the mean data collection rate for the reference anemometer located on the mast (Section 3.5.1.2) and the 5 anemometers located in the street canyon. The proportion of clean data for the in-canyon anemometers was relatively high and suggests that radio modems may be used in future field experiments to reveal mean speed and direction data. However, the number of days when the proportion of clean data from the in-canyon anemometers was an average of 97.7% corresponds to only 10 days, as mentioned earlier, which is why the trial field experiment was disappointing (see Chapter 9). For this reason the field experiment conducted in October and November used a hardwire data acquisition system, which would operate more reliably for a longer period of time.

Attempts were made to improve the RF signals during the field experiment. First, the signals of the receiving modems were attenuated by fitting a 20 cm length of coaxial cable to each modem using a T-piece BNC connector. Second, the orientation of the

transmitting and receiving antennae were changed. Third, the insides of the aluminium cases that housed the transmitting modems were insulated from the lamppost and the mast. Lastly, the RF power output from the transmitting modems was reduced from 500 mW to 5 mW by means of a ten-turn potentiometer located on the inside of the modems. The power output was reduced as it was assumed that the source of the interference was from the other transmitting modems. However, these modifications made very little difference to the overall data quality, particularly in the early part of the experiment.

The factors affecting the performance of a radio link inside a street canyon are shown in Table 3.2. Interference from other networks operating nearby is likely to have been a major contributing factor. BBC Radio York was located only 50 m away from Gillygate and may have been a source of some interference. However, the building and street geometries and street furniture such as lampposts, scaffolding and fall pipes are also likely to have affected the radio signals. As these features are common in street canyons the appropriateness of the radio modem data acquisition system in street canyon experiment is questionable. It is ironic that the weather may also have been an influence as the telemetry system was designed, after all, as a means of collecting anemometer data. However, the radio modems did provide useful data for a short period of time that could be used in future work to reveal spectral properties of the turbulence (see Chapter 9).

Table 3.2. Factors potentially affecting the performance of a radio link

1. Transmitter power output;
2. Height of the transmitter and receiver antennae;
3. Type of antenna used;
4. Surrounding buildings and streets (urban topography);
5. Interference from other networks operating on the same frequency;
6. The weather.

*Data loggers*

In order to achieve a higher proportion of clean data over a longer period of time during the October and November field experiment the telemetry system was replaced with a custom-built data logging system. The anemometers used were configured as described in Section 3.5.1.1.3. Four data loggers were used during the October and November experiment; and each one was housed in secure steel enclosures. One data logger was hardwired to a pair of anemometers via a serial link.

The data loggers situated beside lamppost G3 were powered by DC from a 100 Ah car battery located in a reinforced-alloy enclosure, which was fused and fully-insulated. One battery was used to power two data loggers and four anemometers located on lamppost G3. These battery and data-logger enclosures were painted black prior to the experiment in order to blend in with the surroundings and, thus, reducing the visual impact. Additionally, painting the enclosures black reduced the likelihood of vandalism. A second data logger, which was also painted black, was located at the foot of lamppost G3. The three enclosures located at the foot of lamppost G3 were secured to the lamppost using heavy-duty steel chains and padlocks. The data logger and battery enclosures used for the anemometer pair located on the opposite side of the road on lamppost G4 (Figure 3.8) were secured in the same manner.

The data logger situated beside lamppost G4 was powered by an 85 Ah car battery as it was connected to only two anemometers. A data logger was also connected to the anemometer located on the trailer mounted mast, which was used to measure the above-roof winds (see Section 3.5.1.2). A time-stamp provided by each data logger was synchronised at least every 24 hours to a GPS clock. The data were stored on flashcards, which were removed daily to retrieve the data. The batteries powering the data loggers were also changed daily.

Three anemometers were located on lamppost G3 with the measuring volumes at $z$ = 3.6 m, $z$ = 5.5 m and $z$ = 7.2 m above the pavement. A temporary anemometer, deployed for several hours each day, was located on a stand beside the same lamppost at $z$ = 1.1m. The data from the temporary anemometer was used in the TPT analysis. On lamppost G4, the anemometers were at $z$ = 5.7 m and $z$ = 10.1 m, the former

allowing comparison with the anemometer at $z$ = 5.5 m on the SE side of the street (see also Boddy *et al.*, 2005a).

During the experiment, the operating frequency of the in-canyon anemometers was 20Hz. The anemometers measured the wind and turbulence fields for four weeks, during which measurements were taken from five in-canyon anemometers for 24 hours a day and 7 days a week. However, the sonic anemometer data were not continuous due to the practical need to stop logging while retrieving the flashcards. There were also periods when the mean data collection rate of the in-canyon anemometers dropped below 18 Hz due to a coding error in the data logging software. All time periods corresponding to these events comprised of 7.9% of the total data and were excluded from analysis. However, the performance of the data logging system was far superior in terms of data quality compared to the telemetry system used in the previous experiment. This method of data acquisition provided the statistical means to determine the influence of the in-canyon flow structures in dispersing a traffic-related pollutant.

In summary, measurements of the in-canyon wind flow and turbulence were conducted on both sides of the street during the October and November experiment using the data logger acquisition system. Measurements were conducted at 4 different heights on lamppost G3 and at 2 different heights on lamppost G4. Two anemometers were located at the same height on each lamppost at approximately mid-canyon level in order to allow for comparison.

### *3.5.1.2. Background wind speed and direction*

Measurements of the background wind speed, $U_{ref}$, and direction, $\theta_{ref}$, were conducted during both field experiments. On both occasions a trailer-mounted mast was located in a car park compound approximately 125 m to the NW of Gillygate (Figure 3.8). The compound was secured by a remote-controlled steel gate and walls that were 5 m tall with razor wire across the top edges. Vehicular access to the compound was via Bootham Row. A Gill R3-50 ultrasonic anemometer was bolted to a supporting bracket that was attached to the top of the mast. The telescopic mast, which was also pneumatic, was raised using a pump powered by two 85 Ah car batteries. The

anemometer located on the fully-raised mast was at $z = 19.5$ m. Guy ropes were used to secure the mast during the experiment. During the October and November experiment the anemometer was connected to a data-logger and operated at 10 Hz.

The car park was considered to be the most suitable location in the vicinity to measure the background winds, as from almost all directions the anemometer was approximately 1.8 times the average height of the surrounding buildings, i.e. $1.8H$. During winds from the west, however, the influence resulting from flow distortion caused by a large tree approximately 10 m west of the anemometer was considered in the following chapters.

The wind direction data collected at the mast during the October and November experiment were compared with data sampled at 7 m using an aerovane located at the City of York Council's automatic weather station in the grounds of Bootham Hospital, as shown in Figure 3.9. The aerovane was located approximately 140 m to the N of the mast and unfortunately was situated in the lee of a large building.

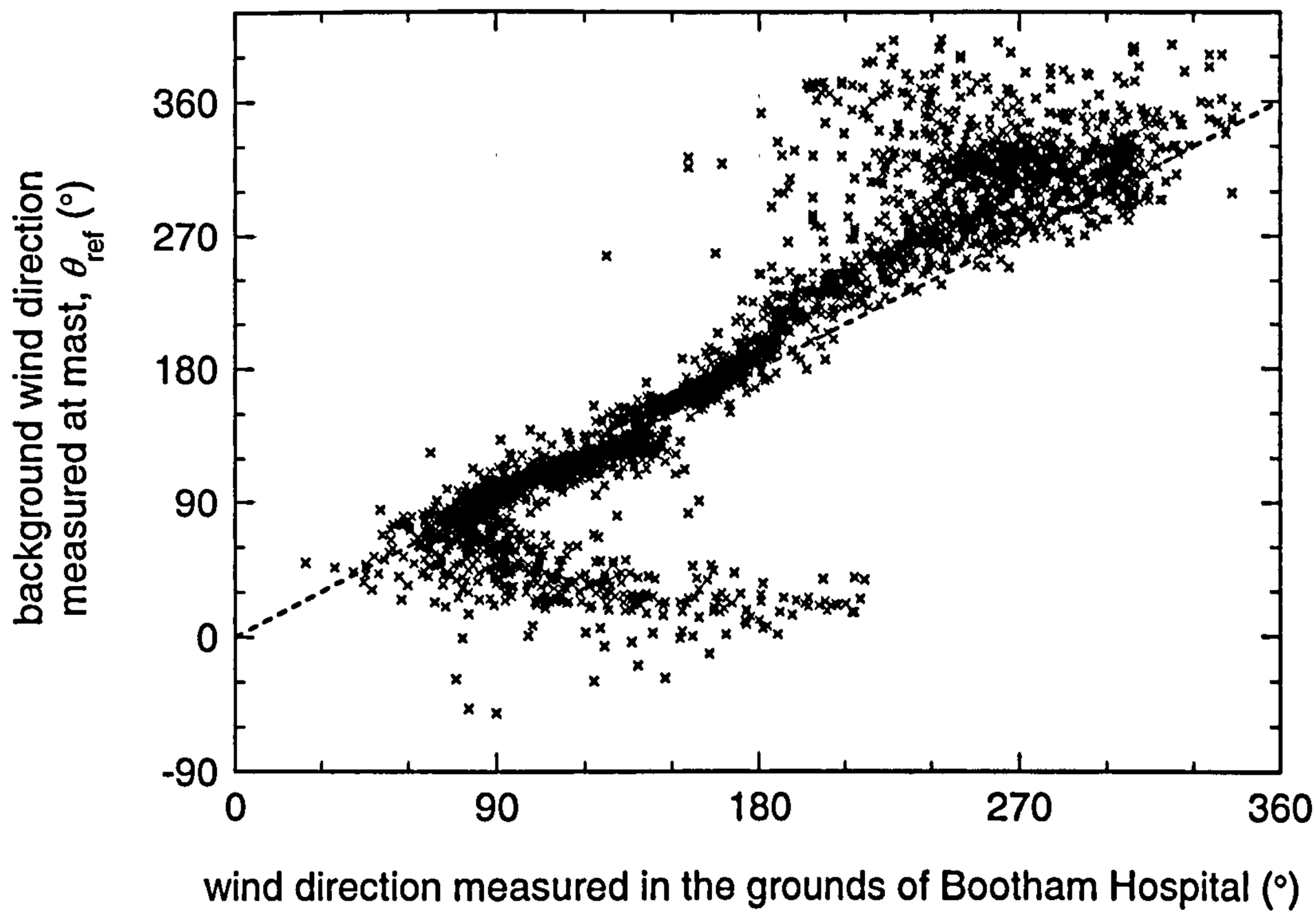


Figure 3.9. Comparison between the background wind direction, $\theta_{ref}$, measured at the mast during the October and November 2003 experiment against the wind direction measured in grounds of Bootham Hospital.

The suitability of the Bootham Hospital monitoring site for obtaining background wind measurements for street canyon studies was brought into question following the analysis of the wind and CO concentration data collected along Gillygate between 1 August and 9 December 2002. Boddy *et al.* (2003a) described the dispersion of CO inside Gillygate and Bootham using the Bootham Hospital reference wind data. However, as the aerovane was located in the lee of the building the instrument was positioned within a flow recirculation zone during winds from the N. As a result, background winds from 315 – 45° were excluded from the concentration rose analysis presented in Boddy *et al.* (2003a,b,c).

The dashed line shown in Figure 3.9 represents the 1:1 regression line. It is clear from the regression analysis that the Bootham Hospital wind data compares well with the mast data, particularly for $90° \leq \theta_{ref} < 180°$ when most of the data points fall on the regression line. This is likely to be attributable to the relatively large homogenous fetch associated with the park, which is vegetated mainly by grass for these wind directions. However, a noticeable departure from the regression line is evident for background winds corresponding to the northerly directions, during which southerly winds were recorded in the park. This is likely to be due to the development of flow recirculation in the lee of the hospital building. The data shown in Figure 3.9, therefore, demonstrates the importance of establishing a suitable reference location to measure the background wind prior to conducting a field experiment. Further discussion into the importance of establishing a suitable background reference location is given in Chapter 5, particularly in relation to the influence of the Minster on the urban wind field.

*3.5.1.3. Temperature and humidity*

During the October and November experiment the temperature and humidity fields were measured inside radiation-shielded screens using Gemini Tinytag Plus data loggers. The screens were attached to the anemometer brackets at $z = 2.9$ m and $z = 4.5$ m on lamppost G3 and at $z = 5.0$ m on lamppost G4. The data collected by the Gemini loggers were averaged over 5-minute intervals and stored in memory. The temperature and humidity data were collected in order to create a comprehensive data set from the street canyon field experiment.

However, analysis of the temperature and humidity data is not included in this study and the effects of convection on the dispersion of the traffic-related pollutant were assumed to be negligible, particularly for winds >1.2 $ms^{-1}$ (Chapter 4). Although wind tunnel studies (e.g. Kovar-Panskus *et al.*, 2002) and computational studies (e.g. Sini *et al.*, 1996; Kim and Baik, 2001) suggest that street canyon walls heated by the sun influence the mechanically driven recirculating flow (see also Chapter 2), it seems unlikely to be operationally important in most scenarios (see Britter and Hanna, 2003). It was mentioned in Chapter 2 that any effect is far less evident in field measurements (e.g. Louka *et al.*, 2002) probably because, in the field, the physical width of the free convective boundary layer on the heated wall is small compared to the scale of the mechanically driven motion (Britter and Hanna, 2003), which is of course on the street scale.

### 3.5.2. Concentrations of a traffic-related pollutant

The traffic-related pollutant measured in this study was carbon monoxide (CO). Learian streetboxes incorporated electrochemical sensors located on the outside of the logger unit. Each streetbox was configured to sample at 1-minute intervals and to calculate and store the concentration data as 15-minute averages in parts per million (ppm). The mean CO concentration data were reported at the end of each time period. Each streetbox unit was a battery powered stand-alone pollution monitoring and logging system. The batteries used were lithium and their performance and longevity were tested during trial runs and were found to be of a high standard.

Furthermore, due to their relatively light weight and small size of approximately 280 by 170 by 120 mm they could be easily attached to an item of street furniture, such as a lamppost, using 3/8" width Band-It banding. At the top and bottom of the backplate of each unit were reinforced alloy hoops. When attaching the units to lampposts the banding was passed through the hoops and the slack was pulled tight using a banding clamp. Once the unit was located at the appropriate height the bandings were securely fastened using Band-It buckles. The Band-It materials were found to be the most secure way of fixing the anemometer brackets and streetboxes to lampposts during trial experiments conducted prior to the field experiments.

One of the major advantages of the streetbox over other pollution monitoring equipment was its ability to be located at any height on lampposts. For the duration of the October and November experiment, 26 streetboxes were attached to 15 roadside lampposts within each street canyon. One streetbox was located in Portland Street and provided a measure of the background CO concentration. This large spatial coverage allowed the spatial variability in concentrations to be investigated. Furthermore, as the streetboxes were stand-alone logging units they could be left relatively undisturbed. However, each streetbox was regularly monitored during the experiment in case the lithium battery voltage dropped below 10.4 volts, after which the unit was likely to fail. Section 3.5.2.2 describes how regular communication was kept with the streetboxes. The analysis of the data from the streetboxes located on the lampposts shown in Figure 3.8 is presented in Chapters 5 and 7 (see also Boddy *et al.*, 2005a,b).

*3.5.2.1. Operating principle of the streetbox*

The streetbox is a pollution monitoring unit comprising integral power and communications, electrochemical sensors and a data logger. This is shown schematically in Figure 3.10. The streetbox differs from other roadside pollution monitoring equipment as it is self-powered and can run for several weeks without external intervention. The exact period of time that the lithium batteries lasted in the field was dependent upon the sampling and averaging intervals chosen and the external temperature. However, the batteries lasted approximately six weeks during the October and November experiment. The capabilities of the streetbox were achieved as the unit uses a low power data logger and sensor assembly and because it does not utilise external devices such as pumps, active filters or switched airflow for automatic baseline or span corrections (Learian, 2002). The ease of deployment and operation flexibility meant that the streetbox had distinct advantages. However, because of the absence of automatic baseline and span corrections it was necessary to manually correct for these during post-processing based on the most recent calibration. A detailed description of the data quality assurance and control procedure undertaken is given in Section 3.5.2.3.

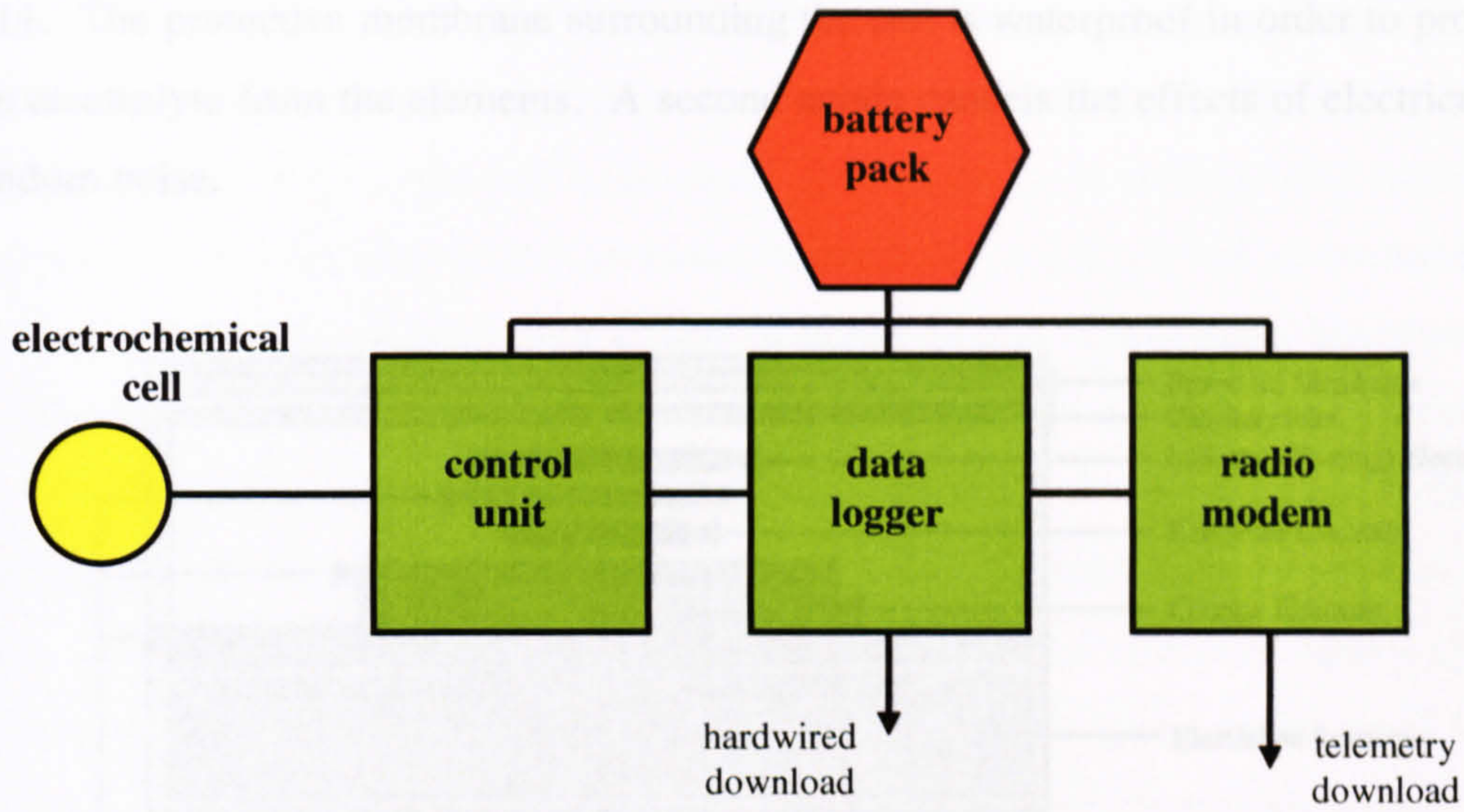


Figure 3.10. Schematic representation of the Learian streetbox electrochemical cell monitoring unit showing the hardwired and telemetry methods of establishing a connection (Modified from Ropkins *et al.*, 2000).

Electrochemical cells are used to measure electrochemical current and, therefore, ion migration between electrodes connected by an electrolytic medium. Thus, electrochemical cells can be used to detect or quantify analytes that react within the electrochemical cell to offset the cell's internal electrochemical equilibrium (Ropkins *et al.*, 2000) and thereby generating electrical current. Electrochemical cells contain two electrodes, one which acts as an indicator electrode (which is analyte sensitive) and the other is used as a reference electrode (which has a fixed voltage, often set to zero) and current flow and resistance is measured between the two electrodes (Ropkins *et al.*, 2000).

The streetbox electrochemical cells function passively by directly exposing the cells to ambient air. The Siemens RPM system, which also uses electrochemical cell technology, differs in the way it incorporates complex air intake systems and delicate analysis chambers. Whilst an air intake system is likely to reduce the chances of electrochemical cell damage, fouling and/or contamination it is also likely to increase the purchase cost of the instrument and the utilisation of moving parts, such as an air intake pump, can significantly reduce the operational reliability of an instrument (Ropkins *et al.*, 2000).

The electrochemical cell of the type incorporated in the streetbox is shown in Figure 3.11. The protective membrane surrounding the cell is waterproof in order to protect the electrolyte from the elements. A second anode cancels the effects of electrical or random noise.

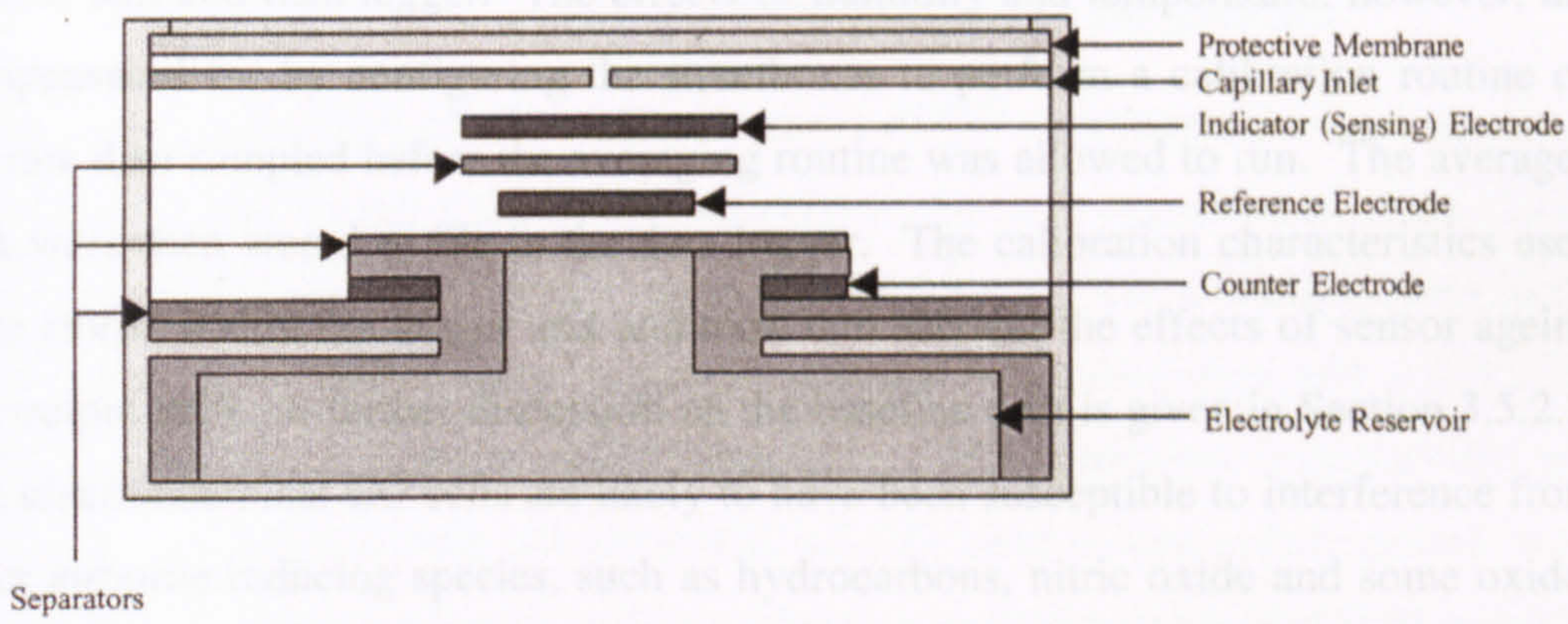


Figure 3.11. Side view of the electrochemical cell of the type fitted in the Learian streetbox (Ropkins *et al.*, 2000).

The electrochemical carbon monoxide cells are reduction-sensitive that measure CO based upon the general reaction:

$$CO + [O] \rightarrow CO_2 .$$

The detection limits of the streetbox fitted with an electrochemical CO sensor are reported to be in the order of 0.5 ppm, quantification ranges of the order of 2000 ppm and precisions of the order of 1% (Learian, 2002). Table 3.3 shows the accuracy of the streetbox electrochemical CO sensor.

Table 3.3. Learian streetbox fitted with an electrochemical CO sensor (Learian, 2002).

| | |
|---|---|
| Operating life | 3 years exposed to air |
| Maximum range | 0-2000 ppm |
| Resolution | 0.5 ppm |
| Maximum zero shift | 3 ppm |
| Temperature range | -20°C to +50°C |
| Pressure range | Atmospheric +/- 10% |
| RH range | 15% to 90% (non-condensing) |
| Long term output drift | < 5% per year |
| Repeatability | 1% of signal |

The trade-off with the construction of the electrochemical cells is that the sensor will always be exposed to external influences such as temperature and humidity. In particular, moisture can affect the viscosity of the electrolyte, which in turn would affect the accuracy of the results obtained. However, it is unlikely that rainwater entered the cells as they were positioned beneath an overhang that constituted the control unit and data logger. The effects of humidity and temperature, however, are compensated for by configuring the streetboxes to perform a calibration routine on the raw data sampled before the averaging routine was allowed to run. The averaged data were then stored to file in the data logger. The calibration characteristics used were stored within the logger unit and took into account the effects of sensor ageing and output drift. A further discussion on the baseline drift is given in Section 3.5.2.3. The electrochemical CO cells are likely to have been susceptible to interference from other airborne reducing species, such as hydrocarbons, nitric oxide and some oxides of sulphur. However, it is assumed in this study that these effects were negligible.

*3.5.2.2. Establishing a connection with the streetbox*

The streetbox could be connected via an RS232 serial link direct to the laptop using the Learian streetbox software. The hardwired method was used in the laboratory prior to the field experiments in order to configure the sampling and logging routines. Once communication had been established it was also possible to check the status of the logger and to synchronise the time. However, there were occasions during the field experiment when it was necessary to connect via RS232 to the lowest streetboxes at $z = 3.5$ m when radio communication could not be achieved.

It was usual to download the data from the streetboxes located in the field using an integral licence exempt radio modem that could be remotely configured to transmit the data to a kerbside laptop. Once radio communication with a streetbox was established it was also possible to check the data and to monitor the voltage of the lithium batteries. Although the voltages of lithium batteries decayed non-linearly they were usually ~10.6 volts during operational mode. During tests conducted prior to the field experiments it was revealed that the streetboxes failed below 10.4 volts. Therefore, it was important to establish regular communication with all streetboxes deployed during the field experiments in order to monitor the battery voltages.

Although the streetbox voltages were routinely checked one streetbox located on lamppost G4 did fail during the October and November experiment due to the voltage dropping below 10.4 volts. The data from this streetbox was excluded from the analysis presented in Chapter 5.

*3.5.2.3. Data quality assurance and control procedures for the streetbox*

Fifteen-minute averages of one-minute samples of CO concentrations were measured using streetboxes during trials conducted prior to the field experiments. Tate (2005) conducted co-location surveys at a street side location in Central London prior to the March and April 2003 field experiment utilising two streetboxes and a US EPA certified Gas Filter Correlation CO Analyser. The precision, repeatability and reliability of the streetbox measurement of CO over a one-month period were demonstrated. When compared with the reference analyser $r^2$ values of 0.95 and 0.96 were achieved (Tate, 2005).

The streetboxes were calibrated prior to the field experiments using an Environics multi-gas calibrator. The calibration gases used were zero-gas and CO concentrations of 3 ppm. The zero-gas was supplied by a Sabio Model 1001 zero air generator. An aspirator was fitted over the electrochemical CO sensor on the streetbox and the flow from the zero air generator was controlled by the multi-gas calibrator. The multi-gas calibrator was fitted with a series of mass-flow controllers and mixing chambers. The 3 ppm CO concentrations were derived by mixing a concentration of CO at 466 ppm with zero-gas using the multi-gas calibrator. The aspirator was then used to pass the 3 ppm CO gas over the electrochemical sensor.

The zero-gas and 3 ppm CO concentration calibrations were each carried out for a period of at least ten minutes and the mean concentrations measured by the streetboxes were determined. All streetbox data collected during the field experiments were linearly corrected according to the most recent zero-gas calibration. A check of CO concentrations using the calibration gas at concentrations of 3 ppm confirmed that the span was accurate to within 10%. This suggests that the variability in the CO concentrations measured during the field experiment caused by the resolution of the sensor was considerably less than the variability attributed to

meteorological and traffic conditions (Chapters 5 and 7, respectively). For all streetboxes used in the study the data collected were continuous. Data quality was assessed through the combined analysis of the concentration frequency distributions to identify outliers, coupled with analysis of the time-series concentration plots for noise spikes. No further [CO] data were excluded on this basis.

### 3.5.3. Traffic

#### *3.5.3.1. Traffic characteristics*

Traffic flow along Gillygate and Bootham was controlled by the Split, Cycle and Offset Optimisation Technique (SCOOT) Urban Traffic Control system. SCOOT uses inductive loops buried in the road surface to collect information on detector occupancy. This information is used in the SCOOT traffic model to optimise signal timings at traffic lights (Hunt et al., 1991). The flow of information in a SCOOT-based Urban Traffic Control system is shown in Figure 3.12. The term '*link*' refers to the length of road between the SCOOT detector and the stop line at the traffic light.

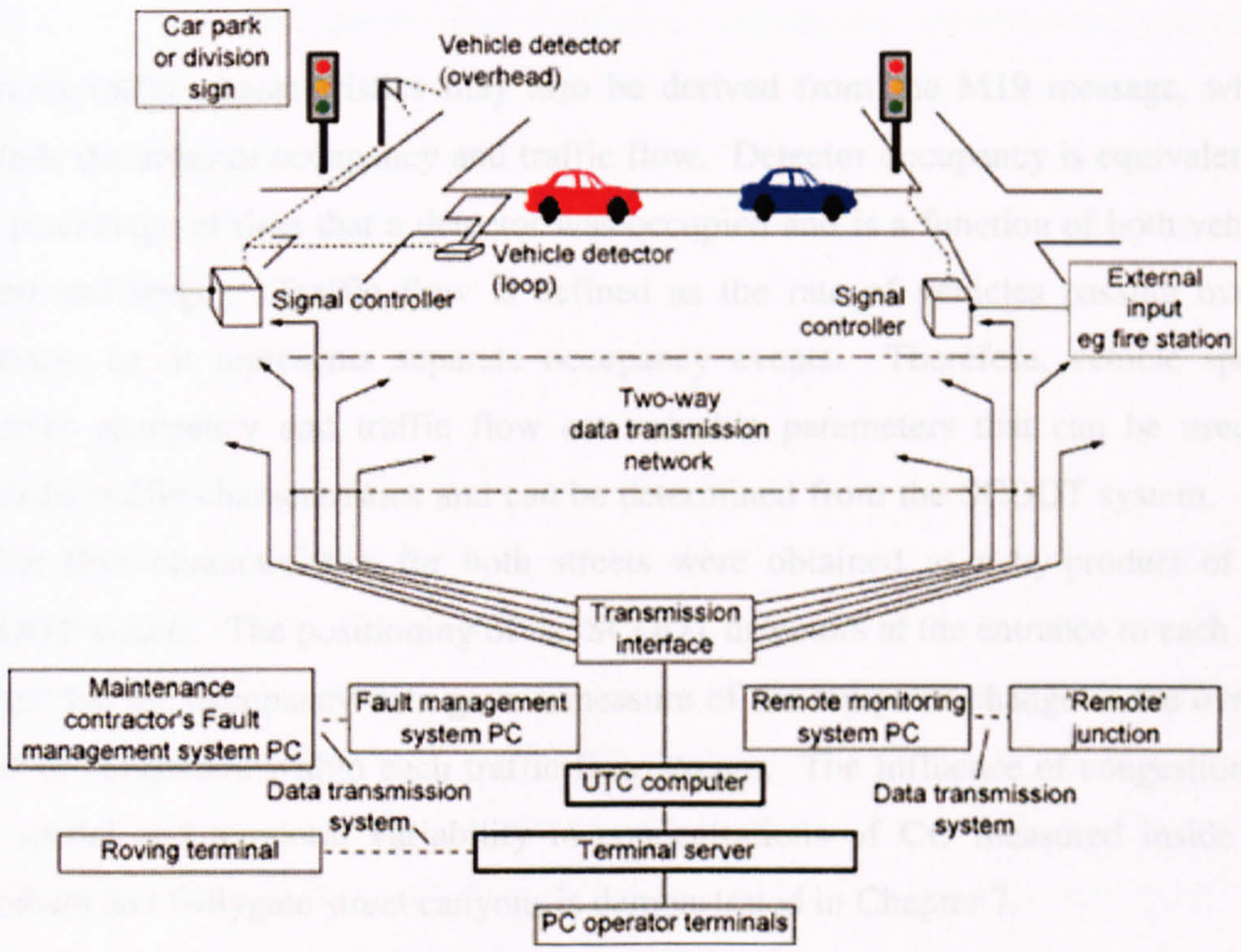


Figure 3.12. Schematic of the flow of information in a SCOOT-based Urban Traffic Control system (SCOOT, 2003).

Each SCOOT detector was located upstream of the stop line on Bootham and Gillygate and the direction of the traffic flow stream that each detected and controlled is shown in Figure 3.8. The detectors were located at the upstream end of each link in order to maximise the effectiveness of traffic monitoring by decreasing the probability of vehicles remaining stationary on them during congested traffic flows. The inductive loop detectors cover approximately 4 $m^2$ of the road surface on Bootham and Gillygate.

Although the loop detectors used by SCOOT do not explicitly classify vehicles, they do record occupancy '*events*' at a frequency of 4 Hz. A single event was recorded when a vehicle occupied the detector loop area within a ¼ s period. The raw SCOOT detector data is referred to as the M19 message and were collected during the investigation, allowing the identification of individual vehicle events at the entry to each link in the study area. Detector occupancy and traffic flow for each inbound and outbound flow direction were averaged over periods of 15-minutes in order to compare with the mean CO concentrations. The 15-minute averages obtained were reported at the end time for each time period.

Various traffic characteristics may also be derived from the M19 message, which include the detector occupancy and traffic flow. Detector occupancy is equivalent to the percentage of time that a detector was occupied and is a function of both vehicle speed and length. Traffic flow is defined as the rate of vehicles passing over a detector, i.e. it represents separate occupancy events. Therefore, vehicle speed, detector occupancy and traffic flow are valuable parameters that can be used to describe traffic characteristics and can be determined from the SCOOT system. The traffic flow characteristics for both streets were obtained as a by-product of the SCOOT system. The positioning of the SCOOT detectors at the entrance to each link meant that the occupancy data gave a measure of the temporal change in the overall level of congestion within each traffic flow stream. The influence of congestion on the spatial and temporal variability in concentrations of CO measured inside the Bootham and Gillygate street canyons is demonstrated in Chapter 7.

Under some circumstances, however, the detection area of each loop can vary by up to 25%, depending on the individual vehicle chassis characteristics (e.g. height above

the road or metallic content). Therefore, vehicles such as motorcycles and scooters may not always have been explicitly recorded within the traffic flow. SCOOT detectors can also be susceptible to 'nose-to-tail' masking, i.e. two or more slow moving vehicles travelling close together may register as a single vehicle event. Additionally, SCOOT detectors are omni-directional, meaning that a vehicle travelling opposite to the expected flow direction over the loop (e.g. emergency vehicles) would have been recorded in that traffic stream.

An important part of the current study was, therefore, to evaluate the SCOOT system using manually recorded traffic data. In Chapter 7 the accuracy of the SCOOT system was determined through a comparison between the direct observations of traffic recorded manually and the synchronised detector data. Observations of the bi-directional traffic flow in Gillygate and Bootham comprised both off-peak and the afternoon-peak flows along all four links. It is demonstrated in Chapter 7 that the SCOOT system is reliable method of measuring traffic flow.

The quality of the traffic data was assessed using the method described in Section 3.5.2.3 for [CO]. Data quality was determined through the combined analysis of the flow and detector occupancy frequency distributions to identify outliers, coupled with analysis of the time-series flow and detector occupancy plots for noise spikes. Following this assessment only one value was removed, which corresponded to detector occupancy.

*3.5.3.2. Traffic-produced turbulence*

Measurements of traffic-produced turbulence (TPT) were conducted inside the Gillygate street canyon using ultrasonic anemometers located on lamppost G3 (see Figure 3.8). The wind flow and turbulence measurements were conducted at 20 Hz to determine the turbulence produced within the inbound traffic flow along Gillygate. The lowest anemometer ($z$ = 1.1 m) was attached to a supporting stand positioned 1.5m from centre of lane, 0.21m from the kerb and 0.65m from the lamppost. The anemometer was positioned directly beneath the anemometers attached to lamppost G3 (Section 3.5.1.1.4). A certain amount of flow distortion from the lamppost cannot be excluded, particularly during parallel background winds and is discussed in more

detail in Chapter 6. The anemometer was located in the centre of a 4 m section of the inbound lane that was demarcated by lines, which were painted white. The anemometer was connected to a data logger located at the foot of the lamppost (Section 3.5.1.1.4).

The lowest anemometer was only deployed during the TPT measurements in order to reduce the likelihood of vandalism. Data was also used from the other anemometers located at the G3-G4 experiment cross-section. The periods when the mean data collection rate of anemometers dropped below 18 Hz due to a coding error in the data logging software were excluded from the analysis, as mentioned earlier.

The background wind speed and direction were measured by the anemometer located at a height of 19.5 m on top of the trailer-mounted mast (Section 3.5.1.2). The TPT analysis presented in Chapter 6 excluded all data corresponding to $U_{ref}$ >1.2 m s$^{-1}$ in order to focus purely on traffic-produced flow components. As a result of the data quality control procedures described in Section 3.5.1.1.4 and the conditional analysis, only 12% of the total anemometer data available were used in the work presented in Chapter 6. This was mainly caused by low frequency of $U_{ref}$ ≤1.2 m s$^{-1}$ rather than poor data quality.

Manual surveys of the inbound traffic flow, including vehicle speed and classification, were conducted beside lamppost G3 using an in-house traffic counting computer program. The traffic surveys were conducted for several hours over a period of 14 days during the October and November experiment. The vehicles were classified according to the following five categories: cars; motorcycles; light goods vehicles (LGVs); buses and heavy goods vehicles (HGVs). Depending on the vehicle type, each keystroke of the right-hand represented the moment the front axle of the vehicle crossed the first white line marked beside lamppost G3. The keystroke by the left-hand represented the moment the rear axle of the same vehicle crossed the second line painted 4 m downstream. This method allowed the measurement of the average speed of each vehicle passing through the 4 m section beside the anemometer. The limitations of this method are discussed in Chapter 9 and the error calculations are shown in the Appendix.

The wind and traffic data were all averaged over 1-minute periods in order to allow for a suitably large data set. The wind velocity data collected during the TPT investigations comprised a maximum of 1200 samples for each 1-minute mean and variance value, which provided statistical convergence. This averaging period also allowed for the determination of the turbulence parameters, such as the standard deviation of the vertical velocity component, $\sigma_w$, and TKE. The measurement of the TPT field and a comparison with the calculated TPT produced using the parameterisations of Di Sabatino *et al.* (2003) and Kastner-Klein *et al.* (2003) is presented in Chapter 6.

### 3.5.4. Street canyon flow and dispersion modelling

The MISKAM CFD flow model was used to help in the interpretation of the mean wind and turbulence analysis from the October and November field experiment. MISKAM consists of a 3-D non-hydrostatic flow model and an Eulerian dispersion model (Eichhorn, 1996) and uses $k$-$\varepsilon$ turbulence closure. Results from the dispersion model were used qualitatively in a sensitivity study into the influence of variable emissions along Gillygate in causing the spatial variations in concentrations of a tracer (Chapter 8). Verification of the model is beyond the scope of this study and is not presented in this thesis.

The numerical simulation of dispersion in MISKAM can be described as having two stages. First, there is the steady state flow field over an arbitrary building configuration set by the domain using the flow component of the model. Second, the derived mean wind and turbulence parameters from MISKAM are input into the Eulerian dispersion model.

The $k$-$\varepsilon$ turbulence model developed in 1972 by Jones and Launder is a two-equation eddy-viscosity turbulence model used to derive the TKE, $k$, and the dissipation rate of TKE, $\varepsilon$. The $k$-$\varepsilon$ model provides empirical transport equations for both $k$ and $\varepsilon$, and the primary function of the model is to provide an estimate of the eddy viscosity at each point in the flow. Some of the advantages of the model over others relate to the fact that $k$ and $\varepsilon$ appear naturally in the TKE equation (Section 3.5.1.1.2) and can be

derived from the Navier-Stokes equation without introducing additional variables. According to Davidson (2004) the $k$-$\varepsilon$ model has become the standard working model of turbulence for scientists and engineers as it is simple to use and generally gives reasonable results.

The wind flow over the Gillygate experiment site near to the G3-G4 cross-section was simulated using the MISKAM numerical model (Eichhorn, 1996). The flow model used a $k$-$\varepsilon$ turbulence closure scheme to parameterise the sub-grid scale turbulence. In this Section a description of the code is given. The method used to build the domain is also described.

*3.5.4.1. Description of the MISKAM code*

The mean flow velocities were derived in MISKAM following the continuity equation (see Chapter 2) and the Navier-Stokes equation, which governs the motion of most fluids. The Navier-Stokes equation is shown below, with buoyancy omitted:

$$\frac{\partial u_i}{\partial t} + u_j \frac{\partial u_i}{\partial x_j} = \frac{1}{\rho}\frac{\partial P}{\partial x_i} - \frac{\partial \overline{u_i u_j}}{\partial x_j}; \tag{3.24}$$

where

$u_i$ are the three velocity components ($i$=1,2,3 or $x,y,z$);

$u_j$ are the turbulent fluctuation components (deviations from the mean velocity, where over bar denotes time averaging);

$p$ is pressure;

$\rho$ is density of air.

It is possible to manipulate the Navier-Stokes Equation to produce a perfectly deterministic equation, thus given initial conditions we are able to integrate forward to obtain the actual instantaneous wind velocity, $U(t)$, from the mean velocity and the random fluctuating component, as shown in Figure 3.6.

However, since $U(t)$, has been shown in Section 3.5.1.1.2 to be random and unpredictable and the statistical properties such as the mean velocity $U$ are reproducible, then it makes sense to focus predictive theories of turbulence not on $U(t)$ itself, but where its statistical properties, such as $U$ and $(u')^2$, play a central role. Thus we need a set of dynamical equations for these statistical quantities analogous to the deterministic equation we are able to produce when dealing with $U(t)$. It is possible to manipulate the deterministic equation for $U(t)$ into a set of statistical equations.

This system of equations contains more statistical unknowns than equations relating them, i.e. the system of equations is not closed (Davidson, 2004). This is a problem that is common to non-linear dynamical systems, and arises due to the non-linear term contained in the right hand side of the Navier-Stokes equation. The problem was referred to in Chapter 2 as the *closure problem* of turbulence. Consequently, there can be no complete statistical theories of turbulence and the theories and models that do exist effectively 'fill-in' the unknowns based upon experimental data (Davidson, 2004). These unknowns are referred to as Reynolds stresses (Chapter 2). The success or failure of these types of models, therefore, depends upon how well they are able to explain the experimental results. Reynolds stresses, $\overline{u_i'u_j'}$, arise as a result of the turbulence and act on the mean flow, shaping its evolution and maintaining the turbulent fluctuations (Davidson, 2004). The Reynolds stresses mentioned in Chapter 2 can apply time averages to the Navier-Stokes and continuity equations used in MISKAM.

The eddy-viscosity concept, also known as the "*first order closure method*", is analogous with molecular diffusion and assumes the turbulent stresses are proportional to the local velocity gradients (Berkowicz *et al.*, 1997a). In MISKAM the Reynolds stresses are defined as follows:

$$-\overline{u_i u_j} = \nu_t\left(\frac{\partial u_i}{\partial x_j}+\frac{\partial u_j}{\partial x_i}\right)-\frac{2}{3}\partial_{ij}k\,; \tag{3.25}$$

where $\nu_t$ is eddy viscosity and is proportional to some appropriate velocity and length scale. The last term in Equation (3.25) is assumed part of pressure perturbation.

MISKAM, therefore, uses the complete 3-D equations of motion of the flow field and the advection-diffusion equation to determine the concentrations of substances with neutral density (see Sahm *et al.*, 2002). The transport equation for pollutants used by MISKAM is based on the conservation equation for a scalar (Chapter 2) and is shown below:

$$\frac{\partial C}{\partial t}+u_j\frac{\partial C}{\partial x_j}=-\frac{\partial \overline{u_j c}}{\partial x_j}+\beta, \tag{3.26}$$

where $C$ denotes the mean concentration and $c$ is the deviation from the mean, while $\beta$ represents all possible sources and sink terms, such as emissions and chemical reactions. The key problem is once again determining the parameterisation of the turbulent flux term $\overline{u_j c}$ and MISKAM uses the pollutant concentration flux equation:

$$-\overline{u_j c}=\frac{\nu_t}{Sc_t}\frac{\partial C}{\partial x_j}, \tag{3.27}$$

where $\nu_t$ is the eddy viscosity and $Sc_t$ is a constant equal to 0.74. The mean wind fields and diffusivity coefficients and can be supplied by a particular flow model and Equation (3.26) solved numerically subject to appropriate boundary conditions (Berkowicz *et al.*, 1997a). The model produces pollutants only in the source cells (i.e. volume source) in grams per second (g $s^{-1}$). The model, therefore, calculates the stationary flow and pressure field, diffusivity coefficients and the concentration field within the entire domain. The TKE, $k$, is calculated in MISKAM using:

$$\frac{\partial k}{\partial t}+u_j\frac{\partial k}{\partial x_j}=-\overline{u_i u_j}\frac{\partial u_i}{\partial x_j}+\frac{\partial}{\partial x_j}\left(\frac{\nu_t}{\sigma_k}\frac{\partial k}{\partial x_j}\right)-\varepsilon, \tag{3.28}$$

where $\sigma_k$ is a constant equal to 1. While dissipation, $\varepsilon$, is derived using:

$$\frac{\partial \varepsilon}{\partial t} + u_j \frac{\partial \varepsilon}{\partial x_j} = -C_{\varepsilon 1} \frac{\varepsilon}{k} \overline{u_i u_j} \frac{\partial u_i}{\partial x_j} + \frac{\partial}{\partial x_j}\left(\frac{\nu_t}{\sigma_\varepsilon} \frac{\partial \varepsilon}{\partial x_j}\right) - C_{\varepsilon 2} \frac{\varepsilon^2}{k}, \quad (3.29)$$

where $\sigma_\varepsilon$ is a constant equal to 1.3; and $C_{\varepsilon 1}$ and $C_{\varepsilon 2}$ are constants equal to 1.44 and 1.92, respectively. The code description described above was prepared by P. Louka and can be found on the TRAPOS website (http://www.dmu.dk/Atmospheric-Environment/trapos/).

*3.5.4.2. The model domain*

The domain used in the flow and dispersion modelling is shown in Figure 3.13. The configuration of the buildings and streets shown in Figure 3.13 were incorporated into the MISKAM model domain using a scaled plan of the street canyon geometry. The heights of the buildings were measured in the field using the inclination method described in Section 3.4 and were incorporated into the domain.

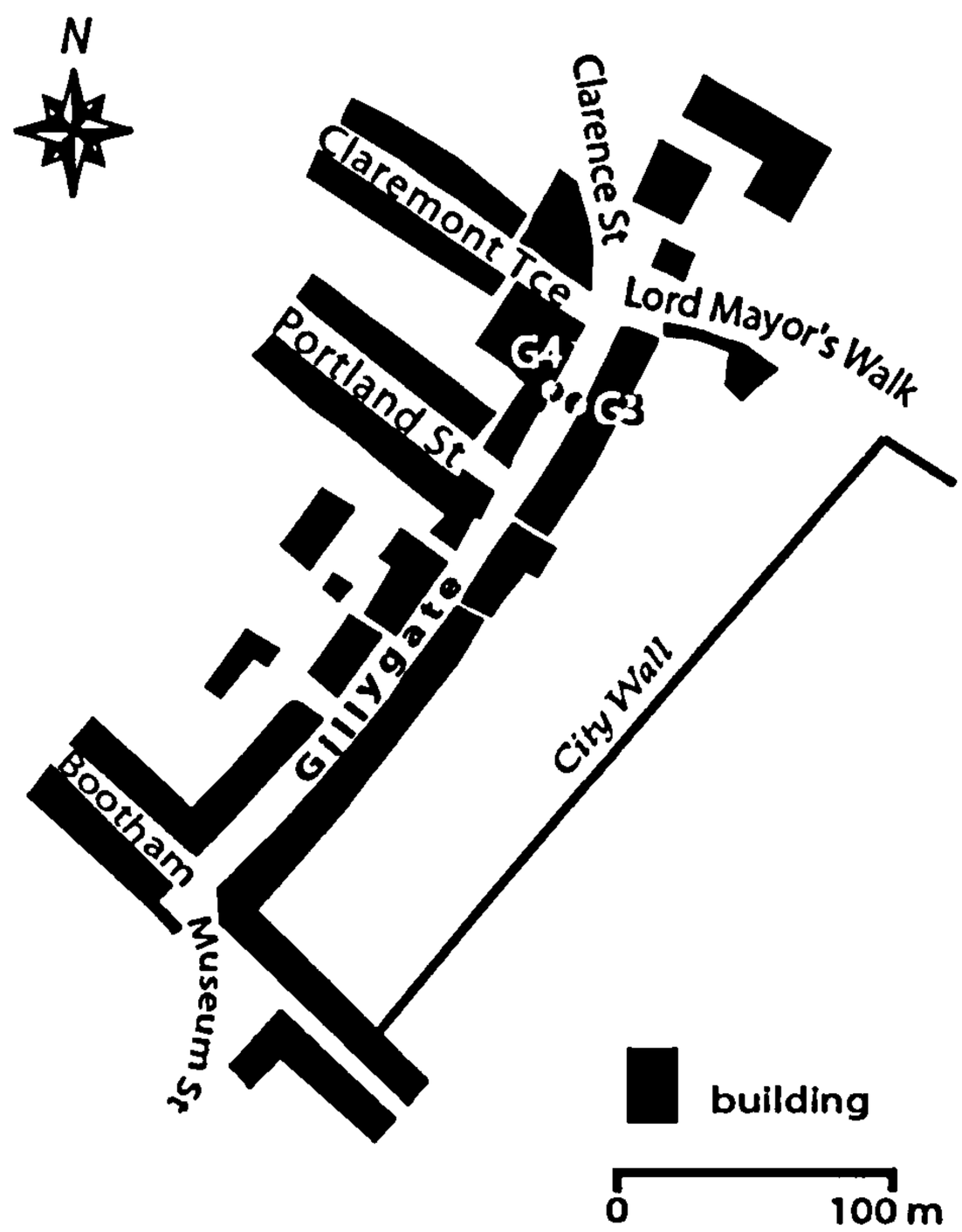


Figure 3.13. Plan view of the buildings in the modelling domain; showing the Gillygate street canyon and adjoining streets.

The buildings heights were specified within each grid of the domain as an integer. Each integer corresponded to the vertical extent of the building within the grid and, thus, a zero corresponded to the absence of a building at that grid point. The modelling domain included the side streets adjoining Gillygate and incorporated the significant structures within approximately 100m of the street, as shown in Figure 3.13.

The model interpreted all buildings as having flat roof geometries. The domain extended 270m in the across-canyon direction and 510m in the along-canyon direction. The domain included the common junction and part of the Bootham street canyon and a section of the street leading to the Minster (Figure 3.13). However, the Minster itself was not included in the model domain. The city wall was included in the domain and was approximately parallel to the along-canyon axis.

The maximum extent of the domain in the vertical direction was 50m, which was over three times the height of the tallest building in the domain. The total grid size (number of cells) in the across-canyon ($x$), along-canyon ($y$) and vertical ($z$) directions was 89 by 168 by 23, respectively. The grid was 3-D and the resolution of the domain could be adjusted by the user in order to allow for a higher resolution along the street. The model was configured to allow for higher resolution in the area of the grid corresponding to the G3-G4 experiment cross-section in order to allow for future comparison with measured concentrations, as mentioned in Chapter 9. The resolution of the model at this location was 1m by 2m by 1m in the $x$, $y$ and $z$ directions, respectively. This resolution was set for the section of Gillygate corresponding to 74m from the Bootham/Gillygate intersection to a point ~30m along Clarence St (see Figure 13). However, the model resolution from the junction between Museum St and Bootham to a point 74m along Gillygate was 2m by 4m by 1m in the $x$, $y$ and $z$ directions, respectively. The lower resolution was chosen for this section of the domain in order to allow the model to run more efficiently.

*3.5.4.3. Running MISKAM*

The MISKAM flow model assumed that the wind speed increased logarithmically upstream and that there was neutral static stability (i.e. isothermal conditions were assumed). In the model, the height of the reference wind was configured to 50 m and the reference wind speed was set to 5 m $s^{-1}$. The height at which the vertical logarithmic wind profile extrapolates to a zero wind speed is known as the roughness length, $z_0$. The model was configured to $z_0$ = 0.5 m in order to define this profile. Roughness parameters describe how effective a surface area is in transforming the energy of the mean wind, which flows over it, into turbulent motion, in the boundary layer above (Davenport *et al.*, 2000). According to the recently revised roughness length described by Davenport *et al.* (2000) 'very rough' terrain corresponds to $z_0$, = 0.5 m (e.g. relatively low buildings with interspaces and no high trees). This roughness length, therefore, corresponds to flow over suburban housing, which constituted the majority of the upstream fetch. For comparison, city centres with a mixture of low-rise and high-rise buildings are likely to have roughness lengths of $z_0$ ≥2 m.

The flow model was run for certain background wind directions including perpendicular, oblique and parallel winds. The *U*, *V* and *W* components of wind velocity were calculated at each grid point within the domain using the equations described earlier. A FORTRAN program converted the flow model outputs into a format that was able to be imported into Origin. Origin is a program that is part of the OriginLab suite of software and provides a wide range of features from data analysis to the creation of publication quality graphics. A particularly useful feature is the facility to import data from Microsoft Excel into Origin graphs.

The calculated mean velocity data was then shown graphically through the creation of vector plots. The vector plots showed the mean horizontal and vertical wind velocities during certain background winds at the experiment (G3-G4) cross-section and for other locations along Gillygate.

The turbulence module was run to derive turbulence parameters based on the outputs from the flow model for each background wind direction. The contour plots were

created by converting the derived TKE values into a matrix using the weighted average gridding method in Origin. The derived mean wind (vector plots) and TKE (contour plots) were used in Chapter 4 in order to assist in the interpretation of the dispersion characteristics of the in-canyon flow features. The evaluation of the model was beyond the scope of the study.

A sensitivity study into the influence of variable emission rates on the spatial variations along the street canyon was conducted using the MISKAM Eulerian dispersion model (Chapter 8). Tate (2005) presented the development and implementation of an integrated traffic microsimulation and instantaneous emission model in order to study the spatial and temporal variations in vehicular emissions along Bootham and Gillygate. In particular, the Dynamic Route Assignment Combining User Learning and microsimulAtion (DRACULA) traffic micro-simulation was integrated with the Comprehensive Model Emission Model (CMEM). This accounted for tailpipe emissions now largely associated with acceleration events (see Tate, 2005). For more information on DRACULA, reference should be made to Tate *et al.* (2005b).

The variability in the traffic network (e.g. signal timings) and traffic characteristics (e.g. free-flow, congested-flow) throughout a typical weekday was incorporated into the modelling study conducted by Tate (2005). The aim of the work was to derive the spatial and temporal variability in emissions at the microscopic scale. This was used to generate second-by-second vehicle trajectory data and CO tailpipe emissions. The second-by-second modelling approach was implemented in order to estimate the temporal (15-minute time intervals) and spatial variations in CO emissions and to verify the instantaneous emission model using transient emission measurements over a standard drive cycle as well as in real-world traffic conditions. A more detailed description of the DRACULA microsimulation model and the CMEM is provided in Chapter 8 (see also Tate *et al.*, 2005b). The location and magnitude of the CO emissions were averaged in Tate (2005) over 15-minute time periods and 10m sections along Bootham and Gillygate, therefore, the common intersection was included. The variable emission rates of CO were interpolated over 2m sections along Gillygate from the common Bootham/Gillygate intersection to the junction with Lord Mayor's Walk at the far end of the street.

The source cells of the tracer in the domain were located in the centre of Gillygate. These cells were ~8m wide and covered the entire length of the street from the Bootham/Gillygate intersection to the junction with Lord Mayor's Walk. The source cells of the tracer were set using the constant (i.e. mean) and variable emissions profile. The influence of parallel ($\theta_{ref}$ = 210°), oblique ($\theta_{ref}$ = 165°) and perpendicular ($\theta_{ref}$ = 120°) background winds on the in-canyon concentration field was investigated. The influence of the spatial variability in emissions on the resulting in-canyon concentrations was also investigated. The variable emissions profile is a more realistic representation of the actual emissions along Gillygate as the influence of traffic characteristics and driving mode was considered. Incorporating variable emissions into such a dispersion modelling study aimed to increase the accuracy of the predictions of roadside concentrations of traffic-related pollutants. This is particularly important for traffic management assessments as the mean (or constant) profile may drastically over-predict parts of the street (e.g. mid-link), while under-estimating emissions in other areas (e.g. intersections).

A FORTRAN code converted the concentration outputs from MISKAM into a format that was able to be imported into Origin. The contour plots were created in a similar way to the TKE plots by converting the derived concentration values into a matrix using the weighted average gridding method.

### 3.6. Summary and Conclusions

This Chapter described the Bootham and Gillygate street canyons that were used in the field experiments, including the surrounding building and street layout. A description was given into the instruments that were used to determine the influence of meteorology, urban topography and traffic on the spatial and temporal variability in concentrations of CO measured inside the street canyons. Data quality assurance and control techniques employed were also described. A modelling study was conducted into the mean wind, turbulence and concentration fields inside the Gillygate street canyon in order to help interpret the results from the experimental experiment.

# CHAPTER 4

## Mean wind flow and turbulence inside the Gillygate street canyon

### 4.1. Introduction

The mean wind flow and turbulence characteristics in the urban canopy are highly variable and strongly depend on the building, roof and street geometries in the local environment. In Chapter 3 the variance and standard deviation of the velocity components were introduced. A description was given into how these can be used as an indication of the turbulence intensity, with larger values corresponding to greater intensities. The rate of dispersion of a pollutant depends on the mean flow and the turbulent velocity components. An overall measure of the turbulence intensity is the TKE, as was mentioned in Chapter 3. Pollutants emitted by traffic travelling along the Gillygate street canyon, for instance, are likely to have been transported by the mean wind flow and turbulence. The turbulent velocity components, which contribute to the TKE, can be used in street canyon studies to investigate the characteristics of the in-canyon airflows and the implications for pollutant dispersion. The mean flow inside street canyons, therefore, will not only transport (or advect) pollutants but also turbulence. Additional characteristics of the in-canyon flow structures can be determined by including turbulence with the mean flow analysis.

The influence of the building, roof and street geometries of Gillygate and the surrounding local environment is described in Chapter 5 in relation to the dispersion of a traffic-related pollutant by the background wind. However, this Chapter will explore the in-canyon flow features in detail in order to investigate the potential influence they have on the dispersion of traffic-related pollutants. As these flow

structures represent time-averages of fluctuating phenomena it is important to explore not only the mean flow inside the canyon but also the turbulence. Analysis using turbulence statistics will also provide evidence to determine the flow features present within a street canyon. In particular, the 2-D archetypal recirculating street canyon flow is investigated, paying attention to its symmetry about the across-canyon axis.

However, other flow patterns caused by the interaction between buildings and the local wind field and shown schematically in Chapter 2 are also likely to have further implications for the dispersion of air pollutants inside street canyons (see also Hosker, 1985). For example, corner vortices may develop at an isolated building corner during perpendicular background winds. However, this scenario can be related to street canyon environments with side streets aligned perpendicular to the axis. In such street canyons the mean perpendicular flow is allowed to channel along the adjoining side streets, producing counter-rotating corner vortices with vertical axes inside the canyon. The corner vortex pair is likely to force the air inside the canyon into two converging flows. However, an alternative view, although related, is that the corner vortices may be the result of the flow being forced into the street canyon from the adjoining side streets, i.e. the corner vortex pair was *caused* by along canyon flow. This explanation should be kept in mind during the course of this Chapter.

Clearly such flow structures would have significant consequences for the dispersion of pollutants emitted inside street canyons that have openings along the canyon walls. To date, the consequences of such 3D flow phenomena have largely been ignored in dispersion modelling studies. Previous studies have focused predominantly on the 2D archetypal street canyons of aspect ratios equal to unity and usually with large length-to-height ($L/H$) ratios. However, in street canyons with relatively small $L/H$ ratios (i.e. ~5) it is likely that flow features, such as the along-canyon flow convergence described above, are potentially more significant during perpendicular winds than the 'classic' recirculating flow. As street canyons with relatively small $L/H$ ratios, caused by openings along the canyon walls, such as side streets, are more common in real urban environments the effects of these flow structures are potentially more significant in terms of dispersion modelling studies than the classic 2D recirculating flow models. A more detailed discussion of these flow features is given in Section 4.3. In summary, for more complicated street geometries, it has been demonstrated

numerically (e.g. Sini *et al.*, 1996; Leitl and Meroney, 1997), and by using wind tunnel modelling (Hoydysh and Dabberdt, 1988; Kastner-Klein *et al.*, 1997, 2001; Rafailidis, 1997; Park *et al.*, 2004), that wind flow and pollutant dispersion within continuous street canyons essentially depend on the aspect ratio, the street length and building roof geometry (Theurer, 1999).

### 4.1.1. Perpendicular winds and the classic skimming flow regime

The majority of field experiments conducted within full-scale street canyons have predominantly investigated the influence of the classic skimming flow regime with its characteristic single across-canyon recirculating flow (with a horizontally-aligned axis). DePaul and Sheih (1986) measured wind velocities inside a street canyon with an aspect ratio of ~1.4 in Chicago by analysing the trajectories of tracer balloons that were released in the canyon and photographed in rapid succession. The trajectories confirmed a recirculating flow developed inside the canyon during wind directions approximately perpendicular to the street axis and provided that the background wind speed was greater than 1.5 – 2.0 m $s^{-1}$. The recirculating flow was characterised by vertical velocity and reverse flow at street level, which were significantly large in magnitude. The mean velocities associated with the downdraughts on the windward side of the canyon were approximately a factor of two greater than the mean velocities in the updraughts on the leeward side. The mean vertical velocities in the centre of the canyon were found to be approximately zero.

Louka *et al.* (2000) investigated the airflow within and above a street canyon during perpendicular winds. The geometry of a street canyon is usually defined by its height ($H$) to width ($W$) ratio (or aspect ratio). The experiment was performed between two long barns with pitched roofs, which had an aspect ratio of $H/W \approx 0.7$. Using profiles of mean wind and turbulent statistics (standard deviations and TKE) they found that the conventional picture of a persistent recirculating in a single across-canyon vortex flow within the street with small-scale turbulent fluctuations about this mean needs to be revised. Instead, the mean recirculating inside the canyon was found to be much weaker than the unsteady turbulent fluctuations and, therefore, the mean flow is merely a residual of an unsteady turbulent recirculation (see Chapter 2).

Louka *et al.* (2000) also found that the recirculation in the canyon is coupled to the wind aloft through a shear layer that develops at roof level. They calculated from the measurements the shear production and turbulent transport terms described in the TKE budget formulation in Chapter 3. They found that above-roof level production equals dissipation, as expected in a horizontally homogenous boundary layer. They observed that the shear production of TKE reached a maximum around roof-level and stated that the maximum production of TKE by shear close to the roof-level is associated with turbulence within the shear layer being shed from the upstream roof. These findings are supported by the observations of Kastner-Klein and Rotach (2004). Vachon *et al.* (2002) performed full-scale measurements of the carbon monoxide (CO), wind and turbulence fields within a street canyon in Nantes, France. During low background wind conditions traffic was associated with an increase in TKE at the lowest levels in the street, especially on the leeward side of the canyon (Chapter 2).

Berkowicz *et al.* (1997a) performed preliminary measurements of the wind and turbulence inside a street canyon in Copenhagen, Denmark. Although, the analysis includes moderate and high background wind speeds, the measurements were only taken at one point in the street and different flow features with contrasting dispersion characteristics can be expected at other locations inside a street canyon. Nielsen *et al.* (2000) presented analysis from measurements in the same street canyon in Copenhagen and the influences of side streets and trees on the in-canyon flow characteristics were reported.

The majority of the numerical models currently used to determine the skimming flow regime involve idealised building configurations i.e. the buildings have rectangular shapes with flat roofs and are arranged in a uniform manner. Sini *et al.* (1996) built a numerical model to simulate the small-scale atmospheric flows within the urban canopy, based on the standard $k$-$\varepsilon$ two-equation turbulence model. The model was used to study the flows and vertical exchanges of pollutants within the street and at the interface with the atmospheric layer above the roofs for a street canyon of infinite length. They found that the number and arrangement of flow structures within the street canyon largely influenced the vertical exchange rates.

Kim and Baik (2003) examined the effects of inflow turbulence intensity on flow and pollutant dispersion inside a street canyon with an aspect ratio of 1 using a 2-D numerical model. TKE was found to increase inside the street canyon as the inflow turbulence intensity increased. Furthermore, as the inflow turbulence intensity increased the pollutant concentration in the street decreased as pollutants escaped from the street canyon.

Kastner-Klein and Rotach (2004) measured the vertical profiles of the velocity components in a wind tunnel study using a Laser-Doppler velocimeter in order to investigate the mean flow and turbulence within the urban roughness sublayer. They distinguished two types of velocity profiles within the canopy. They found that within street canyons the mean wind velocities were almost zero or negative below roof level. They also observed significantly higher mean velocities close to intersections or open spaces. They also found that the turbulent velocities inside the canopy were higher than within the street canyon. TKE and shear stress profiles showed pronounced maxima immediately above roof level.

### 4.1.2. Perpendicular winds and the influence of pitched roofs

Longley *et al.* (2004a) conducted measurements of the airflow and turbulence in two street canyons with buildings of pitched roof geometries on only one side of the canyon in Manchester. Their analysis of the in-canyon vertical wind angles and horizontal flow directions revealed some features of a recirculating flow (see also Chapter 5). They observed evidence of flow reflection off the windward canyon wall during perpendicular background winds, suggesting that the street level flow opposed the direction of the above-roof flow. They also observed downdraughts on the windward side of the canyon and updraughts on the leeward side. In Gillygate the roofs of the buildings on both sides of the street were pitched. Therefore, one of the objectives of the analysis presented in this Chapter will be to investigate whether or not a recirculating flow occurred in a real street canyon with pitched roofs.

The work presented by Louka *et al.* (1998; 2000) has revealed substantially more about the turbulence inside a street canyon with pitched roofs and for $H/W \approx 0.7$. The unsteady fluctuations in the position of the shear layer are believed to have forced the

unsteady fluctuations in the street, as was mentioned in Chapter 2. The shapes of the roofs are likely to have affected the depth and strength of the shear layer. Pitched roofs were more likely to be associated with energetic eddies (Louka *et al.*, 1998) and stronger turbulence intensity (Rafailidis, 1997) than flat roofs. Although it should be made clear that these studies only used an isolated set of street canyons, which may have resulted in contrasting in-canyon flow dynamics. The influence of urban roughness on the in-canyon flow is discussed in more detail below.

It was mentioned earlier that the majority of the numerical models currently use idealised building configurations with buildings that have rectangular shapes and flat roofs and are arranged in a uniform manner. However, the wind tunnel studies conducted by Kastner-Klein and Plate (1999) and Rafailidis (1997) have demonstrated that building and roof geometries (such as pitched roofs) are likely to result in contrasting in-canyon dispersion characteristics, compared to street canyons with flat roofs. Kastner-Klein *et al.* (2004) studied the flow patterns in the central vertical plane for three different *L/H* ratios and three different roof configurations for an isolated street canyon with an aspect ratio of unity in a wind tunnel. It was mentioned in Chapter 2 that for all cases with flat roofs, they found that flow separation occurred at the upwind edge of the upwind building and a recirculating flow formed within the canyon. A shear layer was found to develop; and the greatest turbulence intensity was observed above the roof of the upwind building. However, for all cases studied with pitched roofs, the typical street-canyon recirculating vortex did not develop (Chapter 2).

Meroney *et al.* (1996) investigated the dispersion of a tracer gas in wind tunnel studies of an isolated street canyon in open country and a street canyon in an urban environment. The street canyons had aspect ratios of unity and the roofs were flat. They found that the dynamics and, thus the dispersion characteristics, of the flow were quite different. The isolated canyon was observed to have better ventilation than the urban roughness case. They reported that a recirculating flow with a horizontally-aligned axis formed only intermittently in the isolated street canyon, whereas it was much more stable amidst urban roughness. However, in real street canyons with pitched roofs and non-isolated (i.e. urban roughness) configurations the

typical in-canyon flow features are more likely to form over a broader range of background wind directions. This will be explored in more detail in this Chapter.

### 4.1.3. Oblique and parallel background winds

Whilst the majority of the previous work has focused on the influence of perpendicular background winds on the development of a skimming flow regime and an across-canyon recirculating flow, consideration should also be given to other wind directions. Background winds oblique to the street axis winds may cause recirculating helical flows with strong along-canyon components. Therefore, helical flow regimes would be driven by winds above the urban canopy (Chapter 2).

Helical flows are likely to transport turbulence and traffic-related pollutants at street level towards the leeward side of the canyon in the reverse flow portion of the recirculating flow. However, the reflection off the windward canyon wall during oblique background winds is likely to show greater along-canyon tendencies, unlike in the case of the single across-canyon recirculating flow (with a horizontally-aligned axis). The establishment of firm evidence of recirculating flows associated with skimming and helical regimes in the study conducted by Nielsen (2000) was complicated by the presence of trees located along the Copenhagen street canyon.

On the other hand, parallel background winds in the study conducted by Nielsen (2000) were found to enhance the efficiency of the street canyon ventilation as a result of turbulent winds causing pulsating circulation patterns (see also Chapter 2). Channel flows were also described by Longley *et al.* (2004) and are likely to have had a 'flushing' effect, causing lower in-canyon mean concentrations than during perpendicular and oblique background winds associated with recirculating flows.

### 4.1.4. Chapter synopsis

Our attention in this Chapter focuses on the mean flow and turbulence characteristics inside the Gillygate street canyon and their potential to disperse traffic-related pollutants. The influence of the background winds and street canyon geometry on the dispersion of a traffic-related pollutant is described in Chapter 5. Investigations in

this Chapter are focused on the factors influencing the production of turbulence during background wind speeds greater than 1.2 m $s^{-1}$ in order to exclude most of the effects from traffic and convection. An explanation as to why this threshold was chosen is provided in Section 4.4.1. The analysis presented in this Chapter uses quantities of flow and turbulence averaged over 15-minute time periods in order to be consistent with the study into CO and traffic characteristics presented in Chapters 5 and 7.

Specific research questions include: (i) the variation of the mean in-canyon wind flow and turbulence relative to background wind speed and direction, and (ii) the influence of building, roof and street geometries on flow and dispersion characteristics. Questions are also raised in relation to the effects of street corners and side streets and the morphology of buildings on the in-canyon wind flow and turbulence and their significance for pollutant dispersion.

## 4.2. Experimental Method

### 4.2.1. The site

The field study of the mean wind flow and turbulence was conducted for one month between 13 October 2003 and 12 November 2003 inside the Gillygate street canyon situated along an arterial route to the inner-ring road in the city of York, U.K. It was mentioned in Chapter 3 that Gillygate is aligned perpendicular to Bootham; and whilst Gillygate is orientated predominantly at 45° from N, it is aligned approximately 30° from N at the opposite end to the common intersection. Portland Street and Claremont Terrace are two residential streets that adjoin Gillygate perpendicular to the street axis (Figure 4.1). Overall, Gillygate is a relatively narrow symmetrical street canyon, with $H/W \approx 0.8$.

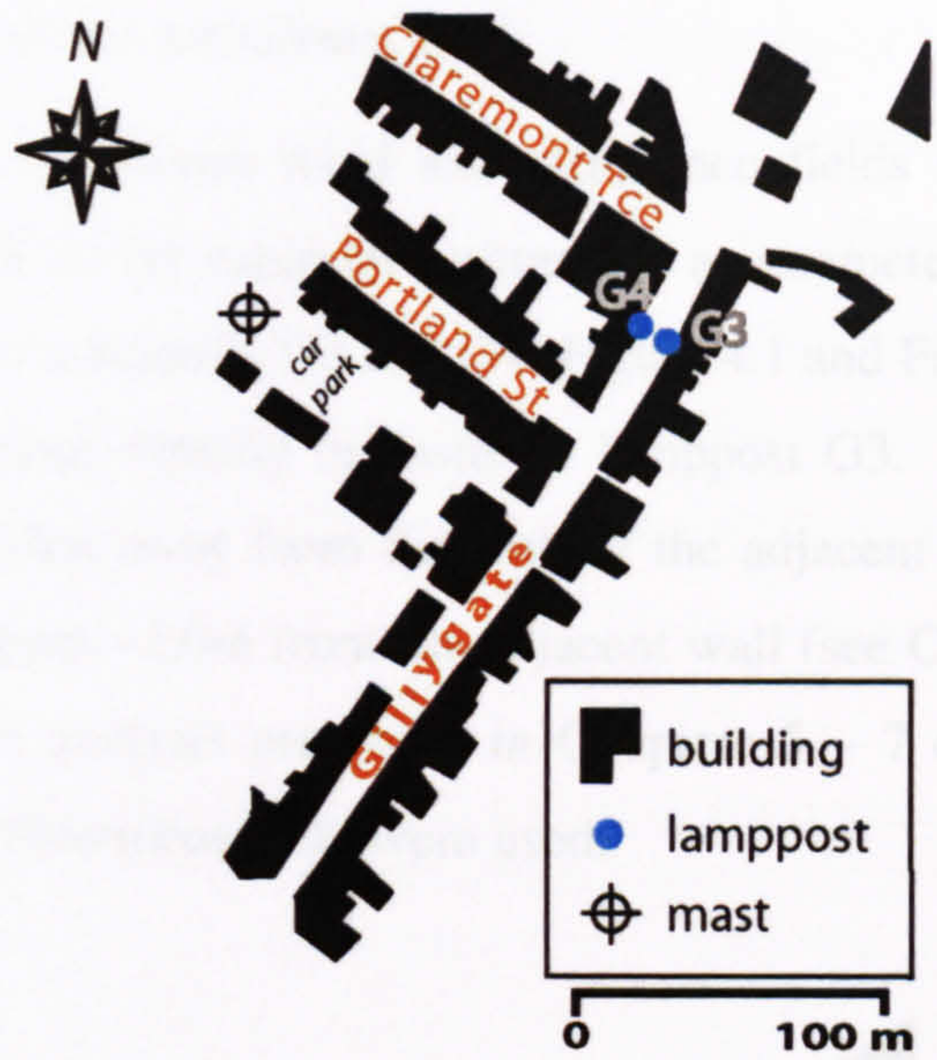


Figure 4.1. Plan view of the Gillygate street canyon, showing the lampposts that support the anemometers and the reference anemometer mast.

Attention is focused on the mean and standard deviation of the velocity components as this Chapter aims to evaluate the effects of the mean flow as a mechanism for pollution dispersion. The effects of additional sources of turbulence caused by traffic-produced turbulence and convection are not considered here as all data corresponding to background wind speeds ≤1.2 m $s^{-1}$ are excluded from most of the analysis. The influence of traffic-produced turbulence was potentially more significant during low wind speed conditions (Chapter 6).

### 4.2.2. Instrumentation and Experiments

*4.2.2.1. Background wind speed and direction*

The background wind speed, $U_{ref}$, and direction, $\theta_{ref}$, were measured using an ultrasonic anemometer that was attached to a trailer-mounted mast at a height of 19.5m. The anemometer was connected to a data-logger and operated at 10Hz, as was mentioned in Chapter 3. The mast was located in a secure car park compound, approximately 125m to the NW of Gillygate (Figure 4.1). The car park was considered to be the most suitable location in the vicinity to measure the background winds as the anemometer was ~1.8$H$ from almost all directions.

*4.2.2.2. In-canyon wind and turbulence fields*

Measurements of the in-canyon wind and turbulence fields were carried out at a sampling frequency of 20 Hz using five ultrasonic anemometers located at different heights in Gillygate on lampposts G3 and G4 (Figure 4.1 and Figure 4.2). For clarity, lamppost G4 was located directly opposite to lamppost G3. The anemometers on lamppost G4 were ~1.0m away from the wall of the adjacent building, whereas the anemometers on G3 were ~2.0m from the adjacent wall (see Chapter 3). In order to be consistent with the analysis presented in Chapters 5 – 7 only data between 13 October 2003 and 12 November 2003 were used.

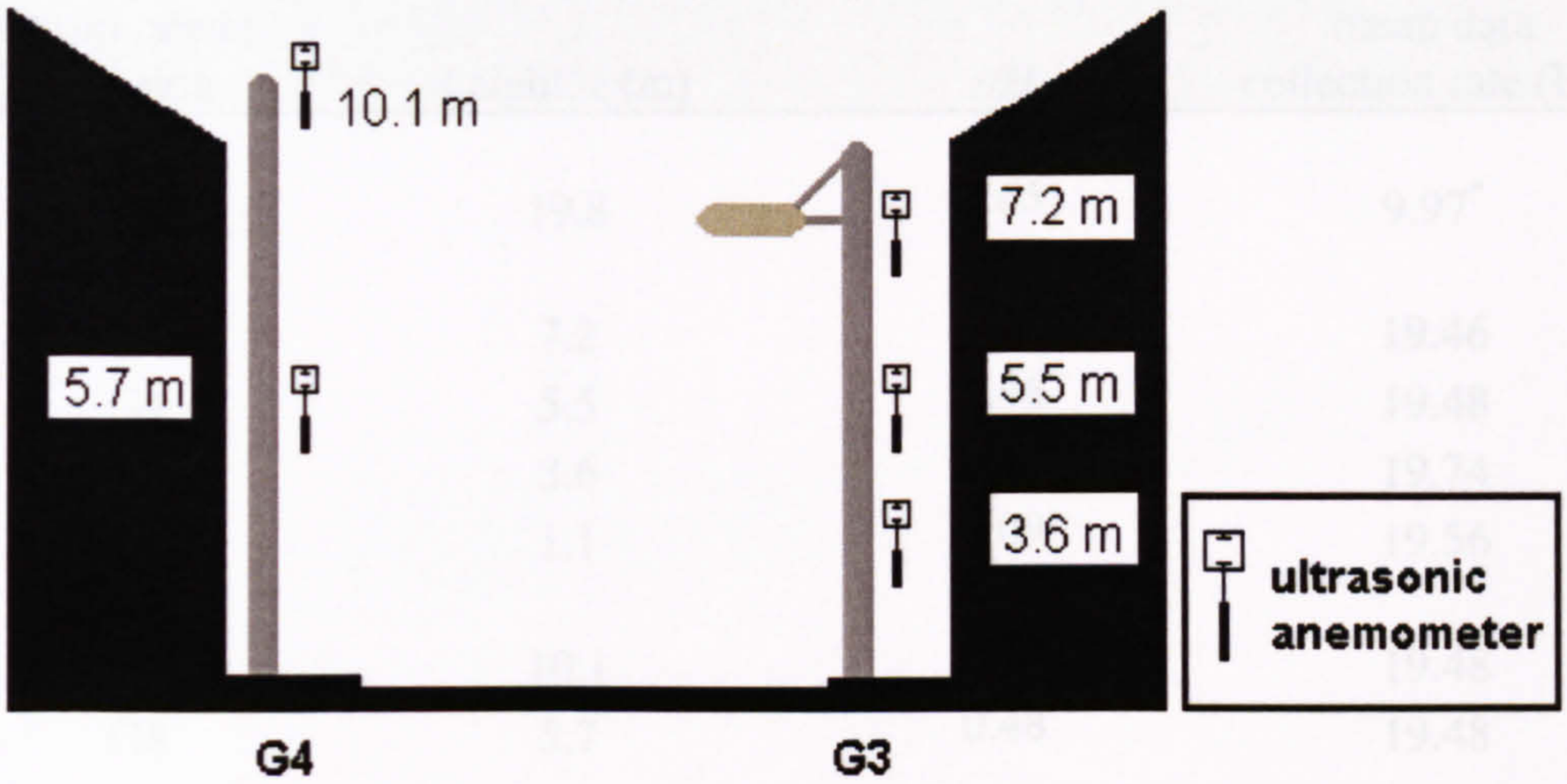


Figure 4.2. Schematic of the Gillygate canyon cross-section at G3-G4, showing relative locations of the ultrasonic anemometers.

The data were post-processed and averaged over 15-minute time periods. Clearly, in each 15-minute averaging period there should be 18000 samples measured by each anemometer operating at 20 Hz. Time periods with less than 90% of the total number of samples were excluded, i.e. the mean data collection rate was greater than 18 Hz. After these time periods were excluded, however, the mean data collection rates for each 15-minute period across the entire monitoring period were much higher than the minimum value for data rejection (Table 4.1). For example, at the mid-canyon anemometers the mean data collection rates were as high as 19.48 Hz.

Comparisons were made between the mean and standard deviation of the flow at mid-canyon height at lampposts G3 and G4 ($z/H$ = 0.46 and $z/H$ = 0.48, respectively).

However, analysis is also shown from the data collected by the sonic anemometers located on lamppost G3 at $z/H$ = 0.30 and $z/H$ = 0.60 and from the anemometer located on lamppost G4 at $z/H$ = 0.84. The highest anemometer on lamppost G4 is closest measurement location to the shear layer. Comparisons between the mean and turbulent parts of the flow measured by the in-canyon anemometers against the background wind should give an indication of the variation in turbulence within the canyon volume.

Table 4.1. The mean data collection rate for all ultrasonic anemometers deployed during the experiment. *Note that all instruments were set to sample at 20 Hz except for the reference anemometer located on the mast, which was set at 10 Hz.

| anemometer location | height, $z$ (m) | $z/H$ | mean data collection rate (Hz) |
|---|---|---|---|
| mast | 19.8 | 1.65 | 9.97* |
| G3 | 7.2 | 0.60 | 19.46 |
| G3 | 5.5 | 0.46 | 19.48 |
| G3 | 3.6 | 0.30 | 19.74 |
| G3 | 1.1 | 0.09 | 19.56 |
| G4 | 10.1 | 0.84 | 19.48 |
| G4 | 5.7 | 0.48 | 19.48 |

For clarity, Gillygate is orientated at approximately 30° from north at the G3-G4 cross-section. The SE side of the street canyon is relatively unbroken along its entire length. However, the NW side of the canyon is broken by Portland Street and Claremont Terrace, which are two residential streets that adjoin Gillygate perpendicular to the along-street axis (Figure 4.1). It is expected that two very different flow regimes occurred during perpendicular background winds of $\theta_{ref}$ = 120° (i.e. SE) and $\theta_{ref}$ = 300° (i.e. NW). There are no trees or bus shelters or any other street furniture along the entire length of the canyon that would have caused significant sheltering effects. However, some flow distortion was to be expected from the lampposts upon which the anemometers were located.

The wind flow over the experiment site near to the G3-G4 cross-section was simulated using the MISKAM numerical model (Eichhorn, 1996). The flow model used a $k$-$\varepsilon$ turbulence closure scheme to parameterise the turbulence. Chapter 3 described the method used to build the domain. The model assumed that the wind speed increased logarithmically with height upstream and that there was neutral static stability. A roughness length of 0.5 m was used in order to define this profile. This roughness length corresponds to flow over suburban housing (Oke, 1987; Davenport *et al.*, 2000), which constituted the majority of the upstream fetch. The model was also used to derive turbulence parameters. The derived mean wind and turbulence parameters were compared with the experimental results in order to assist in the interpretation of the dispersion characteristics of the in-canyon flow features.

## 4.3. Results

This Section presents all the results from the mean flow and turbulence analysis. The discussion of the results has been placed in Section 4.4. The results in the subsequent chapters are contained within the discussion. However, as the figures in this Chapter present data as a function of the background wind direction it was necessary to separate the results and discussion sections for ease of cross-referencing.

### 4.3.1. Standard deviation of the mean vertical wind velocity

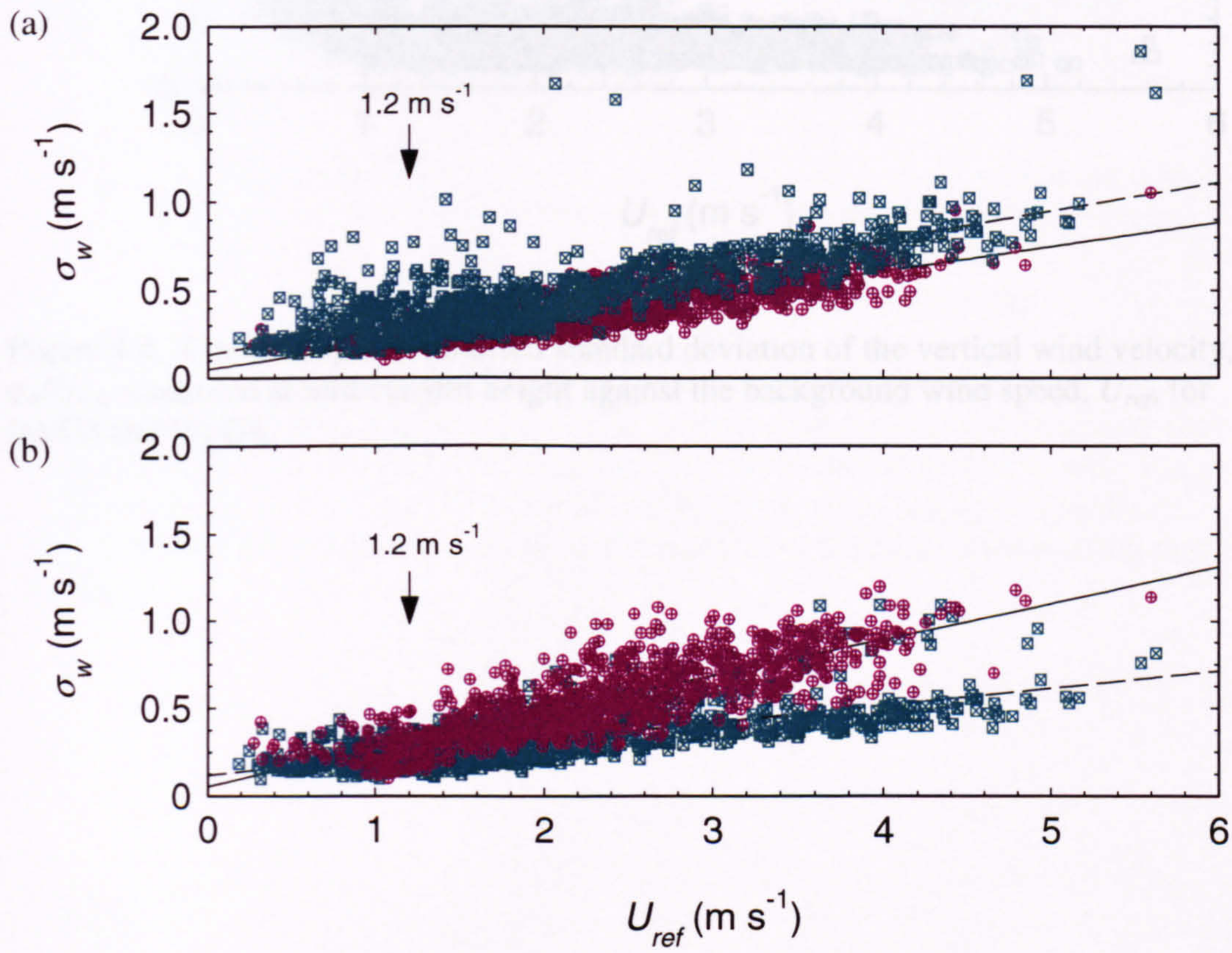


Figure 4.3. Standard deviation of the vertical wind velocity, $\sigma_w$, measured at mid-canyon height against the background wind speed, conditioned on background wind directions ⊠ $\theta_{ref}$ = 120° ±90° and ⊕ $\theta_{ref}$ = 300° ±90° for (a) G3 and (b) G4. — — curve fit for $\theta_{ref}$ = 120° ±90° and —— curve fit for $\theta_{ref}$ = 300° ±90°.

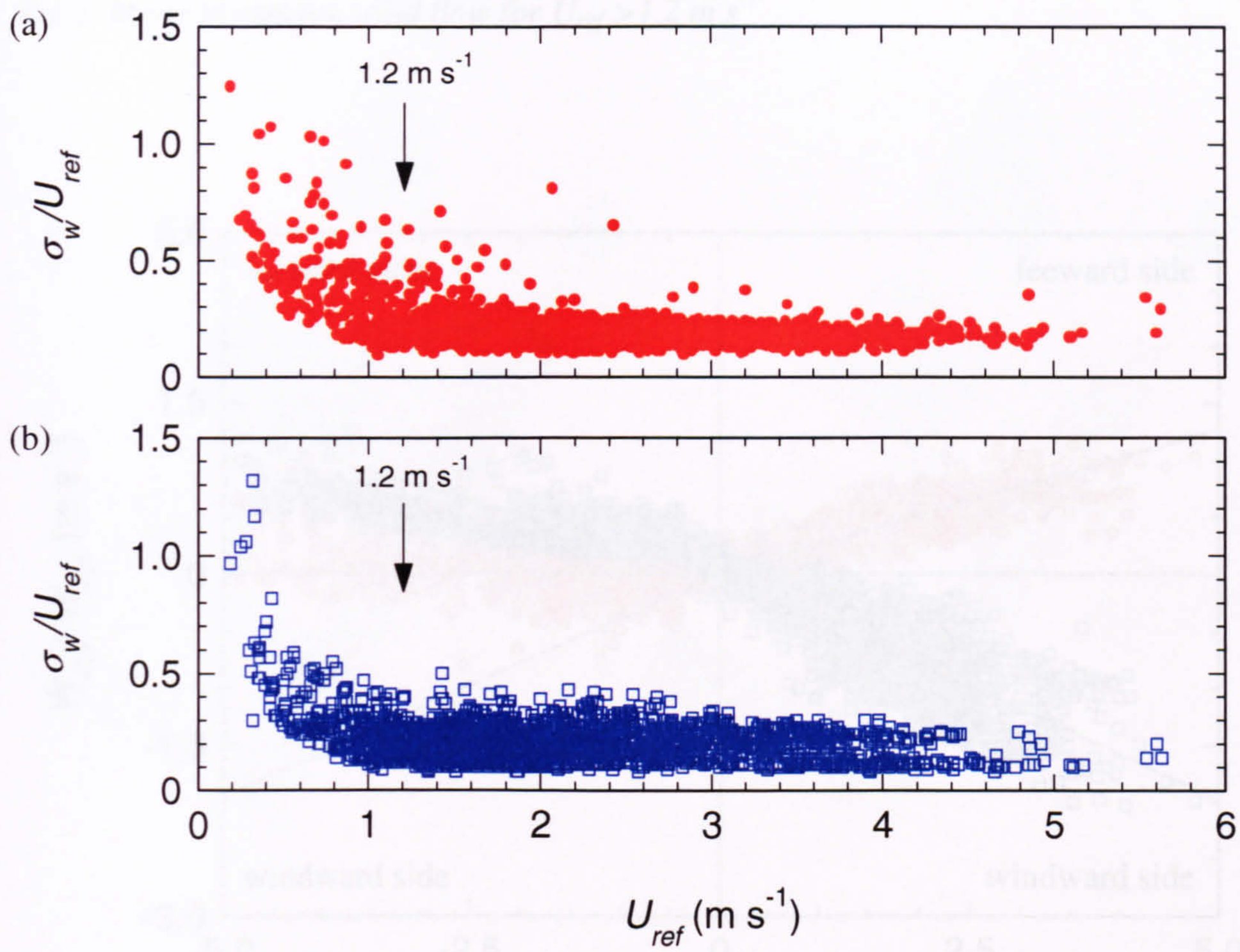


Figure 4.4. Compensated normalised standard deviation of the vertical wind velocity, $\sigma_w/U_{ref}$, measured at mid-canyon height against the background wind speed, $U_{ref}$, for (a) G3 and (b) G4.

*4.3.2. Mean in-canyon wind flow for $U_{ref}$ >1.2 m s$^{-1}$*

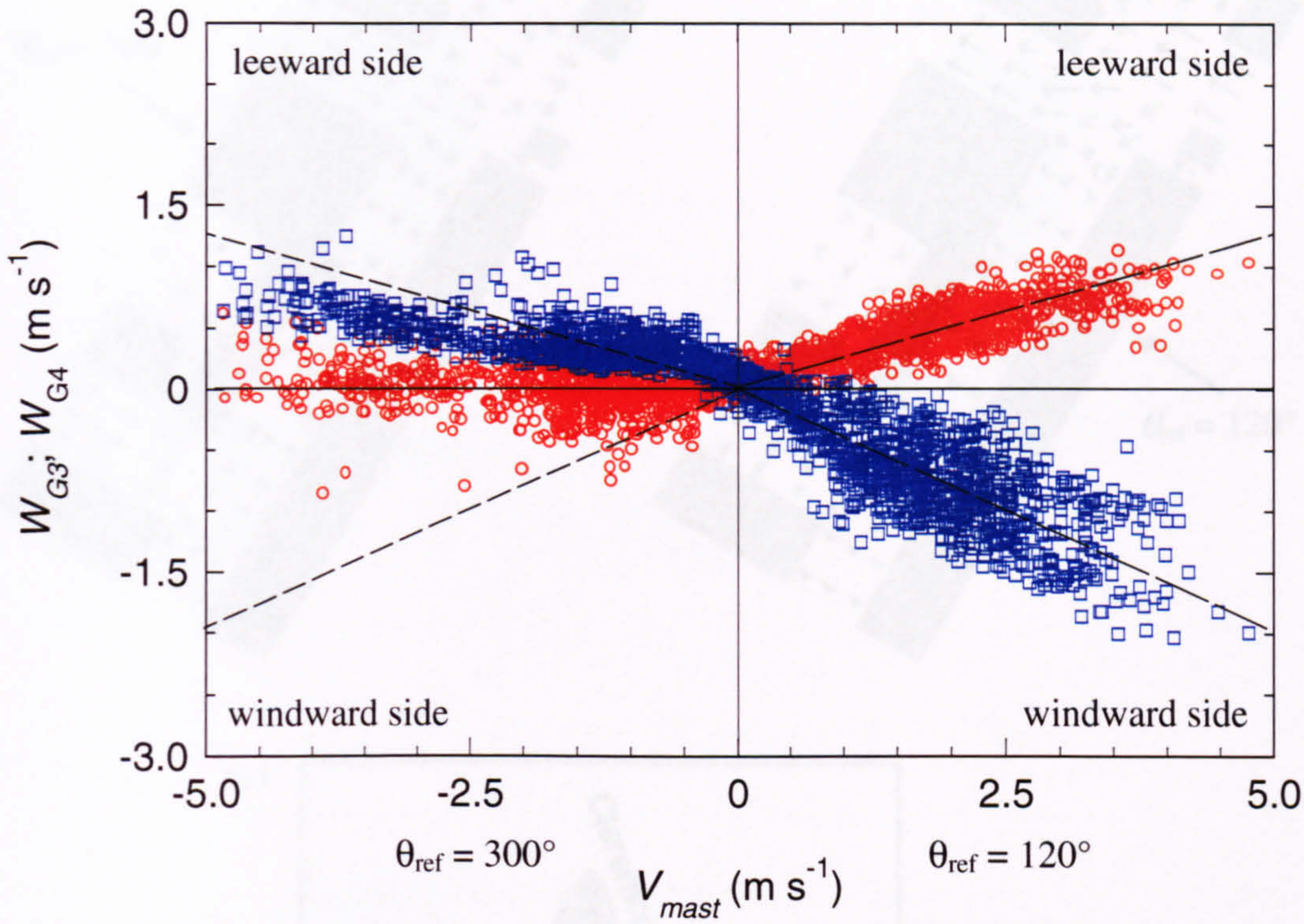


Figure 4.5. Vertical velocity component, *W*, measured at mid-canyon height on each lamppost as a function of the across-canyon component measured at the mast, $V_{mast}$: ○ G3 and □ G4. — — curve fits for SE background winds and – – – predicted curve fits for NW backgrounds based on the analysis of the data corresponding to the SE winds.

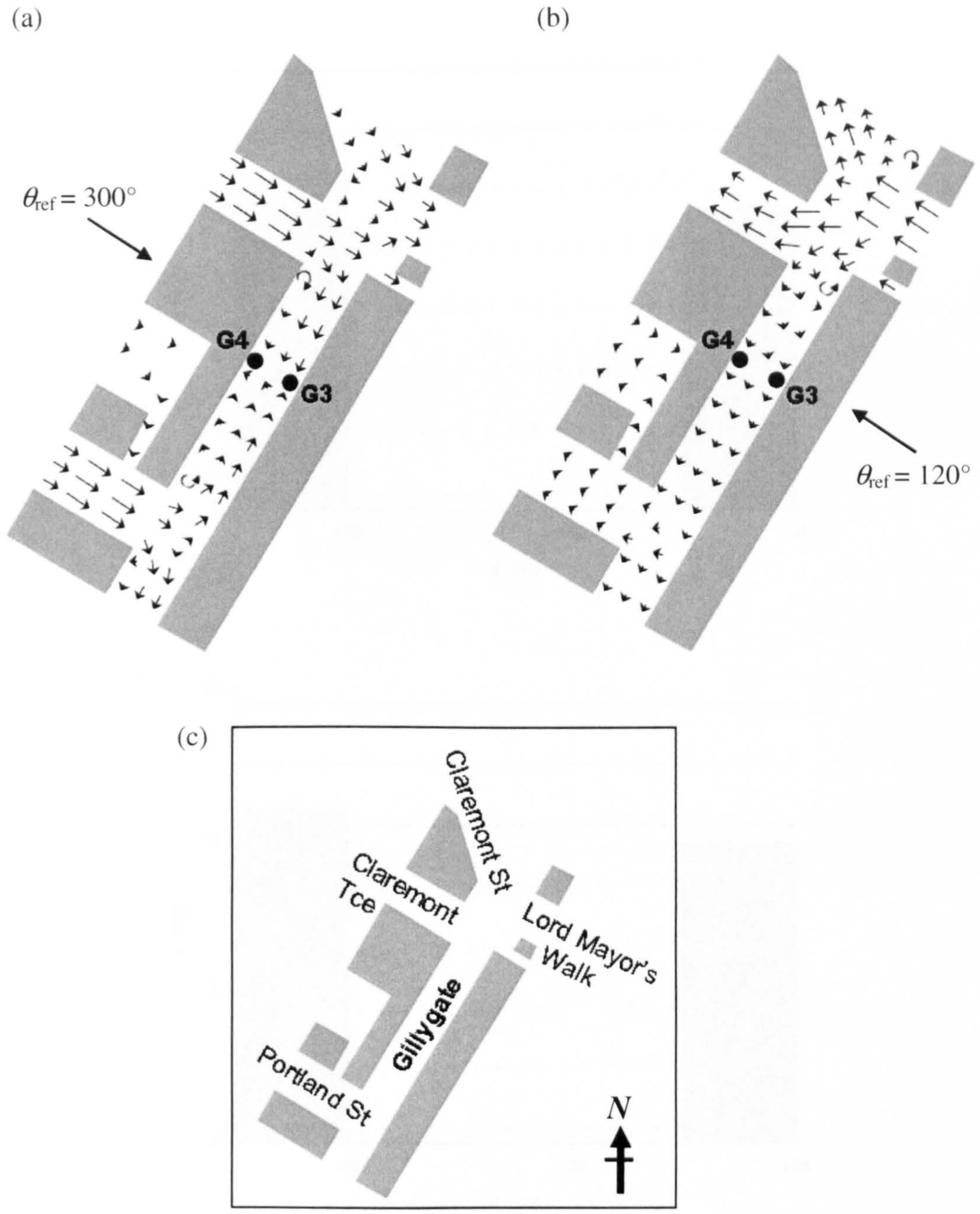


Figure 4.6. Schematic of the mean horizontal flow vectors computed by MISKAM at a height of 5m for perpendicular background winds from: (a) $\theta_{ref}$ = 300° and (b) $\theta_{ref}$ = 120°. The section of the model domain used was around cross-section G3-G4 and is shown in (c). The buildings are shown as shaded rectangles. The reference wind speed (at 50 m) was configured to 5 m $s^{-1}$.

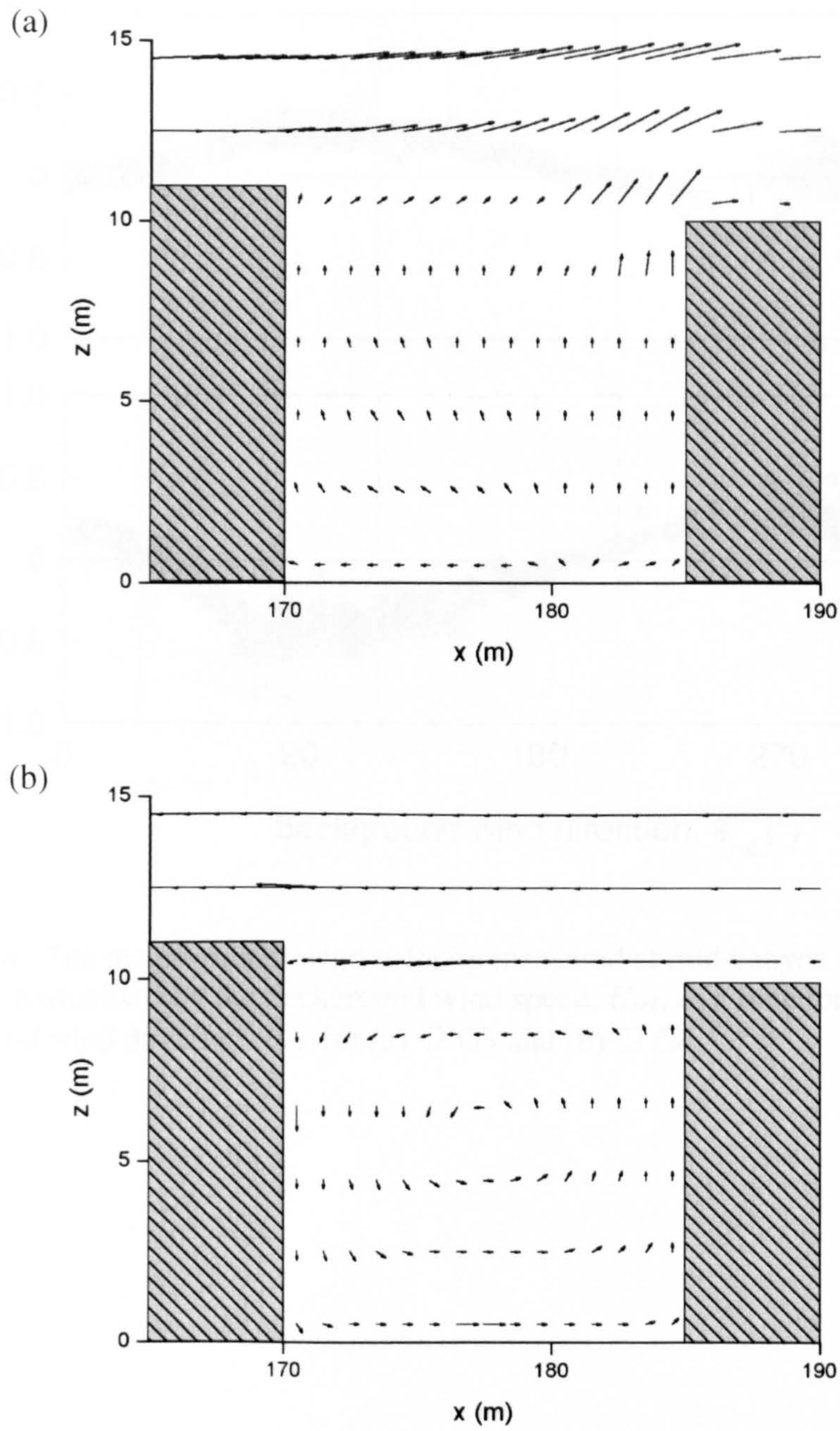


Figure 4.7. The mean flow vectors computed by MISKAM at cross-section G3-G4 for perpendicular background winds from: (a) $\theta_{ref} = 300°$ and (b) $\theta_{ref} = 120°$. The buildings are shown as shaded rectangles with diagonal hatches. The reference wind speed (at 50 m) was configured to 5 m $s^{-1}$.

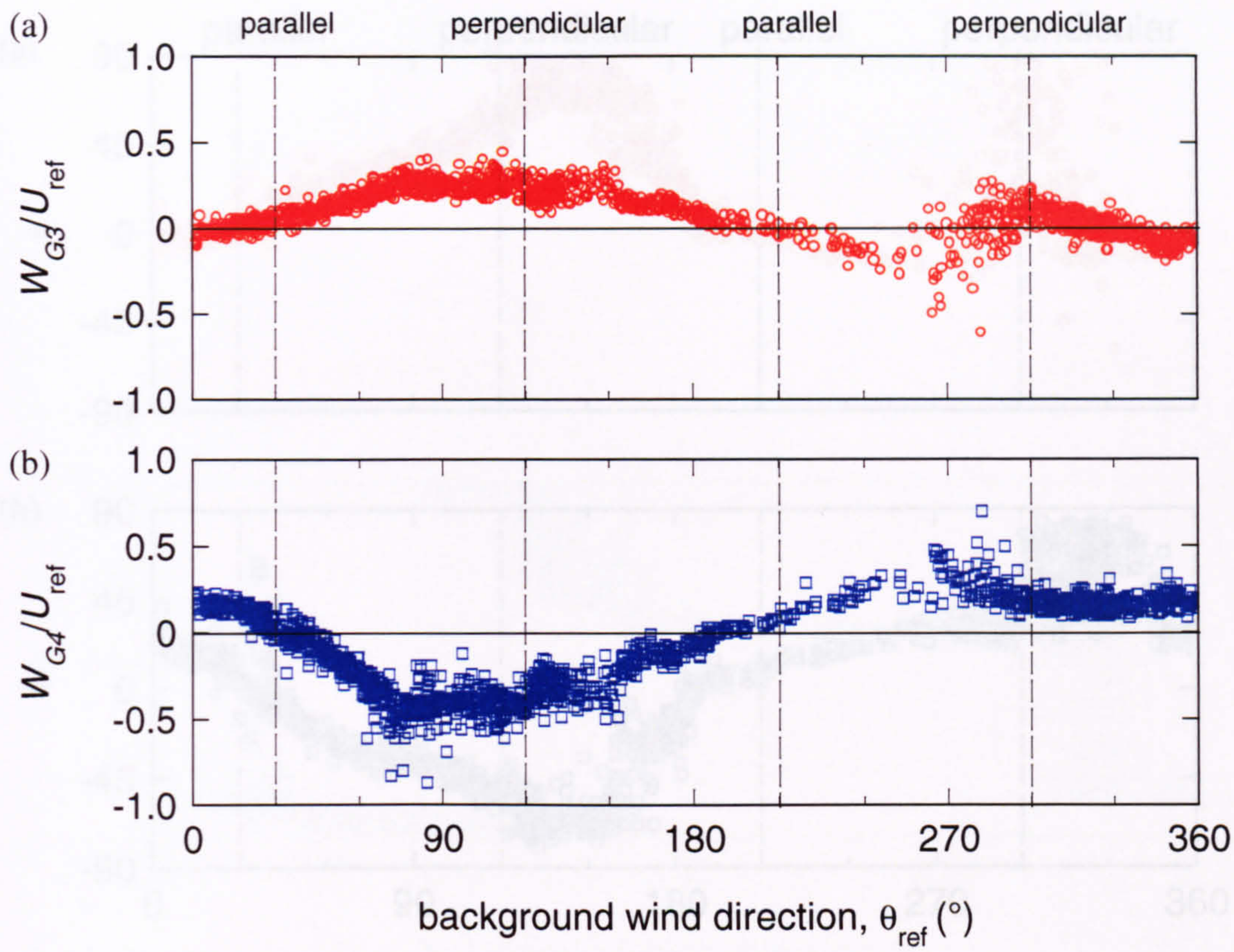


Figure 4.8. The mean vertical wind velocity measured at mid-canyon height inside Gillygate normalised by the background wind speed, $U_{ref}$, as a function of the background wind direction, $\theta_{ref}$, for (a) ○ G3 and (b) □ G4.

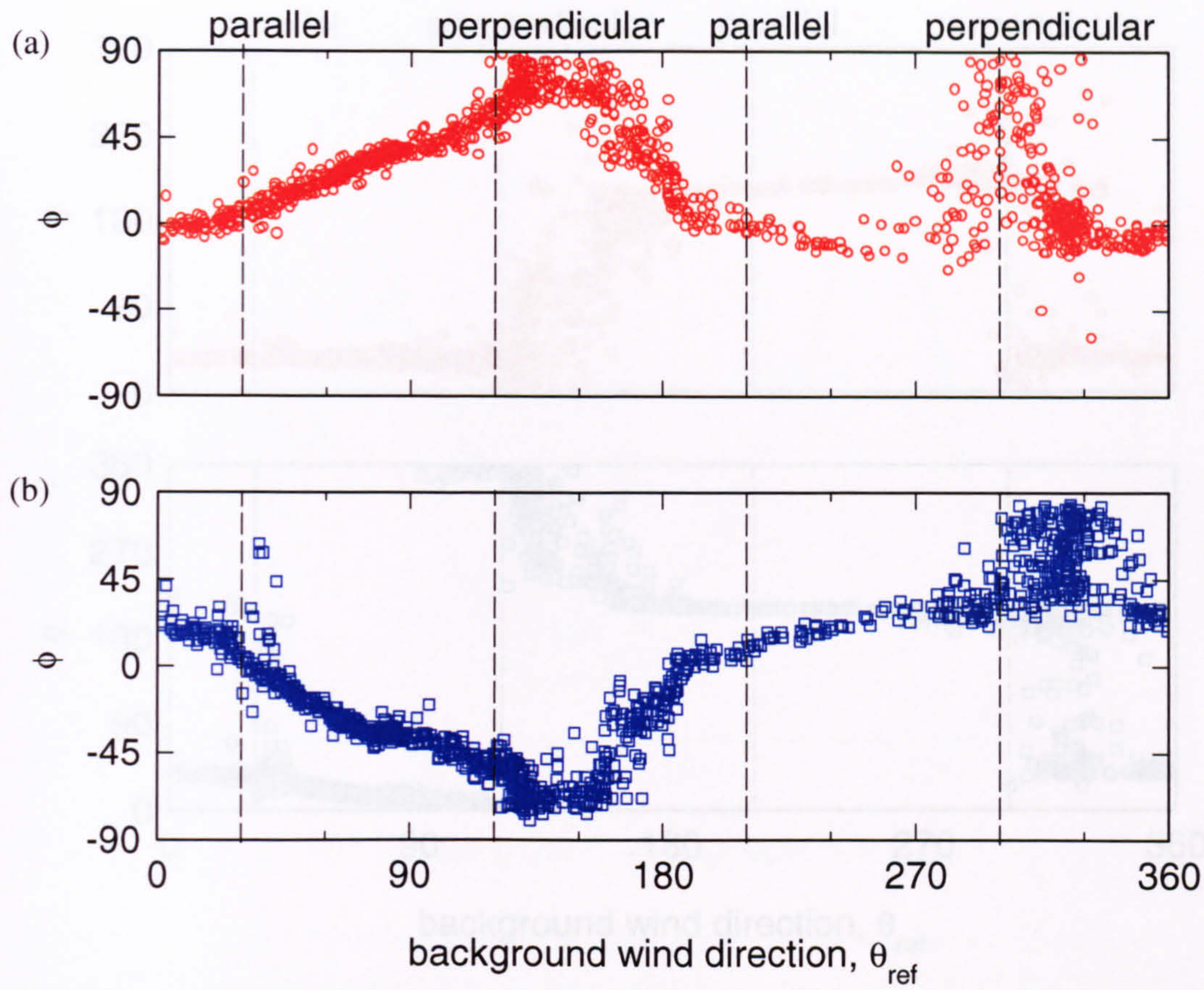


Figure 4.9. Vertical wind velocity angle, $\phi$, as a function of background wind direction, $\theta_{ref}$, for: (a) ○ G3 and (b) □ G4.

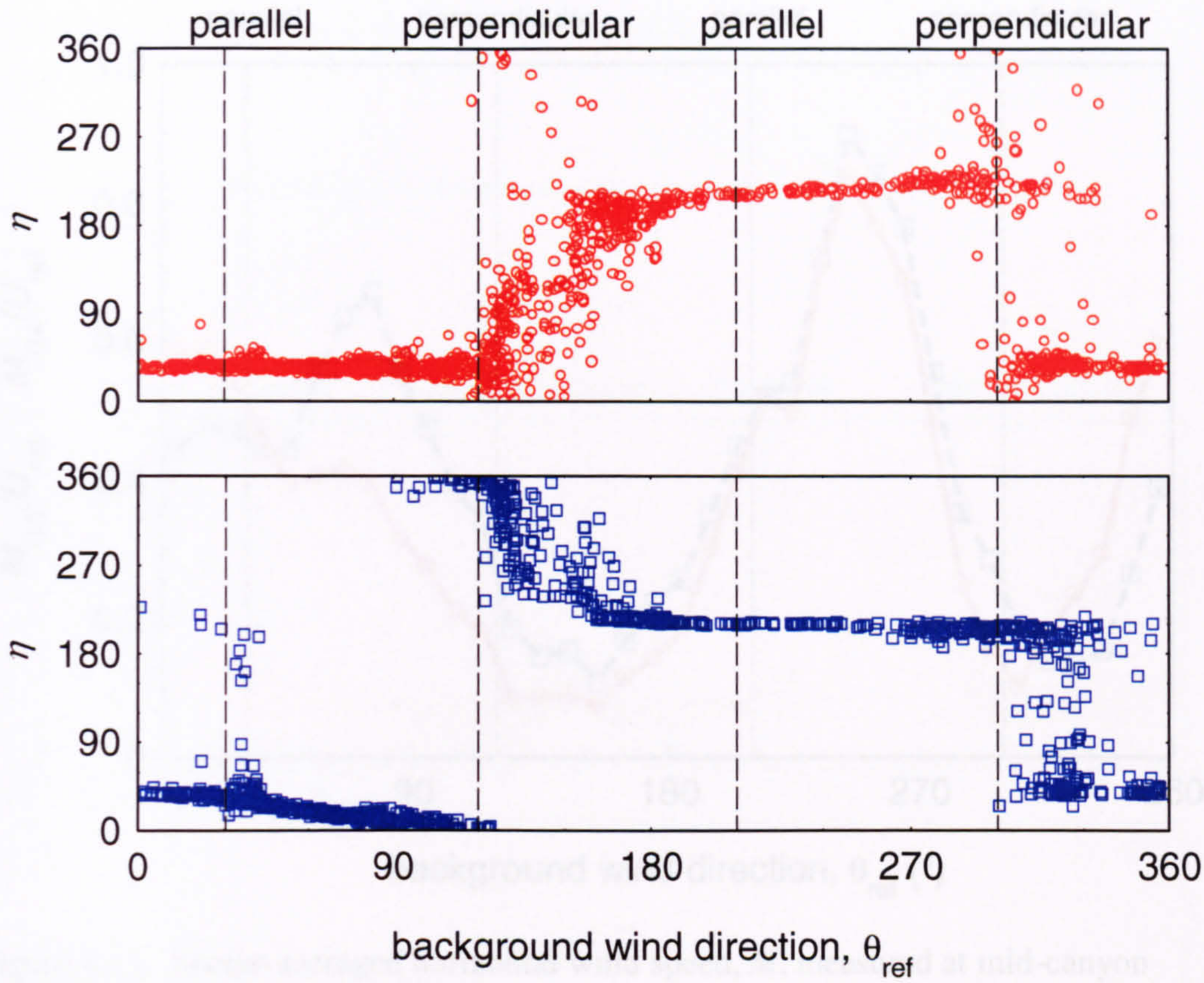


Figure 4.10. In-canyon wind direction, $\eta$, as a function of background wind direction, $\theta_{ref}$, for: (a) ○ G3 and (b) □ G4.

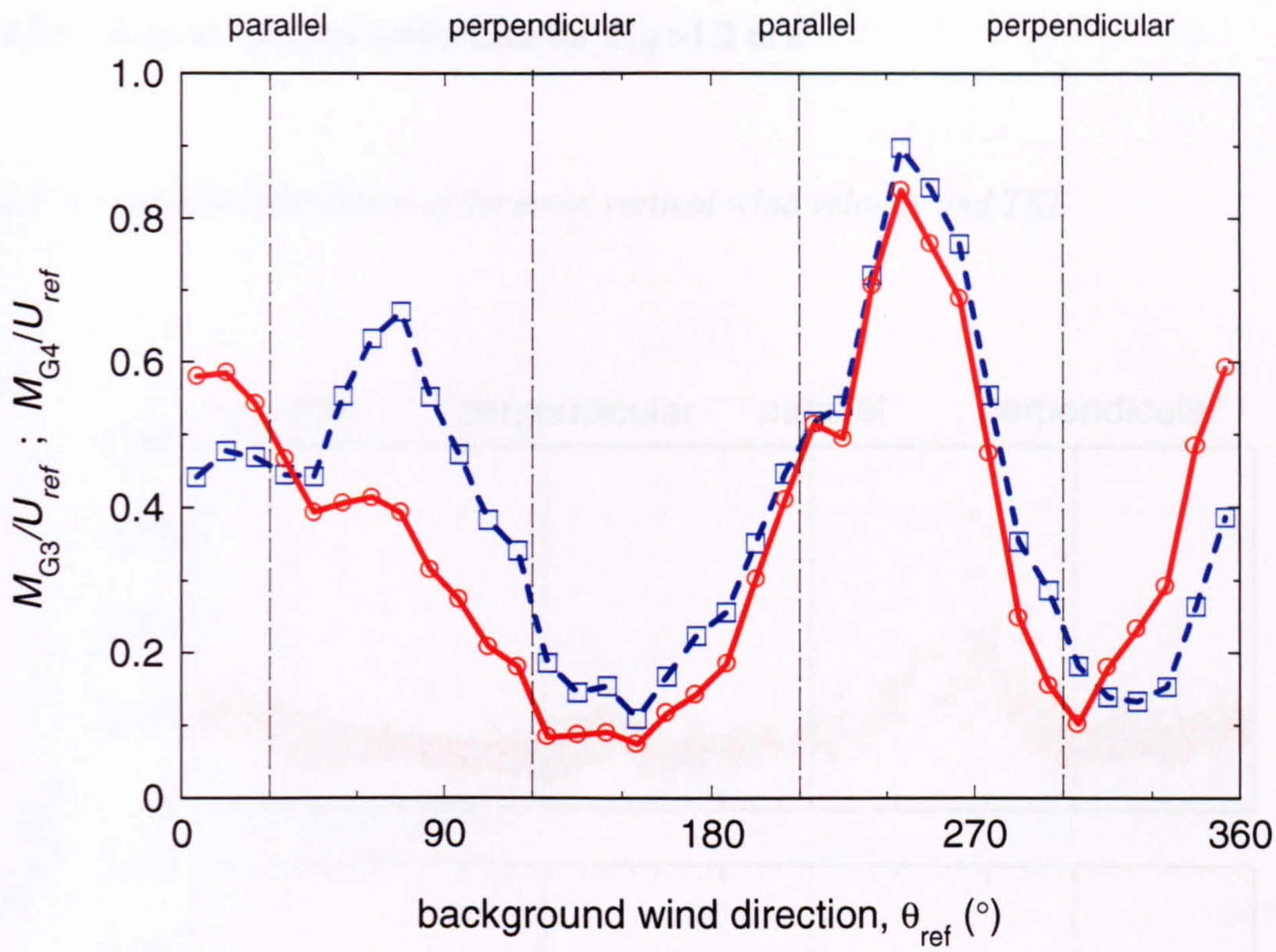


Figure 4.11. Sector-averaged horizontal wind speed, $M$, measured at mid-canyon height normalised by the background wind speed, $U_{ref}$, as a function of $\theta_{ref}$: —○— G3 and --□-- G4.

### 4.3.3. Mean in-canyon turbulence for $U_{ref}$ >1.2 m s$^{-1}$

*4.3.3.1. Standard deviation of the mean vertical wind velocity and TKE*

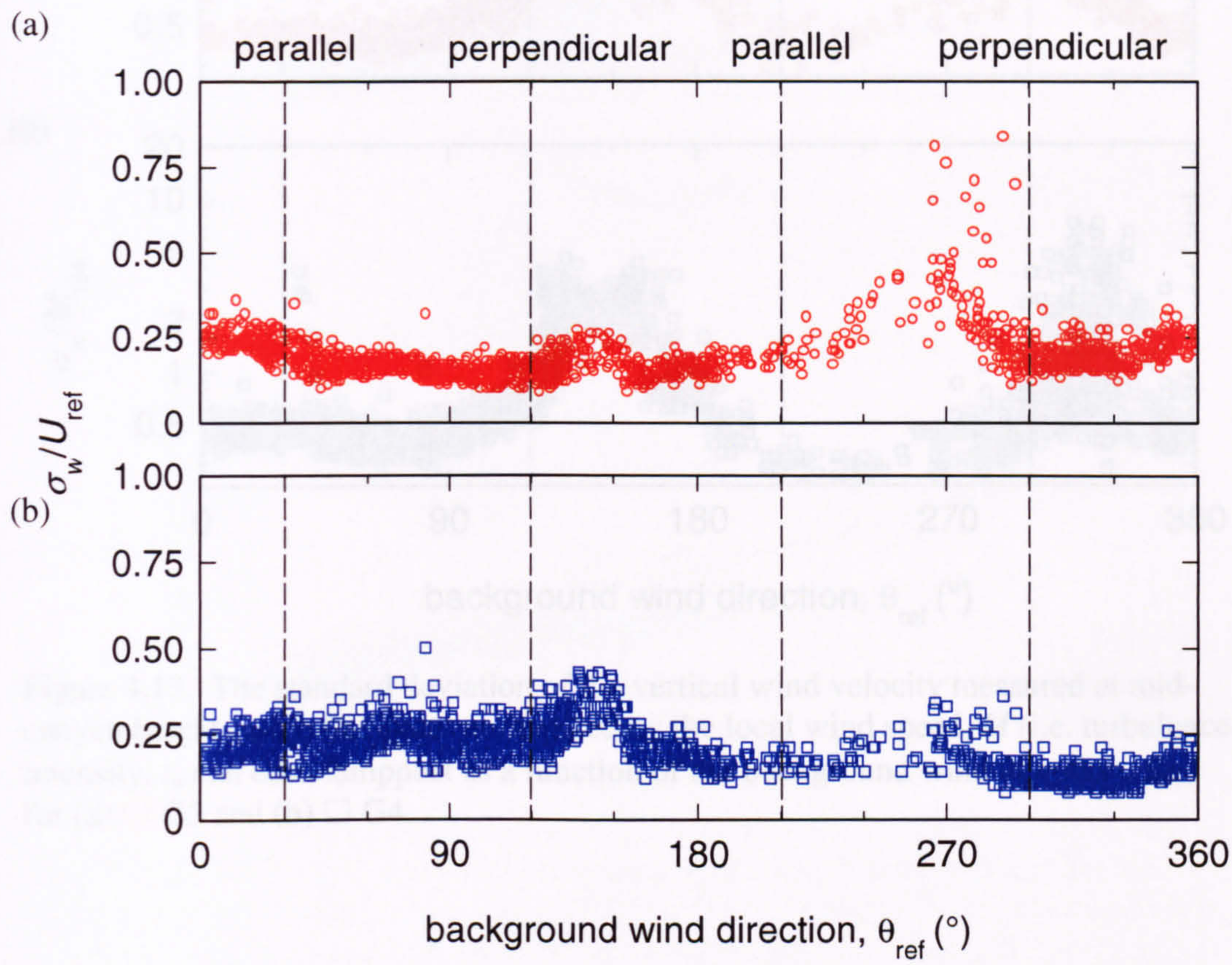


Figure 4.12. The standard deviation of the vertical wind velocity measured at mid-canyon height inside Gillygate normalised by the background wind speed, $U_{ref}$, as a function of the background wind direction, $\theta_{ref}$, for (a) ○ G3 and (b) □ G4.

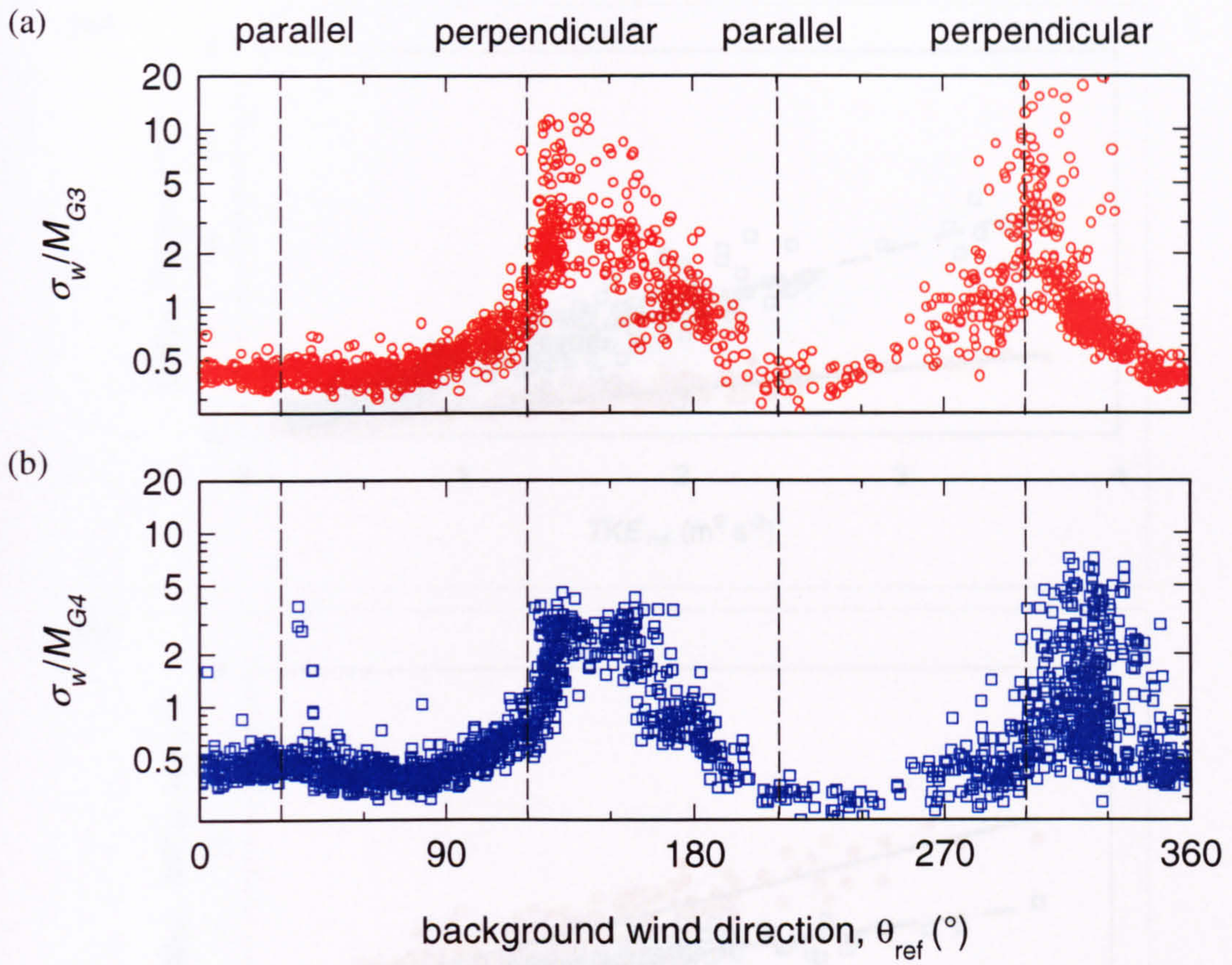


Figure 4.13. The standard deviation of the vertical wind velocity measured at mid-canyon height inside Gillygate normalised by the local wind speed, $M$ (i.e. turbulence intensity, $t_w$) on each lamppost as a function of the background wind direction, $\theta_{ref}$, for (a) ○ G3 and (b) □ G4.

(a)

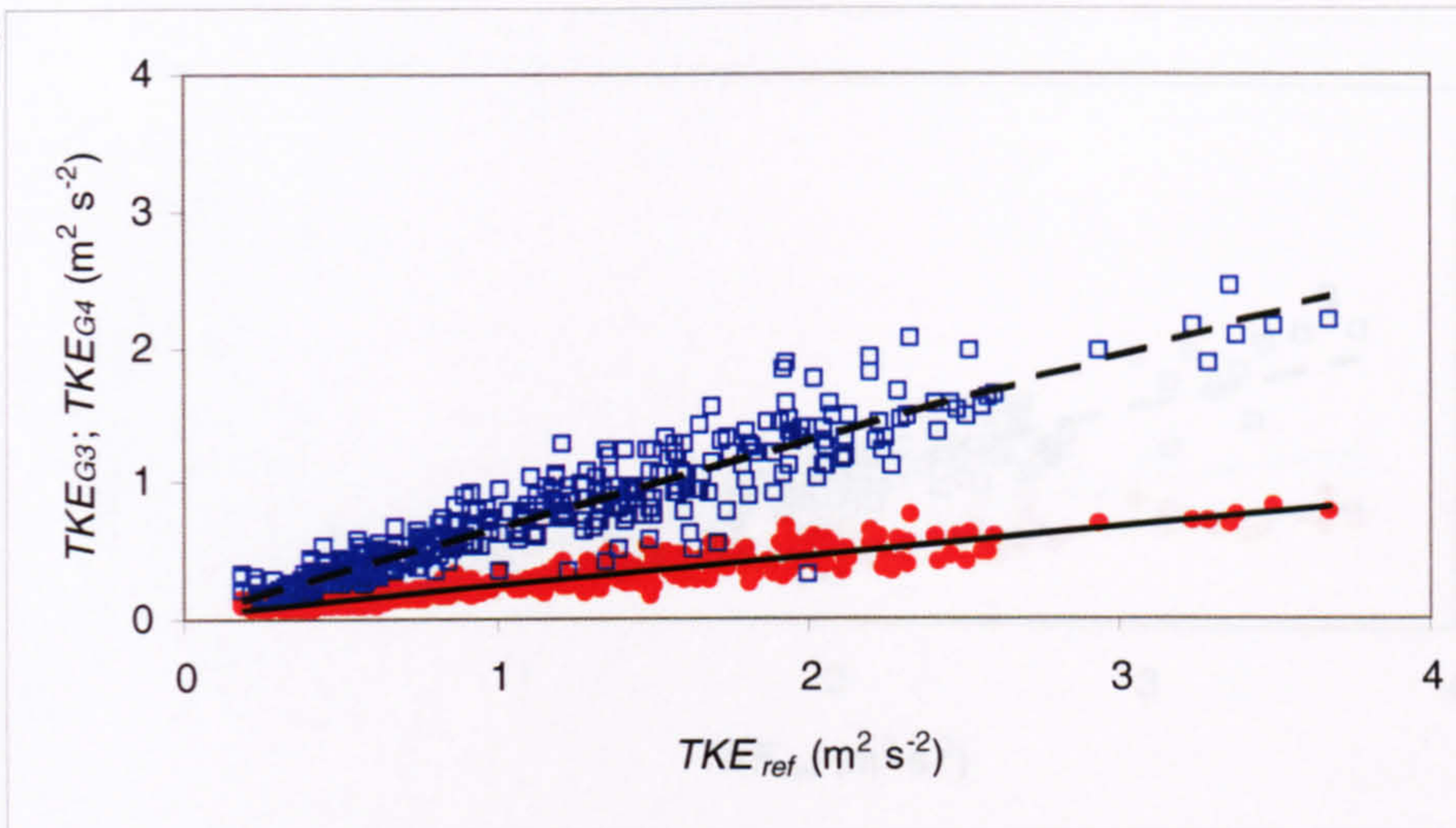


(b)

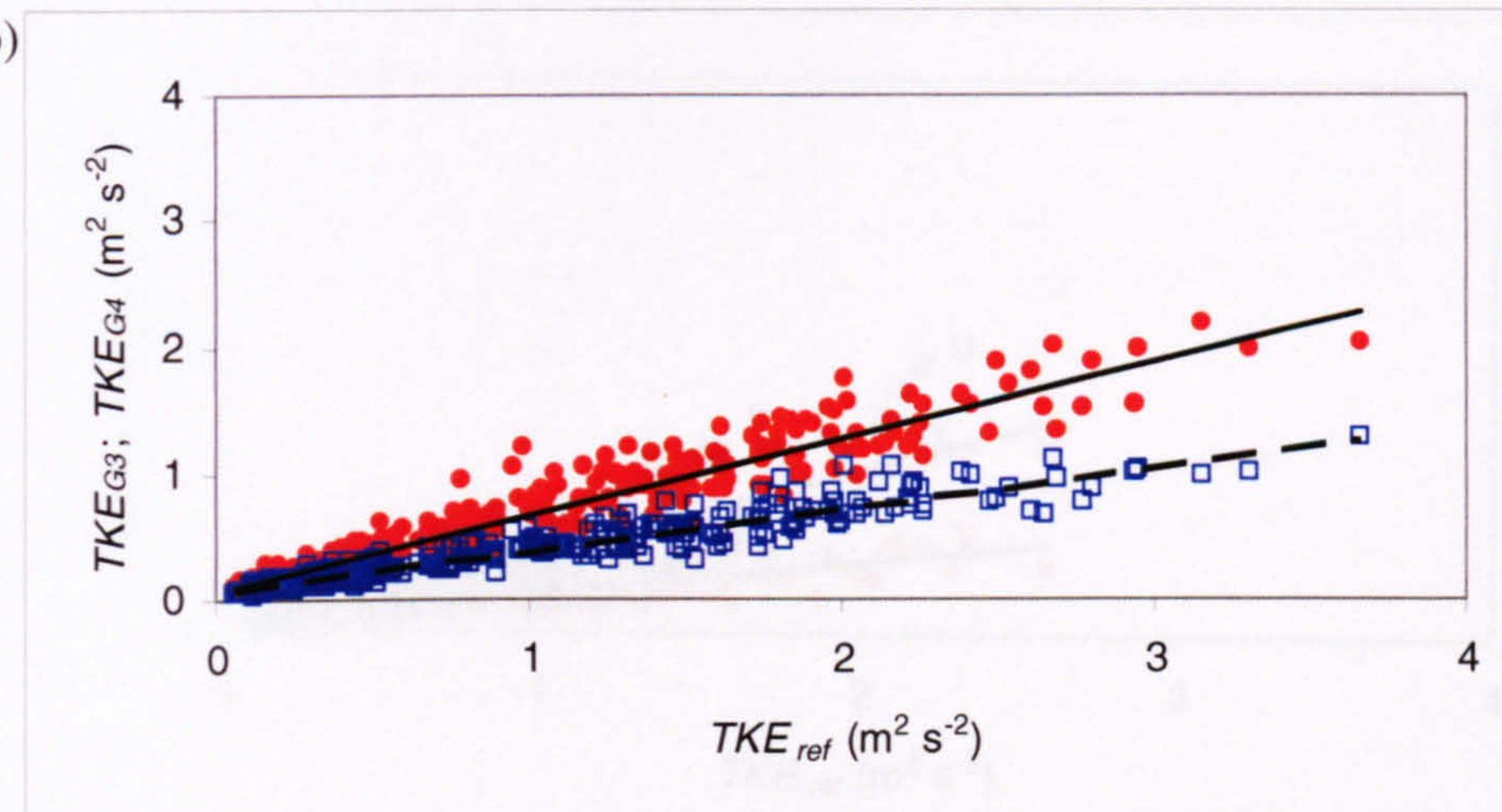


Figure 4.14. TKE measured at mid-canyon height on each lamppost against the background turbulence kinetic energy, $TKE_{ref}$, for • G3 and □ G4, conditioned on $U_{ref}$ >1.2 m s$^{-1}$ and: (a) $\theta_{ref}$ = 120° ±30°; (b) $\theta_{ref}$ = 300° ±30°. —— curve fit for G3 and — — curve fit for G4.

(a)

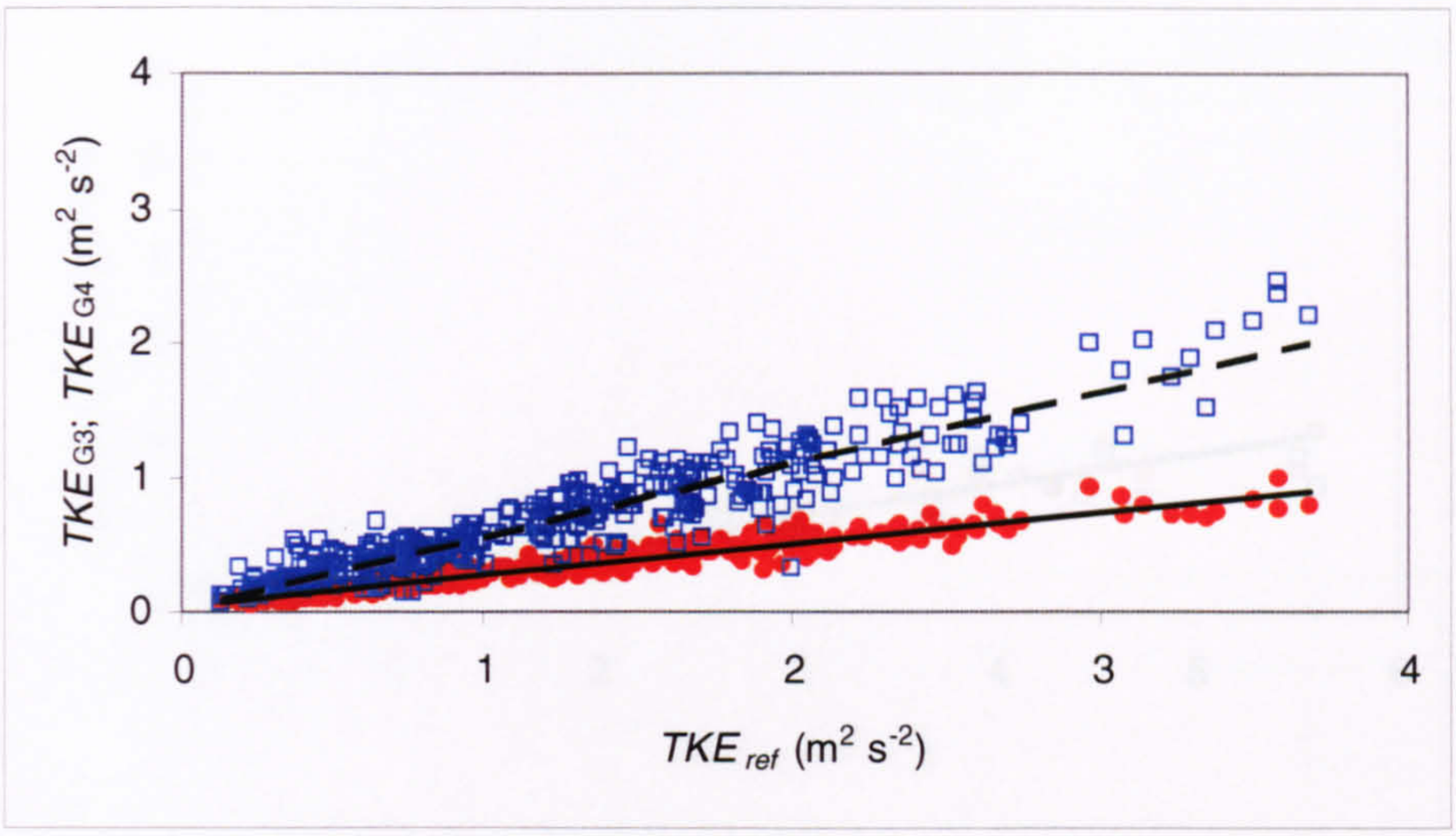


(b)

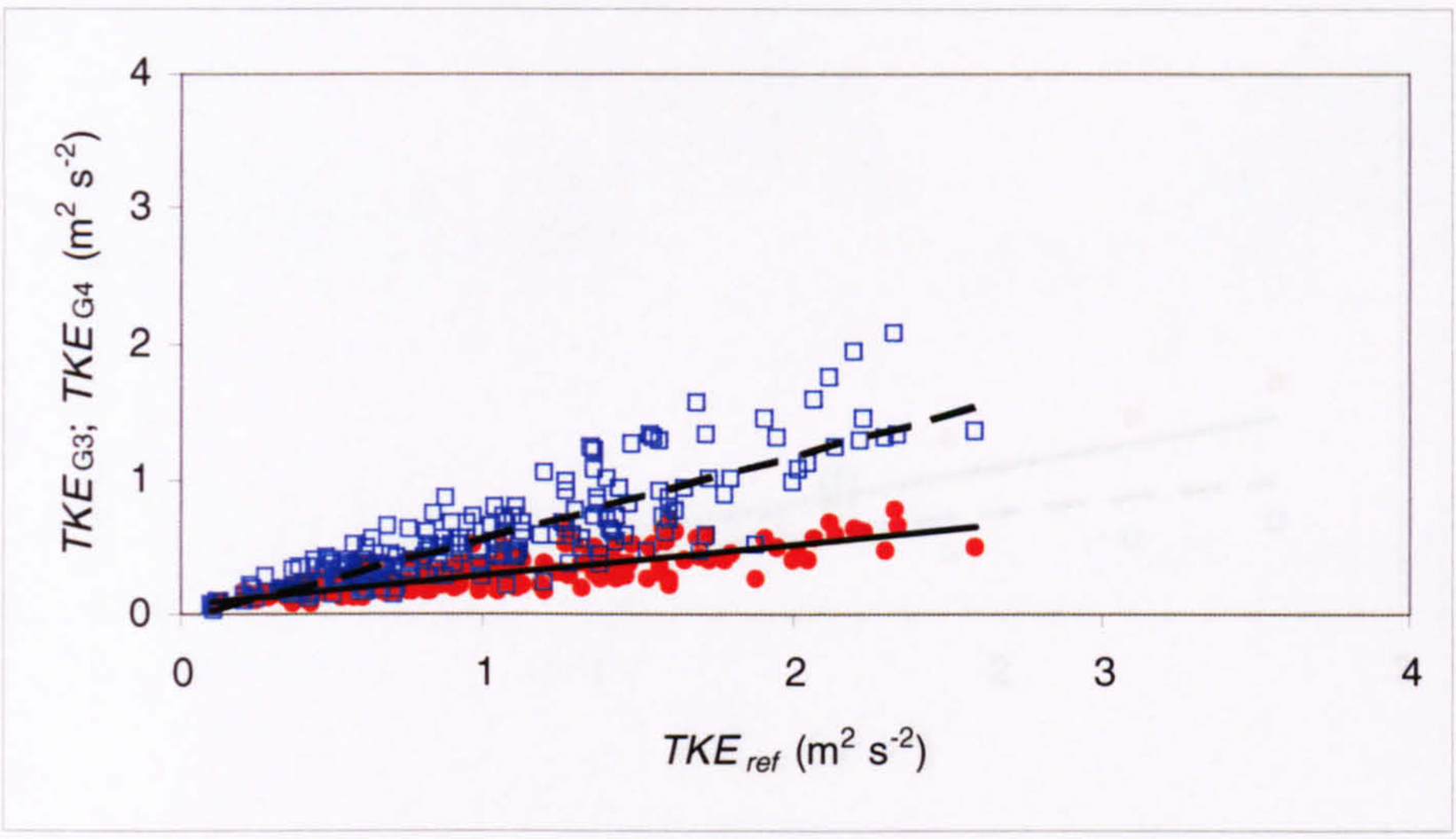


Figure 4.15. TKE measured at mid-canyon height on lampposts G3 and G4 against the background turbulence kinetic energy, $TKE_{ref}$, for • G3 and □ G4, conditioned on $U_{ref}$ >1.2 m s$^{-1}$ and: (a) $\theta_{ref}$ = 75° ±30°; (b) $\theta_{ref}$ = 165° ±30°. —— curve fit for G3 and — — curve fit for G4.

(a)

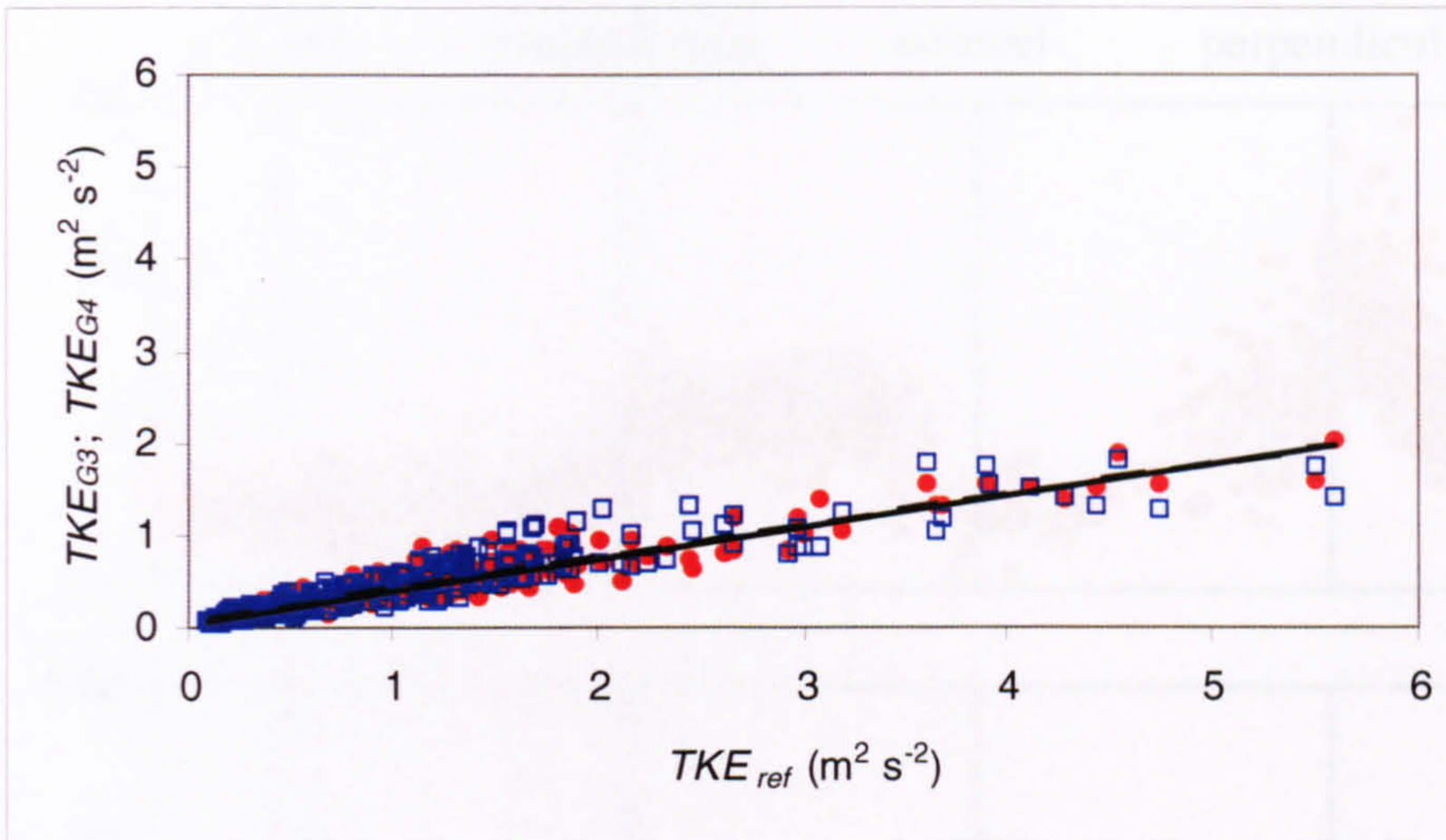


(b)

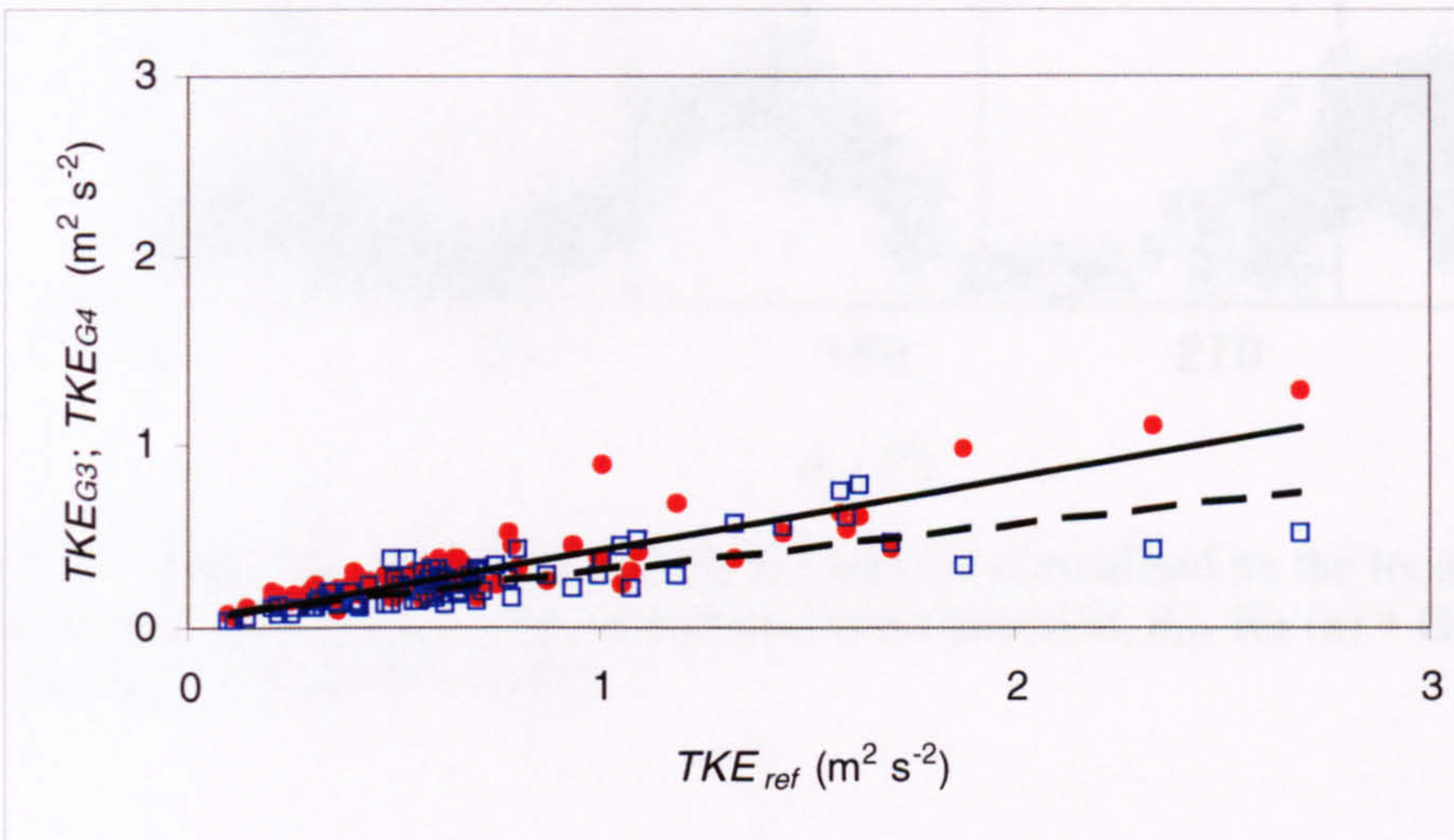


Figure 4.16. TKE measured at mid-canyon height on each lamppost against the background turbulence kinetic energy, $TKE_{ref}$, for • G3 and □ G4, conditioned on $U_{ref}$ >1.2 m s$^{-1}$ and: (a) $\theta_{ref}$ = 30° ±30°; (b) $\theta_{ref}$ = 210° ±30°. —— curve fit G3 and — — curve fit for G4.

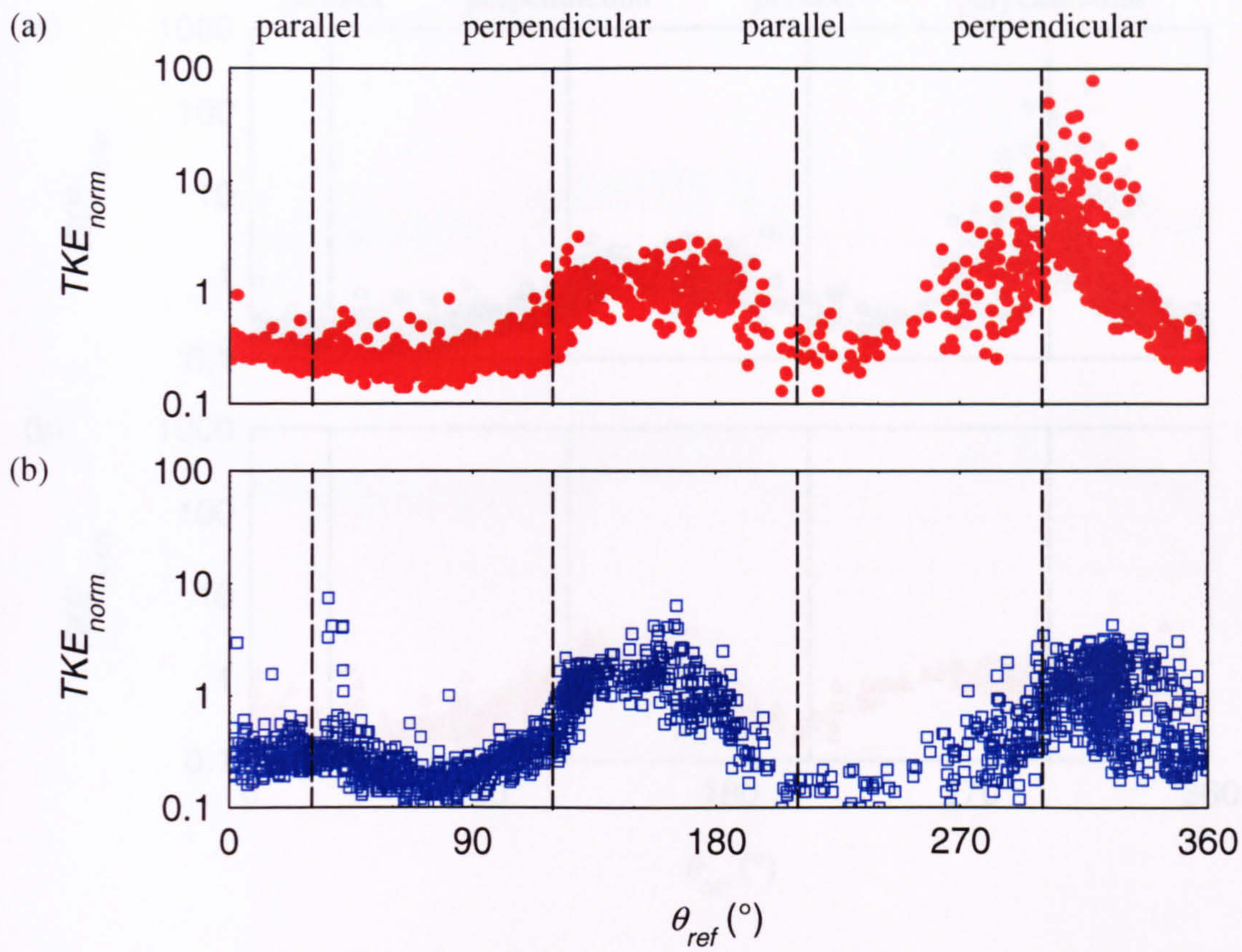


Figure 4.17. TKE measured on lampposts G3 and G4 normalised by the local horizontal wind speed against the background wind direction, $\theta_{ref}$, for (a) • G3 at $z/H$ = 0.46 and (b) □ G4 at $z/H$ = 0.48.

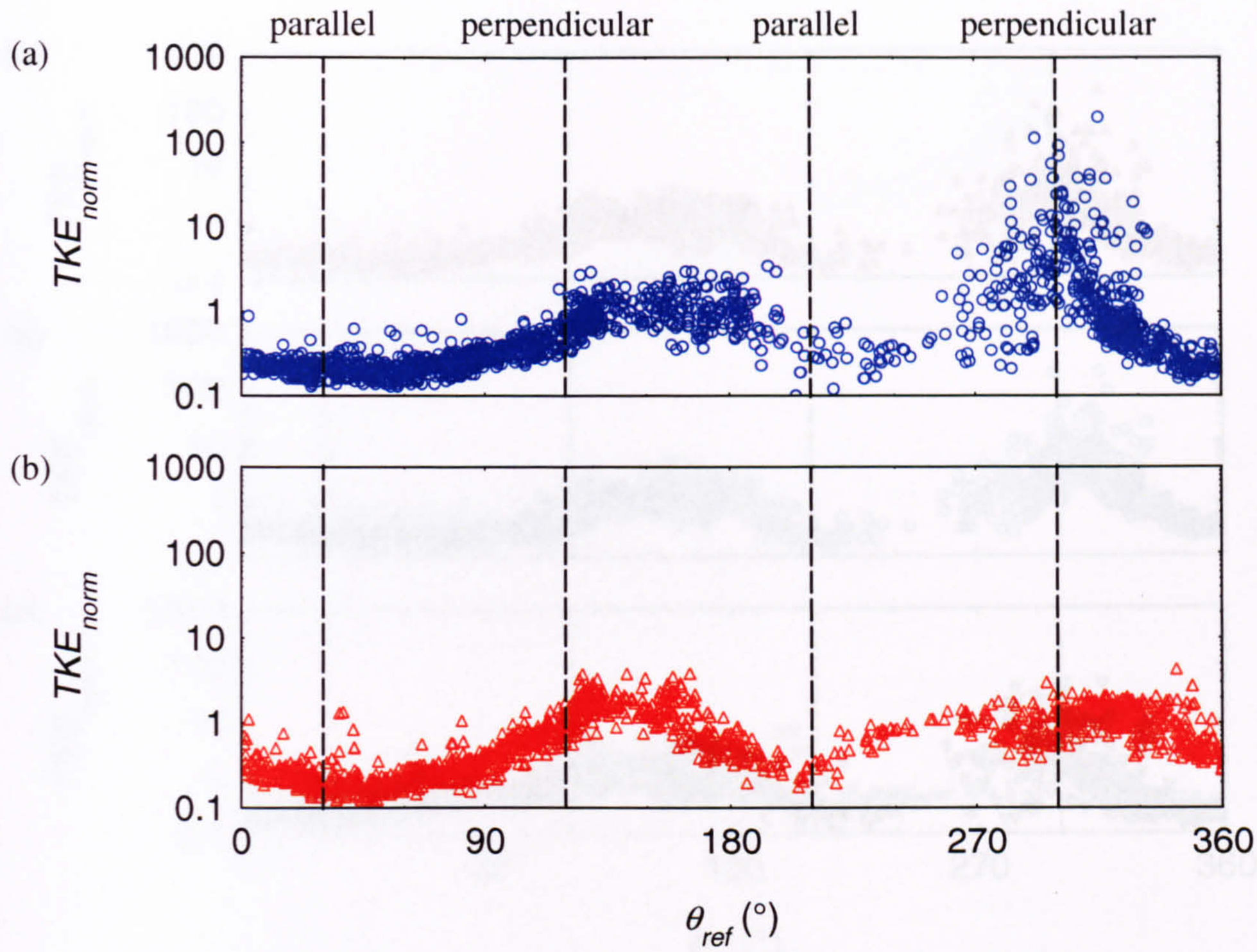


Figure 4.18. TKE measured on lampposts G3 and G4 normalised by the local horizontal wind speed, $M$, against the background wind direction, $\theta_{ref}$, for (a) ○ G3 at $z/H = 0.60$ and (b) △ G4 at $z/H = 0.84$.

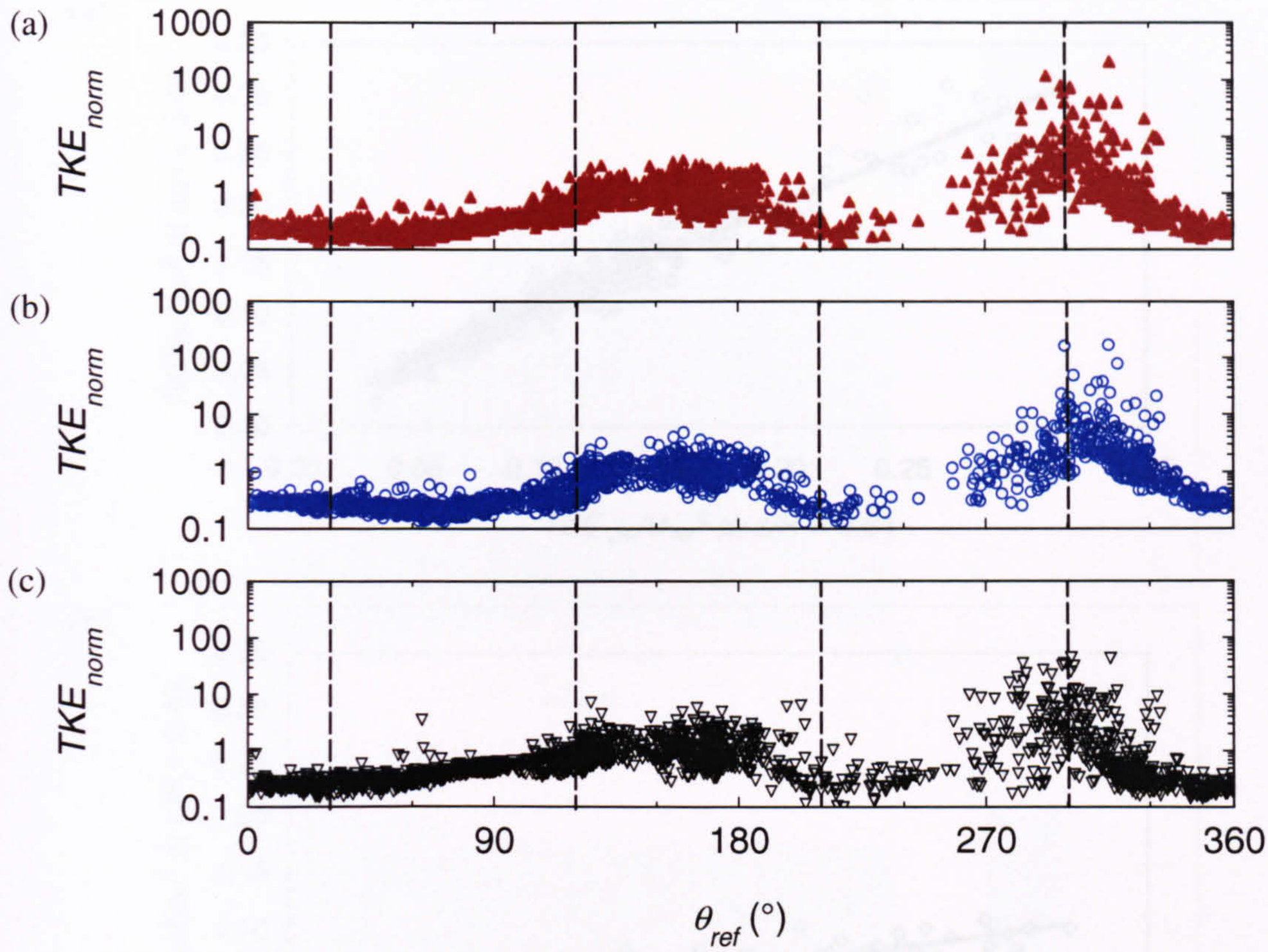


Figure 4.19. TKE measured on lamppost G3 normalised by the local horizontal wind speed, $M$, against the background wind direction, $\theta_{ref}$, for (a) ▲ $z/H = 0.60$; (b) ○ $z/H = 0.46$; and (c) ▽ $z/H = 0.30$.

(a)

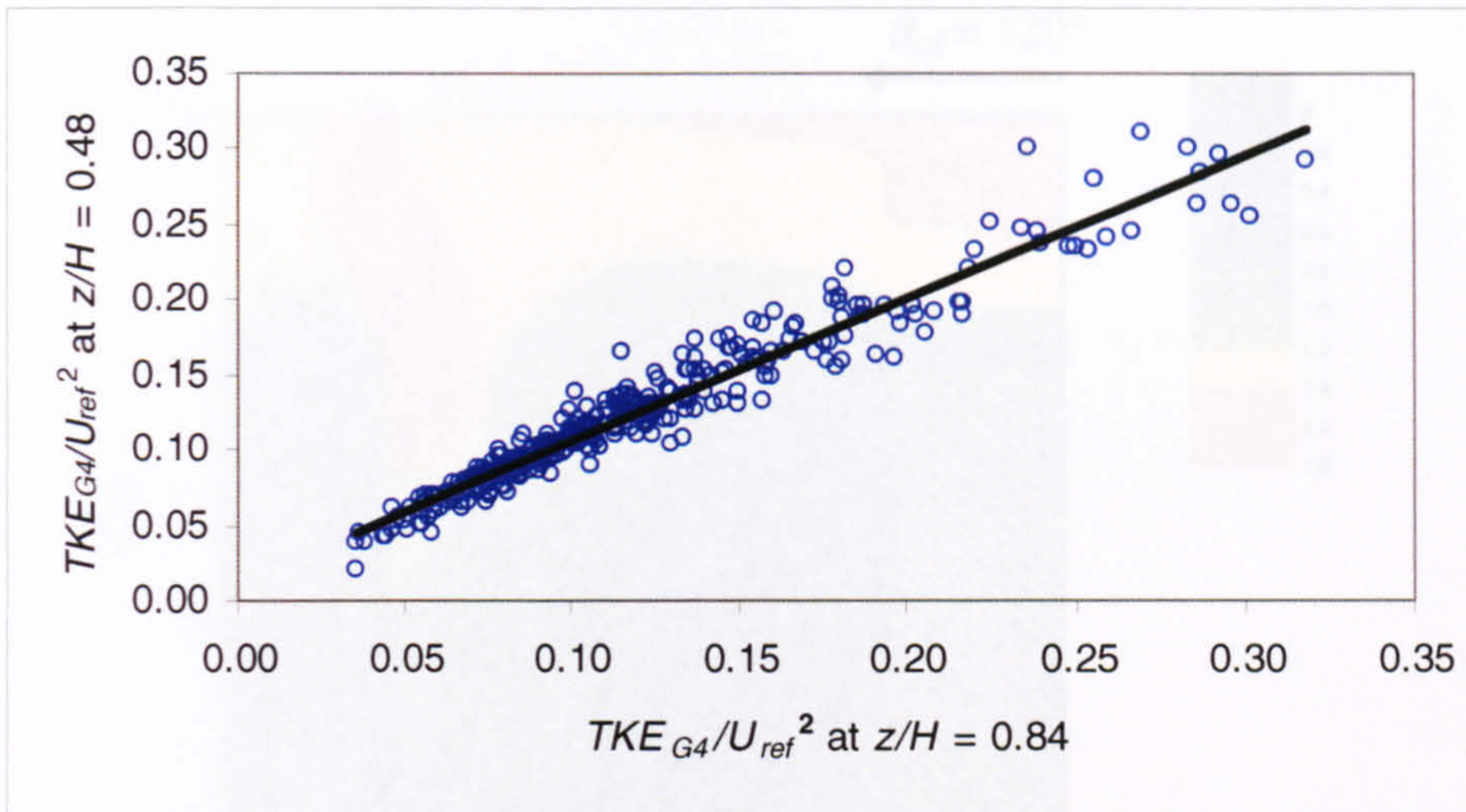


(b)

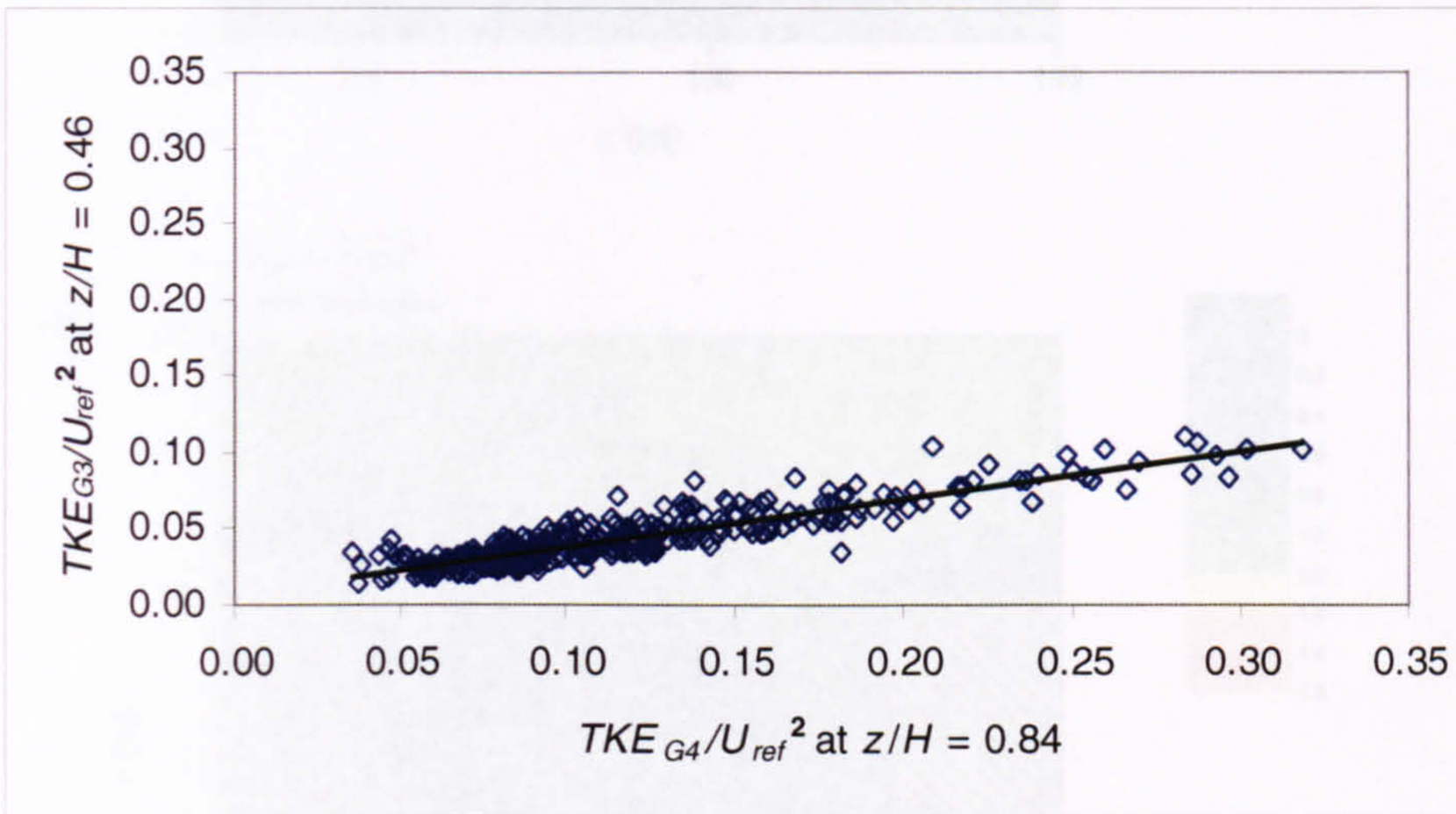


(c)

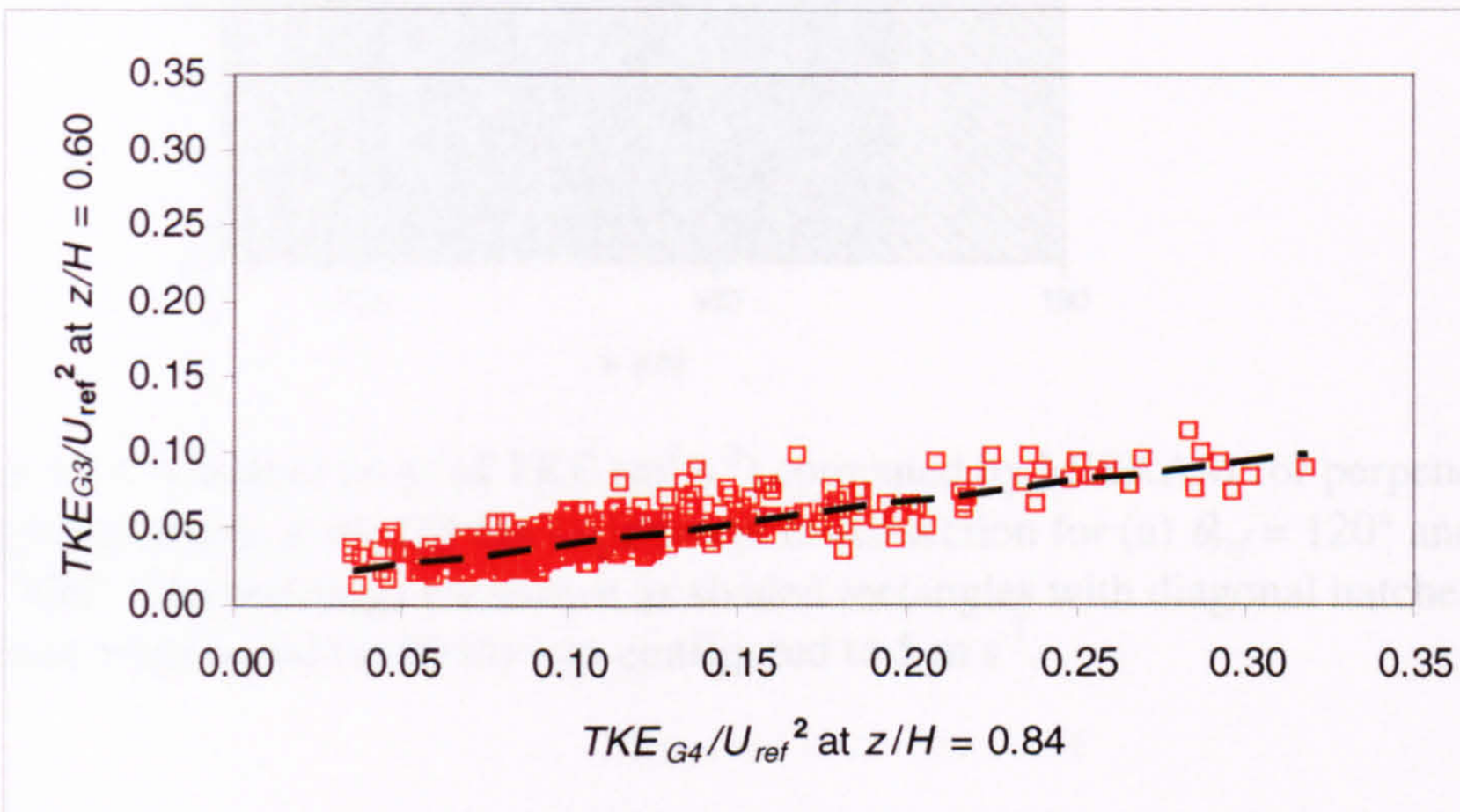


Figure 4.20. TKE measured on each lamppost normalised by $U_{ref}^2$ as a function of the TKE measured close to the shear layer at $z/H = 0.84$ on lamppost G4 conditioned on $\theta_{ref} = 120° \pm 30°$ for (a) G4 at $z/H = 0.48$, (b) G3 at $z/H = 0.46$ and (c) G3 at $z/H = 0.60$.

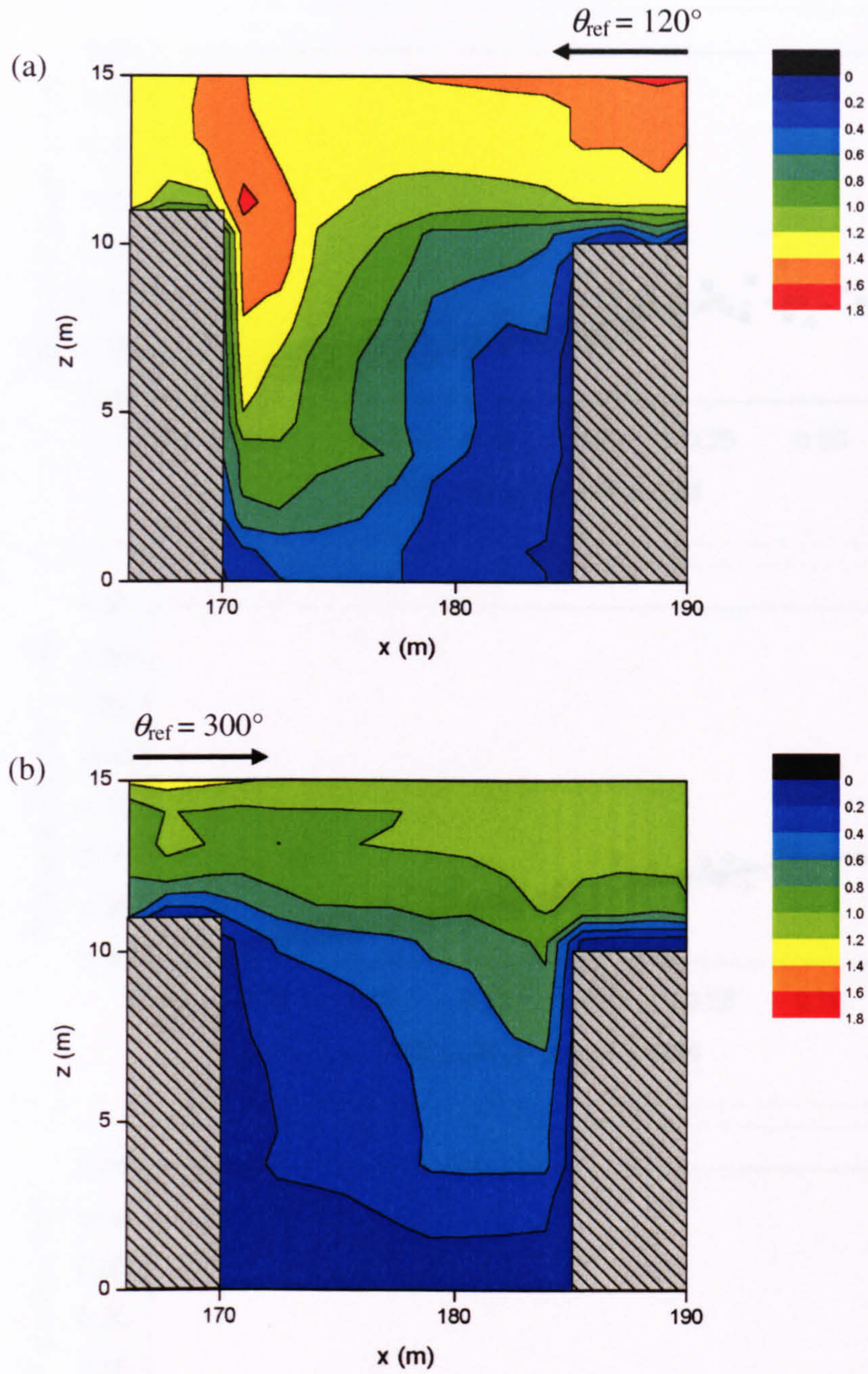


Figure 4.21. Contour plots of TKE ($m^2\ s^{-2}$) computed by MISKAM for perpendicular background winds at the G3-G4 experiment cross-section for (a) $\theta_{ref} = 120°$ and (b) $\theta_{ref} = 300°$. The buildings are shown as shaded rectangles with diagonal hatches. The reference wind speed (at 50 m) was configured to 5 m $s^{-1}$.

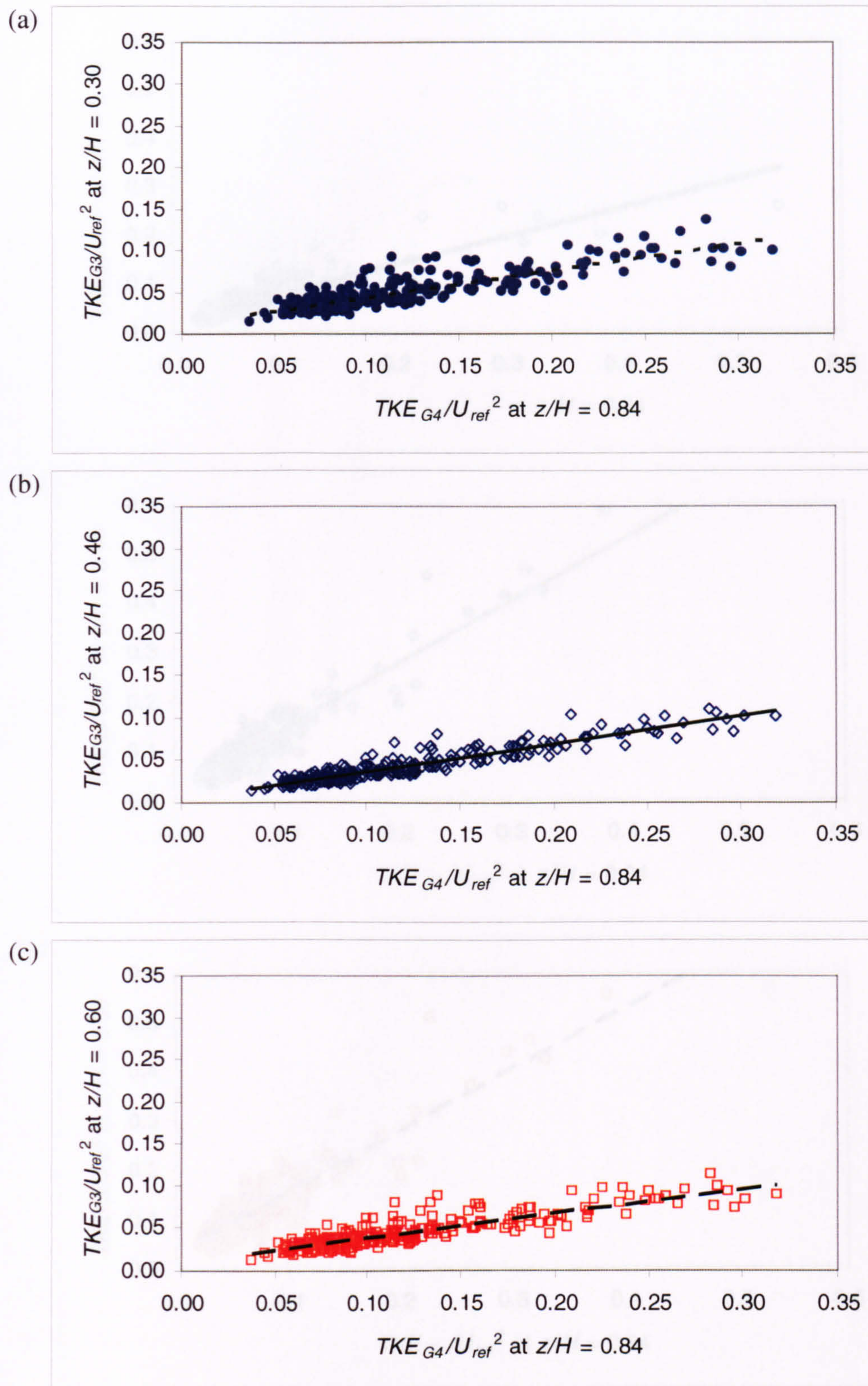


Figure 4.22. TKE measured on lamppost G3 normalised by $U_{ref}^2$ as a function of the normalised TKE measured close to the shear layer at $z/H = 0.84$ on lamppost G4 conditioned on $\theta_{ref} = 120° \pm 30°$ for (a) $z/H = 0.30$, (b) $z/H = 0.46$ and (c) at $z/H = 0.60$.

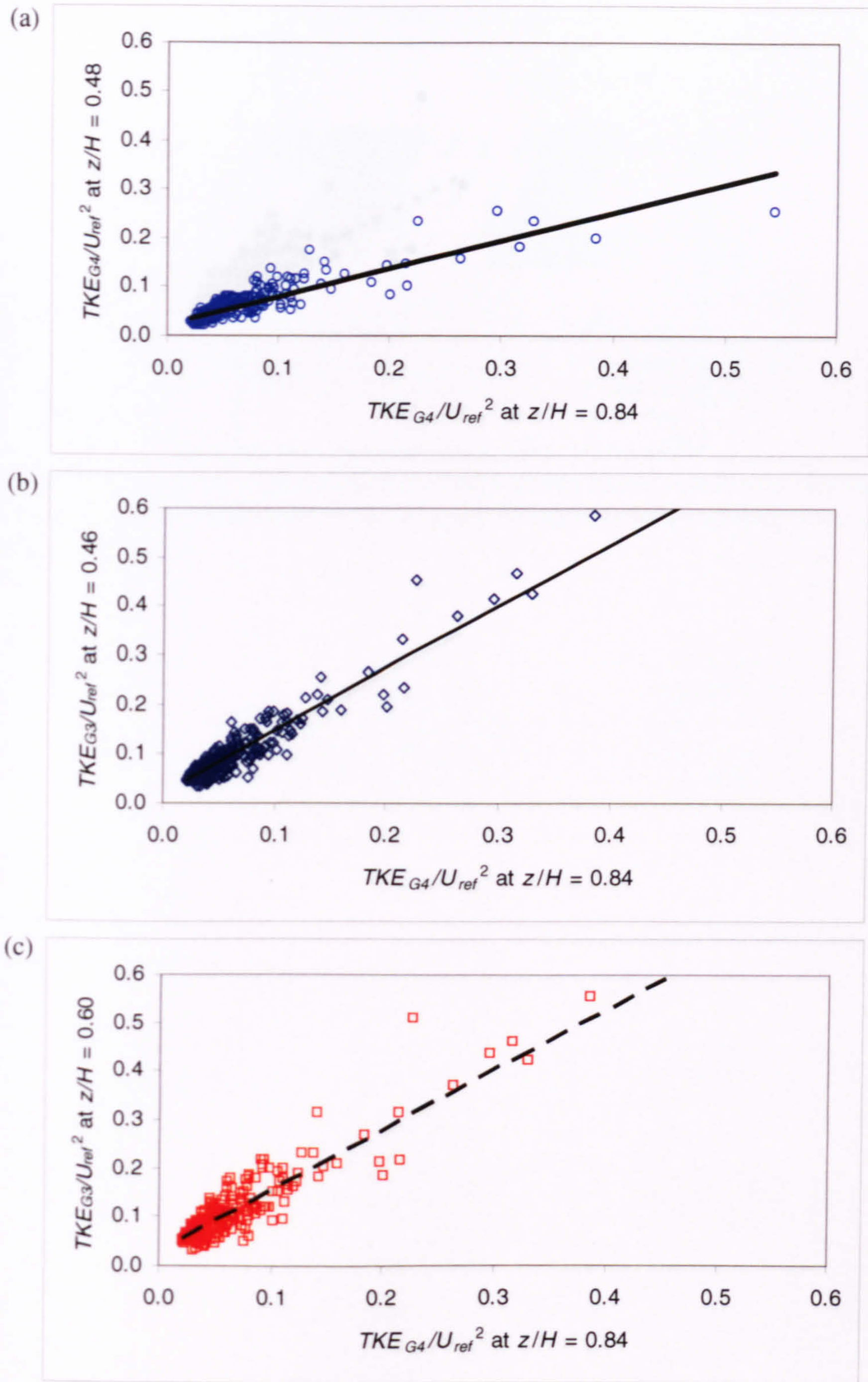


Figure 4.23. TKE measured on each lamppost normalised by $U_{ref}^2$ as a function of the normalised TKE measured close to the shear layer at $z/H = 0.84$ on lamppost G4 conditioned on $\theta_{ref} = 300° \pm 30°$ for (a) G4 at $z/H = 0.48$, (b) G3 at $z/H = 0.46$ and (c) G3 at $z/H = 0.60$.

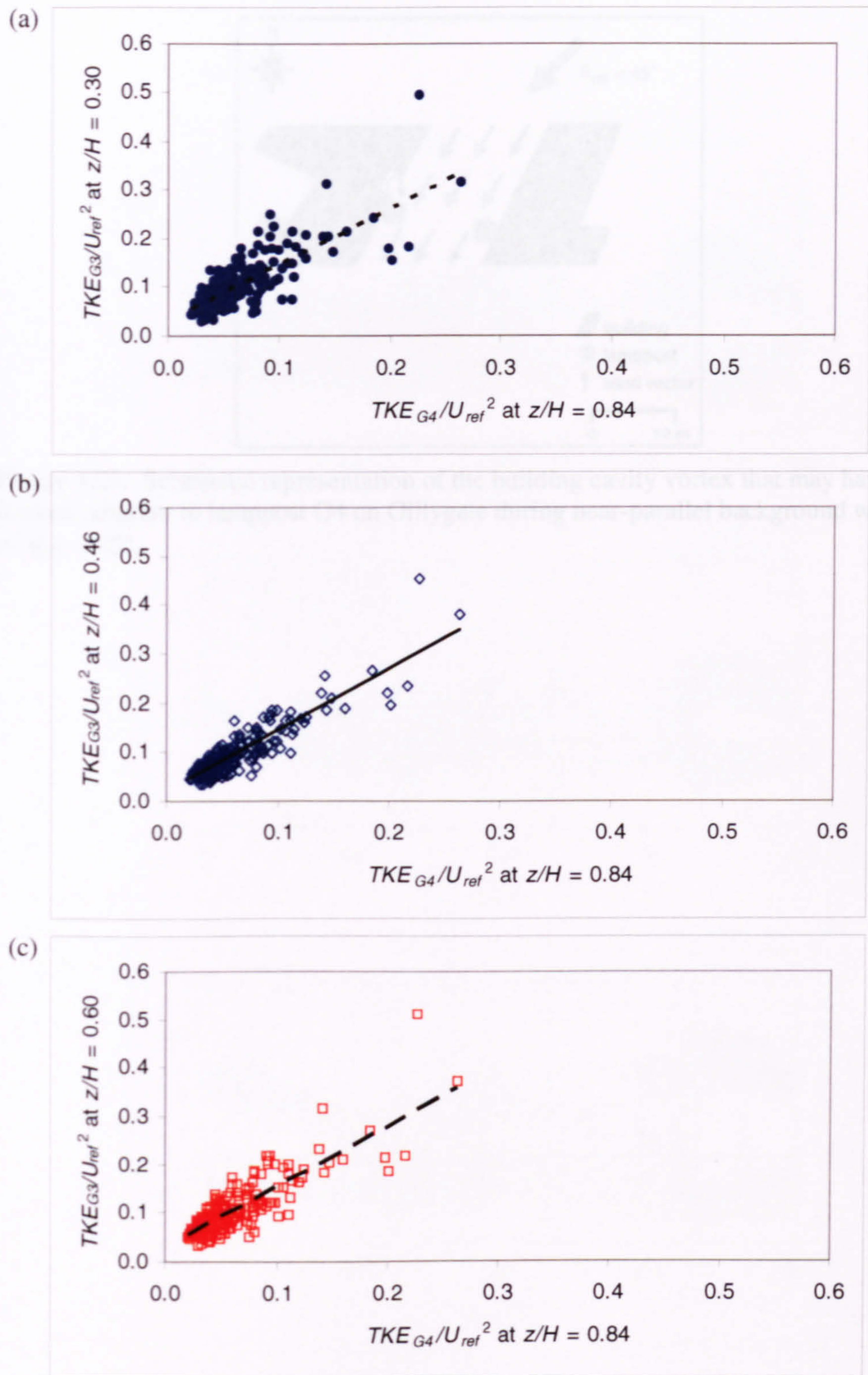


Figure 4.24. TKE measured on lamppost G3 normalised by $U_{ref}^2$ as a function of the normalised TKE measured close to the shear layer at $z/H = 0.84$ on lamppost G4 conditioned on $\theta_{ref} = 300° \pm 30°$ for (a) $z/H = 0.30$, (b) $z/H = 0.46$ and (c) at $z/H = 0.60$.

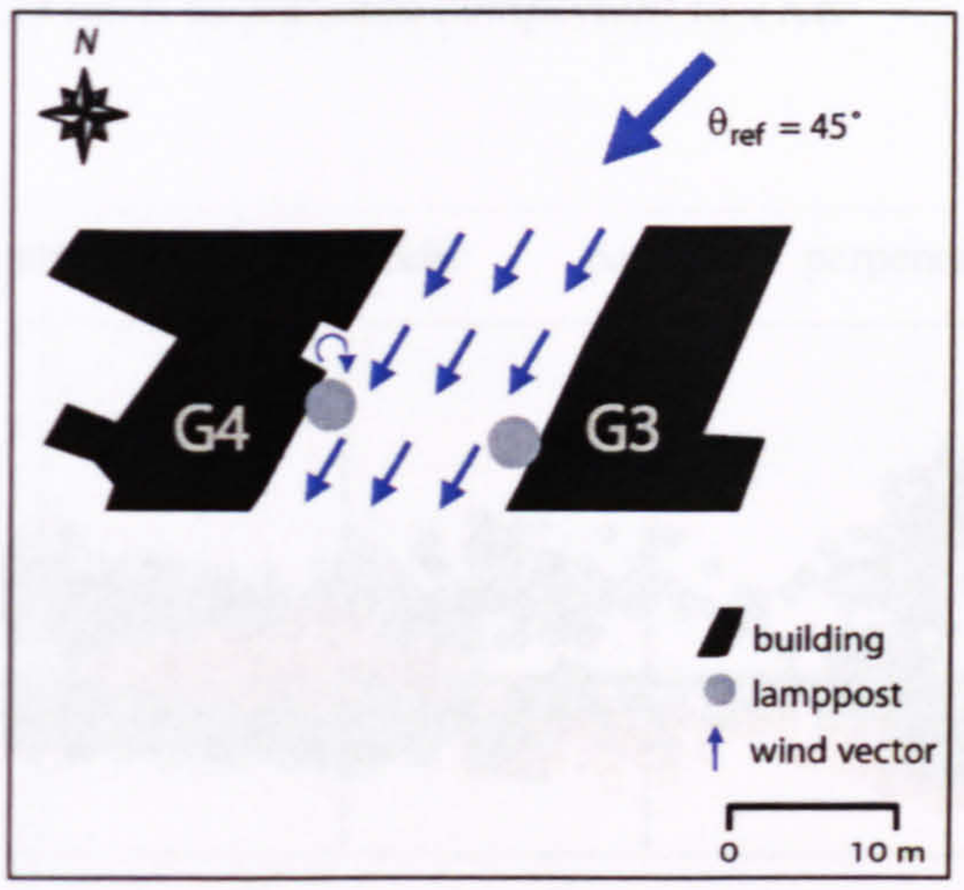


Figure 4.25. Schematic representation of the building cavity vortex that may have formed adjacent to lamppost G4 on Gillygate during near-parallel background winds of $\theta_{ref} = 45°$.

*4.3.3.2. Contribution of each turbulence component to TKE*

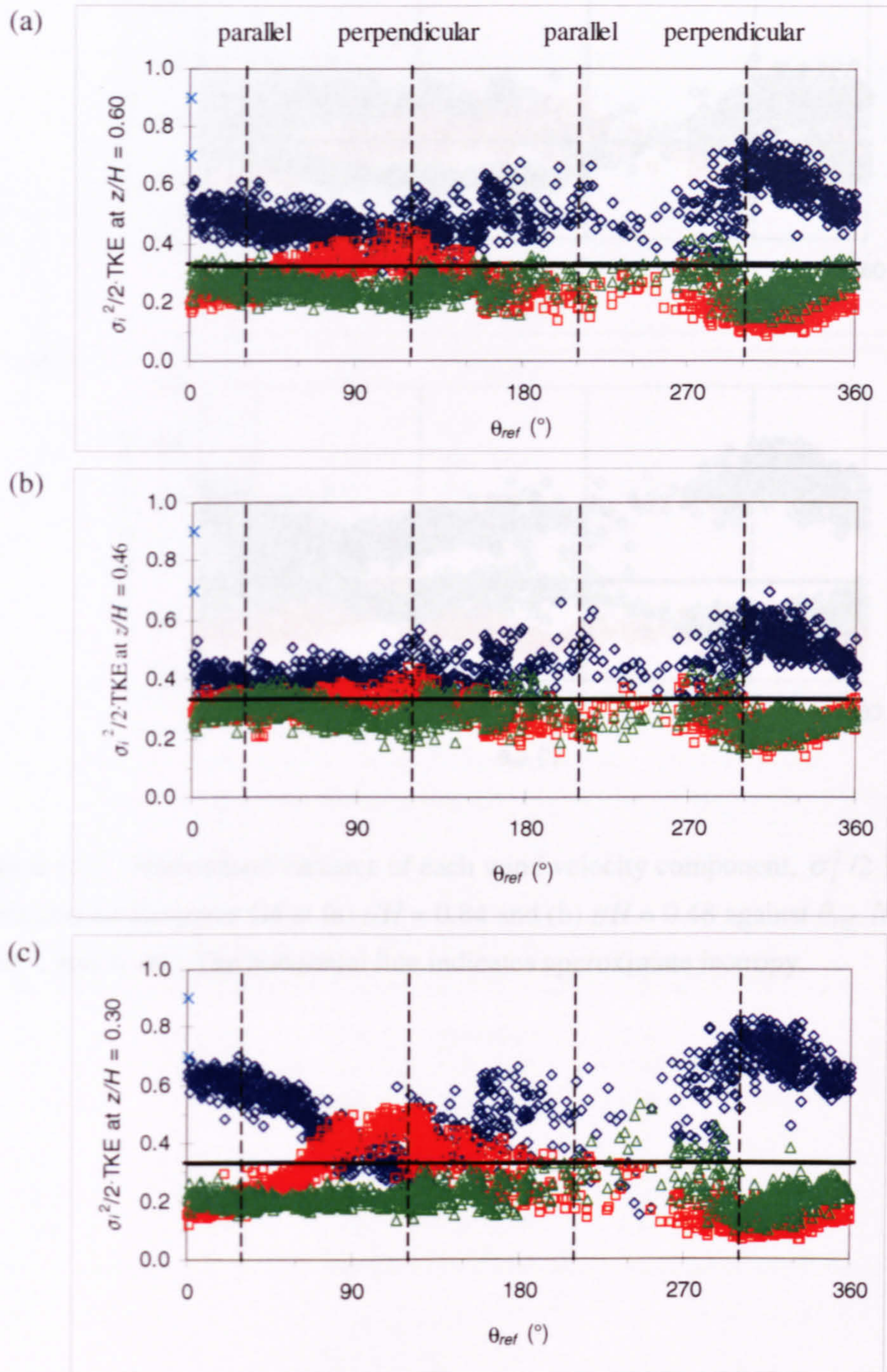


Figure 4.26. Normalised variance of each wind velocity component, $\sigma_i^2/2{\cdot}TKE_{G3}$, measured on lamppost G3 at (a) $z/H = 0.60$, (b) $z/H = 0.46$ and (c) $z/H = 0.30$ against $\theta_{ref}$, for: ◇ $\sigma_u^2$; □ $\sigma_v^2$; and △ $\sigma_w^2$. The horizontal line indicates approximate isotropy.

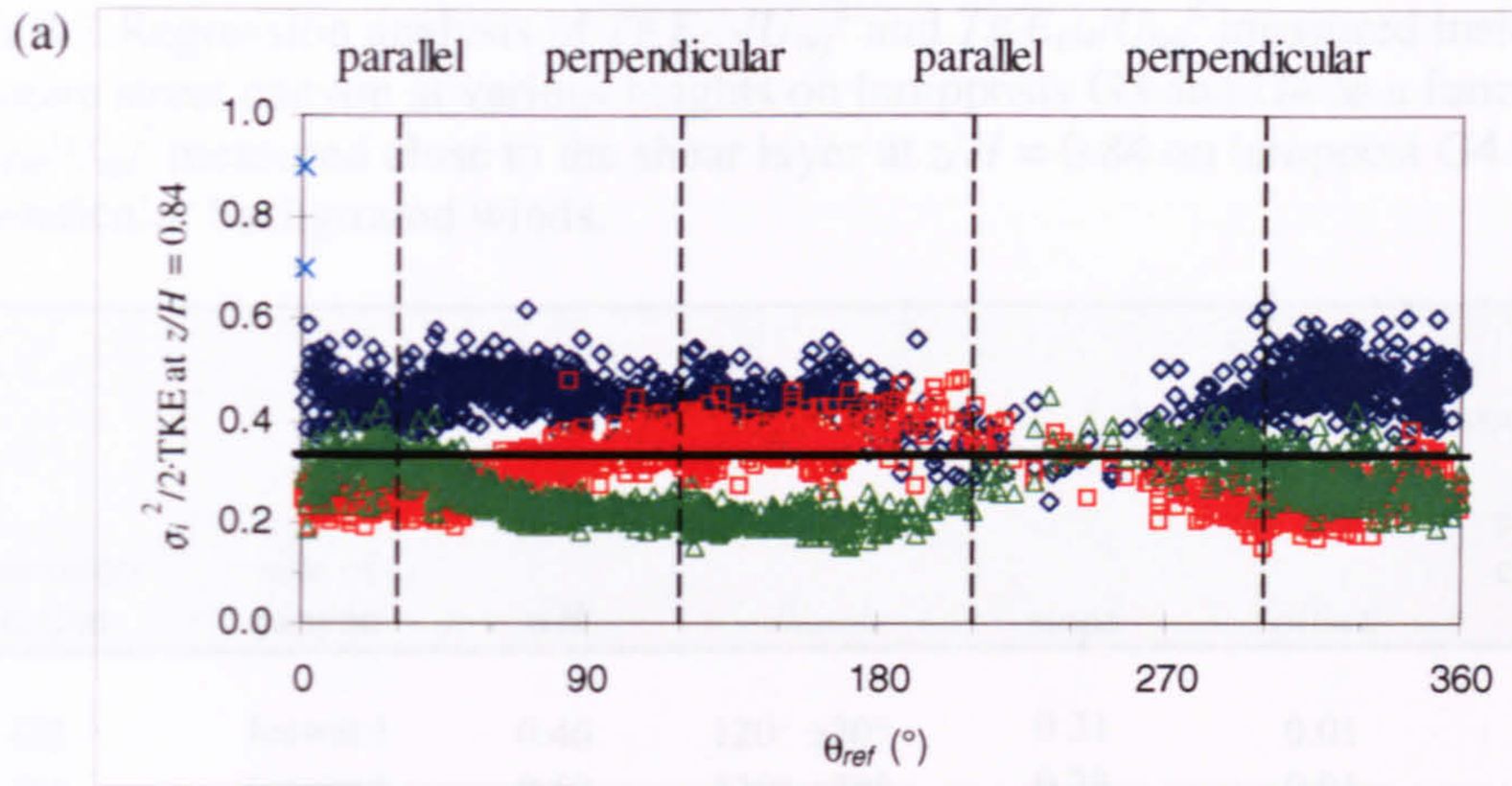


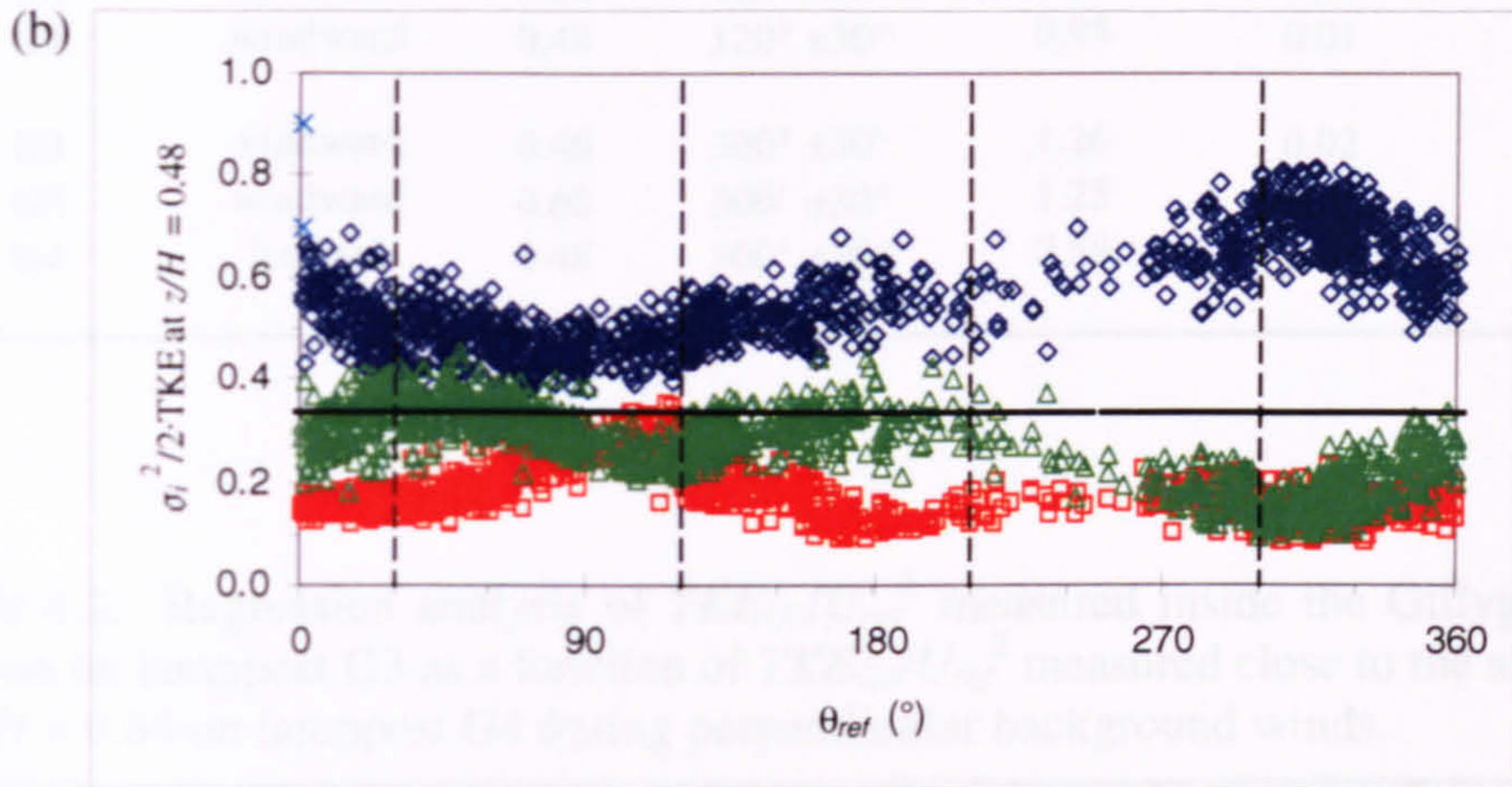


Figure 4.27. Normalised variance of each wind velocity component, $\sigma_i^2/2{\cdot}TKE_{G4}$, measured on lamppost G4 at (a) $z/H = 0.84$ and (b) $z/H = 0.48$ against $\theta_{ref}$, for: ◇ $\sigma_u^2$; □ $\sigma_v^2$; and △ $\sigma_w^2$. The horizontal line indicates approximate isotropy.

Table 4.2 Regression analysis of $TKE_{G3}/U_{ref}^2$ and $TKE_{G4}/U_{ref}^2$ measured inside the Gillygate street canyon at various heights on lampposts G3 and G4 as a function of $TKE_{G4}/U_{ref}^2$ measured close to the shear layer at $z/H = 0.84$ on lamppost G4 during perpendicular background winds.

| | | | | least-squares regression | | |
|---|---|---|---|---|---|---|
| anemometer location | side of canyon | $z/H$ | $\theta_{ref}$ | slope | offset | correlation coefficient ($r^2$) |
| **G3** | leeward | 0.46 | 120° ±30° | 0.31 | 0.01 | 0.81 |
| **G3** | leeward | 0.60 | 120° ±30° | 0.28 | 0.01 | 0.68 |
| **G4** | windward | 0.48 | 120° ±30° | 0.95 | 0.01 | 0.94 |
| **G3** | windward | 0.46 | 300° ±30° | 1.26 | 0.02 | 0.91 |
| **G3** | windward | 0.60 | 300° ±30° | 1.25 | 0.03 | 0.86 |
| **G4** | leeward | 0.48 | 300° ±30° | 0.58 | 0.02 | 0.78 |

Table 4.3. Regression analysis of $TKE_{G3}/U_{ref}^2$ measured inside the Gillygate street canyon on lamppost G3 as a function of $TKE_{G4}/U_{ref}^2$ measured close to the shear layer at $z/H = 0.84$ on lamppost G4 during perpendicular background winds.

| | | | | least-squares regression | | |
|---|---|---|---|---|---|---|
| anemometer location | side of canyon | $z/H$ | $\theta_{ref}$ | slope | offset | correlation coefficient ($r^2$) |
| **G3** | leeward | 0.30 | 120° ±30° | 0.33 | 0.01 | 0.73 |
| **G3** | leeward | 0.46 | 120° ±30° | 0.33 | 0.00 | 0.87 |
| **G3** | leeward | 0.60 | 120° ±30° | 0.29 | 0.01 | 0.76 |
| **G3** | windward | 0.30 | 300° ±30° | 1.16 | 0.03 | 0.64 |
| **G3** | windward | 0.46 | 300° ±30° | 1.23 | 0.02 | 0.81 |
| **G3** | windward | 0.60 | 300° ±30° | 1.26 | 0.03 | 0.72 |

Table 4.4. Regression analysis of TKE measured inside the Gillygate street canyon at mid-canyon height on lampposts G3 and G4 as a function of $TKE_{ref}$ measured at the reference mast during oblique background winds.

| | | | | least-squares regression | | |
|---|---|---|---|---|---|---|
| anemometer location | side of canyon | $z/H$ | $\theta_{ref}$ | slope | offset | correlation coefficient ($r^2$) |
| **G3** | leeward | 0.46 | 75° ±30° | 0.23 | 0.03 | 0.93 |
| **G4** | windward | 0.48 | 75° ±30° | 0.54 | 0.02 | 0.88 |
| **G3** | leeward | 0.46 | 165° ±30° | 0.22 | 0.06 | 0.68 |
| **G4** | windward | 0.48 | 165° ±30° | 0.61 | 0.05 | 0.74 |
| **G3** | windward | 0.46 | 255° ±30° | 0.92 | 0.08 | 0.51 |
| **G4** | leeward | 0.48 | 255° ±30° | 0.33 | 0.03 | 0.57 |
| **G3** | windward | 0.46 | 345° ±30° | 0.58 | 0.07 | 0.89 |
| **G4** | leeward | 0.48 | 345° ±30° | 0.31 | 0.05 | 0.86 |

## 4.4. Discussion

In the following Section the findings from the analysis of the mean flow measured inside the Gillygate street canyon are compared with the mean flow derived by MISKAM in order to help interpret the dispersion characteristics of the flow features. The turbulence is also investigated in Section 4.4.3 as the mean flow will have advected turbulent eddies inside the canyon. Therefore, the analysis of the turbulence measured inside the Gillygate canyon complements the mean flow study. The discussion of the turbulence analysis is split into two parts: first, the standard deviation of the vertical velocity and TKE are considered; second, the contribution of each turbulence component to TKE is examined.

It is a characteristic of turbulence that the irregular fluctuations occur in all three velocity components and are unpredictable in detail, as was described in Chapter 3. It was demonstrated above, however, that statistically distinct properties of the turbulence can be identified and analysed. For example, the turbulence intensity measured in the vertical velocity component, $t_w$, involves normalising the standard deviation of the vertical velocity, $\sigma_w$, by the local horizontal wind speed, $M$, using:

$$t_w = \frac{\sigma_w}{M} \tag{4.1}$$

where $M = \sqrt{(U^2+V^2)}$ and is measured by the same anemometer (i.e. at the same location). However, Nielsen (2000) in his work on the turbulent ventilation of a street canyon in Copenhagen did not follow this normalisation method. Instead, Nielsen (2000) normalised $\sigma_w$ by the background wind speed, $U_{ref}$, measured on a flat roof 500m from the street as trees located along the canyon are likely to have sheltered the in-canyon anemometers during certain wind directions. Had Nielsen (2000) normalised by $M$, the sheltering effects of the trees are likely to have implied stronger turbulent intensities than the opposite side of the street where sheltering effects were absent, which would not necessarily have been the case. There are no major obstructions to the flow within the Gillygate street canyon and, therefore, the procedure described in Equation (4.1) is considered most appropriate in order to

compare turbulent intensities measured at one location against another. This is particularly so when comparing the turbulence measured at mid-canyon height on either side of the street. Deriving the turbulence intensity is also a useful method of determining the relative proportion of mixing of turbulence compared to the mean local wind speed, $M$. On the other hand, the method of normalising $\sigma_w$ by $U_{ref}$ is more appropriate for comparisons between the data collected at different heights and locations within the same canyon and between experiments. The two normalisation methods are presented in Section 4.4.3 for completeness.

In addition to investigating the turbulent intensity of the vertical velocity component measured inside the Gillygate street canyon, analysis is also presented of the overall measure of turbulence intensity by including all three velocity components i.e. by studying TKE. A full definition of TKE and the method used to calculate it was given in Chapter 3. Further consideration of the contribution of each component to the turbulence measured is presented by investigating the isotropic nature of the turbulence. Although the analysis only provided an approximate measure of isotropy, the study revealed that the turbulence was generally anisotropic across most background wind directions. The following Section introduces the discussion of the turbulence findings.

### 4.4.1. Standard deviation of the mean vertical wind velocity

The standard deviation of the mean vertical wind velocity, $\sigma_w$, measured by the mid-canyon sonic anemometers located at lampposts G3 and G4 against the background wind speed, $U_{ref}$, is shown in Figure 4.3. The data was conditioned on $\theta_{ref} = 120°$ $\pm 90°$ (or $30° < \theta_{ref} \leq 210°$) and $\theta_{ref} = 300°$ $\pm 90°$ (or $210° < \theta_{ref} \leq 30°$). Therefore, the conditional analysis was based on using the along-street axis as a separator and no data were excluded. As expected, there was a strong dependence between $\sigma_w$ and $U_{ref}$ at G3 during $\theta_{ref} = 120°$ $\pm 90°$ and $\theta_{ref} = 300°$ $\pm 90°$ as shown by the curve fits with $r^2 =$ 0.73 and 0.64, respectively. The similarities in the slopes of the regression lines are shown by the values 0.14 and 0.16, respectively. There was also a strong dependence between $\sigma_w$ and $U_{ref}$ at G4 during $\theta_{ref} = 120°$ $\pm 90°$ and $\theta_{ref} = 300°$ $\pm 90°$ as shown by the curve fits with $r^2 = 0.68$ and 0.53, respectively. The slopes of the regression lines are

not similar, however, as shown by the values 0.21 and 0.10, respectively. During $\theta_{ref}$ = 120° ±90° lampposts G4 and G3 were located on the windward and leeward sides of the canyon, respectively. The steeper slope for G4 during $\theta_{ref}$ = 120° ±90° compared to G3 indicates that there were greater fluctuations about the mean vertical velocity on the windward side of the canyon, which is likely to be a result of an across-canyon recirculating flow (with a horizontally-aligned axis). This supports the suggestion that the recirculating flow produced stronger fluctuations in the mean vertical velocity on the windward side of the canyon compared to the leeward side. However, this will be explored in more detail in Section 4.4.3 using comparisons between the turbulence intensities. If the greater fluctuations about the mean vertical velocity during $\theta_{ref}$ = 120° ±90° were related to the development of a horizontally-aligned recirculating flow then the absence of such a flow during $\theta_{ref}$ = 300° ±90° may explain why the values are not of the same magnitude.

The scatter in the data points above the regression line presented in Figure 4.3a during $\theta_{ref}$ = 120° ±90 at G3 caused the offset to be higher than for $\theta_{ref}$ = 300° ±90, although the slopes are similar. A more detailed discussion of the regression line slopes is given in Section 4.4.3 and forms part of the TKE analysis. The offsets in Figure 4.3a are 0.05 m $s^{-1}$ and 0.13 m $s^{-1}$ for $\theta_{ref}$ = 120° ±90 and $\theta_{ref}$ = 300° ±90, respectively. This scatter is also the reason for the lower $r^2$ value and indicates that the windward side experiences greater fluctuations in the mean vertical velocity than the leeward side for these background wind conditions. This suggests that during background winds from the SE sector (i.e. $\theta_{ref}$ = 120° ±90) there was a different flow structure present within the Gillygate street canyon, compared to background winds from the NW sector (i.e. $\theta_{ref}$ = 300° ±90). It is unlikely that a street-level flow reversal associated with a skimming flow regime occurred during perpendicular NW winds. In order to investigate whether or not this is in fact the case the analysis must be continued by studying in more detail the mean velocity and turbulence fields measured by the in-canyon anemometers (Sections 4.4.2 and 4.4.3).

Whilst the departure of the data points from the regression line for $U_{ref} \leq 1.2$ m $s^{-1}$ is indicative of a weaker relationship, it is not immediately obvious that the relationship

actually collapses during these weak background winds. The standard deviation of the vertical wind, $\sigma_w$, measured by the mid-canyon sonic anemometers located at G3 and G4 were normalised by the background wind speed, $U_{ref}$, and plotted against $U_{ref}$ in Figure 4.4. The figure shows that the normalised standard deviations are insensitive to $U_{ref}$ for $U_{ref} > 1.2$ m s$^{-1}$, suggesting a linear relationship between $\sigma_w$ and $U_{ref}$. However, the normalised standard deviations rise sharply during weak background winds. This shows that $\sigma_w$ does not correlate with $U_{ref}$ for $U_{ref} \leq 1.2$ m s$^{-1}$ and probably reflects the greater significance of other sources of turbulence, such as traffic-produced turbulence (Chapter 6). These results suggest that the single across-canyon recirculating vortex that was produced in the street canyon during background wind directions of 120° ±30 was more likely to occur for $U_{ref} > 1.2$ m s$^{-1}$. Although the results presented here are from 15-minute averages, they appear to be in agreement with the findings presented by Nielsen (2000) who used 1-hour averages.

### 4.4.2. Mean in-canyon wind flow for $U_{ref} > 1.2$ m s$^{-1}$

The following section will describe the results of the mean flow measurements conducted at mid-canyon height on lampposts G3 and G4 inside Gillygate. The analysis aims to determine the in-canyon flow features that developed during certain background wind conditions. Reference is also made of the potential of each flow feature in transporting traffic-related pollutants inside the canyon, although this will be investigated in more detail in Chapter 5. Following the work shown previously, the effects of additional sources of turbulence caused by traffic-produced turbulence and convection are not considered in this Section as all data corresponding to background wind speeds $\leq 1.2$ m s$^{-1}$ are excluded from the analysis. The analysis presented in Section 4.4.3 of the turbulence measured inside the Gillygate canyon complements the observed characteristics of some of the in-canyon flow features described below.

*4.4.2.1. Perpendicular SE background winds*

Figure 4.5 shows the mean vertical wind velocity measured at mid-canyon height, $W$, as a function of the across-canyon component of the background mean wind, $V_{mast}$, for $U_{ref}$>1.2 ms$^{-1}$. The subscript assigned to $W$ refers to the lamppost upon which the anemometer was attached (i.e. G3 or G4). The Cartesian (right-hand) co-ordinate system was used with $U$ aligned along the canyon and was positive from 210 °N, $V$ was positive from 120 °N and $W$ was positive upwards (see Chapter 3).

Figure 4.5 shows that during perpendicular background SE winds (i.e. $\theta_{ref}$= 120° and $V_{mast}$ >0) the mean vertical wind velocities measured at mid-canyon height on either side of the canyon were of opposite sign. During $\theta_{ref}$ = 120° the vertical velocity component on the leeward (G3) side was predominantly upwards, as indicated by the slope of the regression line of 0.25. However, the vertical velocity component on the windward (G4) side was predominantly downwards during $\theta_{ref}$= 120° and the mean velocities were significantly higher than on the leeward side, as indicated by the steeper slope of -0.38. These features are typical of a single across-canyon recirculating flow with a horizontally-aligned axis (e.g. DePaul and Sheih, 1986; Berkowicz *et al.* 1996, 1997a; Nielsen, 2000). DePaul and Sheih (1986) found that the recirculating flow was characterised by significant vertical velocities and reverse flow at street level. On the windward side of the street canyon they found that the mean velocities associated with the downdraughts were approximately a factor of two greater than the mean velocities in the updraughts on the leeward side.

Berkowicz *et al.* (1997a) conducted a similar analysis of the vertical velocity component to that shown in Figure 4.5 as a function of the across-canyon component of the mean background wind and found similar characteristics of an across-canyon recirculating flow. However, the in-canyon data was only collected by a single sonic anemometer located at $z/H$ = 0.33 inside a deep street canyon of $H/W$ = 0.72 in Copenhagen, Denmark. The regression slopes shown in Figure 4.5 that were formed from the data corresponding to $\theta_{ref}$= 120° have zero intercepts, which indicates that parallel background winds are likely to have had strong along-canyon velocity components. The correlation coefficients for the data collected on the leeward (G3) and windward (G4) sides indicated relatively strong correlations as shown by the $r^2$

values of 0.63 and 0.55, respectively. Therefore, stronger relationships between the two quantities appear to have been observed at mid-canyon height inside the Gillygate street canyon than were observed by Berkowicz *et al.* (1997a). It should be noted that Berkowicz *et al.* (1997a) did not perform any regression analysis on the Copenhagen data and, therefore, the comparisons between the results shown in Figure 4.5 with the findings of Berkowicz *et al.* (1997a) are based on a qualitative assessment. However, these findings would appear to suggest that the mid-canyon height ($z/H \approx 0.5$) used in the present study is likely to be a better location to measure the airflow inside street canyons. This is particularly important to bear in mind when conducting experiments attempting to determine the influence of across-canyon recirculating flows on the dispersion of traffic-related pollutants inside street canyons.

The in-canyon horizontal velocity field was computed at a height of 5m for perpendicular background winds that correspond to $\theta_{ref} = 120°$ and 300° using the MISKAM numerical flow model. The horizontal velocity field is shown schematically in Figure 4.6. Note that the vectors shown in the figure are only an indication of the velocity magnitude. The section of the domain and the names of the adjoining side streets are shown in Figure 4.6c. During $\theta_{ref} = 120°$ the background wind flows over a relatively long length of buildings uninterrupted by openings. For these background winds, the model predicted negligible in-canyon horizontal velocities (Figure 4.6b). The horizontal velocity vectors show some across-canyon flow from the windward side towards the leeward side of the canyon near to G3-G4. However, the vectors generally indicate an along-canyon flow resulting from the development of a corner vortex at the junction of Gillygate and Lord Mayor's Walk.

Confirmation of a classic 2-D recirculating flow with across-canyon street level flow reversal is shown by the vertical cross-section of the velocity field computed at the G3-G4 measurement cross-section (Figure 4.7b). The figure clearly shows that during $\theta_{ref} = 120°$ a skimming flow regime develops above the street canyon cavity with a recirculating flow characterised by downdraughts on the windward side and updraughts on the leeward side of the canyon. The vertical velocity vectors shown in Figure 4.7b also show that the downdraughts were stronger on the windward side of the street canyon than the updraughts on the leeward side. These findings give

further support to the higher mean vertical velocities measured on the windward (G4) side compared to the leeward (G3) side during these background wind conditions (Figure 4.5).

Figure 4.8 presents the mean vertical wind velocity measured at mid-canyon height inside Gillygate on lampposts G3 and G4 normalised by the background wind speed, $U_{ref}$, as a function of the background wind direction, $\theta_{ref}$. Figure 4.8 shows that during $\theta_{ref} = 120°$ the normalised mean vertical wind velocities, $W/U_{ref}$, measured on either side of the canyon were of opposite sign. During $\theta_{ref} = 120°$, negative values of $W_{G4}/U_{ref}$ indicate that there were downdraughts on the windward (G4) side of the canyon; while positive values of $W_{G3}/U_{ref}$ indicate that there were updraughts on the leeward (G3) side. Figure 4.8 appears to show almost perfect qualitative symmetry in the $W_{G3}/U_{ref}$ and $W_{G4}/U_{ref}$ values measured by the mid-canyon anemometers during background winds from $30° < \theta_{ref} \leq 210°$. The normalised mean vertical velocities during parallel background winds, therefore, were approximately zero (Section 4.4.2.4). Although the results show qualitative symmetry during background winds from $30° < \theta_{ref} \leq 210°$ there are quantitative differences between the two sides of the canyon as the magnitude of $W_{G4}/U_{ref}$ were greater on the windward (G4) side than the values of $W_{G3}/U_{ref}$ for the leeward (G3) side. Therefore, these results for $\theta_{ref} = 120°$ support the findings of DePaul and Sheih (1986), where $W_{G4} \approx 2W_{G3}$.

The analysis was continued by determining the dependence of the vertical velocity vector angle, $\phi$, on the background wind direction, as shown in Figure 4.9. The data shown in the figure are from the mid-canyon anemometers located on lampposts G3 and G4. The vertical velocity vector angle, $\phi$, was calculated using the formula below, where $U$, $V$ and $W$ refer to the three mean velocity components:

$$\phi = \tan^{-1}[W/(U^2 + V^2)^{1/2}].$$

For an across-canyon recirculating flow during background winds with a perpendicular component, $\phi$ on either side of the canyon should be antisymmetric. Figure 4.9 indicates that for most data, $\phi$ for each anemometer was antisymmetric

about $\phi = 0$ when the background wind was approximately between 30° and 250°. The change in sign of $\phi$ for both anemometers at 30° and 210° corresponds to parallel background winds, i.e. when $\theta_{ref}$ was aligned with the street axis. Therefore, the data shown in Figure 4.9 is in agreement with the mean vertical wind velocity analysis presented in Figure 4.8, and suggests that an across-canyon recirculating flow (with a horizontally-aligned axis) developed during background SE winds.

Figure 4.10 presents the in-canyon wind direction, $\eta$, as a function of background wind direction, $\theta_{ref}$, for mid-canyon height on lampposts G3 and G4. During SE background winds, the figure shows a distinct in-canyon flow direction between 90° and 150° and a slight linear dependence for $\eta_{G4}$ with $\theta_{ref}$ between 30° and 120°. In fact, this shows evidence of reflection of the in-canyon airflow, with the angle of reflection relative to the street axis increasing as the background wind became more perpendicular to the street axis, which gives further support to the presence of an across-canyon recirculating flow.

Figure 4.11 shows the normalised sector-averaged horizontal wind speed measured at mid-canyon height on lampposts G3 and G4, $M_{G3}$ and $M_{G4}$, as a function of $\theta_{ref}$. The figure was formed from the average of all 15-minute in-canyon horizontal wind speed values within each 10° background wind direction sector for the entire monitoring period. As expected, the minimum values in $M_{G3}$ and $M_{G4}$ occurred during perpendicular background winds. However, the minimum values in $M_{G3}$ and $M_{G4}$ are offset by approximately 20° during near-perpendicular background winds. This has significant consequences in the normalisation procedures described below, which use $M_{G3}$ and $M_{G4}$.

In the light of the evidence that supports the development of a recirculating flow inside the Gillygate street canyon during perpendicular SE background winds >1.2 $ms^{-1}$, it follows that such flow features do occur in real urban environments. Although the MISKAM model used flat-roof geometries (Figure 4.6 and Figure 4.7), the findings from the experimental data are contrary to those of Kastner-Klein *et al.* (2004) as a recirculating flow appears to be a feature of a skimming flow in a real street canyon with pitched roof geometries. Kastner-Klein *et al.* (2004) used wind

tunnel investigations of the flow and dispersion inside an isolated street canyon. However, Kastner-Klein *et al.* (2004) recognised the limitations of their study and stated that the flow, turbulence and dispersion conditions in an isolated street canyon are largely determined by the flow separation at the first edge of the upwind building. In real street canyon configurations the upwind fetch is disturbed by complicated urban topographies, causing distortions in the mean above-roof winds. Therefore, isolated street canyons of the type used by Kastner-Klein *et al.* (2004) and Meroney *et al.* (1996) are likely to produce somewhat unrealistic urban flow and dispersion characteristics.

#### *4.4.2.2. Perpendicular NW background winds*

The mean vertical velocity component measured at mid-canyon height at lampposts G3 and G4 shown in Figure 4.5 reveal contrasting flow features during perpendicular NW background winds (i.e. $\theta_{ref} = 300°$ and $V_{mast} < 0$). Although there is a degree of scatter in the data points, generally downdraughts on the windward (G3) side appear to have been absent, indicating that a single across-canyon recirculating flow (with a horizontally-aligned axis) is unlikely to have developed inside the canyon during these conditions. During $\theta_{ref} = 300°$ the mean vertical flow on the windward (G3) and leeward (G4) sides were generally upwards.

This is supported by the analysis of $W_{G3}/U_{\mathrm{ref}}$ and $W_{G4}/U_{\mathrm{ref}}$ from data collected at mid-canyon height, which is presented in Figure 4.8 as a function of $\theta_{\mathrm{ref}}$. Figure 4.8 also shows that the normalised mean vertical velocity is positive on both sides of the canyon during $\theta_{ref} \approx 300°$. However, Figure 4.8 shows that increased scatter in the $W_{G4}/U_{\mathrm{ref}}$ values during $\theta_{ref} \approx 285°$ may be caused by updraughts within a helical flow regime. Section 4.4.2.3 describes the influence of helical flows in more detail. However, it is also possible that normalising $W_{G3}$ and $W_{G4}$ by $U_{ref}$ is likely to have been complicated by the sheltering effect of the large tree located at ~270° from the mast. The mean wind speeds measured at the mast during westerly winds, therefore, are likely to have been reduced by the tree, exaggerating the normalised $W_{G3}$ and $W_{G4}$ values. The analysis of the vertical wind velocity, $\phi$, presented in Figure 4.9 also supports the findings shown in Figure 4.8. The figure indicates that a single across-

canyon recirculating flow (with a horizontally-aligned axis) cannot occur for $\theta_{ref}$ between 210° and 30°, as $\phi$ on both sides of the canyon is positive.

The mean vertical velocities measured on the leeward (G4) side were stronger than those measured on the windward (G3) side during perpendicular background NW winds (Figure 4.5). The figure shows the curve fit based on the slope of 0.25 that was observed on the leeward side during $\theta_{ref}$= 120°. During $V_{mast} > 2.0$ m s$^{-1}$, $W_{G4}$ departs from the slope, which suggests that the mean leeward vertical velocities were lower than those measured on the leeward side during $\theta_{ref}$= 120°. Furthermore, the mean windward vertical velocities were close to zero during $\theta_{ref}$= 300°, which is a much greater departure from the slope of -0.38 observed on the windward side during $\theta_{ref}$= 120°. The results presented in Figure 4.5 clearly show that the features of a recirculating flow are not symmetrical relative to the across-street axis (120° - 300°). This is in contrast to what would be expected in a street canyon of infinite length and uniform symmetric cross-section. However, the side streets that adjoin Gillygate provide openings along the NW side of the canyon. Nielsen (2000) in the study of the airflow and turbulence inside a street canyon in Copenhagen also reported that openings along the downwind canyon wall influenced the in-canyon recirculation patterns.

The outputs from the MISKAM flow model of the in-canyon horizontal velocity field at 5m (Figure 4.6a) for $\theta_{ref}$ = 300° near the G3-G4 cross-section supports the assumption that during these conditions a classic across-canyon recirculating flow was generally absent. Figure 4.6a indicates that the mean perpendicular flow channels along the adjoining side streets of Portland Street and Claremont Terrace, producing counter-rotating corner vortices with vertical axes inside the canyon. The model predicted that the corner vortex pair is likely to have forced the air inside the canyon into two converging flows. However, an alternative explanation should be noted: the counter-rotating corner vortices may have been the result of along-canyon flows. The convergence of the horizontal velocity field near to G3-G4 suggests that significant vertical momentum flux must have occurred. The horizontal vectors are greater on the windward (G3) side than on the leeward (G4) side. This perhaps explains why the mean vertical velocity components measured on the windward side

were weaker than those measured on the leeward side (Figure 4.5), as the horizontal components of velocity are likely to have been more significant. Figure 4.10 provides supporting evidence for the convergence of the horizontal flow at G3 and G4 in addition to Figure 4.9. For $\theta_{ref}$ between 300° and 345° (NW background winds), the in-canyon horizontal angle ($\eta$) indicates a significant level of flow switching between the two directions that are parallel to the street axis (30° and 210°). Flow convergence may also account for higher than expected values in $M_{G4}$ (Figure 4.11), with the minimum values occurring during background winds that were offset to perpendicular by 20°, i.e. when the converging flow ceased.

The computed vertical velocity vectors shown in Figure 4.7a indicate updraughts on both sides of the canyon. However, the computed vertical velocity vectors indicate that during these conditions below mid-canyon height there was also an across-canyon flow from the windward (G3) side of the canyon towards the leeward (G4) side.

The presence of the counter-rotating corner vortices contributed to increasing the complexity of the flow structures that developed within the street canyon and will have influenced the local dispersion of traffic-related pollutants. Although it is unlikely that a single across-canyon recirculating flow developed inside the canyon during $\theta_{ref} = 300°$ the across-street flow is likely to have transported traffic-related pollutants towards the leeward side of the canyon (see Chapters 5 and 8). The flow reversal at street level is likely to be associated with the counter-rotating corner vortices. The model, therefore, served as a useful tool to help explain, in particular, the complex flow features associated with $\theta_{ref} = 300°$, which are likely to be local to the G3-G4 experiment cross-section.

#### *4.4.2.3. Oblique background winds*

Background winds orientated oblique to the street axis influence along-canyon flow. The coupling of a strong along-canyon flow with across-canyon recirculation supports the existence of a helical flow regime. Johnson and Hunter (1999) provided support for such an in-canyon flow structure in a study within a traffic-free canyon. They suggested that the along-canyon component is initiated by pressure differences

at the canyon ends, although relatively steady conditions are necessary for it to be fully established.

Figure 4.8 presents the mean vertical wind velocity, $W$, measured at mid-canyon height inside Gillygate on each lamppost (i.e. G3 and G4) normalised by the background wind speed, $U_{ref}$, as a function of the background wind direction, $\theta_{ref}$. The figure clearly shows that off-perpendicular background winds, particularly those oblique to the street axis, produced helical flow regimes inside Gillygate. For instance, during $\theta_{ref} \approx 90°$ and $\theta_{ref} \approx 150°$ the values of $W_{G4}/U_{ref}$ measured on the windward side of the canyon were negative; while the $W_{G3}/U_{ref}$ values measured on the leeward side were positive. On the other hand, during $\theta_{ref} \approx 240°$ negative $W_{G3}/U_{ref}$ values were observed on the windward side of the canyon and positive values of $W_{G4}/U_{ref}$ were recorded on the leeward side. Therefore, oblique background winds from the NW sector are likely to have produced across-canyon recirculating flows with horizontally-aligned axes, while perpendicular background NW winds generated across-canyon recirculating flows with vertically-aligned axes.

Figure 4.10 shows that during oblique background winds the in-canyon wind direction, $\eta_{G4}$, is nearly equally divided between 30° and 210°, indicating that the flows were dominated by in-canyon flow channelling. Figure 4.11 presents the mean horizontal wind velocity, $M$, measured at mid-canyon height on lampposts G3 and G4 normalised by $U_{ref}$ as a function of $\theta_{ref}$. The figure shows that during $\theta_{ref} \approx 240°$ high values of $M_{G3}$ and $M_{G4}$ were measured at mid-canyon height. These findings support the assumption that during oblique background winds, increased momentum of the recirculating flow is caused by strong along-canyon flow components. However, it should also be reaffirmed that normalising $M_{G3}$ and $M_{G4}$ by $U_{ref}$ is likely to have been complicated by the sheltering effect of the large tree located at ~270° from the mast. The mean wind speeds measured at the mast during westerly winds, therefore, are likely to have been reduced by the tree, exaggerating the normalised $M_{G3}$ and $M_{G4}$ values.

During oblique background winds, fresh air would have entered the canyon from the shear layer and the mean flow would have been reflected off the windward canyon

wall, producing across-canyon flow at street level (Chapter 2). Updraughts on the leeward side would be expected following the interaction between the street level flow and the upwind (leeward) canyon wall. The helical flow regime would be expected to have had stronger along-canyon velocity components than during the classic skimming flow single-across canyon vortex as the helical recirculating flow would have been driven by the oblique winds aloft. It is likely that the street level across-canyon flow that is produced during oblique winds will have transported traffic-related pollutants towards the leeward side of the canyon where they may have accumulated. The strong along-canyon flow component is also likely to have transported pollutants down the street away from emission hot-spots (e.g. junctions) where accelerating driving modes are common (see Chapter 8). Helical flows, therefore, are likely to have had a significant influence on the dispersion of traffic-related pollutants inside Gillygate and will form the subject of further investigation in Chapters 5 and 8.

#### *4.4.2.4. Parallel background winds*

Figure 4.8 presents the normalised mean vertical wind velocities, $W/U_{ref}$, measured at mid-canyon height inside Gillygate on each lamppost (i.e. G3 and G4) as a function of the background wind direction, $\theta_{ref}$. The figure shows that during parallel background winds (i.e. $\theta_{ref} = 30°$ and $\theta_{ref} = 210°$) the values of $W_{G3}/U_{ref}$ and $W_{G4}/U_{ref}$ were approximately zero on both sides of the canyon, as mentioned earlier. These findings support those of Longley *et al.* (2004a), who observed that channel flows produced small vertical components. Weak mean vertical velocities during parallel background winds were expected as the majority of the flow measured at G3 and G4 will have been channelled along the canyon. This is supported by Figure 4.10, which shows that the in-canyon wind direction, $\eta_{G4}$, at mid-canyon height on G3 and G4 is nearly equally divided between 30° and 210°, indicating no preferred direction of the in-canyon winds, apart from being dominated by in-canyon flow channelling.

Figure 4.11 presents the mean horizontal wind velocity, $M$, measured at mid-canyon height on lampposts G3 and G4 normalised by $U_{ref}$ as a function of $\theta_{ref}$. Similar values in $M_{G3}$ and $M_{G4}$ occurred during parallel background winds from 30° and 210°

on both sides of the street. The higher values in $M_{G4}$ during background winds from approximately 75° compared with $M_{G3}$ may suggest that a corner vortex was present at the end of the row of buildings on the inbound side of the canyon opposite Claremont Terrace. A corner vortex would accelerate the airflow around its centre, which would account for $M_{G4}$ being higher than $M_{G3}$ during these wind conditions.

It is plausible that channel flows produced during parallel background winds will have 'flushed' traffic-related pollutants along the street and ultimately out of the canyon. It is acknowledged that the sources of the pollutants (i.e. road traffic) were aligned with the background wind during parallel background winds. However, the mean concentrations measured during these wind conditions would be expected to be lower due to flushing than during oblique and perpendicular winds, when recirculating flows are likely to have developed inside Gillygate. This will be explored in more detail in Chapters 5 and 8.

### 4.4.3. In-canyon turbulence for $U_{ref}$>1.2 m s$^{-1}$

The analysis of the turbulence presented in this Section complements the preceding investigation into the mean wind flow measured inside the Gillygate street canyon. The turbulence analysis, therefore, supports the evidence of the mean in-canyon flow features that developed during certain background wind conditions. The analysis focuses on the influence of the perpendicular background winds and the production of turbulence inside Gillygate. However, the influence of oblique and parallel background winds is also mentioned. First, the merits and limitations of the two normalisation procedures used for $\sigma_w$ are discussed. The discussion is continued by investigating $\sigma_w$ and TKE measured in the canyon.

The turbulence intensity in the vertical wind component, $t_w$, was calculated by normalising $\sigma_w$ measured on lampposts G3 and G4 by the mean local horizontal wind speed, $M$, as described in Equation (4.1). High values of turbulence intensity, $t_w$, correspond to low mean local wind velocities, $M$, therefore, $t_w$ is useful for determining the relative proportion of local mixing that is due to turbulence as opposed to $M$. This is particularly the case during perpendicular background winds,

when the $\sigma_w/M_{G3}$ and $\sigma_w/M_{G4}$ values may be somewhat exaggerated by the lower values of $M_{G3}$ and $M_{G4}$ measured at mid-canyon height (Figure 4.11). On the other hand, normalising $\sigma_w$ by $U_{\mathrm{ref}}$ is more appropriate for comparisons between data from anemometers located at different heights and locations inside the same canyon and between data sets collected from other experiments.

Figure 4.12 presents $\sigma_w/U_{ref}$ measured at mid-canyon height inside Gillygate on lampposts G3 and G4 as a function of the background wind direction, $\theta_{\mathrm{ref}}$. Figure 4.13 presents the turbulence intensity, $\sigma_w/M_{G3}$ and $\sigma_w/M_{G4}$, measured at mid-canyon height inside Gillygate on lampposts G3 and G4 as a function of $\theta_{\mathrm{ref}}$. Thus, the normalisation method in which $U_{ref}$ was used in place of $M$ is presented in order to allow for comparison between the two methods.

Figure 4.13 shows that the values of the normalised standard deviations of the mean vertical velocity measured at G3, $\sigma_w/M_{\mathrm{G3}}$, indicate that the greatest values of $t_w$ occurred during perpendicular background winds. Therefore, normalising $\sigma_w$ by the mean local wind speeds $M_{G3}$ and $M_{G4}$ the dependence of the turbulence intensity on $\theta_{ref}$ is much clearer, particularly during perpendicular background winds.

However, caution is needed when normalising $\sigma_w$ by $M$, as the local wind speeds would be expected to vary at different heights and locations within the canyon. It was mentioned earlier that the values of $t_w$ may have been exaggerated by low values of $M_{G3}$ and $M_{G4}$ measured during perpendicular background winds (Figure 4.11). It is as a result of these high turbulence intensities measured during perpendicular winds that it is difficult to ascertain the sensitivity of the normalised quantities for other background wind directions. Therefore, Figure 4.13 presents the values of $t_w$ measured at mid-canyon height on lampposts G3 and G4 on a logarithmic scale. Due to variations in $M$ across the canyon, the method of normalising $\sigma_w$ by $U_{ref}$ is more appropriate for comparisons between the data collected at different locations within the canyon (see Figure 4.12) and between other experiments. This was kept in mind during the analysis of the TKE measured within the entire canyon volume.

It should also be reaffirmed that normalising $\sigma_w$ by $U_{ref}$ is likely to have been complicated by the sheltering effect of the large tree located at ~270° from the reference mast. The mean wind speeds measured at the mast during westerly winds, therefore, are likely to have been reduced by the tree, exaggerating the normalised $\sigma_w$ values. For this reason, for comparisons between the data collected at mid-canyon height $\sigma_w/M$ is preferred over $\sigma_w/U_{ref}$. In order to compare levels of turbulence measured in the canyon with those measured close to the shear layer the turbulence statistics are better normalised by $U_{ref}$. This is shown in the following Section with regards to the TKE analysis. The analysis of the flow structures was continued by investigating the turbulence in all three velocity components. The TKE analysis is presented below and complements the findings of $t_w$ (i.e. $\sigma_w/M$) as a function of $\theta_{ref}$. The analysis begins by exploring the turbulence measured at mid-canyon height on lampposts G3 and G4. However, discussion is also made of the turbulence measured at other locations within the canyon.

#### *4.4.3.1 Standard deviation of the mean vertical velocity and TKE*

##### *4.4.3.1.1. Perpendicular SE background winds*

The analysis of the mean vertical wind velocity presented in Section 4.4.2 produced a discussion of the potential for a single across-canyon recirculating flow with a horizontally-aligned axis developing during perpendicular SE background winds. The classic recirculating flow that is expected to have developed during skimming flow regimes is likely to have advected turbulence from the shear layer into the cavity of the canyon and to have generated turbulence as a result of flow impingement and separation. More specifically, the turbulence would be advected from the shear layer to the windward (G4) side of the canyon and then across the street towards the leeward (G3) side in the reverse flow portion of the recirculating flow. Therefore, the turbulence measured inside the canyon during $\theta_{ref}$ = 120° is likely to relate to the turbulence that is advected from the shear layer within the recirculating flow. However, during the process of advection across the canyon volume some turbulent energy is expected to have been lost.

The values of $W_{G3}/U_{ref}$ and $W_{G4}/U_{ref}$ (Figure 4.8) can be compared with the values of $\sigma_w/U_{ref}$ measured at mid-canyon height on G3 and G4 (Figure 4.12) in order to give an indication of the stability of the recirculating flow that formed during $\theta_{ref}$ = 120°. During these wind conditions the values of $\sigma_w/U_{ref}$ measured on both sides of the canyon are approximately half the values of $W_{G3}/U_{ref}$ and $W_{G4}/U_{ref}$. Therefore, it seems likely that the classic single-across canyon recirculating flow that formed inside Gillygate during $\theta_{ref}$ = 120° was relatively stable. It should be stressed that the recirculating flow is unlikely to have been entirely stable as it is represented by time-averages of fluctuating phenomena. However, Louka *et al.* (2000) and Nielsen (2000) stated evidence of more intermittent recirculating patterns, probably as a result of the lower aspect ratio of each canyon. The presence of trees in the street canyon used by Nielsen (2000) is also likely to have weakened the overall structure of the recirculating flow inside the Copenhagen canyon and may have inhibited the development of downdraughts on the windward side.

The turbulence intensities, $t_w$, measured on both sides of Gillygate during $\theta_{ref}$ = 120° is shown in Figure 4.13 by the relationship between $\sigma_w/M_{G3}$ and $\sigma_w/M_{G4}$ (i.e. $t_w$) and $\theta_{ref}$. The values of $t_w$ indicate that the greatest turbulence intensities measured inside Gillygate at mid-canyon height occurred during perpendicular and near-perpendicular background winds. Although slightly off-set, the turbulence measured during $\theta_{ref} \approx$ 120° is likely to have resulted from the single-across canyon recirculating flow. During $\theta_{ref} \approx$ 120° the off-set is likely to have been caused by low values of $M_{G3}$ and $M_{G4}$ measured at mid-canyon height (Chapter 5).

Figures 4.14 – 4.16 present the TKE measured at mid-canyon height on lampposts G3 and G4 against the TKE measured at the reference location on the mast, $TKE_{ref}$, conditioned on $U_{ref}$ >1.2 m s$^{-1}$. Each figure is further conditioned on the background wind directions, which allows comparison of perpendicular ($\theta_{ref}$ = 120° ±30°; $\theta_{ref}$ = 300° ±30°); oblique ($\theta_{ref}$ = 75° ±30°; $\theta_{ref}$ = 165° ±30°) and parallel winds ($\theta_{ref}$ = 30° ±30°; $\theta_{ref}$ = 210° ±30°). These correspond to Figures 4.14, 4.15 and 4.16, respectively. A detailed discussion into the influence of oblique and parallel background winds is given in Sections 4.4.3.1.3 and 4.4.3.1.4, respectively.

Figure 4.14a shows strong linear correlations between the TKE measured at mid-canyon height against the TKE measured at the reference location on the mast, $TKE_{ref}$, during $\theta_{ref}$ = 120° ±30° (or 90° < $\theta_{ref}$ ≤ 150°) with $r^2$ values of 0.87 and 0.82 for G4 and G3, respectively. During these background winds, lampposts G4 and G3 were located on the windward side and the leeward side of the canyon, respectively. The slopes of the regression lines are 0.64 and 0.23, respectively. The stronger dependence of $TKE_{G4}$ against $TKE_{ref}$ indicates that the turbulence was greatest on the windward side during these background wind conditions. This also supports the findings of the vertical mean wind velocities presented earlier, which showed that the greatest velocities were measured on the windward side of the canyon and were associated with the downdraughts of a recirculating flow (with a horizontally-aligned axis). It also indicates that the turbulence measured at mid-canyon height does vary across the canyon during $\theta_{ref}$ = 120° ±30°. The lower slope for the leeward side suggests that turbulent energy is likely to have been lost as the flow recirculated within the canyon. Therefore, the lower TKE that was measured at mid-canyon height on the leeward side compared to the windward side is also further evidence in support of a recirculating flow.

Furthermore, it was mentioned in Chapter 2 that the turbulence intensities measured in street canyons were typically a factor of 10 lower than the above-roof intensities (see also Britter and Hanna, 2003). However, the actual figure will not only depend on the turbulence present in the background flow, but will also be specific to each street canyon and will primarily depend on the aspect ratio, roof geometry and the presence of additional roughness elements (e.g. trees, bus shelters, signs) within the street. However, the leeward TKE values measured at mid-canyon height during the classic skimming flow inside the Gillygate street canyon indicate that the turbulence intensities were a factor of 5 lower than the intensities measured above roof level.

The TKE measured at the mid-canyon anemometers were normalised by the sum of the squares of the local mean wind components (i.e. $U^2 + V^2 + W^2$) in order to allow for comparison across all background wind directions. Figure 4.17 presents the normalised turbulence kinetic energy, $TKE_{norm}$, measured at G3 and G4 against $\theta_{ref}$. The profiles of the $TKE_{norm}$ curves are similar to those presented for $\sigma_w/M_{G3}$, and

$\sigma_w/M_{G4}$ (Figure 4.13) with the strongest turbulence intensities occurring during perpendicular background wind conditions. As mentioned earlier with regards to Figure 4.13, the off-set is likely to be a function of the lower values of $M_{G3}$, and $M_{G4}$ measured at mid-canyon height (Figure 4.11). For $\theta_{ref}$ = 120° ±30° the $TKE_{norm}$ values indicate that stronger turbulence intensities were measured on the windward (G4) side than the leeward (G3) side.

The analysis up to this point has only comprised of the data collected from the anemometers at mid-canyon height on lampposts G3 and G4. However, it is also important to consider the overall turbulence intensity measured at different heights within the canyon volume. Figure 4.18 presents the TKE normalised by the local wind speed, $TKE_{norm}$, measured at $z/H$ = 0.60 on lamppost G3 and at $z/H$ = 0.84 on lamppost G4 as a function of $\theta_{ref}$. While the profiles of the $TKE_{norm}$ scatter points are similar for 0° < $\theta_{ref}$ ≤ 120°, the values measured on lamppost G4 at $z/H$ = 0.84 are almost a factor of two lower than those measured within the recirculating region at $z/H$ = 0.48 (Figures 18b and 17b, respectively). However, this is not necessarily an indication of lower normalised TKE at roof-level, compared to locations deeper within the canyon. Instead, these lower normalised values were most likely caused by higher local mean wind speeds compared to those measured deeper inside the canyon. Figure 4.19 presents the vertical variation in $TKE_{norm}$ measured at $z/H$ = 0.60, $z/H$ = 0.46 and $z/H$ = 0.30 on lamppost G3 across all background wind directions. Figure 4.19 shows that the turbulence intensities measured on the G3 side of the canyon were similar at each height not only during $\theta_{ref}$ = 120° ±30°, but across all background wind directions. These findings give further support to the discussions of Britter and Hanna (2003), who stated that turbulence intensities may be assumed to be approximately uniform throughout the urban canopy (i.e. below roof height).

However, it would also be useful to compare the turbulence measured inside the canyon with the turbulence measured closer to the shear layer. The anemometer located closest to the shear layer was at $z/H$ = 0.84 on lamppost G4. However, it should be stressed that the actual proximity to the shear layer is likely to differ depending on $\theta_{ref}$. Nevertheless, shear generated turbulence is likely to have been advected towards the anemometer located at $z/H$ = 0.84 on lamppost G4 during $\theta_{ref}$ =

120° ±30°. Therefore, this anemometer is expected to have measured higher levels of turbulence than the anemometers located deeper inside the canyon.

The analysis is continued by comparing the turbulence measured at each location inside the canyon against the turbulence measured just above the roof eves on the G4 side by normalising TKE by $U_{ref}^2$. Figure 4.20 presents $TKE_{G3}/U_{ref}^2$ measured on lamppost G3 at $z/H$ = 0.46 and $z/H$ = 0.60, as a function of $TKE_{G4}/U_{ref}^2$ measured close to the shear layer at $z/H$ = 0.84 on G4. The figure also presents $TKE_{G4}/U_{ref}^2$ measured on lamppost G4 at $z/H$ = 0.48 as a function of $TKE_{G4}/U_{ref}^2$ measured close to the shear layer at $z/H$ = 0.84 on G4. The data were conditioned on $\theta_{ref}$ = 120° ±30. The plots show strong, positive correlations between $TKE_{G3}/U_{ref}^2$ measured on the leeward (G3) side of the canyon at $z/H$ = 0.46 and $z/H$ = 0.60 and $TKE_{G4}/U_{ref}^2$ measured close to the shear layer on the windward (G4) side with $r^2$ values of 0.81 and 0.68, respectively. The figure also shows a strong, positive correlation between $TKE_{G4}/U_{ref}^2$ measured at mid-canyon height on the windward side and $TKE_{G4}/U_{ref}^2$ measured close to the shear layer, with $r^2$ = 0.94.

Table 4.2 presents the results of the linear regression analysis of $TKE_{G3}/U_{ref}^2$ and $TKE_{G4}/U_{ref}^2$ measured inside the canyon as a function of $TKE_{G4}/U_{ref}^2$ measured close to the shear layer at $z/H$ =0.84 on lamppost G4 during perpendicular background winds. The slopes of the regression lines reveal some interesting features of the single across-canyon recirculating flow that developed during these background winds. The slope of the regression line for $TKE_{G4}/U_{ref}^2$ measured at mid-canyon height on lamppost G4 and $TKE_{G4}/U_{ref}^2$ measured close to the shear layer is 0.95. Therefore, the normalised TKE was slightly lower at the mid-canyon location than close to the downwind portion of the shear layer. However, the slope is almost 1, which implies that only a small amount of turbulence energy was lost from the roof eves to mid-canyon level. Therefore, shear turbulence produced at roof-level on the upstream (leeward) side of the canyon is likely to have been transported towards the windward side. The downdraughts associated with the recirculating flow are likely to have then advected the turbulence first towards the highest anemometer on the windward side and then to the mid-canyon anemometer, during which some turbulent energy was lost.

Figure 4.20 shows that the slope of the regression line for $TKE_{G3}/U_{ref}^2$ measured at mid-canyon height on the leeward (G3) side and $TKE_{G4}/U_{ref}^2$ measured close to the shear layer on the windward (G4) side is a factor of ~3 lower. The slopes for the regression lines are 0.31 and 0.95 for G3 and G4, respectively. This is in agreement with the TKE values derived from MISKAM (Figure 4.21a), although the model results are used here qualitatively to help interpret the experimental results. The computed TKE values were not normalised by $U_{ref}$ as they were created simply to allow for comparison between the two perpendicular wind directions. The computed TKE values would need to be normalised by $U_{ref}$ for more detailed comparisons with the experimental results, see the recommendations for future work described in Chapter 9.

Figure 4.21 shows the computed TKE as contour plots within and above the cavity of the street canyon for the two perpendicular background wind directions. The contour plots were created by converting the derived values into a matrix using the weighted average gridding method in Origin. Figure 4.21a clearly shows that for $\theta_{ref} = 120°$ the model predicted TKE to be at its greatest within the canyon volume close to the roof level of the windward building. Recall that the model predicted that during $\theta_{ref} = 120°$ a skimming flow was present above a single across-canyon recirculating flow (Figure 4.7b). Therefore, the experimental and computed in-canyon TKE results both indicate either that significantly more energy was lost in the reverse flow portion of the single across-canyon recirculating flow or that less turbulence was produced locally.

The anemometer located on lamppost G4 at $z/H = 0.84$ was positioned just above the eves of the roof and was the closest location to the shear layer. Louka *et al.* (2000) found that TKE was at its greatest magnitude at roof-level as shear turbulence was produced near the upstream roof and was transported by the mean wind within the shear layer. Although no measurements were taken close to the upstream roof, the lower values of normalised TKE measured in the recirculating zone inside the Gillygate canyon compared to those for $z/H = 0.84$ on the windward (G4) side during $\theta_{ref} = 120° \pm 30°$ and predicted by MISKAM agree with the findings of Louka *et al.* (2000).

The variation of $TKE_{G3}/U_{ref}^2$ measured on the leeward (G3) side at $z/H$ = 0.30, $z/H$ = 0.46 and $z/H$ = 0.60 during $\theta_{ref}$ = 120° ±30° as a function of $TKE_{G4}/U_{ref}^2$ measured close to the shear layer on lamppost G4 at $z/H$ = 0.84 is shown in Figure 4.22. Figure 4.22 compares with the $TKE_{G3}$ values normalised by the local wind speed presented in Figure 4.19, except that the data were conditioned on $\theta_{ref}$ = 120° ±30°. This analysis is presented for completeness, although 26% of the data shown previously in Figure 4.20 has been excluded in order to allow for comparison with the $TKE_{G3}/Uref^2$ data from the lowest anemometer on lamppost G3 (i.e. at $z/H$ = 0.30). Table 4.3 presents the results of the regression analysis for $TKE_{G3}/U_{ref}^2$ measured at each height on lamppost G3 as a function of $TKE_{G4}/U_{ref}^2$ measured close to the shear layer at $z/H$ = 0.84 on lamppost G4 during perpendicular background winds. The regression analysis shows strong, positive correlations between the two quantities with $r^2$ values of 0.73, 0.87 and 0.76, respectively. The slopes of the regression lines are 0.33, 0.33 and 0.29, respectively. While the slopes are similar, they show a slight decrease with height. The similarities in the slopes are probably due to the fact that the measurements were taken relatively close to the canyon wall and greater differences in TKE with respect to height may be expected towards the centre of the canyon.

*4.4.3.1.2. Perpendicular NW background winds*

During perpendicular NW winds (i.e. $\theta_{ref}$ = 300°) the values of turbulence intensity, $t_w$, measured at mid-canyon height on lamppost G3 are approximately equal to the values of $t_w$ measured during $\theta_{ref}$ =120° (Figure 4.13). However, the positive values of $W_{G3}/U_{\mathrm{ref}}$ and $W_{G4}/U_{\mathrm{ref}}$ (Figure 4.8) measured on each side of the canyon during $\theta_{ref}$ ≈ 300° indicate that the turbulence produced during these winds is likely to be caused by a different mechanism to a classic single across-canyon flow (with a horizontally-aligned axis). It was described in Section 4.4.2 that NW winds channelled through the side streets adjoining Gillygate perpendicular to the canyon axis. Counter-rotating corner vortices with vertically-aligned axes are likely to have developed at the junctions with Gillygate, caused by converging airflows inside the canyon. The along-canyon flows are believed to have converged at a point near to the G3-G4 cross-section, causing updraughts and strong turbulence intensities on both sides of the canyon. Significant vertical momentum flux would be expected at the point of flow convergence due to mass conservation. Figure 4.13 also shows that during $\theta_{ref}$ =

300° greater values of $t_w$ were measured on the windward (G3) side of the canyon than on the leeward (G4) side.

The values of $W_{G3}/U_{ref}$ and $W_{G4}/U_{ref}$ (Figure 4.8) can be compared with the values of $\sigma_w/U_{ref}$ measured at mid-canyon height on G3 and G4 (Figure 4.12) in order to give an indication of the stability of the in-canyon flow structures that formed during $\theta_{ref}$ = 300°. During these wind conditions the values of $\sigma_w/U_{ref}$ measured on the windward (G3) side of the canyon are a factor of ~2 greater than the values of $W_{G3}/U_{ref}$. This gives further evidence of strong turbulence intensity associated with these background winds. Recall that the values of $\sigma_w/U_{ref}$ measured on both sides of the canyon during $\theta_{ref}$ = 120° were approximately half the values of $W_{G3}/U_{ref}$ and $W_{G4}/U_{ref}$, indicating that the classic single across-canyon recirculating flow (with a horizontally-aligned axis) was much more stable, as would be expected. This gives further emphasis to the complexity of the in-canyon flow structures that developed during background winds from the NW.

Figure 4.14 presents the values of $TKE_{G3}$ and $TKE_{G4}$ measured at mid-canyon height against the values of $TKE_{ref}$, conditioned on $U_{ref}$>1.2 m s$^{-1}$. Figure 4.14b shows that during $\theta_{ref}$ = 300° ±30° (or 270° < $\theta_{ref}$ ≤ 330°) the slopes of the regression lines are more similar, as shown by the values 0.61 and 0.32 for G3 and G4, respectively. During these background wind directions, lampposts G3 and G4 were located on the windward side and the leeward side of the canyon, respectively. The relationship between the two quantities is strong and positive, as shown by the $r^2$ values of 0.93 and 0.91 for G3 and G4, respectively. The fact that the slopes are more similar than for $\theta_{ref}$ = 120° ±30° is further evidence to support the view that a single across-canyon recirculating flow (with a horizontally-aligned axis) was less likely to have occurred during these background wind conditions. The smaller difference in the turbulence intensities can be attributed to the along-canyon flow convergence that produced updraughts on both sides of the street. During these background winds, the updraughts were strongest on the leeward (G4) side of the canyon compared to the windward (G3) side, as shown earlier by the higher mean vertical velocities presented in Figure 4.5 and Figure 4.8. The analysis shown in Figure 4.14b reveals that the TKE was slightly greater on the windward (G3) side of the canyon than on the

leeward (G4) side. The TKE is likely to have been higher on the windward side due to greater turbulence within the horizontal flow components. This will be explored in more detail in Section 4.4.3.2.

By continuing the analysis, Figure 4.17 presents the normalised turbulence kinetic energy, $TKE_{norm}$, measured at G3 and G4 against $\theta_{ref}$. Figure 4.17a also shows that the greatest turbulence intensities were measured on the windward (G3) side during $\theta_{ref}$ = 300° ±30° than on the leeward (G3) side during $\theta_{ref}$ = 120° ±30°. Figure 4.18a and Figure 4.19 reveal that the turbulence intensities measured on the windward (G3) side of the canyon during $\theta_{ref}$ = 300° ±30° at $z/H$ = 0.60 are comparable to those presented for $z/H$ = 0.46 and $z/H$ = 0.30. This implies that during perpendicular NW winds, local turbulence production was still significant on the windward side at $z/H$ = 0.60. Even at mid-canyon height, the turbulence was found to be less intense on the leeward (G4) side than those on the windward (G3) side during these background wind conditions. These findings are likely to be a function of the proximity of the anemometer located at mid-canyon height on lamppost G3 to the momentum flux caused by flow convergence.

However, the source of the turbulence measured at the point of flow convergence may not purely be related to the momentum flux and, therefore, its origins may not be entirely local. Instead, the turbulence may have been generated in an above-roof shear layer and transported into the canyon in a mean flow further down the street (i.e. either side of the G3-G4 experiment cross-section) and then advected by horizontal along-canyon flows to the point of convergence. The differences in the across-canyon turbulence may be explained by the influence of the street-level across-canyon flow from the windward (G3) side of the canyon to the leeward (G4) side, which is likely to have advected turbulence. As a result, the intensities on the leeward side of the canyon were found to be lower than on the windward side during these winds.

Figure 4.23 presents $TKE_{G3}/U_{ref}^2$ measured on lamppost G3 located on the windward side of the canyon at $z/H$ = 0.46 and $z/H$ = 0.60, as a function of $TKE_{G4}/U_{ref}^2$ measured close to the shear layer at $z/H$ = 0.84m on G4, conditioned on $\theta_{ref}$ = 300°

±30. Once again, the relationship between the two quantities were strong and positive, as shown by the $r^2$ values of 0.91 and 0.86 for at $z/H = 0.46$ and $z/H = 0.60$ on lamppost G3, respectively (Table 4.2). The figure also presents $TKE_{G4}/U_{ref}^2$ measured on lamppost G4 located on the leeward side of the canyon at $z/H = 0.48$ as a function of $TKE_{G4}/U_{ref}^2$ measured close to the shear layer at $z/H = 0.84$ on lamppost G4. The relationship between the two quantities was also strong and positive, as shown by the $r^2$ value of 0.78.

Normalising TKE by the local wind speed (Figure 4.18 and Figure 4.19) rather than by $U_{ref}^2$ (Figure 4.22 and Figure 4.23) may have only shown the variation in the local mean wind speed measured at each location rather than the variability in the turbulence intensities across the canyon. Instead, normalising $TKE_{G3}$ and $TKE_{G4}$ by $U_{ref}^2$ would give a better indication of the level of turbulence measured at different locations inside the canyon. The slopes of the regression lines presented in Figure 4.23, therefore, reveal more accurately the effects of in-canyon flow and turbulence. During $\theta_{ref}$ = 120° ±30° and $\theta_{ref}$ = 300° ±30°, lampposts G3 and G4 were located on the leeward side of the canyon, respectively. The slopes for the regression analysis of the data collected at mid-canyon height on the leeward sides of the canyon during $\theta_{ref}$ = 120° ±30° and $\theta_{ref}$ = 300° ±30° are shown in Figure 4.20b and Figure 4.23a and are 0.31 and 0.58, respectively (see Figure 4.1). There is almost a factor of two difference between the slopes. The higher slope for $\theta_{ref}$ = 300° ±30° reveals that the normalised TKE measured at mid-canyon height on lamppost G4 is more similar to the anemometer on the same lamppost at $z/H = 0.84$.

Figure 4.23a also shows that the slope of 0.58 for $TKE_{G4}/U_{ref}^2$ measured at $z/H = 0.48$ on the leeward (G4) side against $TKE_{G4}/U_{ref}^2$ measured $z/H = 0.84$ indicates that the turbulence was greater at the closest location to the shear layer than at mid-canyon height on the leeward side during $\theta_{ref}$ = 300° ±30°. Recall that Louka *et al.* (2000) measured greater levels of TKE in the shear layer compared to locations deeper inside the canyon. However, Figure 4.23 shows the slopes for $TKE_{G3}/U_{ref}^2$ measured at $z/H = 0.46$ and at $z/H = 0.60$ on the windward (G3) side against $TKE_{G4}/U_{ref}^2$ measured close to the shear layer during these background wind conditions. The slopes are 1.26 and 1.25, respectively.

The analysis was continued by investigating $TKE_{G3}/U_{ref}^2$ measured at each height on lamppost G3 compared to the values of $TKE_{G4}/U_{ref}^2$ measured close to the shear layer on lamppost G4 during perpendicular NW winds. The variation of $TKE_{G3}/U_{ref}^2$ measured on the windward side at $z/H = 0.30$, $z/H = 0.46$ and $z/H = 0.60$ as a function of $TKE_{G4}/U_{ref}^2$ measured at the closest location to the shear layer on lamppost G4 at $z/H = 0.84$, conditioned on $\theta_{ref} = 300° \pm 30°$ is shown in Figure 4.24. This figure continues the analysis of the features of the converging along-canyon flows presented in Figure 4.23, but includes the data for the lowest anemometer at $z/H = 0.30$ and, therefore, 26% of the data shown previously in Figure 4.23 has been excluded. Table 4.3 presents the results of the regression analysis for $TKE_{G3}/U_{ref}^2$ measured at each height on lamppost G3 as a function of $TKE_{G4}/U_{ref}^2$ measured close to the shear layer at $z/H = 0.84$ on lamppost G4 during perpendicular background winds. The regression analysis shows strong, positive correlations between the two quantities with $r^2$ values of 0.64, 0.81 and 0.72, respectively. The slopes of the regression lines are 1.16, 1.23 and 1.26, respectively. The slopes are similar, which suggests that there was little variation in TKE with height. Furthermore, the slopes are all greater than 1, which indicates that the TKE measured in the canyon on the windward (G3) side was higher than the TKE measured at roof-level on lamppost G4. Figure 4.24, therefore, confirms that although more than a quarter of the data shown previously in Figure 4.23 was removed, the TKE measured on the windward (G3) side was still found to be higher at each vertical location than the TKE measured just above roof-eve level on lamppost G4.

The contour plot shown in Figure 4.21b shows the TKE derived from MISKAM for $\theta_{ref} = 300°$. The contour plot in Figure 4.21b contrasts considerably with Figure 4.21a, with TKE showing much less variation across the canyon in the former (i.e. during $\theta_{ref} = 300° \pm 30°$). It was mentioned earlier that comparisons between the measured and modelled values of the in-canyon TKE would require the results to be normalised. Additionally, it should be noted that the model is unlikely to represent the turbulence measured in the field as the model cannot represent the unsteadiness that must generate a large proportion of the fluctuations during along-canyon converging flows. Although this must be borne in mind when interpreting the results of the modelling study, the findings give further support to the likelihood that a single

across-canyon flow with a horizontally-aligned axis was generally absent during perpendicular NW winds.

The along-canyon converging flow scenario (with two counter-rotating vertically-aligned corner-vortices) shows less penetration into the canyon of the above-roof turbulence compared to the classic single-across canyon horizontally-aligned recirculating flow. Recall that there were updraughts on both sides of the canyon at the point of flow convergence (i.e. the G3-G4 experiment cross section). However, the suggestion that there was some penetration of turbulence from the shear layer during $\theta_{ref}$ = 300° implies that the mean background wind flow must have penetrated the canyon either side of the convergence point. An alternative explanation may relate to the potential for greater vertical velocity gradients at the top of the canopy on the windward side of the canyon, even for the converging flow scenario. This would lead to a TKE production term within the model. Future work should include further analysis of the vertical velocity gradients and TKE at multiple experiment cross-sections either side of the flow convergence point, as discussed in Chapter 9.

*4.4.3.1.3. Oblique background winds*

The turbulence intensities, $t_w$, presented in Figure 4.13 also show that turbulence occurred when helical flows are suspected to have formed inside the Gillygate canyon. This analysis of the $t_w$ measured inside the canyon during oblique background winds, therefore, supports the observations of the mean vertical velocity presented in Figure 4.8. The analysis of the mean vertical wind velocity suggested that these background winds produced downdraughts on the windward side of the canyon and updraughts on the leeward side.

In particular, oblique background winds from $\theta_{ref} \approx 150°$ appear to have produced high turbulence intensities that were similar in magnitude to those measured during the classic recirculating flow associated with $\theta_{ref} = 120°$. The high $t_w$ values measured on both sides of the street during $\theta_{ref} \approx 150°$ suggests that the mean in-canyon wind velocities were low.

The analysis into the variation in the turbulence intensities across the canyon during oblique background winds was continued by considering TKE. Figure 4.15 presents $TKE_{G3}$ and $TKE_{G4}$ measured at mid-canyon height as a function of $TKE_{ref}$ conditioned on $U_{ref}$>1.2 m s$^{-1}$. The data was also conditioned separately on $\theta_{ref}$ = 75° ±30° (or 45° < $\theta_{ref}$ ≤ 105°) and $\theta_{ref}$ = 165° ±30° (or 135° < $\theta_{ref}$ ≤ 195°) in order to investigate the influence of oblique winds on the production of turbulence inside the street canyon. It should be noted that the data used for $\theta_{ref}$ = 120° ±30° and $\theta_{ref}$ = 75° ±30° and for $\theta_{ref}$ = 120° ±30° and $\theta_{ref}$ = 165° ±30° overlap by 15°, respectively. During $\theta_{ref}$ = 75° ±30°, lampposts G4 and G3 were located on the windward and leeward sides of the canyon, respectively. These background winds produced downdraughts on the windward (G4) side of the canyon and updraughts on the leeward (G3) side (Figure 4.8). This gives further support to the view that helical flow regimes developed inside Gillygate during these background winds.

Figure 4.15 indicates that during $\theta_{ref}$ = 75° ±30° the slopes of the regression lines are 0.54 and 0.23 for the windward (G4) and leeward (G3) sides, respectively. The $r^2$ values indicate strong, positive correlations between the two quantities and are 0.88 and 0.93 for the windward and leeward sides, respectively. A similar trend can be observed for oblique background winds from $\theta_{ref}$ = 165° ±30°. For these background winds the slopes of the regression lines are 0.61 and 0.22 for the windward (G4) and leeward (G3) sides, respectively. The results of the linear regression analysis performed for the oblique background wind directions are presented in Table 4.4.

The analysis was also conducted for $\theta_{ref}$ = 255° ±30° (or 225° < $\theta_{ref}$ ≤ 285°) and $\theta_{ref}$ = 345° ±30° (or 315° < $\theta_{ref}$ ≤ 15°). It should be noted that the data used for $\theta_{ref}$ = 300° ±30° and $\theta_{ref}$ = 255° ±30° and for $\theta_{ref}$ = 300° ±30° and $\theta_{ref}$ = 345° ±30° overlap by 15°, respectively. During $\theta_{ref}$ = 255° ±30° the slopes of the regression lines are 0.92 and 0.33 for the windward (G3) and leeward (G4) sides, respectively. Similarly, for $\theta_{ref}$ = 345° ±30° the slopes of the regression lines are 0.58 and 0.31 for the windward (G3) and leeward (G4) sides, respectively. The stronger dependence of $TKE_{G3}$ and $TKE_{G4}$ against $TKE_{ref}$ for data corresponding to the windward sides of the canyon indicates that during oblique background winds the turbulence was greatest on the windward sides (Table 4.4).

The findings of the TKE analysis for oblique background winds, therefore, support the mean flow analysis, which suggested that these winds produced recirculating helical flows along Gillygate. It should be stressed that oblique background winds from the NW sector produced across-canyon recirculating flows with horizontally-aligned axes, while perpendicular background NW winds generated across-canyon recirculating flows with vertically-aligned axes. TKE was found to be higher on the windward side of the canyon than on the leeward side, which complements the results for perpendicular SE background winds. It also indicates that the turbulence measured at mid-canyon height does vary across the canyon during these wind conditions by a factor of ~2. The advection of turbulence by the mean flow from the windward side of the canyon to the leeward side is likely to have been the cause of the lower leeward TKE.

Oblique background winds from 45° N, however, appear to have caused a different in-canyon recirculating flow structure. During $\theta_{ref} \approx 45°$ high turbulence intensities, $t_w$, were observed at mid-canyon height on lamppost G4, although they were absent at mid-canyon height on lamppost G3 (Figure 11). These elevated $t_w$ values were probably caused by a vortex (with a vertically-aligned axis) developing in the cavity of the building adjacent to lamppost G4. The building cavity vortex that formed during these background winds is shown schematically in Figure 4.25. Figure 4.17 also shows that the building cavity vortex that may have formed adjacent to lamppost G4 during near-parallel background winds of $\theta_{ref} = 45°$ (Figure 4.25) is also likely to be the cause of the moderately high $TKE_{norm}$ values measured at G4 during these conditions. However, consideration should also be given to the possibility of residual turbulence being produced as a result of the air motions interacting with the lamppost itself.

*4.4.3.1.4. Parallel background winds*

During parallel background winds low turbulence intensities, $t_w$, were measured at mid-canyon height on lampposts G3 and G4 (Figure 4.13), which supports the assertion that channel flows with strong along-canyon flow components are likely to have developed. Recall that the mean vertical velocity, $W$, measured at mid-canyon

height on both sides of the street was low (although $W$ >0 m s$^{-1}$) during parallel background winds (Figure 4.8), while along-canyon flows dominated (Figure 4.10).

By continuing the analysis, Figure 4.16 presents the $TKE_{G3}$ and $TKE_{G4}$ measured at mid-canyon height as a function of $TKE_{ref}$ conditioned on $U_{ref}$ >1.2 m s$^{-1}$. The data was also conditioned separately on $\theta_{ref}$ = 30° ±30° and $\theta_{ref}$ = 210° ±30° in order to investigate the influence of parallel winds on the production of turbulence inside the street canyon. During parallel background winds the slopes of the regression lines are even closer together (e.g. compared to $\theta_{ref}$ = 120° ±30° and $\theta_{ref}$ = 300° ±30°), indicating that the turbulence intensities measured on both sides of the street are similar in magnitude. During $\theta_{ref}$ = 30° ±30° the slopes of the linear regression lines are 0.35 and 0.34 for G3 and G4, respectively, while the $r^2$ values are both 0.9. The similarities in the turbulence intensities also imply that the building cavity vortex that formed during near parallel winds of $\theta_{ref}$ = 45° shown schematically in Figure 4.25 is unlikely to have been a significant mechanism of turbulence production.

During $\theta_{ref}$ = 210° ±30° the slopes of the regression lines are 0.39 and 0.25 for G3 and G4, respectively; while the $r^2$ values are 0.78 and 0.62, respectively. Furthermore, the slopes of the regression lines shown in Figure 4.16 for $TKE_{G3}$ and $TKE_{G4}$ against $TKE_{ref}$ during parallel background winds are comparable to those presented in Figure 4.14 and Figure 4.15 for the leeward sides of the canyon during perpendicular and oblique background winds, respectively. The maximum values are also similar to those found on the leeward side of the canyon during the background wind directions that resulted in across-canyon recirculating flows. This may indicate that that there was a lack of transfer of turbulent energy into the canyon during channel flows or that there was a significant loss of energy once inside the canyon.

#### *4.4.3.2. Contribution of each turbulence component to TKE*

The analysis of the turbulence, particularly the turbulence intensity shown in the previous Section, investigated the dependency of $\sigma_w$ on the background wind direction. The analysis was continued by investigating the overall turbulence intensity by using TKE. The following sub-section continues the turbulence analysis by looking at the contribution of each turbulence component to TKE. This was

performed by investigating the variance, $\sigma^2$, of each mean velocity component, $i$, and their overall contribution to TKE. The variance of the along-canyon, across-canyon and vertical components of velocity are referred to as $\sigma_u^2$, $\sigma_v^2$ and $\sigma_w^2$, respectively. Although no analysis is presented of the co-variance of the mean velocity components, this analysis is a useful way of approximating the isotropy of the turbulence. Of course, this method is also useful to determine the degree of anisotropy of the turbulence across all background wind directions.

In Chapter 3 turbulence was defined as being homogenous and isotropic when the variance, $\sigma^2$, of each mean velocity component (i.e. $U$, $V$ and $W$) were equal. Isotropy, and consequently anisotropy, can be approximated by the ratio of $\sigma_u^2$, $\sigma_v^2$ and $\sigma_w^2$ to 2·TKE, where TKE was measured at the same location, i.e. $TKE_{G3}$ and $TKE_{G4}$ were used. As the ratio of $\sigma_u^2$, $\sigma_v^2$ and $\sigma_w^2$ to 2·TKE determines the contribution of each turbulence component to TKE as a fraction of 1, the turbulence inside the canyon would be approximately isotropic if the three components were all equal to 0.33. As mentioned in Chapter 3, turbulence in street canyons is expected to be generally anisotropic due to the proximity to locally produced turbulence.

Figures 4.26 and 4.27 present the ratio of the variance of the mean velocity components $\sigma_u^2$, $\sigma_v^2$ and $\sigma_w^2$ to 2·TKE as a function of the background wind direction, $\theta_{ref}$, at various heights on lampposts G3 and G4, respectively. In order to compare the data from the lowest anemometer located on lamppost G3 ($z/H$ = 0.30), 26% of the data presented in Figures 4.17 – 4.20 and Figure 4.23 for the remaining anemometers were excluded. Therefore, Figures 4.26 and 4.27 are consistent with the data shown in Figures 4.21 and 4.23. It is evident in Figures 4.26 and 4.27 that the turbulence measured at each location inside the canyon appears to have been generally anisotropic across most background wind directions, with the along-canyon component having the greatest proportion of turbulence.

However, Figure 4.26 shows that during $0° \leq \theta_{ref} < 90°$ the turbulence measured on G3 at mid-canyon height (i.e. $z/H$ = 0.46) was likely to have been more isotropic than at $z/H$ = 0.60 and $z/H$ = 0.30, which probably reflects the mid-canyon location of the

anemometer. Figure 4.26c shows that as $\theta_{ref}$ increases from 0° to 120° N (i.e. towards perpendicular) the proportion of $TKE_{G3}$ contributed by the along-canyon turbulent component decreases at $z/H$ = 0.30 on the leeward (G3) side, while the proportion from the across-canyon component increases. Figure 4.26c shows that the across-canyon component consisted of a greater proportion of the turbulence measured at the lowest anemometer on the leeward (G3) side of the canyon during perpendicular SE winds (i.e. $\theta_{ref}$= 120°). Although it is less obvious, a similar trend can also be seen in the values presented in Figure 4.26a for $z/H$ = 0.60 during the same background wind directions. The greatest proportion of $TKE_{G3}$ measured at the lowest anemometer on G3 ($z/H$ = 0.30) during $\theta_{ref}$= 120° correspond to the across-canyon component, while the contribution from the along-canyon component was much lower. Isotropy, therefore, appears to have decreased with distance away from the canyon mid-height. This suggests that the mid-canyon anemometer was closer to the centre of the recirculating flow, where the turbulence was more equally distributed in all three components.

The mid-canyon anemometer located on the windward (G4) side measured a greater proportion of turbulence within the vertical components compared to the data collected from the highest anemometer on lamppost G4 (Figure 4.27). It should be mentioned, however, that the greater proportion of turbulence in the vertical components at mid-canyon height on the windward (G4) side of the canyon compared to the highest anemometer on G4 may also be caused by the closer proximity of the mid-canyon anemometer on G4 to the canyon wall. Recall that, the anemometers on lamppost G4 were ~1.0m away from the wall of the adjacent building, whereas the anemometers on G3 were ~2.0m from the adjacent wall. The highest anemometer on lamppost G4 was located above the roof-eves. Therefore, the downdraughts were likely to have been of greater intensity at mid-canyon height on the windward side than closer to the shear layer.

The turbulence measured by the mid-canyon anemometer located on the windward (G4) side was always anisotropic. The turbulence measured at mid-canyon height on the windward side of the canyon consisted of a greater proportion in the along-canyon components, compared to mid-canyon height on lamppost G3. During $\theta_{ref}$ = 120° lamppost G4 was located on the windward side of the canyon and the greater

proportion of turbulence in the along-canyon component may be related to the impingement of the mean flow on the windward canyon wall. Therefore, comparisons between the proportion of turbulence measured by the mid-canyon anemometers as a function of $\theta_{ref}$ indicates that the turbulence was generally more anisotropic on the windward (G4) side than it was on the leeward (G3) side, due to the greater contribution from along-canyon components. This may be partly due to the anemometer on G4 being located closer to the wall of the canyon than the anemometer on G3. However, these findings generally strengthen the argument that a single across-canyon recirculating flow with a horizontally-aligned axis developed inside the canyon during these perpendicular background winds.

During perpendicular NW winds (i.e. $\theta_{ref}$ = 300° ±30) the along-canyon components at all locations inside the canyon contributed up to 80% of the turbulence, except at $z/H$ = 0.84 on lamppost G4 where the contribution remained relatively constant at ~50%. The highest anemometer located on lamppost G4 on the leeward side of the canyon, therefore, generally showed more isotropy across $\theta_{ref}$ than the anemometer located at mid-canyon level on G4. The large proportion of turbulence measured within the along-canyon components at all in-canyon locations, except at the highest position on the leeward (G4) side, suggests that the cause is local. The suggestion that along-canyon fluctuations dominate everywhere under these conditions implies that they are likely to be of large scale caused by the transient nature of the convergence point, i.e. the convergence point coincides only periodically with the G3-G4 experiment cross-section. During parallel background winds (i.e. $\theta_{ref}$ = 30° ±30 and $\theta_{ref}$ = 210° ±30) the greatest proportion of turbulence measured at each location in the canyon was found in the along-canyon components, as would be expected during channel flows.

## 4.5. Summary and Conclusions

In this Chapter the influence of the Gillygate street canyon geometry on the mean wind flow and turbulence measured inside the canyon was investigated over a period of one month. The analysis provided support for the evidence of in-canyon flow structures. The results have allowed for greater understanding of the dynamics and dispersion characteristics of the in-canyon flow features, which will be explored

further in Chapter 5. In order to help interpret the results from the field experiment the MISKAM model was used to derive the mean wind flow and turbulence inside the canyon during certain background wind directions.

A single across-canyon recirculating flow with a horizontally-aligned axis is likely to have occurred during perpendicular SE winds of speeds greater than 1.2 m $s^{-1}$, even though the roofs on the upwind building were pitched. During these background winds, downdraughts were observed on the windward side of the canyon, while updraughts occurred on the leeward side. The downdraughts were characterised by stronger mean vertical velocities and higher values of TKE than the updraughts. The analysis of the contribution of the variance of the three turbulence components (i.e. $\sigma_u^2$, $\sigma_v^2$ and $\sigma_w^2$) to TKE demonstrated a useful way to approximate the isotropy of the turbulence. The analysis provided greater insight into the in-canyon flow and dispersion mechanisms. The analysis demonstrated that at locations deep inside the canyon on both sides of the street the greatest proportion of turbulence was found in the along-canyon velocity components.

Comparisons between the normalised values of the mean vertical velocity measured at mid-canyon height and their standard deviations revealed that the single across-canyon recirculating flow was likely to have been relatively stable under averaging times of 15-minutes. The analysis of the TKE suggested that the across-canyon recirculating flow is likely to have transported shear turbulence from the upstream roof in downdraughts towards the windward side. Turbulence was transported towards the leeward side of the canyon in the street-level reverse flow portion of the recirculating flow. The flow direction at street-level is expected to have been reflected off the windward canyon wall and is likely to have generally opposed the direction of the mean flow aloft. The TKE was found to be greatest in magnitude at the level of the roof eves on the windward side of the street canyon, i.e. at the closest location to the shear-layer. However, TKE is likely to have been reduced during advection in the mean flow from mid-canyon height on the windward side to mid-canyon height on the leeward side and then vertically within the updraughts.

The loss of turbulent energy from one side of the canyon to the other in a classic single across-canyon recirculating flow (with a horizontally-aligned axis) also revealed that the turbulence varied with height and proximity to the centre of the recirculating flow. As a result, turbulence intensities were lowest on the leeward side of the canyon during perpendicular SE background winds. The proportion of the turbulence measured on the leeward side during these background winds was a factor of 5 lower than the turbulence measured at the reference mast (at ~1.8*H*). This revealed a significant TKE gradient across the canyon during these background winds when the classic single across-canyon recirculating flow (with a horizontally-aligned axis) occurred.

Three-dimensional flows inside street canyons were also shown to exhibit more complex characteristics than a single across-canyon recirculating flow. The importance of understanding 3-D flows was demonstrated in the analysis of the effects of perpendicular NW winds. The horizontal mean flow vectors computed at mid-canyon height by MISKAM revealed that during these background winds, counter-rotating corner vortices with vertically-aligned axes are likely to have developed at the junctions of the side streets off Gillygate. The model predicted that the corner vortex pair was caused by two converging flows. Upon convergence, the along-canyon flows formed updraughts on both sides of the street. During these background winds, the turbulence intensity was found to be greater on the windward side of the canyon than on the leeward side. Significant vertical momentum flux would be expected at the point of flow convergence. During perpendicular NW background winds TKE was greatest on the windward side of the canyon than at roof-eve height on the leeward side. Turbulence is likely to have been advected towards the leeward side in a street-level flow associated with the counter-rotating corner vortices. The advection of turbulence in the across-canyon flow from the windward side of the canyon is likely to have caused the lower TKE on the leeward side. The flow outputs computed by MISKAM supported the assumption that there was an across-canyon flow during these background winds.

Oblique background winds are also thought to have produced in-canyon recirculating flows with horizontally-aligned axes. During these background winds, recirculating helical flows developed inside the canyon with downdraughts on the windward side

of the street and updraughts on the leeward side. The recirculating helical flows, therefore, were driven by the oblique winds aloft. A helical flow is likely to have transported turbulence predominantly in an along-street flow, but also in a recirculating flow from the windward side of the canyon to the leeward side. Advection of turbulence in the across-canyon flow is likely to have caused the turbulence intensities on the leeward side of the canyon to be lower than on the windward side. On the other hand, parallel background winds produced channel flows with strong along-canyon flow components and low vertical velocities on both sides of the street canyon.

# CHAPTER 5

# The influence of background winds on the spatial variability in concentrations of a traffic-related pollutant

## 5.1. Introduction

Pollutants emitted by vehicle traffic in urban areas have now generally been accepted to be a cause of chronic health effects. In urban areas, where the population and traffic flows are often relatively high, human exposure to traffic-related pollutants is significant (Fenger, 1999). Increased incidence of congestive heart disease among the elderly and those with pre-existing conditions has been linked to increases in background concentrations of carbon monoxide (Morris *et al.*, 1995). However, the concentrations of traffic-related pollutants in street canyons are controlled by a balance between factors that contribute to both pollutant accumulation and dispersion. What is currently required is not only a reduction in the emissions of harmful pollutants but also a method whereby it is possible to predict wind flow and pollutant dispersion accurately using numerical models. These models could then be used within strategic planning activities aimed at assessing the influence of a range of traffic management procedures on air quality within urban areas. In order to assess the validity of available models, a range of experimental data is required in networks of urban streets with varying geometries.

It was discussed in Chapter 2 and demonstrated in Chapter 4 that complex building and street geometries modify the in-canyon flow structures and, therefore, influence the dispersion of vehicle emissions. The first step in achieving a greater understanding of complex urban wind flows and their implication for pollutant

dispersion should, therefore, be to conduct a study of the wind flow and pollutant concentrations within urban street canyons of varying building and street geometry.

It was shown in Chapter 4 that the classic single across-canyon recirculating flow with a horizontally-aligned axis is likely to have developed inside Gillygate during perpendicular background SE winds, during which the majority of the background flow is believed to have skimmed over the canyon, thus producing the *skimming* flow regime (Oke, 1987; Johnson and Hunter, 1999). During these background wind conditions, downdraughts were observed on the windward side of the canyon, while updraughts occurred on the leeward side. The downdraughts were characterised by stronger mean vertical velocities and higher values of TKE than the updraughts. The flow direction at street-level is expected to have opposed the direction of the mean flow aloft, as was shown in Chapter 4.

The classic recirculating flow with a horizontally-aligned axis has also been observed in the field by DePaul and Sheih (1986) and in the wind tunnel by Hoydysh and Dabberdt (1988). Kim and Baik (2004) conducted a numerical study into the effects of the background wind direction on flow and dispersion in short street canyons with cubic building geometries. They identified three in-canyon flow patterns with considerably different dispersion characteristics depending on the incidence wind angle. They found that as the incidence angle becomes oblique to the street axis more pollutants escaped from the street canyon. In addition, side streets interrupt street canyons within real urban networks and additional 3-D effects may influence the dispersion of emissions. Pollution may also accumulate in small cavities where additional recirculation regions occur (Oke, 1987), and whirling eddies, or corner vortices, developing around buildings are likely to accumulate traffic-related pollutants.

Many previous street canyon models have concentrated on skimming flow, since pollutants released by vehicles at street level during these background wind conditions are transported by a single across-canyon recirculating flow (see Chapter 2). Louka *et al.* (2000) implied that a recirculating flow occurred during perpendicular winds, although measurements of the wind flow in their study were made above the urban canopy, i.e. at or above roof-level. The classic across-canyon

recirculating flow (with a horizontally-aligned axis) observed in the present study may, therefore, cause an increase in the concentrations of traffic-related pollutants on the leeward (or up-wind) side of the canyon relative to the windward side.

Despite the range of idealised numerical studies, few full-scale experiments have been conducted which provide data from simultaneous measurements of in-canyon wind flow and pollutant concentrations, relative to a suitable background wind measurement. Three-dimensional flows inside street canyons also have more complex dispersion characteristics. Full-scale street canyon experiments, however, are only representative of local conditions and data from more locations are required to identify general properties (Longley *et al.*, 2004a). Inter-comparisons must also be made between street canyons of different geometry, as not all street canyons are symmetrical. Most streets have a non-uniform width or have buildings that differ in height on either side. Dispersion models are widely used in air quality and traffic management, urban planning, pollution forecasting and for predicting personal exposure to pollutants. However, for dispersion models to achieve their full potential, they must be able to represent the influence of traffic emissions on roadside concentrations accurately for a range of street geometries and background wind conditions.

The importance of understanding 3-D flows was demonstrated in the analysis of the effects of perpendicular NW winds in Chapter 4. In particular, the horizontal mean flow vectors computed at mid-canyon height by the MISKAM CFD model supported the findings from the field experiment. It was shown that during these background winds, counter-rotating corner vortices with vertically-aligned axes are likely to have developed at the junctions of the side streets off Gillygate (see also Chapter 2). The model predicted that the vortex pair forced the air inside the canyon into two converging flows. An alternative explanation was also mentioned in Chapter 4 in that the corner vortex pair may have been caused by the along-canyon flows. However, the along-canyon flows, upon convergence, formed updraughts on both sides of the street. During these background winds, the intensities of the turbulence were found to be greater on the windward side of the canyon than on the leeward side. There was also evidence of an across-canyon flow at street level from the windward side of the canyon to the leeward side. These in-canyon flow features are likely to have had a

significant influence in the dispersion of traffic-related pollutants and will be explored in more detail in this Chapter.

Oblique background winds are also thought to have produced across-canyon recirculating flows with horizontally-aligned axes inside the Gillygate street canyon (Chapter 4). During these background winds, recirculating helical flows are thought to have developed with downdraughts on the windward side of the street and updraughts on the leeward side. The recirculating helical flows, therefore, were driven by the oblique winds aloft (Chapter 2). A helical flow is likely to have transported traffic-related pollutants predominantly in an along-street flow, but also in a recirculating flow from the windward side of the canyon to the leeward side.

During parallel background winds, channel flows with strong along-canyon flow components are expected to have flushed traffic-related pollutants along and ultimately out of the canyon (Chapter 2). The influence of channel flows will be explored in more detail in this Chapter, although they are expected to have produced the lowest in-canyon concentrations due to the absence of flow recirculation.

### 5.1.1. Chapter synopsis

Chapter 4 described the in-canyon wind flow and turbulence features that were observed for different background winds during the experiment. In this Chapter the interaction of the background wind with the surrounding building and street geometries on the in-canyon pollutant concentrations has been studied experimentally in two street canyons of different geometry. Boddy *et al.* (2005a) described the work presented in this Chapter. Specific investigations in this Chapter are focused on the factors influencing the spatial variability of in-canyon pollutant concentrations and include the influence of building and street geometries on flow and dispersion characteristics. Questions are also raised as to the effect of street corners and side streets on the in-canyon wind flow and dispersion characteristics. Chapters 5 and 6 will investigate the influences of traffic, both as contributing to dispersion mechanisms and as a source of pollution, respectively.

## 5.2. Experimental method

### 5.2.1. The site

The field study was conducted for one month between 13 October 2003 and 12 November 2003 in the Bootham and Gillygate street canyons. The measurements of the mean in-canyon wind and turbulence fields were undertaken inside the Gillygate street canyon (Chapter 4). The measurements of the concentration fields and traffic characteristics were undertaken along both Bootham and Gillygate, which are two streets aligned perpendicular to each other. Chapter 3 mentioned that the field experiment allowed for the simultaneous and continuous measurement of the mean in-canyon wind, turbulence and concentration fields and traffic characteristics. For clarity, the streets have a common traffic-signal controlled intersection as depicted in Figure 5.1. Bootham is aligned at approximately 312° clockwise from N. Gillygate is orientated predominantly at 45° from N, although it is aligned approximately 30° from N at the opposite end to the common intersection. Portland Street and Claremont Terrace are two residential streets that adjoin Gillygate perpendicular to the street axis.

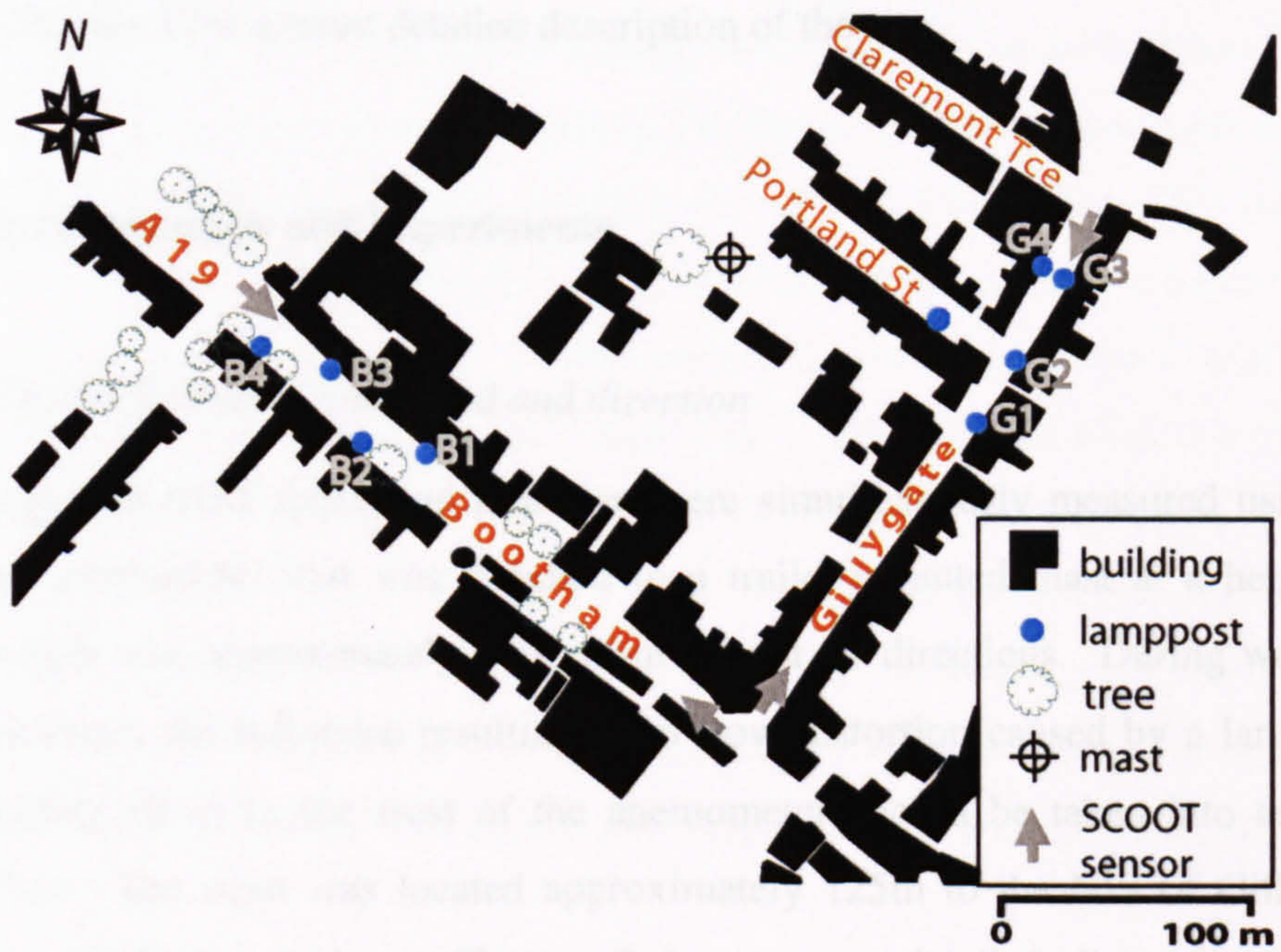


Figure 5.1. Plan view of the study area showing the street canyons, the lampposts that support the instruments, the reference anemometer mast, the locations of the significant trees and the four SCOOT sensors (arrows indicate the direction of traffic flow measured).

Buildings of different heights and with complex roof shapes surround both streets allowing for a range of street canyon geometries to be studied within one experiment. The geometry of a street canyon is usually described by its height ($H$) to width ($W$) ratio (or aspect ratio). The height of the buildings on both sides of the Gillygate street canyon was 12 m. Therefore, Gillygate is a relatively narrow symmetrical street canyon, with $H/W \approx 0.8$.

The Bootham street canyon geometry is more varied, and although $H/W$ was nominally 0.65 throughout the canyon, it was asymmetrical in places at the cross-sections near the instruments. The aspect ratio at the experiment section of Bootham was different for the two perpendicular wind directions as the building heights were different on both sides of the street. The height of the buildings on the SW and NE sides of the canyon was 14 m and 12 m, respectively. For background winds from the SW the aspect ratio was ~0.75, whereas it was ~0.6 for background winds from the NE. There are also several trees along Bootham, some of which were adjacent to the instruments used in the study (see Figure 5.1). Both streets have high traffic flows, with significant periods of congestion. The influence of congestion and the associated stop-start driving modes is investigated in Chapter 7. Reference should be made to Chapter 3 for a more detailed description of the site.

### 5.2.2. Instrumentation and Experiments

#### *5.2.2.1. The background wind speed and direction*

The background wind speed and direction were simultaneously measured using an ultrasonic anemometer that was attached to a trailer-mounted mast at a height of 19.5m, which was approximately 1.8H from almost all directions. During westerly winds, however, the influence resulting from flow distortion caused by a large tree approximately 10 m to the west of the anemometer should be taken into account (Figure 5.1). The mast was located approximately 125m to the NW of Gillygate. Reference should be made to Chapter 3 for a more detailed discussion of the experimental methodology.

*5.2.2.2. Carbon monoxide concentrations*

The traffic-related pollutant measured in this study was carbon monoxide (CO). One of the reasons for choosing CO was because petrol engine vehicles are the primary source in street canyons (Derwent *et al.*, 1995). Additionally, CO can be regarded as being an inert tracer due to the very short distance between source and receptor in street canyon experiments and its low reactivity on these short timescales. This is not the case with $NO_2$, which rapidly dissociates in the presence of light, or with NO, which reacts very quickly with ozone (Palmgren *et al.*, 1996). The chemical lifetime of CO is very long (several weeks) compared to other pollutants (Dennis *et al.*, 1996). Therefore, CO can be used as a traffic-related 'tracer' in a study of the influence of dispersion within a street canyon. Furthermore, the mean diurnal concentrations of other traffic-related pollutants such as $NO_x$ (Väkevä *et al.*, 1999) and particle number concentration in the range 0.01 to 10μm (Penttinen *et al.*, 2001, Ketzel *et al.* 2003) have been found to correlate reasonably well with CO close to traffic sources allowing it to be used as an effective traffic-related tracer.

15-minute averages of one minute samples (reported at the end of each time period) of CO concentrations were measured using electrochemical sensors, incorporated within Learian streetboxes. It was mentioned in Chapter 3 that co-location surveys conducted at a street side location in central London prior to the experiment utilising two streetboxes and a US EPA certified Gas Filter Correlation CO Analyser demonstrated the precision, repeatability and reliability of the streetbox measurement of CO over a one-month period. When compared with the reference analyser $r^2$ values of 0.95 and 0.96 were achieved (Tate, 2005). CO has been used as a tracer to indicate significant differences in traffic-related pollutant concentrations between neighbouring streets in London (Croxford *et al.*, 1996) and between different sides of the same street (Croxford and Penn, 1998). On both occasions, experiments were conducted on the performance of two streetboxes against conventional non-dispersive infrared (NDIR) equipment. The results also indicated excellent correlations, with $r^2$ of better than 0.8.

The streetbox locations discussed in this Chapter for both street canyons are depicted in Figure 5.1. Figure 5.2 shows the relative location of the streetboxes and the

anemometers attached to lampposts G3 and G4 at the Gillygate experiment cross-section, although it should be noted that no in-canyon anemometer data is presented in this Chapter (see Chapter 4). All streetboxes in Bootham were at a height of 3.5m, allowing for an investigation into the spatial variability in the concentrations of CO along a street canyon. Whilst the spatial survey was still of interest in Gillygate, the streetboxes in this canyon were located at heights of 3.5m and 7.0m in order to investigate the vertical gradient in the concentration of CO. Streetboxes were unable to be located along the entire length of Gillygate from the common intersection due to the absence of lampposts.

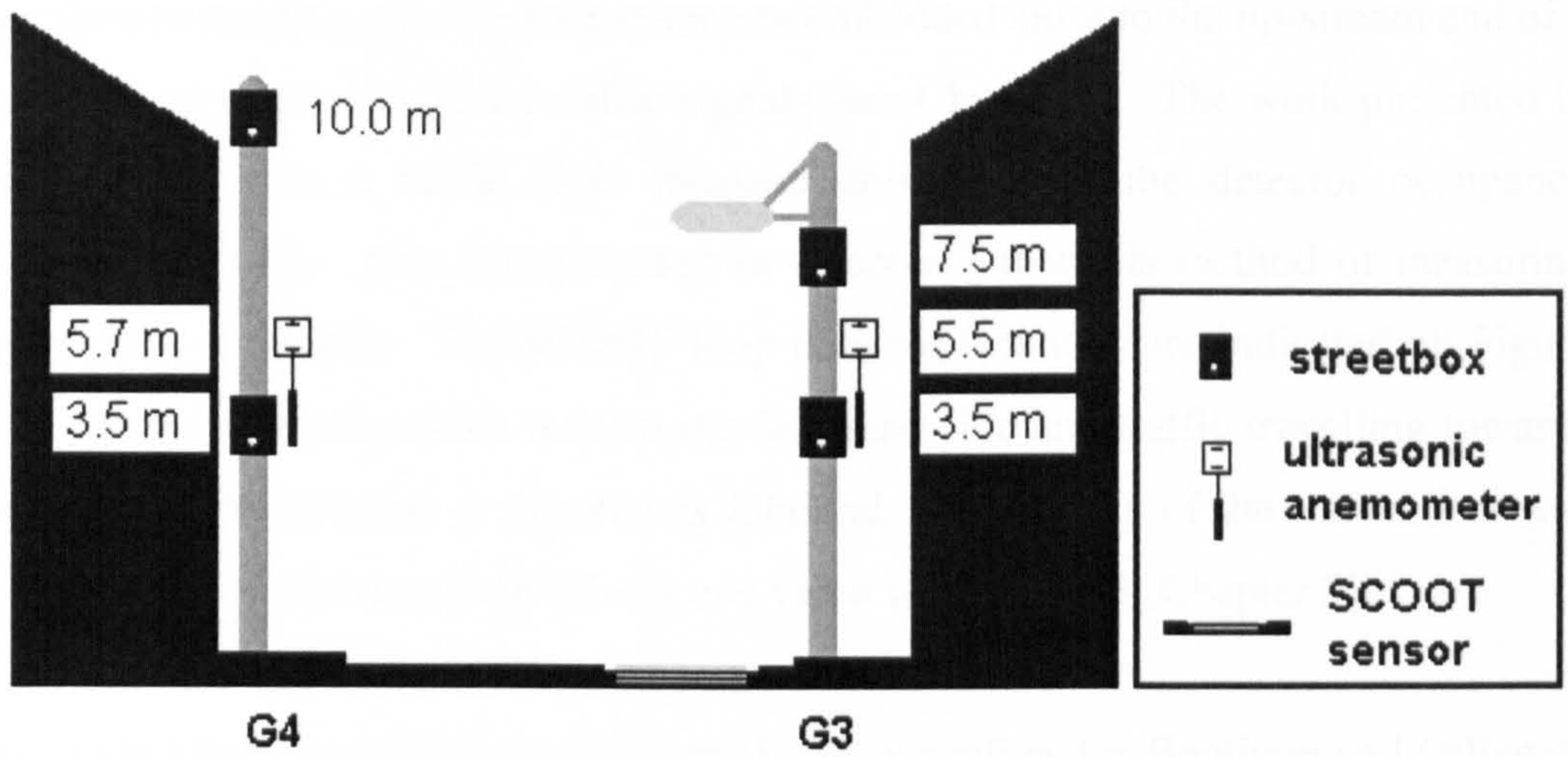


Figure 5.2. Schematic of the Gillygate canyon cross-section at G3-G4, showing relative instrument locations.

In addition to the co-location survey, further QA-QC techniques were applied as detailed in Chapter 3. Prior to the experiment all streetboxes were calibrated using a multi-gas calibrator. The calibration gases used were zero-gas and CO concentrations of 3 ppm. All streetbox data were linearly corrected according to the most recent zero-gas calibration. A check of CO concentrations using the calibration gas at concentrations of 3 ppm confirmed that the span was accurate to within 10%. This suggests that the variability in the CO concentrations measured during the experiment caused by the resolution of the sensor was considerably less than the variability attributed to meteorological and traffic conditions. The streetbox on G4 at 7.0 m failed halfway through the experiment, therefore, comparison is made with the streetbox data on the same lamppost at 10.0 m (Figure 5.2). For all other streetboxes used in the present study the data collected were continuous. Data quality was

assessed through the combined analysis of the concentration frequency distributions to identify outliers, coupled with analysis of the time-series concentration plots for noise spikes. No further [CO] data were excluded on this basis. Conditional analysis of the data did remove some values and each technique will be described in turn below.

*5.2.2.3. The traffic flow characteristics*

The traffic flow characteristics for both streets were obtained as a by-product of the SCOOT system (Hunt *et al.*, 1991). SCOOT provides a variety of traffic flow measures from piezo-electric loop detectors embedded close to the up-stream end of a link, or road section, between traffic signals (see Chapter 3). The work presented in this Chapter uses a traffic flow measure derived from the detector occupancy operating at 4 Hz. It is demonstrated in Chapter 7 that this method of measuring traffic flow is reliable. The SCOOT loop detector locations are indicated on Figure 5.1. For both streets, traffic was on the left hand side and traffic travelling towards the common intersection is denoted as inbound. The quality of the traffic data was assessed in a similar way to [CO] and one value was removed (Chapter 3).

The bi-directional (or total) weekday traffic flow profiles for Bootham and Gillygate are represented as 15-minute aggregates and diurnal averages for the whole monitoring period in Figure 5.3. Overall, the average diurnal total traffic flow for Gillygate between 06:30 and 22:00 was 860 vehicles $h^{-1}$ compared with 750 vehicles $h^{-1}$ for Bootham. Gillygate had a distinct peak in the total traffic flow at 08:00 and a less distinct peak at 18:00. However, in Bootham the average diurnal total traffic flow profile shows a more distinct peak at 19:00 than for the morning. The lowest average diurnal flow of approximately 40 vehicles $h^{-1}$ occurred in both streets at 04:00. The variability between days is quite low but is highest in Gillygate during the late morning period.

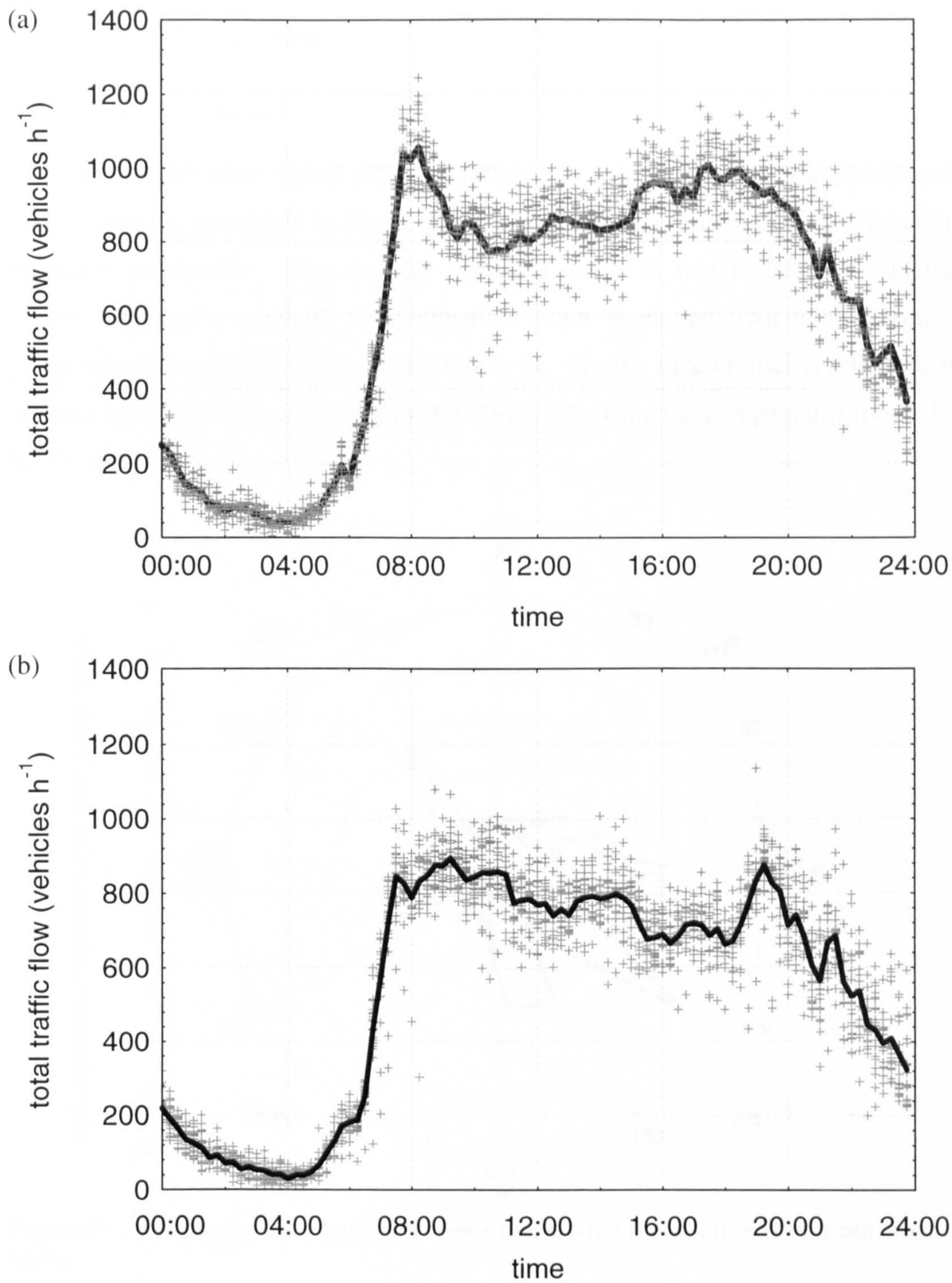


Figure 5.3. Total traffic flow during the experiment period for (a) Gillygate and (b) Bootham: +15-minute aggregate; ▬ average diurnal profile.

## 5.3. Results and Discussion

### *5.3.1. Background winds*

The background wind speed ($U_{ref}$) and direction ($\theta_{ref}$) data from the above-roof anemometer are presented in Figure 5.4 as a wind speed rose and a wind direction frequency distribution. The data are averaged using 15 minute intervals and the overall average for each 10° wind direction sector is plotted. All wind direction angles reported increase clockwise relative to N. For the sake of clarity, reference is made to wind direction sector angles at 45° intervals using the compass directions: N; NE; E; SE; S; SW; W; and NW.

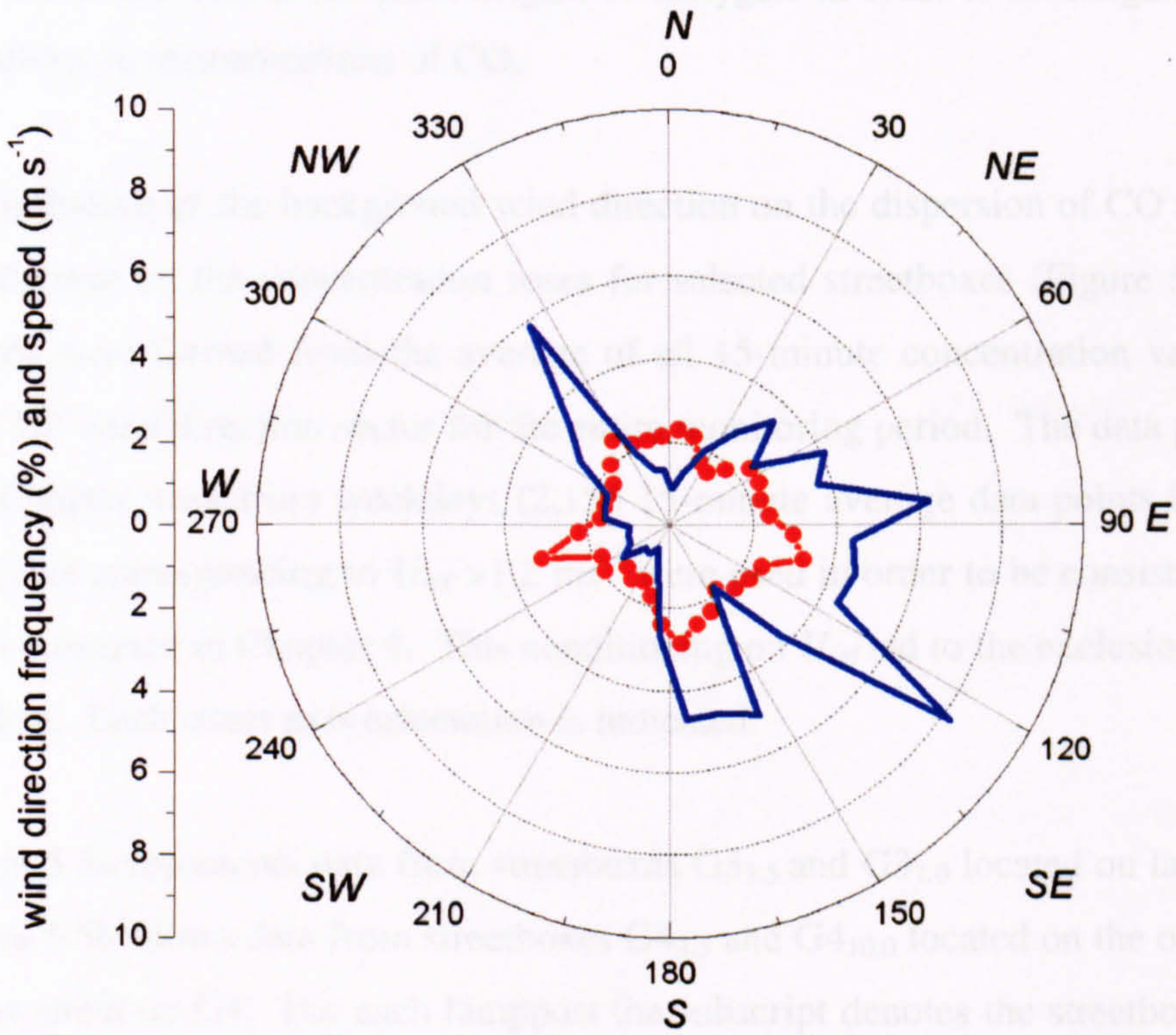


Figure 5.4. Frequency distribution of: —— mean wind direction; —●— mean wind speed.

The predominant winds were from the SE and NW, with only very few occurrences from the SW. Since each street canyon is approximately perpendicular, a direct comparison could be made between simultaneous CO concentrations in one canyon with predominantly parallel background winds and the adjacent canyon with predominantly perpendicular background winds. The maximum background wind speeds were from the S and WSW, although the mean speeds from other wind

direction sectors remained relatively high with $U_{ref}$ >2.0 m $s^{-1}$ occurring 50% of the time.

*5.3.2. Spatial variability in CO concentrations in the Gillygate street canyon*

The turbulent mixing of the in-canyon volume of air implies that any two measurements of a pollutant conducted at close proximity to each other in a street can differ significantly (Croxford *et al.*, 1996). Furthermore, traffic congestion and the characteristic stop-start traffic flows may also provide substantial variability with distance from a traffic-signal controlled intersection (see Chapter 7). With this in mind, the streetboxes were located at the same height on different lampposts along each street and also at different heights in Gillygate in order to investigate the spatial variability in concentrations of CO.

The influence of the background wind direction on the dispersion of CO in Gillygate is indicated on the concentration roses for selected streetboxes (Figure 5.5). These figures were formed from the average of all 15-minute concentration values within each 10° wind direction sector for the entire monitoring period. The data presented in this Chapter were from weekdays (2,156 15-minute average data points in total) and only data corresponding to $U_{ref}$ >1.2 $ms^{-1}$ were used in order to be consistent with the work presented in Chapter 4. This conditioning on $U_{ref}$ led to the exclusion of 25% of the data. Each street axis orientation is indicated.

Figure 5.5a represents data from streetboxes $G3_{3.5}$ and $G3_{7.0}$ located on lamppost G3. Figure 5.5b shows data from streetboxes $G4_{3.5}$ and $G4_{10.0}$ located on the opposite side of the street on G4. For each lamppost the subscript denotes the streetbox height (in metres). The highest concentrations were measured at the lowest streetboxes, $G3_{3.5}$ and $G4_{3.5}$. The vertical variation in mean concentrations on each side of the street is also indicated by the greater difference in concentrations between $G4_{3.5}$ and $G4_{10.0}$, when compared with the difference between $G3_{3.5}$ and $G3_{7.0}$. Whilst there is some evidence of vertical dilution, further studies are required at heights up to and including the rooftop, in order to fully understand the degree of mixing along vertical gradients within street canyons (see Väkevä *et al.*, 1999).

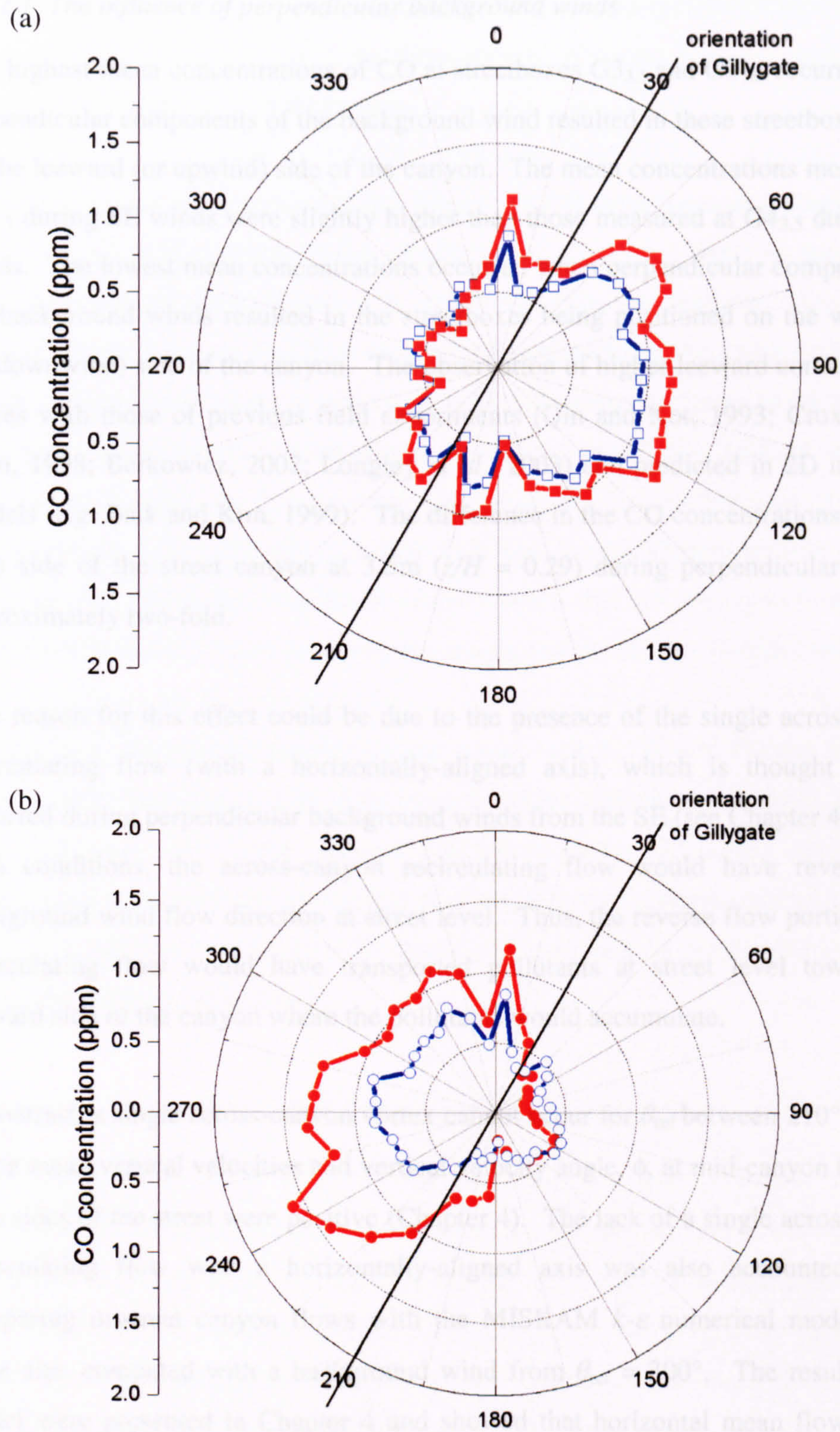


Figure 5.5. Sector-averaged CO concentrations (ppm) in Gillygate: (a) —■— streetbox $G3_{3.5}$ and —□— streetbox $G3_{7.0}$; (b) —●— streetbox $G4_{3.5}$ and —○— streetbox $G4_{10.0}$.

*5.3.2.1. The influence of perpendicular background winds*

The highest mean concentrations of CO at streetboxes $G3_{3.5}$ and $G3_{7.0}$ occurred when perpendicular components of the background wind resulted in these streetboxes being on the leeward (or upwind) side of the canyon. The mean concentrations measured at $G3_{3.5}$ during SE winds were slightly higher than those measured at $G4_{3.5}$ during NW winds. The lowest mean concentrations occurred when perpendicular components of the background winds resulted in the streetboxes being positioned on the windward (or downwind) side of the canyon. The observation of higher leeward concentrations agrees with those of previous field experiments (Qin and Kot, 1993; Croxford and Penn, 1998; Berkowicz, 2002; Longley *et al.*, 2003) and predicted in 2D numerical models (e.g. Baik and Kim, 1999). The difference in the CO concentrations between each side of the street canyon at 3.5m ($z/H$ = 0.29) during perpendicular $\theta_{ref}$ was approximately two-fold.

One reason for this effect could be due to the presence of the single across-canyon recirculating flow (with a horizontally-aligned axis), which is thought to have occurred during perpendicular background winds from the SE (see Chapter 4). Under such conditions, the across-canyon recirculating flow would have reversed the background wind flow direction at street level. Thus, the reverse flow portion of the recirculating flow would have transported pollutants at street level towards the leeward side of the canyon where the pollutants would accumulate.

In contrast, a single across-canyon vortex cannot occur for $\theta_{ref}$ between 210° and 30°, as the mean vertical velocities and vertical velocity angle, $\phi$, at mid-canyon height on both sides of the street were positive (Chapter 4). The lack of a single across-canyon recirculating flow with a horizontally-aligned axis was also accounted for by comparing in-street canyon flows with the MISKAM $k$-$\varepsilon$ numerical model of the same site, computed with a background wind from $\theta_{ref}$ = 300°. The results of the model were presented in Chapter 4 and showed that horizontal mean flow at mid-canyon height was channelled by the background wind along Portland Street and Claremont Terrace (see Figure 5.1). Counter-rotating corner vortices (with vertically-aligned axes) formed at the corners of the streets inside the Gillygate street canyon, producing two opposing along-canyon flows. Flow convergence occurred within the

canyon at a location close to the G3-G4 experiment cross-section. The converging along-canyon flow coupled with the development of corner vortices contributed to updraughts on either side of the canyon.

It is believed that the counter-rotating corner vortices (with vertically-aligned axes), which formed at the corners of the adjoining side streets are likely to have lead to flow reversal at the canyon floor i.e. the street-level flow was opposite to the direction of the above-roof flow. The flow reversal is expected to be the cause of the higher concentrations of CO on the leeward (G4) side of the canyon relative to the windward (G3) side. With the CO concentration data alone it would have seemed sensible to have concluded that the flow reversal was caused by the development of a classic across-canyon vortex of the type that develops during skimming flow regimes. However, one of the particular merits of this study is that the in-canyon flow features were investigated simultaneously with the measurements of the CO concentrations.

In summary, the concentration roses for streetboxes at G3 and G4 are in general axisymmetric (see Figure 5.5), they are a result of completely different in-canyon flow structures. The higher leeward concentrations for G3 during perpendicular background flows are likely to be due to a single across-canyon recirculating flow, whereas at G4 there are likely to be due to the formation of corner vortices formed due to the adjoining side streets.

*5.3.2.2. The influence of parallel and oblique background winds*

The concentration roses (Figure 5.5) for Gillygate also indicate significant dependence of CO concentrations on $\theta_{ref}$ when the background winds were parallel or oblique to the street axis. Significantly higher concentrations during parallel winds from 210° were measured by streetbox $G4_{3.5}$ compared with $G4_{10.0}$ (see Figure 5.5b). Whilst this may indicate more limited vertical mixing of pollutants during parallel conditions, there is a reduced difference in CO concentration with height on the opposite side of the street, possibly suggesting the influence of more localised flow features. Low mean concentrations occurred on both sides of the street during parallel winds from 30°. During $\theta_{ref}$ = 30°, the in-canyon flow was associated with shorter traffic queues in this direction, compared with winds from 210° for which $\theta_{ref}$

is upstream of a long section of the street canyon that extends from the common intersection.

The results from the Gillygate and Bootham street canyon field experiment suggest that the mean concentrations are also lower during parallel wind flows compared with near-parallel flows. Parallel background winds are likely to have 'flushed' the pollutant along and ultimately out of the canyon in a channel flow (see Chapter 4). It is acknowledged that parallel winds may not always be the cause of low in-canyon concentrations as the concentrations measured are dependent upon sources, such as junctions or roundabouts, located upwind (see Vardoulakis *et al.*, 2002).

Recall from Chapter 4 that the results from the present filed experiment suggest that the minimum values in the mean horizontal wind speeds measured at mid-canyon height (i.e. $M_{G3}$ and $M_{G4}$) occurred during perpendicular background winds. However, the minimum values in $M_{G4}$ are offset by approximately 20° during near-perpendicular background winds. Similar values in $M_{G3}$ and $M_{G4}$ occurred during parallel background winds from 30° and 210° on both sides of the street.

The highest mean concentration measured at streetbox $G4_{3.5}$ occurred during oblique winds from the SW rather than from the perpendicular NW. Furthermore, oblique winds from between 5° and 10° coincide with high mean concentrations at both $G3_{3.5}$ and $G4_{3.5}$. Oblique NE winds also caused high mean concentrations at streetbox $G3_{3.5}$ although this feature is absent at $G4_{3.5}$ due to the likely influence of an across-canyon vortex. Furthermore, traffic commonly queued in the streets leading up to the junction at the NE end of Gillygate during periods of extreme congestion. Oblique background winds may have induced a helical flow regime along the canyon (see Nakamura and Oke, 1988), which may explain the higher concentrations measured during oblique winds compared with parallel winds in Gillygate. The coupling of a strong along-canyon flow with across-canyon recirculation supports the existence of a helical flow. Background wind flows oblique to the street axis, therefore, influence along-canyon flow (Chapter 4).

An additional feature of interest is that whilst a single across-canyon recirculating flow was shown to not be present during perpendicular background flows from the

NW (Chapter 4), it is possible that for oblique background winds (e.g. $\theta_{ref} = 240°$) a helical recirculating flow may have existed. For this case $\phi_{G3} = -\phi_{G4}$ (Chapter 4) and the across-canyon recirculating flow (with a horizontally-aligned axis) appears to have been strong enough to overcome the influence of channelled flows from the adjoining side streets. A possible reason for this is the increased momentum of the vortex due to a strong along-canyon flow component for background winds from this direction, as shown in Chapter 4. This is also supported by the high in-canyon wind speeds found on both sides of the street under these conditions, as shown in Chapter 4. The presence of downdraughts on the windward side of the canyon and updraughts on the leeward side during oblique background winds is further supported by the observations of the mean vertical wind velocity, which was of opposite sign (Chapter 4). This analysis was continued in Chapter 4, which shows that asymmetrical vertical wind angles were measured on either side of the canyon, particularly during $\theta_{ref} = 240°$. The recirculating helical flows, therefore, are likely to have been driven by the oblique winds aloft. Helical flows are likely to have transported CO predominantly in an along-street flow, but also in a recirculating flow from the windward side of the canyon to the leeward side.

Helical flows are likely to produce reasonably good mixing of pollutants along the canyon. This is supported by evidence in Figure 5.6a showing similar mean concentration profiles at positions G1, G2 and G3 along the canyon for most background wind directions despite variations in building and street geometries. Overall, the profile of the $G1_{3.5}$ concentration rose is similar to $G3_{3.5}$. However, some differences in the concentration roses for streetboxes $G1_{3.5}$, $G2_{3.5}$ and $G3_{3.5}$ do occur due to the presence of side streets. For instance, Portland Street adjoins Gillygate directly opposite streetbox $G2_{3.5}$ and, therefore, high buildings exist on only one side (as shown in Figure 5.1). This may be accounted for if a weaker across-canyon vortex (with a horizontally-aligned axis) developed at G2 compared to the vortex described earlier at G3, resulting in an almost two-fold difference in mean CO concentrations for background winds from the SE sector. It is possible that an isolated roughness regime developed during $\theta_{ref} = 120°$ at G2 rather than a skimming flow regime, which would have transported some pollutants out of Gillygate and into Portland Street.

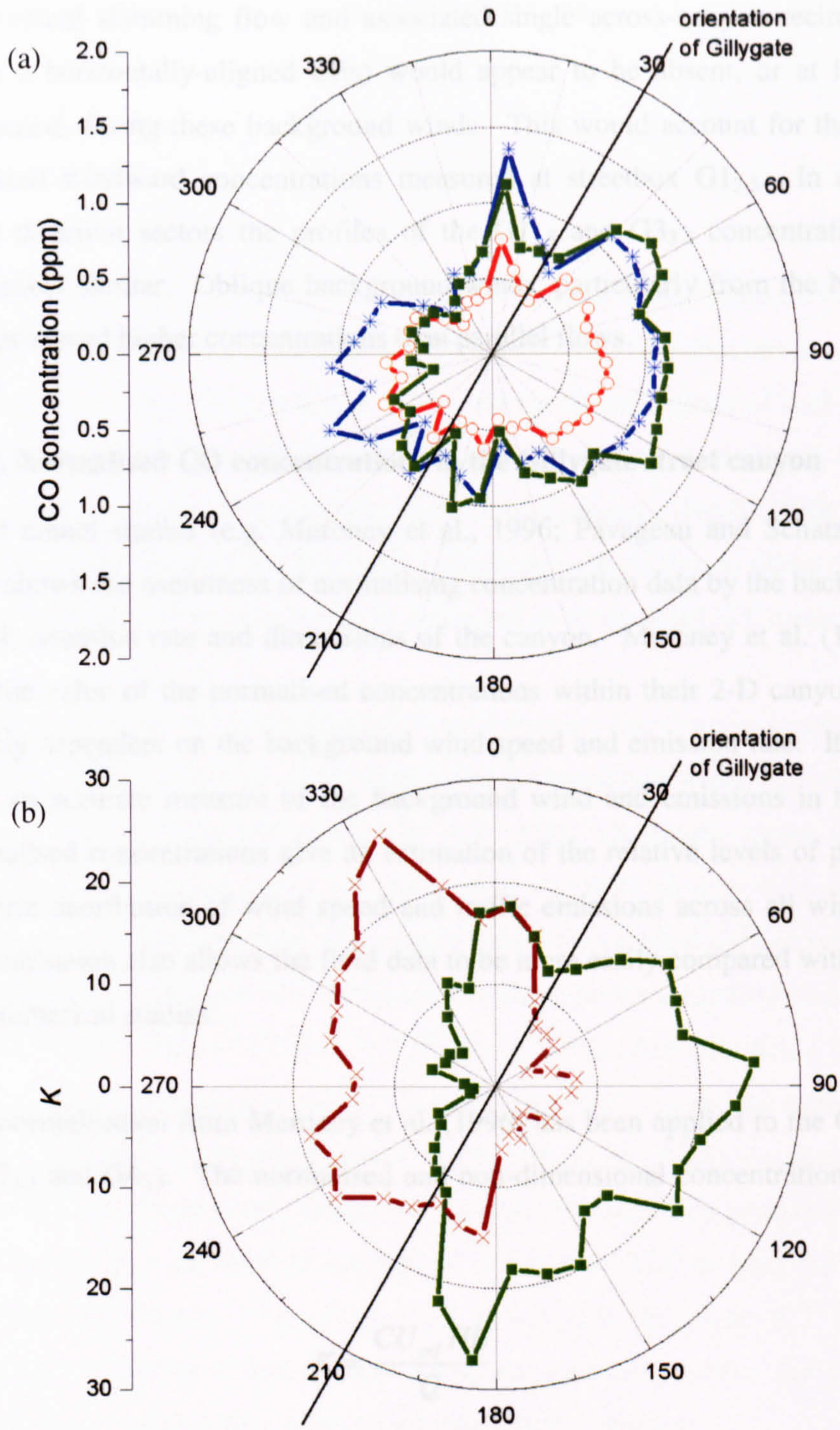


Figure 5.6. Sector-averaged CO concentrations (ppm) in Gillygate: (a) —✳— streetbox $G1_{3.5}$; —○— streetbox $G2_{3.5}$ and —■— streetbox $G3_{3.5}$; (b) Normalised sector-averaged CO concentrations using Equation (5.1) for: —■— $G3_{3.5}$ and —×— $G4_{3.5}$.

A small opening also exists along the NW canyon wall opposite streetbox $G1_{3.5}$. During background winds from the W and WNW a portion of the flow is likely to have transported CO at street level towards the sensor on the other side of the canyon.

The typical skimming flow and associated single across-canyon recirculating flow (with a horizontally-aligned axis) would appear to be absent, or at least severely weakened, during these background winds. This would account for the higher than expected windward concentrations measured at streetbox $G1_{3.5}$. In all remaining wind direction sectors the profiles of the $G1_{3.5}$ and $G3_{3.5}$ concentration roses are noticeably similar. Oblique background winds, particularly from the NNE and NE, also produced higher concentrations than parallel flows.

### 5.3.3. Normalised CO concentrations in the Gillygate street canyon

Wind tunnel studies (e.g. Meroney et al., 1996; Pavageau and Schatzmann, 1999) have shown the usefulness of normalising concentration data by the background wind speed, emission rate and dimensions of the canyon. Meroney et al. (1996) showed that the value of the normalised concentrations within their 2-D canyons were only weakly dependent on the background wind speed and emission rate. It follows that, with an accurate measure of the background wind and emissions in the street, the normalised concentrations give an estimation of the relative levels of pollutant for a uniform distribution of wind speed and traffic emissions across all wind directions. Normalisation also allows the field data to be more easily compared with wind tunnel and numerical studies.

The normalisation from Meroney et al. (1996) has been applied to the Gillygate data at $G3_{3.5}$ and $G4_{3.5}$. The normalised and non-dimensional concentration $K$ is defined as:

$$K = \frac{CU_{ref}HL}{Q}, \tag{5.1}$$

where $C$ is the raw concentration of CO (mg m$^{-3}$ converted from ppm and with the background concentration subtracted), $U_{ref}$ (m s$^{-1}$) is the wind speed measured at the mast, $H$ (m) is the height of the canyon and $Q/L$ (mg s$^{-1}$ m$^{-1}$) is the CO emission per unit length along the canyon. As it is not possible to directly measure the actual emissions along the streets during the experiment an estimate has to be made from the

SCOOT traffic data. For simplicity, a linear relationship between the emissions and the total traffic flow is assumed:

$$\frac{Q}{L} \approx e\mathcal{T}, \tag{5.2}$$

where $\mathcal{T}$ is the total traffic flow in vehicles $s^{-1}$ and $e$ is an averaged emission factor for vehicles using the street. A value of 7.81 mg $m^{-1}$ $veh^{-1}$ was derived for $e$ on Gillygate during peak flows, which is based on the vehicle classifications of traffic in Gillygate from a large number of traffic counts and the emissions database from the UK government's National Atmospheric Emissions Inventory (NAEI, 2004). Using such a simple model for the emissions will exclude any effects due to idling or acceleration within the traffic flow, which will be discussed in more detail in Chapters 7 and 8.

Figure 5.6b shows the normalised CO concentration rose for the streetboxes at $G3_{3.5}$ and $G4_{3.5}$. The plot shows the average value for weekdays when $U_{ref}$ was greater than 1.2 $ms^{-1}$ and for times between 06:30 and 22:00. Overnight values were excluded because the low values of CO recorded led to a large relative error in the normalised concentration. Unfortunately, no suitable urban background concentration data were available for CO in the NAEI Air Quality Archive (www.airquality.co.uk). However, a background value of 0.2 ppm (~0.25 mg $m^{-3}$) has been subtracted from each 15-minute mean concentration value. The estimate of 0.2 ppm was typical of the CO values measured in Portland Street during 06:30 to 22:00 on weekdays and is consistent with tropospheric background levels. The streetbox used in Portland Street was attached to a lamppost at a height of 3.0 m and ~25.0 m from the junction with Gillygate (see Figure 5.1). Figure 5.7 shows that the mean CO concentrations measured in Portland Street were found to have very little variation with the background wind direction when conditioned in this manner.

Figure 5.7 also shows the unit standard deviation of the mean concentration for each 10° wind direction sector. The diurnal mean CO concentrations measured in Portland Street did show a distinct peak at approximately 08:45 and a less distinct peak at approximately 18:30 (not shown). These times most likely relate to the peak commuting periods. However, it should be stressed that there was little variability in

the mean concentrations measured for the times between the peak periods, when the mean concentrations were ~0.2 ppm.

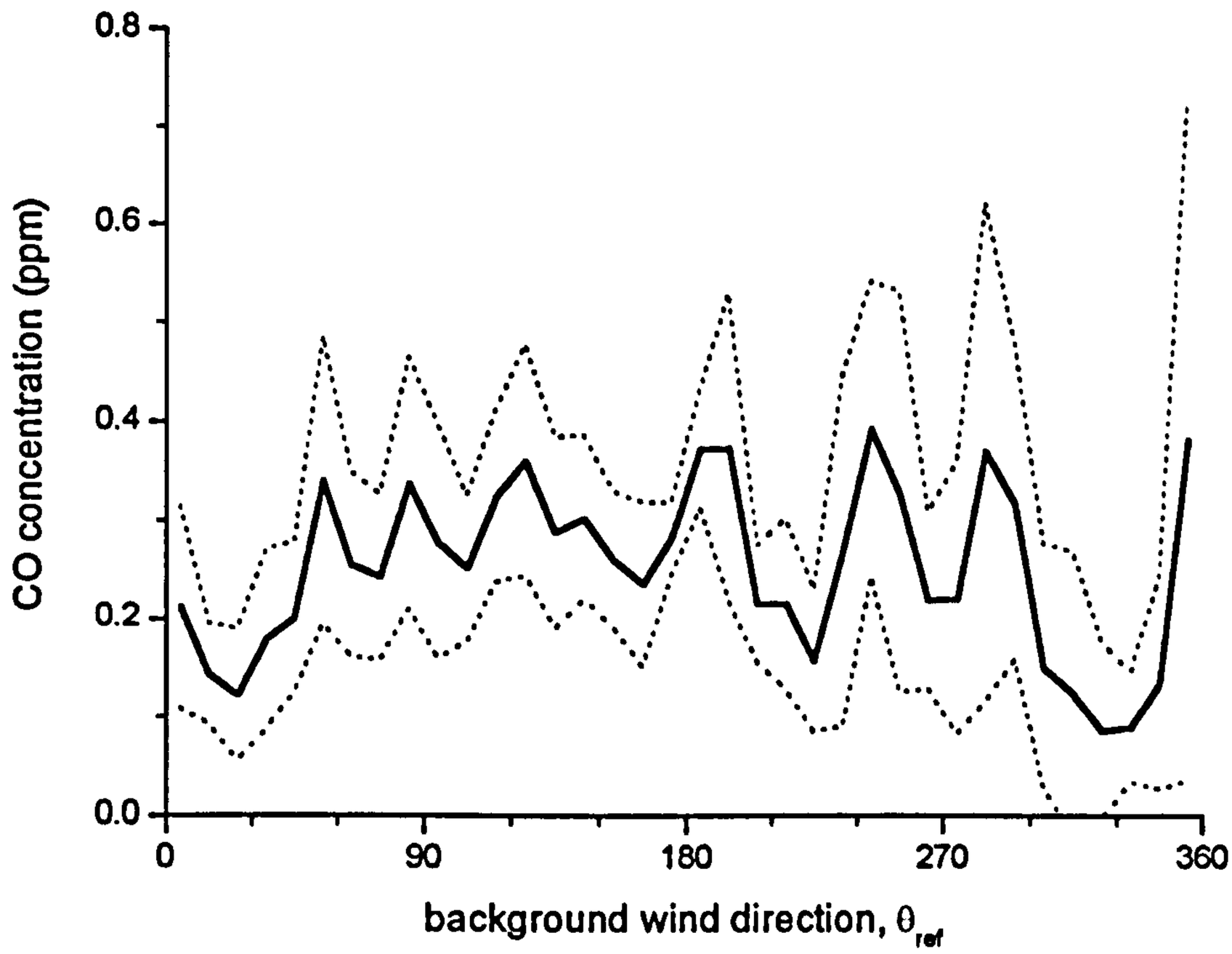


Figure 5.7. The variability in the mean CO concentrations measured in Portland Street against the background wind direction, $\theta_{ref}$, conditioned on $U_{ref}$ >1.2 $ms^{-1}$ and times between 06:30 and 22:00. The mean concentrations are shown as ——— and the unit standard deviation is shown as ------.

By comparing the normalised and raw concentration roses (Figure 5.6a and Figure 5.5) it can be seen that the normalisation has reduced the relative values for winds from 210° – 250° and at approximately 5° for both $G3_{3.5}$ and $G4_{3.5}$. Conversely, new maximum values occur at 185° for $G3_{3.5}$ and 335° for $G4_{3.5}$. The ratio of normalised concentrations between leeward and windward sides of the street is now over 3 for perpendicular winds from both the NW and SE, compared with approximately 2 in the raw concentrations. Pavageau and Schatzmann (1999) recorded values of $K$ around 85 and 35 on the leeward and windward sides of the canyon in their wind tunnel study at similar relative heights to the streetboxes in Gillygate. The higher values in the wind tunnel possibly reflect the higher aspect ratio ($H/W$ = 1) and also the reduced ventilation in a 2-D canyon compared to the real street canyons studied here.

The normalisation procedure raises some interesting issues relating to the use of the background (or reference) measurements of the wind flow for comparison between measured data and model predictions. For example, it is likely that the large tree located in close proximity to the mast anemometer distorted the background winds, reducing the measured wind speed for background winds from 270°. This resulted in lower normalised concentrations measured by $G3_{3.5}$ and $G4_{3.5}$ during winds from 270°, compared with adjacent wind directions (Figure 5.6b).

A similar effect also exists for background winds from between 135° and 175°. York Minster is approximately 370 m upwind of the mast anemometer for $135° < \theta_{ref} < 150°$. By computing the standard deviation of the background wind direction, $\sigma_{\theta ref}$, using the method of Skibin (1984), both the influence of the tree and the Minster correspond to data over wind direction ranges for which $\sigma_{\theta ref}$ is relatively large (greater than 40°), compared with non-affected directions ($\sigma_{\theta ref} \cong 20°$, not shown). Since the Minster is a large building with the main structure at a height of approximately $3H$ and three towers extending to approximately $5H$, it is expected that the building is likely to cause significant disturbances to background winds from the SE and S, as was measured by the mast anemometer.

Additionally, the in-canyon anemometers are 320 m upwind of the Minster for $150° < \theta_{ref} < 175°$). Therefore, relative to the Minster, differences in the locations of the in-canyon anemometers and the mast implies that the use of the background wind speed measured at the mast (i.e. $U_{ref}$) within the normalisation procedure for winds from this direction causes some problems. This is because $U_{ref}$ does not necessarily give an accurate representation of the flow directly above the roof of the study canyon for these background wind directions. Chapter 4 also discussed problems associated with using $U_{ref}$ to normalise mean wind and turbulence parameters. In urban environments with complex building structures of a similar type to those studied in this Chapter, the use of a single reference measurement for the whole city could be problematic. In this case, the relatively small displacement of 125 m between the mast anemometer and G3 and G4 highlights this issue.

*5.3.4. Mean concentrations in the Bootham street canyon*

Figure 5.8 shows mean CO concentration roses in the Bootham street canyon. The streetbox pairs $B1_{3.5}$ and $B3_{3.5}$ were on the leeward side of the canyon during NE background winds; whereas the streetbox pairs $B2_{3.5}$ and $B4_{3.5}$ were on the leeward side during SW winds (see Figure 5.1). Overall, the CO concentrations were approximately a factor of two lower in Bootham compared with Gillygate, despite total traffic flows measured in the street being only 20% lower compared with Gillygate. The higher mean concentrations of CO during perpendicular winds suggest evidence of an across-canyon recirculating flow (with a horizontally-aligned axis), although it does not necessarily imply a skimming flow regime as strong as the one observed for Gillygate due to the lower aspect ratio of Bootham. However, the scale of difference between the leeward concentrations compared with those measured on the windward side was up to two-fold larger than those measured in Gillygate.

The lower observed CO concentrations along Bootham might be partly related to the greater predominance of parallel background wind flows measured during the experiment, as well as its lower aspect ratio compared to Gillygate. The lower aspect ratio provides a larger cross-sectional area within which pollutants may be diluted. Additionally, if a weaker recirculating flow occurs in a canyon of this aspect ratio, then the across-canyon vortex would break down more easily during winds from directions off-perpendicular to the street axis. The across-canyon recirculating flow may also be destabilised by the trees located in the canyon (see Figure 5.1). This would account for the relatively large change in concentration shown in Figure 5.8b.

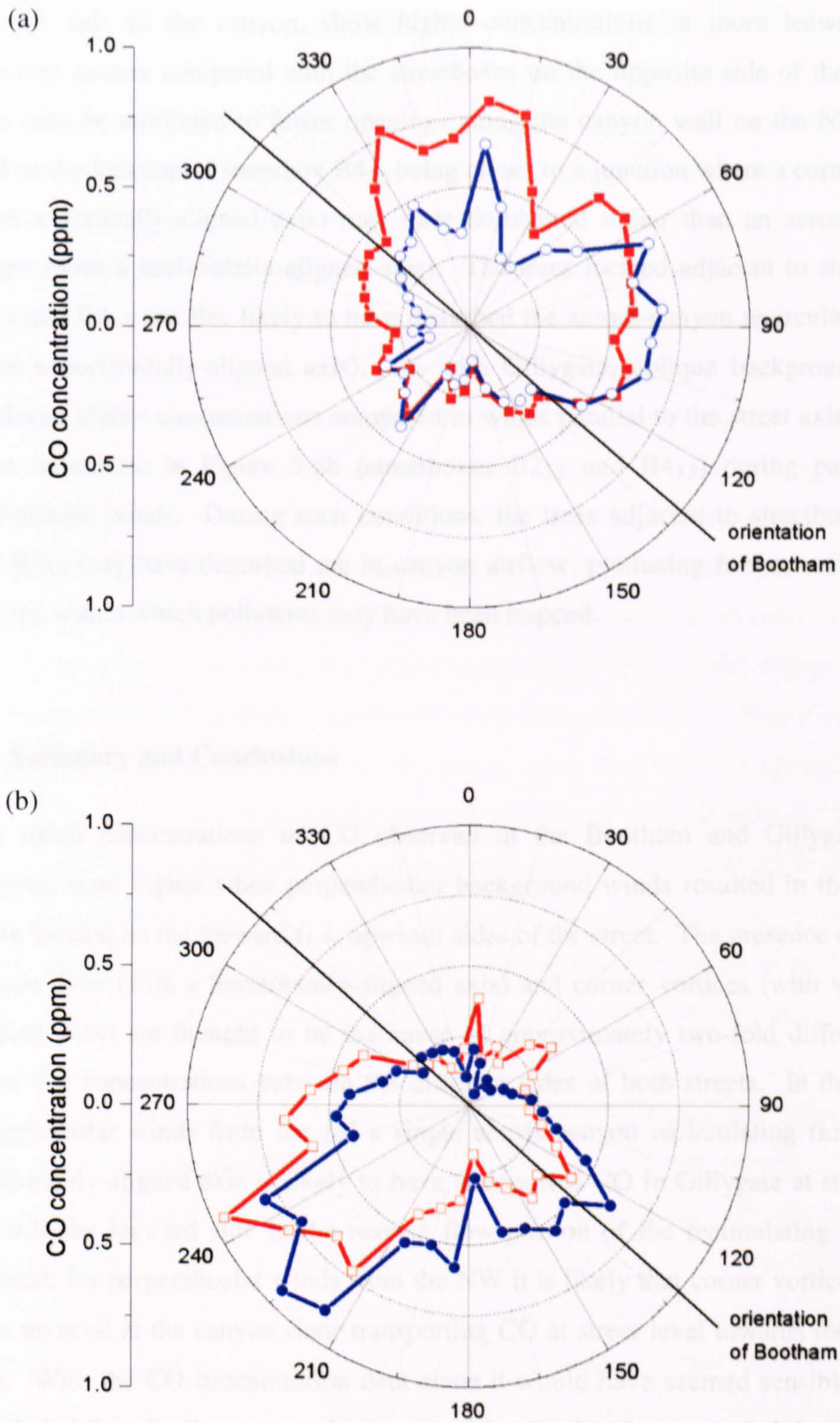


Figure 5.8. Sector-averaged CO concentrations (ppm) in Bootham: (a) —■— streetbox $B1_{3.5}$; and —○— streetbox $B3_{3.5}$ (b) —□— streetbox $B2_{3.5}$ and —●— streetbox $B4_{3.5}$.

The concentration roses (Figure 5.8a) for streetboxes $B1_{3.5}$ and $B3_{3.5}$, which were on the NE side of the canyon, show higher concentrations in more leeward wind direction sectors compared with the streetboxes on the opposite side of the canyon. This may be attributed to fewer openings along the canyon wall on the NE side as well as the location of streetbox $B4_{3.5}$ being closer to a junction where a corner vortex (with a vertically-aligned axis) may have dominated rather than an across-canyon vortex (with a horizontally-aligned axis). The trees located adjacent to streetboxes $B2_{3.5}$ and $B4_{3.5}$ are also likely to have disturbed the across-canyon recirculating flow (with a horizontally-aligned axis). As with Gillygate, oblique background winds produced higher concentrations compared to winds parallel to the street axis. This is most noticeable in Figure 5.8b (streetboxes $B2_{3.5}$ and $B4_{3.5}$) during parallel SE background winds. During such conditions, the trees adjacent to streetboxes $B2_{3.5}$ and $B4_{3.5}$ may have disturbed the in-canyon airflow, producing further recirculation regions within which pollutants may have been trapped.

## 5.4. Summary and Conclusions

The mean concentrations of CO observed in the Bootham and Gillygate street canyons were higher when perpendicular background winds resulted in the sensors being located on the leeward (i.e. upwind) sides of the street. The presence of across-canyon flow (with a horizontally-aligned axis) and corner vortices (with vertically-aligned axes) are thought to be the cause of approximately two-fold differences in mean CO concentrations between the different sides of both streets. In the case of perpendicular winds from the SE a single across-canyon recirculating flow with a horizontally-aligned axis is likely to have transported CO in Gillygate at street level towards the leeward side in the reverse flow portion of the recirculating flow. In contrast, for perpendicular winds from the NW it is likely that corner vortices lead to flow reversal at the canyon floor transporting CO at street level towards the leeward side. With the CO concentration data alone it would have seemed sensible to have concluded that the flow reversal was caused by the development of a classic across-canyon vortex with a horizontally-aligned axis of the type that develops during skimming flow regimes. However, one of the particular merits of this study was that

the in-canyon flow features were investigated simultaneously with the measurements of the CO concentrations and this was found not to be the case.

Comparisons between the concentration roses and the normalised concentrations also revealed the influence of the traffic upwind of the background flow. Comparisons of CO concentrations measured at different heights in Gillygate indicate a degree of vertical mixing, which also gives support to the presence of an across-canyon vortex under certain conditions.

The mean CO concentrations measured in Bootham were presented as a function of the background wind direction and also revealed that concentrations were a factor of two larger on the leeward side of the canyon compared to the windward side. The CO concentration data can produce an indirect method of determining in-canyon flow features. Therefore, it seems reasonable to conclude that a single across-canyon is the most likely cause of difference in concentrations given the absence of large openings of the type that Portland Street produced in the Gillygate canyon. However, without simultaneous measurements of the in-canyon wind flow and turbulence it is not possible to accurately determine the flow characteristics inside Bootham. Therefore, when using the indirect method to determine in-canyon flow features for other street canyons consideration must be given to the likelihood of corner vortices (with vertically-aligned axes and across-canyon flow) developing rather than the classic single across-canyon recirculating vortex (with a horizontally-aligned axis).

Comparisons between the mean concentrations observed in the two street canyons indicate lower concentrations in the wider Bootham canyon despite only small differences between the total traffic flows within each street. In addition to the presence of trees, the lower aspect ratio would be expected to cause the development of a weaker across-canyon vortex structure (with a horizontally-aligned axis) during perpendicular background flows as well as providing a larger volume in which emissions may be diluted. Significantly lower concentrations in Bootham due to its overall geometry, despite only small differences in total traffic flows, raises important issues related to traffic management within such streets (see also Chapter 7). Traffic activity and urban and physical topography need to be considered in tandem when developing traffic management and control strategies to manage the spatial

distribution of emissions better within street canyons, since the dispersion of emissions is more efficient in some streets than in others.

The study also shows evidence that oblique background winds play a significant part in the dispersion of CO in both street canyons. High CO concentrations either side of the street axis coincide with oblique background winds. Background winds from 45° either side of the street axis resulted in horizontally channelled flows along the canyon. During oblique background winds, helical flows were shown to cause significantly higher concentrations on the leeward side of the canyon due to across-canyon flow recirculation than during parallel background winds.

Parallel background winds were found to have limited across-canyon and vertical mixing and are associated with channel flows. As a result lower mean concentrations of CO were measured during parallel background winds than for other background wind directions. This suggests that channel flows with strong along-canyon flow components are likely to have flushed traffic-related pollutants along and ultimately out of the canyon.

Concentrations normalised by the background wind speed and total traffic flow showed similar structures to non-normalised results, although a threefold difference between the leeward and windward sides of the street was observed. The normalisation procedure is essential for any comparison with model predictions of concentrations and it highlighted problems in defining appropriate reference measurements across a complex city. In particular, the large structure of York Minster was found to influence the normalised profiles.

This Chapter investigated the dispersion of CO in two street canyons and the focus was primarily on the interaction of the background winds with the local building and street geometries. It has been demonstrated that differences in geometry along a canyon and differences in the traffic flow result in contrasting in-canyon wind flows and dispersion characteristics. The streets used in the present study are not untypical of UK urban areas and, therefore, it is likely that the flow features found would be present in other situations. The helical flow regime, for example, has been identified in recent field studies carried out in a central London location (Dobre *et al.*, 2005).

What is important is that numerical models attempting to represent the dispersion of traffic-related pollutants within urban areas should be capable of describing such features. The study presented in this Chapter, therefore, provides a useful data set for the evaluation of such numerical models in more complex situations than the idealised street canyon case (see Dixon *et. al.*, 2005). Model predictions of the spatial variability of any traffic-related pollutant in a non-regular canyon with adjoining side streets should, thus, incorporate understanding of the complex in-canyon flows that develop under certain background wind conditions. This has special relevance to predicting the relative exposure of people to pollutants not only within street canyons but also indoors according to the predominant background wind direction frequency and speed.

# CHAPTER 6

## The influence of traffic-produced turbulence as a potential pollutant dispersion mechanism

### 6.1. Introduction

High concentrations of traffic-related pollutants in street canyons are associated with low background wind speed conditions, as mentioned in Chapter 2. However, operational street canyon dispersion models commonly perform poorly under these conditions. Typically these models are structured to have an inverse relationship between the concentration field and the background wind speed, $U_{ref}$, and this relationship leads to substantial overestimation of the concentrations during low wind speeds (Britter and Hanna, 2003).

It was stated in Chapter 2 that mechanically produced turbulence depends on the roughness of the surface and the speed of the horizontal wind flow. Other sources of turbulence include convection, which involves the vertical exchanges of air, from heated urban surfaces and from vehicle exhausts and engines, as mentioned in Chapter 2. There is also the mechanical production of turbulence from the motion of vehicles, which is known as traffic-produced turbulence (TPT). Therefore, mechanically produced turbulence inside street canyons is assumed to be composed of two parts: one is dependent upon the background wind speed, $U_{ref}$, and direction, $\theta_{ref}$, causing shear turbulence production (see Chapter 4); and the other is due to TPT. When $U_{ref}$ is low TPT dominates and because the highest concentrations often occur during these conditions, appropriate modelling of these features is crucial (Kastner-Klein *et al.*, 1998; Ketzel *et al.*, 1999).

### 6.1.1. Previous studies

The generation of turbulence by moving vehicles has been the subject of several theoretical and experimental investigations, although the TPT effects are applicable to fast moving cars on open roads (see Eskridge and Hunt, 1979; Eskridge and Thompson, 1982; Eskridge and Rao, 1986; Rao *et al.*, 1986; Thompson and Eskridge, 1987; Grønskei, 1988; Eskridge *et al.*, 1991; Watkins *et al.*, 1995). There have been a number of studies on the dispersion of traffic-related pollutants in street canyons (e.g. Bauman *et al.*, 1992; Rotach, 1995; Sini *et al.*, 1996; Louka *et al.*, 1998, 2000; Väkevä *et al.*, 1999; Longley *et al.*, 2004a). However, only a limited number of full-scale field experiments have focused on investigating the influence of TPT on the dispersion of such pollutants. The lack of field measurements of TPT can be attributed to the fact that it is difficult to separate traffic from other sources of turbulence, such as thermally-generated turbulence or shear turbulence associated with the background wind (Chapter 4).

Previous studies conducted to investigate the influence of TPT effects have already been mentioned in Chapter 2 and, therefore, this Section will be kept relatively short. Vachon *et al.* (2002) described the influences of traffic motions on the production of turbulence inside a deep three-lane street canyon with one-way traffic and $H/W$ of 1.4 in Nantes, France (Chapter 2). They attributed the increased levels of TKE found in the lower half of the canyon to TPT. They found turbulence enhancement close to the traffic region on both windward and leeward sides of the street. The influence was more pronounced on the leeward side and the vertical extent of the TPT region was much larger than on the windward side. Vachon *et al.* (2002) propose that this phenomenon is caused by the advection of turbulence produced in the traffic region towards the leeward side due to the wind-induced single across-canyon flow (with a horizontally-aligned axis). Therefore, a single across-canyon flow with a somewhat destabilized structure may develop in street canyons even during weak perpendicular background winds. Data are presented in this Chapter from the Gillygate street canyon field experiment, which will allow for a more detailed examination of this explanation.

As described in Chapter 2, the recently obtained wind tunnel and field results have significantly contributed to a better understanding of TPT effects on street canyon airflow and dispersion and their interaction with wind-induced flow phenomena. However, the incorporation of traffic effects in dispersion models is still rudimentary (Di Sabatino *et al.*, 2003). Recently, however, there have been studies of the influence of TPT on street canyon concentration fields using wind tunnel experiments for no traffic, one-way traffic and two-way traffic flows (Kastner-Klein *et al.*, 1998; 1999; 2000; 2001; Di Sabatino *et al.*, 2003). For instance, Kastner-Klein *et al.* (1998; 1999; 2001) released a tracer gas ($SF_6$) at a constant rate from the floor of the canyon and found that during one-way traffic flows, there were pronounced along-canyon airflow and dispersion conditions. The concentration distribution along the canyon displayed strong lateral skewness, with concentrations increasing in the direction of traffic-produced airflow. Pearce and Baker (1997) fired single and multiple numbers of vehicles along a wind tunnel model of a street canyon with a simulated perpendicular airflow and a tracer gas that was released from the floor of the wind tunnel as a line source along the length of the canyon. Reference should be made to Chapter 2 for a more detailed discussion of these results.

Di Sabatino *et al.* (2003) estimated the magnitude of TPT, or at least it was an appropriate scaling, from a production-dissipation balance for TKE (Chapter 2). They estimated TPT by considering three vehicle-wake conditions: isolated vehicle-wakes, wake-interfering vehicles and totally overlapping wakes. These conditions are analogous to the isolated, wake-interference and skimming flow regimes described by Oke (1988) to explain the effects of buildings on the wind flow (see Chapter 2).

Kastner-Klein *et al.* (1999) developed and evaluated a scaling concept based on the background wind speed and vehicle speed for pollutant concentration data against field and wind tunnel data. They found that their scaling more realistically described concentration distributions than the standard method, which assumes the concentrations are inversely proportional to the background wind speed, $U_{ref}$, as mentioned earlier. Kastner-Klein *et al.* (2003) compared these results with kerbside measurements of $NO_x$ that were collected over a period of several years in three separate street canyons in Hanover and Berlin in Germany and in Copenhagen, Denmark. They found that the traditional concentration scaling, which employs the

background wind speed as a normalising factor, was inappropriate in urban street canyon situations during low $U_{ref}$.

The incorporation of TPT into the semi-empirical Operational Street Pollution Model (OSPM) led to a marked improvement in the model performance, especially for the extreme events (Berkowicz, 2000a). According to Di Sabatino *et al.* (2003), the OSPM considers traffic inside a street canyon as the superposition of individual vehicles. They also stated that the TPT parameterisation is based on the assumption that the motion of vehicles produces an overall variance of the velocity fluctuations proportional to the square of the vehicle velocity. The coefficient of proportionality is linked to the drag coefficient of the vehicles and its value is empirically determined by fitting velocity variances and concentration data obtained in field experiments (Chapter 2). However in this Chapter the coefficient of proportionality is taken to be unity due to the absence of mean CO concentration collected within the layer in which TPT effects are most active. In other words, the aim of the analysis was to test the functional dependence only.

Kastner-Klein *et al.* (2003) suggested that the analysed experimental data gave indications of different scaling laws for TPT and resulting concentration fields during different traffic conditions. In particular, they were able to distinguish between light density and intermediate density traffic conditions. However, their analysis also had a number of uncertainties within the field data. For example, traffic velocity was not measured and the estimates used may be erroneous. These uncertainties would also affect the estimation of the emission rates that depend on the traffic velocity (see Chapters 7 and 8). In order to make more definitive conclusions, therefore, any further field experiments must incorporate a method to include traffic speed.

### 6.1.2. Chapter synopsis

In this Chapter the interaction of the background winds with the surrounding building and street geometries on in-canyon turbulence intensities produced by moving vehicles has been studied experimentally in the Gillygate street canyon. In addition to traffic producing an additional pollutant dispersion mechanism to the in-canyon airflow (Chapter 4), characteristics of the traffic flow also cause variability in

pollutant concentrations (Chapter 7). However, specific investigations in this Chapter are focused on the factors influencing the production of turbulence during low background wind speed conditions, and include: (i) the variation of the in-canyon turbulence relative to the background wind direction, and (ii) the effect of the background wind speed. The measured in-canyon vertical velocity standard deviations and TKE are compared against results from TPT formulations.

## 6.2. Theoretical Background

Mechanical turbulence is produced in a street canyon by the wind and passing traffic, as mentioned earlier. The effects of thermal stratification in enhancing or suppressing turbulence are neglected in this work and neutral stability is always assumed. Berkowicz *et al.* (1997a) suggested that vehicles in street canyons are considered in OSPM to be moving flow distortion elements creating additional turbulence. It should be stressed that the OSPM only calculates the vertical turbulence component, $\sigma_w$ (Berkowicz, 2000b). Reference should be made to Berkowicz *et al.* (1997a) for more information on the TPT parameterisation incorporated into OSPM.

Buckland (1998) employed the formulation used in OSPM to incorporate TPT effects into an operational model. More recently, Gidhagen *et al.* (2004) used the TPT parameterisation of OSPM following a similar method to Buckland (1998) in order to formulate the effect of TPT in traffic flow of cars and HGVs, rather than total traffic flow. However, the use of actual drag coefficients for the two vehicle classes, rather than using the value of 0.3, would possibly improve the predictive quality of the models. Furthermore, traffic flow in street canyons is often unstable, i.e. the traffic flow switches between periods of free flow and congested flow (Chapter 7) and it is, therefore, necessary to consider traffic characteristics when formulating TPT. Unstable traffic flows usually comprise of platoons of vehicles travelling at low speed with interacting wakes, i.e. vehicles travelling close together one after the other.

Di Sabatino *et al.* (2003) developed a conceptual framework to parameterise TPT under various traffic densities, which is required for the incorporation of traffic effects in dispersion models. Di Sabatino *et al.* (2003) focussed on integral,

operational models in which TPT and wind-generated turbulence components are implemented. However, aspects of the TPT parameterisation are also likely to be applicable in numerical dispersion models. As stated by Di Sabatino *et al.* (2003), the principle aim of employing TPT parameterisation is to improve concentration predictions during conditions when wind- and thermally-generated turbulence play insignificant roles and TPT components are the dominant dispersion mechanism.

The TPT analysis of Di Sabatino *et al.* (2003) and Kastner-Klein *et al.* (2003) is based on the production-dissipation balance for TKE generated by a single vehicle or a platoon of vehicles travelling in a street canyon. For clarity, the two articles are published back-to-back in the same journal as part I and part II, respectively. The TKE produced by traffic-produced velocity fluctuations, $TKE_t$, must be represented by:

$$TKE_t = 0.5(\sigma_{ut}^2 + \sigma_{vt}^2 + \sigma_{wt}^2).$$

The subscript notation $t$ refers to the component of turbulence related to TPT. Therefore, if $(\sigma_{ut}^2 + \sigma_{vt}^2 + \sigma_{wt}^2)$ is equal to $\sigma_t^2$ then $TKE_t$ should be equal to $0.5 \cdot \sigma_t^2$. Since these traffic-related velocity fluctuations vary in space, Di Sabatino *et al.* (2003) state that a representative TPT magnitude must be based on a spatially averaged value of the standard deviation, $\sigma_{mt}$. The TPT analysis presented in Di Sabatino *et al.* (2003) is based on the production-dissipation balance for TKE generated by a single vehicle or a platoon of vehicles in a street canyon, using adequate averaging volumes discussed in detail below.

Di Sabatino *et al.* (2003) described the general form for the TKE production, $P$, for one or several vehicles as:

$$P = N \cdot v \cdot C_D \cdot \left(0.5\rho \cdot v^2\right) \cdot h^2, \tag{6.1}$$

where $N$ is the number of vehicles producing turbulence (dimensionless), $C_D$ is the average drag coefficient of the vehicles, $v$ is the vehicle speed, $h$ is the geometrical length scale of the vehicles and $\rho$ is the density of air. The cross-sectional area of the

vehicles, $A_c$, can be defined using $h^2$ and must be the area used in defining the drag coefficients. The square root of $A_c$, therefore, defines $h$.

The production of TKE per unit mass of air, $P_t$, for TPT is:

$$P_t = \frac{N \cdot v \cdot C_D \cdot (0.5\rho \cdot v^2) \cdot h^2}{\rho \cdot V_t} = \frac{0.5N \cdot C_D \cdot v^3 \cdot h^2}{V_t}, \tag{6.2}$$

According to Di Sabatino *et al.* (2003), the averaging volume, $V_t$, could be identified as either the volume of a relatively thin layer at the floor of the street canyon that is restricted to the traffic region; or the volume of the whole canyon. Using the spatially averaged TPT value, $\sigma_{mt}$, where the subscript refers to mean turbulence, the dissipation of TKE per unit mass, $\varepsilon$, is formulated by:

$$\varepsilon = c_1 \cdot \frac{\sigma_{mt}^3}{l_\varepsilon}, \tag{6.3}$$

where $l_\varepsilon$ is the length scale used to model the dissipation of TKE and $c_1$ is the dimensionless constant. Equating (6.2) and (6.3) gives the general expression for $\sigma_{mt}^3$:

$$\sigma_{mt}^3 = c_2 \cdot N \cdot \frac{C_D \cdot h^2 \cdot l_\varepsilon \cdot v^3}{V_t}, \tag{6.4}$$

where $c_2$ is equal to $(2\ c_1)^{-1}$. It should be mentioned that there is confusion in the TPT parameterisation formulated by Di Sabatino *et al.* (2003) and Kastner-Klein *et al.* (2003) and a detailed discussion is given in Section 6.2.4.

Before it is possible to consider the averaging volumes and length scales to be used in the analysis, consideration of the relevant traffic characteristics is required. Figure 6.1 presents a theoretical time-series of the turbulent wakes produced by vehicles travelling along a street canyon, where $T$ is the time period of passing vehicles and $\tau$ is the lifetime of the turbulent wake produced by a single vehicle. Traffic flow $q$ can

be used to determine $T$, as $T$ is equal to $1/q$ (Berkowicz, 2000b). Although turbulence is shown schematically in Figure 6.1 it is acknowledged that turbulence traces tend to go to zero relatively quickly. However, the figure is a useful representation of turbulence in the wake of a passing vehicle, as will be demonstrated in the following sections.

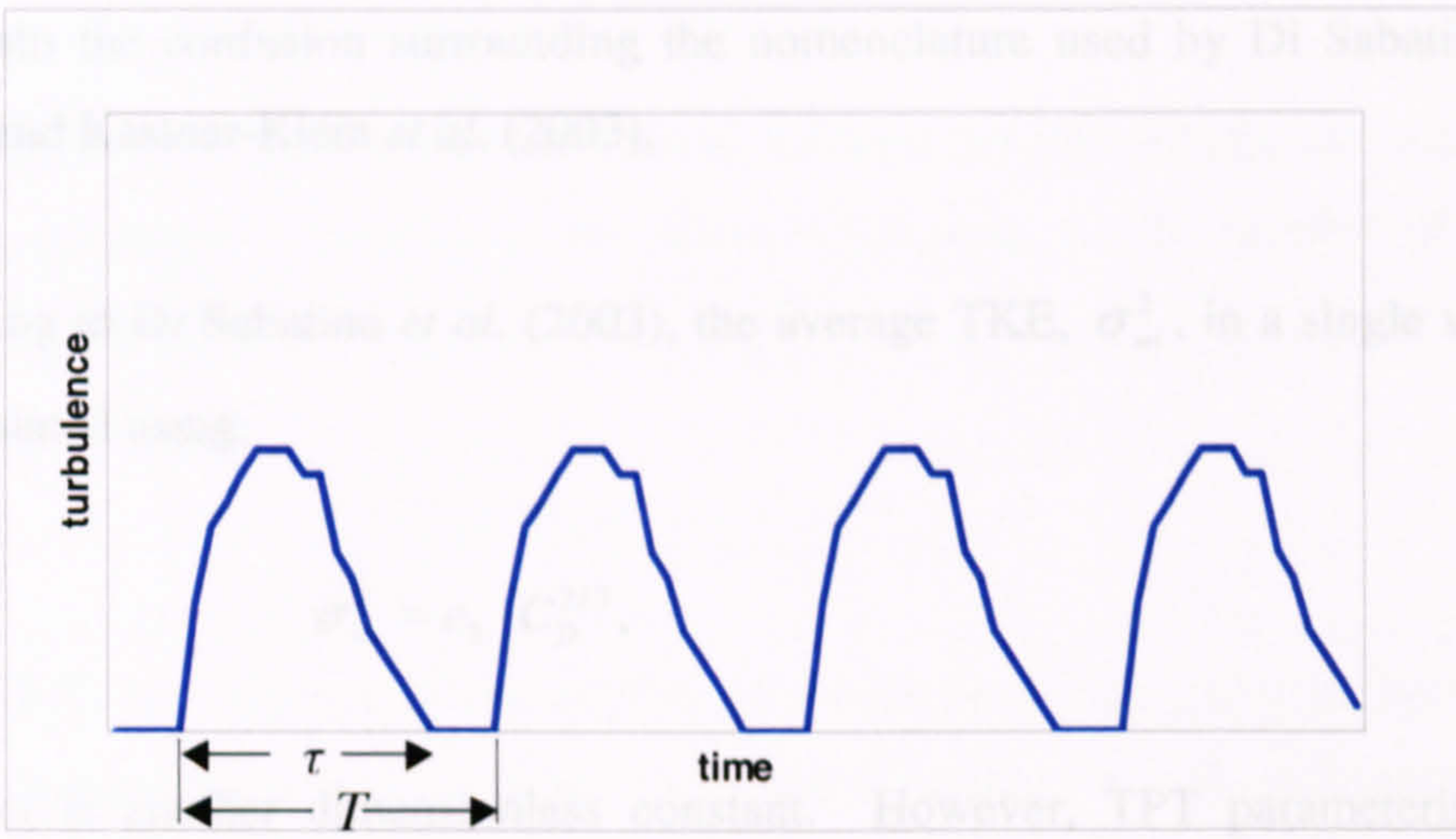


Figure 6.1. Theoretical representation of the turbulence produced by vehicles travelling at constant speed along a street canyon and with equal distance between consecutive vehicles (modified from Berkowicz, 2000b).

### 6.2.1. Low traffic density: no interaction between vehicle wakes

In the case of low traffic density with large gaps between successive vehicles there will be little interaction between the turbulent wakes, i.e. $\tau << T$ (Figure 6.1). According to Di Sabatino *et al.* (2003), the size of the wake will be related to the geometrical length scale of the vehicle, which will also determine the dissipation length scale. Thus, the unknown parameters in Equation (6.4) can be described as:

$$N = 1\,; \tag{6.5}$$

$$V_t \propto h^3\,; \tag{6.6}$$

$$l_\varepsilon \propto h \quad . \tag{6.7}$$

The parameter described above in (6.6) can be deduced from Equation (6.4) where $V_t \propto h^2 \cdot l_\varepsilon$ and incorporating $l_\varepsilon$ from (6.7).

Di Sabatino *et al.* (2003) used (6.5) – (6.7) in order to derive a measure of the average TKE, $\sigma_{wt}^2$, in a single wake. A degree of confusion may be partly created by the choice of subscript used by Di Sabatino *et al.* (2003) and it is unclear whether the subscript *w* refers to the vertical velocity component, *W*, or vehicle wake. It is also unclear whether the subscript *t* is consistent with previous notation and, thus, refers to TPT or instead refers to TKE. In Section 6.2.4 a more detailed discussion will be given into the confusion surrounding the nomenclature used by Di Sabatino *et al.* (2003) and Kastner-Klein *et al.* (2003).

According to Di Sabatino *et al.* (2003), the average TKE, $\sigma_{wt}^2$, in a single wake can be calculated using:

$$\sigma_{wt}^2 = c_3 \cdot C_D^{2/3}, \tag{6.8}$$

where $c_3$ is another dimensionless constant. However, TPT parameterisation in dispersion models does not require a measure of the turbulence produced in one particular wake, $\sigma_{wt}^2$. Instead, what is required is an average value of the turbulence produced over a part of the street canyon, $\sigma_{ct}^2$, of length, *L*, width, *W*, and height, *H*. The subscript refers to the calculated turbulence averaged over a section of the canyon. Di Sabatino *et al.* (2003) stated that for the case of non-interacting wakes the $\sigma_{ct}^2$ value could be defined by volume averaging:

$$N \cdot \sigma_{wt}^2 \cdot V_w = \sigma_{ct}^2 \cdot V_c, \tag{6.9}$$

where $V_w \propto h^3$ corresponds to the volume of the wake and $V_c$ describes the averaging volume chosen for inside the canyon. However, the volume $V_c$ is not necessarily related to $L \cdot W \cdot H$ and it can be defined as:

$$V_c = L \cdot S_t, \tag{6.10}$$

where $S_t$ is the cross-sectional area of the street canyon in which TPT occurs, i.e. $S_t \leq W \cdot H$. Di Sabatino *et al.* (2003) mentioned that turbulence could be averaged over the whole canyon or over just the traffic layer. In other words, $S_c = W \cdot H$ describes turbulence averaged over the whole canyon and, perhaps more appropriately, $S_t = W \cdot h$ describes turbulence averaged over the traffic layer. In the work presented in this Chapter the turbulence was averaged over the traffic layer $S_t$.

Using traffic density, $\kappa$, or the number of vehicles per unit length, and the spacing between consecutive vehicles, or the distance headway, $L_v$, the number of vehicles can be expressed by:

$$N = L / L_v = L \cdot \kappa . \tag{6.11}$$

Traffic flow, $q$, is defined as the number of vehicles passing a point in the street per unit time or $q = N/t$, where $t$ is time. Using the definition for $\kappa$ from Equation (6.11) and $v$ = L/$t$, traffic density can be expressed as follows:

$$\kappa = \frac{q}{v} . \tag{6.12}$$

Using Equations (6.9) – (6.11), Di Sabatino *et al.* (2003) finally describe the average turbulence produced over the traffic layer for the case of non-interacting wakes:

$$\sigma_{ct}^2 = c_4 \cdot \kappa \cdot C_D^{2/3} \cdot v^2 \cdot \frac{h^3}{S_t} . \tag{6.13}$$

The above expression contains a new dimensionless constant, $c_4$. Once again, it is not made explicitly clear in Di Sabatino *et al.* (2003) whether the calculated spatially averaged turbulence, $\sigma_{ct}^2$, is for TKE or simply the standard deviation of the vertical velocity component (see Section 6.2.4.). Equation (6.13), according to Di Sabatino *et al.* (2003), describes the expected behaviour $\sigma_{ct}^2 \propto \kappa \cdot v^2$ and it is conceptually in agreement with the TPT parameterisation used in the OSPM (see Berkowicz *et al.*, 1997a). More specifically, Equation (6.13) follows the OSPM parameterisation if $S_t$

$= W \cdot h$ and $c_4 = b^2 \cdot \frac{A_c}{A_p} \cdot C_D^{-2/3}$ where $b^2$ is a factor related to the drag coefficient and $A_c$ and $A_p$ are the average frontal area and plan area of the vehicle, respectively. Therefore, the traffic parameterisation used in the OSPM is appropriately derived for the case of light traffic density during which there is expected to be no interaction between vehicle wakes.

### 6.2.2. Intermediate traffic density: moderate interaction between vehicle wakes

In a real street canyon environment traffic density is usually higher due to congestion and, therefore, consideration must be given to the interaction between the wakes of consecutive vehicles. Di Sabatino *et al.* (2003) considered the average turbulence produced by a platoon of vehicles during intermediate traffic density conditions, i.e. using the terms introduced in Figure 6.1: $\tau > T$. Traffic flow, $N$, in this case was considered in Equation (6.13) to be $N = L \cdot \kappa$.

The volume of the traffic layer, $V_t$, was considered to be:

$$V_t = V_c = L \cdot S_t . \tag{6.14}$$

Furthermore, Equation (6.7) indicates that $l_\varepsilon \propto h$. Taking these factors into account, Di Sabatino *et al.* (2003) expressed the average TKE over the traffic layer for the case of wake-interfering vehicles as:

$$\sigma_{ct}^2 = c_5 \cdot (\kappa \cdot C_D)^{2/3} \cdot v^2 \cdot \frac{h^2}{S_t^{2/3}}, \tag{6.15}$$

where another dimensionless proportionality constant, $c_5$, is introduced. Di Sabatino *et al.* (2003) stated that Equation (6.15) can be used to express the average TKE, although there is some confusion with the TPT parameterisation (see Section 6.2.4).

Di Sabatino *et al.* (2003) stated that during intermediate traffic densities the drag coefficient, $C_D$, remains almost constant or changes modestly as the vehicles are not

densely packed. For a given street canyon geometry, therefore, $\frac{\sigma_{ct}^2}{v^2}$ changes with traffic density according to $\kappa^{2/3}$, i.e. the rate of change is slower than for the case with no wake interaction, which showed a linear dependence of $\frac{\sigma_{ct}^2}{v^2}$ with $\kappa$. Equation (6.15) corresponds to a similarity criterion for the interaction of wind and TPT inside street canyons that has been proposed by Plate (1999) and verified by Kastner-Klein *et al.* (2000).

### 6.2.3. High traffic density: strong interaction between vehicle wakes

Congestion occurs when traffic flow exceeds the network capacity (see Chapter 7). When traffic flow approaches the level at which congestion occurs the traffic density is high and the distance headway is reduced, i.e. high traffic density is characterised by totally overlapping wakes and using the terms introduced in Figure 6.1: $\tau >> T$. The approach to the TPT parameterisation is similar to the case of interacting wakes. However, Di Sabatino *et al.* (2003) assumed that the vehicles are densely packed so that the effective length scale for dissipation is the distance headway and no longer the length scale of the wake:

$$l_\varepsilon \propto L_v = 1/\kappa . \tag{6.16}$$

Therefore, the average turbulence produced in the traffic region of a street canyon for the case of totally overlapping wakes can be described as:

$$\sigma_{ct}^2 = c_6 \cdot C_D^{2/3} \cdot v^2 \cdot \frac{h^{4/3}}{S_t^{2/3}} . \tag{6.17}$$

A new dimensionless constant, $c_6$, is introduced in Equation (6.17). Although Equation (6.17) is quoted accurately from Di Sabatino *et al.* (2003) it is dimensionally incorrect and would require reworking if it is to be used in future studies. The equation shows the TPT effect is expected to become independent of traffic flow if traffic density is high. Di Sabatino *et al.* (2003) also stressed that as the

distance headway decreases, $C_D$ will reduce due to slipstream effects and $\frac{\sigma_{ct}^2}{v^2}$ will consequently decrease. The study by Hong *et al.* (1998) documents the drag reduction for a two-vehicle platoon by operating two full-scale Ford Windstar vans in tandem on an open desert road. Drag forces were measured using a system developed at the University of Southern California. The testing procedure consisted of a smooth acceleration of the platoon. The data collected during acceleration allows the calculation of the drag force on the vehicle following. They found that both vans experience substantial drag savings at headways of a fraction of a vehicle length. These results highlight the importance of incorporating the drag reduction experienced in densely packed platoons into the TPT parameterisation.

### 6.2.4. Confusion concerning the calculated spatially averaged turbulence, $\sigma_{ct}^2$

There is confusion surrounding the calculations described in Equations (6.13), (6.15) and (6.17), which were taken from Di Sabatino *et al.* (2003) to derive the calculated spatially averaged turbulence, $\sigma_{ct}^2$. It is unclear whether $\sigma_{ct}^2$ is best compared against measured $\sigma_w$ or TKE. The confusion is caused by the fact that the equations appear to represent the spatially averaged TKE. In particular, in Di Sabatino *et al.* (2003) Equation (18) described above is to be used to express 'the average turbulent kinetic energy.' However, in part II of the article, Kastner-Klein *et al.* (2003) explicitly state that the standard deviation of the vertical velocity, $\sigma_w$, was calculated using Equations (6.13), (6.15) and (6.17) and compared against $\sigma_w$, which was measured in the street canyon at 10.0 m.

It perhaps should be noted that a simple scaling factor may be used if the mean turbulence is isotropic. However, it is unlikely that the mean turbulence will be isotropic close to the floor of the street canyon, particularly during low background wind conditions when TPT effects dominate. The analysis of the anisotropy of the turbulence presented in Chapter 4 for $U_{ref} > 1.2$ m s$^{-1}$ showed the contribution of each turbulence component measured at various heights within the Gillygate street canyon to TKE. It was found that the turbulence was generally anisotropic across most background wind directions, with the greatest contribution occurring from the along-

canyon component. Given that turbulent wakes produced by passing vehicles are likely to produce strong along-canyon fluctuations during low background wind speed conditions the mean turbulence is even more likely to be anisotropic. Therefore, a simple scaling factor to incorporate into Equations (6.13), (6.15) and (6.17) is unlikely to be suitable but does merit further investigation in future studies.

The confusion also surrounds the claim that Equation (6.13), according to Di Sabatino *et al.* (2003), is conceptually in agreement with the TPT parameterisation used in the OSPM. As the OSPM parameterisation derives the variance of the vertical velocity fluctuations, $\sigma_w^2$, the OSPM parameterisation can only be in agreement with Equation (6.13) if the latter is also used to calculate $\sigma_w^2$.

It was discussed at the start of this Section that TPT can be generated in all three velocity components and that traffic-produced fluctuations must be represented by all three components (i.e. $\sigma_{ut}$, $\sigma_{vt}$ and $\sigma_{wt}$ or simply $\sigma_t$). Ketzel and Berkowicz (2005, pers. comm.) stated that the 'transition' from $\sigma_t$ to only the vertical component fluctuations, $\sigma_{wt}$, used in Equations (6.8), (6.9) and (6.13) was already performed. This implies that the calculated turbulence, $\sigma_{ct}$, is the volume average of the vertical component of TPT, $\sigma_{wt}$. Based on this assumption, therefore, the use of Equations (6.13), (6.15) and (6.17) by Kastner-Klein *et al.* (2003) to calculate $\sigma_w$ was in fact correctly used in the comparisons with measured $\sigma_w$.

Referring to the confusion over the use of the TPT parameterisation, Kastner-Klein (2005, pers. comm) stated that it is somewhat imprecise to compare the TPT parameterisations with measured $\sigma_w$. The stated reasons for doing so included that the dispersion models of the type used in OSPM often use a line source approach to incorporating traffic emissions. Therefore, it could be argued that the TPT effect on the horizontal turbulence components is already accounted for and, consequently, it is only necessary to explicitly parameterise the vertical component of TPT (e.g. OSPM). Therefore, the TPT parameterisation used in Di Sabatino *et al.* (2003) and Kastner-Klein *et al.* (2003) focused on the average vertical component of TPT by following the box-model approach and considering the vertical ventilation of the street canyon due to traffic motions. Furthermore, Kastner-Klein (2005, pers. comm) stated that the

influence of traffic travelling inside street canyons on $\sigma_u$ and $\sigma_v$ is not fully understood.

In order to be consistent with the work of Kastner-Klein *et al.* (2003) the analysis presented in this Chapter includes comparisons of the calculated turbulence, stated as being $\sigma_w$, by using Equations (6.13), (6.15) and (6.17) against measured $\sigma_w$. However, comparisons are also made between calculated turbulence, stated as being TKE, using the same equations against measured TKE.

## 6.3. Methodology

### 6.3.1. Instrumentation and Experiments

#### *6.3.1.1. Background wind speed and direction*

The background wind speed, $U_{ref}$, and direction, $\theta_{ref}$, were measured by the ultrasonic anemometer located at a height of 19.5 m (i.e. 1.8$H$) on top of the trailer-mounted mast (Chapter 3). The data were post-processed and averaged over 15-minute time periods. In order to be consistent with the work presented in Chapter 4, all time periods with less than 90% of the total number of samples (i.e. 18000) were excluded from analysis, i.e. the mean data collection rate was greater than 18 Hz.

In Chapter 4 the standard deviation of the vertical wind, $\sigma_w$, measured by the mid-canyon sonic anemometers located at G3 and G4 (at 5.5m and 5.7m, respectively) were normalised by the background wind speed, $U_{ref}$, and plotted against $U_{ref}$. It was shown that the normalised standard deviations were insensitive to $U_{ref}$ for $U_{ref} > 1.2$ m s$^{-1}$. However, the normalised standard deviations rose sharply during weak background winds. This shows that $\sigma_w$ does not correlate with $U_{ref}$ alone for $U_{ref} \leq 1.2$ m s$^{-1}$ and probably reflects the greater significance of other sources of turbulence, such as TPT. The analysis presented in this Chapter, therefore, excluded all background wind speeds >1.2 m s$^{-1}$ in order to focus purely on TPT and to eliminate as far as possible the effects of the background wind that were described in Chapter 4.

*6.3.1.2. In-canyon wind flow and turbulence*

Measurements of the in-canyon wind and turbulence fields were carried out at a sampling frequency of 20 Hz using four ultrasonic anemometers located at different heights in Gillygate on lampposts G3 and G4. The data from the two mid-canyon anemometers allowed for the analysis of the mean in-canyon wind field for $U_{ref} \leq 1.2$ m $s^{-1}$. The mid-canyon anemometers were located on lampposts G3 and G4 at $z/H$ = 0.46 and $z/H$ = 0.48, respectively. The data were post-processed and averaged over 15-minute time periods. In order to be consistent with the work presented in Chapter 4, all time periods with less than 90% of the total number of samples (i.e. 18000) were excluded from analysis, i.e. the mean data collection rate was greater than 18Hz.

Data was also collected by the sonic anemometer located on lamppost G3 at 3.6 m ($z/H$ = 0.30). The lowest anemometer was located on a supporting stand at a height of 1.1 m ($z/H$ = 0.09) and was positioned directly beneath the anemometers attached to lamppost G3 (Chapter 3). The data from these two anemometers was used in the TPT analysis and forms the majority of the anemometer data presented in this Chapter. The lowest anemometer was only deployed during the TPT measurement surveys in order to avoid acts of vandalism. The data were post-processed and averaged over 1-minute time periods. In order to be consistent with the work presented in Chapter 4, all time periods with less than 90% of the total number of samples (i.e. 1200) were excluded from analysis, i.e. the mean data collection rate was greater than 18 Hz.

The TPT parameterisation used by Di Sabatino *et al.* (2003) and presented in Section 6.2 was evaluated by comparing the modelled results with the measured turbulence inside the Gillygate street canyon. The root-mean square (rms) values of the measured fluctuations in the mean wind velocities averaged over 1-minute time periods were compared against the traffic flow, traffic density and vehicle speed.

*6.3.1.3. Traffic flow and speed*

Manual observations of the inbound traffic flow, including vehicle speed and classification, were conducted beside lamppost G3 using an in-house traffic counting computer program. These traffic surveys were conducted for several hours over a period of 11 days during the October and November 2003 experiment. The vehicles

were classified according to the following six categories: cars; motorcycles; light goods vehicles (LGVs); buses, heavy goods vehicles (HGVs) and 'others'. Depending on the vehicle type, each keystroke of the right-hand represented the moment the front axle of the vehicle crossed a line marked beside lamppost G3. The keystroke by the left-hand represented the moment the rear axle of the same vehicle crossed the line drawn 4 m downstream. This method allowed the measurement of the average speed of each vehicle passing through the 4m section beside lamppost G3. The Appendix contains the equation used to determine the error of the measured vehicle speed.

Vachon *et al.* (2002) presented data on the effect of vehicle speed on the measured kerbside TKE. Although this is the only dataset from a full-scale study of street canyons it is limited by the fact that the vehicle speed was measured 250 m distant from the study area. In short, Vachon *et al.* (2002) presented traffic flow measured within the study area and vehicle speed 250 m distant but on the same side of the street. The data collected from York during the October/November experiment, therefore, is more comprehensive. In the York study the traffic flow, $q$, per unit time was used to estimate traffic density, $\kappa$, per unit length using vehicle speed, $v$, according to Equation (6.12).

The wind and traffic data were all averaged over 1-minute time periods in order to allow for a suitably large dataset, whilst allowing for the estimation of the standard deviation of the vertical velocities, $\sigma_w$, and TKE caused by TPT effects. The wind velocity data set comprised of 1200 samples for each 1-minute mean velocity, standard deviation and TKE which provides statistical convergence.

*6.3.1.4. Traffic characteristics*

A total number of 10,037 vehicles travelled through the survey section during the TPT field investigation. Over 92% of the total traffic flow was comprised of cars (Figure 6.2). Buses and HGVs made up the majority of the remainder, with LGVs and motorcycles forming an insignificant fraction of the total. As $h \approx 1.4$ m (i.e. $z/H = 0.12$) for cars, the anemometer located at $z/H = 0.3$ on G3 predominantly measured

the airflow and turbulence above the layer in which TPT effects were most active. This is studied in more detail in Section 6.4.

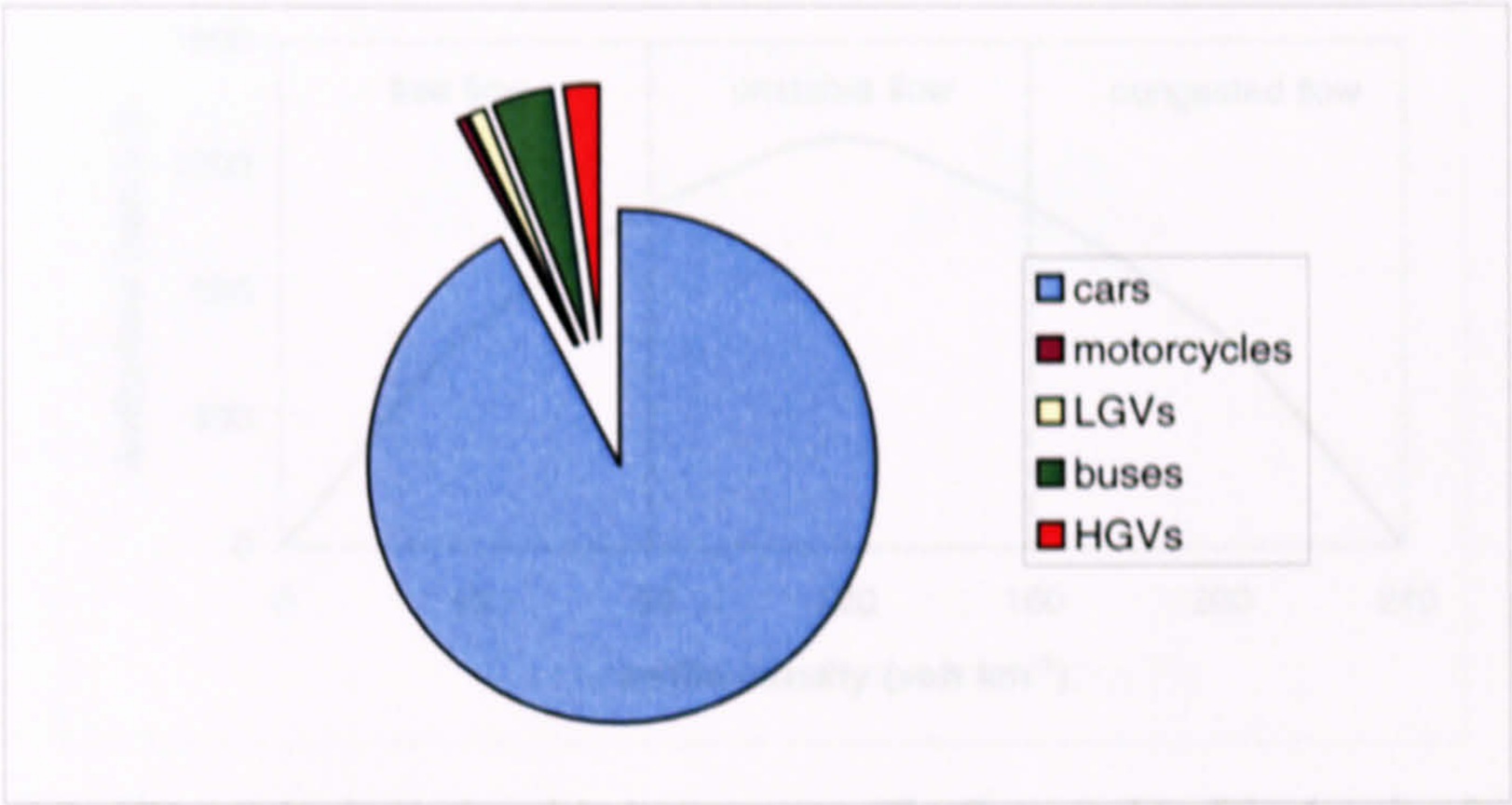


Figure 6.2. Pie chart showing the proportion of vehicles manually surveyed in the inbound traffic flow along Gillygate during the TPT field investigations.

Although traffic surveys were conducted at various times throughout the day the mean vehicle speeds were low. The mean speed of the vehicles travelling inbound along Gillygate during the investigation was only 3.95 m $s^{-1}$ ±0.38. The error calculations for the measured mean vehicle speed determined an error of ~10%. The equations and assumptions used to derive this error value are shown in the Appendix.

Throughout the majority of the time in between the peak traffic flow periods, the platoons of vehicles predominantly travelled inbound along Gillygate in unstable traffic flows, i.e. the traffic switched between periods of free flow and congested flow (Chapter 7). It would appear from the values of the mean vehicle speeds, however, that the traffic flow was predominantly close to or exceeding the capacity of the network.

The theoretical relationship between traffic flow and traffic density described by Dirks *et al.* (2003) is presented in Figure 6.3 for a street with a speed limit of 48 $km^{-1}$ (or 30 miles $h^{-1}$) and a capacity or jam density of 240 veh $km^{-1}$. It should be stressed that jam density refers to the density at which the road is completely blocked due to congestion and traffic flow becomes zero, whereas network capacity can be breached

without traffic flow reaching zero, i.e. capacity is exceeded when congestion occurs (see also Dirks *et al.*, 2002).

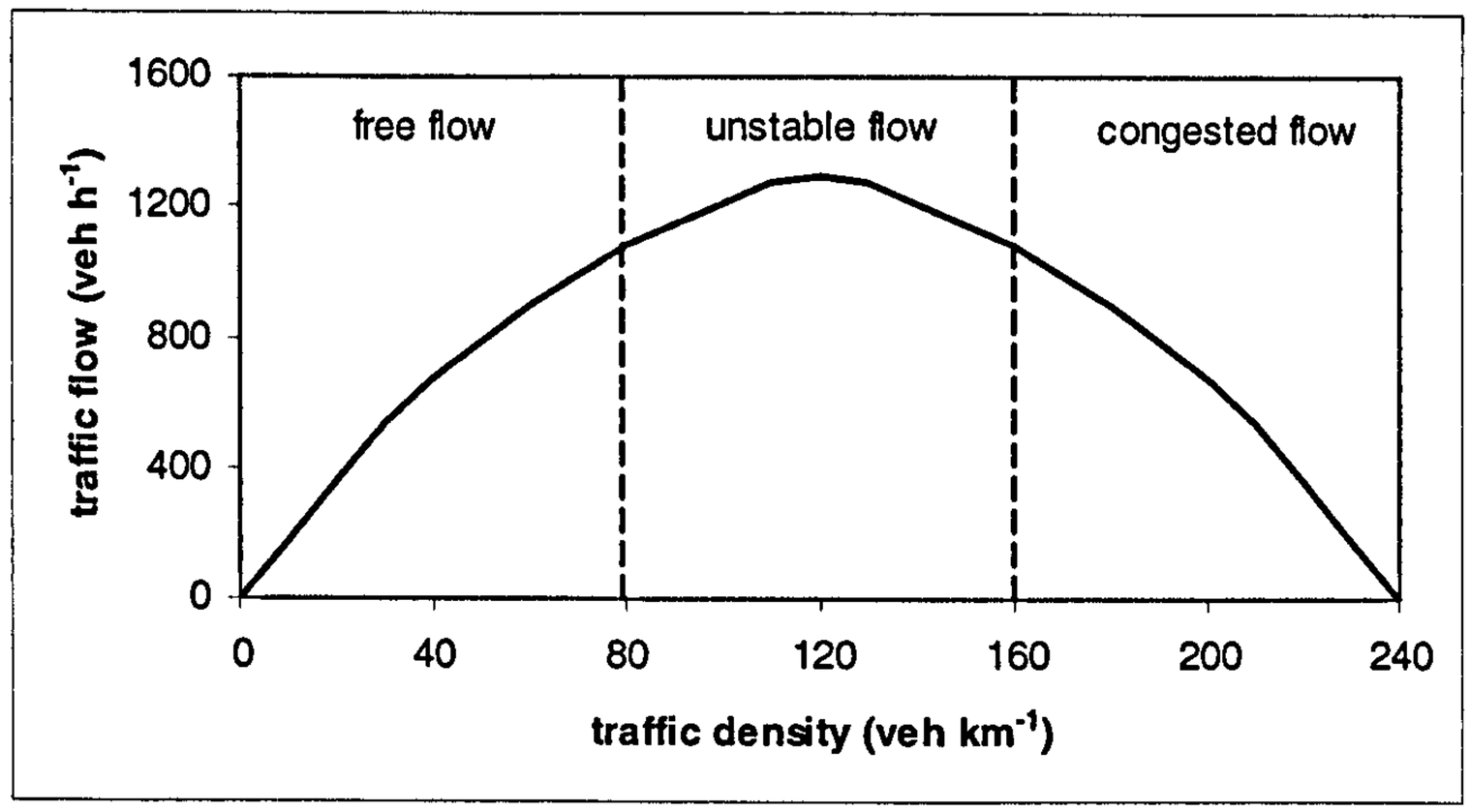


Figure 6.3. Theoretical relationship between traffic flow and traffic density for a street with a speed limit of 48 km $h^{-1}$ (or 30 miles $h^{-1}$) and a jam density of 240 veh $km^{-1}$. The free flow, unstable flow and congested traffic flow conditions are indicated (modified from Dirks *et al.*, 2003).

Figure 6.3 demonstrates that low traffic flow corresponds to either a lack of vehicles on the road or congestion. It also shows that the maximum flow occurs during unstable traffic flow conditions, during which the traffic flow switches between periods of free flow and congested flow. The maximum free flow speed is assumed to be 48 km $h^{-1}$.

Greenshields (1943) found the relationship between traffic density and vehicle speed was suitably represented by:

$$v = v_0\left(1 - \frac{\kappa}{\kappa_j}\right). \tag{6.18}$$

In Equation (6.18) $\kappa_j$ is the jam density and $v_0$ is the maximum free flow speed. This suggests that the highest speeds correspond to free flow conditions and the lowest speeds correspond to congested flow. Figure 6.4 shows the 15-minute averages of inbound traffic flow and detector occupancy measured by SCOOT for the times corresponding to the manual observations. Detector occupancy is equivalent to the percentage of time that a SCOOT detector is occupied and is a function of both

vehicle speed and length. Detector occupancy, therefore, is a useful substitute for traffic density in determining the influence of traffic characteristics on TPT.

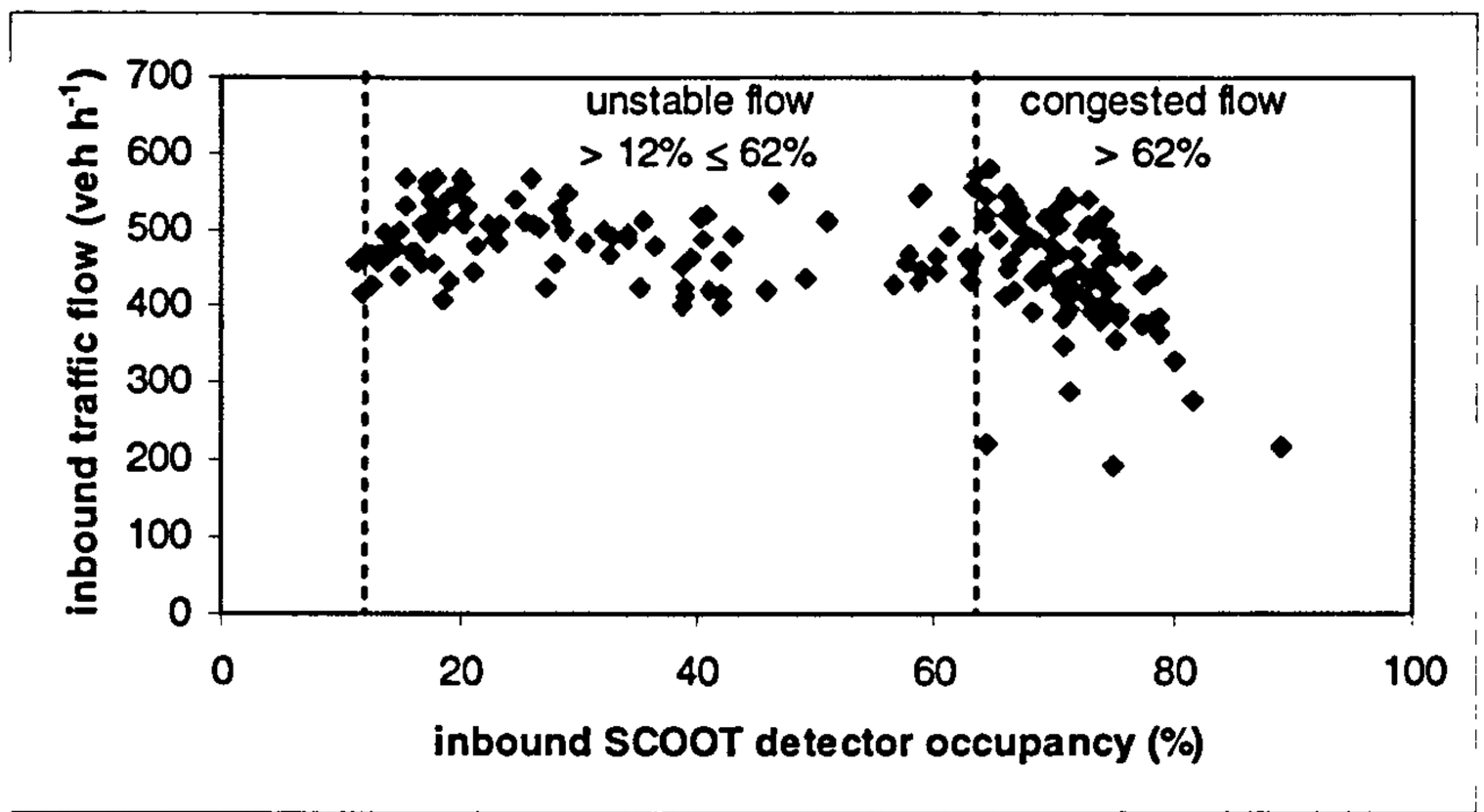


Figure 6.4. Inbound traffic flow and detector occupancy measured by SCOOT and averaged over 15-minute periods during the manual traffic counting survey showing the unstable and congested traffic flow conditions based on the criteria used in Chapter 7. Note the absence of free flow conditions.

In Chapter 7 the analysis of the inbound traffic flow and detector occupancy revealed a linear relationship between the two quantities during free flow conditions. The lower and upper detector occupancy levels are based on the analysis presented in Chapter 7 and they are indicated on Figure 6.4 by vertical dashed lines. It was demonstrated in Chapter 7 that the inbound traffic along Gillygate reached capacity at approximately 12% detector occupancy. An increase in detector occupancy during periods of saturation did not lead to further increases in traffic flow. At very high occupancy the traffic flow decreased, producing a similar parabolic relationship presented in Figure 6.3. This is because the amount of traffic exceeded the capacity of the network and the development of queuing traffic meant vehicles remained stationary on the loop detectors.

However, Figure 6.4 shows no data during free flow conditions, although network capacity was breached above 62% occupancy when congested conditions occurred. This analysis shows that the traffic flow was predominantly unstable or congested during the period of the manual traffic surveys conducted for the TPT investigations. This would account for the low mean vehicle speeds observed during the manual

surveys. Given the absence of long periods of free flow conditions, the figure also suggests that the TPT effects may have been less apparent than expected.

It is important to consider the traffic characteristics observed during the period of the manual observations using the 1-minute average data as this data set will be used to validate the TPT parameterisations. Figure 6.5a shows the traffic flow against traffic density and Figure 6.5b portrays vehicle speed against traffic density. The mean traffic density was derived from the mean traffic flow and traffic speed data using Equation (6.12).

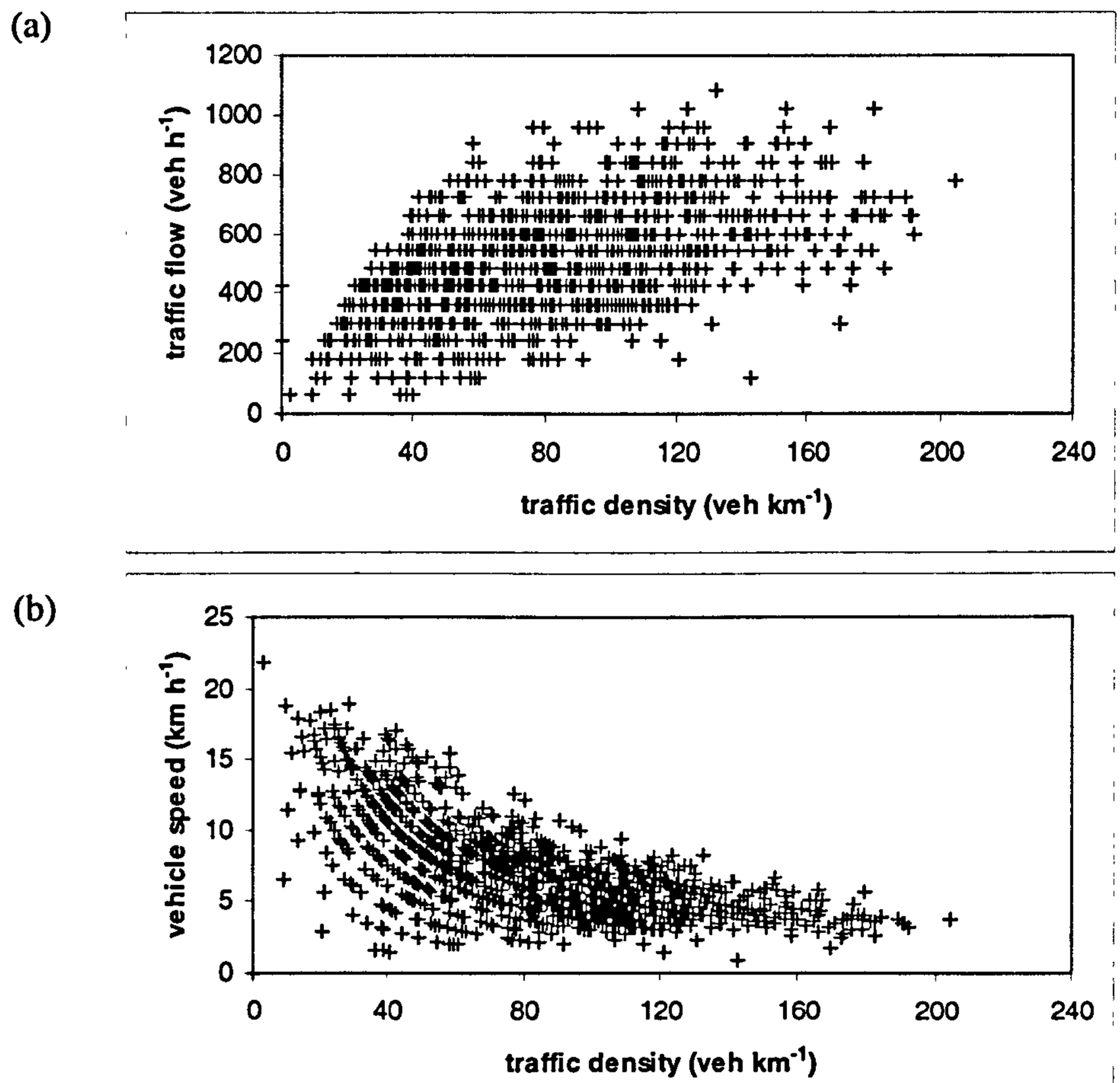


Figure 6.5. Characteristics of the inbound traffic flow using 1-minute averages for: (a) traffic flow and traffic density, and (b) vehicle speed and traffic density.

Figure 6.5a looks very different from the theoretical case presented in Figure 6.3. Figure 6.5a indicates that unstable traffic flows dominated and jam density was never reached. However, the relationship between vehicle speed and traffic density suggests that during high traffic density conditions vehicle speed was greatly reduced.

Whilst some complications may arise from the unstable nature of the traffic flow, using traffic density in the TPT parameterisations should adequately represent the traffic characteristics.

### 6.3.2. TPT parameterisation

The parameterisations for TPT presented in Section 6.2 distinguished between three traffic conditions: (i) low traffic density; (ii) moderate traffic density; and (iii) high traffic density (i.e. congested flow). The traffic flow in the first case is comprised of single vehicles with non-interacting vehicle wakes; whereas moderate traffic density is characterised by platoons of vehicles with interacting vehicle wakes. During congested traffic flows the distance between successive vehicles is shortened and there are strongly interacting wakes. Kastner-Klein *et al.* (2003) used the expressions that incorporated the low and moderate traffic densities (Equations 6.13 and 6.15) but not the high densities (Equation 6.17), as it was not appropriate given the traffic characteristics for the street in Hanover.

It was demonstrated in Figure 6.4 and Figure 6.5 that unstable traffic flows predominantly occurred during the period of the TPT investigations. In particular, the semi-parabolic nature of the relationship between traffic flow and detector occupancy shown in Figure 6.4 implies that for the same value of traffic flow there was either unstable flow (with moderate % detector occupancy) or congested flow (with high % detector occupancy). Clearly, unstable traffic flows produce an inherent difficulty in using traffic flow to estimate traffic density using a formula as simple as Equation (6.12). Therefore, the difficulty in choosing the correct TPT parameterisation based on the three traffic density conditions used by Di Sabatino *et al.* (2003) and Kastner-Klein *et al.* (2003) may cause the empirical models to perform slightly worse than expected. However, in order to calculate the spatially averaged turbulence, $\sigma_{ct}^2$, by following Equations (6.13), (6.15) and (6.17) this caveat can be put aside momentarily whilst consideration is given to certain factors in the TPT parameterisation.

First, it was necessary to consider the portion of the street canyon that TPT effects were likely to have been active. The measured rms of the vertical velocity and TKE

were expected to be highest in the lowest quarter of the canyon due to TPT effects. For this reason, the traffic layer averaging volume $S_t$ was chosen for the TPT parameterisation instead of the whole canyon averaging volume. It was mentioned earlier that Di Sabatino *et al.* (2003) calculated the traffic layer averaging volume $S_t$ using the geometric vehicle length scale $h$ (i.e. $S_t = W \cdot h$). However, Kastner-Klein *et al.* (2003) calculated $S_t$ in the lower half of the canyon using ($S_t = 0.5 \cdot W \cdot H$). The method used by Kastner-Klein *et al.* (2003) accounts for the turbulence that may have been transported vertically in the wakes of passing vehicles, i.e. above vehicle height. By using $h$, therefore, Di Sabatino *et al.* (2003) probably did not report the true height of the traffic layer. Therefore, the method used by Kastner-Klein *et al.* (2003) was used in the analysis presented in this Chapter to calculate $S_t$ in the lower quartile of the canyon (i.e. $S_t = 0.25 \cdot W \cdot H = 45$ m$^2$). It was also necessary to contemplate the drag coefficients of the vehicles and their geometric length scales. The values of the parameters used in this analysis are presented in Table 6.1. The aerodynamic drag coefficient for cars is taken to be 0.3, as used in other studies (e.g. Buckland, 1998; Kastner-Klein *et al.*, 1998; 1999; 2003; Di Sabatino *et al.*, 2003; Gidhagen, 2004). The drag coefficients for the remaining vehicle types were obtained from the Formula One website (www.f1.com) and from literature published in Sport Rider (www.sportrider.com). Gidhagen *et al.* (2004) used a similar method to Buckland (1998) in order to formulate the effect of TPT in traffic flows comprising of cars and HGVs (Chapter 2).

Table 6.1. Estimated traffic parameters showing the drag coefficient $C_D$ and geometric length scale $h$ for each vehicle category.

| vehicle category | $i$ | drag coefficient, $C_D$ | geometric length scale (m), $h = \sqrt{A_c}$ |
|---|---|---|---|
| cars | $i = 1$ | 0.3 | 1.4 |
| motorcycles | $i = 2$ | 0.4 | 0.6 |
| LGVs | $i = 3$ | 0.4 | 2.0 |
| buses | $i = 4$ | 0.6 | 2.6 |
| HGVs | $i = 5$ | 0.9 | 3.0 |

Kastner-Klein *et al.* (2003) used Equations (6.13) and (6.15) to model TPT. However, they only considered two traffic categories, which were cars and HGVs. The average drag coefficient $\overline{C_D}$ and the average geometric vehicle length scale $\bar{h}$ for the two vehicle classes were calculated based on the proportion of each vehicle type present in the total traffic flow. In the present study, the weighted average method was used to calculate the average drag coefficient, $\overline{C_D}$, and the average geometric vehicle length scale, $\bar{h}$, for each 1-minute period. The average drag coefficient $\overline{C_D}$ for a traffic flow, $q_i$, where the index $i$ refers to vehicle category $i$ (Table 6.1) and $q$ is the total inbound traffic flow per unit time, was calculated using the formula:

$$\overline{C_D} = \sum_{i=1}^{n=5} \frac{(q_i \cdot C_{Di})}{q}. \tag{6.19}$$

The average geometric vehicle length scale, $\bar{h}$, for a traffic flow, $q_i$, was calculated in a similar way using:

$$\bar{h} = \sum_{i=1}^{n=5} \frac{(q_i \cdot h_i)}{q}. \tag{6.20}$$

Vehicle speed, $v$, was averaged over 1-minute time periods in order to correspond to the traffic flow and density data. Finally, the values for the dimensionless constants used in Equations (6.13), (6.15) and (6.17) were chosen arbitrarily to equal unity in the absence of concentration data collected within the traffic layer. Consequently, the final slopes of the linear regression analysis will also be arbitrary, although the analysis will determine the significance of the relationship between calculated and measured values of $\sigma_w$.

## 6.4. Results and Discussion

### 6.4.1. Comparisons between measured $\sigma_w$ and traffic characteristics

The work of Vachon *et al.* (2002) has already been briefly mentioned. However, their study, together with the work of Kastner-Klein *et al.* (2003), represent the majority of the current research into both wind flow and traffic conditions in full-scale street canyons. Longley *et al.* (2004a) investigated turbulence in a street canyon in Manchester and found that there was a strong influence of traffic flow on $\sigma_w$ in a layer no deeper than 3 m. However, Longley (2004) mentions that there were fundamental and irreparable errors in the data from one anemometer used in the analysis presented in Longley *et al.* (2004a). Subsequent re-analysis of the data found that conclusions concerning the influence of TPT upon turbulence were dependent on this data and are no longer valid.

Vachon *et al.* (2002) analysed TPT over twelve 1-hour periods and conditioned the data on the background wind direction, $\theta_{ref}$, and speed, $U_{ref}$. In particular, wind directions perpendicular to the street axis and wind speeds of <1.1 m $s^{-1}$ were used. Ultrasonic and propeller anemometers were used in the field experiment to measure the wind component fluctuations at three heights on both sides of the street.

The 1-hour averaged TKE presented by Vachon *et al.* (2002) showed a dependence on traffic flow. On the leeward side of the canyon, TKE increased up to a threshold value of 400 vehicles $h^{-1}$ per lane and then decreased due to shorter distance headways and lower speeds, resulting in a reduction in TPT effects. On the windward side, TKE increased with traffic up to 300 vehicles $h^{-1}$ per lane and this behaviour was most distinctive at the lowest anemometer positioned at a height of ~1.5 m. However, traffic flows >300 vehicles $h^{-1}$ per lane were not observed due to capacity effects and, therefore, a TKE production threshold level could not be determined. Vachon *et al.* (2002) also suggested that TPT affects pollutant dispersion reducing CO concentrations measured at the lowest levels on the leeward side up to a threshold value of TKE approximately equal to 0.15 $m^2$ $s^{-2}$. They also found, however, that high traffic flow generated less turbulence, which in turn lead to lower pollutant dispersion.

In the present study, the fluctuations in the vertical velocity measured at 1.1 m ($z/H$ = 0.09) and 3.6 m ($z/H$ = 0.3) inside the Gillygate street canyon at lamppost G3 reflect turbulent motions produced by the background wind and traffic travelling along the street. The rms values of the measured fluctuations in the 1-minute mean vertical velocities were compared against the traffic flow, traffic density and vehicle speed. Figure 6.6 shows the vertical velocity fluctuations $\sigma_w$ measured on the leeward side of the canyon against mean vehicle speed during background winds $\theta_{ref}$ from 120° ±30°. The data was also conditioned on $U_{ref}$>1.2 m s$^{-1}$ in order to use a larger dataset.

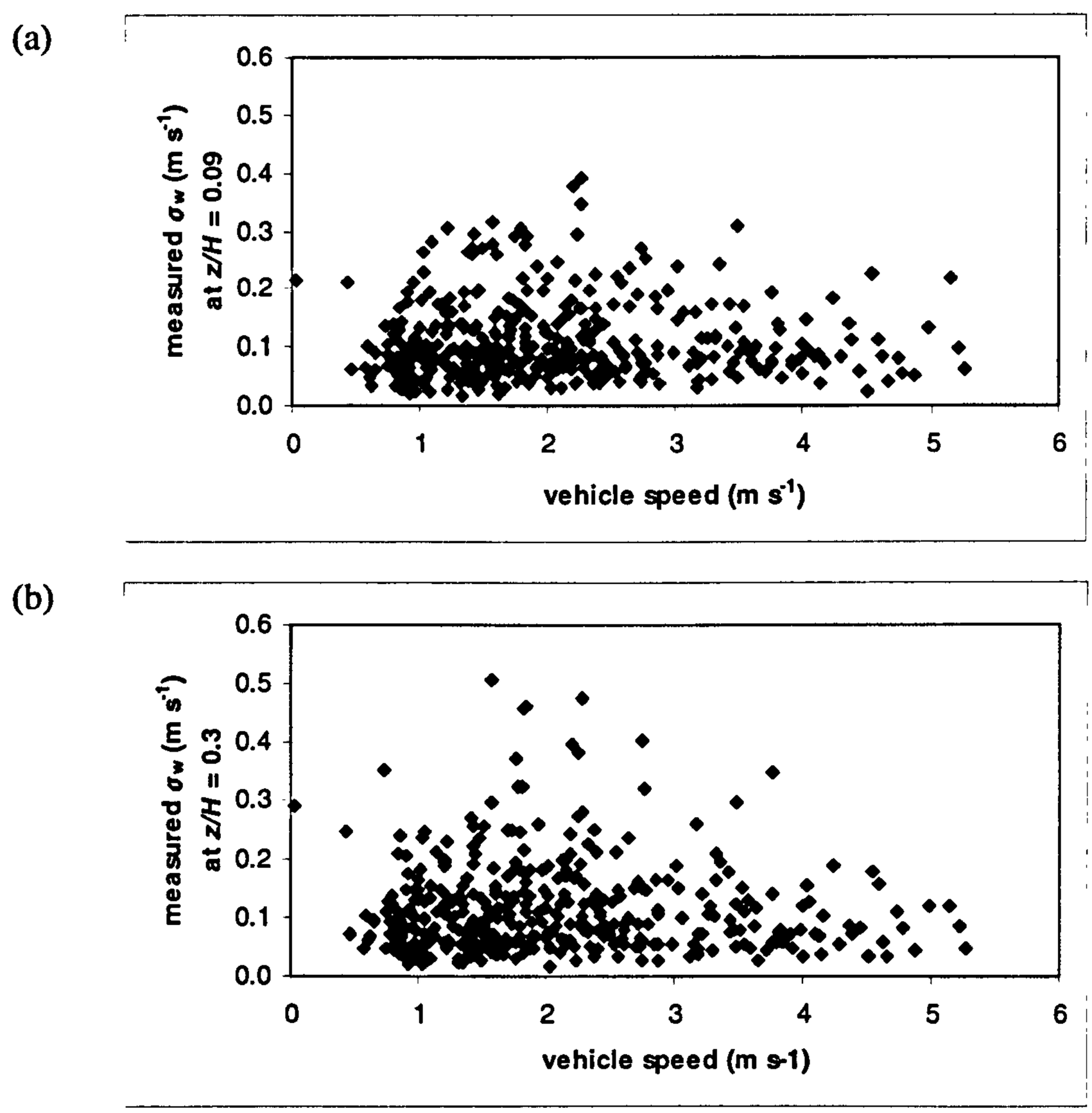


Figure 6.6. Vertical velocity fluctuations $\sigma_w$ against mean vehicle speed conditioned on $U_{ref}$> 1.2 m s$^{-1}$ and $\theta_{ref}$= 120° ±30°, measured on lamppost G3 at (a) $z/H$ = 0.09 and (b) $z/H$ = 0.3.

It is evident from the regression analysis that there is not a statistically significant relationship between $\sigma_w$ measured at both heights on the leeward side of the canyon and mean vehicle speed based on these conditions. Therefore, any turbulence

generated during $U_{ref} \leq 1.2$ m s$^{-1}$ and $\theta_{ref} = 120° \pm 30°$ (i.e. $90° < \theta_{ref} \leq 150°$) is more likely to have been associated with TPT effects. In order to determine the turbulence produced by passing vehicles all subsequent analysis used 1-minute averages of $\sigma_w$ conditioned on $U_{ref} \leq 1.2$ m s$^{-1}$ for a variety of background wind directions. Following the conditional analysis, only 12% of the data presented in Chapters 4, 5 and 7 is included in the work presented in this Chapter. Although the amount of data corresponding to $U_{ref} \leq 1.2$ m s$^{-1}$ is low, it compares with the work of Vachon *et al.* (2002), who presented hourly-averages of TKE over just 12 time periods.

Comparisons between $\sigma_w$ measured at lamppost G3 at $z/H = 0.09$ and $z/H = 0.3$ and mean vehicle speed conditioned on $U_{ref} \leq 1.2$ m s$^{-1}$ and $\theta_{ref} = 120° \pm 30°$ are shown in Figure 6.7a and Figure 6.7b, respectively. Figure 6.7a shows a statistically significant relationship between both $\sigma_w$ at $z/H = 0.09$ and vehicle speed with an $r^2$ value of 0.26. Although there is no statistically significant relationship between both $\sigma_w$ at $z/H = 0.3$ and mean vehicle speed there appears to be a weak relationship that may have been significant with more data points. During perpendicular backgrounds winds from the NW the anemometers at lamppost G3 were located on the windward side of the canyon.

(a)

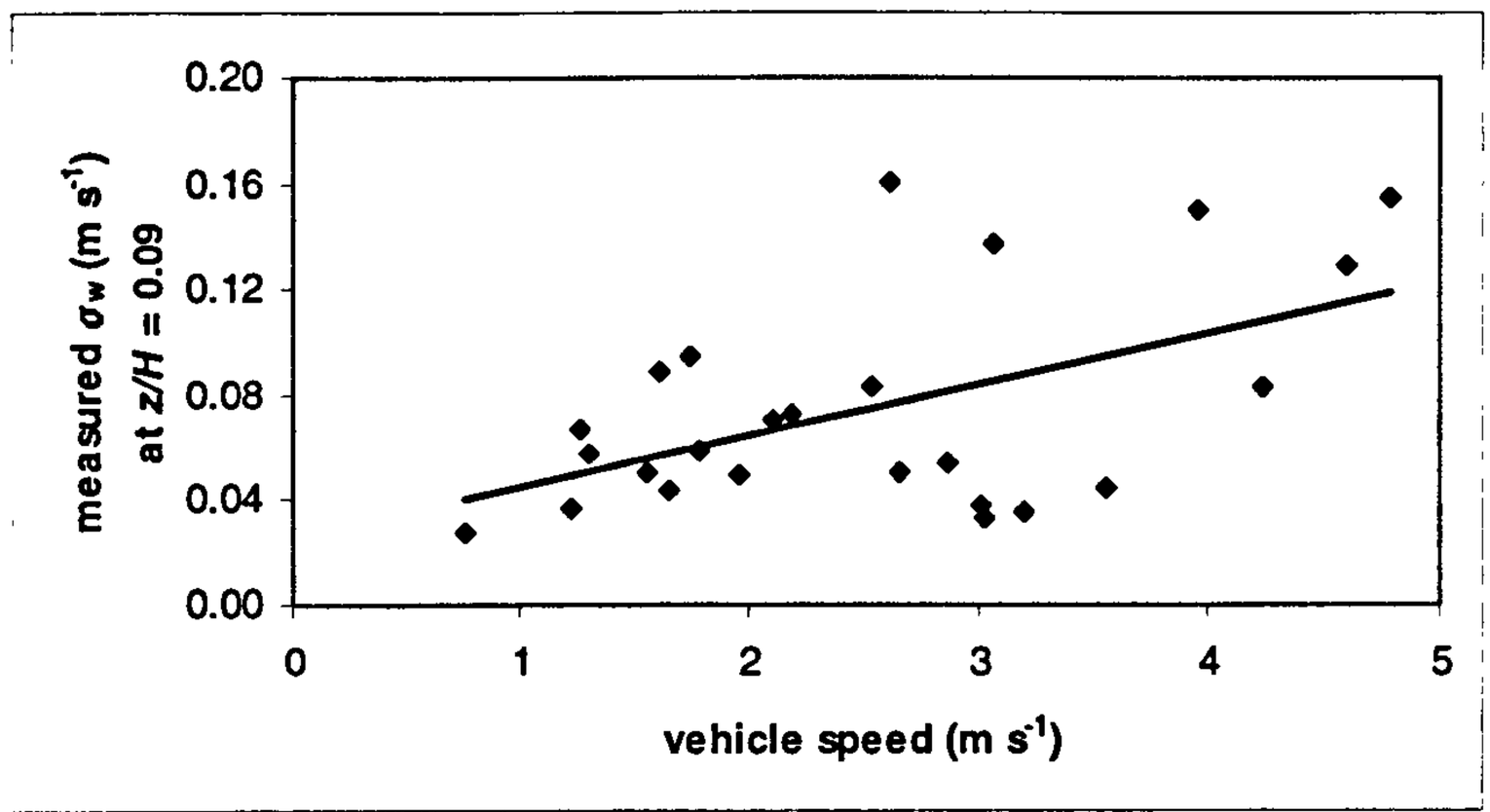


(b)

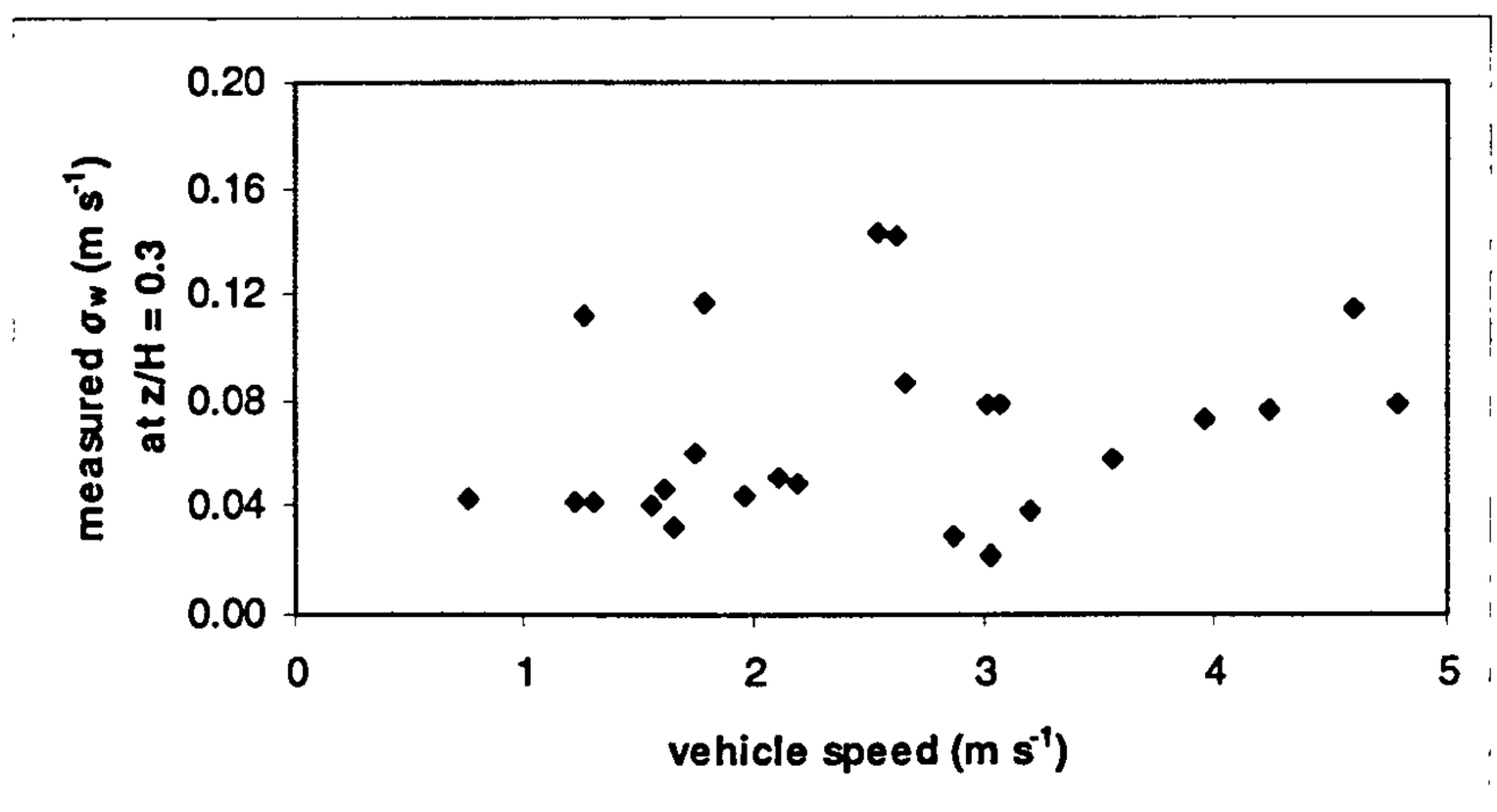


Figure 6.7. Vertical velocity fluctuations $\sigma_w$ against vehicle speed conditioned on $U_{ref}$ $\leq 1.2$ m s$^{-1}$ and $\theta_{ref} = 120° \pm 30°$, measured at lamppost G3 at (a) $z/H = 0.09$ and (b) $z/H = 0.3$.

There was no significant correlation between $\sigma_w$ at $z/H = 0.09$ and vehicle speed when conditioned on $U_{ref} \leq 1.2$ m s$^{-1}$ during background winds $\theta_{ref}$ from perpendicular 300° ±30°, i.e. 270° $< \theta_{ref} \leq$ 330° (not shown). Likewise, there were no significant relationships found between the two variables during parallel background winds from 30° ±30° (i.e. 0° $< \theta_{ref} \leq$ 60°) and 210° ±30° (i.e. 180° $< \theta_{ref} \leq$ 240°). These figures are not shown in this Chapter. The dependence on the background wind direction suggests that a single across-canyon recirculating flow (with a horizontally-aligned axis) may have developed within Gillygate during SE winds, even under low $U_{ref}$ conditions. The weak across-canyon recirculating flow could have potentially transported TPT to the leeward side of the canyon during these background wind conditions.

This prompted further analysis of the vertical wind velocity angle, $\phi$, measured at mid-canyon heights on opposite sides of the street following the method described in Chapter 4 but conditioning the data on $U_{ref} \leq 1.2$ m s$^{-1}$. In Chapter 4 supporting evidence was provided of an across-canyon recirculating flow with a horizontally-aligned axis that developed during background winds from $\theta_{ref} \approx 120°$ and $U_{ref} > 1.2$ m s$^{-1}$. During these background winds, there were strong downdraughts on the windward (G4) side of the canyon and updraughts on the leeward (G3) side. Figure 6.8 shows the 15-minute mean vertical wind velocity angle, $\phi$, measured at mid-canyon height on opposite sides of Gillygate using the method described in Chapter 4. Once again, the figure shows that even during low background winds there were updraughts on the leeward (G3) side of the canyon and downdraughts on the windward (G4) side during perpendicular SE winds. Although, the updraughts and downdraughts were weaker during these low wind speed conditions it does suggest that a single across-canyon vortex was present on average in Gillygate.

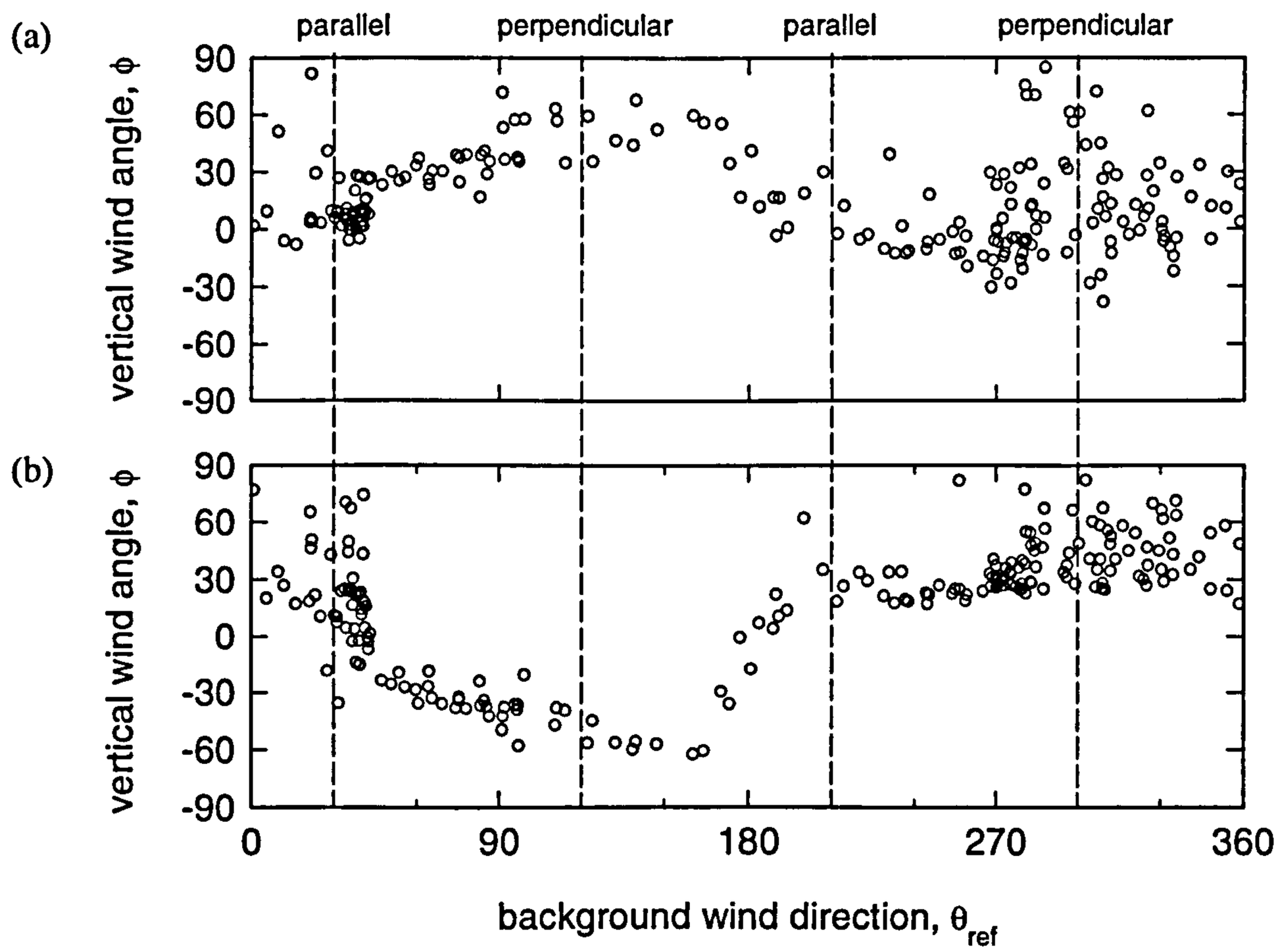


Figure 6.8. 15-minute mean vertical wind velocity angle, $\phi$, as a function of the background wind direction, $\theta_{ref}$, and $U_{ref} \leq 1.2$ m s$^{-1}$ at (a) $z/H = 0.46$ on G3 and (b) $z/H = 0.48$ on G4.

In a traffic-free canyon the turbulence is expected to be weaker at the leeward side than at the windward side due to a loss in energy during transport, as discussed in Section 6.1.1. However, Vachon *et al.* (2002) found that the recirculating flow may have been responsible for transferring additional turbulence produced by vehicles towards the leeward side of the canyon. Unfortunately, no data was collected at $z/H$ = 0.09 on the windward (G4) side during $\theta_{ref}$ = 210° ±30° and so a comparison between the two sides of the canyon was not possible. During perpendicular winds from 300° ±30° the absence of a single-across canyon recirculating flow with a horizontally-aligned axis was most likely caused by the development of corner vortices at the side streets adjoining Gillygate producing along-canyon converging flows, as described in Chapter 4.

Comparisons of $\sigma_w$ at $z/H$ = 0.09 and $z/H$ = 0.3 against both traffic flow and traffic density were statistically insignificant (not shown). However, the differences between the two locations for $\sigma_w$ against mean vehicle speed (Figure 6.7) suggests that TPT effects produced in the inbound lane along Gillygate may have been mainly limited to an area below $z/H$ = 0.3 i.e. the lowest quarter of the canyon. Although more data points may have revealed a stronger influence of TPT at $z/H$ = 0.3. Passing traffic is the likely cause of the turbulence produced in the Gillygate canyon during weak perpendicular SE winds. Therefore, our attention must now turn to the validation of the TPT parameterisation.

### 6.4.2. Model validation using $\sigma_w$

#### *6.4.2.1. The influence of perpendicular background winds*

The vertical velocity fluctuations caused by traffic $\sigma_{ct}$ were calculated using Equations (6.13), (6.15) and (6.17) for light, medium and high traffic densities, respectively. For simplicity, this Section describes the calculated turbulence derived from Equations (6.13), (6.15) and (6.17) as calculated $\sigma_w$. However, in Section 6.3.2 the same calculated turbulence values are compared against measured TKE in order to address the confusion over the parameterisations described in Section 6.2.4.

Figure 6.9 shows good agreement between calculated and measured values of $\sigma_w$ at $z/H = 0.09$ when conditioned on $\theta_{ref} = 120° \pm 30°$ and $U_{ref} \leq 1.2$ m s$^{-1}$ and using Equations (6.13), (6.15) and (6.17), respectively, i.e. when the anemometer was located on the leeward side of the canyon.

The constant of proportionality has different physical meanings in Equation (6.13), (6.15) and (6.17) and can be determined, where available, from vehicle speed and concentration data, as discussed in Section 6.2. It was mentioned that an arbitrary scaling was used in each equation as CO concentrations were not measured within the traffic layer (at $z/H = 0.09$) on lamppost G3. Consequently, comparisons between the results of the regression analysis performed for each equation will imply that the slopes are less important than the statistical significance of the regressions themselves.

The correlation coefficients ($r$), the coefficients of determination ($r^2$) and the slopes of the regression lines are shown in Table 6.2. However, it is worth stressing that although the $r^2$ values for the linear regression correlations shown in Figure 6.9 are relatively low, indicating a moderate relationship between calculated and measured values of $\sigma_w$ at $z/H = 0.09$ during $\theta_{ref} = 120° \pm 30°$, the correlation coefficients are all significant at the 0.5% level. The $r^2$ values for Equations (6.13), (6.15) and (6.17) were 0.33, 0.34 and 0.26, respectively (Table 6.2). These values suggest that the formulations for low and intermediate traffic densities performed slightly better than for high traffic densities. It was expected that the parameterisation used in Equations (6.13) and (6.17) would more accurately predict the turbulence measured in the street as the traffic flow was found to be predominantly unstable, i.e. switching between periods of free-flow and congested flow (as shown in Figure 6.3).

(a)

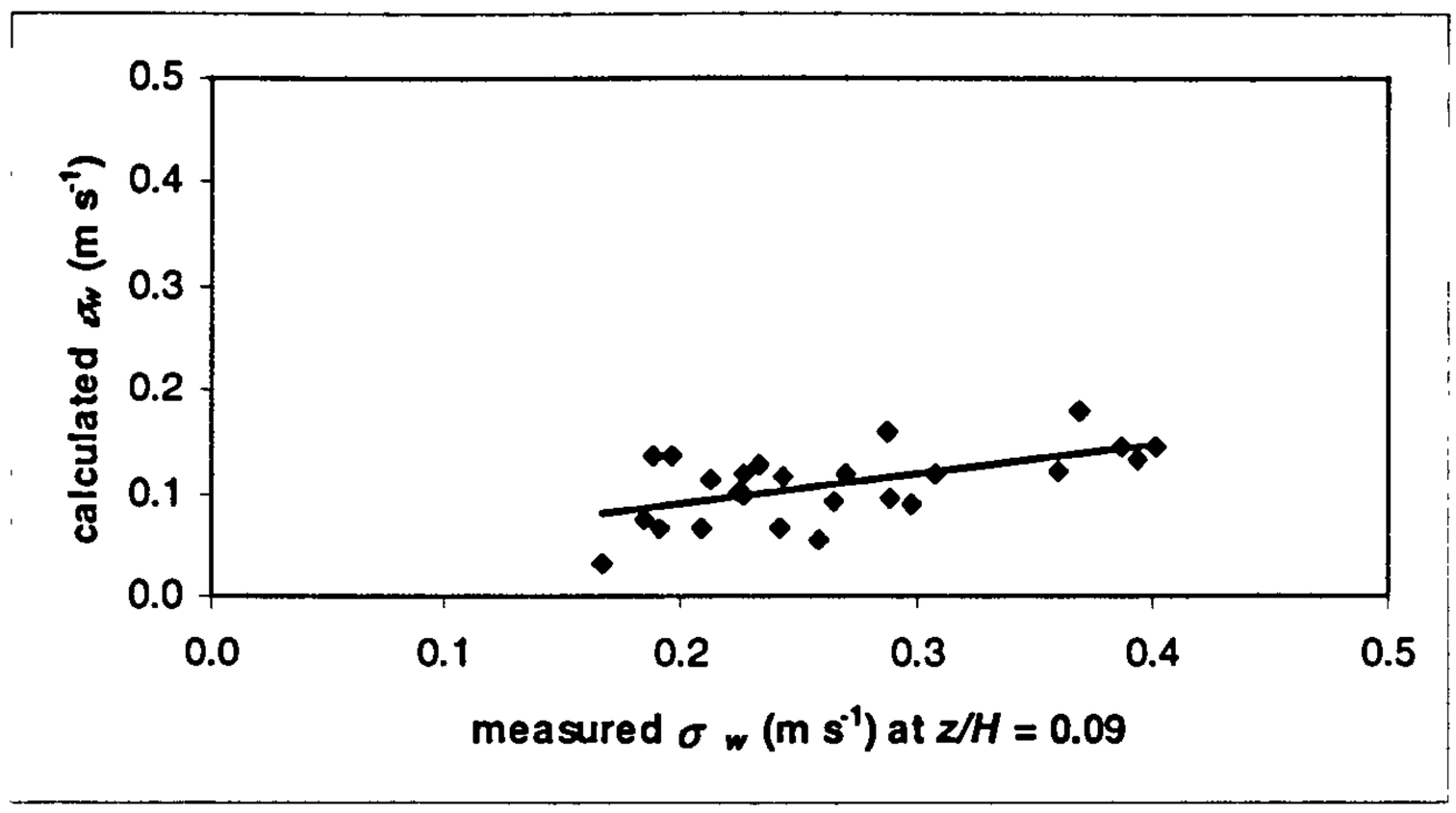


(b)

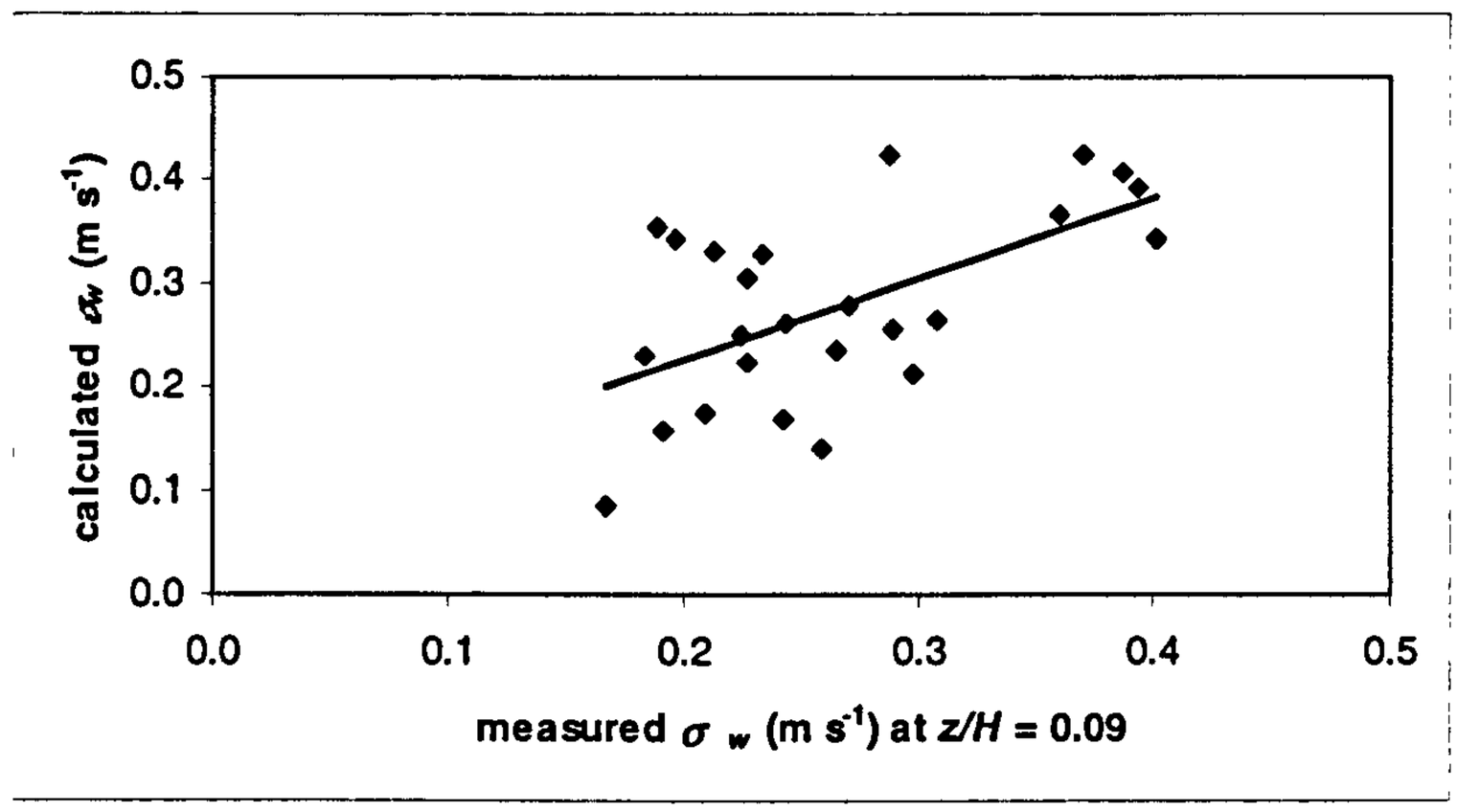


(c)

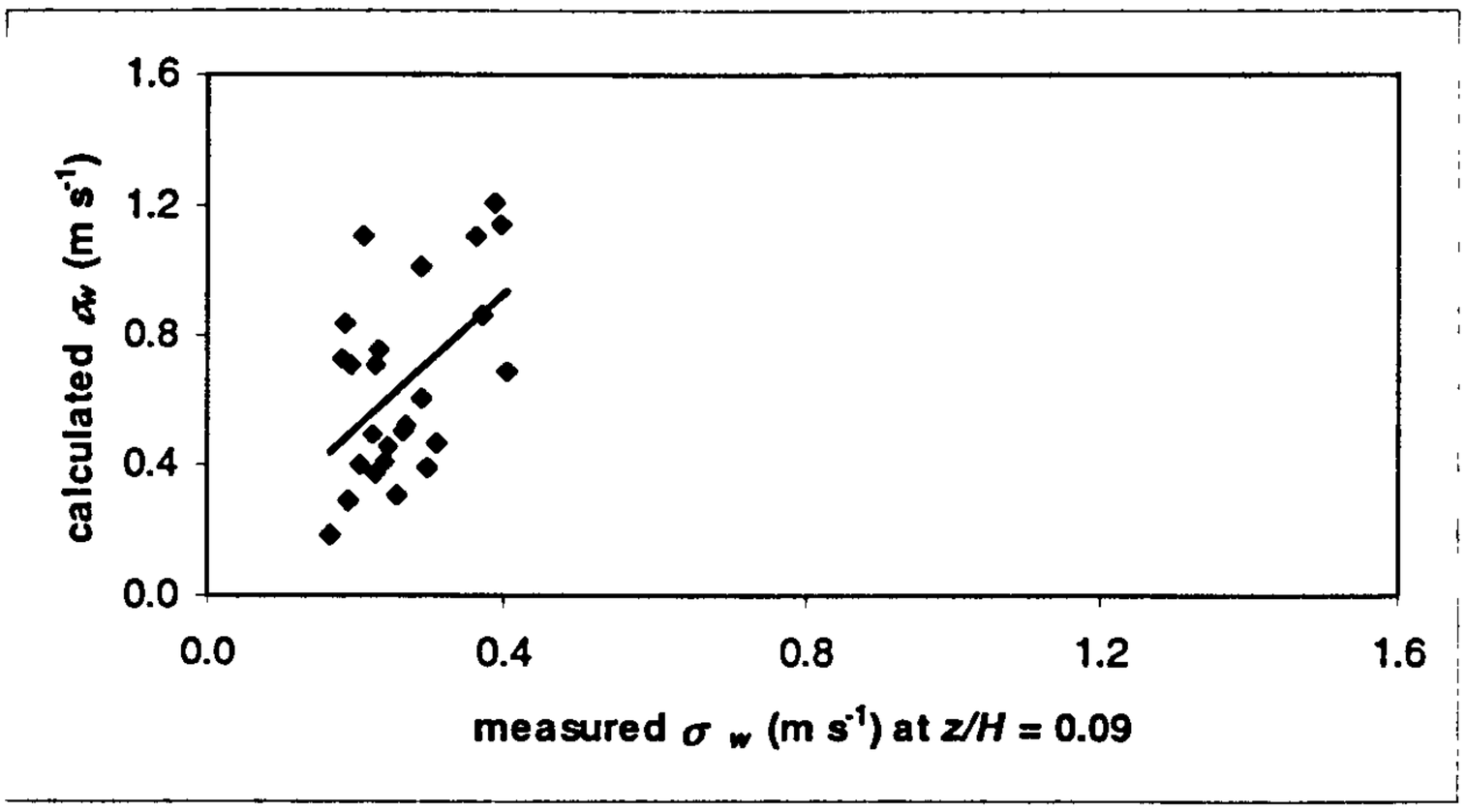


Figure 6.9. Comparison of calculated and measured $\sigma_w$ at $z/H = 0.09$ averaged over 1-minute periods; conditioned on $\theta_{ref} = 120° \pm 30°$ and $U_{ref} \leq 1.2$ m s$^{-1}$ using: (a) Equation (6.13); (b) Equation (6.15); and (c) Equation (6.17).

Table 6.2. Regression analysis of the calculated turbulence and measured vertical velocity variance $\sigma_w$ at lamppost G3 conditioned on $U_{ref} \leq 1.2$ m s$^{-1}$ and as a function of background wind direction, $\theta_{ref}$. #Note that NS is an abbreviation for *Not Significant*.

| | | | linear regression analysis | | | | |
|---|---|---|---|---|---|---|---|
| background wind direction, $\theta_{ref}$ | equation number | $z/H$ | $r$ | $r^2$ | slope | degrees of freedom, $df$ | significance level# (%) |
| 120° ±30° | (6.13) | 0.09 | 0.57 | 0.33 | 0.28 | 23 | 0.5 |
| 120° ±30° | (6.15) | 0.09 | 0.58 | 0.34 | 0.77 | 23 | 0.5 |
| 120° ±30° | (6.17) | 0.09 | 0.51 | 0.26 | 2.14 | 23 | 0.5 |
| 120° ±30° | (6.13) | 0.30 | 0.28 | 0.08 | 0.34 | 23 | NS |
| 120° ±30° | (6.15) | 0.30 | 0.30 | 0.09 | 0.55 | 23 | NS |
| 120° ±30° | (6.17) | 0.30 | 0.22 | 0.05 | 1.14 | 23 | NS |
| 120° ±45° | (6.13) | 0.09 | 0.52 | 0.27 | 0.27 | 28 | 0.5 |
| 120° ±45° | (6.15) | 0.09 | 0.55 | 0.30 | 0.75 | 28 | 0.5 |
| 120° ±45° | (6.17) | 0.09 | 0.52 | 0.27 | 2.17 | 28 | 0.5 |
| 300° ±30° | (6.13) | 0.09 | 0.39 | 0.15 | 0.24 | 10 | NS |
| 300° ±30° | (6.15) | 0.09 | 0.30 | 0.09 | 0.41 | 10 | NS |
| 300° ±30° | (6.17) | 0.09 | 0.06 | 0.004 | 0.28 | 10 | NS |
| 30° ±30° | (6.13) | 0.09 | 0.32 | 0.10 | 0.23 | 15 | NS |
| 30° ±30° | (6.15) | 0.09 | 0.26 | 0.07 | 0.53 | 15 | NS |
| 30° ±30° | (6.17) | 0.09 | 0.17 | 0.03 | 0.97 | 15 | NS |
| 210° ±30° | (6.13) | 0.09 | 0.17 | 0.03 | 0.06 | 28 | NS |
| 210° ±30° | (6.15) | 0.09 | 0.17 | 0.03 | 0.17 | 28 | NS |
| 210° ±30° | (6.17) | 0.09 | 0.14 | 0.02 | 0.30 | 28 | NS |

Kastner-Klein *et al.* (2003) used the TPT parameterisation presented above to compare the calculated and measured values of $\sigma_w$ at 10.0 m inside a deep street canyon in Hanover, Germany. When conditioned on perpendicular background winds ±15°, the correlations between these values obtained from the expressions for both low (Equation 6.13) and intermediate (Equation 6.15) traffic densities were very strong, with correlation coefficients of $r = 0.97$. In the present study, the correlation coefficients presented in Table 6.2 indicate much weaker correlations, although they are statistically significant.

By collecting a sufficiently large data set, Kastner-Klein *et al.* (2003) were also able to condition the data on traffic density in order to use the most appropriate TPT

expression. Unfortunately, it was not possible to condition the data on traffic density, as it would have produced an insufficient quantity of data. Furthermore, even when the data were averaged over 1-minute time periods, the traffic flow was predominantly unstable or congested, which suggests that the TPT effects in Gillygate may be less significant in producing additional turbulence than in the Hanover street canyon. Furthermore, the traffic flow observed by Kastner-Klein *et al.* (2003) in their study was predominantly free flowing, during which mean vehicle speeds would have been higher and TPT effects more active. These reasons are likely to explain why the correlation coefficients found by Kastner-Klein *et al.* (2003) are so much higher than for the Gillygate data.

The relationships between the calculated and measured values of $\sigma_w$ at $z/H = 0.3$, when conditioned on $\theta_{ref} = 120° \pm 30°$ and $U_{ref} \leq 1.2$ m s$^{-1}$, are not statistically significant (Figure 6.10; Table 6.2). This adds further support to the notion that the anemometer located at 3.6 m ($z/H = 0.3$) was situated above the layer in which TPT effects were most active in Gillygate. However, it should be noted that with more data evidence of a significant relationship may have been found, although the relationship is likely to have been weak.

The analysis was continued by using a wider background wind direction sectors in order to include more data. The data was first conditioned $\theta_{ref} = 120° \pm 45°$ (i.e. $75° < \theta_{ref} \leq 165°$) and $U_{ref} \leq 1.2$ m s$^{-1}$, i.e. for weak SE winds with perpendicular and oblique components (Figure 6.11). Even though the wider background wind sector incorporates possible along-canyon helical flow regimes associated with oblique winds (Chapter 4), the correlation coefficients are only slightly lower (as shown in Table 6.2). The correlation coefficients are all statistically significant at the 0.5% level and suggest that TPT effects occurred even during weak oblique background winds. Table 6.2 also shows that the slopes of the regression lines and the $r^2$ values are similar for $\theta_{ref} = 120° \pm 30°$ and $\theta_{ref} = 120° \pm 45°$. This suggests that Equations (6.13), (6.15) and (6.17) are relevant over a fairly wide range of background wind directions.

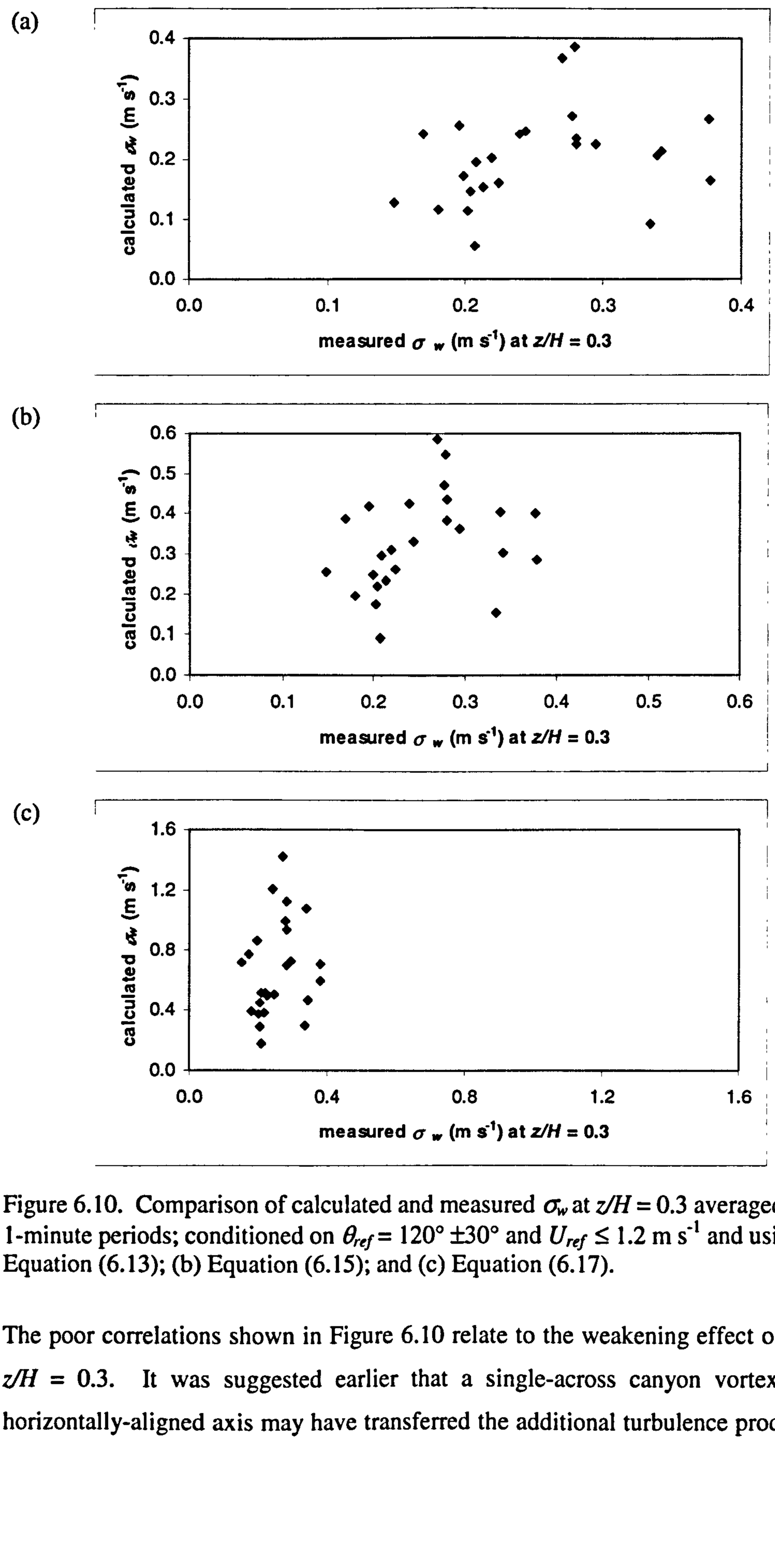


Figure 6.10. Comparison of calculated and measured $\sigma_w$ at $z/H = 0.3$ averaged over 1-minute periods; conditioned on $\theta_{ref} = 120° \pm 30°$ and $U_{ref} \leq 1.2$ m s$^{-1}$ and using: (a) Equation (6.13); (b) Equation (6.15); and (c) Equation (6.17).

The poor correlations shown in Figure 6.10 relate to the weakening effect of TPT at $z/H$ = 0.3. It was suggested earlier that a single-across canyon vortex with a horizontally-aligned axis may have transferred the additional turbulence produced by

vehicles towards the leeward side, which would support the findings shown from the experimental data. However, in order to rule out other effects it is necessary to compare the calculated and measured values of $\sigma_w$ at $z/H = 0.09$ for other background wind directions.

The analysis was continued by first conditioning the calculated and measured values of $\sigma_w$ on $\theta_{ref} = 300° \pm 30°$ and $U_{ref} \leq 1.2$ m s$^{-1}$, i.e. for weak perpendicular NW winds (Figure 6.12). The lack of data for these conditions prevents firm conclusions from being drawn, especially as the correlations were not statistically significant (Table 6.2). However, it is possible that the along-canyon converging flows described in detail in Chapter 4 may have disrupted the turbulent air motions produced by passing traffic, even during $U_{ref} \leq 1.2$ m s$^{-1}$. Figure 6.8 shows the vertical wind velocity angle, $\phi$, as a function of background wind direction $\theta_{ref}$ during $U_{ref} \leq 1.2$ m s$^{-1}$.

During $\theta_{ref} = 300° \pm 30°$ updraughts were observed by the mid-canyon anemometers located on both sides of the street. This suggests that even during weak perpendicular NW winds, corner vortices developed at the junctions with Gillygate producing along-canyon flows, which converged close to the G3-G4 experiment cross-section. Flow convergence is likely to have interfered with the turbulence produced by passing vehicles in the street, resulting in poor correlations between calculated and measured $\sigma_w$ at $z/H = 0.09$.

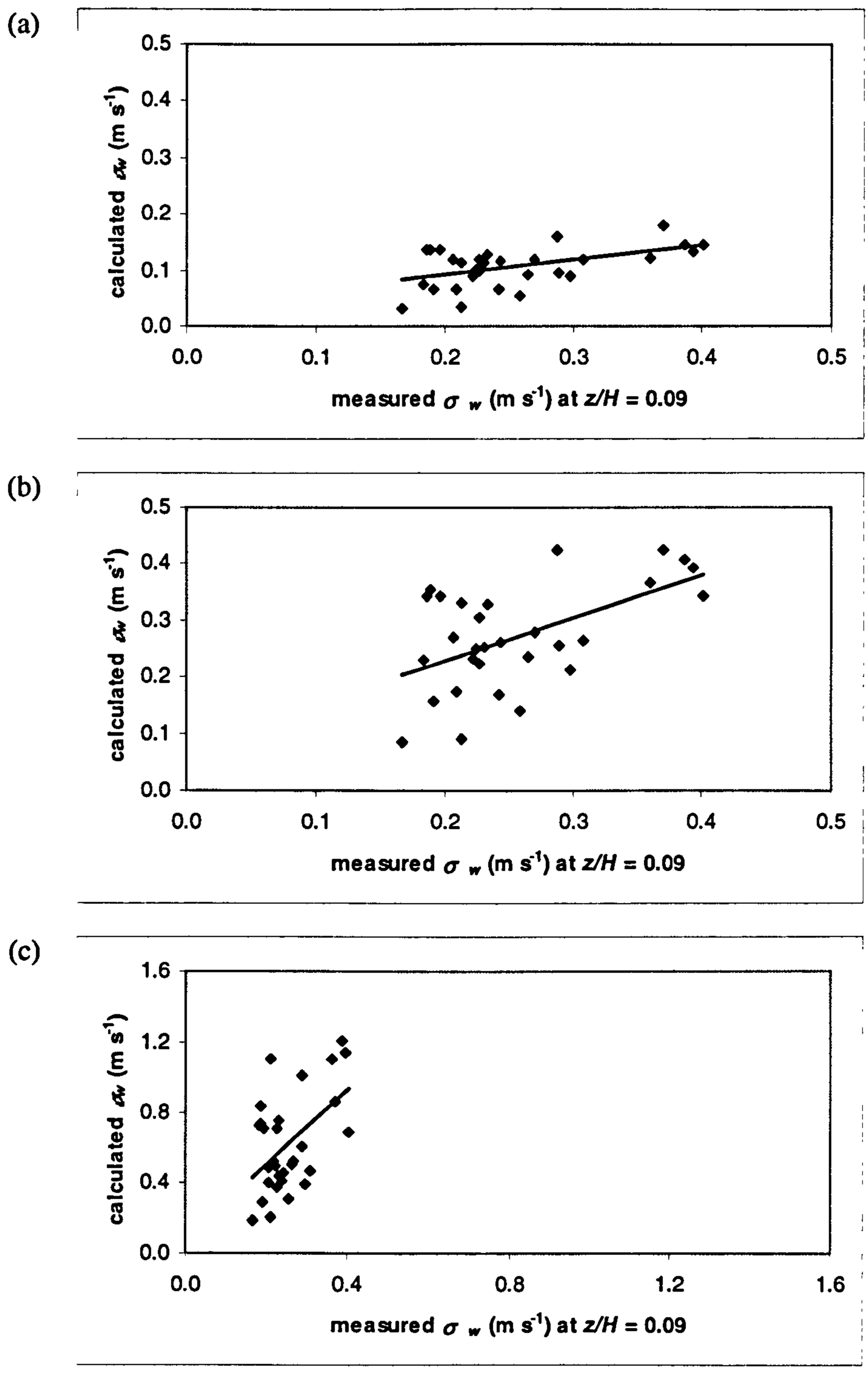


Figure 6.11. Comparison of calculated and measured $\sigma_w$ at $z/H = 0.09$ averaged over 1-minute periods; conditioned on $\theta_{ref} = 120° \pm 45°$ and $U_{ref} \leq 1.2$ m s$^{-1}$ and using: (a) Equation (6.13); (b) Equation (6.15); and (c) Equation (6.17).

*6.4.2.2. The influence of parallel background winds*

The calculated and measured values of $\sigma_w$ at $z/H = 0.09$ were compared for parallel background winds ($\theta_{ref} = 30° \pm 30°$ and $\theta_{ref} = 210° \pm 30°$) as shown in Figure 6.13 and Figure 6.14, respectively. However, the correlations shown in the figures are clearly not statistically significant, even though the number of data points (or more specifically the degrees of freedom) is reasonably high (Table 6.2). The dependence of TPT on perpendicular SE winds was demonstrated in Figure 6.7a and Figure 6.9 and Figure 6.11. However, the inclusion of other wind directions in the analysis demonstrates that the relationship between calculated and measured $\sigma_w$ at $z/H = 0.09$ is only statistically significant during perpendicular SE winds when the anemometer was located on the leeward side of the canyon.

(a)

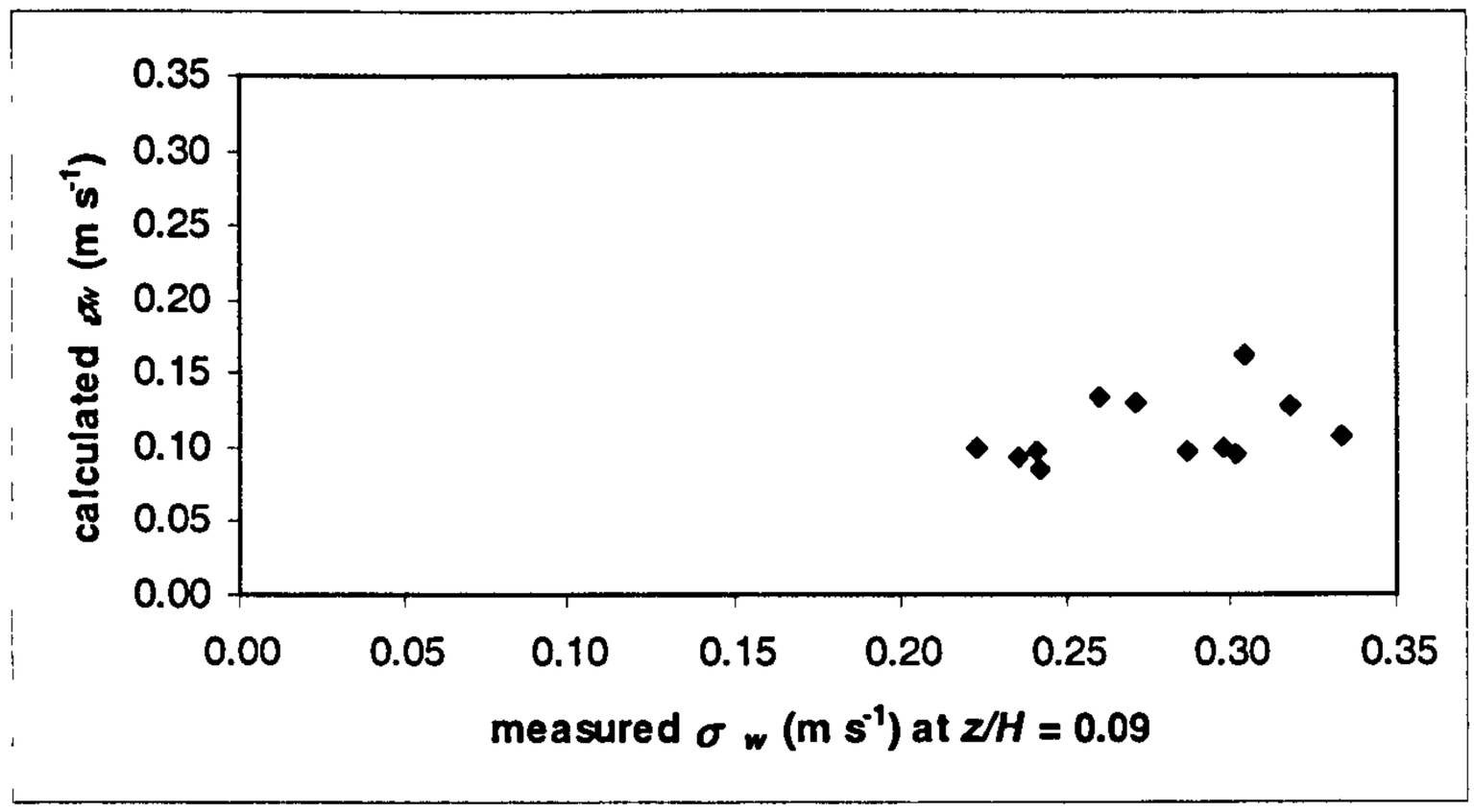


(b)

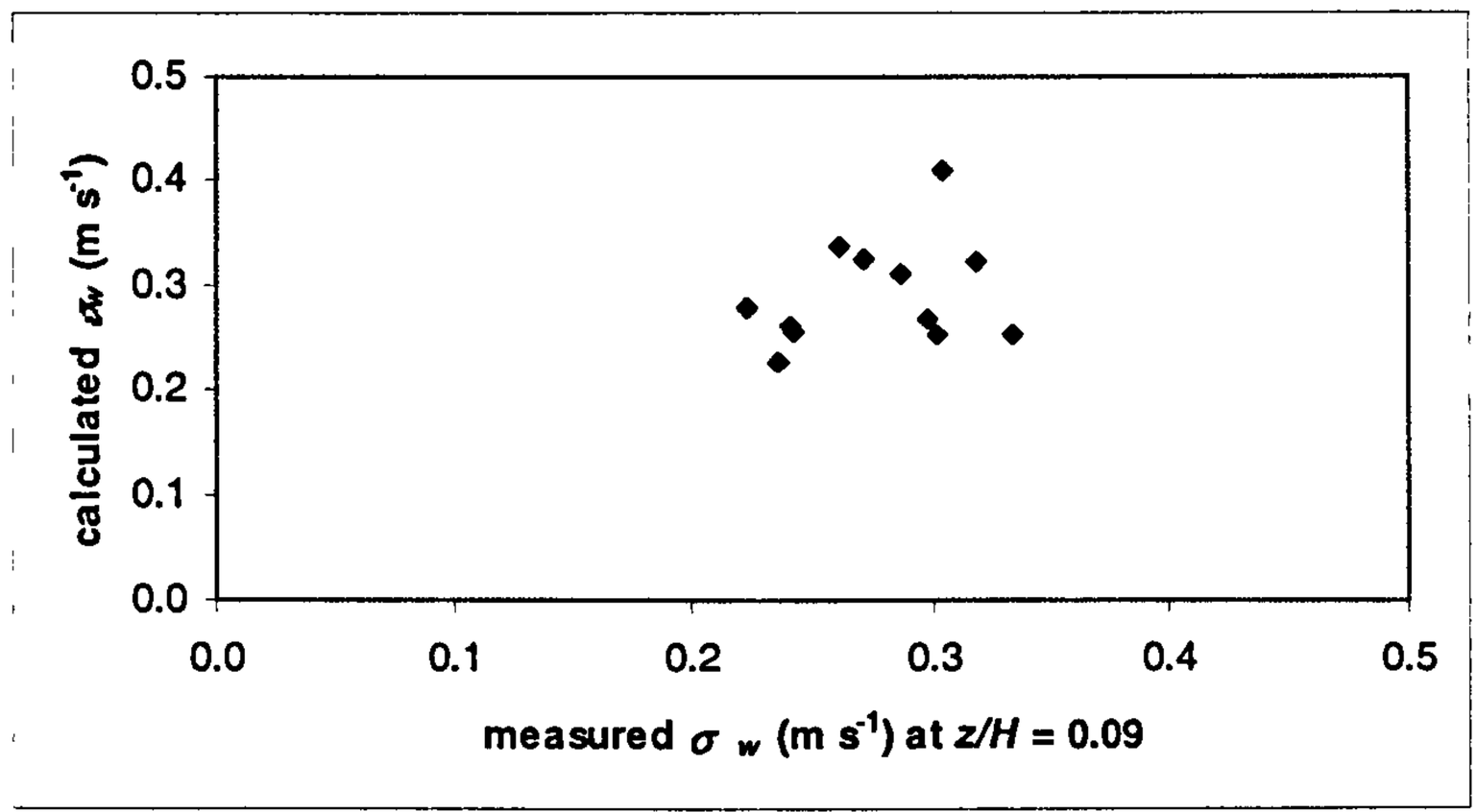


(c)

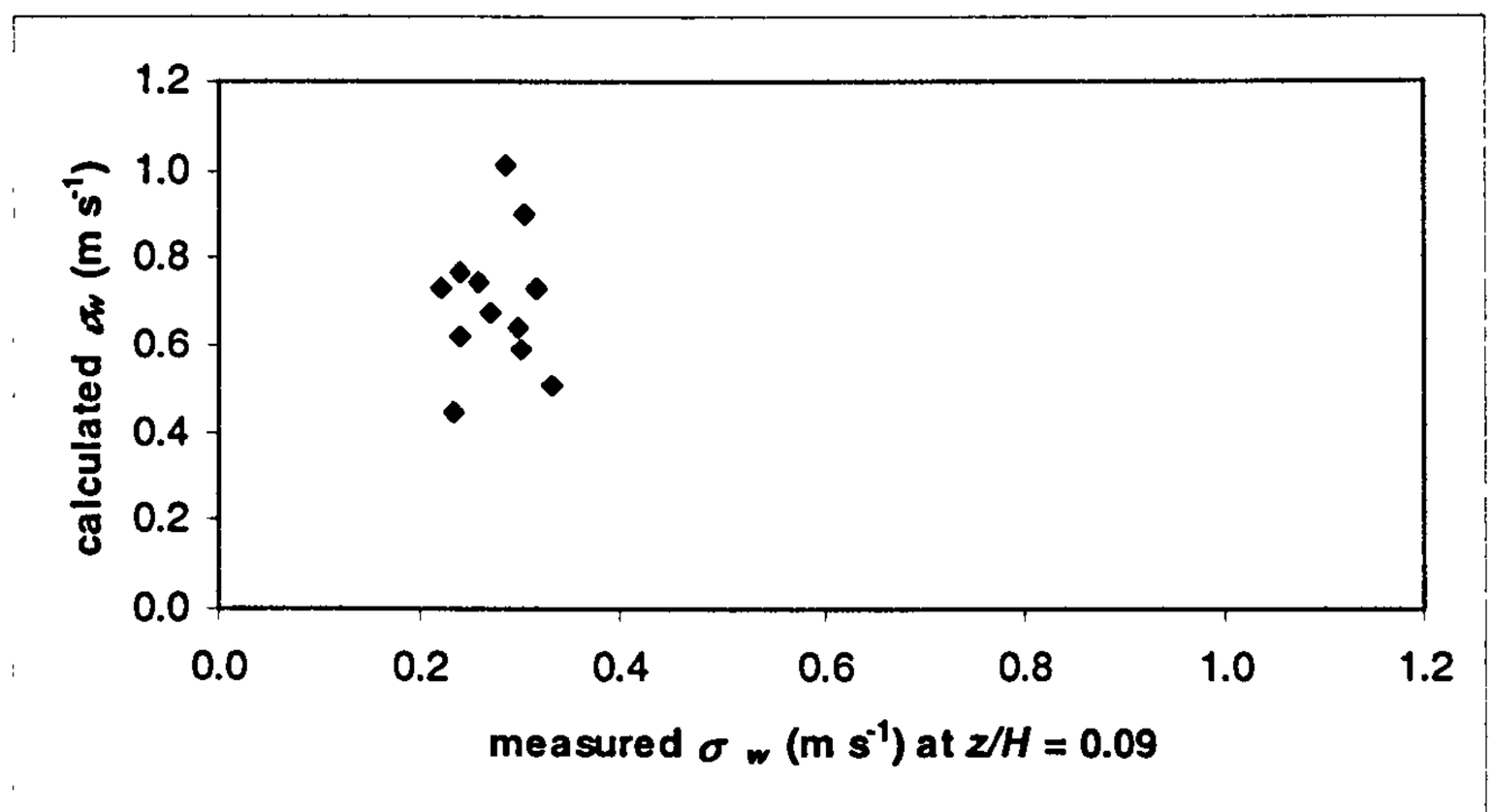


Figure 6.12. Comparison of calculated and measured $\sigma_w$ at $z/H = 0.09$ averaged over 1-minute periods; conditioned on $\theta_{ref} = 300° \pm 30°$ and $U_{ref} \leq 1.2$ m s$^{-1}$ and using: (a) Equation (6.13); (b) Equation (6.15); and (c) Equation (6.17).

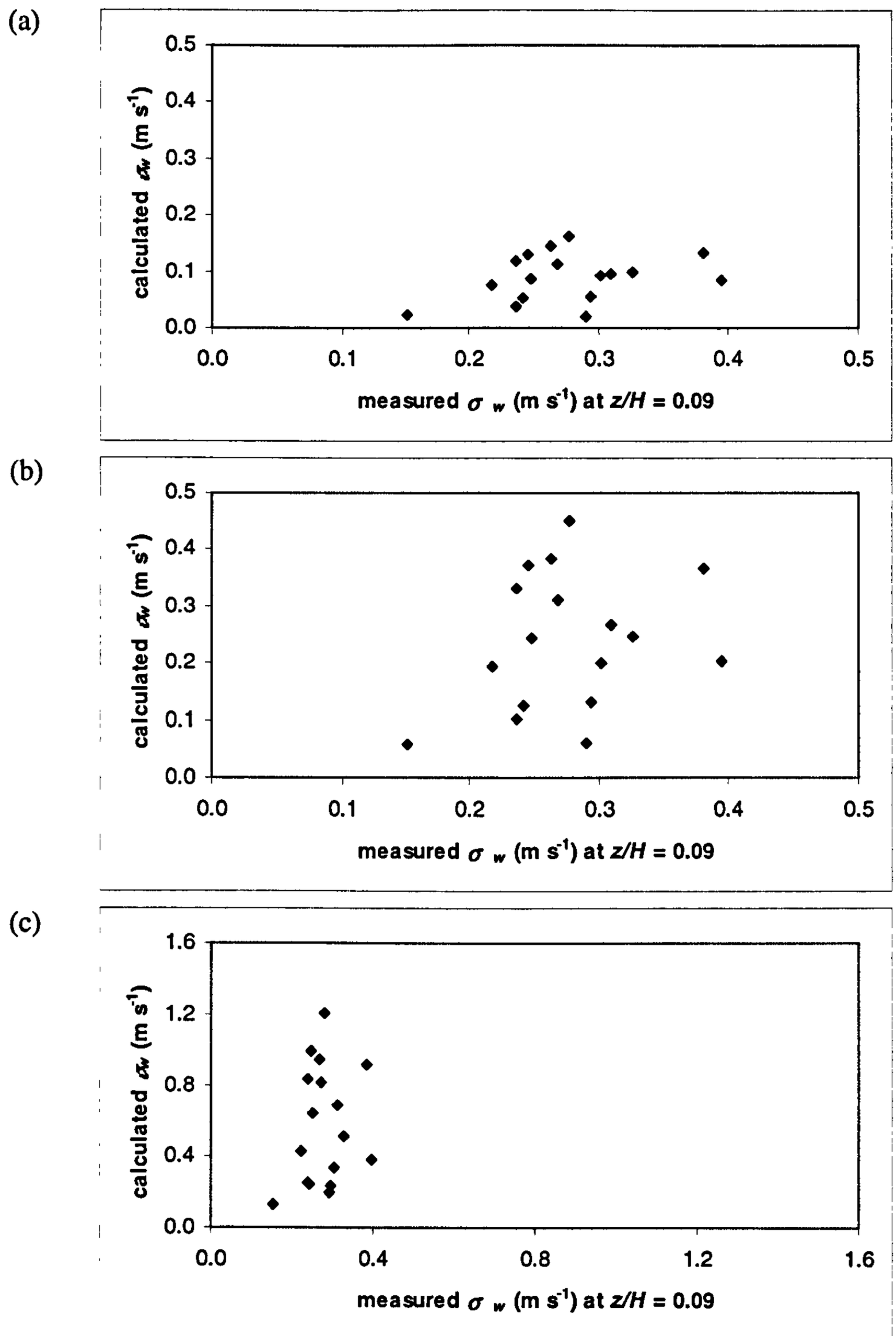


Figure 6.13. Comparison of calculated and measured $\sigma_w$ at $z/H = 0.09$ averaged over 1-minute periods; conditioned on $\theta_{ref} = 30° \pm 30°$ and $U_{ref} \leq 1.2$ m s$^{-1}$ and using: (a) Equation (6.13); (b) Equation (6.15); and (c) Equation (6.17).

(a)

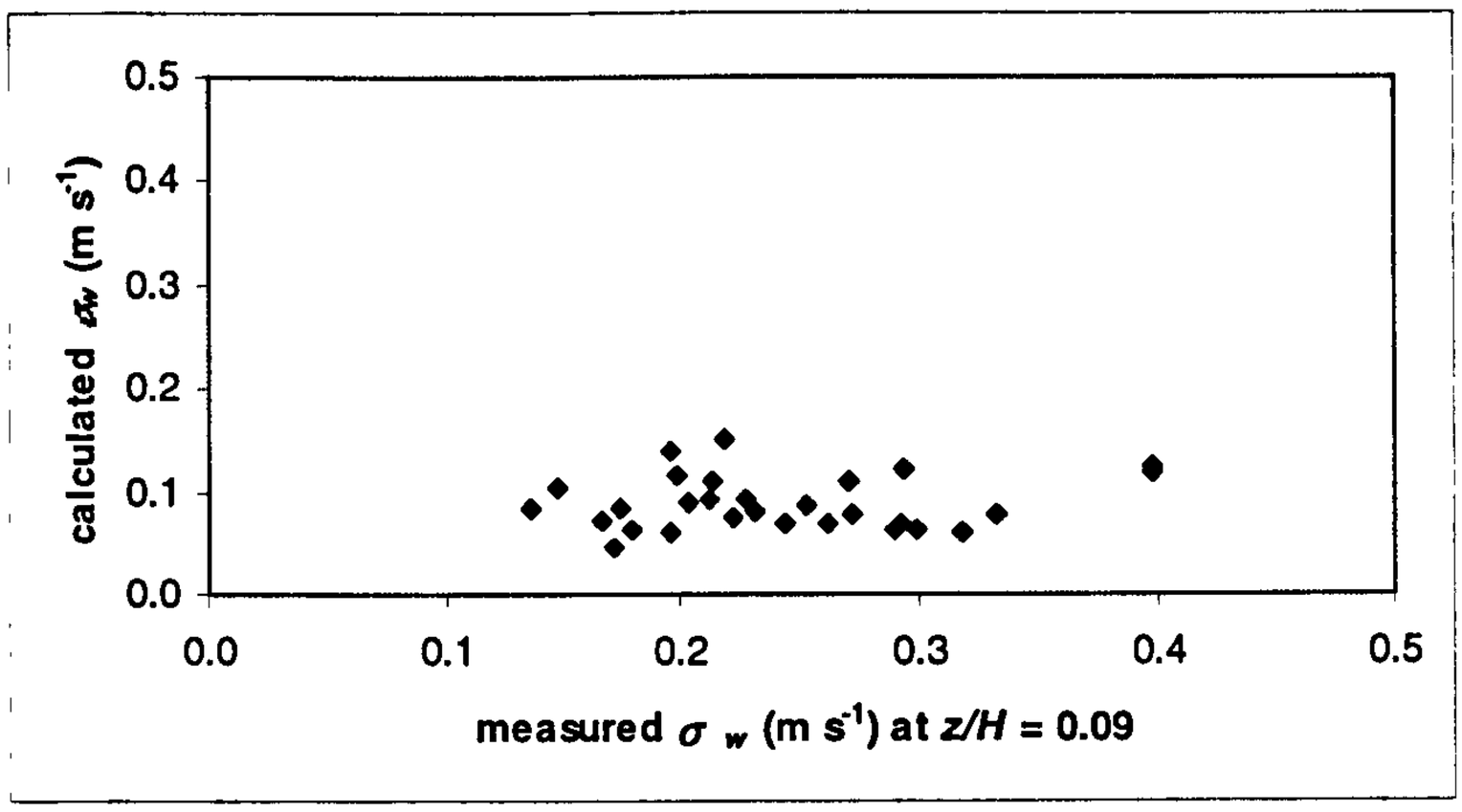


(b)

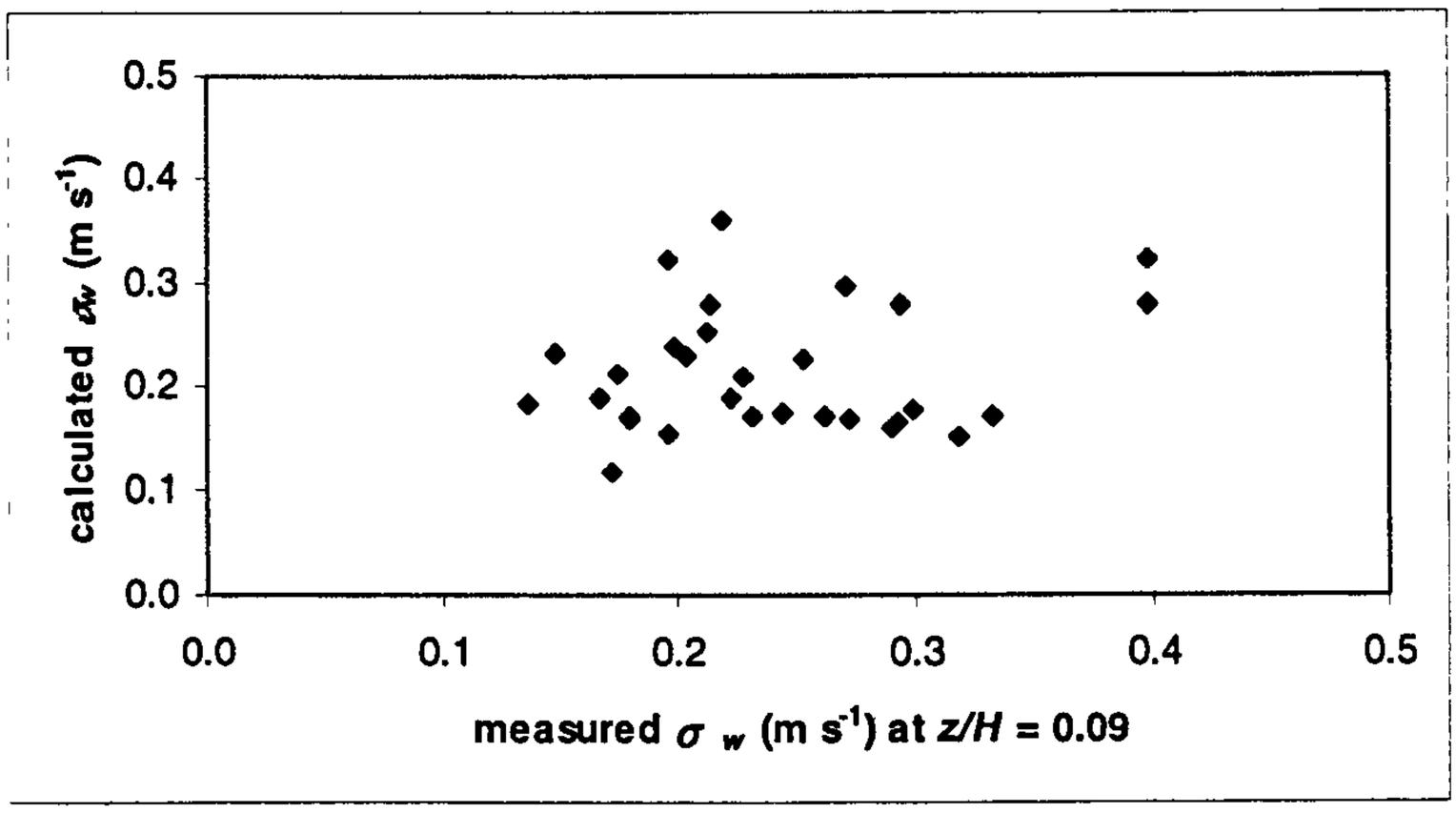


(c)

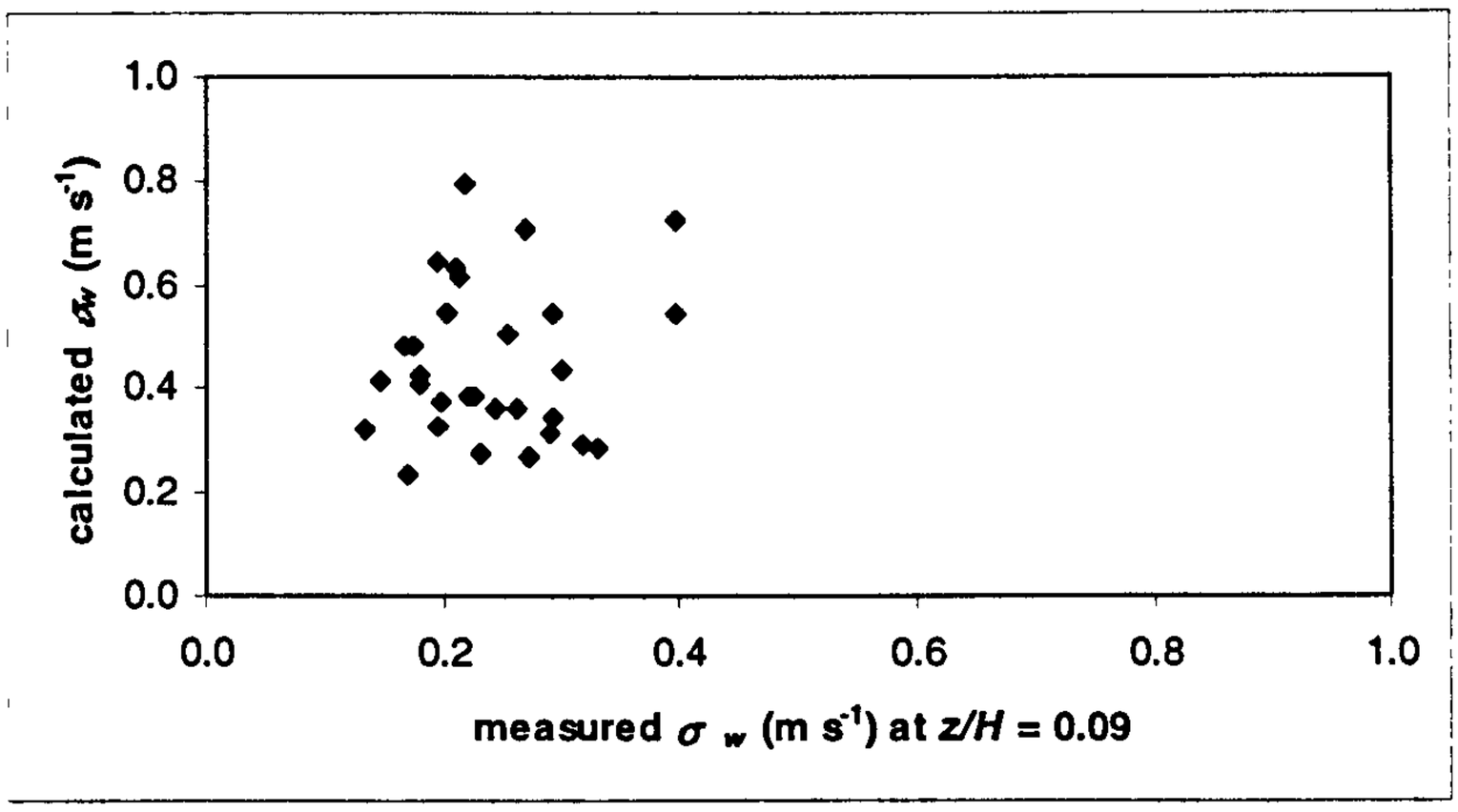


Figure 6.14. Comparison of calculated and measured $\sigma_w$ at $z/H = 0.09$ averaged over 1-minute periods; conditioned on $\theta_{ref} = 210° \pm 30°$ and $U_{ref} \leq 1.2$ m s$^{-1}$ and using: (a) Equation (6.13); (b) Equation (6.15); and (c) Equation (6.17).

### *6.4.3. Model validation using TKE*

Comparisons between the calculated turbulence and measured standard deviation of the vertical velocity, $\sigma_w$, presented in Section 6.4.2 revealed statistically significant correlations between the two quantities, even though the number of data values was small. Equations (6.13), (6.15) and (6.17) were used to calculate the turbulence, believed in this instance to be $\sigma_w$. However, the only statistically significant correlations (at the 0.5% level) were found between the calculated turbulence and the measured $\sigma_w$ at $z/H = 0.09$ when the data were conditioned on $\theta_{ref} = 120°\pm30°$ and $\theta_{ref} = 120°\pm45°$. For all remaining background wind directions and heights there were no statistically significant correlations between the two quantities (Table 6.2).

Due to the confusion between the turbulence parameters calculated by Equations (6.13), (6.15) and (6.17) described in Section 6.2.4, comparisons were made between the calculated turbulence and the measured TKE at $z/H = 0.09$ and at $z/H = 0.3$ on lamppost G3. For clarity, the same calculated turbulence values derived from Equations (6.13), (6.15) and (6.17) were used. The data were conditioned on $U_{ref} \leq 1.2$ m s$^{-1}$ and the same $\theta_{ref}$ sectors shown in Table 6.2 were used. However, including the horizontal turbulence components did not improve the correlations between the two quantities. Table 6.3 presents the regression analysis results for the calculated turbulence against measured TKE. In fact, the correlations between the calculated turbulence values and the measured TKE were generally not statistically significant even at $z/H = 0.09$ when the data were conditioned on $\theta_{ref} = 120°\pm30°$ and $\theta_{ref} = 120°\pm45°$.

The weaker relationships revealed from the TKE analysis may have been caused by the anisotropic nature of the turbulence, even for $U_{ref} \leq 1.2$ m s$^{-1}$. It was revealed in Chapter 4 that for a broad range of background wind directions for $U_{ref} > 1.2$ m s$^{-1}$, the along-canyon fluctuations dominated. Therefore, if it is assumed that the along-canyon fluctuations due to $U_{ref}$ dominated even during $U_{ref} \leq 1.2$ m s$^{-1}$, it is possible that they may have swamped any effects of TPT in the horizontal directions. The only statistically significant correlations were produced between the calculated turbulence values and the measured TKE at $z/H = 0.09$ when the data were conditioned on $\theta_{ref} = 30°\pm30°$. However, this may have been caused by the

production of shear turbulence following flow distortion at lamppost G3 during along-canyon channel flows under near-parallel background winds.

Table 6.3. Regression analysis of the calculated turbulence and measured TKE ($m^2 s^{-2}$) at lamppost G3 conditioned on $U_{ref} \leq 1.2$ m $s^{-1}$ and as a function of background wind direction, $\theta_{ref}$. # Note that NS is an abbreviation for *Not Significant.*

| background wind direction, $\theta_{ref}$ | equation number | $z/H$ | $r$ | $r^2$ | linear regression analysis slope | degrees of freedom, $df$ | significance level# (%) |
|---|---|---|---|---|---|---|---|
| 120° ±30° | (6.13) | 0.09 | 0.25 | 0.07 | 0.12 | 23 | NS |
| 120° ±30° | (6.15) | 0.09 | 0.22 | 0.05 | 0.29 | 23 | NS |
| 120° ±30° | (6.17) | 0.09 | 0.22 | 0.05 | 0.94 | 23 | NS |
| 120° ±30° | (6.13) | 0.30 | 0.20 | 0.04 | 0.29 | 23 | NS |
| 120° ±30° | (6.15) | 0.30 | 0.14 | 0.02 | 0.35 | 23 | NS |
| 120° ±30° | (6.17) | 0.30 | 0.10 | 0.01 | 0.61 | 23 | NS |
| 120° ±45° | (6.13) | 0.09 | 0.25 | 0.06 | 0.12 | 28 | NS |
| 120° ±45° | (6.15) | 0.09 | 0.25 | 0.06 | 0.31 | 28 | NS |
| 120° ±45° | (6.17) | 0.09 | 0.28 | 0.08 | 1.10 | 28 | NS |
| 300° ±30° | (6.13) | 0.09 | 0.35 | 0.12 | 0.17 | 10 | NS |
| 300° ±30° | (6.15) | 0.09 | 0.25 | 0.06 | 0.27 | 10 | NS |
| 300° ±30° | (6.17) | 0.09 | 0.00 | 0.00 | -0.09 | 10 | NS |
| 30° ±30° | (6.13) | 0.09 | 0.48 | 0.23 | 0.04 | 15 | 5.0 |
| 30° ±30° | (6.15) | 0.09 | 0.48 | 0.23 | 0.27 | 15 | 5.0 |
| 30° ±30° | (6.17) | 0.09 | 0.44 | 0.19 | 1.82 | 15 | 10.0 |
| 210° ±30° | (6.13) | 0.09 | 0.20 | 0.04 | 0.04 | 28 | NS |
| 210° ±30° | (6.15) | 0.09 | 0.25 | 0.06 | 0.10 | 28 | NS |
| 210° ±30° | (6.17) | 0.09 | 0.20 | 0.04 | 0.21 | 28 | NS |

## 6.5. Summary and Conclusions

In this Chapter it was mentioned that there was confusion concerning the exact turbulence parameters that were calculated using the formulations of Di Sabatino *et al.* (2003) and Kastner-Klein *et al.* (2003). Separate comparisons between calculated turbulence and measured standard deviation of the vertical velocities, $\sigma_w$, and the calculated turbulence and measured TKE revealed that the parameterisations better represented $\sigma_w$.

The correlation coefficients for the relationship between the calculated and measured $\sigma_w$ at $z/H$ = 0.09 were statistically significant during weak ($U_{ref}$ ≤ 1.2 m $s^{-1}$) perpendicular SE winds, i.e. when the anemometer was located on the leeward side of the canyon. Even during weak SE winds, moderately strong downdraughts and updraughts were observed on the windward and leeward sides of the canyon, respectively. Under these background wind conditions a single across-canyon recirculating flow may have developed inside Gillygate, aiding the advection of TPT to the leeward side of the canyon. This supports the findings of Vachon *et al.* (2002) and may explain why TPT effects were most noticeable at this height during these background wind conditions. A wider perpendicular SE wind direction sector was also used in order to include possible effects associated with helical flows along the canyon during oblique background winds. The correlation coefficients were slightly higher for the calculations based on intermediate traffic densities, which perhaps is not surprising given the predominance of unstable traffic flow conditions during the period of the TPT investigations.

Although statistically significant, the correlation coefficients were lower than those presented in the work of Kastner-Klein *et al.* (2003). This was also probably due to the predominance of unstable traffic flow conditions along Gillygate, leading to overall lower mean vehicle speeds. The traffic flow observed by Kastner-Klein *et al.* (2003) in their study was primarily free flowing, during which vehicle speeds were higher and TPT effects more active. The poor correlations between the calculated and measured $\sigma_w$ at $z/H$ = 0.3 suggests that the TPT effects were weaker at this height, even during perpendicular SE winds. It is believed that this height is above the traffic layer in which TPT effects were most active.

Weak perpendicular NW winds caused updraughts on both sides of the canyon, which indicates that along-canyon flow convergence may have dominated. As a result, the influence of TPT on the windward side of the canyon was not noticeable during these background winds. During near-parallel background winds the correlations between the calculated and measured $\sigma_w$ were not statistically significant. Along-canyon winds are likely to have transported the majority of TPT past the transverse roadside measurement locations.

# CHAPTER 7

# The influence of traffic characteristics on the spatial variability in concentrations of a traffic-related pollutant

## 7.1. Introduction

Despite significant improvements in fuel and engine technology, traffic is still considered to be the major source of urban air pollution. Traffic-related pollutants include: carbon monoxide (CO); oxides of nitrogen ($NO_x$); hydrocarbons; and particulates (Chapter 2). It is now generally accepted that many traffic-related pollutants represent a hazard to human health (e.g. indicated by an increased number of respiratory hospital admissions) and damage costs for the exposed population (Spadaro & Rabl, 2001). Colvile et al. (2001) reviewed a number of studies that provide evidence that fine particles emitted by traffic may be responsible for measurable increases in the manifestations of cardiovascular and respiratory diseases even at the comparatively low levels of air pollution in modern Western cities.

Areas of high, localised pollution are usually found in urban 'hot-spots'. It was mentioned in Chapter 2 that local authorities are required to meet Air Quality Management targets for urban areas. Therefore, many local authorities are considering the application of traffic management strategies for 'hot-spots' projected to exceed these targets. These may include: controlling traffic signals; re-locating traffic queues during congested periods; and the introduction of low emission zones and congestion charging. In many instances local authorities aim to predict the possible influences on roadside pollutant concentrations using air quality dispersion

models before applying such measures. However, these models are often not able to represent urban driving cycles adequately and ignore elevated emissions that are primarily due to vehicles accelerating. Modelling aspects will be discussed in more detail in Chapter 8.

It is important that any dispersion model that is used to inform decisions on air quality and traffic management strategies must be able to represent the influence of traffic on road-side concentrations for a range of realistic street geometries and background (or above-roof) wind flow directions. Presently, many such numerical models are being developed based on, for example, empirical, box model, Gaussian, or CFD approaches (Chapter 2). Comprehensive evaluation of these models requires simultaneous measurements of the key parameters, but very few appropriate data sets currently exist. In the present study, involving field experiments, an attempt is made to determine the influence of different traffic characteristics on the dispersion of a traffic-related pollutant within two urban streets of different geometry. The simultaneous monitoring of the spatial distribution of a traffic-related pollutant alongside detailed information on background wind direction and traffic characteristics allows for the investigation into the relative importance of the factors influencing high roadside pollutant concentrations. Furthermore, it allows for the assessment of the requirements of air quality models to represent the key effects.

The influence of driving mode on vehicle emissions is of particular importance in such a study as higher emission rates are associated with certain traffic characteristics. The four driving modes that are usually referred to in emission studies are: idling, acceleration, deceleration, and cruising. Generally, emission rates are higher for congested traffic conditions with characteristic stop-start conditions associated with periods of idling followed by acceleration (Waters, 1992; André and Pronello, 1997; De Vlieger, 1997; Marsden et al., 2001). During periods of free flow, where traffic is relatively uninterrupted and cruising mode is usual, emission rates are comparatively low. However, the switching between free flow and congested flow coincides with periods of unstable flow when all four driving modes occur. Rapone et al. (2000) studied the emission behaviour of a small capacity catalysed car. The authors found that during highly congested traffic situations the car emits more than twice the amount of CO (g $km^{-1}$) than at higher speeds during free flow. Tate (2005)

applied an integrated modelling approach to study the temporal and spatial variations in vehicular emissions at the local scale. They demonstrated that vehicular emissions of CO were largely associated with accelerating driving modes and consequently emission levels were higher at the intersection in free-flowing traffic conditions than at mid-link locations (see Chapter 8).

### 7.1.1. Chapter synopsis

It was demonstrated in Chapters 4 and 5 that poor dispersion conditions often arise inside street canyons, leading to the occurrence of pollution hot-spots. Our attention in this Chapter focuses on the influence of traffic characteristics on the spatial variability in CO concentrations within two street canyons. Boddy *et al.* (2005b) described the work presented in this Chapter, which continues the investigation of the influence of the background wind on the dispersion of traffic-related pollutants inside street canyons.

This Chapter focuses on the influence of traffic characteristics and driving mode, with particular emphasis on the effects of free, unstable and congested traffic conditions on in-canyon pollutant concentrations. As in Chapter 5, consideration is given to weekday data only in order to exclude the influence of weekend traffic characteristics. The two chapters taken together represent a comprehensive study which attempts to bring together the influences of meteorology, urban topography and traffic characteristics on the spatial and temporal variability in concentrations of CO in two street canyons of differing geometry.

## 7.2. Experimental Method

### 7.2.1. The site

The experiment was conducted within the Bootham and Gillygate street canyons for 4 weeks from 13 October 2003 until 12 November 2003. The canyons are aligned orthogonal to one another and are joined by a common traffic-signal controlled intersection as illustrated in Figure 7.1. Reference should be made to Chapter 3 for a more detailed description of the street canyon geometries. Both streets have high

daytime traffic flow rates (of order $10^3$ vehicles $h^{-1}$), with significant periods of congestion.

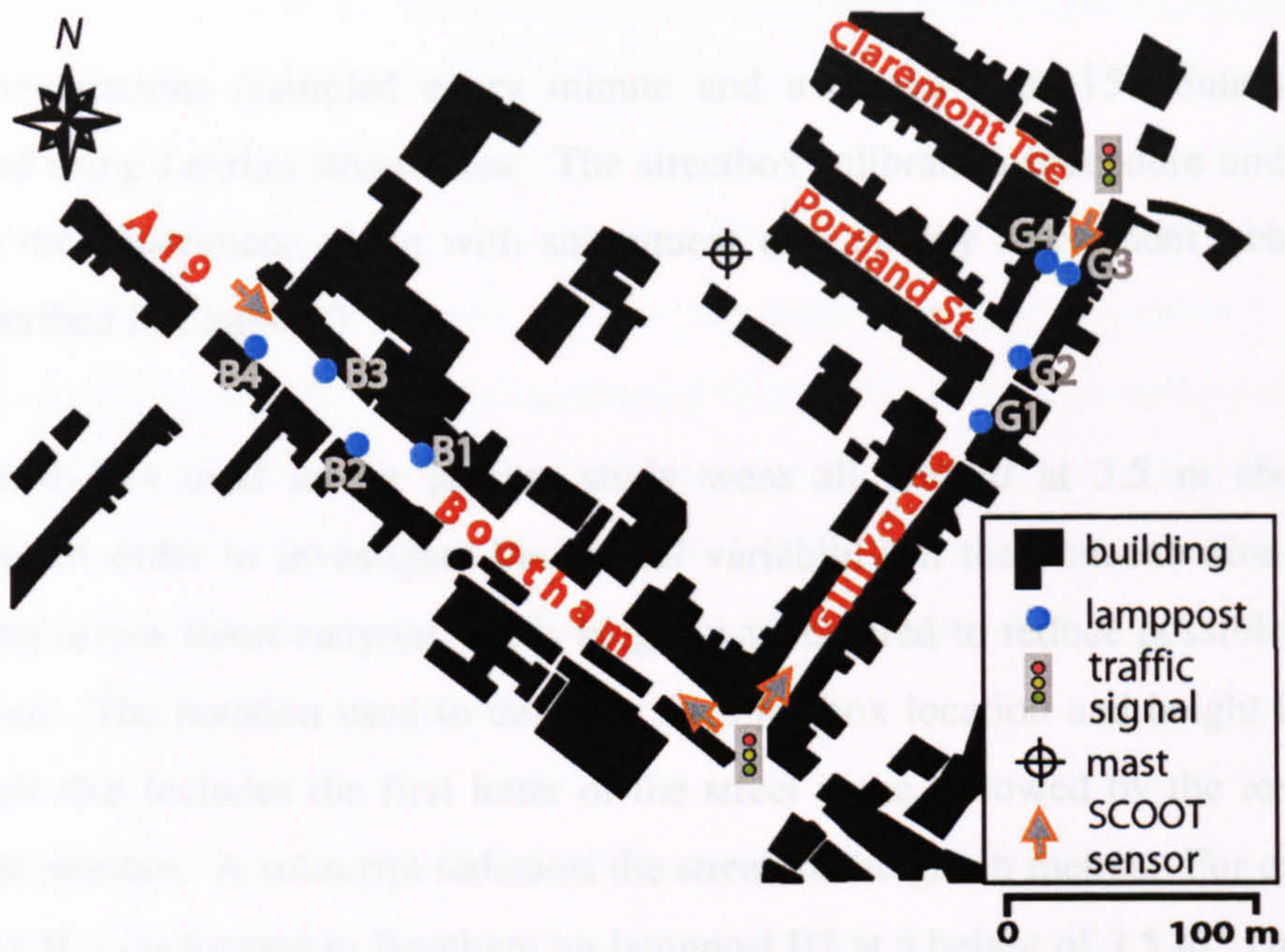


Figure 7.1. Plan view of the study area showing the street canyons, the lampposts that support the instruments, the reference anemometer mast, the traffic signal controlled intersections and the four SCOOT sensors (arrows indicate the direction of traffic flow measured).

### 7.2.2. Instrumentation and Experiments

*7.2.2.1. The background wind speed and direction*

Measurements of the background wind speed and direction were made using an ultrasonic anemometer attached to a trailer-mounted mast at a height of 19.5 m (Figure 7.1). Chapter 3 contains a more detailed description of the experimental methodology.

*7.2.2.2. Carbon monoxide concentrations*

The traffic-related pollutant measured in this study was CO and is consistent with the analysis presented in Chapter 5. Although there have been no recent exceedences of the National Air Quality Standards in the U.K. for CO, the pollutant acts as a useful tracer for traffic related pollutants, particularly in streets where the dominant vehicle

type is the passenger car, as is the case in Gillygate and Bootham. Additional reasons for choosing CO as the pollutant to measure in this study were mentioned in Chapter 3.

CO concentrations (sampled every minute and averaged over 15 minutes) were measured using Learian streetboxes. The streetbox calibration procedure undertaken prior to the experiment, along with subsequent data quality assessment techniques, was described in Chapter 3.

The streetboxes used in the present study were all located at 3.5 m above the pavement in order to investigate the spatial variability in the concentration of CO along and across street canyons. This height was required to reduce possible acts of vandalism. The notation used to describe the streetbox location and height is given by a code that includes the first letter of the street name followed by the respective lamppost number. A subscript indicates the streetbox height in metres. For example, streetbox $B1_{3.5}$ is located in Bootham on lamppost B1 at a height of 3.5 m. Only data from streetboxes $G3_{3.5}$, $G4_{3.5}$, $B1_{3.5}$, and $B2_{3.5}$ are presented in this Chapter. The locations of the streetboxes are shown in Figure 7.1.

*7.2.2.3. The traffic flow characteristics*

Traffic flow along Gillygate and Bootham is controlled by the SCOOT system. SCOOT uses inductive loops buried in the road surface to collect information on detector occupancy (see Chapter 3). This information is used in the SCOOT traffic model to optimise signal timings at traffic lights (Hunt et al., 1991). The term '*link*' refers to the length of road between the SCOOT detector and the stop line at the traffic light. Each SCOOT detector is located upstream of the stop line and the direction of the traffic flow stream that each detects and controls is shown in Figure 1. The detectors are located at the upstream end of each link in order to maximise the effectiveness of traffic monitoring by decreasing the probability of vehicles remaining stationary on them during congested traffic flows.

Although the inductive loop detectors used by SCOOT do not explicitly classify vehicles, they do record occupancy '*events*' at a frequency of 4 Hz. 'Event' refers to

the detection of a vehicle occupying the detector loop area within a ¼ s period. The raw SCOOT detector data (referred to as the M19 message) were collected during the investigation, allowing the identification of individual vehicle events at the entry to each link in the study area. Various traffic characteristics may also be derived from the M19 message, which include the detector occupancy and traffic flow. Detector occupancy is equivalent to the percentage of time that a detector is occupied and is a function of both vehicle speed and length. Traffic flow is defined as the rate of vehicles passing over a detector, i.e. it represents separate occupancy events. Therefore, vehicle speed, detector occupancy and traffic flow are useful parameters that can be used to describe traffic characteristics and can be determined from the SCOOT system. The positioning of the SCOOT detectors at the entrance to each link meant that the occupancy data gave a measure of the temporal change in the overall level of congestion within each traffic flow stream.

However, it was mentioned in Chapter 3 that under some circumstances the detection area of each loop can vary by up to 25%, depending on the individual vehicle chassis characteristics (e.g. height above the road or metallic content). Additionally, SCOOT detectors can be susceptible to 'nose-to-tail' masking, i.e. two or more slow moving vehicles travelling close together may register as a single vehicle event. Furthermore, SCOOT detectors are omni-directional, meaning that a vehicle travelling opposite to the expected flow direction over the loop (e.g. emergency vehicles) would have been recorded in that traffic stream. Therefore, an important part of the current study was to evaluate the SCOOT system using manually recorded traffic data as described in the following Section. Relative to the inbound detector loop for each link, streetboxes $G3_{3.5}$ and $G4_{3.5}$, were each 25 m from Gillygate's inbound detector, whereas $B1_{3.5}$, and $B2_{3.5}$ were 50 m and 40 m, respectively.

## 7.3. Results and Discussion

### 7.3.1. Verification of the SCOOT system

The accuracy of the SCOOT system was determined through a comparison between the direct observations of traffic recorded manually and the synchronised detector data collected for a period of approximately four hours on 10 November 2003.

Observations of the bi-directional traffic flow in Gillygate and Bootham comprised both off-peak and the afternoon-peak flows along all four links.

Vehicles observed along the links were classified according to a six-vehicle category scheme using a computer program described in detail in Chapter 3. During the four-hour period a total of 6,762 vehicles were observed along the four links, of which approximately 91% were cars, 3% were light goods vehicles (LGVs), 3% were buses, 2% were motorcycles (MCs) and 1% were heavy goods vehicles (HGVs). An insignificant fraction of the traffic flows in both streets were classed as 'other'. Table 7.1 and Table 7.2 show the comparison between the manually collected vehicle observations and the processed SCOOT detector data along Gillygate and Bootham, respectively.

Comparison between observations and the SCOOT detector data indicate that for the three traffic flow links, excluding Gillygate inbound, detectors captured an average of 96% of the observed flow. Gillygate inbound was the most heavily congested traffic flow stream with static queues often stretching the entire length of the link throughout the majority of the day. The lower capture rate (90%) for Gillygate inbound was most likely a result of nose-to-tail masking, as shown in Table 7.2.

Table 7.1. Manual vehicle observations compared with SCOOT detector performance along Gillygate on 10 November 2003.

| Classification | Number of events observed | | Number of events detected by SCOOT | | Percentage of detected events in relation to observed events | |
|---|---|---|---|---|---|---|
| Detector location | Gillygate | | Gillygate | | Gillygate | |
| | Inbound | Outbound | Inbound | Outbound | Inbound | Outbound |
| All vehicles | 2282 | 1869 | 2054 | 1800 | 90.0 | 96.3 |
| Cars | 2115 | 1694 | 1905 | 1681 | 90.1 | 99.2 |
| LGVs | 20 | 25 | 17 | 23 | 85.0 | 92.0 |
| Buses | 85 | 82 | 81 | 82 | 95.3 | 100.0 |
| HGVs | 25 | 3 | 25 | 3 | 100.0 | 100.0 |
| MCs | 30 | 64 | 26 | 11 | 86.7 | 17.2 |
| Other | 7 | 1 | 0 | 1 | 0.0 | 100.0 |

The inbound flow determined by SCOOT was compared against manual observations of the inbound flow according to a six-vehicle category scheme for 11 days during the experiment, conducted between 07:45 and 18:00 inclusive, in order to examine the nose-to-tail effect more closely. For clarity, these manual observations were undertaken as part of a separate survey to the one conducted on the 10 November 2003. The manual observations of the traffic flow passing over the inbound SCOOT detector consisted of a total of 118 fifteen-minute mean values, which is equal to 29.5 hours of data. Figure 7.2 presents the mean 15-minute SCOOT inbound traffic flow against the manual observations of the traffic flow. Although the figure demonstrates that there was a strong correlation between the two quantities it is evident from the slope of the regression line (0.694 veh $h^{-1}$) that SCOOT consistently reported lower mean inbound traffic flows. It should be noted that the mean difference (systematic error) may partly be due to synchronisation error of the internal PC clocks used for the manual data collection and SCOOT computer. However, the relatively low slope and $r^2$ value of 0.63 give further indication that the inbound SCOOT detector on Gillygate was likely to have been susceptible to nose-to-tail masking associated with heavily congested traffic with static queues. During periods of stationary or slow moving traffic it is likely that the SCOOT detector was unable to distinguish between the end of one vehicle and the beginning of the vehicle following.

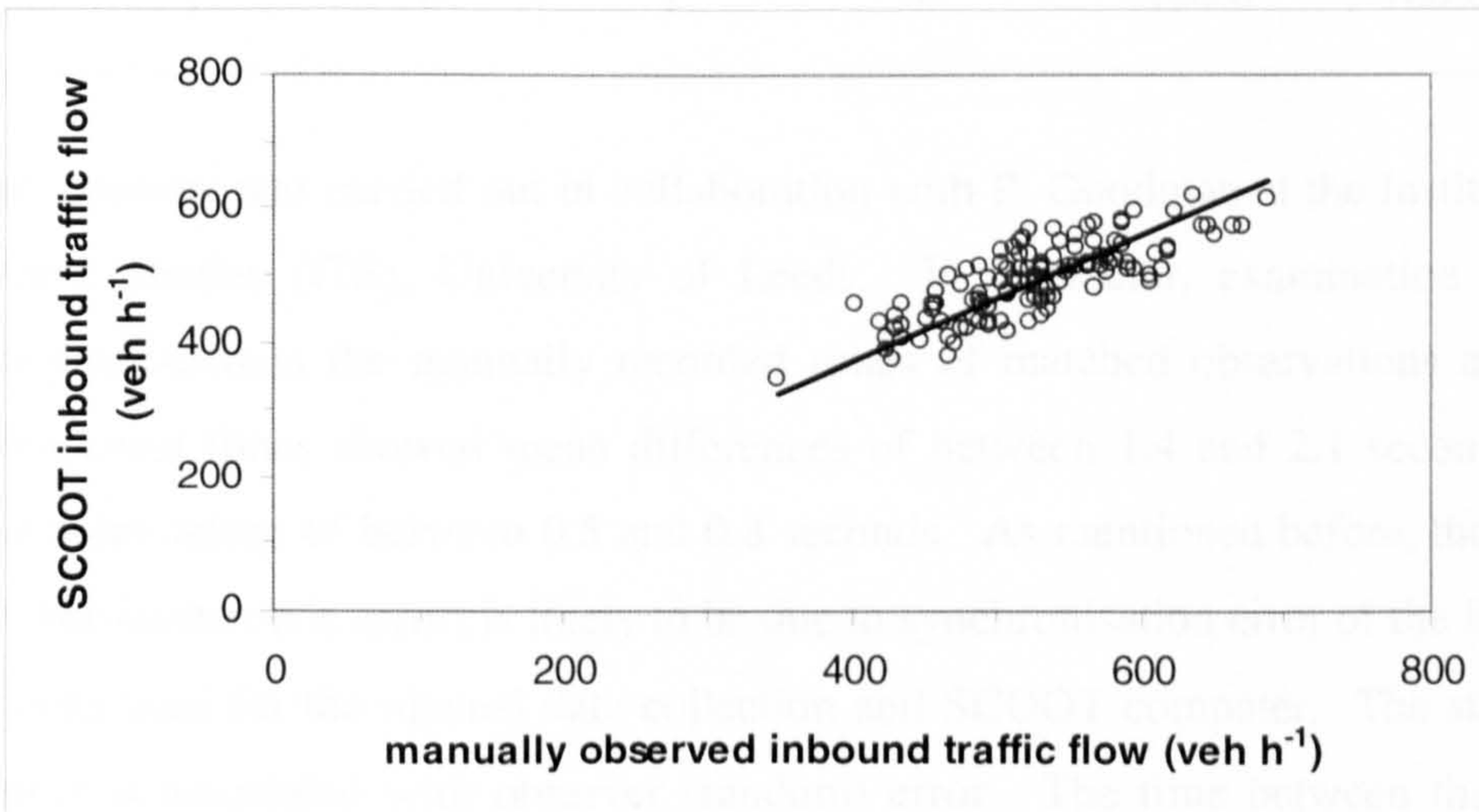


Figure 7.2. Fifteen-minute mean SCOOT inbound traffic flow against the manual observations of the inbound traffic flow along Gillygate during the period of the field experiment.

The manual vehicle observations compared with SCOOT detector performance along Gillygate and Bootham on 10 November also suggest that the reduction in the mean vehicle speed during periods of congestion may also lower the loop detector inductance and reduce the detector's accuracy. The very low capture rate for motorcycles (17%) for Gillygate outbound is attributed to the inductor loop position relative to the junction, resulting in the trajectory of most motorcycles avoiding the loop.

Table 7.2. Manual vehicle observations compared with SCOOT detector performance along Bootham on 10 November 2003.

| Classification | Number of events observed | | Number of events detected by SCOOT | | Percentage of detected events in relation to observed events | |
|---|---|---|---|---|---|---|
| Detector location | Bootham | | Bootham | | Bootham | |
| | Inbound | Outbound | Inbound | Outbound | Inbound | Outbound |
| All vehicles | 1078 | 1538 | 1035 | 1462 | 96.0 | 92.3 |
| Cars | 959 | 1386 | 930 | 1356 | 97.0 | 97.8 |
| LGVs | 63 | 63 | 59 | 59 | 93.7 | 93.7 |
| Buses | 10 | 41 | 9 | 40 | 90.0 | 97.6 |
| HGVs | 17 | 4 | 16 | 4 | 94.1 | 100.0 |
| MCs | 28 | 39 | 20 | 3 | 71.4 | 7.7 |
| Other | 1 | 0 | 1 | 0 | 100.0 | 100.0 |

Further analysis was carried out in collaboration with P. Goodman at the Institute for Transport Studies (ITS), University of Leeds. In particular, examination of the differences between the manually recorded times of matched observations and the detector event times showed mean differences of between 1.4 and 2.1 seconds and standard deviations of between 0.5 and 0.8 seconds. As mentioned before, the mean difference (systematic error) is likely to be due to synchronisation error of the internal PC clocks used for the manual data collection and SCOOT computer. The standard deviation is associated with observer (random) error. The time between the same points on successive vehicles is known as the *headway*. Analysis of headway distribution data showed no statistically significant difference ($\chi^2$ test at the 5% significance level) between observed and detector headways. The mean headway was

determined from headway distributions along the four links and was found to be 4 seconds.

### 7.3.2. Traffic flow and detector occupancy

In order to compare with the mean CO concentrations, 15-minute averages were obtained for both traffic flow and occupancy reported at the end-time for each time period. Figure 7.3 shows the temporal variation in the 15-minute occupancy along Gillygate and Bootham for the whole study period. As the traffic flow exceeded the capacity at the downstream stopline, the maximum detector occupancy threshold was breached and congestion occurred. The data indicate that periods of congestion existed in both streets between 08:00 and 20:00. For the majority of this time the traffic conditions switched between periods of congestion and free flow, as shown by the clustering of data points around low (~10%,) and high (~70%) occupancies, i.e. the traffic conditions were unstable. In both streets between 16:00 and 18:30 congested flow and high occupancy conditions were dominant. This is most noticeable along Gillygate for which only high occupancy occurs.

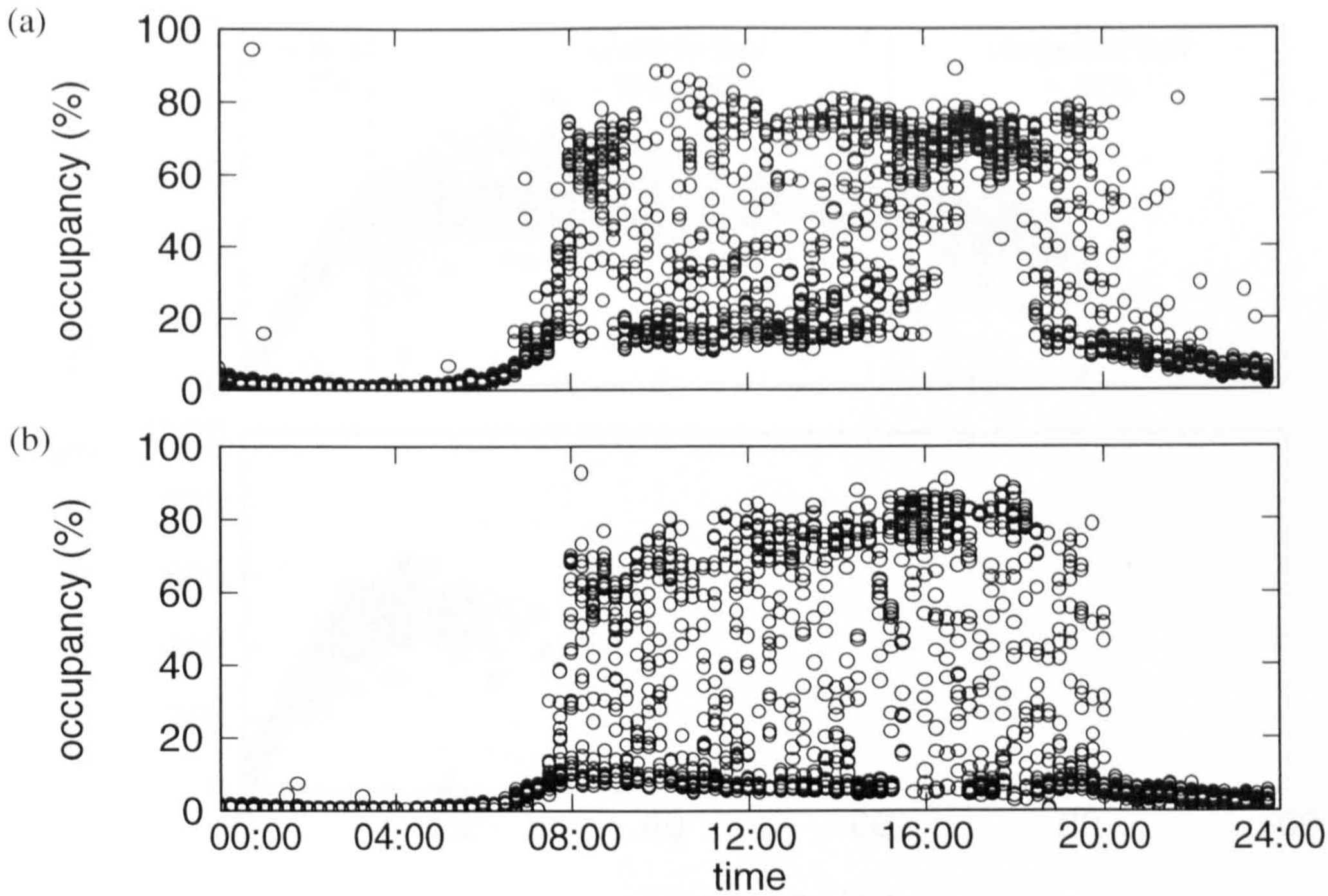


Figure 7.3. Inbound detector occupancy against time for (a) Gillygate and (b) Bootham.

Figures 7.4 and 7.5 show the 15-minute mean traffic flow plotted against the detector occupancy for both the inbound and outbound traffic along Gillygate and Bootham, respectively. For each street the inbound traffic reached capacity at approximately 12% and 10% occupancy, respectively. An increase in detector occupancy during periods of saturation did not lead to further increases in traffic flow. At very high occupancy the traffic flow decreased. This is because the amount of traffic exceeded the capacity of the network and the development of queuing traffic meant vehicles remained stationary on the loop detectors. The traffic flow decrease may also be due to the occurrence of capacity reducing incidents, such as pedestrian movements, opposing flows at downstream junctions, short-term delivery vehicle loading and unloading, which increase the probability of nose-to-tail masking.

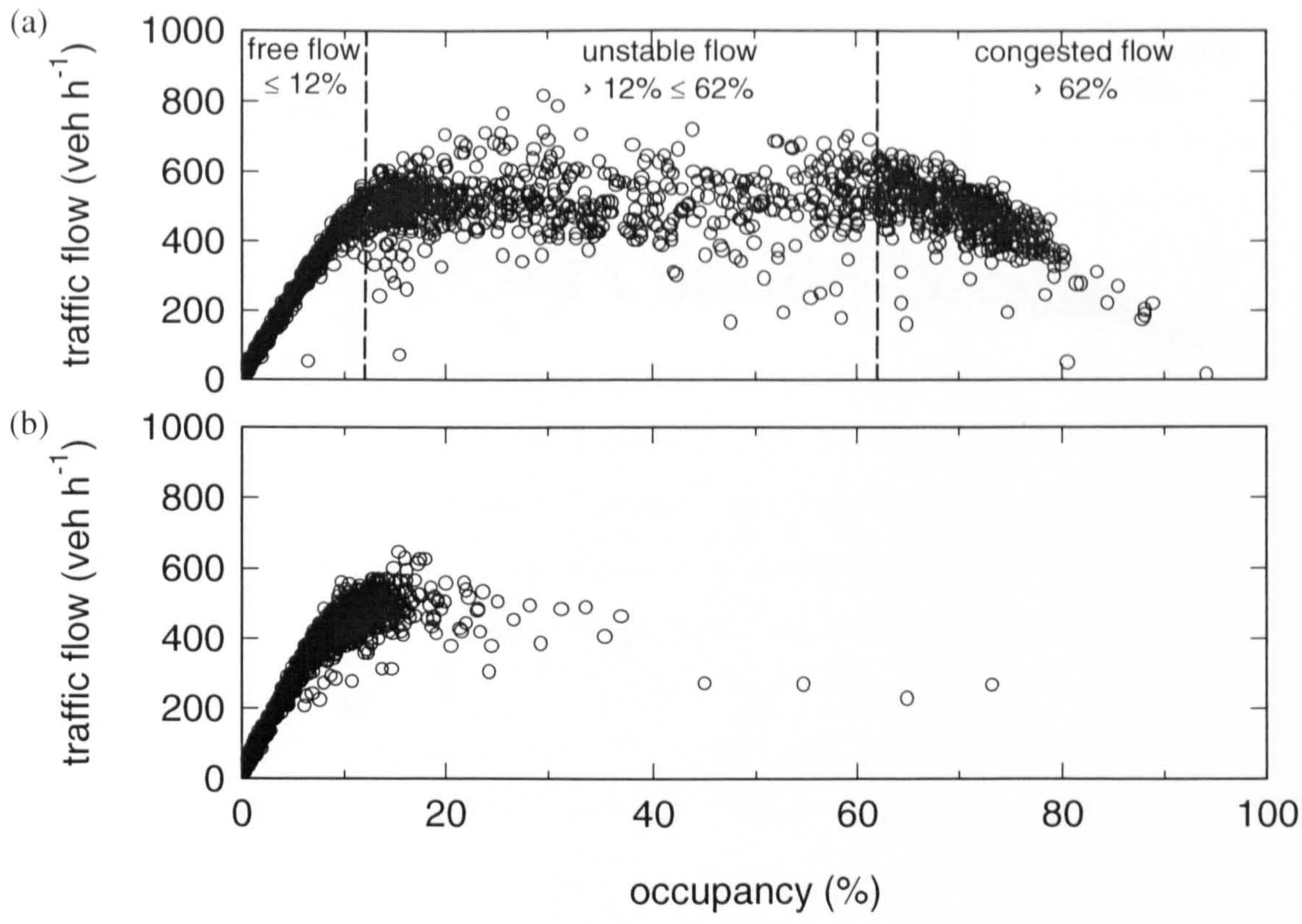


Figure 7.4. Total weekday traffic flow and occupancy along Gillygate for (a) inbound link and (b) outbound link.

The inbound traffic flow along Gillygate exhibited similar traffic conditions to those along Bootham, although Gillygate had a higher capacity flow. The mean total traffic flow during unstable conditions along Gillygate was 947 vehicles $h^{-1}$, compared with 754 vehicles $h^{-1}$ along Bootham. Outbound traffic along Gillygate and Bootham predominantly exhibited free flow conditions (Figure 7.4b and Figure 7.5b). The minority of medium and high occupancy values suggest that network saturation only rarely occurred. An approximately linear relationship exists between traffic flow and occupancy for most outbound flow conditions in both streets. A similar trend occurred during periods of high capacity inbound traffic flows in both streets, suggesting that free flow conditions occurred during these periods.

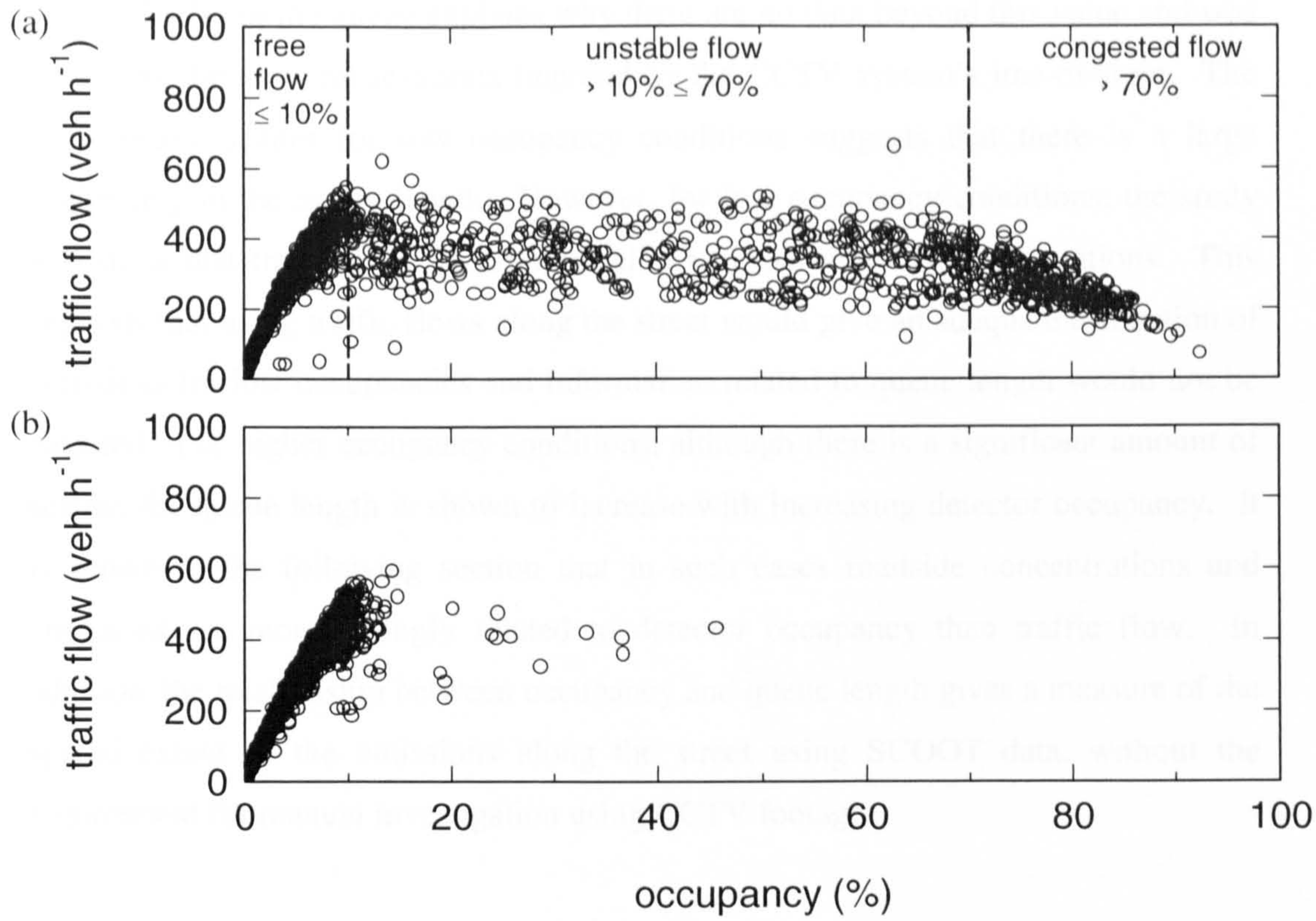


Figure 7.5. Total weekday traffic flow and occupancy along Bootham for (a) inbound link and (b) outbound link.

### 7.3.3. Detector occupancy and queue length for Gillygate inbound

In addition to the detector occupancy analysis, queue length, equal to the total number of queuing vehicles at a stop line, was determined on one link. The number of queuing vehicles within the Gillygate inbound lane were manually counted by S. Parrett, Urban Traffic Management and Control, using CCTV (closed-circuit television) footage between 09:00 – 15:00 for 11 weekdays during the period of the investigation. The stopline was near the Bootham-Gillygate intersection and was 220 m from the SCOOT sensor. Knowledge related to the position of the queue would provide information on the spatial location of emissions within the principle street studied in air quality modelling (Chapter 8). Therefore, it is useful to determine whether data that can be automatically generated from the SCOOT system, such as detector occupancy, can be used to estimate queue length.

Figure 7.6a shows the total number of vehicles in the queue for each 15-minute period against the mean 15-minute detector occupancy. The detection limit threshold

of 40 vehicles in the queue explains why there are no data beyond this value and was caused by the physical restraints imposed by the CCTV system's line-of-sight. The considerable scatter for low occupancy conditions suggests that there is a large uncertainty in the queue length. However, for low occupancy conditions, the study will show that traffic flow is strongly related to roadside CO concentrations. This suggests that using traffic flows along the street would give an adequate estimation of emissions for low occupancies and information related to queue length would not be required. For higher occupancy conditions, although there is a significant amount of scatter, the queue length is shown to increase with increasing detector occupancy. It is shown in the following section that in such cases roadside concentrations and emissions are more strongly related to detector occupancy than traffic flow. In addition, the relationship between occupancy and queue length gives a measure of the spatial extent of the emissions along the street using SCOOT data, without the requirement for manual investigation using CCTV footage.

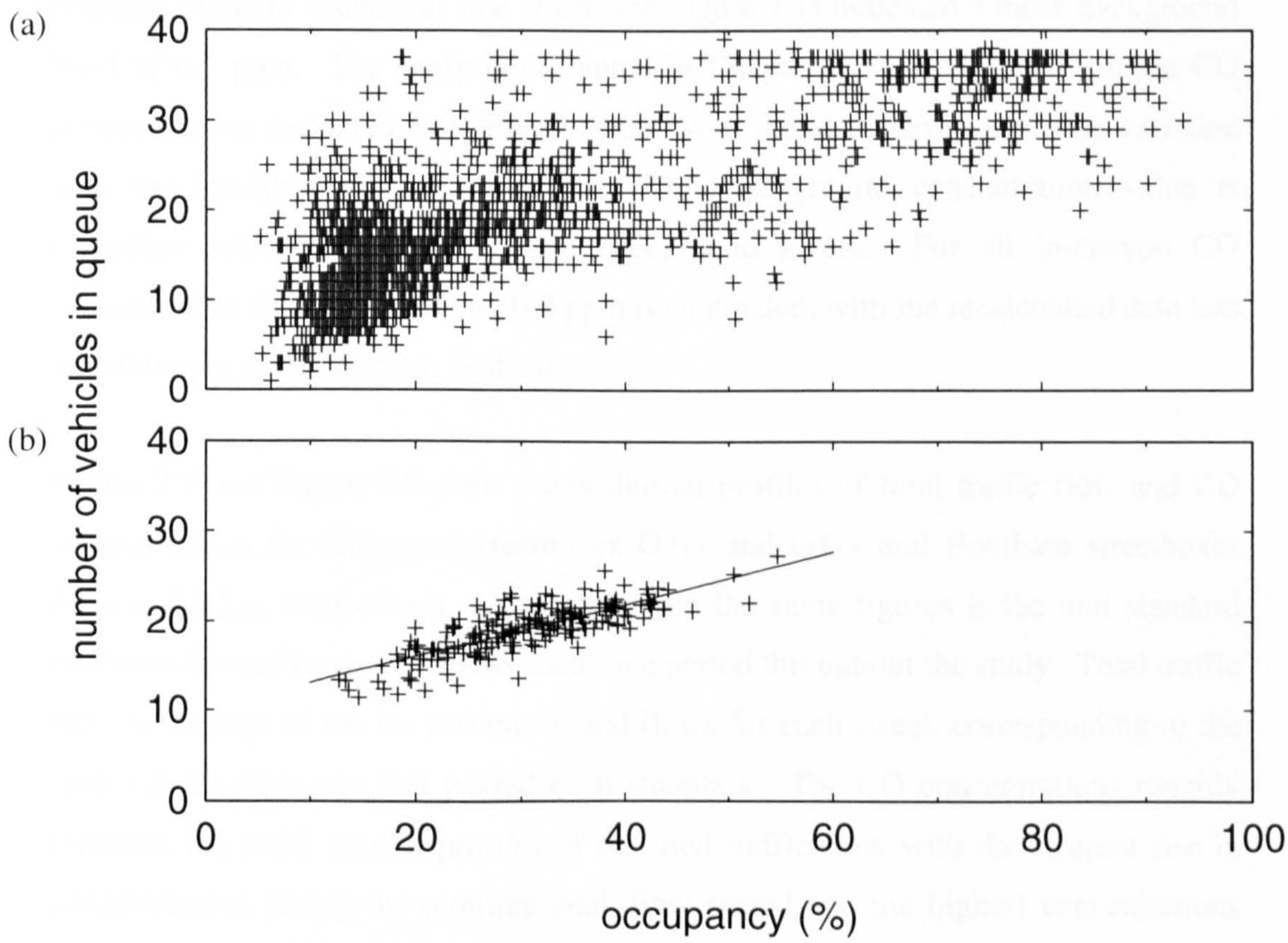


Figure 7.6. Vehicle queue length against inbound detector occupancy along Gillygate for (a) 15-minute means and (b) diurnal means.

Figure 7.6b represents the mean diurnal queue length against detector occupancy for each 15-minute period across the 11 days. As expected, this analysis produced a stronger relationship between detector occupancy and queue length with $r^2 = 0.64$. This analysis indicates the usefulness of using detector occupancy to predict diurnal mean queue length and, therefore, the spatial location of emissions for high occupancy conditions, although clearly with a degree of uncertainty. It is expected that similar relationships may exist for other streets with similar network capacity and traffic characteristics and could possibly be determined through a limited study of CCTV footage for a particular street.

### 7.3.4. Spatial and temporal variability in CO concentrations

To determine the inter-relationship between traffic conditions and in-canyon CO concentrations properly, the background CO concentration due to non-traffic related emissions was estimated. For the duration of the experiment, data from a streetbox in Portland Street (a residential side street, see Figure 7.1) indicated a mean background level of 0.2 ppm. The analysis presented in Chapter 5 showed that the mean CO concentrations measured in Portland Street were found to have very little variation with the background wind direction. This background concentration value is consistent with typical tropospheric background levels. For all in-canyon CO concentration data reported here, 0.2 ppm is subtracted, with the recalculated data less than 0.0 ppm excluded from analysis.

Figure 7.7 and Figure 7.8 show mean diurnal profiles of total traffic flow and CO concentrations for Gillygate streetboxes $G3_{3.5}$ and $G4_{3.5}$ and Bootham streetboxes $B1_{3.5}$ and $B2_{3.5}$, respectively. Also shown on the same figures is the unit standard deviation for each quantity across each time period throughout the study. Total traffic flow is the sum of the in- and out-bound flows for each street, corresponding to the total vehicle flow rate that passed each streetbox. The CO concentrations roughly followed the mean diurnal profiles of the total traffic flow with the steepest rise in concentrations during the morning peak-flow period and the highest concentrations between 07:00 and 20:00. Although total traffic flows were approximately constant throughout the day, maxima in mean CO concentrations occurred during the morning and late-afternoon peak total traffic flow periods. These peaks are clearly not related

to increased traffic flows alone and are consistent with higher CO emissions during periods of idling followed by acceleration that may occur under heavily congested conditions.

Despite the fact that the total traffic flow remained comparatively high throughout most of the time between the peak periods, there was sufficient network capacity maintained to keep vehicles moving steadily at a lower speed. This daytime regime is consistent with calming traffic flows, which results in lower emissions and concentrations. Figure 7.7b shows the diurnal variation of inbound detector occupancy for Gillygate. The figure confirms that although there is little variation in traffic flow throughout the daytime period there is a significant drop in detector occupancy and consequently [CO] following the morning peak-flow period, suggesting more freely moving traffic and a steady rise throughout the afternoon.

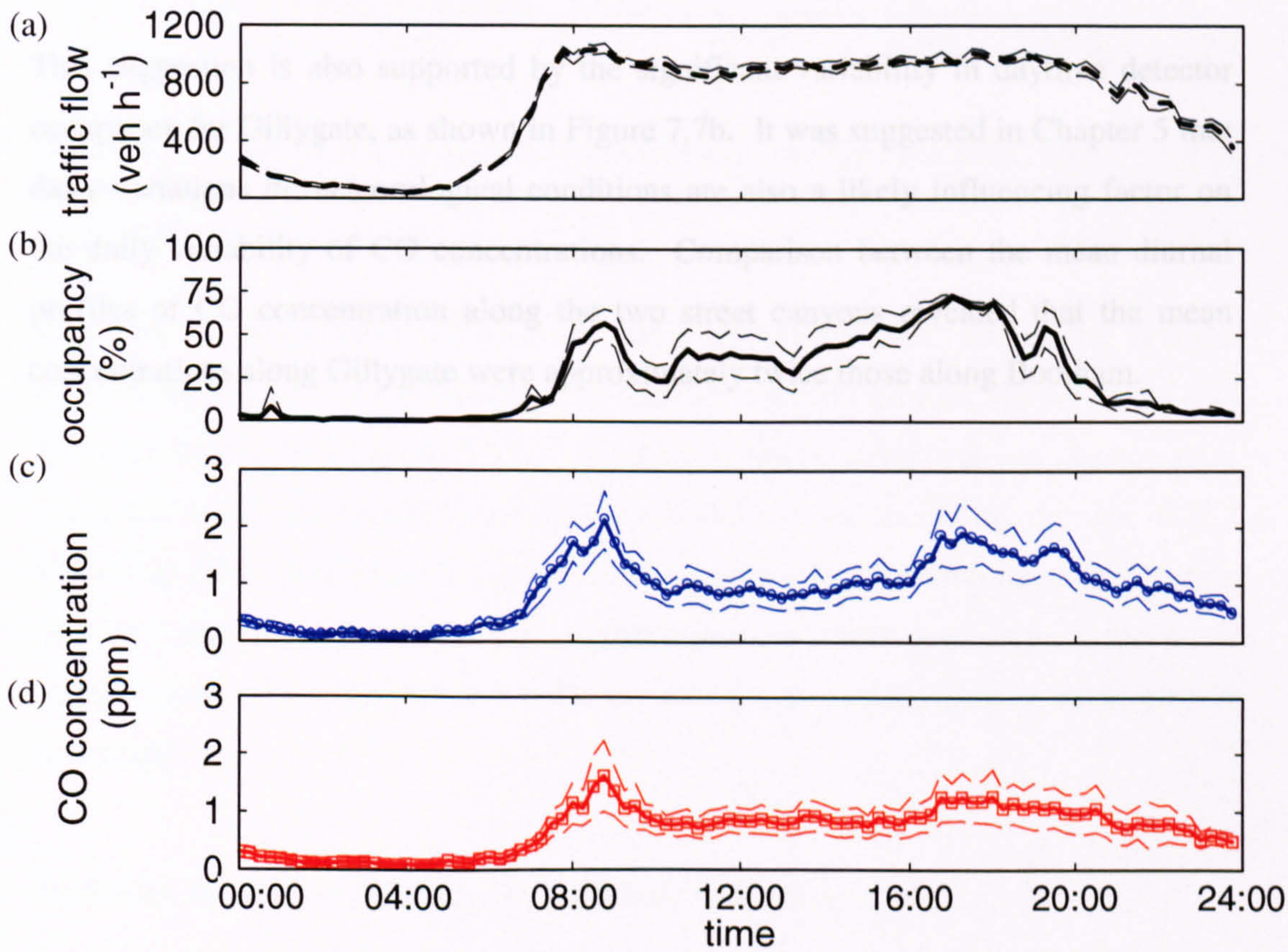


Figure 7.7. Mean diurnal profiles for Gillygate with — — showing unit standard deviation for (a) ▬ ▬ total traffic flow; (b) ▬▬ inbound detector occupancy (c) —○— CO concentration at $G3_{3.5}$; (d) —□— CO concentration at $G4_{3.5}$.

The substantial variability within each 15-minute mean CO concentration measured in both streets is shown by the unit standard deviations in Figure 7.7c, Figure 7.7d, Figure 7.8b and Figure 7.8c. The variability is greater during the daytime than at night. However, this may only be partly attributed to the increased day-to-day variability in daytime traffic flows compared with nighttime values. Other factors, including unaccounted for traffic conditions and meteorology, may also influence the increased variability of CO concentrations. Large variability in the daytime detector occupancy corresponds to traffic switching between free and congested states during unstable flow conditions, as shown in Figure 7.3. Since these traffic conditions are a function of the network capacity, the variability in the traffic flow is likely to have been a dynamic response to network capacity effects, such as across-junction traffic at the downstream intersection. Therefore, network capacity effects during unstable flow conditions are a likely contributor to the variability in the CO concentrations measured in both streets.

This suggestion is also supported by the significant variability in daytime detector occupancy for Gillygate, as shown in Figure 7.7b. It was suggested in Chapter 5 that daily variations in meteorological conditions are also a likely influencing factor on the daily variability of CO concentrations. Comparison between the mean diurnal profiles of CO concentration along the two street canyons revealed that the mean concentrations along Gillygate were approximately twice those along Bootham.

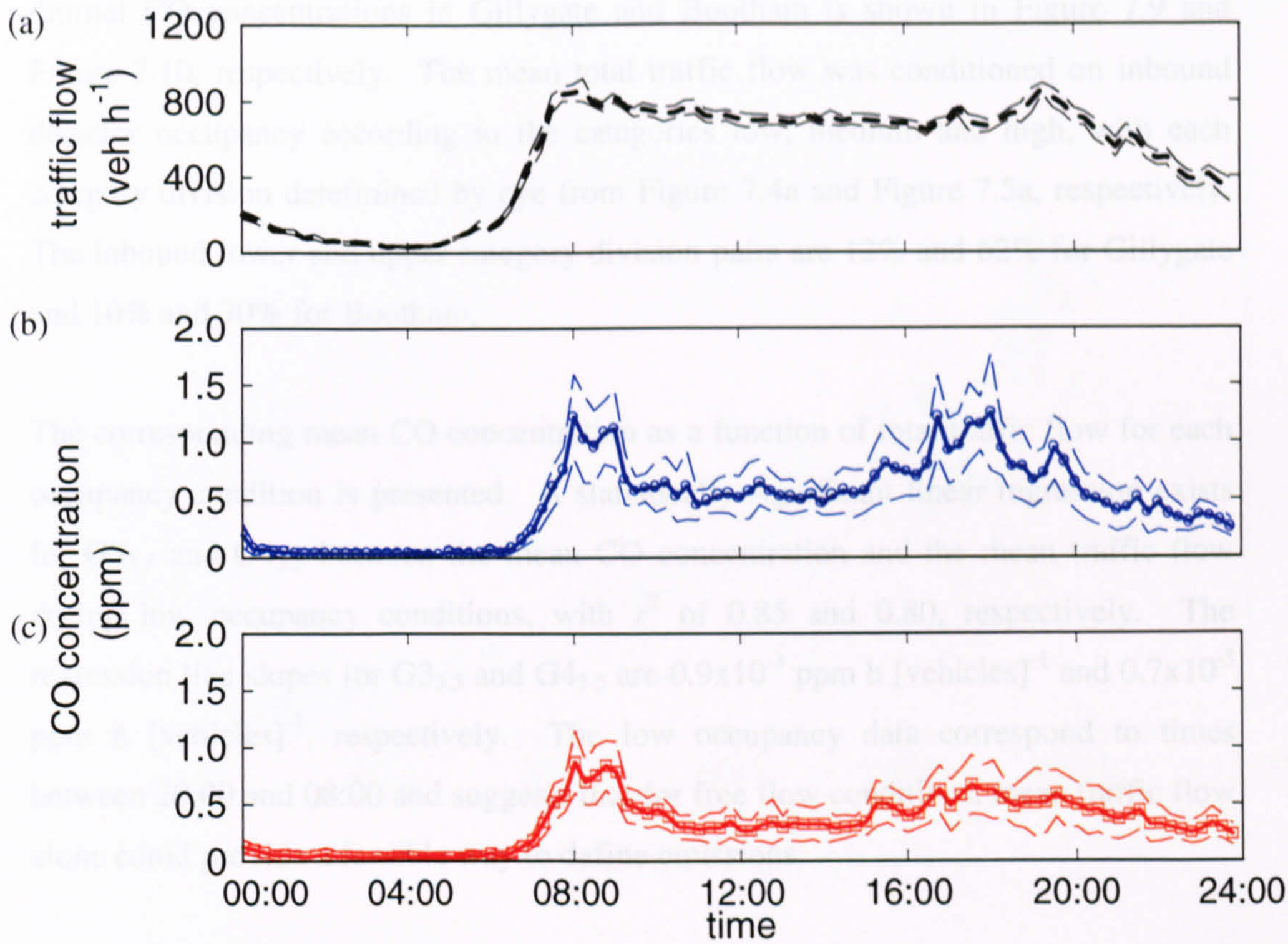


Figure 7.8. Mean diurnal profiles for Bootham with standard deviation lines — — for: (a) — — total traffic flow; (b) —○— CO concentration at $B1_{3.5}$; (c) —□— CO concentration at $B2_{3.5}$.

This may be partly attributed to lower mean total traffic flow during the daytime along Bootham (80% of Gillygate) and network capacity effects. However, it was also mentioned in Chapter 5 that Bootham's lower street canyon aspect ratio increased ventilation and its larger cross-sectional area increased the dilution of CO within the street. Therefore, the study highlights the effects of both network capacity and the interaction of background meteorology with street geometry on the mean concentration of a traffic-related pollutant as well as the day-to-day variability in concentrations.

### 7.3.5. Significance of the study for emissions modelling

Investigation of the influences of traffic-related parameters on road-side concentrations of CO allows us to evaluate how such parameters may potentially be used to estimate emissions. The two parameters investigated here are traffic flow and detector occupancy. The influence of the mean diurnal total traffic flow on the mean

diurnal CO concentrations in Gillygate and Bootham is shown in Figure 7.9 and Figure 7.10, respectively. The mean total traffic flow was conditioned on inbound detector occupancy according to the categories low, medium and high, with each category division determined by eye from Figure 7.4a and Figure 7.5a, respectively. The inbound lower and upper category division pairs are 12% and 62% for Gillygate and 10% and 70% for Bootham.

The corresponding mean CO concentration as a function of total traffic flow for each occupancy condition is presented. A statistically significant linear regression exists for $G3_{3.5}$ and $G4_{3.5}$ between the mean CO concentration and the mean traffic flow during low occupancy conditions, with $r^2$ of 0.85 and 0.80, respectively. The regression line slopes for $G3_{3.5}$ and $G4_{3.5}$ are $0.9 \times 10^{-3}$ ppm h [vehicles]$^{-1}$ and $0.7 \times 10^{-3}$ ppm h [vehicles]$^{-1}$, respectively. The low occupancy data correspond to times between 20:00 and 08:00 and suggests that for free flow conditions, mean traffic flow alone could provide a feasible way to define emissions.

For high occupancy conditions a weaker linear regression also exists for $G3_{3.5}$ and $G4_{3.5}$ with $r^2$ of 0.24 and 0.37, respectively. The poorer fit may be attributed to the increased variability of day-time traffic conditions and suggests that even when conditioned on detector occupancy, traffic flow would give a less reliable estimate of emissions for congested conditions compared to free flow conditions. However, the figure still shows that the regression line slopes are higher than for low occupancy conditions (both are $2.3 \times 10^{-3}$ ppm h [vehicles]$^{-1}$) indicating that CO concentrations vary more strongly with traffic flow under high occupancy conditions.

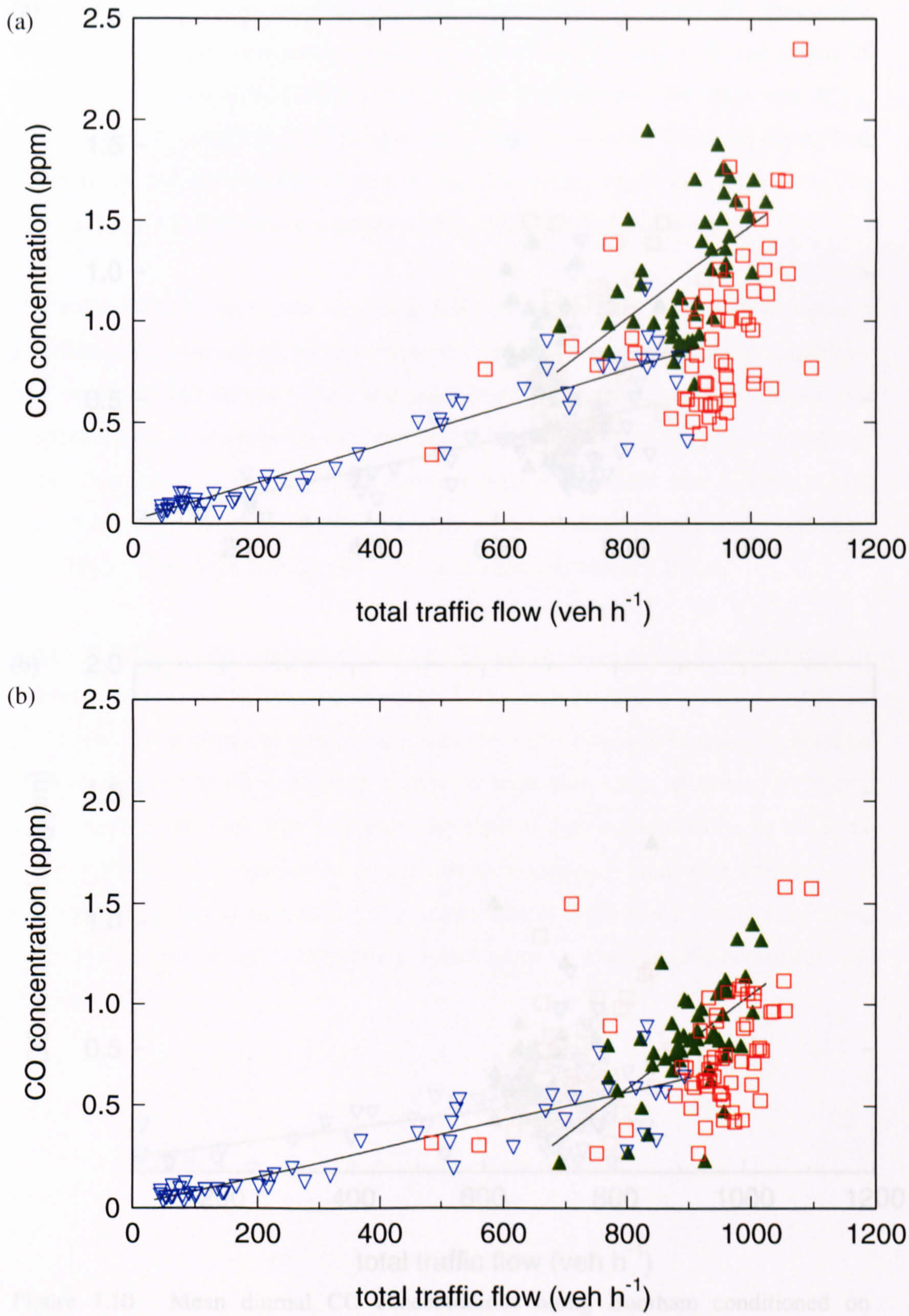


Figure 7.9. Mean diurnal CO concentrations along Gillygate conditioned on inbound detector occupancy and total traffic flow: ▽ low occupancy; □ medium occupancy and ▲ high occupancy for (a) $G3_{3.5}$ and (b) $G4_{3.5}$.

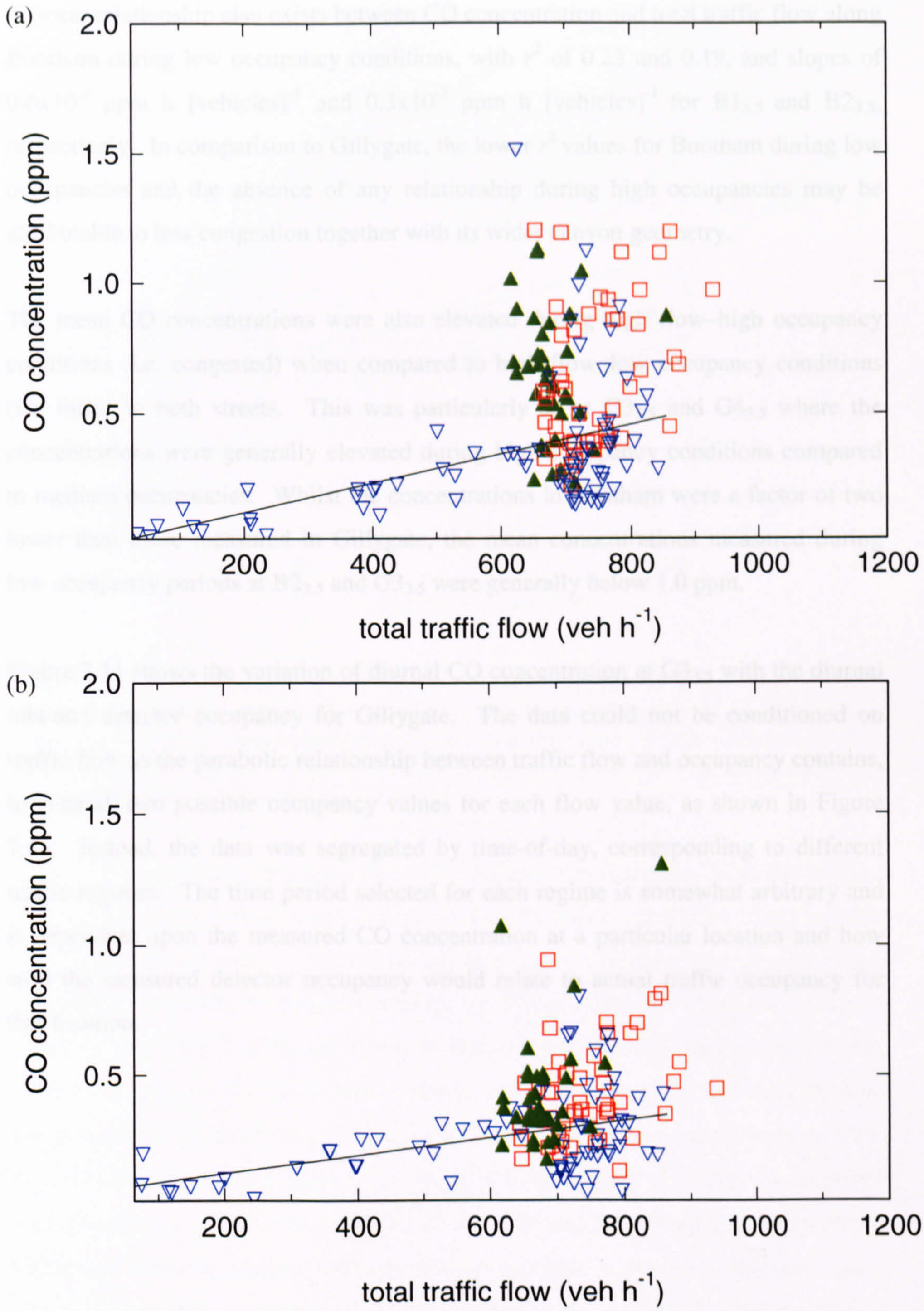


Figure 7.10. Mean diurnal CO concentrations along Bootham conditioned on inbound detector occupancy and total traffic flow: ▽ low occupancy; □ medium occupancy and ▲ high occupancy for (a) $B1_{3.5}$ and (b) $B2_{3.5}$.

A linear relationship also exists between CO concentration and total traffic flow along Bootham during low occupancy conditions, with $r^2$ of 0.23 and 0.19, and slopes of $0.6 \times 10^{-3}$ ppm h [vehicles]$^{-1}$ and $0.3 \times 10^{-3}$ ppm h [vehicles]$^{-1}$ for $B1_{3.5}$ and $B2_{3.5}$, respectively. In comparison to Gillygate, the lower $r^2$ values for Bootham during low occupancies and the absence of any relationship during high occupancies may be attributable to less congestion together with its wider canyon geometry.

The mean CO concentrations were also elevated during high flow–high occupancy conditions (i.e. congested) when compared to high flow–low occupancy conditions (i.e. busy) in both streets. This was particularly so at $G3_{3.5}$ and $G4_{3.5}$ where the concentrations were generally elevated during high occupancy conditions compared to medium occupancies. Whilst the concentrations in Bootham were a factor of two lower than those measured in Gillygate, the mean concentrations measured during low occupancy periods at $B2_{3.5}$ and $G3_{3.5}$ were generally below 1.0 ppm.

Figure 7.11 shows the variation of diurnal CO concentration at $G3_{3.5}$ with the diurnal inbound detector occupancy for Gillygate. The data could not be conditioned on traffic flow as the parabolic relationship between traffic flow and occupancy contains, in general, two possible occupancy values for each flow value, as shown in Figure 7.4a. Instead, the data was segregated by time-of-day, corresponding to different traffic regimes. The time period selected for each regime is somewhat arbitrary and is dependent upon the measured CO concentration at a particular location and how well the measured detector occupancy would relate to actual traffic occupancy for that location.

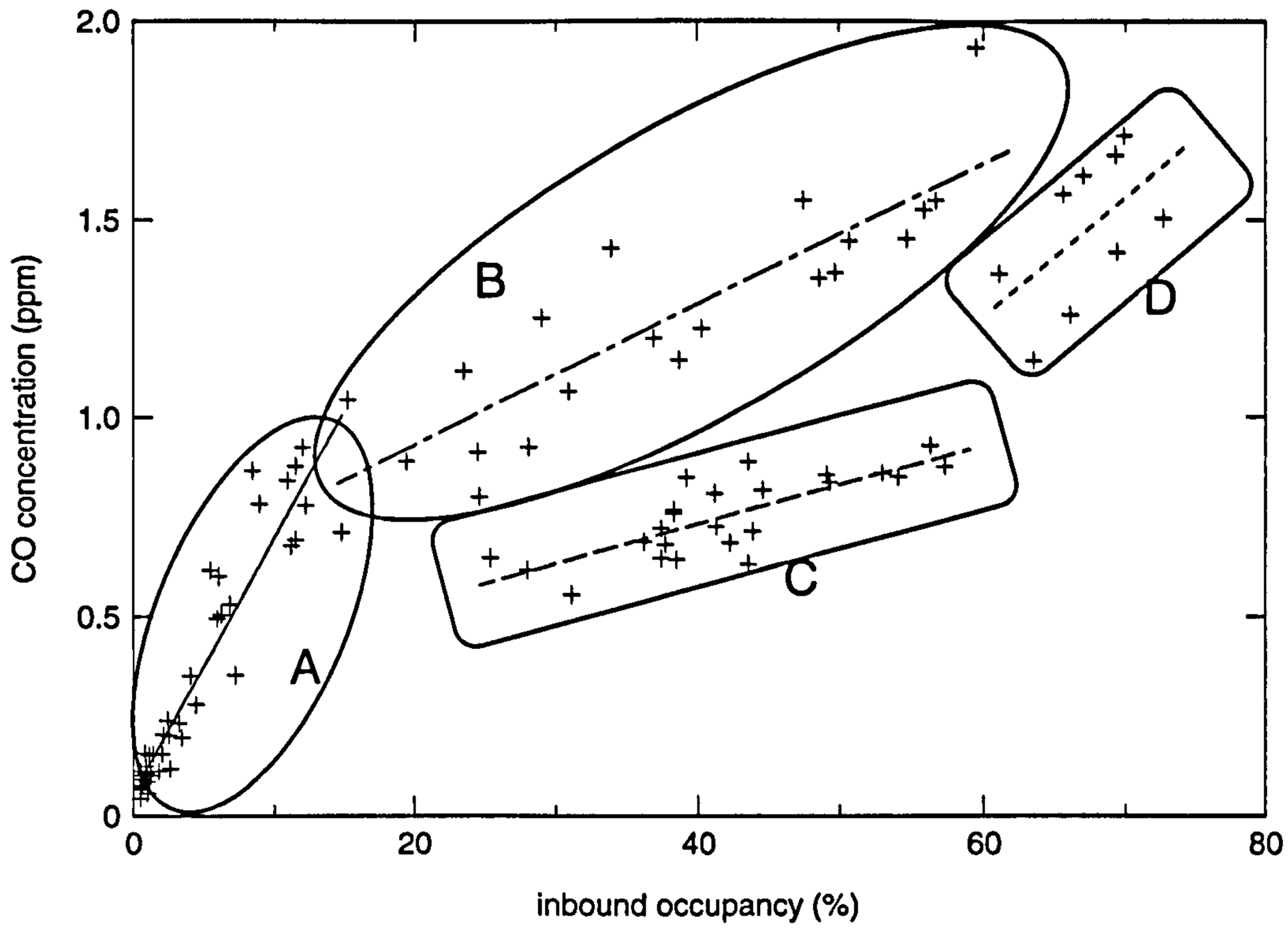


Figure 7.11. Mean diurnal CO concentrations along Gillygate at $G3_{3.5}$ varying with occupancy. Data are segregated according to time-of-day regimes: A, B, C and D. Lines correspond to least-squares regressions over the range of data within each bounded region. Tables 7.3 and 7.4 list the regimes with the corresponding time periods and regression results, respectively.

Table 7.3 summarises four possible traffic regimes for Gillygate, with the relevant time period, vehicle flow range and proportion of traffic conditions (free, unstable and congested) for each 15-minute period as a fraction of the experiment duration. The traffic conditions were determined by the inbound detector occupancy category divisions at 12% and 62%, as shown in Figure 7.4a. During night-time free flow conditions (regime A) there was a one-to-one correspondence between detector occupancy and traffic flow. Consequently, the diurnal CO concentration at $G3_{3.5}$ varied linearly with occupancy, with a slope of $6.4 \times 10^{-2}$ ppm $\%^{-1}$. During the period corresponding to both the morning (07:30 – 10:00) and late evening (18:30 – 20:30) traffic flow maxima, all three traffic conditions occurred (regime B). The lower slope ($1.7 \times 10^{-2}$ ppm $\%^{-1}$) and increased scatter are due to the combined, non-proportional influence of both traffic flow and inbound occupancy on CO concentrations.

Table 7.3. Possible traffic regimes identified from Figure 7.11 using a time-of-day analysis. The dominant traffic condition contribution to each regime is in bold.

| traffic regime | inclusive time period (proportion of day in brackets) | flow range [vehicles $h^{-1}$] | traffic condition proportion (%) | | |
|---|---|---|---|---|---|
| | | | free | unstable | congested |
| **A** | 20:45 – 07:15 (45%) | 45 – 829 | **97** | 3 | 0 |
| **B** | 07:30 – 10:00; 18:30 – 20:30 (21%) | 891 – 1048 | 11 | **63** | 26 |
| **C** | 10:15 – 16:00 (25%) | 854 – 966 | 2 | **68** | 30 |
| **D** | 16:15 – 18:15 (9%) | 951 – 1012 | 0 | 15 | **85** |

Outside these time periods the traffic may be characterised by either medium flow–medium occupancy (regime C) or high flow–high occupancy (regime D). While regimes B and C are predominantly characterised by unstable traffic flows (Table 7.3) the data was segregated due to differences between the off-sets of the regression lines. During regimes C and D, free flow is practically non-existent, with regime D showing that higher congestion occurrences (85%) corresponding to higher CO concentrations and perhaps breaching the network capacity. Although there is a linear relationship with occupancy during the late afternoon - early evening period (16:15 – 18:15) the regression is statistically insignificant ($r^2 = 0.31$) by having only 9 data values (Table 7.4). Overall, in terms of traffic management, regime C would be preferred, with moderately high traffic flows (>966 vehicles $h^{-1}$) and only a weak relationship with occupancy, ($1.0 \times 10^{-2}$ ppm $\%^{-1}$), leading to lower CO concentrations (<1.0 ppm). A combination of SCOOT information and traffic modelling could help to improve the understanding of such complex regimes and should be the subject of further study, as discussed in Chapter 9.

Table 7.4. The linear regression results for the traffic regimes identified from Figure 7.11 using a time-of-day analysis.

| traffic regime | least-squares regression analysis | |
|---|---|---|
| | slope [ppm $\%^{-1}$] | $r^2$ |
| **A** | $6.4 \times 10^{-2}$ | 0.89 |
| **B** | $1.7 \times 10^{-2}$ | 0.75 |
| **C** | $1.0 \times 10^{-2}$ | 0.62 |
| **D** | $3.0 \times 10^{-2}$ | 0.31 |

Analysis of the dependency of CO concentration on inbound detector occupancy indicates the importance of not only traffic flow in each street but also the occurrence of congestion. Congested traffic flows are characterised by a greater number of stop-starts than freely flowing traffic. Waters (1992) states that higher emission levels would be expected during periods of idling and accelerating than during free flow. In fact, it is the acceleration component of stop-start driving during congested conditions that generate the most CO emissions from modern petrol-engine vehicles (André and Pronello, 1997; Barth et al., 2001).

This is also consistent with the findings of Tate (2005), who applied an integrated modelling approach to study the temporal and spatial variations in vehicular emissions along Bootham and Gillygate. Vehicular emissions of CO largely associated with accelerating driving modes are concentrated around the Bootham-Gillygate common intersection in free-flowing traffic conditions. Tate (2005) found that when traffic queues build up with distance from the intersection, emissions are elevated at mid-link locations (i.e. during idling conditions), although they are still significantly lower than at the intersection where accelerating modes are more common. Although some existing air quality models assume a constant emission factor along each road section, these findings suggest that emissions of traffic-related pollutants are not evenly distributed. Therefore, some models may underestimate concentrations at intersections, while overestimating concentrations at mid-link locations. The significance of these findings is explored in more detail in Chapter 8.

### 7.3.6. Combined influence of traffic conditions and background wind flow

Following Croxford and Penn (1998), an analysis of the CO concentration frequency distributions was carried out on Gillygate and Bootham at $G3_{3.5}$ and $B1_{3.5}$, respectively. Figure 7.12 shows the 1, 2, 3, 4, 5, 10, 20, 30, 40, 50, 60, 70, 80, 90, 95, 96, 97, 98, 99 percentiles and the related histogram of the CO concentration data. The percentile plots show that a higher frequency of elevated mean CO concentrations occurred in the narrower Gillygate street canyon compared to Bootham, with the 50$^{th}$ percentile for Gillygate at 0.68 ppm compared to 0.36 ppm for Bootham. Although both monitors show relatively low frequencies at the higher concentration ranges, $G3_{3.5}$ has a much flatter, or platykurtic, distribution compared to $B1_{3.5}$ with a longer tail extending to higher CO concentrations. Figure 7.12 also shows that the mean concentration distribution at $G3_{3.5}$ is more positively skewed than for $B1_{3.5}$. It has been suggested that these high concentrations are associated with periods of congestion, during which stop-starts occurred more frequently within the traffic flow.

However, the differences between the frequency distributions for each street suggest the additional influence of local street geometry and its interaction with background wind flows on the dispersion of traffic-related emissions. The lower aspect ratio of Bootham implies that there was a comparatively larger volume of air inside the canyon within which CO and other pollutants could disperse. The combined influence of traffic conditions, street geometry and background wind flow will be further explored below.

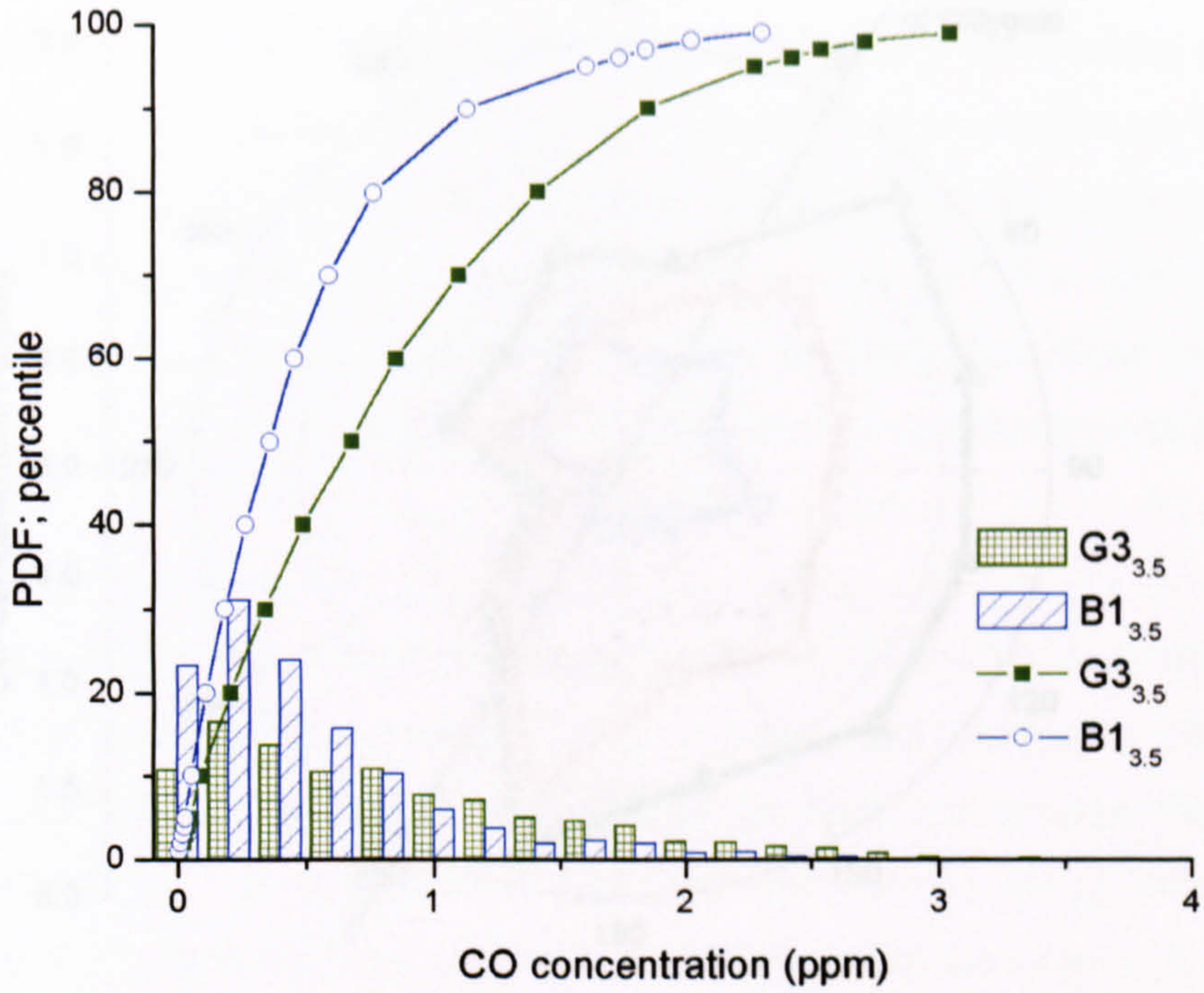


Figure 7.12. Frequency distribution of CO concentrations on Gillygate and Bootham shown as PDFs (bars) and percentiles (lines) for $G3_{3.5}$ and $B1_{3.5}$.

It was shown in Chapter 5 that when CO was measured on the leeward side of the two street canyons the influence of the above-roof wind flow increased the mean CO concentrations. The contribution of traffic characteristics may also be considered when the concentration roses are conditioned on detector occupancy. Figure 7.13 shows the mean CO concentrations as a function of the above-roof wind direction measured at the mast and conditioned on low, medium and high detector occupancies. The normalisation procedure presented in Chapter 5 produced little difference in the overall profiles of the concentration roses presented in Figure 7.13 and is therefore not shown. To achieve statistically significant results, 30° wind direction sectors are used compared to 10° sectors as used in Chapter 5.

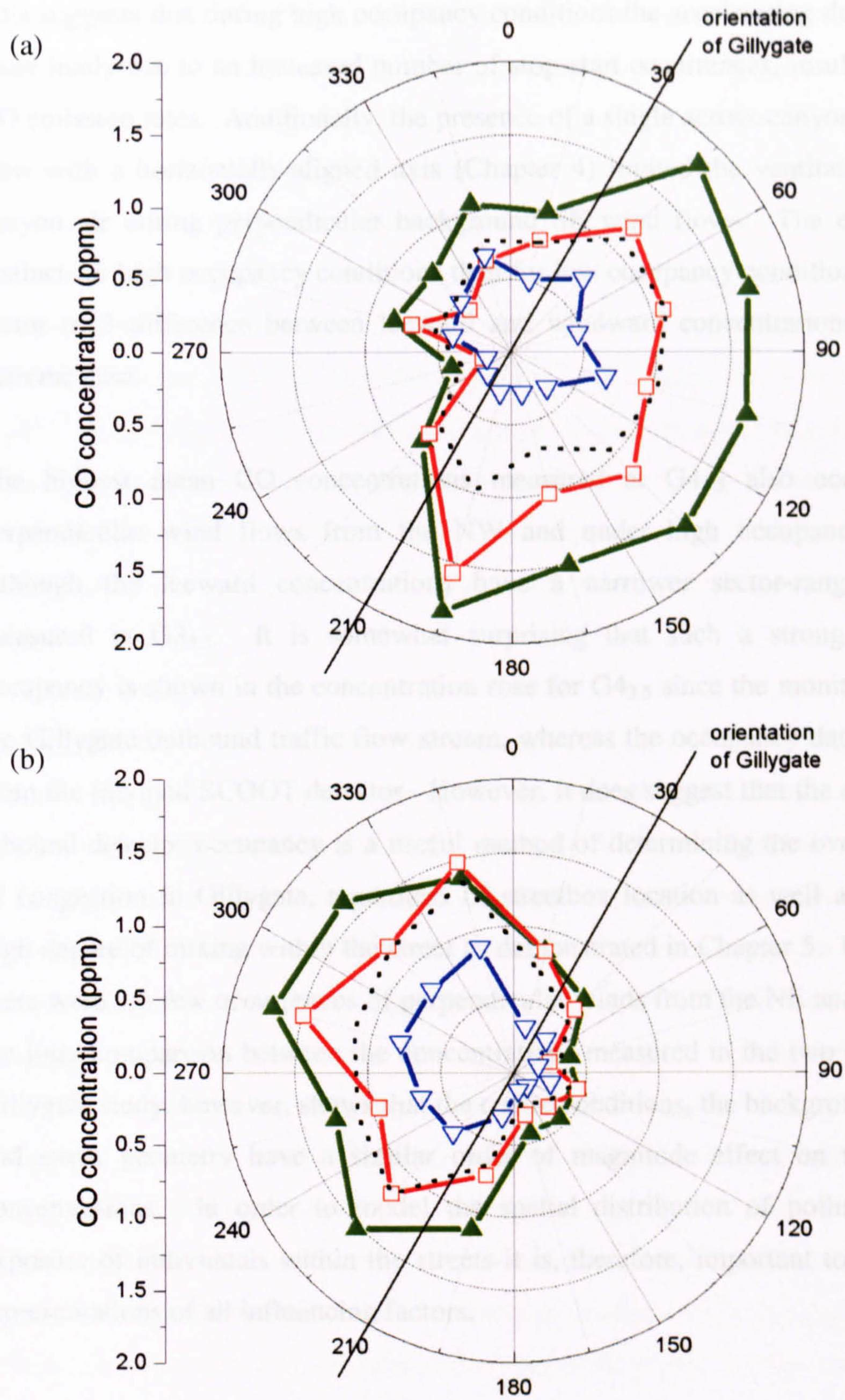


Figure 7.13. Sector-averaged CO concentrations shown as concentration roses conditioned on inbound detector occupancy: ▽ low occupancy; □ medium occupancy; ▲ high occupancy; ····· all data for (a) $G3_{3.5}$ and (b) $G4_{3.5}$.

Higher mean leeward CO concentrations were measured at $G3_{3.5}$ during above-roof wind flows that were perpendicular to the street axis and during high occupancy (i.e. congested) conditions than were measured during parallel above-roof wind flows.

This suggests that during high occupancy conditions the accelerating driving mode is more likely due to an increased number of stop-start occurrences, resulting in higher CO emission rates. Additionally, the presence of a single across-canyon recirculating flow with a horizontally-aligned axis (Chapter 4) limited the ventilation of the in-canyon air during perpendicular background SE wind flows. The effect is more distinct for high occupancy conditions than for low occupancy conditions providing a factor of 3 difference between leeward and windward concentrations in the most extreme case.

The highest mean CO concentrations measured at $G4_{3.5}$ also occurred during perpendicular wind flows from the NW and under high occupancy conditions, although the leeward concentrations have a narrower sector-range than those measured at $G3_{3.5}$. It is somewhat surprising that such a strong influence of occupancy is shown in the concentration rose for $G4_{3.5}$ since the monitor is closer to the Gillygate outbound traffic flow stream, whereas the occupancy data was derived from the inbound SCOOT detector. However, it does suggest that the analysis of the inbound detector occupancy is a useful method of determining the overall influence of congestion in Gillygate, regardless of streetbox location as well as indicating a high degree of mixing within the street as demonstrated in Chapter 5. Unfortunately, there were too few occurrences of perpendicular winds from the NE and SW to allow the inter-comparison between the concentrations measured in the two canyons. The Gillygate study, however, shows that the traffic conditions, the background wind flow and street geometry have a similar order of magnitude effect on the mean CO concentrations. In order to model the spatial distribution of pollutants and the exposure of individuals within the streets it is, therefore, important to find accurate representations of all influencing factors.

## 7.4. Summary and Conclusions

The SCOOT system was found to be a generally reliable method for measuring bi-directional traffic flow and occupancy along Gillygate and Bootham. Occupancy was used as an indication of the traffic flow characteristics (a combination of vehicle type, speed, number and network capacity) along the inbound traffic flow streams in both

streets. The influence of free, unstable and congested traffic conditions on the spatial and temporal variability in CO concentrations in both streets was investigated. Detector occupancy was split into three categories of low, medium, and high occupancy according to its relationship with the traffic flow. High occupancy was used as an indication of congestion and occurred during saturated traffic flows, when increases in occupancy resulted in decreases in traffic flow. High occupancy conditions are expected to be associated with stop-start traffic flows, which are well known to be the cause of elevated emission rates during the accelerating driving mode. Congestion, therefore, has a significant impact on street canyon air quality at both study sites. As congested flow occurs at high occupancy when the link capacity is reached, reductions in emission levels could be achieved if traffic managers were able to maintain traffic flow below the level at which high occupancy conditions arise.

The influence of traffic flow characteristics on CO concentrations varied for different street geometries, with higher mean levels measured in the narrower Gillygate canyon. This can be attributed to a lower mixing volume within Gillygate compared to Bootham and the presence of skimming flow conditions under certain background wind directions, which limit the vertical lofting of pollutants out of the canyon. The study also indicated higher frequencies of elevated CO concentrations within Gillygate compared to Bootham. The lower total traffic flow along Bootham coupled with the predominantly parallel wind flows that were measured during the experiment (Chapter 4) was also a likely contributor to the lower mean concentrations measured in this street. Under low traffic flows and low detector occupancies, a strong linear relationship existed in each canyon between the mean CO concentrations and the traffic flow. This relationship failed under high occupancy (i.e. congested) conditions where the mean CO concentrations were better described by the level of detector occupancy in the street. The study suggests that traffic flow may only be used as a sole indicator of emissions under free flowing traffic conditions and that detector occupancy has a strong influence on emissions under unstable and congested conditions. For the Gillygate inbound detector, which was located close to the CO monitors, the detector occupancy gave a reasonable measure of queue length in the street. The Gillygate outbound detector was found to give a less reliable indication of congestion close to the CO monitors due to it being located at the opposite end of the

traffic link. Traffic modelling, used in combination with SCOOT detector data, may give a more reliable indication of the total detector occupancy at a given location within the street and should be the subject of further study.

Sector-averaged concentration roses conditioned on inbound detector occupancy revealed that the highest mean CO concentrations occurred in Gillygate during high inbound detector occupancy conditions. The inter-relationship between background perpendicular wind flows and congested conditions resulted in higher mean leeward CO concentrations than were measured during parallel wind flows. The development of a single across-canyon vortex under background winds from the SE transported the CO at street level towards the leeward side in the return-portion of a recirculating flow.

The work presented in this Chapter suggests several implications for air quality management strategies and is discussed in more detail in Chapter 8. Significant benefits in street canyon air quality may result from attempts to reduce the level of congestion within narrow streets of similar geometry to those considered here, since this could potentially reduce the emissions from a large number of individual vehicles. Air quality models must represent the complexities associated with building and street geometries as well as those associated with traffic flow characteristics. The ability to represent the influence of stop-start conditions and congestion on traffic-related pollutant emissions could significantly improve the predictive quality of dispersion models, as demonstrated in Chapter 8.

# CHAPTER 8

# Sensitivity study into the influence of the background wind and variable emissions along Gillygate – Final Discussions

## 8.1. Introduction

The findings presented in this thesis, particularly those mentioned in Chapter 7, have several implications for air quality management strategies in urban areas. This could be achieved through local traffic management measures or by city-wide initiatives aimed at reducing the overall levels of traffic such as low emission zones, congestion charging or park and ride schemes. If reductions in overall detector occupancy cannot be achieved then consideration could also be given to moving traffic queues into streets with improved dispersion conditions, i.e. away from narrow street canyons.

Furthermore, air quality models must represent the complexities associated with building and street geometries as well as those associated with traffic flow characteristics. The ability to represent the influence of stop-start conditions and congestion on traffic-related pollutant emissions could significantly improve the predictive quality of dispersion models. This would advance their overall effectiveness in assessing traffic management and control measures and public exposure to traffic-related pollutants. This Chapter describes a sensitivity study that was undertaken following the analysis of the data from the field experiment.

### 8.1.1. Chapter synopsis

This Chapter aims to consolidate the research findings from the experimental study (Chapters 4 – 7) and to present the qualitative results from the dispersion modelling study as a comparison. In Chapter 2 the influence of meteorology, urban topography and traffic was discussed. However, as it was described in Chapters 4 – 7, many of the effects are inter-related and so require a more holistic approach to discuss their impacts on the in-canyon concentration field.

## 8.2. Methodology

Tate (2005) presented the development and implementation of an integrated traffic micro-simulation and instantaneous emission model in order to study the spatial and temporal variations in vehicular emissions along Bootham and Gillygate. In particular, the DRACULA traffic microsimulation was integrated with the Comprehensive Model Emission Model (CMEM), thereby accounting for tailpipe emissions now largely associated with acceleration events, as shown in Chapter 7 (see also Tate *et al.*, 2005b). The variability in the traffic network (e.g. signal timings) and vehicular activity throughout a typical weekday was incorporated into the modelling study in order to derive the spatial and temporal variability in emissions at the microscopic scale (Tate, 2005). This was used to generate second-by-second vehicle trajectory data and CO tailpipe emissions and the results were used to help interpret the spatial and temporal variability in concentrations of CO measured along Bootham and Gillygate. The second-by-second modelling approach was implemented in order to estimate the temporal (15-minute time intervals) and spatial variations in CO emissions and to verify the instantaneous emission model using transient emission measurements over a standard drive cycle as well as in real-world traffic conditions (see Tate, 2005).

The DRACULA microsimulation model simulated the movement and interaction of individual vehicles through a well-defined network such as Bootham and Gillygate by incorporating SCOOT data collected during the field experiment. Vehicle movements and interactions in the network were updated according to traffic characteristics (e.g. performance and desired speed along the street). Additionally,

rules that govern car-following, lane-changing, gap acceptance and driver behaviour at intersections were included. The model was able to simulate vehicles movements as they encounter junctions (e.g. priority and signal control) and the build up and discharge of queues on the network (Tate, 2005). The main purpose of incorporating the CMEM was to predict vehicle tail-pipe emissions in the four different driving modes: idling, accelerating, cruising and decelerating. In Chapter 7 a discussion was given into the influence of these driving modes on the variability in concentrations of CO measured along Bootham and Gillygate.

The location and magnitude of the CO emissions were averaged in Tate (2005) over 15-minute time periods and 10 m sections along Bootham and Gillygate, thus including the common traffic-signal controlled intersection. As total traffic flow along Gillygate was used in the emissions modelling, the results of the emission study were based on the aggregate of inbound and outbound traffic flows. The spatial variations in vehicular CO emissions along Gillygate obtained from Tate (2005) for the time period corresponding to 08:30 – 08:45 were interpolated in the work presented in this Chapter in order to derive emission rates for the dispersion modelling study. Figure 8.1 shows emission rate of CO interpolated over 2 m sections along Gillygate from the common Bootham-Gillygate intersection (i.e. at 0 m) to the junction with Lord Mayor's Walk at the far end of the street. The constant emission profile shown in Figure 8.1 is simply the mean of the variable profile.

During congested traffic flows, particularly in the inbound directions, idling vehicles along Bootham and Gillygate formed queues that extended almost the entire length of the streets. Congested traffic flow conditions are likely to have occurred in Gillygate during 08:30 – 08:45 (see Chapters 5 and 7). Figure 8.1 clearly shows that the emission rate of CO along Gillygate was predicted to be greatest at the common intersection due to vehicles accelerating through the intersection during periods when the traffic signals were green. These findings, therefore, support the observation that the highest concentrations of CO measured inside Gillygate corresponded to congested traffic conditions during which stop-start and, thus, accelerating driving modes, are likely to have occurred.

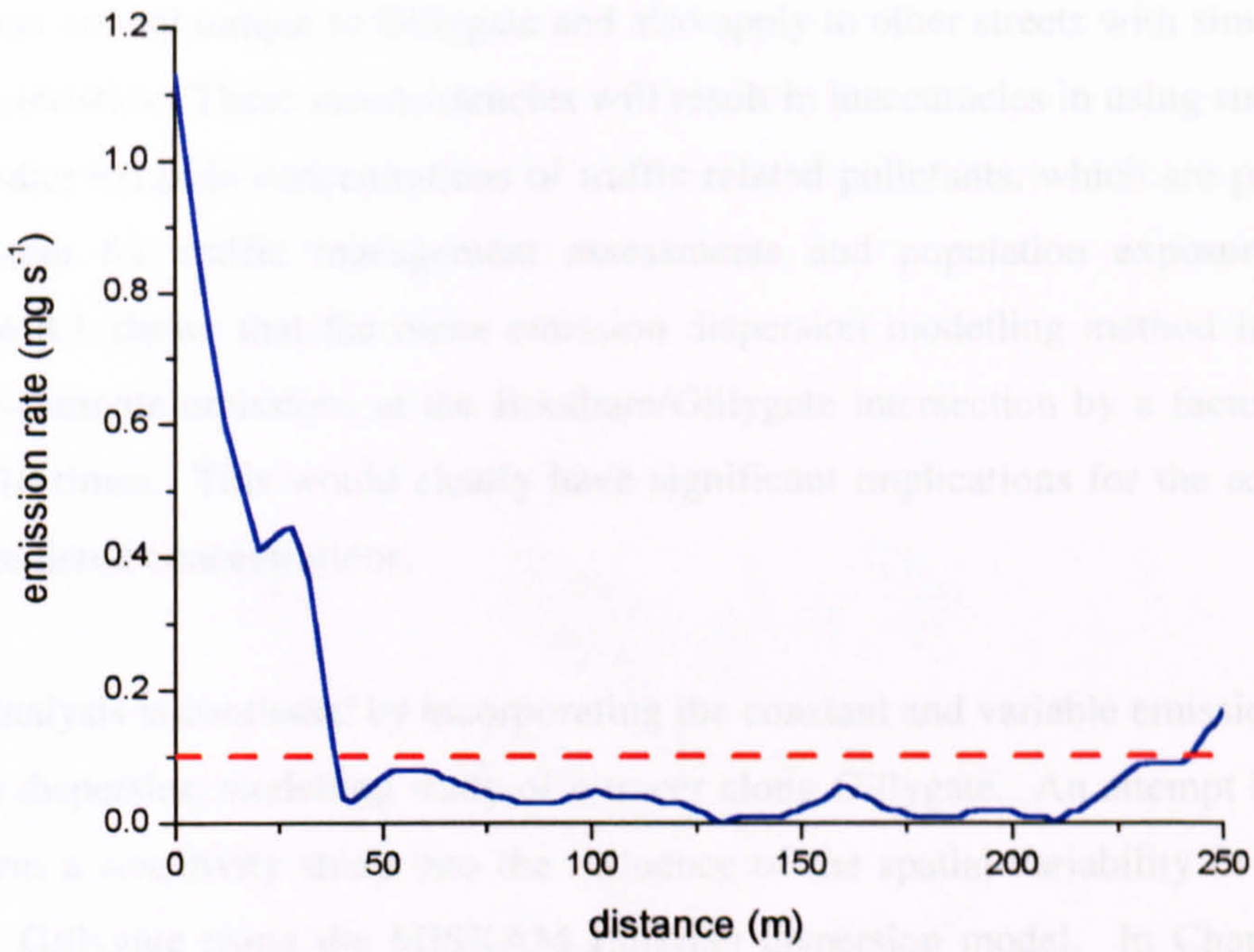


Figure 8.1. Spatial variations in emission rates of CO interpolated over 2 m sections along Gillygate from the common (Bootham/Gillygate) intersection between 08:30 – 08:45: —— variable emissions; — — constant (mean) emissions (adapted from Tate, 2005).

Figure 8.1 also shows that emissions are also higher than the mean emissions profile at the junction with Lord Mayor's Walk, which also indicates the significance of stop-start conditions and accelerating driving modes as vehicles are likely to have accelerated through the signal-controlled intersection. The figure also suggests that the bi-directional traffic travelling along the mid-link section of Gillygate reached optimum cruising speed, causing emissions to fall sharply. Consequently, emissions along the mid-link section fell below the mean. The results of the variable emissions along Gillygate also indicate the possible benefits that may arise if traffic managers were able to minimise the occurrence of congested traffic flows, during which stop-start conditions and accelerating driving modes are more common.

From a street canyon dispersion modelling perspective the spatial variations in emissions along Gillygate during congested traffic flows shown in Figure 8.1 are highly significant. If such models were to assume that emissions are evenly distributed along Gillygate (i.e. using a constant or mean emissions profile) they are likely to not only drastically under-estimate the emissions at the common intersection, but also over-predict the emissions along the mid-link section. Of course, these

findings are not unique to Gillygate and also apply to other streets with similar traffic characteristics. These inconsistencies will result in inaccuracies in using such models to predict roadside concentrations of traffic-related pollutants, which are particularly important for traffic management assessments and population exposure studies. Figure 8.1 shows that the mean emission dispersion modelling method is likely to under-estimate emissions at the Bootham/Gillygate intersection by a factor of more than 10 times. This would clearly have significant implications for the accuracy of the predicted concentrations.

The analysis is continued by incorporating the constant and variable emission profiles into a dispersion modelling study of a tracer along Gillygate. An attempt is made to perform a sensitivity study into the influence of the spatial variability in emissions along Gillygate using the MISKAM Eulerian dispersion model. In Chapter 3, the numerical simulation of dispersion in MISKAM was described as having two stages. First, the steady-state flow field was defined over an arbitrary building configuration using the flow component of the model (see Eichhorn, 1996). The model uses a $k$-$\varepsilon$ turbulence closure scheme to parameterise the subgrid scale turbulence. The model assumed a logarithmic profile upstream at the inflow boundaries. Second, the derived mean wind and turbulence parameters from MISKAM are input into the Eulerian dispersion model.

The building configurations in the domain are shown in Figure 8.2. The configurations were created from a scaled plan and the building heights were measured in the street using the inclination method with an Abney level, as described in Chapter 3. The modelling domain included the side streets adjoining Gillygate and incorporated the significant structures within approximately 100 m of the street, as shown in Figure 8.2. The grid was 3-D and the resolution of the domain could be adjusted by the user in order to allow for a higher resolution along the street. The model resolution from the common intersection to a point 74 m down the street was 2m by 4m by 1m in the across-canyon ($x$), along-canyon ($y$) and vertical ($z$) directions, respectively. The resolution was increased from the point at 74 m to the end of the street and was 1m by 2m by 1m the $x$, $y$ and $z$ directions, respectively. The higher resolution allowed for the comparison between normalised concentrations

derived by MISKAM and the mean concentrations of CO measured in the street (see Smalley *et al.*, 2004). Although the validation of the model is beyond the scope of this present study comparisons have been made between the measured and modelled concentrations using MISKAM for the Gillygate street canyon by Smalley *et al.* (2004a) and Dixon *et al.* (2005).

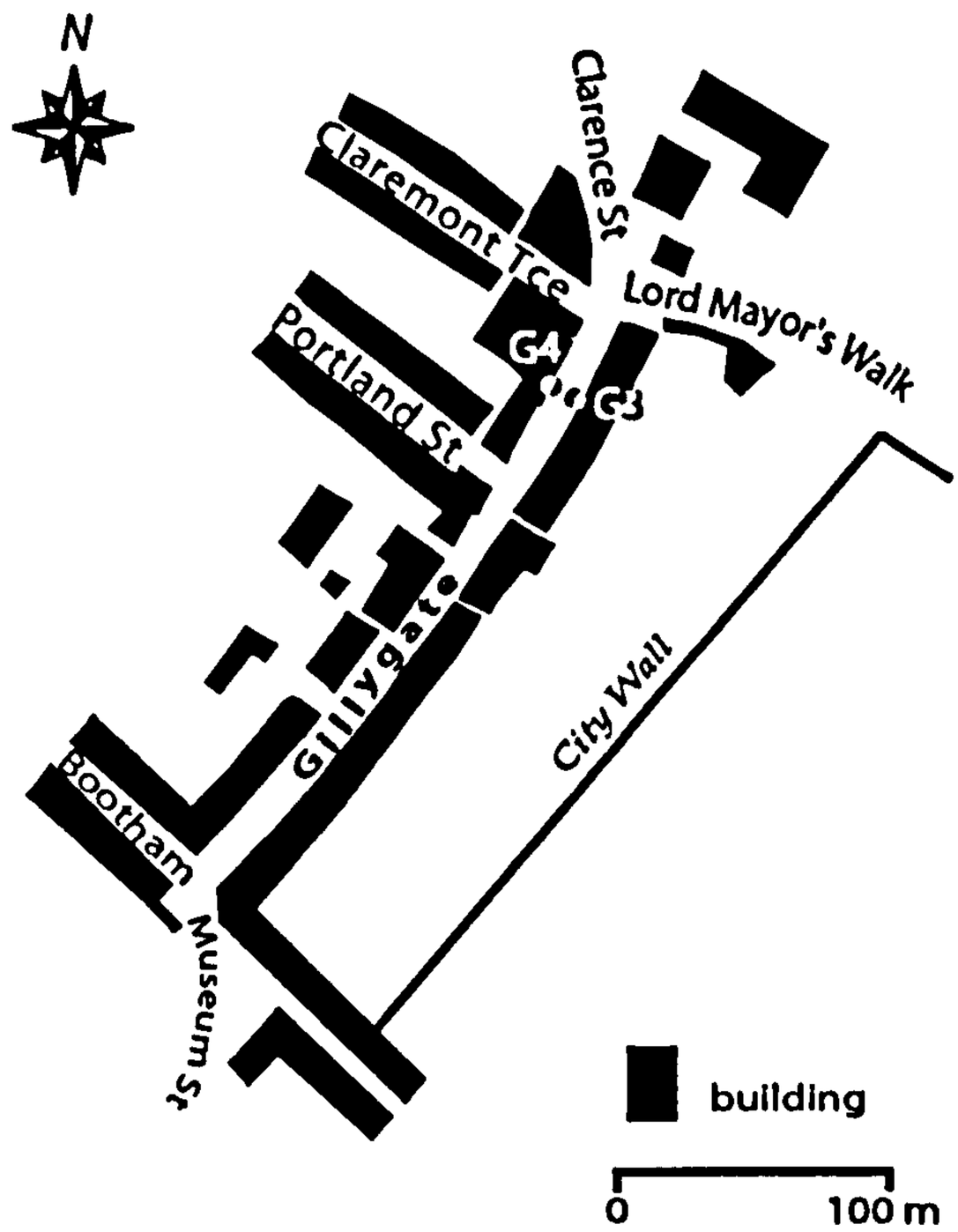


Figure 8.2. The modelling domain, showing the building configurations around the Gillygate street canyon.

The source cells of the tracer used in the domain were located in the centre of Gillygate (~8 m wide) and covered the entire length of the street from the common intersection to the junction with Lord Mayor's Walk. The source cells were first set using the constant (i.e. mean) emission profile shown in Figure 8.1. The influence of parallel ($\theta_{ref}$ = 210°), oblique ($\theta_{ref}$ = 165°) and perpendicular ($\theta_{ref}$ = 120°) background winds on the in-canyon concentration field was investigated. The source cells of the tracer were then set using the variable emission profile shown in Figure 8.1 for the same background wind directions in order to determine the influence of the spatial variability in emissions on the resulting in-canyon concentrations. It was mentioned earlier that the variable emission profile is a more realistic representation of the actual

emissions along Gillygate as the influence of traffic characteristics and driving mode was considered. The derived concentrations from MISKAM were not normalised as there were no comparisons with the measured results presented in Chapters 5 and 7.

Longitudinal cross-sections of the concentration field for each wind direction were desired in order to investigate the spatial variability in concentrations along Gillygate. Therefore, the derived concentrations from MISKAM were interpolated along the leeward side of the street for each wind direction using a FORTRAN code. For comparison, the computed concentrations for perpendicular background winds at the G3-G4 experiment cross-section are also presented. The derived concentrations were then imported into a matrix using the weighted average gridding method in Origin in order to create the longitudinal and transverse (i.e. spatially-averaged) concentration plots. While the transverse concentration plots for perpendicular winds at the measurement cross-section are presented, the transverse plots for other sections of the canyon are not shown.

## 8.3. Results and Discussion

### 8.3.1. Longitudinal cross-section

This Section discusses the qualitative results derived from the modelling study. Figures 8.3 – 8.5 show the contour plots of the concentrations using the constant and variable emission sources for parallel ($\theta_{ref}$ = 210°), oblique ($\theta_{ref}$ = 165°) and perpendicular ($\theta_{ref}$ = 120°), respectively. The contour plots shown in these figures are for longitudinal cross-sections of Gillygate and represent the SE side of the street, i.e. the leeward side during oblique ($\theta_{ref}$ = 165°) and perpendicular ($\theta_{ref}$ = 120°) winds.

The highest mean CO concentrations were measured during the experiment under perpendicular winds and congested traffic conditions (Chapter 7). In the light of this evidence, the aim of the modelling study was to determine, albeit qualitatively, the influence of the background wind and variable emission rates on the predicted concentrations in Gillygate. These three background wind directions were chosen in order to investigate the influence of recirculating in-canyon flow features associated with helical and skimming regimes. In addition, the leeward side of the canyon was

chosen as it was expected that the highest concentrations were to be found on that side of the street as a result of reverse-flow portion of the in-canyon recirculating flows. The influence of street canyon geometry was also investigated, particularly the effect of openings along the canyon walls.

*8.3.1.1. Parallel background winds*

Figure 8.3 shows the concentration plots for the longitudinal cross-section from the common intersection (at $y$ = 0 m) to the stopline beside the outbound traffic light at the far end of the street (at $y$ = 250 m). It was mentioned in Chapter 3 that the flow model used in MISKAM starts with a horizontally uniform flow field and the prognostic equations are solved within the domain until steady-state conditions are reached. Figure 8.3a shows the results for the constant emission source. The figure clearly shows that during parallel ($\theta_{ref}$ = 210°) background winds, concentrations of the tracer increase down the street as a result of advection by along-canyon airflow. The longitudinal effect is shown by the approximately horizontal contour lines for $z$ >2 m at the far end of the street.

The highest concentrations along Gillygate occur in a 'zone' between $y \approx$75 m and $y \approx$250 m. At $y \approx$55 m there is a relatively large opening along the NW canyon wall. The opening is likely to be a possible exit for pollutants. However, the horizontal flow vectors derived from the model suggest that the opening at $y \approx$150 m, which is before Portland Street, causes flow to enter the canyon (not shown). The vectors indicate that the parallel background winds interact with the row of buildings that form the SW flank of Portland Street. As a result, a portion of the flow is forced into the opening at $y \approx$150 m. The flow into the canyon through the opening also caused across-canyon flow towards the SE side of the street. This across-canyon flow is likely to have caused the local pollution hot-spot shown in the figure, particularly given that the derived concentrations are for that side of the street.

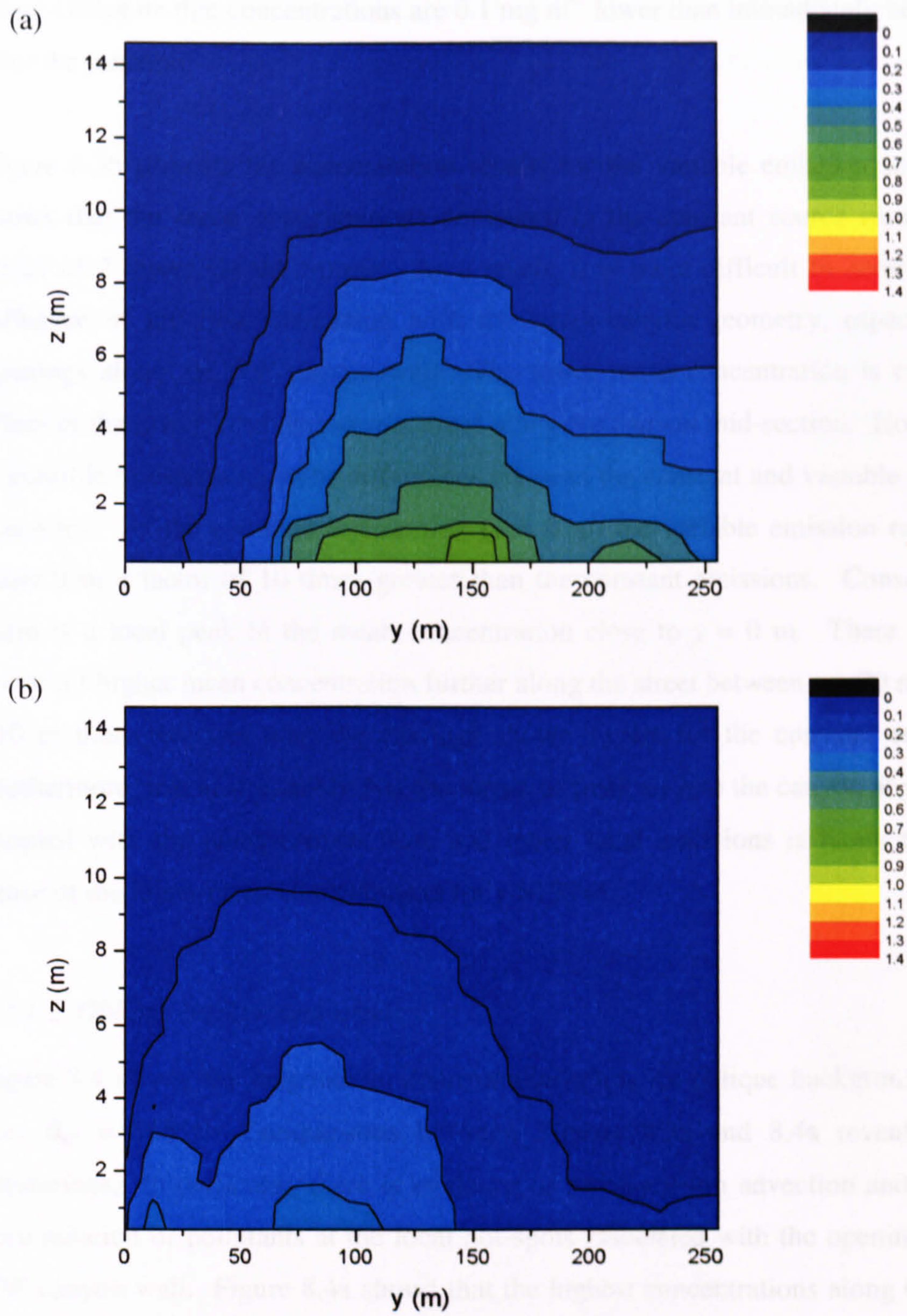


Figure 8.3. Longitudinal cross-section of the mean concentration (mg m$^{-3}$) of the tracer on the SE side of Gillygate during parallel background winds (i.e. $\theta_{ref}$ = 210°) using: (a) the constant and (b) variable emission sources shown in Figure 8.1.

Portland Street (at $y \approx 185$ m) provides a much larger opening and the vector plots revealed that this gap in the canyon wall is more than likely to be an exit for pollutants, as flow entered Portland Street from Gillygate. The width of Portland Street at the junction with Gillygate is ~15 m. The figure shows that at this point

along Gillygate that concentrations are 0.1 mg $m^{-3}$ lower than immediately before and after the junction.

Figure 8.3b presents the concentration results for the variable emission source and shows that the mean concentrations compared to the constant source results are a factor of 2 lower for the former. As a result, it is more difficult to determine the influence of the flow interaction with the street canyon geometry, especially the openings along the NW canyon wall. The lower mean concentration is clearly an effect of the lower local emission sources along the canyon mid-section. However, it is possible to determine some differences between the constant and variable emission scenarios. At the common intersection ($y$ = 0 m) the variable emission rates were more than a factor of 10 times greater than the constant emissions. Consequently, there is a local peak in the mean concentration close to $y$ = 0 m. There is also a 'zone' of higher mean concentration further along the street between $y \approx 70$ m and $y \approx 110$ m that compares with the findings shown earlier for the constant emissions. Furthermore, it is also possible that the influx of fresh air into the canyon at $y \approx 150$ m coupled with the along-canyon flow and lower local emissions is likely to be the cause of the lower mean concentration for $y > 150$ m.

*8.3.1.2. Oblique background winds*

Figure 8.4 shows the longitudinal concentration plots for oblique background winds (i.e. $\theta_{ref}$ = 165°). Comparisons between Figures 8.3a and 8.4a reveal notable similarities. In particular, there is evidence of along-canyon advection and also the accumulation of pollutants at the local hot-spots associated with the openings in the NW canyon wall. Figure 8.4a shows that the highest concentrations along Gillygate were calculated in a 'zone' from $y > 75$ m, which was also calculated for parallel winds. For parallel background winds, the local peak in concentrations at $y \approx 150$ m was associated with across-canyon flow caused by flow entering the canyon through the nearby opening. For oblique background winds there was also found to be a local hot-spot at $y \approx 150$ m, although the mean concentration was higher than for parallel winds. This is likely to be the result of across-canyon advection of pollutants in the reverse flow portion of a recirculating helical flow at street level. During $\theta_{ref}$ = 165°, pollutants are expected to have accumulated on the leeward (SE) side of the canyon

as a result of across-canyon flow recirculation. The additional influence of along-canyon pollutant transport is likely to be the cause of higher mean concentrations calculated at the hot-spot at $y \approx 150$ m.

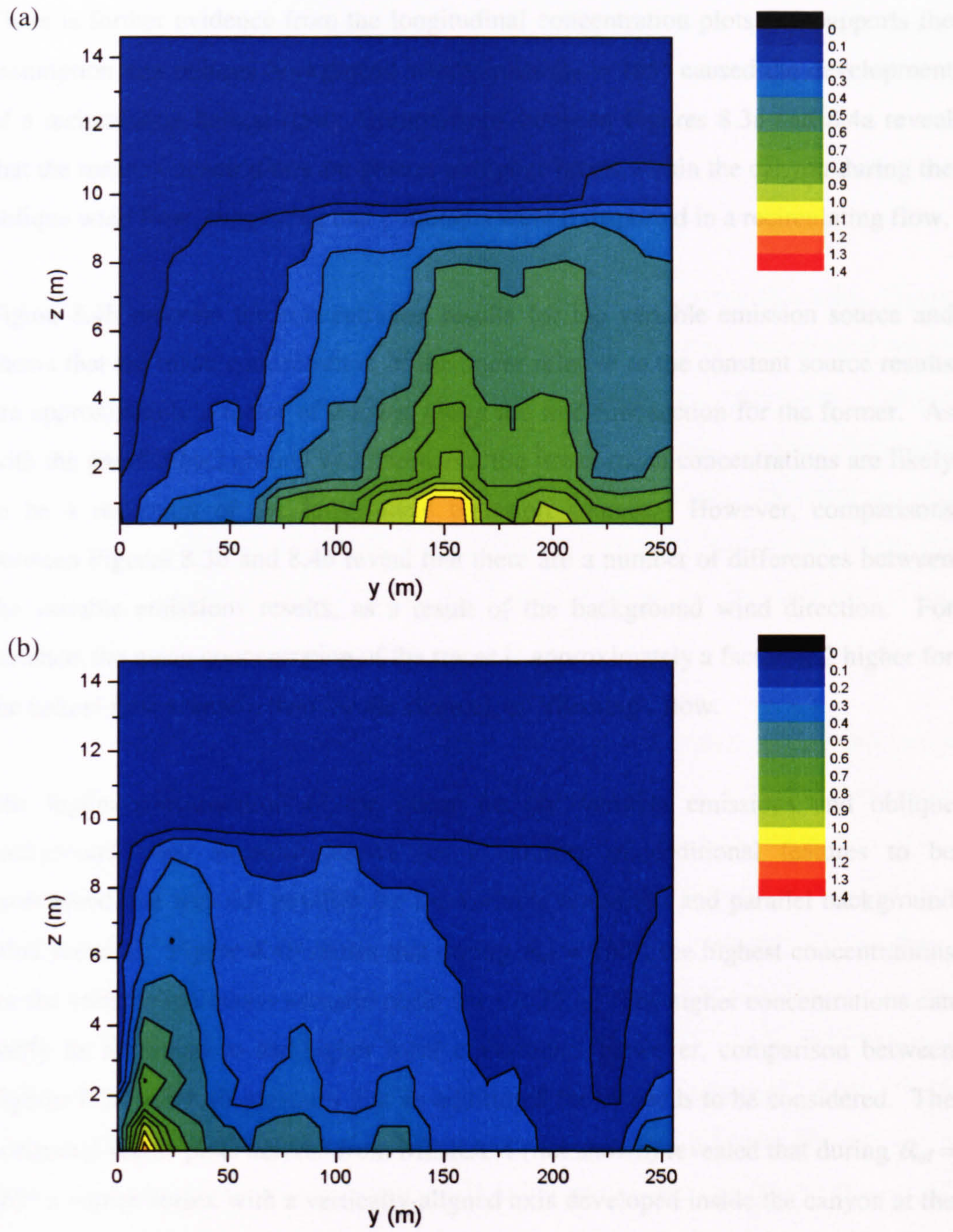


Figure 8.4. Longitudinal cross-section of the mean concentration (mg m$^{-3}$) of the tracer on the leeward (SE) side of Gillygate during oblique background winds (i.e. $\theta_{ref}$ = 165°) using: (a) the constant and (b) variable emission sources shown in Figure 8.1.

Further evidence of a helical flow regime was indicated following the analysis of the vertical flow vectors derived from MISKAM at $y$ = 150 m, which showed the development of a recirculating flow with downdraughts on the windward side of the canyon and updraughts on the leeward side (not shown).

There is further evidence from the longitudinal concentration plots that supports the assumption that oblique background winds from $\theta_{ref}$ = 165° caused the development of a recirculating helical flow. Comparisons between Figures 8.3a and 8.4a reveal that the mean concentrations are greater at higher levels within the canyon during the oblique wind flow, suggesting that pollutants were transported in a recirculating flow.

Figure 8.4b presents the concentration results for the variable emission source and shows that the mean concentration of the tracer relative to the constant source results are approximately a factor of 2 lower along the mid-link section for the former. As with the parallel background wind scenario, the lower mean concentrations are likely to be a reflection of the lower local emission sources. However, comparisons between Figures 8.3b and 8.4b reveal that there are a number of differences between the variable emissions results, as a result of the background wind direction. For instance, the mean concentration of the tracer is approximately a factor of 2 higher for the helical flow scenario than for the channel, or 'flushing', flow.

The higher concentration of the tracer for the variable emissions and oblique background wind scenario allows for a number of additional features to be ascertained that was not possible for the variable emissions and parallel background wind scenario. Figure 8.4b shows that during $\theta_{ref}$ = 165°, the highest concentrations for the variable emissions scenario occur for $y < 25$ m. The higher concentrations can partly be attributed to the higher local emissions. However, comparison between Figures 8.3b and 8.4b indicates that an additional factor needs to be considered. The horizontal vector plots derived from MISKAM (not shown) revealed that during $\theta_{ref}$ = 165° a corner vortex with a vertically-aligned axis developed inside the canyon at the common intersection. This flow recirculation zone was unlikely to have extended significantly beyond 25 m from the street corner. The vertical extent of the corner vortex was also implied in Figure 8.4b, which shows that the recirculating flow was

influential within the entire cavity of the canyon. The across-canyon corner vortex with a vertically-aligned axis was likely to have been responsible for the locally high concentrations on the leeward side of the canyon. The higher concentrations calculated during $\theta_{ref}$ = 165° for variable emissions compared to the constant emission scenario was, however, significantly influenced by the higher local emissions. The hot-spot calculated at $y \approx 250$ m corresponds to the locally higher emission source that is related to the proximity to the traffic-signal controlled junction with Lord Mayor's Walk and Clarence Street.

*8.3.1.3. Perpendicular background winds*

Perpendicular background winds, on the other hand, reveal contrasting results. Figure 8.5 presents the longitudinal concentration plots for perpendicular background winds (i.e. $\theta_{ref}$ = 120°). During these background winds, a single-across canyon recirculating flow with a horizontally-aligned axis is expected to have developed along the mid-link section of the Gillygate canyon uninterrupted by openings (see Chapter 4). As a result, the highest mean concentrations calculated by the model for the constant emission scenario during $\theta_{ref}$ = 120° were on the leeward side of the street canyon.

Figure 8.5a shows the longitudinal cross-section of the calculated concentrations for the constant emission source. Comparisons between Figures 8.5a and 8.4a show many similarities, particularly at the local hot-spot at $y \approx 150$ m and there is evidence of flow recirculation shown by the vertical extent of the concentration distributions. However, there is less evidence of along-canyon pollutant transport during $\theta_{ref}$ = 120°, which is to be expected during the skimming flow regime as it has characteristically poor ventilation conditions. The influence of along-canyon pollutant transport that was reported earlier for oblique background winds ($\theta_{ref}$ = 165°) is likely to be the cause of the higher concentrations at the local hot-spot at $y \approx$ 150 m. Comparisons between Figures 8.5a and 8.3a indicate that during $\theta_{ref}$ = 120° the concentration of the tracer is a factor of 2 greater at $y \approx 150$ m than during $\theta_{ref}$ = 210°, which indicates the significance of the across-canyon flow recirculation. The closeness of the contour lines shown in Figure 8.5a particularly at $y \approx 150$ m reveals the steep decline in the mean concentrations with proximity to the shear layer.

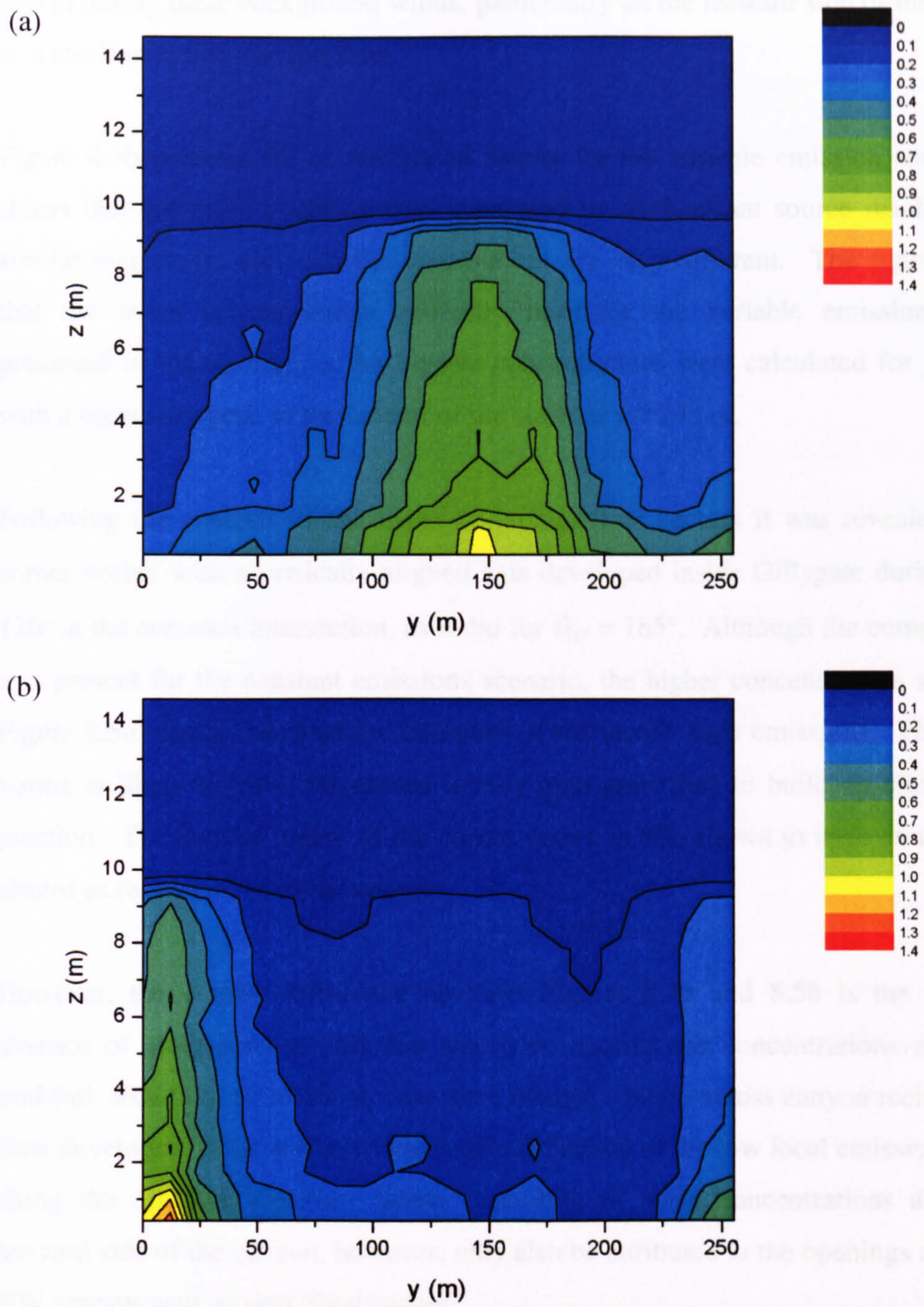


Figure 8.5. Longitudinal cross-section of the mean concentration (mg $m^{-3}$) of the tracer on the leeward (SE) side of Gillygate during perpendicular background winds (i.e. $\theta_{ref}$ = 120°) using: (a) the constant and (b) the variable emission sources shown in Figure 8.1.

At the far end of the canyon ($y \approx 250$ m) the horizontal flow vectors presented in Chapter 4 revealed that a corner vortex with a vertically-aligned axis developed inside Gillygate during $\theta_{ref}$ = 120° at the junction with Lord Mayor's Walk. This corner vortex is likely to be the cause of the higher concentrations that were calculated at $y \approx$

250 m during these background winds, particularly on the leeward side of the canyon as a result of across-canyon flow.

Figure 8.5b presents the concentration results for the variable emission source and shows that the mean concentrations compared to the constant source results are of similar magnitude, although the distributions are very different. The figure shows that the mean concentrations generally resemble the variable emission profile presented in Figure 8.1, i.e. the highest concentrations were calculated for $y$ <25 m with a secondary peak at the far end of the street at $y \approx 250$ m.

Following the analysis of the mean horizontal flow vectors it was revealed that a corner vortex with a vertically-aligned axis developed inside Gillygate during $\theta_{ref}$ = 120° at the common intersection, as it did for $\theta_{ref}$ = 165°. Although the corner vortex was present for the constant emissions scenario, the higher concentrations shown in Figure 8.5b clearly indicates the influence of the locally high emissions. The corner vortex is likely to have caused the locally high emissions to build up close to the junction. The vertical extent of the corner vortex is also shown to have an influence almost as far as the top of the canyon.

However, the notable difference between Figures 8.4b and 8.5b is the apparent absence of along-canyon pollutant transport, causing the concentrations along the mid-link section to be relatively low even though a single-across canyon recirculating flow developed. This is likely to also be a reflection of the low local emission source along the mid-link section. Some variability in mean concentrations along the leeward side of the canyon, however, may also be attributed to the openings along the NW canyon wall, as described earlier.

### 8.3.2. Transverse cross-section

The MISKAM flow and dispersion model was used to calculate the concentrations of the tracer inside the Gillygate street canyon for the two perpendicular background wind directions (i.e. $\theta_{ref} = 120°$ and $\theta_{ref} = 300°$). The model used a constant emission source (i.e. the mean of the variable emission profile shown in Figure 8.1) and the same domain configuration and resolution described in Section 8.2. The contour plots are presented below for completeness.

The contour plots of the calculated mean concentration of the tracer were created using the weighted average gridding method as described in Section 8.2. The contour plots of the concentrations at the experiment G3-G4 cross-section on Gillygate for $\theta_{ref} = 120°$ and $\theta_{ref} = 300°$ are shown in Figure 8.6a and 8.6b, respectively. Figure 8.6a shows that during $\theta_{ref} = 120°$ a single across-canyon recirculating flow (with a horizontally-aligned axis) is likely to have formed inside Gillygate, transporting the tracer towards the leeward side of the canyon. The leeward concentrations are a factor of ~3 greater than the windward concentrations during $\theta_{ref} = 120°$.

Figure 8.6b shows that the worst ventilation conditions were predicted for $\theta_{ref} = 300°$, i.e. when the corner vortices produced across-canyon flow. The across-canyon flow is likely to have transported pollutants towards the leeward side of the canyon, as mentioned in Chapters 4 and 5. It was mentioned that compared to other wind directions the highest concentrations were measured when the sensor was located on the leeward side during perpendicular NW winds, i.e. $\theta_{ref} = 300°$. However, without simultaneous measurements of the in-canyon wind and turbulence fields together with the flow modelling study it would have seemed sensible to have concluded that a single-across canyon vortex typical of skimming flows developed inside the canyon during these background wind conditions.

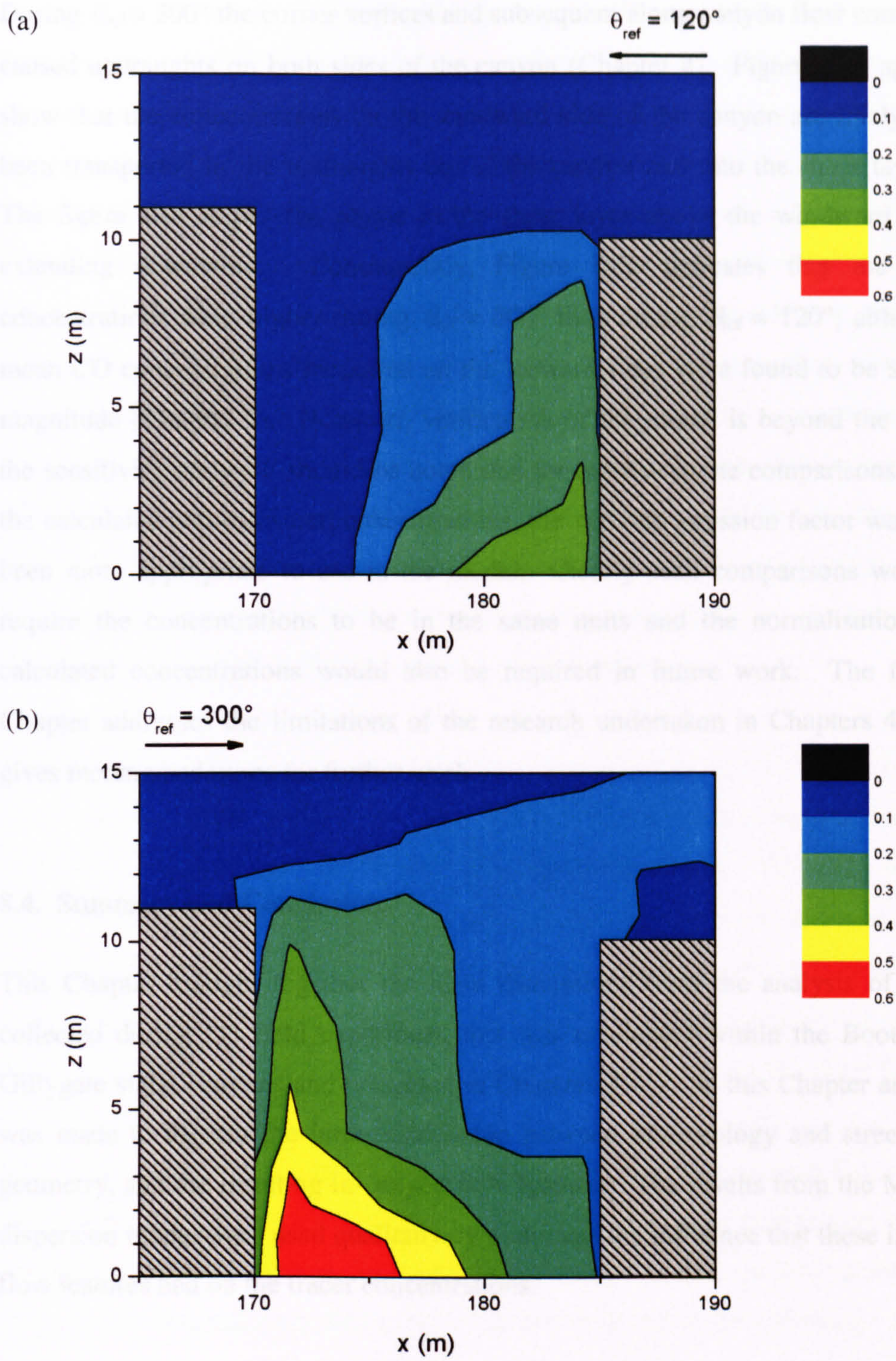


Figure 8.6. Contour plots of the mean concentration (mg m$^{-3}$) of the tracer derived from MISKAM at the transverse G3-G4 cross-section on Gillygate for perpendicular background winds from (a) $\theta_{ref} = 120°$ and (b) $\theta_{ref} = 300°$. Buildings are shown as rectangles with diagonal hatching.

During $\theta_{ref} = 300°$ the corner vortices and subsequent along-canyon flow convergence caused updraughts on both sides of the canyon (Chapter 4). Figure 8.6b appears to show that the concentrations on the windward side of the canyon are likely to have been transported in the updraughts out of the canyon and into the shear layer aloft. The figure also shows the plume in the shear layer above the windward building extending downwind. Consequently, Figure 8.6b indicates that the leeward concentrations were higher during $\theta_{ref} = 300°$ than during $\theta_{ref} = 120°$, although the mean CO concentrations measured on the leeward sides were found to be similar in magnitude (Chapter 5). However, verification of the model is beyond the scope of the sensitivity study. It should be noted that for more accurate comparisons between the calculated and measured concentrations, the variable emission factor would have been more appropriate to use in the model. Clearly such comparisons would also require the concentrations to be in the same units and the normalisation of the calculated concentrations would also be required in future work. The following Chapter addresses the limitations of the research undertaken in Chapters 4 – 8 and gives recommendations for further work.

## 8.4. Summary and Conclusions

This Chapter brought together the main discussions from the analysis of the data collected during the field experiment that was conducted within the Bootham and Gillygate street canyons and presented in Chapters 4 – 7. In this Chapter an attempt was made to discuss the inter-relationship between meteorology and street canyon geometry, and the resulting in-canyon flow features. The results from the MISKAM dispersion model were used qualitatively to discuss the influence that these in-canyon flow features had on the tracer concentrations.

Although qualitative, the analysis provided a useful insight into the importance of using realistic emissions factors in dispersion models. It was shown that the emission factor that represented the actual traffic characteristics at the Bootham-Gillygate intersection was a factor of 10 greater than the mean emission factor. The variable emissions profile was a factor of ~2 lower along the mid-link section of the street canyon. The elevated emissions at the intersection were due to the predominance of

accelerating driving modes within the queuing traffic extending from the stopline. Oblique and parallel background winds produced corner vortices (with vertically-aligned axes) at both ends of Gillygate and across-canyon recirculating flows (with horizontally-aligned axes) along the mid-link section uninterrupted by openings. Consequently, during oblique and perpendicular background winds, the variable emission scenario predicted concentrations at the intersection of ~10 greater than for the constant emission scenario, while concentrations along the mid-link section were a factor of ~2 lower. The higher concentrations at the intersection, however, are likely to have also been partly caused by the development of a corner vortex with vertically-aligned axes, which produced across-canyon flow towards the leeward side of the street. Accelerating driving modes are also responsible for the elevated emission in close proximity to the Gillygate-Lord Mayor's Walk junction. Consequently, the variable emission model results predicted higher concentrations for this section of the link during oblique and parallel winds.

Parallel background winds produced along-canyon flows, which are likely to have flushed the tracer out of the street. As a result, it was difficult to ascertain significant differences between the variable and constant model results. However, the higher local emissions along the mid-link section for the constant emission scenario indicated that flow entered the street through an opening in the canyon wall. This caused across-canyon flow towards the SE side of the canyon, which is likely to have resulted in the development of a local pollution hot-spot at this point along Gillygate.

The results presented in this Chapter helped to bring the findings from the field experiment together, as the influence of meteorology, urban topography and traffic (excluding TPT effects) was discussed. However, the results are only qualitative and further assessment of the model is required, as mentioned in the following Chapter.

# CHAPTER 9

# Limitations of the present study and recommendations for further work

## 9.1. Introduction

This Chapter describes the limitations of the research undertaken in this thesis and recommends areas for future research. The discussion is divided between: street canyon field experiments; modelling studies; conducting measurements of traffic-related pollutant concentrations in addition to CO; and population exposure studies.

### 9.1.1. Street canyon field experiments

#### *9.1.1.1. Weak background winds*

Further research into dispersion of pollutants inside street canyons is expected to focus on topics related to weak background wind conditions. During these conditions, thermal effects due to solar radiation in some European cities may be of greater significance to the stability of the recirculating flow structures that may develop in street canyons compared to those studied in York. In the present experimental study within the Bootham and Gillygate street canyons thermal effects were largely assumed to be negligible during background winds greater than 1.2 m $s^{-1}$ (Chapter 4). Furthermore, it was believed that given the amount of cloud cover over York during the experiment the influence of thermal effects would only have been minimal. Future work should first involve the analysis of the temperature and humidity data collected during the field experiment at various heights on lampposts

G3 and G4 (Chapter 3). Second, further measurements of the heat flux should be conducted inside the canyons during the same time of the year and for different background wind conditions.

Traffic-produced turbulence (TPT) and the micro-scale dispersion around moving vehicles should also be a focus for future work, particularly during weak background winds. In Chapter 6, the value for the dimensionless constants used in the TPT formulations was chosen arbitrarily to equal unity due to the absence of concentration data collected within the traffic layer. Consequently, the final slopes of the linear regression analysis were also arbitrary. Future TPT investigations should include measurements of CO within the layer in which TPT effects are most active, although this will require developing suitable security methods to prevent possible acts of vandalism.

Studies using horizontal arrays of 3-component sonic anemometers at multiple cross-sections of the street canyon where a range of traffic characteristics and driving modes (e.g. idling, accelerating, cruising and decelerating) can be studied would be particularly useful. However, a large longitudinal coverage would only be possible if the anemometers could be secured on street furniture such as lampposts or temporary supports for the entire duration of the experiment as continuous, simultaneous data must be collected. Synchronicity in the measurements of the wind and turbulence fields is necessary in order to conduct the required statistical analysis, particularly of the turbulence parameters (e.g. Smalley *et al.*, 2004b). The problem that will need to be addressed is how to obtain a suitably large data set of synchronous results without the risk of encountering possible acts of vandalism. The results presented in Chapter 6 suggest that locating the instruments well above head height (e.g. at $z/H = 0.3$) in street canyons of similar geometry to Gillygate may measure the wind and turbulence above the layer in which TPT effects are most active. However, this is likely to depend on the traffic characteristics during the investigations. The best option may be to locate the instruments on temporary stands daily at heights within the layer in which TPT effects are most active, while guarding the instruments and conducting manual observations of the traffic speed and flow.

The manual observations of the traffic speed and flow conducted as part of the TPT analysis presented in Chapter 6 also had its limitations and a more accurate method may be preferred for future work. An infra-red speed gun may be a more accurate measure of the actual speed of individual vehicles passing through the survey section. However, it is questionable whether each vehicle in a platoon travelling at speed through the measurement section can be simultaneously counted and classified and also be recorded for its speed. The method of using the computer program to produce a time-stamp each time the front axle of a vehicle entered the 4 m measurement section and when the rear axle left the section, as described in Chapter 6, was at least useful in obtaining traffic flow and speed for each vehicle category. Inaccuracies related to the keystrokes are likely, especially during low traffic flows when the mean vehicle speeds were high. Given that the reaction time is also greatly reduced during these traffic flow conditions there are also likely to be inaccuracies related to the exact times that the vehicle axles crossed the lines marking the entrance and exit to the measurement section. The spatial and temporal error calculations presented in the Appendix indicated that the error was ~10% for the mean vehicle speed of 3.95 m $s^{-1}$ observed during the TPT investigations in the present study. In future studies these inaccuracies may partly be reduced if a larger survey section was used. However, two observers would be required to conduct the observations if this was the case and this is likely to introduce more inaccuracies.

Detector occupancy was used in the present study as an indicator of congestion (Chapter 7). Traffic modelling used in combination with SCOOT detector and queue length data derived from CCTV footage may give a more reliable indication of the total detector occupancy at a given location within the street and should be the subject of further study. The emissions modelling study conducted by Tate (2005) and described in Chapter 8 provided useful insight into the variability of the actual emissions along Gillygate. However, the results from the field experiment presented in Chapters 4 – 7 in addition to the results from the sensitivity study shown in Chapter 8 reveal the importance of understanding the influence of street canyon geometry and meteorology and traffic characteristics. Dispersion models which are able to simulate driving mode and, thus, variable emissions at the micro-scale in tandem with the dispersion characteristics, including TPT effects, at street scale are likely to significantly increase their predictive capabilities. With further studies it may be

possible to assess traffic management plans more accurately and to determine the potential exposure of the population to traffic-related pollutants.

*9.1.1.2. Moderate and strong background winds*

There are also recommendations for future street canyon studies to be conducted during stronger background winds. The work presented in Chapters 4 and 5 revealed that the classic across-canyon recirculating flow (with a horizontally-aligned axis) only occurred inside the Gillygate canyon during perpendicular SE winds, although there was evidence of helical flows during oblique background winds. Perpendicular NW winds produced corner vortices and along-canyon flow convergence. It was mentioned in Chapter 4 that future street canyon studies may wish to include multiple experiment cross-sections with instruments on either side of the canyon. If this was conducted within Gillygate it would allow for further analysis of the wind and turbulence both sides of the flow convergence point and may reveal more about this complex flow feature.

The wind and turbulence data collected inside the Gillygate street canyon and presented in Chapter 4 were averaged over 15-minute periods in order to be consistent with the CO data and the traffic data derived from SCOOT. However, the analysis should be continued by investigating the wind and turbulence parameters over much shorter averaging times. This analysis would complement the work presented in Chapters 4 and 5 and may produce useful insights into the stability of the flow structures (see Dobre *et al.*, 2005).

This work may be combined with the analysis of the mean wind and turbulence data collected in the Gillygate street canyon prior to the main field experiment. It was mentioned in Chapter 3 that a preliminary field study involved using radio modems to acquire the data simultaneously from the in-canyon ultrasonic anemometers. The anemometers used during the trial field experiment are referred by the first letter of their location (i.e. mast or canyon) followed by an identification number. Table 9.1 presents the proportion of clean data and the mean data collection rate for the reference anemometer located on the mast (at 1.8$H$) and the 5 anemometers located in the street canyon. The anemometers located in the canyon were attached to lamppost

G3 or were deployed on stands. The anemometers used in the trial experiment were all set to sample at 5Hz. The proportion of clean data was lowest at the mast (89.5 %). This is likely to have been caused by the greater distance over which the data was sent, causing a greater likelihood of interference (Chapter 3). However, the proportion of clean data for the in-canyon anemometers was relatively high and suggests that radio modems may be used in future field experiments.

Table 9.1. The mean data collection rate for all ultrasonic anemometers deployed during the trial field experiment from 1 April – 9 April 2003 (inclusive). †Note that ID is an abbreviation for *Insufficient Data*.

| anemometer # | location | proportion of clean data† (%) | mean data collection rate* (Hz) |
|---|---|---|---|
| $M_{11}$ | mast | 89.5 | 4.37 |
| $C_{12}$ | canyon | 97.8 | 4.69 |
| $C_{13}$ | canyon | 99.8 | 4.96 |
| $C_{14}$ | canyon | 94.2 | 4.47 |
| $C_{15}$ | canyon | ID | ID |
| $C_{16}$ | canyon | 97.7 | 4.83 |

Although the anemometer data collected during the trial experiment could be used to reveal mean speed and direction data, the number of days with a high percentage of clean data only corresponds to ~10 (Table 9.1). It was for this reason that the field experiment conducted in October and November 2003 used a hardwire data acquisition system, which would operate more reliably for a longer period of time (Chapters 3 and 4).

However, it should be pointed out that the radio modem data acquisition system could potentially be a useful alternative to data loggers in future field experiments if cumbersome data logger boxes were an issue in streets with narrow pavements. In addition to the relatively high proportion of clean data obtained during the trial experiment, post-processing of the data revealed that there were periods of simultaneous and continuous data. There were a total of 5 hours when the data collected simultaneously from anemometers $M_{11}$, $C_{13}$ and $C_{16}$ were continuous (i.e. the data was 100% clean and the mean data collection rate was 5Hz). These time

periods correspond to 1 hour on 06/04/2003 and 4 hours on 08/04/2003. This data potentially allows for the analysis into the spectral characteristics of the turbulence, which would reveal more about the in-canyon flow features that developed inside Gillygate.

Although the field experiments conducted inside the Gillygate street canyon allowed for the interpretation of the in-canyon flow features and their dispersion characteristics, no measurements were undertaken in the more complex Bootham canyon. Further field studies should be conducted to measure the wind and turbulence inside irregular street canyons with, for example, step-up or step-down geometries, and those with side streets or significant changes in the canyon width. This would be useful to determine the dispersion characteristics of the in-canyon flow features. Further investigations in and around other complex urban micro-environments (e.g. intersections) would also provide a greater understanding of micro-scale dispersion conditions (see Dobre *et al.*, 2005). The validation of numerical flow and dispersion models requires thorough validation against experimental data. The accuracy of their predictions is limited by the accuracy of the input data (e.g. emission rates, traffic characteristics, meteorology and street geometry). Therefore, further field experiments are necessary in such complex micro-environments in order to test the accuracy of the street canyon air quality models. This is particularly important when making traffic management decisions and in review and assessment AQM procedures.

### 9.1.2. Street canyon modelling studies

The validation of the MISKAM flow and dispersion model is part of an on-going research programme and was beyond the scope of the study presented in Chapter 8. Smalley *et al.* (2004a) and Dixon *et al.* (2005) provide some useful insight into the performance of the model. However, in further studies it would also be useful to compare the normalised concentrations calculated by MISKAM using the Eulerian dispersion model and a Lagrangian stochastic dispersion model. Smalley *et al.* (2004a) presented results of a modelling study of dispersion inside Gillygate using MISKAM. However, a Lagrangian dispersion model was used in place of the Eulerian dispersion model as it was believed to be more accurate. Concentrations of

pollutants are calculated in the Lagrangian model by tracing the movement of particles as if they were air parcels. The Lagrangian model assumed that for sufficiently small time-steps, the acceleration of particles following the flow is a combination of the 'fading memory' of the velocity of each particle at the previous time-step, the drift correction due to inhomogeneity in the flow field and a random diffusion term (see Smalley *et al.*, 2004a).

On the other hand, the pollution distribution in the Eulerian model is described by changing concentrations at discrete points on a fixed grid (Chapter 3). Comparisons between the normalised concentrations derived from the Eulerian and Lagrangian dispersion models used in MISKAM would be useful for dispersion modellers wishing to use such models in future studies. This would be particularly constructive if the comparison reveals good agreement as the Eulerian dispersion model may be preferred over the more complex Lagrangian model. The complexity of the Lagrangian model has consequences for the time taken to perform each model run. Thus, simpler models often produce quicker results. The findings from the TPT analysis presented in Chapter 6 also revealed that dispersion models may over-predict leeward concentrations during perpendicular background winds given the additional dispersion mechanisms produced by passing traffic. The incorporation of TPT parameterisations into CFD codes such as MISKAM in future work may, therefore, improve their predictive quality, particularly for weak perpendicular background winds.

### 9.1.3. Measurements of other traffic-related pollutant concentrations

The collection of a comprehensive data set reveals a lot about the influences on the variability in concentrations of CO inside street canyons, as was demonstrated in Chapters 4 – 7. Future field experiments should continue to collect meteorological data in addition to pollutant concentration data and traffic characteristics data. Future experiments should, however, include the co-location of instruments used to measure traffic-related pollutants in addition to CO. This would continue the work shown in previous studies (Väkevä *et al.*, 1999; Penttinen *et al.*, 2001; Ketzel *et al.* 2003) into the correlation between other pollutants (e.g. $NO_x$ and particle numbers) and CO close to traffic sources. Additionally, simultaneous measurements of other traffic-

related pollutants such as $NO_x$ and ultrafine particles within street canyons that form part of an AQMA would be useful for making traffic management and urban planning decisions.

Future street canyon experiments should also include measurements of traffic-related pollutants inside the buildings that flank the street. Although measurements of indoor concentrations of CO were conducted during the field experiment using a single streetbox located on a daily basis inside shops along Gillygate the data proved to be unreliable following the QA procedures described in Chapter 3. Further experiments using streetboxes co-located with additional instruments to measure CO and other pollutants (e.g. ultrafine particles) inside such buildings would be useful to investigate the potential exposure of people to traffic-related pollutants. This would be particularly important in street canyons given that across-canyon flows with either vertically- or horizontally-aligned axes would transport pollutants during certain wind conditions. For example, pollutant concentrations measured inside shops and offices located in street canyons that are without air conditioning may be higher in the summer months when windows and doors may be left open.

### 9.1.4. Population exposure studies

In addition to the ambient monitoring of indoor and outdoor concentrations of pollutants in street canyons further work may include conducting exposure studies (see Arnold *et al.*, 2004). Although CO concentrations in ambient air have been monitored for decades in many large urban areas, it is still difficult to assess the overall human exposure to this pollutant adequately. Both the limited number of fixed monitoring sites in each urban area and the extreme temporal and spatial variability of CO concentrations, particularly in street canyons, make exposure assessment problematic. Previous studies of human exposure have shown that the personal CO exposures are poorly correlated with the fixed monitoring site CO concentrations (e.g. Alm *et al.*, 1999). However, some epidemiological studies have reported increased relative risk of daily mortality and morbidity in prevailing urban CO concentrations (Touloumi *et al.*, 1994; Burnett *et al.*, 1998).

Future exposure studies of the type conducted during the DAPPLE field campaign in central London may provide further insight into the variability in the exposure to the population. The principal objective of the exposure assessment conducted during the DAPPLE field campaign was to evaluate the spatial and temporal variability (Arnold *et al.*, 2004). The study also aimed to evaluate the variability within and between different modes of transport and routes of travel at a street canyon intersection and its local environment (see also Kaur *et al.*, 2005).

Personal CO exposures have instead been shown to be strongly affected by the daily activities of individuals, by the time spent in different micro-environments (di Marco *et al.*, *in press*) and by the CO concentrations in various microenvironments where exposed individuals live and work. The present field study in York demonstrated the spatial and temporal variability in the mean concentrations of CO measured within two urban street canyons. The findings of such a study can be used in addition to the collection of information on the activity patterns of the exposed population in order to understand and evaluate the total human exposure. Therefore, future work may also include studies into personal exposure of CO and other traffic-related pollutants. Pollutants such as $NO_x$ and urban particulate matter, particularly $PM_{2.5}$, have potentially greater consequences to human health than CO. Future studies may include conducting exposure studies together with ambient air quality monitoring inside Bootham and Gillygate, or in other street canyons of similar geometry and traffic characteristics.

## 9.2. Summary and Conclusion

Although the research presented in this thesis provided a comprehensive study into the dispersion characteristics inside the Bootham and Gillygate street canyons, further studies are likely to provide even greater understanding. This Chapter described the limitations of the research undertaken in the field experiment and in the qualitative dispersion modelling study. Recommendations for future research were also given. The discussion was divided between: street canyon field experiments; modelling studies; conducting measurements of traffic-related pollutant concentrations in addition to CO; and population exposure studies.

# CHAPTER 10

# Final Remarks and Conclusions

## 10.1. Introduction

In this Chapter final discussions are given into the influence of meteorology, urban topography and traffic on the variability in concentrations of CO measured inside the Bootham and Gillygate street canyons. The Chapter, therefore, aims to consolidate the research findings from the experimental study (Chapters 4 – 7) and the qualitative results from the dispersion modelling study (Chapter 8). In Chapter 2 the influence of meteorology, urban topography and traffic was discussed. Many of the effects are inter-related and so require a holistic approach to discuss their impacts on the in-canyon concentration fields. This Chapter, therefore, describes these effects in such a manner.

## 10.2. The background wind and street canyon geometry

Chapter 4 investigated the influence of the Gillygate street canyon geometry on the mean wind flow and turbulence. The turbulence analysis provided support for the evidence of in-canyon flow structures. The results allowed for a greater understanding of the dynamics and dispersion characteristics of the in-canyon flow features described in Chapter 5. In order to help interpret the results from the field experiment the MISKAM model was used to derive the mean wind flow and turbulence inside the canyon during certain background wind directions.

A single across-canyon recirculating flow (with a horizontally-aligned axis) of the type that develops during skimming flow regimes is likely to have occurred during perpendicular SE winds of speeds greater than 1.2 m $s^{-1}$, even though the roofs on the upwind building were pitched. During these background wind conditions, downdraughts were observed on the windward side of the canyon, while updraughts occurred on the leeward side. The downdraughts were characterised by stronger mean vertical velocities and higher values of TKE than the updraughts. The analysis of the contribution of the variance of the three turbulence components (i.e. $\sigma_u^2$, $\sigma_v^2$ and $\sigma_w^2$) to TKE demonstrated a useful way to investigate the anisotropy of the turbulence. The analysis provided greater insight into the in-canyon flow and dispersion mechanisms.

It was suggested from the analysis of the TKE that the across-canyon recirculating flow is likely to have transported shear turbulence from the upstream roof in downdraughts towards the windward side of the canyon. Turbulence was transported towards the leeward side of the canyon in the street-level reverse flow portion of the recirculating flow. The flow direction at street-level is expected to have been reflected off the windward canyon wall and is likely to have opposed the direction of the mean flow aloft. The turbulence varied with height and proximity to mid-canyon height. The loss of turbulent energy on the leeward side of the canyon relative to the windward side is likely to have been a result of the transport of turbulence in the mean flow. The proportion of the turbulence measured at the mast relative to the turbulence measured on the leeward side of the canyon during these perpendicular background winds was in the order of 0.2.

Three-dimensional (3-D) flows inside street canyons have more complex dispersion characteristics. The importance of understanding 3-D flows was demonstrated in the analysis of the effects of perpendicular NW winds. The horizontal mean flow vectors computed at mid-canyon height by MISKAM revealed that during these background winds, counter-rotating corner vortices with vertically-aligned axes are likely to have developed at the junctions of the side streets off Gillygate. The model predicted that the corner vortex pair was formed as a result of the along-canyon converging flows. Upon convergence, the along-canyon flows formed updraughts on both sides of the

street. During these background winds, the turbulence intensity was found to be greater on the windward side of the canyon than on the leeward side. The flow outputs computed by MISKAM revealed that during these background winds there was an across-canyon flow that opposed the direction of the above-roof winds. The across-canyon flow is likely to have been caused by the counter-rotating corner vortices. Turbulence may have been advected towards the leeward side in the street-level across-canyon, causing lower turbulence intensities on the leeward side of the canyon compared to the windward side. The analysis of the contribution of the turbulence components $\sigma_u^2$, $\sigma_v^2$ and $\sigma_w^2$ to TKE demonstrated that at locations deep inside the canyon on both sides of the street the greatest proportion of turbulence was found in the along-canyon velocity components.

Oblique background winds are thought to have produced in-canyon recirculating helical flows with horizontally-aligned axes. Background winds from 45° either side of the street axis resulted in horizontally channelled flows along the canyon with downdraughts and updraughts on the windward and leeward sides of the canyon, respectively. The helical flows, therefore, were driven by the oblique winds aloft. A helical flow is likely to have transported turbulence predominantly in an along-street flow, but also in a recirculating flow from the windward side of the canyon to the leeward side. Turbulence advection during the across-canyon flow is likely to have caused the turbulence intensities on the leeward side of the canyon to be lower than on the windward side.

### 10.3. In-canyon flow features and resulting in-canyon CO concentrations

The mean concentrations of CO observed in the Bootham and Gillygate street canyons were higher when perpendicular background winds resulted in the sensors being located on the leeward (i.e. upwind) sides of the street (Chapter 5). The presence of across-canyon flow (with a horizontally-aligned axis) and corner vortices (with vertically-aligned axes) are thought to be the cause of approximately two-fold differences in mean CO concentrations between the different sides of both streets.

In the case of perpendicular winds from the SE a single across-canyon recirculating flow with a horizontally-aligned axis is likely to have transported CO in Gillygate at

street level towards the leeward side in the reverse flow portion of the recirculating flow. In contrast, for perpendicular winds from the NW it is likely that corner vortices lead to flow reversal at the canyon floor transporting CO at street level towards the leeward side. With the CO concentration data alone it would have seemed sensible to have concluded that the flow reversal was caused by the development of a classic across-canyon recirculating flow with a horizontally-aligned axis. However, this study investigated the in-canyon flow features simultaneously with the measurements of the CO concentrations and this was found not to be the case.

Comparisons between the concentration roses and the normalised concentrations also revealed the influence of the traffic upwind of the background flow. Comparisons of CO concentrations measured at different heights in Gillygate indicate a degree of vertical mixing, which also gives support to the presence of an across-canyon vortex under certain conditions.

The mean CO concentrations measured in Bootham were presented as a function of the background wind direction and also revealed that concentrations were a factor of two larger on the leeward side of the canyon compared to the windward side. The CO concentration data can produce an indirect method of determining in-canyon flow features. However, it is acknowledged that without simultaneous measurements of the wind flow and turbulence inside the Bootham street canyon a degree of caution is warranted. Given the absence of large openings of the type that Portland Street produced in the Gillygate canyon, it is reasonable to conclude that a single across-canyon recirculating flow with a horizontally-aligned axis is the most likely cause of the higher leeward concentrations.

Comparisons between the mean concentrations observed in the two street canyons indicate lower concentrations in the wider Bootham canyon despite only small differences between the total traffic flows within each street. In addition to the presence of trees, the lower aspect ratio would be expected to cause the development of a weaker across-canyon vortex structure (with a horizontally-aligned axis) during perpendicular background flows as well as providing a larger volume in which emissions may be diluted. Significantly lower concentrations in Bootham due to its

overall geometry, despite only small differences in total traffic flows, raises important issues related to traffic management within such streets (see Section 10.5). Traffic activity and urban and physical topography need to be considered in tandem when developing traffic management and control strategies to manage the spatial distribution of emissions within street canyons better, since the dispersion of emissions is more efficient in some streets than in others.

The study also shows evidence that oblique background winds play a significant part in the dispersion of CO in both street canyons. High CO concentrations either side of the street axis coincide with oblique background winds. During oblique background winds, across-canyon recirculating helical flows (with horizontally-aligned axes) were shown to cause significantly higher concentrations on the leeward side of the canyon than during parallel background winds.

Parallel background winds were found to have limited across-canyon and vertical mixing and are associated with channel flows. As a result lower mean concentrations of CO were measured during parallel background winds than for other background wind directions. This suggests that channel flows with strong along-canyon flow components are likely to have flushed traffic-related pollutants along and ultimately out of the canyon.

Numerical models attempting to represent the dispersion of traffic-related pollutants within urban areas should be capable of describing the in-canyon flow features observed in this study. The field experiment also provided a useful data set for the evaluation of such numerical models in more complex situations than the idealised street canyon case (see Dixon *et. al.*, 2005). Model predictions of the spatial variability of any traffic-related pollutant in a non-regular canyon with adjoining side streets should, thus, incorporate understanding of the complex in-canyon flows that were found to develop under certain background wind conditions. This has special relevance to predicting the relative exposure of people to pollutants not only within street canyons but also indoors, according to the predominant background wind conditions.

## 10.4. The background wind and traffic-produced turbulence

Mechanically produced turbulence inside street canyons is assumed to be composed of two parts: one is dependent upon the background wind speed and direction, causing shear turbulence production during skimming flows; and the other is due to traffic-produced turbulence (TPT). Only during weak perpendicular SE background winds, TPT was found to dominate inside the Gillygate street canyon. Consequently, as the highest concentrations of traffic-related pollutants often occur during these conditions, appropriate modelling of these micro-scale dispersion features is crucial to avoid substantial overestimation of the concentrations. This should form the subject of further study and is discussed in more detail in Chapter 9.

The work presented in Chapter 6 consisted of using the TPT parameterisations of Di Sabatino *et al.* (2003) and Kastner-Klein *et al.* (2003) in order to compare against measured values of turbulence. The measured turbulence parameters included the standard deviation of the mean vertical velocity, $\sigma_w$, and TKE. The correlation coefficients for the relationship between the calculated and measured $\sigma_w$ at 1.1 m ($z/H$ = 0.09) beside lamppost G3 in Gillygate were statistically significant during weak ($U_{ref} \leq 1.2$ m s$^{-1}$) perpendicular SE winds, i.e. when the anemometer was located on the leeward side of the canyon. Even during weak SE winds, moderately strong downdraughts and updraughts were observed on the windward and leeward sides, respectively. Under these background wind conditions a single across-canyon recirculating flow with a horizontally-aligned axis may have developed on average inside Gillygate. The correlation coefficients were higher for the calculations based on intermediate traffic densities. This is perhaps not surprising given the predominance of unstable traffic flow conditions during the period of the TPT investigations, i.e. when the traffic flow switched between periods of free- and congested-flow. Unstable traffic conditions imply that there were likely to have been periods of idling traffic situated beside the anemometer during congested traffic conditions. There are also likely to have been periods of higher mean vehicle speeds during free-flow when accelerating modes were more common.

Although statistically significant, the correlation coefficients were lower than those presented in the work of Kastner-Klein *et al.* (2003). This was also probably due to

the predominance idling, or at least slow cruising, modes. Furthermore, the traffic flow observed by Kastner-Klein *et al.* (2003) in their study was primarily free flowing, during which vehicle speeds are likely to have been higher and TPT effects more active. The poor correlations between the calculated and measured $\sigma_w$ at 3.6 m ($z/H$ = 0.3) suggests a weakening of TPT effects at this height, even during perpendicular SE winds. It is believed that this height is above the traffic layer in which TPT effects were most active in Gillygate. Even during weak background winds, the single across-canyon recirculating flow (with a horizontally-aligned axis) is believed to have transferred TPT towards the leeward side, i.e. in the direction of the anemometer at $z/H = 0.09$. This supports the findings of Vachon *et al.* (2002) and may explain why TPT effects were most noticeable at this height during these background wind conditions.

### 10.5. Traffic characteristics and resulting in-canyon CO concentrations

The SCOOT system was found in Chapter 7 to be a generally reliable method for measuring bi-directional traffic flow and detector occupancy along Gillygate and Bootham. Detector occupancy was used as an indication of the traffic flow characteristics along the inbound traffic flow streams in both streets. The influence of free, unstable and congested traffic conditions on the spatial and temporal variability in CO concentrations in both streets was investigated. Detector occupancy was split into three categories of low, medium, and high occupancy according to its relationship with the traffic flow. High occupancy was used as an indication of congestion and occurred during saturated traffic flows, when increases in occupancy resulted in decreases in traffic flow. High occupancy conditions are expected to be associated with stop-start traffic flows, which are well known to be the cause of elevated emission rates during the accelerating driving mode. Congestion, therefore, has a significant impact on the air quality in both street canyons investigated. If traffic managers were able to maintain traffic flow below the level at which congestion arises, reductions in emission levels could be achieved.

This was further demonstrated in the sensitivity study presented in Chapter 8, which provided a useful insight into the importance of using realistic emissions factors in dispersion models. It was shown that the emission factor that represented the actual

traffic characteristics at the Bootham-Gillygate intersection was a factor of 10 greater than the mean emission factor. The variable emissions profile was a factor of ~2 lower along the mid-link section of the street canyon. The elevated emissions at the intersection were due to the predominance of accelerating driving modes within the queuing traffic extending from the stopline. Oblique and parallel background winds produced corner vortices (with vertically-aligned axes) at both ends of Gillygate and across-canyon recirculating flows (with horizontally-aligned axes) along the mid-link section uninterrupted by openings. Consequently, during oblique and perpendicular background winds, the variable emission scenario predicted that the concentrations at the intersection were a factor of ~10 greater than for the constant emission scenario, while concentrations along the mid-link section were a factor of ~2 lower.

The results from the field experiment revealed that under low traffic flows and low detector occupancies, a strong linear relationship was found between the mean CO concentrations and the traffic flow in each street canyon. This relationship failed under high occupancy (i.e. congested) conditions when the mean CO concentrations were better described by the level of detector occupancy in the street. This suggests that traffic flow may only be used as a sole indicator of emissions under free flowing traffic conditions and that occupancy has a strong influence on emissions under unstable and congested conditions. For the Gillygate inbound detector, which was located close to the G3-G4 experiment cross-section, the detector occupancy gave a reasonable measure of queue length in the street. The Gillygate outbound detector was found to give a less reliable indication of congestion due to it being located at the opposite end of the traffic link.

Sector-averaged concentration roses conditioned on inbound detector occupancy revealed that the highest mean CO concentrations occurred in Gillygate during high inbound detector occupancy conditions. The inter-relationship between background perpendicular wind flows and congested conditions resulted in higher mean leeward CO concentrations than were measured during parallel wind flows. The development of a single across-canyon recirculating flow with a horizontally-aligned axis during perpendicular SE background winds transported CO at street level towards the leeward side in the return-portion of the recirculating flow.

# APPENDIX

## Error Calculations for the Measured Vehicle Speed

The error in the spatial and temporal measurements conducted to derive the speed of each passing vehicle during the TPT investigations (Chapter 6) were calculated as follows. The velocity of the passing vehicle, $v$, is given by:

$$v = \frac{X}{T}, \tag{A.1}$$

where, $X = x_2 - x_1$ and $T = t_2 - t_1$.

Therefore, the error in the spatial and temporal measurements is denoted by $\Delta x_i$ and $\Delta t_i$, respectively.

The relative error in $v$, $\Delta v$, is given by:

$$\frac{\Delta v}{v} = \left[\left(\frac{\Delta X}{X}\right)^2 + \left(\frac{\Delta T}{T}\right)^2\right]^{1/2}. \tag{A.2}$$

Since the error in the spatial ($x_2$ and $x_1$) and temporal ($t_2$ and $t_1$) measurements of are equal, the absolute error for each is given by:

$$(\Delta X)^2 = (\Delta x_1)^2 + (\Delta x_2)^2 = 2(\Delta x_1)^2; \tag{A.3a}$$

$$(\Delta T)^2 = (\Delta t_1)^2 + (\Delta t_2)^2 = 2(\Delta t_1)^2. \tag{A.3b}$$

Substituting Equation (A.3) into Equation (A.2) gives:

$$\frac{\Delta v}{v}=\left[2\left(\frac{\Delta x_1}{X}\right)^2+2\left(\frac{\Delta t_1}{T}\right)^2\right]^{1/2}. \tag{A.4}$$

The temporal error is likely to dominate for larger vehicle speeds. The higher temporal error for greater $v$ can be defined by substituting $T$ in Equation A.4 using Equation A.1 to give:

$$\frac{\Delta v}{v}=\left[2\left(\frac{\Delta x_1}{X}\right)^2+2\left(\frac{v\cdot\Delta t_1}{X}\right)^2\right]^{1/2}. \tag{A.5}$$

The distance over which the vehicle speed was measured, $X$, along Gillygate during the TPT investigations was 4 m (see Chapter 6). Therefore, if $\Delta x_i$ = 0.1 m and $\Delta t_i$ = 0.3 s and if $v$ = 2.53 m s$^{-1}$ the error in $v$ could be derived using:

$$\frac{\Delta v}{v}=\left[2\left(\frac{0.1}{4}\right)^2+2\left(\frac{2.53\cdot 0.3}{4}\right)^2\right]^{1/2}=0.27.$$

Therefore, the error of the measured vehicle speed was ~10%.

The error of the speed measured for each vehicle travelling along the inbound lane along Gillygate during the TPT investigations was calculated using Equation A.5. The maximum value for $v$ was assumed to be 13.41 m s$^{-1}$ (or 30 miles h$^{-1}$). Therefore, data for $v$>13.41 m s$^{-1}$ were excluded from analysis, which corresponded to 2.4% of the total data available. Figure A.1a shows the error in the vehicle speed measured along Gillygate inbound during the TPT investigations as a function of vehicle speed. Figure A.1b presents the frequency distribution of vehicle speed. The mean vehicle speed (and error) was calculated to be 3.95 m s$^{-1}$ ±0.38.

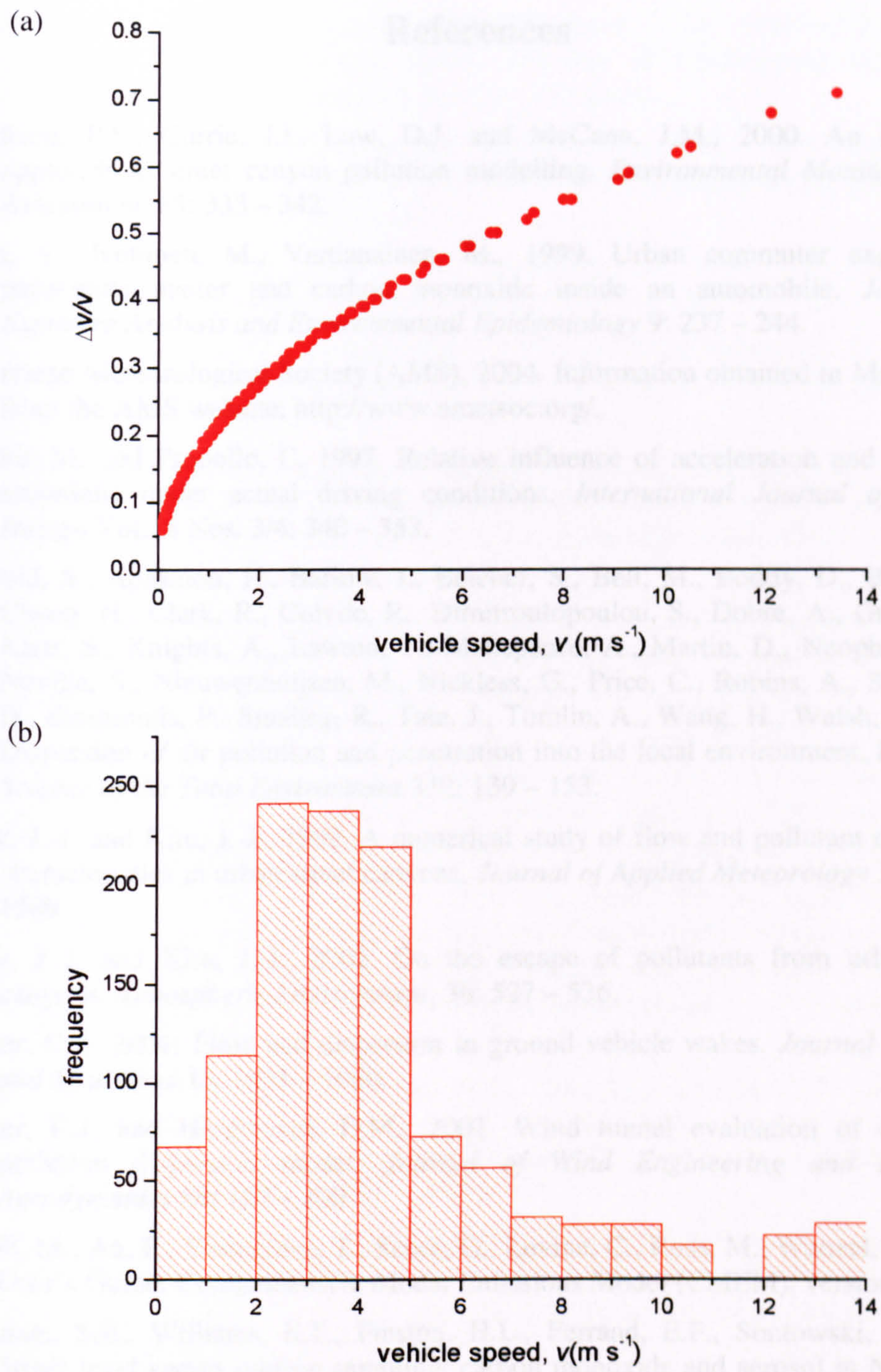


Figure A.1. Plot showing (a) the error in the vehicle speed as a function of vehicle speed and (b) frequency distribution of vehicle speed measured along Gillygate inbound.

# References

Addison, P.S., Currie, J.I., Low, D.J. and McCann, J.M., 2000. An integrated approach to street canyon pollution modelling. *Environmental Monitoring and Assessment*, 65: 333 – 342.

Alm, S., Jantunen, M., Vartianainen, M., 1999. Urban commuter exposure to particulate matter and carbon monoxide inside an automobile. *Journal of Exposure Analysis and Environmental Epidemiology* 9: 237 – 244.

American Meteorological Society (AMS), 2004. Information obtained in March 2004 from the AMS website: http://www.ametsoc.org/.

André, M. and Pronello, C. 1997. Relative influence of acceleration and speed on emissions under actual driving conditions. *International Journal of Vehicle Design* Vol.18 Nos. 3/4: 340 – 353.

Arnold, S., ApSimon, H., Barlow, J., Belcher, S., Bell, M., Boddy, D., Britter, R., Cheng, H., Clark, R., Colvile, R., Dimitroulopoulou, S., Dobre, A., Greally, B., Kaur, S., Knights, A., Lawton, T., Makepeace, A., Martin, D., Neophytou, M., Neville, S., Nieuwenhuijsen, M., Nickless, G., Price, C., Robins, A., Shallcross, D., Simmonds, P., Smalley, R., Tate, J., Tomlin, A., Wang, H., Walsh, P., 2004. Dispersion of air pollution and penetration into the local environment, DAPPLE. *Science of the Total Environment* 332: 139 – 153.

Baik, J.-J. and Kim, J.-J., 1999. A numerical study of flow and pollutant dispersion characteristics in urban street canyons. *Journal of Applied Meteorology* 38, 1576–1589.

Baik, J.-J. and Kim, J.-J., 2002. On the escape of pollutants from urban street canyons. *Atmospheric Environment*, 36: 527 – 536.

Baker, C.J., 2001. Flow and dispersion in ground vehicle wakes. *Journal of Fluids and Structures* 15: 1031 – 1060.

Baker, C.J. and Hargreaves, D.M., 2001. Wind tunnel evaluation of a vehicle pollution dispersion model. *Journal of Wind Engineering and Industrial Aerodynamics* 89: 187 – 200.

Barth, M., An, F., Younglove, T., Scora, G., Levine, C., Ross, M., Wenzel, T., 2001. User's Guide: Comprehensive Modal Emissions Model (CMEM), version 2.02.

Bauman, S.E., Williams, E.T., Finston, H.L., Ferrand, E.F., Sontowski, J., 1982. Street level versus rooftop sampling: carbon monoxide and aerosol in New York City. *Atmospheric Environment*, Vol. 16, No. 10 pp. 2489 – 2496.

Beebe, J., Bell, M.C., and Tate, J., 2003. Analysis of modal emissions – implications for air quality modelling and management. Urban Air Quality: Measurement, Modelling and Management, Proceedings of the 4th International Conference, Prague, Czech Republic.

Berkowicz, R., Palmgren, F., Hertel, O. and Vignati, E., 1996. Using measurements of air pollution in streets for evaluation of urban air quality – meteorological analysis and model calculations. *The Science of the Total Environment* 189/190: 259 – 265.

Berkowicz, R., Hertel, O., Larsen, S.E., Sørensen, N.N., Nielsen, M., 1997a. Modelling traffic pollution in streets. Ministry of Environment and Energy, National Environmental Research Institute, Denmark.

Berkowicz, R., Hertel, O., Sørensen, N.N. and Michelsen, J.A., 1997b. Modelling air pollution from traffic in urban areas. *Institute of Mathematics and its Applications – Conference Series*, 62: 121 – 142.

Berkowicz, R., 2000a. OSPM – a parameterised street pollution model. *Environmental Monitoring and Assessment*, 65: 323 – 331.

Berkowicz, R., 2000b. Human approach to traffic produced turbulence. Contribution to the TRAPOS Working Group on Traffic Produced Turbulence meeting, 25 February, Cambridge.

Berkowicz, R., Ketzel, M., Vachon, G., Louka, P., Rosant, J.M., Mestayer, P.G., Sini, J.F., 2002. Examination of traffic pollution distribution in a street canyon using the Nantes'99 experimental data and comparison with model results. *Water, Air and Soil Pollution: Focus 2*, 311–324.

Boddy, J.W.D., Smalley, R.J., Tate, J.E., Tomlin, A.S., 2003a. The dispersion of a traffic-related pollutant in two urban street canyons. Proceedings of the 12th International Scientific Symposium Transport and Air Pollution, 16 – 18 June, Avignon, France, Vol. 1: 89-96.

Boddy, D., Tomlin, A., Smalley, R., Dixon, N., Tate, J., 2003b. Flow characteristics and the dispersion of a traffic-related pollutant within an urban street canyon. Royal Meteorological Society Conference, 1 – 5 September, UEA, Norwich, U.K.

Boddy, J.W.D., Dixon, N., Smalley, R.J., Tate, J.E., Tomlin, A.S., 2003c. An intercomparison between road-side concentrations of traffic-related pollutants in two urban streets. Proceedings of the 4th International Conference on Urban Air Quality: Measurement, Modelling and Management, 25 – 27 March, Prague, Czech Republic.

Boddy, J.W.D., Smalley, R.J., Dixon, N.S., Tate, J.E., Tomlin, A.S., 2005a. The spatial variability in concentrations of a traffic-related pollutant in two street canyons in York, U.K. – Part I: The influence of background winds. *Atmospheric Environment* 39, Issue 17: 3147 – 3161.

Boddy, J.W.D., Smalley, R.J., Goodman, P.S., Tate, J.E., Bell, M.C., Tomlin, A.S., 2005b. The spatial variability in concentrations of a traffic-related pollutant in two street canyons in York, U.K. – Part II: The influence of traffic, *Atmospheric Environment* 39, Issue 17: 3163 – 3176.

Bootham School, 2003. Aerial photograph supplied by Bootham School, York, UK.

Britter, R.E. and Hanna, S.R., 2003. Flow and dispersion in urban areas. *Annual Review of Fluid Mechanics*, 35: 469 – 496.

Buckland, A.T., 1998. Validation of a street canyon model in two cities. *Environmental Monitoring and Assessment*, 52: 255 – 267.

Burnett, R.T., Cakmak, S., Raizenne, M.E., Stieb, D., Vincent, R., Krewski, D., Brook, J.R., Philips, O., Ozkaynak, H., 1998. The association between ambient carbon monoxide levels and daily mortality in Toronto, Canada. *Journal of Air and Waste Management Association* 48: 689 – 700.

Busch, N.E., 1973. On the mechanics of atmospheric turbulence, In Workshop on Micrometeorology. Editor, D.A. Haugen, *Am. Met. Soc.*, Boston Mass., 1-28.

Carpenter, D.O., 1998. Human health effects of environmental pollutants: new insights. *Environmnetal Monitoring and Assessment* 53: 245 – 258.

Carslaw, D.C. and Beevers, S.D., 2004.Investigating the potential importance of primary $NO_2$ emissions in a street canyon. *Atmospheric Environment* 38, 3585 – 3594.

Census, 2001. Information obtained in April 2005 from the National Statistics website: http://www.neighbourhood.statistics.gov.uk.

Chan, L.Y. and Kwok, W.S., 2000. Vertical dispersion of suspended particulates in urban area of Hong Kong. *Atmospheric Environment* 34, 4403–4412.

Chan, A.T., So, E.S.P. and Samad, S.C., 2001. Strategic guidelines for street canyon geometry to achieve sustainable street air quality. *Atmospheric Environment* 35: 5681 – 5691.

Chan, A.T., Au, W.T.W. and So, E.S.P., 2003. Strategic guidelines for street canyon geometry to achieve sustainable street air quality – Part II: multiple canopies and canyons. *Atmospheric Environment* 37: 2761 – 2772.

Cicolella, A., 1997. Evaluation des risques pour la santé liés au benzène. INERIS, Verneuil, France.

CYC, 2005a. Information obtained in April 2005 from the City of York Council website: http://www.york.gov.uk.

CYC, 2005b. City of York Council - Fourth stage review and assessment of nitrogen dioxide concentrations within the AQMA (http://www.york.gov.uk).

Colvile, R.N., Hutchinson, E.J., Mindell, J.S., Warren, R.F., 2001. The transport sector as a source of air pollution. *Atmospheric Environment* 35, 1537 – 1565.

Croxford, B., Penn, A., Hillier, B., 1996. Spatial distribution of urban pollution: civilising urban traffic. *Science of the Total Environment* 189/190, 3–9.

Croxford, B., and Penn, A., 1998. Siting considerations for urban pollution monitors. *Atmospheric Environment* Vol. 32 No. 6, 1049–1057.

Dabberdt, W.F., Ludwig, F.L., Johnson, W.B, 1973. Validation and applications of an urban diffusion model for vehicular pollutants. *Atmospheric Environment* Vol. 7: 603 – 618.

Davenport, A.G., Grimond, C.S.B., Oke, T.R. and Wieringa, J., 2000. Estimating the roughness of cities and sheltered country. 12th Conference on Applied Climatology, pp. 96 – 99.

Davidson, P.A., 2004. Turbulence – An Introduction for Scientists and Engineers. Oxford University Press, UK.

Dennis, R.L., Byun, D.W., Novak, J.H., Galluppi, K.J., Coats, C.J., Vouk, M.A., 1996. The next generation of integrated air quality modelling: EPA's Models-3. *Atmospheric Environment* 30, 1925–1938.

DePaul, F.T. and Sheih, C.M., 1986. Measurements of wind velocities in a street canyon. *Atmospheric Environment* Vol. 20 No. 3: 455–459.

Derwent, R.G., Middleton, D.R., Field, R.A., Goldstone, M.E., Lester, J.N., Perry, R., 1995. Analysis and interpretation of air quality data from an urban roadside location in central London over the period from July 1991 to July 1992. *Atmospheric Environment* 29, 923–946.

De Vlieger, I., 1997. On-board emmision and fuel consuption measurement campaign on petrol-driven passenger cars. *Atmospheric Environment* 31, 3753 – 3761.

Di Marco, G.S., Kephalopoulos, S., Ruuskanen, J., Jantunen, M., 2005. Personal carbon monoxide exposure in Helsinki, Finland. Submitted to *Atmospheric Environment, in press.*

Dirks, K.N., Johns, M.D., Hay, J.E., Sturman, A.P., 2002. A simple semi-empirical model for predicting missing carbon monoxide concentrations. *Atmospheric Environment*, 36: 5953 – 5959.

Dirks, K.N., Johns, M.D., Hay, J.E., Sturman, A.P., 2003. A semi-empirical model for predicting the effect of changes in traffic flow patterns on carbon monoxide concentrations. *Atmospheric Environment*, 37: 2719 – 2724.

Di Sabatino, S., Kastner-Klein, P., Berkowicz, R., Britter, R.E., Fedorovich, E., 2003. The modelling of turbulence from traffic in urban dispersion models – Part I: theoretical considerations. *Environmental Fluid Mechanics*, 3: 129 – 143.

Dixon, N.S., Boddy, J.W.D., Smalley, R.J., Tomlin, A.S., 2005. Evaluation of a turbulent flow and dispersion model in a typical street canyon in York, U.K. *Atmospheric Environment,* in press, corrected proof.

Djenidi, L., Elavarasan, R., Antonia, R.A. (1999), The turbulent boundary layer over transverse square cavities. *Journal of Fluid Mechanics* 395, 271–294.

Dobre, A., Arnold, S., Smalley, R., Boddy, J.W.D., Barlow, J.F., Tomlin, A.S. and Belcher, S.E., 2005. Flow field measurements in the proximity of an urban intersection in London, UK, *Atmospheric Environment* 39, Issue 26: 4647 – 4657.

EDINA, 2004. Ordnance Survey (OS) maps obtained from the EDINA website: http://edina.ac.uk.

Eichhorn, J., 1996. Validation of a microscale pollutant dispersal model. 21st International Meeting on Air Pollution Modeling and its Application, Baltimore, USA, 6 – 10 November 1995.

Eskridge, R.E. and Hunt, J.C.R., 1979. Highway modelling: Part I – prediction of velocity and turbulence fields in the wakes of vehicles. *Journal of Applied Meteorology*, 18: 387.

Eskridge, R.E. and Thompson, R.S., 1982. Experimental and theoretical study of the wake of a block-shaped vehicle in a shear-free boundary flow. *Atmospheric Environment* Vol. 16 No. 12: 2821 – 2836.

Eskridge, R.E. and Rao, S.T., 1986. Turbulent diffusion behind vehicles: experimentally determined turbulence mixing parameters. *Atmospheric Environment* Vol. 20 No. 5: 851 – 860.

Eskridge, R.E., Petersen, W.B. and Rao, S.T., 1991. Turbulent diffusion behind vehicles: effect of traffic speed on pollutant concentrations. *Journal of the Air and Waste Management Association*, 41: 312 – 317.

Fenger, J., 1999. Urban air quality. *Atmospheric Environment* 33, 4877–4900.

Formula One, 2005. Information on drag coefficients for various vehicle types was obtained from the Formula One website in April 2005: www.f1.com.

Gidhagen, L., Johansson, C., Langner, J., Olivares, G., 2004. Simulation of $NO_x$ and ultrafine particles in a street canyon in Stockholm, Sweden. *Atmospheric Environment*, 38: 2029 – 2044.

Gill Instruments, 2002. Omnidirectional (R3-50) Research Ultrasonic Anemometer – User Manual, 1210-PS-0011, Issue 01.

Goldstein, I.F. and Landovitz, L., 1977a. Analysis of air pollution patterns in New York City – 1. Can one station represent the large metropolitan area? *Atmospheric Environment* 11: 47 – 52.

Goldstein, I.F. and Landovitz, L., 1977b. Analysis of air pollution patterns in New York City – 1. Can one aerometric station represent the area surrounding it? *Atmospheric Environment* 11: 53 – 57.

Grønskei, K.E., 1988. The influence of car speed on dispersion of exhaust gases. *Atmospheric Environment*, Vol. 22 No. 2: 273 – 281.

Hertel, O., de Leeuw, F.A.A.M., Raaschou-Nielsen, O., Jensen, S.S., Gee, D., Herbarth, O., Pryor, S., Palmgren, F., Olsen, E., 2001. Human exposure to outdoor air pollution. *Pure and Applied Chemistry* 73 (6), 933–958.

Heywood, J.B., 1988. Internal Combustion Engine Fundamentals. McGraw-Hill, New York.

Holmén, B.A. and Niemeier, D.A., 1998. Characterizing the effects of driver variability on real-world vehicle emissions. *Transpn. Res.-D*, Vol. 3, No. 2: 117 – 128.

Hong, P., Marcu, B., Browand, F. and Tucker, A., 1998. Drag forces experienced by two full-scale vehicles at close spacing, *SAE Technical Paper* No. 980396.

Hosker, R.P., 1985. Flow around isolated structures and building clusters: a review. *American Society of Heating, Refrigeration and Air Conditioning Engineers Incorporated* 91: 1671 – 1692.

Hoydysh, W.G. and Dabberdt, W.F., 1988. Kinematics and dispersion characteristics of flows in asymmetric street canyons. *Atmospheric Environment* 22, 2677–2689.

Hoydysh, W.G. and Dabberdt, W.F., 1994. Concentration fields at urban intersections: fluid modelling studies. *Atmospheric Environment* 28, 11: 1849–1860.

Hunt P.B., Robertson D.I., Bretherton R.D., Winton R. I., 1991. SCOOT - A traffic responsive method of co-ordinating signals. Laboratory Report 1014, TRRL, Crowthorne, Berkshire.

Hunter L. J., Watson I. D. and Johnson G. T., 1991. Modelling airflow regimes in urban canyons. *Energy Bldng* 15-16, 315 324.

Hunter, L.J, Johnson, G.T. and Watson, I.D., 1992. An investigation of three-dimensional characteristics of flow regimes within the urban canyon. *Atmospheric Environment* 26B No. 4: 425 – 432.

Hussain, M. and Lee, B.E., 1980. An investigation of wind forces on three-dimensional roughness elements in a simulated atmospheric boundary layer flow: Part II Flow over large arrays of identical roughness elements and the effect of frontal and side aspect ratio variations, Report BS 56, Dept. Building Science, University of Sheffield.

Jeong, S.J. and Andrews, M.J., 2002. Application of the $k$-$\varepsilon$ turbulence model to the high Reynolds number skimming flow field of an urban street canyon. *Atmospheric Environment* 36, 1137–1145.

Jicha, M., Pospisil, J. and Katolicky, J., 2000. Dispersion of pollutants in street canyon under traffic induced flow and turbulence. *Environmental Monitoring and Assessment* 65: 343 – 351.

Jicha, M., Katolicky, J. and Pospisil, J., 2002. Dispersion of pollutants in a street canyon and street intersection under traffic induced flow and turbulence using a low Re $k$-$\varepsilon$ model. *International Journal of Environment and Pollution* Vol. 18 No. 2: 160 – 170.

Johnson, G.T. and Hunter, L.J., 1995. A numerical study of dispersion of passive scalars in city canyons, *Boundary-Layer Meteorology* 75, 235-262.

Johnson, G.T. and Hunter, L.J., 1999. Some insights into typical urban canyon airflows. Atmospheric Environment 33, 3991–3999.

Joumard, R. Lamure, C., Lambert, J. and Tripiana, F., 1996. The Science of the Total Environment 189/190: 57 – 67.

Kastner-Klein, P., Fedorovich, E., Plate, E.J., 1997. Gaseous pollutant dispersion around urban-canopy elements: wind tunnel case studies. *International Journal of Environmental Pollution* 8, 727–737.

Kastner-Klein, P., Berkowicz, R., Rastetter, A., Plate, E.J., 1998. Modelling of vehicle induced turbulence in air pollution studies for streets. Proceedings of the 5th International Conference on Harmonisation within Atmospheric Dispersion Modelling, Rhodes, Greece, 18 – 21 May.

Kastner-Klein, P. and Plate, E.J., 1999. Wind-tunnel study of concentration fields in street canyons. *Atmospheric Environment* 33: 3973 – 3979.

Kastner-Klein, P., Fedorovich, E., Rotach, M.W., 1999. Organised and turbulent air motions in a wind tunnel model of a street canyon with and without moving vehicles. Proceedings of the 6th International Conference on Harmonisation within Atmospheric Dispersion Modelling, Rouen, 11 – 14 October.

Kastner-Klein, P., Fedorovich, E., Sini, J.-F., Mestayer, P.G., 2000. Experimental and numerical verification of similarity concept for diffusion of car exhaust gases in urban street canyons. *Environmental Monitoring and Assessment*, 65: 353 – 361.

Kastner-Klein, P., Fedorovich, E., Rotach, M.W., 2001. A wind tunnel study of organised and turbulent air motions in urban street canyons. *Journal of Wind Engineering and Industrial Aerodynamics* 89, 849–861.

Kastner-Klein, P., Fedorovich, E., Ketzel, M., Berkowicz, R., Britter, R., 2003. The modelling of turbulence from traffic in urban dispersion models – Part II: evaluation against laboratory and full-scale concentration measurements in street canyons. *Environmental Fluid Mechanics*, 3: 145 – 172.

Kastner-Klein, P., Berkowicz, R., and Britter, R., 2004. The influence of street architecture on flow and dispersion in street canyons. *Meteorology and Atmospheric Physics* 87, 121 – 131.

Kastner-Klein, P. and Rotach, M.W., 2004. Mean flow and turbulence characteristics in an urban roughness sublayer. *Boundary-Layer Meteorology* 111: 55 – 84.

Kastner-Klein, P., 2005. Personal communication: by email.

Kaur, S., Nieuwenhuijsen, M. and Colvile, R., 2005. Personal exposure of street canyon intersection users to $PM_{2.5}$, ultrafine particle counts and carbon monoxide in central London, UK. *Atmospheric Environment* 39, Issue 20: 3629 – 3641.

Ketzel, M., Berkowicz, R., Müller, W., Lohmeyer, A., 1999. Dependence of street canyon concentrations on above roof wind speed – implications for numerical modelling. Proceedings of the 6th International Conference on Harmonisation within Atmospheric Dispersion Modelling, Rouen, 11 – 14 October.

Ketzel, M., Berkowicz, R. and Lohmeyer, A., 2000. Comparison of numerical street dispersion models with results from wind tunnel and field measurements. *Environmental Monitoring and Assessment*, 65: 363 – 370.

Ketzel, M., Louka, P., Sahm, P., Guilloteau, E., Sini, J.-F., and Moussiopoulos, N., 2002a. Intercomparison of numerical urban dispersion models – Part II: street canyon in Hannover, Germany. *Water, Air and Soil Pollution*: Focus 2: 603 – 613.

Ketzel, M., Berkowicz, R., Müller, W., Lohmeyer, A., 2002b. Dependence of street canyon concentrations on above roof wind speed – implications for numerical modelling. *International Journal of Environment and Pollution* Vol. 17, No. 4: 356 – 366.

Ketzel M., Wåhlin P., Berkowicz R., Palmgrena F., 2003. Particle and trace gas emission factors under urban driving conditions in Copenhagen based on street and roof-level observations. *Atmospheric Environment*, 37: 2735-2749.

Ketzel, M. and Berkowicz, R., 2005. Personal communication: by email.

Kim, J.-J. and Baik, J.-J., 2001. Urban street canyon flows with bottom heating. *Atmospheric Environment* 35: 3395 – 3404.

Kim, J.-J. and Baik, J.-J., 2003. Effects of inflow turbulence intensity on flow and pollutant dispersion in an urban street canyon. *Journal of Wind Engineering and Industrial Aerodynamics* 91: 309 – 329.

Kim, J.-J. and Baik, J.-J., 2004. A numerical study of the effects of ambient wind direction on flow and dispersion in urban street canyons using the RNG $k$-$\varepsilon$ turbulence model. *Atmospheric Environment* 38, 3039–3048.

Kingham, S., Briggs, D., Elliott, P., Fischer, P., Lebret, E., 2000. Spatial variations in the concentrations of traffic related pollutants in indoor and outdoor air in Huddersfield, England. *Atmospheric Environment* 34, 905–916.

Kovar-Panskus, A., Moulinneuf, L., Savory, E., Abdelqari, A., Sini, J.-F., Rosant, J.-F., Robins, A., Toy, N., 2002. A wind tunnel investigation of the influence of solar-induced wall-heating on the flow regime within a simulated urban street canyon. *Water, Air and Soil Pollution Focus* 2: 555 – 571.

Kukkonen, J. Valkonen, E., Walden, J., Koskentalo, T., Karppinen, A., Berkowicz, R. and Kartastenpää, R., 2000. Measurements and modelling of air pollution in a street canyon in Helsinki. *Environmental Monitoring and Assessment*, 65: 371 – 379.

Lamb, R.G., Hogo, H. and Reid, L.E., 1979. A Lagrangian approach to modeling air pollution dispersion: development and testing in vicinity of a roadway, EPA-600/4-79-023.

Lanzini, G. and Tamponi, M., 1995. A microscale Lagrangian particle model for the dispersion of primary pollutants in a street canyon. Sensitivity analysis and first validation trials. *Atmospheric Environment* Vol. 29 No. 23: 3465 – 3475.

Laxen, D.P.H. and Noordally, E., 1987. Nitrogen dioxide distribution in street canyons. *Atmospheric Environment* Vol. 21 No. 9: 1899 – 1903.

Learian, 2002. Streetbox Urban Pollution Monitor – Training Manual. pp. 34.

LeBlanc, D.C., Meyer, M.D., Saunders, F.M., Mulholland, J.A., 1994. Carbon monoxide emissions from road driving: evidence of emissions due to power enrichment. *Transportation Research Record* 1444: 126-134.

Lee, I.Y. and Park, H.M., 1994. Parameterization of the pollutant transport and dispersion in urban street canyons, *Atmospheric Environment* 28, 2343 – 2349.

Leonardi, S., Orlandi, P., Smalley, R.J., Djenidi, L., Antonia, R.A., 2003. Direct numerical simulations of turbulent channel flow with transverse square bars on one wall. *Journal of Fluid Mechanics* 491: 229–238.

Leitl, B.M. and Meroney, R.N., 1997. Car exhaust dispersion in a street canyon: numerical critique of a wind tunnel experiment. *Journal of Wind Engineering and Industrial Aerodynamics* 67/68, 293–304.

Lingard, J.J.N., Tomlin, A.S., Clarke, A.G., Healey, K., Hay, A.W.M., Wild, C.P., Routledge, M.N., 2003. A study of trace metal concentrations of urban airborne particulate matter and its free radical activity. Proceedings of the 12th International Scientific Symposium Transport and Air Pollution, 16 – 18 June, Avignon, France.

Lingard, J.J.N., 2004. Size distributional analysis of urban airborne particulate matter. PhD thesis, Department of Fuel and Energy, University of Leeds.

Longley, I.D., Gallagher, M.W., Dorsey, J.R., Flynn, M., Allan, J.D., Alfarra, M.R., Inglis, D., 2003. A case study of aerosol (4.6 nm $<D_p<10\mu m$) number and mass size distribution measurements in a busy street canyon in Manchester, UK. *Atmospheric Environment* 37, 1563–1571.

Longley, I.D., Gallagher, M.W., Dorsey, J.R., Flynn, M., Barlow, J.F., 2004a. Short-term measurements of airflow and turbulence in two street canyons in Manchester. *Atmospheric Environment* 38, 69–79.

Longley, I.D., Gallagher, M.W., Dorsey, J.R., Flynn, M., 2004b. A case-study of fine particle concentrations and fluxes measured in a busy street canyon in Manchester, U.K. *Atmospheric Environment* 38, 3595–3603.

Longley, I.D., 2004. Corrections to a description of turbulence in a trafficked street canyon in Manchester. *Atmospheric Environment* 38, 4589 – 4592.

Louka, P. Belcher, S.E. and Harrison, R.G., 1998. Modified street canyon flow. *Journal of Wind Engineering and Industrial Aerodynamics*, 74 – 76: pp. 485 – 493.

Louka, P. Belcher, S.E., Harrison, R.G., 2000. Coupling between air flow in streets and the well-developed boundary layer aloft. *Atmospheric Environment* 34, 2613–2621.

Louka, P., Vachon, G., Sini, J.-F., Mestayer, P. G. and Rosant, J.-M., 2002. Thermal effects on the airflow in a street canyon – Nantes'99 experimental results and model simulations. *Water, Air and Soil Pollution: Focus* 2: 351 – 364.

Marsden, G., Bell, M., Reynolds, S., 2001. Towards a real-time microscopic emissions model. *Transportation Research - Part D*: 6, 37 – 60.

Meroney, R.N., Pavageau, M., Rafailidis, S., Schatzmann, M., 1996. Study of line source characteristics for 2-D physical modelling of pollutant dispersion in street canyons. Journal of Wind Engineering and Industrial Aerodynamics 62, 37 – 56.

Midenet, S., Boillot, F. and Pierrelée, J.-C., 2004. Signalized intersection with real-time adaptive control: on-field assessment of $CO_2$ and pollutant emission reduction. *Transportation Research – Part D*, 9: 29 – 47.

Morris, R.D., Naumova, E.N., Munasinghe, R.L., 1995. Background air pollution and hospitalisation for congestive heart failure among elderly people in seven large US cities. *American Journal of Public Health* 85, 1361.

Mukherjee, P. and Viswanathan, S., 2001. Carbon monoxide modelling from transportation sources. Chemosphere, 45: 1071 – 1083.

NAEI, 2004. National Atmospheric Emissions Inventory website: http://www.aeat.com/netcen/airqual/naei/roadproj/contents.html.

Nakamura, Y., and Oke, T.R., 1988. Wind, temperature and stability conditions in an E-W oriented urban canyon. *Atmospheric Environment* 22, 2691–2700.

Namdeo, A.K., Colls, J.J., Baker, C.J., 1999. Dispersion and resuspension of fine and coarse particulates in an urban street canyon. *Science of the Total Environment* 235: 3–13.

National Air Quality Information Archive, 2005. Information obtained from the website managed by NETCEN: http://www.airquality.co.uk.

Nicholson, S.E., 1975. A pollution model for street-level air. *Atmospheric Environment* 9, 19–31.

Nielsen, M., 2000. Turbulent ventilation of a street canyon. *Environmental Monitoring and Assessment*, 65: 389 – 396.

Nikolaou, K., 1999. Emissions reduction of high and low polluting new technology vehicles equipped with a $CeO_2$ catalytic system. *The Science of the Total Environment* 235: 71 – 76.

Oke, T.R., 1987. Boundary Layer Climates, 2nd Edition, Methuen UK.

Oke, T.R., 1988. Street design and urban canopy layer climate. *Energy and Buildings* 11: 103 – 113.

Palmgren, F., Berkowicz, R., Hertel, O., Vignati, E., 1996. Effects of reduction of $NO_x$ on the $NO_2$ levels in urban streets. *Science of the Total Environment* 189/190, 409–415.

Park, S.-K., Kim, S.-D., Lee, H., 2004. Dispersion characteristics of vehicle emission in an urban street canyon. *Science of the Total Environment* 323, 263–271.

Pavageau, M., Rafailidis, S., Schatzmann, M., 1996. A comprehensive experimental databank for the verification of urban car emission dispersion models. Fourth Workshop on Harmonisation within Atmospheric Dispersion Modelling for Regulatory Purposes, Ostende, Vol. 2, pp. 443–450.

Pavageau, M. and Schatzmann, M., 1999. Wind tunnel measurements of concentration fluctuations in an urban street canyon, *Atmospheric Environment* 33, 3961 – 3971.

Pearce, W. and Baker, C.J., 1997. Wind-tunnel investigation of the effect of vehicle motion on dispersion in urban canyons. *Journal of Wind Engineering and Industrial Aerodynamics*, 69 – 71: 915 – 926.

Pegg, R.E. and Ramsden, A.W., 1966. Towards clear diesel exhausts. Proceedings of the International Clean Air Congress Part 1: 154 – 156.

Penttinen, P. Timonen, K.L., Tiittanen, P., Mirme, A., Ruuskanen, J., Pekkanen, J., 2001. Ultrafine particles in urban air and respiratory health among adult asthmatics. *European Respiration Journal* 17, 428 – 435.

Pfeffer, H.U., Friesel, J., Elbers, G., Beier, R., Ellermann, K., 1995. Air pollution monitoring in street canyons in North Rhine-Westphalia, Germany. *Science of the Total Environment* 169: 7–15.

Plate, E.J., 1999. Methods of investigating urban wind fields – physical models. *Atmospheric Environment* 33: 3981 – 3989.

Piringer, M., Grimmond, C.S.B., Joffre, S.M., Mestayer, P., Middleton, D.R., Rotach, M.W., Baklanov, A., De Ridder, K., Ferreira, J., Guilloteau, E., Karppinen, A., Martilli, A., Masson, V., Tombrou, M., 2002. Investigating the surface energy balance in urban areas – recent advances and future needs. *Water, Air and Soil Pollution: Focus* 2: 1 – 16.

Qin, Y. and Kot, S.C., 1993. Dispersion of vehicular emission in street canyons, Guangzhou City, South China (P.R.C.). *Atmospheric Environment* 27B, 283–291.

Rafailidis, S., 1997. Influence of building area density and roof shape on the wind characteristics above a town. *Boundary-Layer Meteorology* 85, 255–271.

Rafailidis, S., 2000. Near-field geometryeffects on urban street canyon measurements for model validation. *International Journal of Environment and Pollution* 14 (1–6), 538–546.

Rao, S.T., Sistla, G., Eskridge, R.E. and Petersen, W.B., 1986. Turbulent diffusion behind vehicles: evaluation of roadway models. Atmospheric Environment Vol. 20 No. 6: 1095 – 1103.

Rapone, M., Della Ragione, L., Prati, M.V., Violetti, N., 2000. Driving behaviour and emission results for a small size gasoline car in urban operation. Society of Automotive Engineers, Inc. SAE Technical Paper Series No. 2000-01-2960.

Riain, C.M.N., Fisher, B., Martin, C.J. and Littler, J., 1998. Flow field and pollution dispersion in a central London street. *Environmental Monitoring and Assessment* 52: 299 – 314.

Robins, A. and MacDonald, R., 2001. Review of flow and dispersion in the vicinity of groups of buildings: Annex B, University of Surrey.

Robins, A., Savory, E., Scaperdas, A. and Grigoriadis, D., 2002. Spatial variability and source receptor relations at a street intersection. *Water, Air and Soil Pollution*: Focus 2: 381 – 393.

Robins, A., 2003. Wind tunnel dispersion modelling some recent and not so recent achievements. *Journal of Wind Engineering and Industrial Aerodynamics* 91: 1777 – 1790.

Rodi, W., 1995. Introduction to the numerical simulation approaches in wind engineering, In: Wind Climate in Cities, Editors, J.E. Cermak *et al.*, Kluwer Academic Publishers, 633-647.

Ropkins, K., Ames, D.L. and Colvile, R.N., 2000. Final report: evaluation of sensors to provide real-time air quality information for UTMC systems.

Rotach, M.W., 1993. Turbulence close to a rough urban surface – Part 1: Reynolds Stress. *Boundary-Layer Meteorology* 65: 1 – 28.

Rotach, M.W., 1995. Profiles of turbulence statistics in and above an urban street canyon. *Atmospheric Environment*, Vol. 29, No. 13: 1473–1486.

Sahm, P., Louka, P., Ketzel, M., Guilloteau, E. and Sini, J.-F., 2002. Intercomparison of numerical urban dispersion models – Part I: street canyons and single building configurations. *Water, Air and Soil Pollution*: Focus 2: 587 – 601.

Schatzmann, M., Leitl, B. and Liedtke, J., 2000. Dispersion in urban environments: comparison of field measurements with wind tunnel results. *Environmental Monitoring and Assessment* 65: 249–257.

Schorling, M., 1994. Computation of ambient concentration distributions due to vehicle emissions, *Science of the Total Environment* 146/147: 445-450.

SCOOT, 2003. Information obtained from the SCOOT Urban Traffic Control (UTC) website: http://www.scoot-utc.com/.

Seshari, P. and Harrison, R., 1993. Workzone mobile source emission prediction. Research Report, SWUTC/92/60021-3, Centre for Transportation Research, University of Texas, Austin, USA.

Sharma P. and Khare, M., 2001. Modelling of vehicular exhausts – a review. *Transportation Research Part D*, 6: 179 – 198.

Sini, J.F., Anquetin, S., Mestayer, P.G., 1996. Pollutant dispersion and thermal effects in urban street canyons. *Atmospheric Environment* 30, 2659–2677.

Skibin, D., 1984. A simple method for determining the standard deviation of wind direction. *Journal of Atmospheric and Oceanic Technology* 1, 101-102.

Smalley, R.J., Dixon, N.S., Boddy, J.W.D., Tate, J.E. and Tomlin, A.S., 2004a. The influence of 3-dimensional flow structures on the dispersion of a traffic related pollutant in a complex urban street canyon. 13th Transport and Air Pollution Conference, Boulder, Colorado, USA.

Smalley, R.J., Boddy, J.W.D., Dixon, N.S., and Tomlin, A.S., 2004b. Anisotripic Reynolds stress invariants in an urban street canyon. 13th Transport and Air Pollution Conference, Boulder, Colorado, USA.

Spadaro, J.V. and Rabl, A., 2001. Damage costs due to automotive air pollution and the influence of street canyons. *Atmospheric Environment* 35, 4763 – 4775.

Sport Rider, 2005. Information on drag coefficients for various vehicle types was obtained from the Sport Rider website in April 2005: www.sportrider.com.

Stern, R. and Yamartino, R.J., 2001. Development and first evaluation of micro-calgrid: a 3-D, urban canopy-scale photochemical model. *Atmospheric Environment*, 35 Supplement No. 1, S149 – S161.

Stull, R.B., 1988. An Introduction to Boundary Layer Meteorology. Kluwer Academic Publishers, The Netherlands.

Stull, R.B., 2000. Meteorology for Scientists and Engineers, Second Edition. Brooks/Cole, Pacific Grove, CA, USA.

Tate, J.E., 2005. A Study of Vehicular Emissions and Ambient Air Quality at the Local-scale. PhD thesis, Institute for Transport Studies, University of Leeds.

Tate, J., Bell, M.C., Tomlin, A.S., Smalley, R.J. and Boddy, J.W.D., 2005a. An experimental investigation of the variability in traffic characteristics and air pollutant concentrations at the local scale. Urban Air Quality: Measurement, Modelling and Management, Proceedings of the 5th International Conference.

Tate, J.E., Bell, M.C. and Liu, R., 2005b. The Application of an Integrated Traffic Microsimulation and Instantaneous Emission Model to study the Temporal and Spatial Variations in Vehicular Emissions at the Local-scale. 14th International Conference, Transport and Air Pollution, Graz, 2005, Heft 85/1, pp.138 – 147.

Theurer, W., 1999. Typical building arrangements for urban air pollution modelling. *Atmospheric Environment* 33, 4057–4066.

Thompson, R.S., and Eskridge, R.E., 1987. Turbulent diffusion behind vehicles: experimentally determined influence of vortex pair in vehicle wake. *Atmospheric Environment*, Vol. 21, No. 10: 2091–2097.

Touloumi, G., Pocock, S.J., Katsouyami, K., Trichopoulos, D., 1994. Short term effects of air pollution on daily mortality in Athens: a time series analysis. *International Journal of Epidemiology* 23: 957 – 967.

Uehara, K., Murakami, S., Oikawa, S., Wakamatsu, S., 2000. Wind tunnel experiments on how thermal stratification affects flow in and above urban street canyons. *Atmospheric Environment* 34: 1553–1562.

Vachon, G., Rosant, J.-M., Mestayer, P.G., Sini, J.-F., 1999. Measurements of dynamic and thermal field in a street canyon – URBCAP Nantes99. Proceedings of the 6th International Conference on Harmonisation within Atmospheric Dispersion Modelling for Regulatory Purposes, 11 – 14 October, Rouen, France, Paper No. 124.

Vachon, G., Rosant, J.-M., Mestayer, P.G., Louka, P., Sini, J.-F., Delaunay, D., Antoine, M.-J., Ducroz, F., Garreau, J., Griffiths, R., Jones, C., Lorin, Y., Molle, F., Peneau, J-P., Tetard, Y., Violleau, M., 2000. Experimental investigation of pollutant dispersion within a street in low wind conditions – the experiment Nantes'99. Proceedings of the 9th International Scientific Symposium Transport and Air Pollution, 5 – 8 June, Avignon, France.

Vachon, G., Louka, P., Rosant, J.-M., Mestayer, P.G., Sini, J.-F., 2002. Measurements of traffic-induced turbulence within a street canyon during the Nantes '99 experiment. *Water, Air and Soil Pollution: Focus*, 2: 127 – 140.

Väkevä, M. Hämeri, K., Kulmala, M., Lahdes, R., Ruuskanen, J., Laitinen, T., 1999. Street level versus rooftop concentrations of submicron aerosol particles and gaseous pollutants in an urban street canyon. Atmospheric Environment 33, 1385–1397.

Vardoulakis, S., Gonzalez-Flesca, N., and Fisher, B.E.A., 2002. Assessment of traffic-related air pollution in two street canyons in Paris: implications for exposure studies. *Atmospheric Environment* 36: 1025 – 1039.

Vardoulakis, S., Fisher, B.E.A., Pericleous, K. and Gonzalez-Flesca, N., 2003. Modelling air quality in street canyons – a review. *Atmospheric Environment* 37: 155 – 182.

Venegas, L.E. and Mazzeo, N.A., 2000. Carbon monoxide concentration in a street canyon of Buenos Aires city (Argentina). *Environmental Monitoring and Assessment* 65, 417–424.

Vignati, E., Berkowicz, R., Hertel, O., 1996. Comparison of air quality in streets of Copenhagen and Milan, in view of the climatological conditions. *Science of the Total Environment* 189/190, 467–473.

Waters, M.H.L., 1992. Road vehicle fuel economy: state-of-the-art review, 3, HMSO, London.

Watkins, S., Saunders, J.W., Hoffmann, P.H., 1995. Turbulence experienced by moving vehicles. Part I Introduction and turbulence intensity. *Journal of Wind Engineering and Industrial Aerodynamics*, 57: 1 – 17.

World Health Organisation (WHO), 2003. Health aspects of air pollution with particulate matter, ozone and nitrogen dioxide. Report on a WHO Working Group, Bonn, Germany, 13 – 15 January, pp. 95.

Xia, J. and Leung, D.Y.C., 2001a. Pollutant dispersion in urban street canopies. *Atmospheric Environment*, 35: 2033 – 2043.

Xia, J. and Leung, D.Y.C., 2001b. Some interesting phenomena on air pollutant dispersion in urban street canyons. Proceedings of the 7th International Conference on Harmonisation within Atmospheric Dispersion Modelling for Regulatory Purposes.

Xie, S., Zhang, Y., Qi, L. and Tang, X., 2003. Spatial distribution of traffic-related pollutant concentrations in street canyons. *Atmospheric Environment* 37: 3213 – 3224.

Xie, X., Huang, Z., Wang, J. and Xie, Z., 2005. The impact of solar radiation and street layout on pollutant dispersion in street canyon. *Building and Environment* 40: 201 – 212.

Yamartino, R.J. and Wiegand, G., 1986. Development and evaluation of simple models for the flow, turbulence and pollutant concentration fields within an urban street canyon. *Atmospheric Environment*, Vol. 20, No. 11: 2137 – 2156.